Physics of Atomic Nuclei, Vol. 63, No. 12, 2000, pp. 2051–2066. Translated from Yadernaya Fizika, Vol. 63, No. 12, 2000, pp. 2147–2162.

REVIEW

Nuclear-Physics Aspects of Controlled Thermonuclear Fusion: Analysis of Promising Fuels and Gamma-Ray Diagnostics of Hot Plasma

V. T. Voronchev[1)] and V. I. Kukulin

Institute of Nuclear Physics, Moscow State University, Vorob'evy gory, Moscow, 119899 Russia

Received February 15, 2000

Abstract—A brief survey of nuclear-physics aspects of the problems of controlled thermonuclear fusion is given. Attention is paid primarily to choosing and analyzing an optimal composition of a nuclear fuel, reliably extrapolating the cross sections for nuclear reactions to the region of low energies, and exploring gamma-ray methods (as a matter of fact, very promising methods indeed) for diagnostics of hot plasmas (three aspects that are often thought to be the most important ones). In particular, a comparative nuclear-physics analysis of hydrogen, DT, and DD thermonuclear fuels and of their alternatives in the form of D^3He, D^6Li, DT^6Li, H^6Li, $H^{11}B$, and H^9Be is performed. Their advantages and disadvantages are highlighted; a spin-polarized fuel is considered; and the current status of nuclear data on the processes of interest is analyzed. A procedure for determining cross sections for nuclear reactions in the deep-subbarrier region is discussed. By considering the example of low-energy D + ^{6}Li interactions, it is shown that, at ion temperatures below 100 keV, the inclusion of nuclear-structure factors leads to an additional enhancement of the rate parameters $\langle\sigma v\rangle$ for the (d, pt) and (d, $n\tau$) channels by 10–40%. The possibility of using nuclear reactions that lead to photon emission as a means for determining the ion temperature of a thermonuclear plasma is discussed. © *2000 MAIK "Nauka/Interperiodica".*

1. INTRODUCTION

Among important applications of nuclear physics, that which is dealing with the problem of controlled thermonuclear fusion stands out in many respects. One of the main problems to be solved here is to evolve and implement a large-scale thermonuclear reactor that would represent an economical source of energy and which would be safer than fission reactors. Searches for an optimum composition of a nuclear fuel have so far been one of the main lines in such investigations. Both one- and multicomponent mixtures of light elements have been considered. Despite many years of efforts in these realms, preference has not yet been given to a unique fuel cycle. Of factors that are of prime importance for this, we would like to mention knowledge of the properties of light isotopes and the possibilities for their production, understanding of mechanisms that govern nuclear reactions between light nuclei, and precise information about cross sections for such processes.

The present survey, which is based in part on previous studies of the present authors, is devoted to nuclear-physics aspects of controlled thermonuclear fusion—namely, to the role of nuclear-structure factors in reactions between light nuclei, to radiative-capture processes of the $A(B, \gamma)C$ type in the deep-subbarrier region of energies, and to the possibilities of using such reactions for extracting required information about the dynamics of hot plasmas. In our opinion, attention given to these important problems in review articles on controlled thermonuclear fusion and in original investigations into the allied range of problems is insufficient. It is shown in the present study, however, that such issues are of nonnegligible importance for further advancements in the problem of controlled thermonuclear fusion and that they may even become crucial for solving some problems. We hope that the present survey, which is pioneering in these realms, will fill, at least partly, the gap between a vast body of currently available information about the structure of light nuclei and specific investigations into the problem of controlled thermonuclear fusion.

Bearing in mind the technological potential of the first experimental facilities of the tokamac type for heating and confining hot plasmas, researchers had focused, for a long time, on two types of hydrogen thermonuclear fuel, deuterium (DD) and deuterium–tritium (DT) fuels [1]. It should be recalled that large cross sections for the process $T(d, n)^4He$ at low energies ($E \leq$ 100 keV) and a considerable energy release in the reaction, Q = 17.6 MeV, seemed to give sufficient ground to hope for experimentally implementing the ignition of the reaction as early as the 1970s at plasma temperatures of a few keV, which were thought to be quite realistic at that time. These were the reasons why, despite serious drawbacks of a DT mixture—a low efficiency of the transformation of nuclear energy into electric

[1)] Institute of Crystallography, Russian Academy of Sciences, Leninskiĭ pr. 59, Moscow, 117333 Russia.

energy because of the generation of an extremely intense neutron radiation in the reaction being discussed and a need for producing and employing radioactive tritium, which is extremely hazardous—it was justifiably thought that there was no serious alternatives to DT fuels.

However, radical improvements of tokamacs, the advent of a new fusion reactor within the ITER international project, and a vigorous development of different reactor schemes (for example, open-type devices and a configuration featuring a so-called inverted magnetic field), as well as the emergence of the concept of inertial thermonuclear fusion, created preconditions for considering initial plasma heating to a few tens of keV followed by the working range of burning temperatures reaching a few hundred keV. This gave impetus to studying alternative, non-hydrogen, fuels like D^3He, H^6Li, D^6Li, and $H^{11}B$, which require higher ignition temperatures (in relation to D + T fusion), but which possess a number of important ecological and economical advantages. For example, burning in the H + ^{6}Li and H + ^{11}B systems generates neutron fluxes and hazardous radionuclides only in negligible amounts. At the same time, such fuels are not expensive, since they consist of stable light-element isotopes abundant on the Earth.

At present, however, physical processes in the majority of non-hydrogen fuels have received much less study than analogous processes in DT or DD cycles. Even the first investigations revealed that a theoretical analysis of some alternative cycles is very involved because burning in hot plasmas is a highly ramified process involving a few tens of exothermic reactions proceeding simultaneously with commensurate probabilities. This type of process dynamics is markedly different from the character of the burning of a DT fuel, where the channel $T(d, n)^4He$ dominates over all possible reactions.

In studying thermonuclear fuels that show considerable promise, it is necessary to take into account two types of processes. Of these, the first is associated with first-generation reactions representing direct channels of the burning of a nuclear fuel in reactions between light elements originally present in the reactor region. As a rule, such processes provide a major part of the energy released in the fusion process. There are also, however, secondary phenomena that accompany the burning of any fuel and which play a very important role in some cases. We will break up secondary processes into two classes that differ in the physics underlying the phenomena that occur.

In the first class, we include processes that do not lead directly to nuclear transformations, but which appear to be a basic mechanism of fuel self-heating. Above all, this is the elastic Coulomb scattering of fast charged particles, products of nuclear reactions, on plasma ions and electrons. In addition to Coulomb scattering, there can occur the nuclear elastic scattering of fast particles, both charged particles and neutrons, on the ions of the fuel. The latter process proceeds at small values of the impact parameter, but it involves high momentum transfers. In the literature, the above elastic-scattering processes are referred to as CES (Coulomb elastic scattering) and NES (nuclear elastic scattering) processes. Either leads to the heating of the plasma and to an increase in its reactivity. Ion scattering is a dominant mechanism of heating, but the role of neutron scattering is nonnegligible in severely compressed laser targets characterized by large values of the parameter ρR, where ρ and R are, respectively, the density and the radius of the target.

The second class of secondary phenomena accompanying the burning of a thermonuclear fuel includes those that lead to nuclear transformations. These are, in particular, catalytic nuclear reactions between fuel ions and active isotopes produced in the plasma. Catalytic processes proceed on both thermalized and nonthermalized nuclei. In the latter case, the processes being discussed are in-flight reactions—that is, some fast particles enter into nuclear reactions prior to undergoing thermalization. It is necessary to take such phenomena into account because particles produced in a plasma have, on average, the mean energy of a few MeV, at which the cross sections for nuclear reactions are much larger than the corresponding cross sections at thermal energies (10–50 keV). The set of in-flight processes is not exhausted by reactions on the products of nuclear fusion—reactions between fast fuel ions accelerated in elastic collisions are also of importance. The above suprathermal fusion reactions produce charged particles and neutrons of energies as great as a few tens of MeV [2]. Among other secondary processes of nonnegligible importance, mention should be made of neutron-induced reactions leading to the production of active isotopes. The role of second-generation processes is greater in non-hydrogen fuels, where a large number of active-isotope species are produced owing to the occurrence of a wide variety of nuclear reactions (see, for example, [3]).

Inputs necessary for a realistic analysis of the kinetics of processes proceeding in thermonuclear-fusion reactors must include reliable data on the cross sections for many reactions in a broad range of energies. Above all, this concerns reactions involving light nuclei and proceeding in the low-energy region $E < 500$ keV, which is of prime importance for controlled thermonuclear fusion. An additional incentive to study the relevant cross sections at a high-precision level comes from nuclear astrophysics, where many fundamental problems cannot be solved without this. At present, experimentalists have accumulated a vast body of relevant data. Compilations of measured cross sections and computed reaction-rate parameters are presented in the well-known reference literature [4–8]. For example, the DATLIB database [8] contains 270 data files for 77 channels of nuclear reactions involving isotopes of light elements from hydrogen to boron. References to

other databases can be found in [8, 9]. We would also like to mention the Russian handbook [10] on nuclear processes and cross sections, which covers a very broad range of energies and which additionally presents a spline approximation of experimental data. A precision *R*-matrix parametrization of the cross sections for low-energy D + T, D + D, and D + ^{3}He interactions, as well as of their Maxwell reactivities, is given in [11].

In some cases, however, available experimental data are insufficient for a detailed analysis of fuel burning and of the possibility for monitoring this burning. Here, we only note the following. First, low-energy radiative-capture reactions like T(t, γ)^{6}He, ^{3}He(τ, γ)^{6}Be, ^{6}Li(d, γ)^{8}Be, ^{6}Li(τ, γ)^{9}B, ^{7}Li(d, γ)^{9}Be, and ^{7}Li(t, γ)^{10}Be, which can be used to determine the ion temperature of a plasma or to monitor its dynamics, have not yet received adequate study. Moreover, there are no data on some of such processes whatsoever. Second, neither reliable measurements of some reactions involving light radionuclides and proceeding at subbarrier energies nor relevant theoretical investigations have been performed so far. For example, the interesting catalytic reaction ^{7}Be(d, p)2^{4}He in a D^{6}Li fuel—this reaction, which is accompanied by a large heat release of $Q \sim$ 17 MeV, produces only charged particles—has been studied insufficiently. Third, the situation is not absolutely clear in what is concerned with cross sections for low-energy reactions on polarized nuclei. This is especially important since the use of spin-polarized fuels can increase the energy released by a thermonuclear plasma and suppress simultaneously the generation of neutron fluxes. By way of example, we indicate that, for the D + T resonance process, the estimate of the nuclear-spin-polarization effect is known [12], but that, for the D + D direct reaction, the situation is much more complicated [13]. For the majority of non-hydrogen thermonuclear fuels, no detailed investigations of polarization processes have been undertaken thus far.

One of the objectives of the present study is to analyze various thermonuclear cycles based on the use of hydrogen, helium, lithium, beryllium, and boron isotopes. We pay attention primarily to nuclear-physics aspects of the issue—in particular, to the nuclear-structure effect on the cross sections for fusion reactions and on the rates of these reactions.

The ensuing exposition is organized as follows. In Section 2, we consider DT, DD, D^{3}He, D^{6}Li, DT^{6}Li, H^{6}Li, H^{11}B, and H^{9}Be fuel mixtures and analyze their advantages and disadvantages. The important case of spin-polarized fuels is also analyzed. It should be emphasized that difficulties encountered in simulating the burning of some alternative fuels are associated with uncertainties in the predicted cross sections for nuclear reactions in the deep-subbarrier energy region, where there are no experimental data. For this reason, we further discuss (in Section 3) extrapolation methods for determining cross sections in the region of low (thermonuclear) energies. By studying some important examples, we demonstrate there, among other things, how the special features of the nuclear structure of ^{6}Li and ^{7,9}Be affect the behavior of the cross sections for low-energy thermonuclear reactions. In Section 4, we consider the possibility of determining the ion temperature of a fuel by measuring the fluxes of reactor photons. The basic results of our consideration are summarized in the Conclusion (Section 5).

2. THERMONUCLEAR FUELS

According to the classification of McNally [14], thermonuclear fuels can be broken down by convention into three groups: classical (DT), promising (DD, D^{3}He, D^{6}Li), and exotic (^{3}He^{3}He, H^{6}Li, H^{11}B, H^{9}Be) fuels. We will consider them precisely in this order.

2.1. DT Fuels

A DT mixture of hydrogen isotopes is the most traditional form of fuel for nuclear reactors. The following processes are usually considered in studying the deuterium–tritium cycle:

(i) the primary exothermic reactions

$$\mathrm{D} + \mathrm{T} \longrightarrow {}^4\mathrm{He} + n + 17.59\ \mathrm{MeV}, \quad (1)$$

$$\mathrm{D} + \mathrm{D} \longrightarrow \mathrm{T} + p + 4.03\ \mathrm{MeV}, \quad (2)$$

$$\mathrm{D} + \mathrm{D} \longrightarrow {}^3\mathrm{He} + n + 3.27\ \mathrm{MeV}, \quad (3)$$

$$\mathrm{T} + \mathrm{T} \longrightarrow {}^4\mathrm{He} + 2n + 11.33\ \mathrm{MeV}; \quad (4)$$

(ii) the main secondary exothermic reaction

$$\mathrm{D} + {}^3\mathrm{He} \longrightarrow {}^4\mathrm{He} + p + 18.34\ \mathrm{MeV}; \quad (5)$$

(iii) the tritium production in a lithium blanket,

$$n + {}^6\mathrm{Li} \longrightarrow \mathrm{T} + {}^4\mathrm{He} + 4.78\ \mathrm{MeV}; \quad (6)$$

(iv) the neutron-breeding processes

$$n + {}^9\mathrm{Be} \longrightarrow 2n + 2{}^4\mathrm{He} - 1.57\ \mathrm{MeV}, \quad (7)$$

$$n + \mathrm{D} \longrightarrow 2n + p - 2.23\ \mathrm{MeV}. \quad (8)$$

Among all promising reactions, the D + T process provides the highest energy release and is characterized by the largest value of the reaction-rate parameter (reactivity) $r = \langle \sigma v \rangle$, a quantity obtained by averaging the product of the nuclear cross section $\sigma(E)$ and the relative velocity v of the reacting particles over their Maxwell velocity distribution $f(v)$. That the reactivity is so high in this case is due to a manifestly resonance character of the D + T reaction in the region of low subbarrier energies. It proceeds through the $J^\pi T = [(3/2)^+, 1/2]$ level of the compound nucleus ^{5}He at the excitation energy of $E^* = 16.76$ MeV; this corresponds to an incident-deuteron kinetic energy of $E_d \sim 100$ keV [15]. In [16], it was shown that this "thermonuclear" resonance is a typical three-body near-threshold resonance of the $t + n + p$ structure and that the coupling of the input and output channels ($td \rightleftharpoons \alpha n$) is due both to noncentral (tensor) and to central forces. Additional gain in the reactivity can be obtained owing to a spin

polarization of the fuel [12, 17]. In the presence of an external magnetic field **B**, the cross section for the D + T interaction can be represented in the form

$$\sigma = \left(a + \frac{2}{3}b + \frac{1}{3}c\right)\sigma_{3/2} + \left(\frac{1}{3}b + \frac{2}{3}c\right)\sigma_{1/2}, \qquad (9)$$

where $a = d_+t_+ + d\_t\_$, $b = d_0$, and $c = d_+t\_ + d\_t_+$, $d_+(t_+)$, $d\_(t\_)$, and d_0 being the fraction of deuterons (tritons) oriented, respectively, parallelly, antiparallelly, and orthogonally to the field **B**. Since the reaction being considered proceeds through the $J = 3/2$ channel at low energies, a parallel orientation of the D and T spins increases the cross-section value by 50% in the resonance region [12]. However, the eventual estimate of the gain in the energy release is complicated by various depolarization effects associated with binary collisions, fluctuations, nonuniformities of magnetic fields, and other similar factors. In the literature, there are both optimistic and pessimistic estimates of the depolarization rate (see, for example, [12, 17–21]).

In contrast to the D + T process (1), the D + D processes (2) and (3) are not of a resonance character. These reaction channels have approximately identical probabilities and are both characterized by smaller energy-release values and considerably reduced (in relation to the D + T process) cross sections at low energies. As a result, the above D + D processes make a relatively small contribution to the energy released in the burning of DT fuels, and they are often referred to as a satellite component. There exists, however, a third possible channel of D + D interactions, $D(d, \gamma)^4He$; this channel involves the production of high-energy photons and can have diagnostic applications—in particular, it can be used to determine the ion temperature of the fuel [22]. The T + T process (4), which is the last in the list of primary processes, does not make a significant contribution to the reaction energy release either and appears to be a by-process. At actual temperatures, its rate is two orders of magnitude less than the rate of reaction (1).

A DT mixture possesses important advantages. First, the $n\tau$ value satisfying the Lawson criterion is much less for D + T interactions than for other kinds of thermonuclear fuels. Second, the D + T fusion reaction is triggered at relatively low temperatures. The ideal threshold temperature determined as the temperature at which the energy release is equal to the energy loss by bremsstrahlung in the case of a complete particle confinement is about 4 keV [23]; an optimum temperature of burning is estimated at 15 keV in [23] and at 20 keV in [1]. Finally, the specific-power release is at least two orders of magnitude greater than similar energy characteristics of other mixtures.

Nonetheless, the DT cycle has some serious drawbacks. First of all, the burning process is accompanied by intense neutron fluxes. High-energy neutrons carry about 80% of the energy released in the D + T fusion process (about 14 MeV per reaction event). This entails very serious technological problems of protecting structural reactor materials from formidable neutron fluxes. Moreover, the energy of neutrons escaping from the reactor can be utilized with an efficiency not exceeding 40%—in other words, immense energy fluxes will circulate in the system at a typical thermonuclear-reactor power of 5×10^3 GW if energy converters are included in the reactor circuit. But this is not the whole story: tritium is radioactive; it must be produced artificially; and the extraction of tritium from a lithium blanket presents a nontrivial problem. To summarize, the presence of a source of high-energy and high-density neutron radiation, together with the use of a strongly radioactive material, imposes severe radiation-safety requirements on the implementation of a DT reactor.

2.2. DD Fuels

Primary D + D interactions have two almost equiprobable exothermic channels (2) and (3). They lead to the production of the active isotopes T and ^3He in the plasma. This in turn initiates the important secondary catalytic processes (1) and (5). Although the burning of a DD fuel is also accompanied by the generation of neutron fluxes, they are less intense than those in the D + T process. The DD cycle does not require specially producing tritium; hence, the application of this cycle makes it possible to avoid using a lithium blanket and involved tritium technologies associated with this. It has already been indicated, however, that, at low energies, the D + D cross sections are much smaller than the D + T cross sections and that triggering the D + D process requires much higher plasma temperatures. By way of example, we indicate that the ideal threshold temperature becomes as high as about 40 keV in this case [23].

2.3. D^3He Fuels

By convention, such fuels are categorized as neutron-free fuels. In such a helium–hydrogen mixture, the D + ^3He process (5), the D + D processes (2) and (3), and the reaction

$$^3He + {}^3He \longrightarrow {}^4He + 2p + 12.86\ \text{MeV} \qquad (10)$$

appear to be primary reactions. Predominantly, useful energy is released in the D + ^3He channel (5). This reaction, which has the greatest Q value of 18.34 MeV, leads to the production of only charged particles, a circumstance that improves conditions for fuel self-heating. Of course, the neutron-free process (10), which is accompanied by a considerable energy release per fusion event, is also very appealing. The use of ^3He fuels as such seems tempting, but it is very difficult to implement reaction (10) in practice because of a high threshold for its ignition. At an operating ion temperature of the plasma about 100 keV, its rates are approximately two orders of magnitude less than the rates of

the D + ^{3}He reaction; as a consequence, the contribution of reaction (10) to the burning of D^{3}He fuels is negligibly small.

The group of secondary processes in the D^{3}He cycle includes the catalytic reactions (1) and (4) (D + T and T + T, respectively), as well as two reactions involving fast protons,

$$\mathrm{D} + p \longrightarrow 2p + n - 2.23\ \mathrm{MeV}, \quad (11)$$

$$\mathrm{T} + p \longrightarrow {}^3\mathrm{He} + n - 0.76\ \mathrm{MeV}. \quad (12)$$

Owing to dominance of the D + ^{3}He channel (5), the fuel being discussed can be thought to be neutron-free by convention [24]. Here, the primary neutron channel (3) of D + D interactions and the D + T catalytic reaction (1) appear to be the sources of neutron contamination in the D^{3}He cycle, the contribution of the latter often being dominant [25]. The fraction of the neutron component in the energy release is estimated at about 3% [26]. This is a serious advantage of reactors employing D^{3}He mixtures, and the relevant possibility attracts much attention at present.[2)] A detailed survey of the current status of the problem can be found in [29].

Some gain in the energy release can be achieved by burning a spin-polarized D^{3}He fuel. It is difficult, however, to obtain an accurate estimate of the increase in the reactivity because, near the $d + \tau$ threshold, there are two (not one as in the case of $d + t$) excited states of the intermediate nucleus ^{5}Li at $E^* \sim 16.66$ MeV [$J^\pi T = (3/2)^+, 1/2$] and $E^* \sim 18 \pm 1$ MeV [$(1/2)^+, 1/2$] [15] that contribute to the $S = 1/2$ and 3/2 reaction channels (both channels of the reaction being considered). The cross-section-enhancement values adopted in the literature fall within the range 44–49%. Another important objective pursued in using nuclear spin polarization is to suppress selectively the D + D reactions and neutron yields associated with them [12, 30], but the degree of this suppression is still debated. Previously, it was shown in [31] that, for the low-energy D + D reactions, the contribution of the $^5S_2$ input channel is small in relation to the contribution of the $^1S_0$ channel, and this made it possible to consider the possibility of suppressing this reaction in the case of parallel deuteron spins. Later on, however, a pessimistic estimate of this suppression was obtained upon taking into account the D-wave state in ^{3}He [32], because an additional allowed contribution of central forces arises in this case. After a number of studies on the subject, the highly reliable analysis of Zhang *et al.* [13], who considered the D + D reactions in a polarized deuterium plasma, nonetheless revealed that the ratio $\eta = \sigma_{1,1}/\sigma_0$ (ratio of the cross sections for reactions involving spin-polarized and unpolarized nuclei) for deuteron energies between 30 and 90 keV decreases monotonically from 0.86 to 0.22. The last value corresponds to a 4.5-fold suppression of the D + D process. That the neutron channels in a polarized D^{3}He fuel can be suppressed so strongly gave incentive to developing a conceptual design of a D^{3}He fusion reactor on the basis of a linear tandem device [33, 34].

Apart from a high ignition temperature, D^{3}He fuels have yet another serious drawback: ^{3}He is a very rare isotope on the Earth; moreover, there are presently no efficient sources for its production. However, the possibility of delivering ^{3}He from the Moon's surface, which can contain, according to estimates based on studying Moon rocks, about 10^6 t of this isotope [35], is discussed in the literature.

2.4. D^{6}Li and DT^{6}Li Fuels

The presence of the ^{6}Li isotope in a hydrogen plasma complicates dramatically an analysis of thermonuclear fusion. Nuclear reactions in a D^{6}Li mixture are multistep branched processes, a number of isotopes of light elements being produced in them with commensurate probabilities. In the first generation alone, the possible processes include the two D + D channels (2) and (3) and the seven exothermic D + ^{6}Li reactions

$$\mathrm{D} + {}^6\mathrm{Li} \longrightarrow {}^4\mathrm{He} + {}^4\mathrm{He} + 22.37\ \mathrm{MeV}, \quad (13)$$

$$\mathrm{D} + {}^6\mathrm{Li} \longrightarrow {}^7\mathrm{Li} + p + 5.03\ \mathrm{MeV}, \quad (14)$$

$$\mathrm{D} + {}^6\mathrm{Li} \longrightarrow {}^7\mathrm{Li}^* + p + 4.55\ \mathrm{MeV}, \quad (15)$$

$$\mathrm{D} + {}^6\mathrm{Li} \longrightarrow {}^7\mathrm{Be} + n + 3.38\ \mathrm{MeV}, \quad (16)$$

$$\mathrm{D} + {}^6\mathrm{Li} \longrightarrow {}^7\mathrm{Be}^* + n + 2.95\ \mathrm{MeV}, \quad (17)$$

$$\mathrm{D} + {}^6\mathrm{Li} \longrightarrow {}^4\mathrm{He} + \mathrm{T} + p + 2.56\ \mathrm{MeV}, \quad (18)$$

$$\mathrm{D} + {}^6\mathrm{Li} \longrightarrow {}^4\mathrm{He} + {}^3\mathrm{He} + n + 1.80\ \mathrm{MeV}. \quad (19)$$

We do not present here other possible reactions in the ^{6}Li + ^{6}Li system, which are characterized by very small cross sections and which do not therefore make a noticeable contribution against the background of reactions (13)–(19). Among secondary processes, whose number exceeds 80, we only mention the strong reactions (1) and (5) between D and T and between D and ^{3}He, respectively, and the high-Q catalytic processes

$$\mathrm{D} + {}^7\mathrm{Be} \longrightarrow 2{}^4\mathrm{He} + p + 16.77\ \mathrm{MeV}, \quad (20)$$

$$\mathrm{D} + {}^7\mathrm{Li} \longrightarrow 2{}^4\mathrm{He} + n + 15.12\ \mathrm{MeV}. \quad (21)$$

In studying prospects for a D^{6}Li fuel, it is necessary to take into account its special features [3, 36].

(A) Branched character of burning. The reaction cross sections at low energies are small in relation to the D + T cross sections, but the number of processes proceeding in the D^{6}Li cycle is as large as a few tens. For this reason, the total contribution of a large number of channels—of these, some (for example, D + ^{7}Be and D + ^{7}Li) have energy releases commensurate with the energy release in the D + T processes—may prove to be significant.

[2)] Yamagiwa [27] proposed using an ^{18}O admixture in a D^{3}He reactor in order to produce the positron-unstable radionuclide ^{18}F in the reaction ^{18}O(p, n)^{18}F. Along with ^{11}C, ^{13}N, ^{15}O, and ^{19}Ne, this element can be employed in positron tomography and find diagnostic applications in cancer radiotherapy [28].

(B) Relatively large yields of fast and slow charged particles. Slow charged particles can efficiently heat a fuel via elastic Coulomb collisions. As to fast charged particles, their presence enhances the role of other secondary phenomena like NES processes and in-flight reactions. By way of example, we indicate the following catalytic chain [37]:

the inelastic-scattering process

$$^4\text{He (fast)} + {}^6\text{Li} \longrightarrow {}^6\text{Li}^*(2.18\ \text{MeV}) + {}^4\text{He (slow)},$$

the decay process

$$^6\text{Li}^*(2.18\ \text{MeV}) \longrightarrow {}^4\text{He (slow)} + \text{D (fast)}, \quad (22)$$

and the reaction

$$\text{D (fast)} + {}^6\text{Li} \longrightarrow 2{}^4\text{He (fast)} + 22.37\ \text{MeV}.$$

This chain results in the doubling of the number of fast alpha particles (they appear to be some kind of a catalyst for the process) and releases a large amount of energy.

(C) Monotonic energy dependence of the reaction cross sections. As was indicated above, the main reaction of thermonuclear fusion (D + T) is of a resonance character. Accordingly, its cross sections are large in the region of subbarrier energies, but they begin to decrease upon achieving a maximum at $E_d \sim 100$ keV. On the contrary, the cross sections for the D + D and D + ^{6}Li processes at low energies are much smaller than the D + T cross section, but they increase monotonically (and quite sharply for D + ^{6}Li) as the deuteron energy increases up to $E_d \sim 1$ MeV. This type of behavior is peculiar to many secondary reactions of the D^{6}Li cycle as well. As a result, there can arise an additional positive feedback in the mechanism of plasma self-heating.

(D) Presence of the fluxes of neutrons having moderate energies. It should be recalled that D^{6}Li is not a neutron-free fuel, but that its burning is accompanied primarily by the generation of neutrons with energies between 1 and 3 MeV (in contrast to 14-MeV neutrons coming from the D + T process), so that a major part of the energy release is associated with charged particles. Neutron radiation makes but a small contribution to the total energy release, but it leads to the additional production of tritium in the blanket reaction $^6\text{Li}(n, t)^4\text{He}$, which proceeds in this case directly in the region of burning. We also note that neutrons from the D + ^{6}Li processes can be used in mixed reactors of the breeder type [38].

(E) Uncertainties in the cross-section values. For the first-generation D + D and D + ^{6}Li processes, the situation around nuclear data on low-energy cross sections is quite clear. The D + D processes were intensively investigated earlier—for example, reliable data on their cross sections in the region of thermonuclear energies and on the rate parameters $\langle\sigma v\rangle$ were published in [11]. The D + ^{6}Li cross sections, which can be found, for example, in the DATLIB database [8] or in the handbook of Abramovich *et al.* [10], are known to a somewhat poorer precision, which is nonetheless quite sufficient for simulating the ignition and burning processes. We would also like to mention the interesting study of Cherubini *et al.* [39], who used quasielastic data on the reaction $^6\text{Li}(^6\text{Li}, 2\alpha)^4\text{He}$ in the region of above-barrier energies to extract the $^6\text{Li}(d, \alpha)^4\text{He}$ excitation function at very low relative energies. This indirect method of analysis is based on the so-called Trojan Horse model proposed in [40]. However, there also remain unresolved questions. For example, the contribution to the reaction being discussed from ^{8}Be highly excited states near the d + ^{6}Li threshold at about 22 to 23 MeV has yet to be clarified conclusively. In particular, it was shown in [41] that the D + ^{6}Li processes can be described satisfactorily without resort to a resonance mechanism. On the contrary, the contribution of the excited state $^8\text{Be}(2^+)$ at about 22.28 MeV was found to be large in the experimental study of Czersky *et al.* [42], who measured the cross sections for the reaction $^6\text{Li}(d, \alpha)^4\text{He}$ in the energy range E_d = 50–180 keV. Thus, the highly exothermic reaction (13) receives a considerable contribution from a resonance mechanism. In this connection, it should be recalled that, despite many years of strenuous efforts, there is presently no reliable general method for extrapolating the cross sections for low-energy reactions to those near-threshold energies that are of immediate importance for calculating the plasma reactivity $\langle\sigma v\rangle$. In Section 3, we will discuss some extrapolation procedures and allied problems. Among other things, it will be shown that nuclear-structure factors play an important role in extrapolating cross sections to the deep-subbarrier region.

For some second-generation nuclear reactions in the D^{6}Li cycle, the cross sections required for studying the role of these reactions in the heating of the fuel and their contribution to the energy release have not yet been determined to a sufficient precision. In some cases, there are only fragmentary experimental data or only theoretical estimates. For example, neither experimental nor theoretical studies have been performed thus far for the interesting second-generation reaction $^7\text{Be}(d, p)2^4\text{He}$ + 16.77 MeV, which has an energy release virtually identical to that from one event of the D + T process, but which produces, in contrast to the latter, only charged particles. The two-step process

$$\text{D} + {}^7\text{Be} \longrightarrow {}^8\text{Be}^*(2^+) + p + 0.05\ \text{MeV}, \quad (23)$$

$$^8\text{Be}^*(2^+) \longrightarrow 2{}^4\text{He} + 16.72\ \text{MeV} \quad (24)$$

appears to be the most probable mechanism of the reaction being discussed, since there is no Coulomb barrier for neutron transfer in reaction (23) and since the ^{8}Be nucleus features the well-known $J^\pi = 2^+$ 16.63-MeV level [15], whose population in the above process corresponds to a nearly vanishing energy release. The first step leads to the formation of a relatively long-lived ^{8}Be* state, which then decays into two fast alpha parti-

cles. Since $Q \approx 0$ in process (23), the reaction cross section is given by

$$\sigma \sim \int \frac{\varphi_{\mathrm{Coul}}(q^2)dq}{Q + q^2}, \qquad (25)$$

where the function $\varphi_{\mathrm{Coul}}(q^2)$ is proportional to the penetrability of the Coulomb barrier. It follows that, for $Q \longrightarrow 0$, the reaction cross section can sharply grow slightly above the threshold [43][3)] and that its values at moderately small energy values must considerably exceed simple barrier estimates.

The above exemplifies problems encountered in these realms when one studies only one of more than 80 second-generation reactions in the D^{6}Li cycle. A nonconventional procedure for directly determining the cross sections for a broad range of nuclear reactions at low energies not yet explored by that time was proposed in [44] on the basis of a laser compression of a thermonuclear target. In contrast to conditions prevalent in conventional nuclear-physics experiments, high matter densities, exceeding typical solid-state densities by many orders of magnitude, are achieved in a laser compression of a target. Despite very small cross-section values for energies $E \leq 10$ keV and despite a comparatively low hydrodynamic efficiency of targets, we can therefore expect that the yields of nuclear products—in particular, neutrons and photons—will be sufficient for purposes of reliable detection. Within this approach, one determines not the absolute value of the cross section for the reaction of interest at a specific energy value, but its relative yield with respect to some reference reaction [like D$(d, n)^3$He] whose cross section is well known. The absolute yield of products from thermonuclear reactions is then found as the convolution of the required cross section with the velocity distribution of plasma ions, which is not known very well. However, the parameters of this distribution can be corrected on the basis of a series of measurements of the yields of particles from a reference reaction thoroughly studied in advance. The yields from both the reference reaction and the reaction under study change in response to variations in the conditions under which the laser target is compressed. If one has sufficient statistics of particle yields in the two reactions at his disposal and if one knows the effective plasma temperature in the target upon each shot of the laser gun used, it is possible to establish the behavior of the required cross section in the deep-subbarrier region [44]. By way of example, we indicate that, according to the estimates presented in [44], the cross sections for the D + ^{6}Li processes can be determined at extremely low energies of E = 1–10 keV by applying the proposed procedure, provided that the relative yield of fast particles from these processes has been measured.

(F) Effect of nuclear-spin polarization. At low energies, the reaction ^{6}Li$(d, \alpha)^4$He (13), which is characterized by the highest energy release among the first-generation processes, proceeds predominantly through the $S = 2$ channel, provided that the 2^+ level in ^{8}Be at $E^* \approx 22.28$ makes a dominant contribution (see above). If this process is implemented with polarized particles whose spins are parallel, the energy release must therefore increase by a factor close to 2, all other conditions being the same.

In analyzing the prospects of D^{6}Li fuels, it is impossible to take into account completely all the aforementioned features. However, a simplified model incorporating all first-generation reactions and some secondary processes that was developed in [3, 36] permitted drawing some important conclusions on the role of ^{6}Li in a plasma consisting of hydrogen isotopes. In the first of those studies, the kinetics of 13 D + D, D + ^{6}Li, D + T, D + ^{3}He, D + ^{7}Be, and D + ^{7}Li nuclear processes was investigated under the conditions of magnetic plasma confinement. There, the mechanism of self-heating was described within the CES process; that is, the plasma temperature increased owing to the elastic Coulomb scattering of fast particles on fuel ions.

On the basis of the results obtained in [3], one can draw two important conclusions. First, a 10% admixture of ^{6}Li to a deuterium fuel can increase the plasma reactivity. This means that an additional energy release owing to the presence of ^{6}Li exceeds the enhancement of radiative losses because of a contamination of a hydrogen plasma by an admixture with charge number $Z_{\mathrm{Li}} = 3$. At the same time, the threshold ignition temperature increases insignificantly, amounting to $T_{\mathrm{thr}} \sim$ 50 keV—the corresponding temperature for a pure DD fuel is about 40 keV [23]. The second conclusion concerns a dominant mechanism of energy generation. It turned out that it is of manifest catalytic character and is due to the production of the active elements T, ^{3}He, and ^{7}Be. Their fusion proceeds so vigorously that, within some 10 to 14 s from the commencement of burning, the concentration of these nuclei exceeds the current value of the ^{6}Li concentration. Characteristic curves describing the dynamics of fuel burnup and the production of active isotopes in a D + ^{6}Li plasma are presented in Fig. 1.

For yet another example of the use of ^{6}Li nuclei in fusion reactors, we can indicate a relatively simple means for the ignition of a DD fuel at initial temperatures of $T_0 \leq 10$ keV by injecting a T^{6}Li pellet into the reactor core [36]. This composition of a solid-state igniter is recommended for the following two reasons. First, it initiates a self-sustaining process of burning, with an energy release in the three-component DD + T^{6}Li mixture being not less than that in the two-component DD + T mixture.[4)] Second, the use of lithium tritide (that is, tritium-substituted lithium hydride) makes

[3)]In the absence of a Coulomb barrier—that is, for neutrons—the reaction cross section must grow indefinitely in this case from the threshold.

[4)]This notation for the plasma composition emphasizes that a T ^{6}Li or a T admixture is introduced in a deuterium plasma.

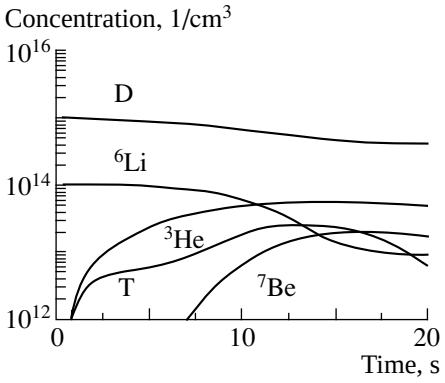

Fig. 1. Concentrations of a fuel and of some active isotopes produced in a D + ^{6}Li plasma as functions of time [3].

unnecessary a separation of tritium from a lithium blanket and its subsequent transportation to the zone of burning.

A diagnostic application of the reactions ^{6}Li(d, p)^{7}Li* (478 keV) and ^{6}Li(d, n)^{7}Be* (431 keV) furnishes an additional motivation for introducing a ^{6}Li admixture in a deuterium-containing plasma [45]. By detecting monochromatic photons produced in these reactions, one can attempt to measure the ion temperature T_i (see Section 4) or to control the dynamics of burning.

However, Kernbichler and Heindler [46] assessed more pessimistically the use of ^{6}Li as a possible component of a thermonuclear fuel and showed that the energy released in a D^{6}Li mixture decreases monotonically as its concentration is increased. In order to draw a definitive conclusion on the prospects for the use of a D^{6}Li fuel, we need more detailed models taking into account many second-generation processes; it is also necessary to consider various reactor designs. Such an analysis is hindered, however, by formidable computational difficulties and by the absence of some nuclear data on cross sections.

A new attempt at refining the model for laser thermonuclear fusion was made by Nakao *et al.* [47], who additionally studied the role of suprathermal nuclear reactions in a DT + ^{6}Li target. A numerical simulation was performed there on the basis of coupled transport and hydrodynamic processes [48]. This simulation took into account all first-generation reactions in the DT + ^{6}Li system; charged-particle and neutron scattering; the deuteron-breakup reaction D(n, 2n)p; and the D + T, D + D, and D + ^{6}Li processes of suprathermal fusion on deuterons and tritons accelerated in neutron scattering. For the case of the volume fuel-ignition mechanism, typical results are quoted in Table 1. The initial conditions were characterized by the value of ρR = 10 g/cm^2, the equal ion and electron temperatures of $T_i = T_e$ = 1.5 keV, the degree of compression (on the scale of the solid-state density) of ρ/ρ_0 = 5000, and the ^{6}Li content of 5% in the DT mixture. Table 1 shows that the D + T process, the main thermonuclear-fusion reaction, is dominant here. This result might have been expected from the outset, but it is of interest to compare the relative contributions of other channels. It can be seen that the energy release is 30% greater in the D + ^{6}Li processes than in the D + D processes. The data quoted here cannot be considered to be conclusive, since some important issues associated with the optimization of the nonhomogeneous structure of the target and with the regime of its compression have yet to be clarified. In addition, it is of interest to study the kinetics of nuclear reactions at higher initial temperatures as well.

2.5. H^{6}Li Fuels

The above special features of the D + ^{6}Li nuclear processes are inherent in part in H^{6}Li fuels. As in the case of D^{6}Li, the burning of the fuel is highly branched here, and the number of relevant reactions is as high as a few tens [49]. However, the spectrum of the first-generation reactions is much narrower here than that for D + ^{6}Li. If we discard the suppressed ^{6}Li + ^{6}Li channel and the weak radiative-capture process ^{6}Li(p, γ)^{7}Be, there remains, in a H^{6}Li mixture, only one exothermic reaction

$$\mathrm{H} + {}^6\mathrm{Li} \longrightarrow {}^4\mathrm{He} + {}^3\mathrm{He} + 4.02\ \mathrm{MeV}, \qquad (26)$$

which is pure in the sense that it produces neither neutrons nor radionuclides. The second-generation exothermic reactions

$$^3\mathrm{He} + {}^6\mathrm{Li} \longrightarrow 2{}^4\mathrm{He} + \mathrm{H} + 16.88\ \mathrm{MeV}, \qquad (27)$$

$$^3\mathrm{He} + {}^6\mathrm{Li} \longrightarrow {}^7\mathrm{Be} + \mathrm{D} + 0.11\ \mathrm{MeV} \qquad (28)$$

do not lead to neutron production either; the first of these regenerates protons. The processes in (26) and (27) can be combined into the chain

$$\mathrm{H} + 2{}^6\mathrm{Li} \longrightarrow \mathrm{H} + 3{}^4\mathrm{He} + 20.90\ \mathrm{MeV}. \qquad (29)$$

In relation to the direct reaction ^{6}Li(^{6}Li, α)2^{4}He, this chain provides an easier means for burning ^{6}Li with the

Table 1. Energy release in a DT + ^{6}Li laser target

Initial internal energy, MJ	Energy release, MJ	Relative contribution of channels, %					
		thermal			suprathermal		
		D + T	D + D	D + ^{6}Li	D + T	D + D	D + ^{6}Li
0.634	476.2	90.1	0.8	1.2	7.6	0.2	0.1

generation of three fast alpha particles. This process was simulated, for example, in [28].

Despite the obvious attractiveness of H^{6}Li fuels (owing to the absence of strong neutron fluxes and their cheapness), it has proven to be impossible at present to accomplish its ignition.[5)] An analysis of the cycle in (29) with allowance for the ^{6}Li + ^{6}Li thermonuclear reactions does not lead to ignition even in the case of large values of $\beta \sim nT/B^2$ (where n and T are the plasma density and temperature, respectively, while B is the external-magnetic-field induction), in which case losses by cyclotron radiation are minimal [51]. The more recent investigation of Kernbichler and Heindler [46] also demonstrated that, even at optimal operating temperatures in the range 300–650 keV, the energy characteristics of H^{6}Li mixtures are below the threshold values by about one order of magnitude. Nonetheless, H + ^{6}Li plasmas may still be of interest for different settings—for example, in the case of collisions between plasma bunches [52].

2.6. H^{11}B Fuels

As in the preceding case, the almost complete absence of neutron generation and cheapness are important advantages of boron–hydrogen mixtures. In the first generation, the two possible exothermic reactions are

$$\mathrm{H} + {}^{11}\mathrm{B} \longrightarrow 3{}^4\mathrm{He} + 8.68\ \mathrm{MeV}, \quad (30)$$

$$\mathrm{H} + {}^{11}\mathrm{B} \longrightarrow \gamma + {}^{12}\mathrm{C} + 15.96\ \mathrm{MeV}, \quad (31)$$

the latter being severely suppressed. In the energy region of our prime interest, the branching ratio for these channels is about 10^{-5} [53]. The dominant reaction (30) yields alpha particles of moderate energies, $E_\alpha \sim 2.9$ MeV; this favors the heating of the ion component with an efficiency of 80–90% [54]. Over a broad energy range, the reaction in question is of a resonance character associated with a few excited states of the ^{12}C nucleus. Of these, the lowest is responsible for the low-energy peak in the cross section at $E_p \sim 163$ keV. The reactivity of secondary processes in H^{11}B fuels is very low. The weak reactions ^{11}B(p, n)^{11}C and ^{11}B(α, n)^{14}N may prove to be neutron sources, the neutron contribution to the energy release being estimated at about 0.1% [55]. A H^{11}B fuel was proposed in [56] and was investigated, for example, in [53–57]. The reactivity attains a maximum only at high temperatures (about 300 keV); together with large losses by radiation because of a large boron charge of $Z = 5$, this complicates fulfillment of the energy-balance conditions. The general conclusion from the aforementioned investigations is that it is necessary to use laser thermonuclear facilities for implementing the H + ^{11}B process and that magnetic confinement proves to be inefficient because of large radiative losses. According to [58], the volume ignition is achievable at $\rho R = 16$ g/cm^2 under certain conditions. For ignition, Martinez-Val *et al.* [59] propose using particle beams under the conditions of the inertial compression of a target with the aim of generating a thermal-detonation wave. A new type of a thermonuclear reactor, CBFR (colliding-beam fusion reactor, which is appropriate for the use of a H^{11}B fuel), was proposed by Rostoker *et al.* [52], who argue that a CBFR is convenient for the burning of a spin-polarized fuel, since the depolarization rate is insignificant on the time scale of nuclear fusion or diffusion [60]. It was shown that the use of a polarized H^{11}B mixture ensures a 60% enhancement of the cross section [60].

2.7. H^{9}Be Fuels

The H + ^{9}Be process has two approximately equiprobable exothermic channels of the production of slow charged particles,

$$\mathrm{H} + {}^9\mathrm{Be} \longrightarrow {}^4\mathrm{He} + {}^6\mathrm{Li} + 2.13\ \mathrm{MeV}, \quad (32)$$

$$\mathrm{H} + {}^9\mathrm{Be} \longrightarrow 2{}^4\mathrm{He} + \mathrm{D} + 0.65\ \mathrm{MeV}, \quad (33)$$

which are able to transfer a major part of their energy to plasma ions. Although the total energy release is as small as some 2.8 MeV, the low-energy behavior of the reaction is determined by the presence of a strong resonance at an incident-proton energy of $E_p \sim 330$ keV [61], which corresponds to the excited state ^{10}B(1$^-$) at $E^* \sim 6.88$ MeV [15]. This conclusion was confirmed in the earlier experimental study of Sierk and Tombrello [62] as well. In this region, the reaction cross sections are extremely large; the product σv exceeds that for the D + ^{3}He processes, falling short of only the corresponding quantity for the D + T process [63]. It was also indicated in [61] that the additional reason for extremely large low-energy cross sections may be concealed in the structural features of the ^{9}Be nucleus as well. This nucleus has a neutron weakly bound to the ^{8}Be core, its separation energy being as low as some 1.7 MeV [15, 64]. The ^{9}Be density profiles found in [65] indicate that the neutron wave function extends over a large distance, so that the direct reaction mechanism is quite possible. This is confirmed by the latest experimental study of the reaction on polarized protons at $E_p \sim 80$–300 keV in [66], where it was shown that the direct mechanism provides a good description of the cross sections for the (p, d) channel (33) at very low energies.

It is of paramount importance that all products of the H + ^{9}Be processes (32) and (33) cause the second-generation exothermic processes [63]

$$\mathrm{D} + {}^9\mathrm{Be} \longrightarrow 4 \text{ reactions with total } Q \sim 21\ \mathrm{MeV}, \quad (34)$$

$${}^6\mathrm{Li} + {}^9\mathrm{Be} \longrightarrow 8 \text{ reactions with c } Q \approx 2\text{–}15\ \mathrm{MeV}, \quad (35)$$

$${}^4\mathrm{He} + {}^9\mathrm{Be} \longrightarrow n + {}^{12}\mathrm{C} + 5.70\ \mathrm{MeV}, \quad (36)$$

[5)] It is interesting to note that, under astrophysical conditions, the reaction ^{6}Li(p, α)^{3}He plays an important role. Together with the radiative-capture process ^{4}He(d, γ)^{6}Li, it is responsible for the abundance of the ^{6}Li isotope in the Universe [50].

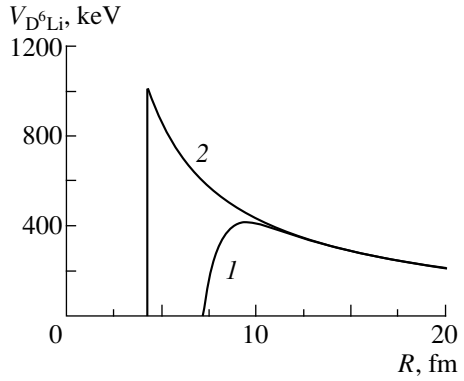

Fig. 2. (*1*) Realistic ([70]) and (*2*) purely Coulomb potential barrier in the D + ^{6}Li system. For the Coulomb barrier, the channel radius was taken to be a = 4.3 fm.

$$^6\mathrm{Li} + \mathrm{H} \longrightarrow {}^3\mathrm{He} + {}^4\mathrm{He} + 4.02\ \mathrm{MeV}, \qquad (37)$$

and that their role in plasma heating may prove to be significant. However, no detailed investigations of H^{9}Be fuels have been performed thus far. Moreover, a comprehensive simulation of its burning has not yet been performed, and the role of secondary processes has not been clarified. It is clear, however, that the resonance H + ^{9}Be process can at least utilize moderated protons very efficiently in the energy region below 1 MeV [63].

3. EXTRAPOLATION OF CROSS SECTIONS FOR NUCLEAR REACTIONS TO THE REGION OF LOW ENERGIES AND ROLE OF NUCLEAR-STRUCTURE FACTORS

In order to extrapolate the cross sections for nuclear reactions to the region of low (deep-subbarrier) energies, where there are usually no experimental data, the cross section $\sigma(E)$ is represented as the product of a factor that changes slowly with energy and a factor that changes fast. Specifically, we set

$$\sigma(E) = \frac{S(E)}{E}P(E), \qquad (38)$$

where the structural factor $S(E)$ is weakly dependent on energy or is taken to be a constant, a dominant energy dependence being absorbed primarily in the potential-barrier penetrability factor $P(E)$.

It is clear, however, that, if the potential-barrier shape or a method for computing the penetrability $P(E)$ is chosen inappropriately, the relevant error will translate into the factor S. Thereby, the factor $S(E)$ will acquire an additional unphysical energy dependence adversely affecting the extrapolation of cross sections to the deep-subbarrier region. We recall in this connection that, since direct measurements at low energies of $E < 300$ keV usually involve sizable errors, any uncontrollable energy dependence in $S(E)$ will inevitably impair the accuracy of the extrapolation. By way of illustration, we indicate that, in the D + D system, the p-wave contribution is of importance up to 15 keV, so that a conventional use of an s-wave extrapolation (discard of the p-wave contribution) leads to large errors.

Within the standard extrapolation, the penetrability factor is usually calculated for a purely Coulomb shape of the potential barrier in the semiclassical approximation, which leads to the Gamow formula [67]

$$P_{\mathrm{Gamow}} \sim \exp\left(-\frac{4\pi^2 e^2 Z_1 Z_2}{\hbar v}\right), \qquad (39)$$

where v is the relative velocity of particles with charge numbers Z_1 and Z_2.

Within the more precise quantum-mechanical model, we have (see, for example, [68])

$$P_{\mathrm{quant}} \sim \left[\frac{kR}{F^2 + G^2}\right]_{R=a}, \qquad (40)$$

where F and G are, respectively, the regular and the irregular Coulomb wave function, k is the wave number, and a is the channel radius. The extrapolation procedure developed in [69, 70] is more correct. There, the quantum-mechanical-tunneling factor $P(E)$ is determined for a realistic shape of the potential barrier (rather than for an ideal Coulomb shape) that contains information about the inner structure of particles involved in the reactions being considered. This is especially important in describing the interaction of nuclei having a pronounced cluster structure. The realistic barrier is constructed with allowance for the peripheral attractive component of nuclear interaction in the system, whereby the shape of the barrier is strongly modified, its height being reduced.[6)] This can clearly be seen in Fig. 2, which displays the Coulomb and the realistic potential barrier for the D + ^{6}Li system [70]. The latter was computed on the basis of the double-folding model with reliable three-body wave functions of the ^{6}Li nucleus, $\Psi_{^6\mathrm{Li}}(\alpha n_1 p_1)$, that provide a good description of its structure and of many processes in which this nucleus participates [72–74] and with the realistic deuteron wave functions $\Psi_{\mathrm{D}}(n_2 p_2)$ obtained by using the Reid soft-core nucleon–nucleon (NN) potential [75]. In our approach, both the nuclear and the Coulomb pair potentials (V_{ij} and U_{ij}, respectively) of the αN and NN interactions are weighted with the internal wave functions of the nuclei involved in the reactions being considered. In the D + ^{6}Li system, the binary interaction is represented as

$$V_{D^6Li}(R) = \langle \Psi_{^6\mathrm{Li}}(\alpha n_1 p_1)\Psi_{\mathrm{D}}(n_2 p_2)|V_{\mathrm{nucl}} + U_{\mathrm{Coul}}|\Psi_{^6\mathrm{Li}}(\alpha n_1 p_1)\Psi_{\mathrm{D}}(n_2 p_2)\rangle, \qquad (41a)$$

[6)] In passing, we would like to mention the independent investigation of Rowley and Merchant [71], who analyzed the effect of the shape of the barrier on its penetrability in astrophysical reactions.

where

$$V_{\text{nucl}} = V_{\alpha n_2} + V_{\alpha p_2} + V_{n_1 n_2} + V_{n_1 p_2} + V_{p_1 n_2} + V_{p_1 p_2},$$
$$U_{\text{Coul}} = U_{\alpha p_2} + U_{p_1 p_2} \quad (41b)$$

and R is the distance between the D and ^{6}Li centers of mass. It is important to note that the $\Psi_{^6\text{Li}}$ wave functions in (41a) were found by solving the three-body problem with the same αN and NN potentials (41b) as those used in the folding model. Thus, the shape of the potential barrier in the D + ^{6}Li system was calculated in a fully self-consistent way without resort to adjustable parameters (*ab initio* calculation); hence, it can be thought to be quite reliable.

For the realistic barrier in (41), the tunneling factors $P(E)$ are depicted in Fig. 3. The P_{semicl} curve corresponds to the penetrability factor found in the semiclassical approximation [76],

$$P_{\text{semicl}}(E) \sim \exp\left\{-\frac{2}{\hbar}\int_{R_1}^{R_2}\sqrt{2\mu(V_{\text{D}^6\text{Li}}(R)-E)}\,dR\right\}, \quad (42)$$

where μ is the reduced mass of the nuclei, E is their c.m. energy, and $R_{1,2}$ are the coordinates of the classical turning points [they are determined from the condition $V_{\text{D}^6\text{Li}}(R_1) = V_{\text{D}^6\text{Li}}(R_2) = E$]. The P_{pres} curve corresponds to a precise calculation where the tunneling penetrability factor is defined as the ratio of the flux densities for the transmitted and reflected waves. It can be seen that these two approaches lead to different energy dependences for the tunneling factor $P(E)$, as is additionally illustrated in Fig. 4, which displays the ratio of the penetrability factors $P_{\text{pres}}(E)$ and $P_{\text{semicl}}(E)$. This comes as no surprise: the semiclassical expression (42) is highly accurate only in the case of smooth potentials (that is, potentials slowly varying with distance), but the interaction potential in (41) does not possess this property—it decreases fast to the left of the maximum (see Fig. 2), not ensuring the required accuracy. Thus, we have revealed that there arise sizable errors when precise quantum-mechanical penetrability of the actual potential barrier is replaced by that in the semiclassical approximation.

The above barrier corrections proved to be of importance in describing the reaction between loosely bound nuclei D and ^{6}Li, which are characterized by a high degree of clustering. We will demonstrate this by considering the example of the reaction rate in a D + ^{6}Li plasma under the condition of thermal equilibrium at temperature kT. In this case, the velocity distribution of particles has a Maxwellian form, and the reaction-rate parameter $\langle\sigma v\rangle$ is given by

$$\langle\sigma v\rangle = \left(\frac{8}{\mu\pi}\right)^{1/2}(kT)^{-3/2}\int_0^\infty E\sigma(E)e^{-E/kT}\,dE. \quad (43)$$

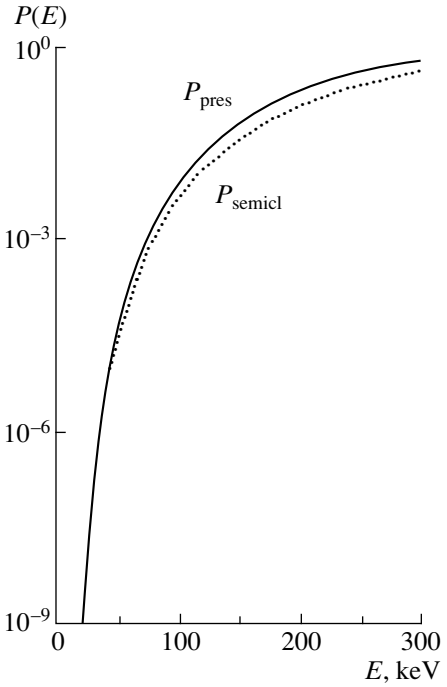

Fig. 3. Precise and semiclassical penetrability [$P_{\text{pres}}(E)$ and $P_{\text{semicl}}(E)$, respectively] of a realistic potential barrier in the D + ^{6}Li system.

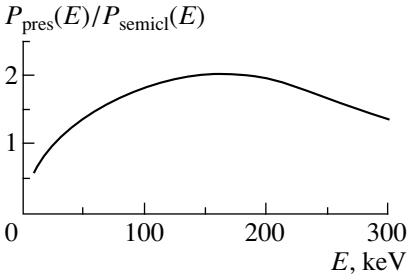

Fig. 4. Ratio $P_{\text{pres}}/P_{\text{semicl}}$ for a realistic potential barrier in the D + ^{6}Li system as a function of energy.

The equilibrium rate parameters $\langle\sigma v\rangle$ calculated for the $(d, n\tau)$ and (d, pt) channels of D + ^{6}Li interaction, which are responsible for the production of ^{3}He and tritium, are quoted in Table 2. In the ion-temperature range $T_i \equiv kT$ = 1–100 keV, these results exceed those presented in [77] by about 10–40%, the difference between the rate parameters found from the two calculations becoming greater with decreasing ion temperature.

In the above methods for extrapolating relevant cross sections, the slowly changing structural factor $S(E)$ is parametrized analytically—for example, in the form of a Padé approximant. In many cases, this approach unfortunately does not ensure the required accuracy and reliability of extrapolation, since the errors in extracting the factor S from experimental data often grow so sharply with decreasing energy that the confidence interval ΔS for a determination of $S(0)$ in an

Table 2. Rate parameters $\langle \sigma v \rangle$ of the reactions ^{6}Li(d, $n\tau$)^{4}He and ^{6}Li(d, pt)^{4}He for the case of a Maxwell velocity distribution of ions

Ion temperature T_i, keV	Rate parameter $\langle \sigma v \rangle$, cm^3/s	
	(d, $n\tau$)	(d, pt)
1	2.03 (–31)	2.46 (–31)
2	1.29 (–27)	1.59 (–27)
3	8.67 (–26)	1.08 (–25)
4	1.20 (–24)	1.52 (–24)
5	7.71 (–24)	9.83 (–24)
6	3.12 (–23)	4.03 (–23)
7	9.49 (–23)	1.23 (–22)
8	2.35 (–22)	3.14 (–22)
9	5.11 (–22)	6.68 (–22)
10	9.77 (–22)	1.27 (–21)
20	3.82 (–20)	5.43 (–20)
30	2.03 (–19)	3.22 (–19)
40	5.54 (–19)	9.70 (–19)
50	1.11 (–18)	2.05 (–18)
60	1.87 (–18)	3.63 (–18)
70	2.79 (–18)	5.65 (–18)
80	3.91 (–18)	8.01 (–18)
90	5.14 (–18)	1.08 (–17)
100	6.54 (–18)	1.37 (–17)

Note: In the second and in the third column, the numbers in front of parentheses and the numbers presented parenthetically stand, respectively, for the mantissa and the integral (negative) power of ten in the floating-point representation of numbers—for example, 2.03 (–31) denotes 2.03×10^{-31}.

extrapolation to the threshold becomes commensurate with the $S(0)$ value itself.

In those frequent cases where there are no pronounced compound resonance states near the threshold (that is, where the existing near-threshold resonances are of a so-called potential character—this is so in systems like D + D and ^{3}He + ^{3}He), it is possible to develop an alternative, very promising approach to extrapolating cross sections, which is especially efficient for reactions featuring spin-polarized particles. It consists in using well-known data at not very low energies of $E \sim$ 0.5–5 MeV to construct a reliable multichannel interaction potential with allowance for important reaction channels $a + b \longrightarrow c_i + d_i$ ($i = 0, 1, \ldots, n$). In contrast to the scattering amplitude, this potential is in general a very smooth function of E, and the threshold energy is not a peculiar point for it. Therefore this potential can be used to predict cross sections near the threshold for the $a + b$ channel. Although this approach had been known for quite a long time, its specific realization on the basis of a new method for constructing the multichannel potential being discussed was proposed only in recent years (see [78–80]). The potential in question is based on a direct iterative solution to the inverse scattering problem. This solution proceeds directly from experimental data on cross sections, as well as on vector and tensor analyzing powers. Although this method has hitherto been harnessed only in elastic-scattering problems featuring channel coupling, it can obviously be applied to the general problem of predicting near-threshold cross sections for rearrangement reactions.

4. TEMPERATURE DIAGNOSTICS OF A THERMONUCLEAR PLASMA BY THE GAMMA-RAY METHOD

A determination of the ion temperature and of its profiles and time evolution is an important problem of diagnostics of a thermonuclear plasma. At present, a great number of diagnostic procedures that primarily employ data from atomic physics have been proposed for measuring the parameters of a thermonuclear plasma. By and large, these procedures furnish only indirect information about the ion plasma component, but direct nuclear physics methods that make it possible to monitor straightforwardly the dynamics of ions may prove to be of paramount importance here. Of particular value are nuclear-physics methods relying on reactions between charged particles. Such reactions may proceed in a fuel initially, but they can also be activated in a dedicated way by introducing diagnosing admixtures in a plasma.

Let us consider the possibility of determining the ion temperature of a fuel, T_i, by using processes that produce high-energy photons freely escaping from the reactor core both in the case of a magnetic plasma confinement and in the case of inertial confinement. We restrict ourselves to considering DT and D^{3}He fuels, which have received so far the most detailed study, and choose, for activating (diagnosing) admixtures, ^{3}He and ^{6}Li isotopes for DT mixtures and T and ^{6}Li for D^{3}He mixtures. Presented below are the radiative-capture reactions proceeding in the systems under consideration and involving the emission of photons of energies E_γ in excess of 10 MeV [processes (15) and (17) could also be included in this list]:

$$\begin{gathered} \mathrm{T}(d,\gamma)^5\mathrm{He} + 16.70, \quad {}^3\mathrm{He}(t,\gamma)^6\mathrm{Li} + 15.79, \\ \mathrm{D}(d,\gamma)^4\mathrm{He} + 23.85, \quad \mathrm{T}(t,\gamma)^6\mathrm{He} + 12.31, \\ {}^3\mathrm{He}(d,\gamma)^5\mathrm{Li} + 16.39, \quad {}^6\mathrm{Li}(d,\gamma)^8\mathrm{Be} + 22.28, \\ {}^3\mathrm{He}(\tau,\gamma)^6\mathrm{Be} + 11.49, \quad {}^6\mathrm{Li}(\tau,\gamma)^9\mathrm{B} + 16.60, \\ {}^6\mathrm{Li}(d,p)^7\mathrm{Li}^*[0.478]\ (\longrightarrow {}^7\mathrm{Li} + \gamma + 0.478) + 4.55, \\ {}^6\mathrm{Li}(d,n)^7\mathrm{Be}^*[0.431]\ (\longrightarrow {}^7\mathrm{Be} + \gamma + 0.431) + 2.95 \end{gathered} \tag{44}$$

(the energies released in these reactions are given in MeV). Of the reactions listed here, T(d, γ), D(d, γ), and ^{3}He(d, γ) have received adequate experimental study; the same can be said about the last two processes ^{6}Li(d, $p\gamma$) and ^{6}Li(d, $n\gamma$) [22, 81–83]. For the first time, the use of these reactions for a hot-plasma thermometer was proposed in [45, 84–86].

The idea of determining the ion temperature T_i is based on the fact that the yield of photons from $A + B$ interactions, $Y_\gamma(AB)$, is proportional to the concentration of reaction products, $n_{A(B)}$, and to the γ-channel reactivity $\langle \sigma v \rangle_{AB_\gamma}$, which depends greatly on T_i. By choosing an appropriate combination of a few reactions from (44), it is possible to find the required temperature, irrespective of plasma-density values [45]. By way of example, we indicate that, for a DT mixture, a simultaneous detection of photon yields in the reactions T(d, γ) and D(d, γ) leads to

$$\frac{Y_\gamma(\mathrm{TD})}{Y_\gamma(\mathrm{DD})} = \frac{2n_\mathrm{T}}{n_\mathrm{D}} \frac{\langle \sigma v \rangle_{\mathrm{TD}_\gamma}}{\langle \sigma v \rangle_{\mathrm{DD}_\gamma}} = f(T_i), \qquad (45)$$

where the ratio of the concentrations n_T and n_D can be considered as a constant to a high precision. It follows that the ratio of the yields of photons from the above two reactions is a known function of the ion temperature T_i. Therefore, a simultaneous independent measurement of the two photon fluxes provides a means for determining T_i. The monitoring of three photon fluxes from the reactions T(d, γ), D(d, γ), and T(t, γ) could be very useful, but there are no nuclear data on the cross sections for the last process.

The smallness of cross sections is a drawback common to all radiative-capture reactions, which are governed by electromagnetic interaction. For example, the ratio of the branching fractions for the radiative and the main channel at low energies is about 5×10^{-5} for D + T and D + ^{3}He interactions and about 10^{-7} for D + D interactions [22]. Therefore, the problem of experimentally detecting photons in such reactions is nontrivial. However, Lerche *et al.* [87] reported that they recorded 16.7-MeV gamma radiation from D + T interactions at the Nova laser facility and used it in studying the dynamics of burning.

The last two processes in (44), which yield monochromatic photons of energy E_γ about 500 keV, do not have this drawback. These reactions are governed by strong interaction, and the relevant low-energy cross sections are relatively large. Their photon yield as estimated for a facility implementing a magnetic plasma confinement [45] is quite sizable even at a 1% concentration of ^{6}Li. That the reactions ^{6}Li(d, $n\gamma$) and ^{6}Li(d, $p\gamma$) represent different output channels of the same process is also of importance, because any current fluctuation of the plasma density or some other parameter of the plasma under study would not affect the accuracy in determining T_i. However, the energy dependences of the cross sections $\sigma(E)$ for these channels differ only slightly in subbarrier region [82], so that the question of whether this distinction is sufficient for attaining the required degree of accuracy in determining the temperature is still open. Anyway, a direct measurement of photon yields from nuclear reactions proceeding in a thermonuclear reactor would nevertheless furnish unique information about the most important properties of plasmas.

5. CONCLUSION

In the present review article, we have considered some important nuclear-physics facets of the problem of controlled thermonuclear fusion. Attention has been given primarily to (i) choosing an optimum thermonuclear cycle for future thermonuclear power engineering, (ii) analyzing the problem of a reliable extrapolation of measured cross sections to the deep-subbarrier energy region, and (iii) discussing gamma-ray diagnostics of a hot plasma on the basis of radiative-capture reactions.

We have shown that special features of nuclear structure—for example, pronounced clustering in light nuclei—often play an important role in the low-energy behavior of relevant cross sections for nuclear reactions and can also affect the choice of strategies for investigations in these realms. At the same time, these factors have been virtually disregarded not only in monographs and review articles devoted to the problem of controlled thermonuclear fusion but also in a large number of original specific studies. Fortunately, interest in these issues has quickened somewhat in recent years, and a series of studies, which are surveyed in our article, have been performed along these lines.

We have conducted a comparative nuclear-physics analysis of the following eight promising thermonuclear fuels based on isotopes of light elements: DT, DD, D^{3}He, D^{6}Li, DT^{6}Li, H^{6}Li, H^{11}B, and H^{9}Be. Of these, DT, DD, and D^{3}He mixtures have received the most detailed study. Among all cycles considered above, a DT fuel possesses the lowest ignition temperature ($T <$ 10 keV). However, practical uses of this fuel are restricted by many disadvantages like the presence of intense neutron fluxes carrying about 80% of the energy released in D + T interactions, a relatively low reactor efficiency, and the fact that one has to deal with radioactive tritium. In what is concerned with radiation safety and with the efficiency of conversion of nuclear energy into electric energy, a D^{3}He fuel is preferable because, here, neutrons carry only about 3% of the total energy release. Unfortunately, the ignition of this fuel requires higher plasma temperatures of a few tens of keV; in addition, there are practical difficulties in obtaining the ^{3}He isotope, one of the fuel components. Additional gain in the energy release can be achieved through the use of spin-polarized fuels, where the cross sections for the two reactions increase by about 50%. However, it is difficult to estimate this gain definitively, since the result depends on the role of depolarization

effects. Another objective pursued by the use of spin-oriented nuclei is that there are hopes for suppressing the neutron flux associated with the D + D by-process. The degree of this suppression, which depends on the cross sections for low-energy D + D interactions involving polarized deuterons, is still hotly debated; sometimes, the estimates presented in the literature are at odds with one another.

A high ignition temperature is the main (and sometimes the only) drawback of non-hydrogen fuels. If, however, operating temperatures of a few hundred keV are achieved, the use of alternative fuels can prove to be advantageous from the ecological and economical points of view. For example, the cheap and "pure" fuel $H^{11}B$, for which the adopted estimate of the neutron contribution to the total energy release is as low as 0.1%, is very appealing in this respect. Unfortunately, the kinetics of nuclear processes has been studied much more poorly in alternative fuels than in hydrogen fuels. Virtually no investigations have been performed for $H^{9}Be$ fuels, although σv values for H + ^{9}Be interactions are inferior only to those for D + T. Analysis of some alternative fuels is extremely difficult because of a complicated multistep character of their burning, which results in the generation of a number of active light isotopes in such plasmas. Although the most recent development of supercomputer technologies and the advent of teraflop supercomputers capable of performing about 10^{12} operations per second make it possible to overcome many computational difficulties in simulating plasma dynamics, there unfortunately remains the problem of sufficient motivation for performing this formidable work.

Another factor complicating the analysis of non-hydrogen thermonuclear fuels stems from the absence of reliable nuclear data on some important processes. By considering the example of D + ^{6}Li interactions alone, we have shown that, at ion temperatures of $T_i < 100$ keV, the Maxwellian reactivities $\langle \sigma v \rangle$ for the (d, pt) and (d, $n\tau$) channels are additionally enhanced by 10–40% upon correctly taking into account nuclear-structure factors. Similar investigations have yet to be performed for many other interesting reactions induced by light nuclei showing a considerable degree of clustering (for example, H + ^{9}Be).

Reactions that produce photons and which accompany burning or which are deliberately activated by diagnostic admixtures of light isotopes can serve as an efficient thermometer of a hot plasma. The yield of gamma radiation freely escaping from the reactor core depends greatly on the ion temperature T_i in the thermonuclear region and can therefore be used to determine T_i. Under the condition that the above photon yields exceed the gamma-radiation background, the possibility of simultaneously detecting a few radiative processes opens the way to determine absolute values of the ion temperature, irrespective of the initial plasma densities and their current fluctuations.

ACKNOWLEDGMENTS

We are grateful to many physicists, including V.I. Kogan, V.N. Pomerantsev, G.V. Sklizkov, V.A. Chuyanov, and H. Nakashima, with whom we discussed, over various periods of time, the range of problems considered in the present review article.

Special thanks are due to V.M. Krasnopolsky, Y. Nakao, and K. Kudo, who were our collaborators in many original studies.

REFERENCES

1. L. A. Artsimovich, *Controlled Thermonuclear Reactions*, Ed. by A. Kolb and R. S. Pease (Fizmatgiz, Moscow, 1961; Gordon and Breach, New York, 1964).
2. Y. Nakao, T. Honda, Y. Honda, *et al.*, Fusion Technol. **20**, 824 (1991).
3. V. T. Voronchev, V. I. Kukulin, and V. M. Krasnopolsky, Nucl. Fusion **24**, 1117 (1984).
4. G. H. Miley, H. Towner, and N. Ivich, Illinois Univ. Rep., No. COO-2218-17, 1974.
5. W. A. Fowler, G. R. Caughlan, and B. A. Zimmerman, Annu. Rev. Astron. Astrophys. **13**, 69 (1975).
6. J. R. McNally, K. E. Rothe, and R. D. Sharp, Oak Ridge Nat. Lab. Rep., No. ORNL-TM-6914, 1979.
7. S. T. Perkins, A. M. Hansen, and R. J. Howerton, California Univ. Rep. **26**, UCRL-50400 (1984).
8. R. Feldbacher and M. Heindler, Nucl. Instrum. Methods Phys. Res. A **271**, 55 (1988).
9. L. T. Cox, F. B. Mead, and C. K. Choi, Fusion Technol. **18**, 325 (1990).
10. S. N. Abramovich, B. Ya. Guzhovskiĭ, V. A. Zherebtsov, and A. G. Zvenigorodskiĭ, *Nuclear-Physics Constants for Thermonuclear Fusion* (TsNIIatominform, Moscow, 1989).
11. H.-S. Bosch and G. M. Hale, Nucl. Fusion **32**, 611 (1992).
12. R. M. Kulsrud, H. P. Furth, E. J. Valeo, and M. Goldhaber, Phys. Rev. Lett. **49**, 1248 (1982).
13. J. S. Zhang, K. F. Liu, and G. W. Shuy, Phys. Rev. C **60**, 054614 (1999).
14. J. R. McNally, in *Proceedings of the 2nd International Conference on Emerging Nuclear Energy Systems, Lausanna, 1980.*
15. F. Ajzenberg-Selove, Nucl. Phys. A **413**, 1 (1984).
16. V. T. Voronchev, V. I. Kukulin, V. M. Krasnopol'skiĭ, and P. L. Polyakov, Yad. Fiz. **37**, 271 (1983) [Sov. J. Nucl. Phys. **37**, 161 (1983)].
17. R. M. Kulsrud, E. J. Valeo, and S. C. Cowley, Nucl. Fusion **26**, 1443 (1986).
18. R. M. More, Phys. Rev. Lett. **51**, 396 (1983).
19. J. J. Lodder, Phys. Lett. A **98A**, 179 (1983).
20. G. Kamelander, Atomkernenerg./Kerntech. **45**, 200 (1984).

21. T. Takahashi and Y. Nakao, Report No. NIFS-592 (Nat. Inst. Fusion Research, Nagoya, 1999).
22. F. E. Cecil, D. M. Cole, F. J. Wilkinson III, and S. S. Medley, Nucl. Instrum. Methods Phys. Res. B **10/11**, 411 (1985).
23. M. Hagler and M. Kristiansen, *An Introduction to Controlled Thermonuclear Fusion* (Lexington Books, Lexington, 1977; Mir, Moscow, 1980).
24. J. R. McNally, Nucl. Fusion **18**, 133 (1978).
25. C. Powell, J. Nering, B. C. Maglich, and A. Wilmerding, Nucl. Instrum. Methods Phys. Res. A **271**, 41 (1988).
26. T. Honda, Y. Nakao, Y. Honda, *et al.*, Nucl. Fusion **31**, 851 (1991).
27. M. Yamagiwa, Nucl. Sci. Eng. **125**, 218 (1997).
28. A. Chatterjee, E. Takada, M. Torikoshi, and M. Kanazawa, Nucl. Phys. A **616**, 478 (1997).
29. W. R. Fundamenski and A. A. Harms, Fusion Technol. **29**, 313 (1996).
30. R. V. Kulsrud, Nucl. Instrum. Methods Phys. Res. A **271**, 4 (1988).
31. B. P. Ad'yasevich and D. E. Fomenko, Yad. Fiz. **9**, 283 (1969) [Sov. J. Nucl. Phys. **9**, 167 (1969)]; B. P. Ad'yasevich *et al.*, Yad. Fiz. **33**, 601 (1981) [Sov. J. Nucl. Phys. **33**, 313 (1981)].
32. H. M. Hofmann and D. Fick, Phys. Rev. Lett. **52**, 2038 (1984).
33. G. W. Shuy, A. E. Dabiri, and H. Guraol, Fusion Technol. **9**, 459 (1986).
34. G. W. Shuy and D. Dobrott, Science Applications Int. Corp. Report, No. APPAT-20, 1983.
35. L. J. Wittenberg, J. F. Santarius, and G. L. Kulcinski, Fusion Technol. **10**, 167 (1986).
36. V. M. Krasnopolsky, V. T. Voronchev, and V. I. Kukulin, Nucl. Fusion **28**, 2135 (1988).
37. J. R. McNally, Nucl. Data Sci. Technol., Proc. Symp. **2**, 41 (1973).
38. E. P. Velikhov, V. A. Glukhikh, V. V. Gur'ev, *et al.*, At. Énerg. **45**, 3 (1978).
39. S. Cherubini, V. N. Kondratyev, M. Lattuada, *et al.*, Astrophys. J. **457**, 855 (1996).
40. G. Baur, Phys. Lett. B **178**, 135 (1986).
41. A. J. Elwyn and J. E. Monahan, Phys. Rev. C **19**, 2114 (1979).
42. K. Czersky *et al.*, Phys. Rev. C **55**, 1517 (1997).
43. N. Austern, *Direct Nuclear Reaction Theory* (New York, 1970).
44. V. I. Kukulin, V. M. Krasnopolsky, and V. T. Voronchev, Laser Part. Beams **5**, 399 (1987).
45. M. Kamal, V. I. Kukulin, and V. T. Voronchev, Vopr. At. Nauki Tekh., Ser. Termoyad. Sintez, No. 3, 37 (1989).
46. W. Kernbichler and M. Heindler, Nucl. Instrum. Methods Phys. Res. A **271**, 65 (1988).
47. Y. Nakao, V. N. Voronchev, Y. Tabaru, *et al.*, in *Proceedings of the International Conference on Plasma Physics, Nagoya, 1996*, Vol. 2, p. 1774.
48. Y. Nakao *et al.*, J. Nucl. Sci. Technol. **30**, 18 (1993).
49. J. R. McNally, Nucl. Instrum. Methods Phys. Res. A **271**, 5 (1988); Nucl. Fusion **11**, 187 (1971).
50. K. M. Nollett, M. Lemoine, and D. N. Schramm, Phys. Rev. C **56**, 1144 (1997).
51. J. R. McNally, Nucl. Technol./Fusion **2**, 9 (1982).
52. N. Rostoker, M. W. Binderbauer, and H. J. Monkhorst, Science **278**, 1419 (1997).
53. D. C. Moreau, Nucl. Fusion **17**, 13 (1977).
54. A. B. Kukushkin and V. I. Kogan, Fiz. Plazmy **5**, 1264 (1979) [Sov. J. Plasma Phys. **5**, 708 (1979)].
55. J. D. Gordon, T. K. Samec, S. A. Freije, and B. I. Hauss, Nucl. Technol./Fusion **4**, 348 (1983).
56. J. R. McNally, Oak Ridge Nat. Lab. Report, No. ORNL-TM-3233, 1970.
57. W. Kernbichler, R. Feldbacher, and M. Heindler, in *Proceedings of the 10th International Conference on Plasma Physics and Controlled Nuclear Fusion Research, London, 1984*, Vol. 3, p. 429.
58. G. H. Miley and H. Hora, in *Proceedings of the 2nd International Symposium on Aneutronic Power, Washington, 1989.*
59. J. M. Martínez-Val, S. Eliezer, M. Piera, and G. Velarde, Phys. Lett. A **216**, 142 (1996).
60. H. J. Monkhorst, N. Rostoker, and M. W. Binderbauer, in *Proceedings of the Mini-Conference on Advanced Fuels for Fusion, 1998*, Paper R8M3.09.
61. A. J. Elwyn, J. E. Monahan, and J. P. Schiffer, Nucl. Fusion **11**, 551 (1971).
62. A. J. Sierk and T. A. Tombrello, Nucl. Phys. A **210**, 341 (1973).
63. J. R. McNally, Nucl. Fusion **11**, 554 (1971).
64. V. T. Voronchev, V. I. Kukulin, V. N. Pomerantsev, and G. G. Ryzhikh, Few-Body Syst. **18**, 191 (1995).
65. V. T. Voronchev, V. I. Kukulin, V. N. Pomerantsev, *et al.*, Yad. Fiz. **57**, 1964 (1994) [Phys. At. Nucl. **57**, 1890 (1994)].
66. C. R. Brune, W. H. Geist, H. J. Karwowski, *et al.*, Phys. Rev. C **57**, 3437 (1998).
67. G. Gamow, Z. Phys. **51**, 204 (1928).
68. J. E. Monahan, A. J. Elwyn, and F. J. D. Serduke, Nucl. Phys. A **269**, 61 (1976).
69. V. I. Kukulin, M. Kamal, V. T. Voronchev, and V. M. Krasnopolsky, J. Phys. G **10**, L213 (1984).
70. V. T. Voronchev, V. I. Kukulin, V. M. Krasnopolsky, *et al.*, Mem. Fac. Eng., Kyushu Univ. **50**, 517 (1990).
71. N. Rowley and A. C. Merchant, Astrophys. J. **381**, 591 (1991).
72. V. I. Kukulin, V. M. Krasnopolsky, V. T. Voronchev, and P. B. Sazonov, Nucl. Phys. A **417**, 128 (1984); **453**, 365 (1986).
73. V. I. Kukulin, V. T. Voronchev, T. D. Kaipov, and R. A. Eramzhyan, Nucl. Phys. A **517**, 221 (1990).
74. V. I. Kukulin and G. G. Ryzhikh, Prog. Part. Nucl. Phys. **34**, 397 (1995).
75. R. V. Reid, Ann. Phys. (N.Y.) **50**, 393 (1968).
76. L. D. Landau and E. M. Lifshitz, *Quantum Mechanics: Non-Relativistic Theory* (Nauka, Moscow, 1974; Pergamon, New York, 1987).
77. A. J. Elwyn, J. E. Monahan, and F. J. D. Serduke, Nucl. Sci. Eng. **63**, 343 (1977).

78. V. I. Kukulin, in *Proceedings of the 2nd International Workshop on Nuclear Research at the UKP-2 Accelerator, Almaty, 1998*, p. 16.
79. R. S. Mackintosh, S. G. Cooper, and V. I. Kukulin, Nucl. Phys. A **645**, 399 (1999).
80. S. G. Cooper, V. I. Kukulin, R. S. Mackintosh, and E. V. Kuznetsova, Phys. Rev. C **58**, R31 (1998).
81. F. E. Cecil, R. F. Fahlsing, and R. A. Nelson, Nucl. Phys. A **376**, 379 (1982).
82. F. E. Cecil, R. J. Peterson, and P. D. Kunz, Nucl. Phys. A **441**, 477 (1985).
83. A. J. Elwyn, R. E. Holland, C. N. Davids, *et al*., Phys. Rev. C **16**, 1744 (1977).
84. S. S. Medley and H. Hendel, Bull. Am. Phys. Soc. **26**, 980 (1982).
85. F. E. Cecil and D. E. Newman, Nucl. Instrum. Methods Phys. Res. A **221**, 449 (1984).
86. A. Fubini and M. Haegi, Fusion Technol. **25**, 330 (1994).
87. R. A. Lerche, M. D. Cable, and P. G. Dendooven, in *Proceedings of the 2nd International Conference on Laser Interaction and Related Plasma Phenomena, Osaka, 1995*, p. 527.

Translated by A. Isaakyan

Physics of Atomic Nuclei, Vol. 63, No. 12, 2000, pp. 2067–2072. From Yadernaya Fizika, Vol. 63, No. 12, 2000, pp. 2163–2168.

NUCLEI
Experiment

Study of the Gamma Emission from the 31-yr Isomer of ^{178}Hf Induced by X-Ray Irradiation*

C. B. Collins[1], F. Davanloo[1], M. C. Iosif[1], R. Dussart[1], J. M. Hicks[1], S. A. Karamian, C. A. Ur[2], I. I. Popescu[2], V. I. Kirischuk[3], J. M. Pouvesle[4], P. McDaniel[5], and C. E. Crist[6]**

Joint Institute for Nuclear Research, Dubna, Moscow oblast, 141980 Russia

Received September 20, 1999; in final form, January 14, 2000

Abstract—A sample containing 6.3×10^{14} nuclei of the 16^+ isomer of ^{178}Hf having a half-life of 31 yr and an excitation energy of 2.446 MeV was irradiated with x-ray pulses from a device operated at 15 mA to produce bremsstrahlung with an endpoint energy of 90 keV. The gamma spectra of the isomeric target were taken with a Ge detector. The intensity of the 325.5-keV ($6^+ \longrightarrow 4^+$) transition in the ground-state band of ^{178}Hf was found to increase by about 2%. Such an enhanced decay of the ^{178}Hf isomer is consistent with an integrated cross section value of 3×10^{-23} cm^2 keV if resonance absorption occurs within energy ranges corresponding to the maxima of the x-ray flux, either near 20 keV or at the energies of the characteristic emission lines of *W.*

1. INTRODUCTION

The four- and five-quasiparticle isomers of Lu, Hf, and Ta are of interest because they have relatively long lifetimes for states at excitation energies of 2 to 3 MeV. They are referred to as *K* isomers because spontaneous radiative decay is hindered by structural changes forbidden by *K*-quantum numbers. In this mass region, nuclei are deformed and the projection of the total angular momentum onto the symmetry axis contributes this quantum number *K*, which can change by no more than the multipolarity of the electromagnetic transition. Decays from a high-*K* isomer to the rotational states of a low-*K* band are forbidden; therefore, a relatively long lifetime is inevitable. The most interesting example may be the 31-yr, four-quasiparticle ^{178}Hf isomer having an excitation energy of 2.446 MeV.

Proposals to trigger the energy release of a nuclear isomer by exciting it to some higher level associated with freely radiating states have been known for over a decade [1]. To be efficient, such schemes should be applied at an energy near that of the *K*-mixing state of the isomer. It was proposed in [1] to use the resonant absorption of x rays from a bremsstrahlung source to excite some fraction of a high-*K* isomeric population to the *K*-mixing level. Then, the decay to the ground state via one or more γ cascades could subsequently release the total energy of the isomer plus that of the absorbed trigger photon. The types of *K*-mixing states needed in such schemes to induce the decay of nuclear isomers have been reported [2] in ^{180}Ta and described in ^{174}Hf and other isomers [3].

In 1999, the use of soft x-ray irradiation to enhance the decay of the ^{178}Hf isomer was reported in [4, 5]. In that study, the continuous x-ray spectrum was most intense in the range between 20 and 60 keV. While the energy of the particular component causing the transition that initiated the process was not determined, the data were analyzed under the assumption that the energy lies near the 40-keV mean value of the spectral distribution.

The two-step process leading to the excitation of the intermediate level and following the decay to the ground state is assumed here to be the same as earlier for ^{180m}Ta [2]. The integrated cross section of $\sigma\Gamma \approx 10^{-25}$ cm^2 keV measured for ^{180m}Ta corresponds to the presence of an activation level of width $\Gamma \approx 0.5$ eV. The same width assumed for ^{178m_2}Hf leads to $\sigma\Gamma \approx 10^{-21}$ cm^2 keV when the cross section in the Breit–Wigner resonance is used. This is in accord with the experimental results reported in [4, 5], but the rescaling from ^{180m}Ta to ^{178m_2}Hf looks straightforward. The level schemes of the two nuclei are very different, and so are the energy and the wavelength of the incident radiation: nearly 3 MeV for ^{180}Ta [2] and about 40 keV for ^{178}Hf [4, 5]. The integrated cross section (ICS) for photon resonance absorp-

* This article was submitted by the authors in English.

[1] Center for Quantum Electronics, University of Texas at Dallas, Richardson, USA.
[2] H. Hulubei National Institute of Physics and Nuclear Engineering and IGE Foundation, Bucharest, Romania.
[3] Institute for Nuclear Research, National Academy of Sciences of Ukraine, pr. Nauki 47, UA-252028 Kiev, Ukraine.
[4] GREMI, CNRS–Universite d'Orleans, France.
[5] Air Force Research Laboratory, DEPA, Kirtland Air Force Base, Albuquerque, New Mexico, USA.
[6] Sandia National Laboratory, Albuquerque, New Mexico, USA.
** e-mail: karamian@cv.jinr.dubna.su

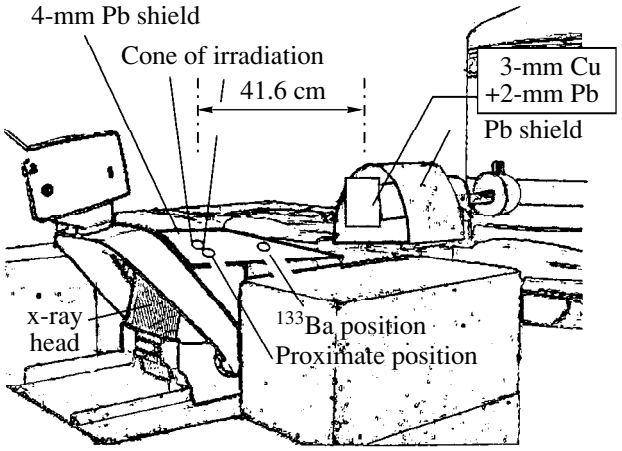

Fig. 1. Scheme of the experimental arrangement showing the geometric placements and dimensions of the components.

tion has been recently discussed in [6], and the possibility of modifying the recommended equations was concluded. More experimental information is necessary for calibrating ICS at photon energies in the region $E_\gamma <$ 100 keV.

On the other hand, the systematics of nuclear transition strengths do not predict the widths of levels as large as those known from the ^{180m}Ta experiment [2] and obtained for ^{178m_2}Hf [4, 5]. The value of $\Gamma = 0.5$ eV corresponds to a short lifetime ($\approx 10^{-15}$ s), while a typical lifetime of nuclear states at excitation energies of 2 to 3 MeV is two orders of magnitude greater. Accordingly, $\sigma\Gamma \approx 3 \times 10^{-27}$ cm^2 keV could be predicted for ^{180m}Ta by using the value of $B(E1) = 0.01$ Weisskopf units recommended in systematics. This is lower than the experimental value by one order of magnitude. The corresponding disagreement is even more impressive in the ^{178}Hf case, mainly because of the deficit of levels with appropriate quantum numbers for the decay of the high-spin intermediate state excited after the absorption of a photon by the ^{178m_2}Hf isomer. As a consequence, the properties of intermediate *K*-mixing states appear as an extraordinary phenomenon that naturally stimulates more focused studies. In particular, more details on the enhancement of the decay of the ^{178m_2}Hf isomer are necessary in order to clarify the mechanism of the x-ray induced deexcitation of the isomer. By focusing upon a confirmation of the work previously reported [4, 5], while extending it to include a study of a fragment of a cascade not present in the spontaneous decay of the isomer, the present study is aimed at meeting these requirements.

2. EXPERIMENTAL DETAILS

The experimental work was performed at the Center for Quantum Electronics, University of Texas at Dallas. The irradiating bremsstrahlung beam was provided by an x-ray unit operated at 15 mA and an endpoint energy up to 90 keV. The device was operated in a way that ensured a duty cycle for the irradiation of about 0.6%.

The irradiated sample consisted of a sealed plastic target containing 6.3×10^{14} ^{178m_2}Hf isomeric nuclei placed in a 1-cm diameter well. The main radioactive contaminants in the sample were the ^{172}Hf nuclide and its daughters at a level of activity comparable to the intensity of the 31-yr spontaneous decay of the ^{178}Hf isomer. The sample was placed at 5.5-cm distance from the emission point of the x-rays, and the only absorption was due to the glass of the x-ray tube and the 2-mm plastic sealing of the x-ray device. The absorption in the sealing of the sample was negligible.

Figure 1 shows the experimental arrangement. The HP coaxial Ge detector was placed at 41.6-cm distance from the sample being irradiated. The detector had the efficiency of 10% relative to the standard NaI for ^{60}Co lines. A shielding built of 3-mm Cu and 2-mm Pb was used in order to prevent detection of scattered x-rays in the Ge detector. Thus, the pulse rate of scattered x-rays allowed to get into the detector was measured to be about 1500 counts/s. The count rate produced by the radioactive target in the absence of the x-rays was about 4000 counts/s. Such an experimental arrangement resulted in a low value of the total dead time of the acquisition tract of about 9% during the irradiation. The energy and efficiency calibration of the Ge detector was done using standard calibration sources, ^{60}Co, ^{133}Ba, and ^{137}Cs. We estimated the maximum absolute detection efficiency to be of about 1.5×10^{-4} at a γ-ray energy near 300 keV in the described geometry with absorbers.

Data acquisition was enabled only when a signal was presented from a *p–i–n* diode which monitored the x-ray beam. The signal from the diode was processed in order to produce a 4-ms gate centered on the burst of the x-ray flux. We recorded γ-ray energies up to 2 MeV with amplification set to give 0.25 keV/channel, allowing for a good analysis of the possible admixtures in the lines of interest. Spectra were stored during each three hours and gain matched using internal γ lines before adding them in order to compensate a weak variation (within 0.05%) of the electronics gain.

Special attention was devoted to the measurement of the incident x-ray flux. For this purpose, the x-ray device was aligned to direct the flux to the Ge detector placed at 8.2-m distance. The direct x-ray flux could reach the active area of the detector only through a 1-mm-diameter hole placed near the detector. High count rate still required the application of absorbers for the measurement of the direct radiation spectrum. The final spectra could be reconstructed from a few mea-

surements with different absorbers. They are shown in Fig. 2 for two conditions, with and without a 2.7-mm equivalent thickness of Al available for covering the output window. The spectrum taken with 1.5-mm Cu absorber is given in the inset. It was one of the component measurements from which the composite spectrum was assembled. In previous work [4, 5], the ^{178m_2}Hf sample was irradiated with the presence of the Al absorber between x-ray tube and the sample, while in the experiment reported here it had been removed. One can see from curve *1* in Fig. 2 that there is a high intensity, above 4×10^{11} photons cm^{-2} keV^{-1} s^{-1}, at low energies near 20 keV; drastic decrease of the intensity with increasing E_x values; and a clear manifestation of the characteristic *K-X* lines of *W* (material of the converter in the x-ray device). All these special features of the incident radiation are important for conclusively determining the integrated cross section, as discussed below.

3. RESULTS

Acquired with the Ge detector, spectra of the induced emission of γ radiation generally resembled those obtained in the earlier work [4, 5]. However, in the present experiment, normalization of the spectra taken with and without x-ray irradiation was facilitated by the deliberate inclusion of lines from the ^{133}Ba source placed near the Hf target, but not irradiated. Those fiducial lines were within about 30 keV of the 325.5-keV ($6^+ \longrightarrow 4^+$) component of the ground-state band (GSB) and therefore reduced any effects of a drift or a nonlinear energy dependence of the efficiency. An empty target holder, the "blank," of a mass and construction similar to the one carrying the isomeric nuclei was available for use. Comparative measurements showed that over 95% of the elastic and inelastic scattering of the irradiating beam arose from the mass of the holder, not from its contents.

Three geometric arrangements were important during the collection of data: (1) "inbeam," when the isomeric target was centered in the cone of irradiation as shown in Fig. 1; (2) "outbeam," when the target was placed out of the beam of x-rays at the position denoted as "proximate" in Fig. 1 and the "blank" target holder replaced it in the cone of irradiation; and (3) "baseline," when the isomeric target was placed in the position of the cone of irradiation, but the x-ray source was turned off. During analysis, both inbeam and outbeam spectra were scaled to the baseline spectrum, so that the areas of the fiducial line in each spectra were the same.

Figure 3 shows the results of 16 h of acquisition time, during which there were 340 s of actual counting time enabled by the gate coincident with the detection of x-rays. From top to bottom are shown the inbeam, outbeam, and baseline spectra: when the spectra were subtracted, the data were acquired so that the total numbers of photons collected in the 356.0-keV line of ^{133}Ba

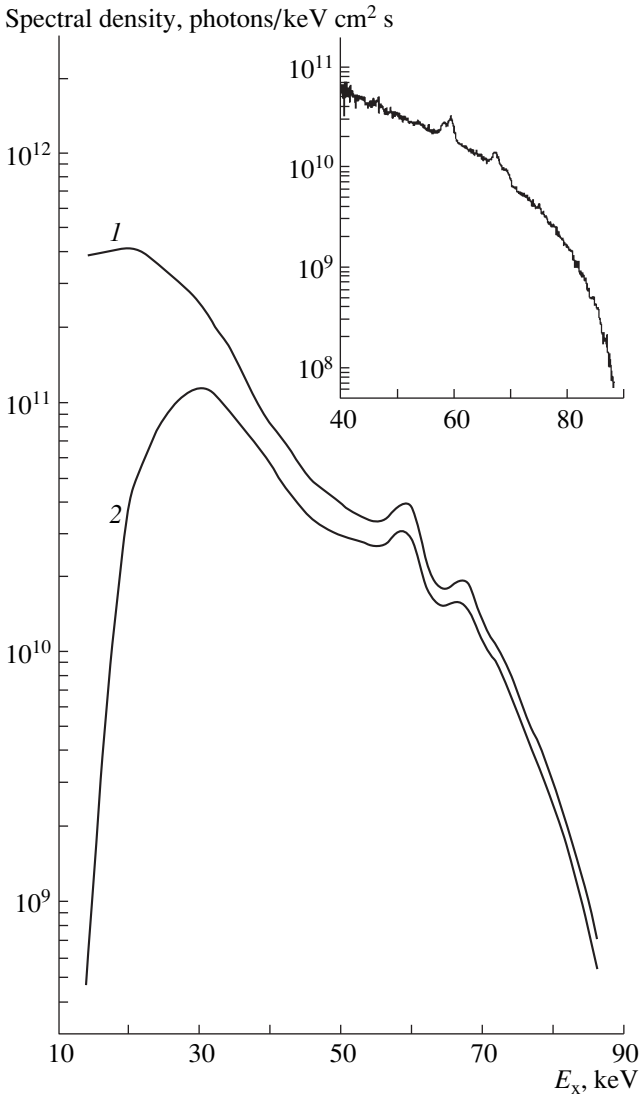

Fig. 2. Photon spectral flux expected at the inbeam position of the isomeric target. These experimental data for a 90-keV endpoint were measured by using a Ge detector from input attenuated with a pin hole and placed at 8.2-m distance from the x-ray tube. The radiation spectra correspond to this experiment (curve *1*) and the measurements in [4, 5] (curve *2*), where the Al absorber was used. The inset shows the raw data taken with a 1.5-mm Cu absorber.

were as nearly equal as could be arranged. The counts in the areas under the relevant peaks are summarized in Tables 1 and 2. In this case, more counts were used for a better accuracy of the baseline spectrum accumulated.

It was mentioned above that the efficiency of the γ-ray detection had a maximum near 300 keV, decreasing to lower energies due to a presence of absorbers and to higher energies due to an intrinsic efficiency of the Ge detector. Accordingly, in this series of measurements, we concentrated to detect the enhancement of the 325.5-keV line providing the best resolution and reasonably good statistics. Some other lines of the ^{178m_2}Hf

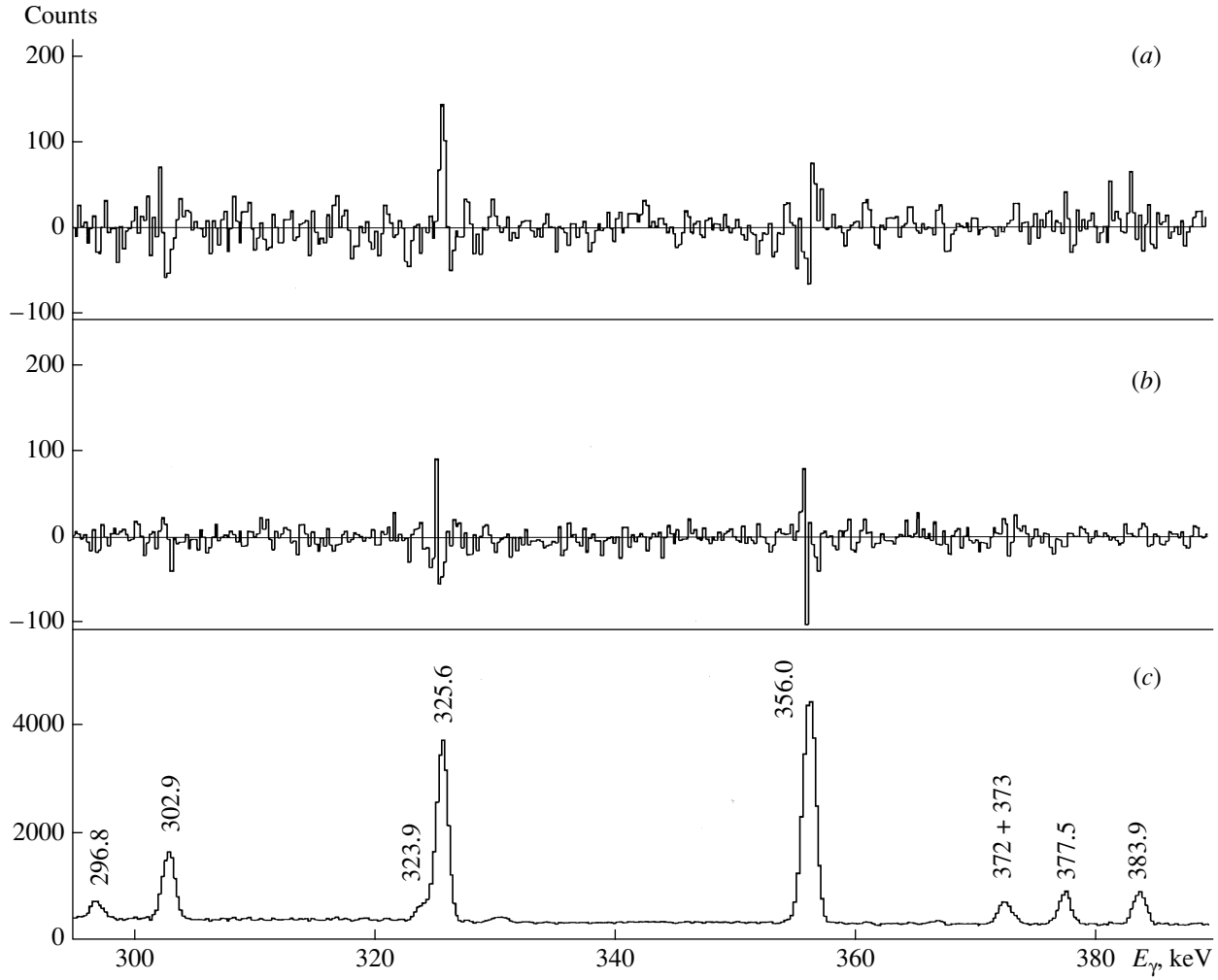

Fig. 3. Spectra of the ^{178m_2}Hf from the irradiated target: (*a*) target inbeam minus scaled baseline, (*b*) target outbeam minus scaled baseline, and (*c*) baseline spectrum. The region shown could be dependably normalized by comparing the areas under the 356.0-keV line of ^{133}Ba and included the 325.5-keV ($6^+ \longrightarrow 4^+$) component of the GSB of ^{178}Hf.

decay could be also enhanced (for instance 213.4 and 426.6 keV) under irradiation, but a statistical accuracy for them was lower than that for the 325.5-keV line.

In addition, the difficulties in establishing precise fiducial lines exist in other regions of the spectra; differences in areas under peaks could not be attained with the same high level of confidence as accomplished for the 325.5-keV line. Previous reports [4, 5] suggested that not all components of the spontaneous decay cascade were enhanced by the x-rays. If several transitions feeding the GSB in spontaneous decay are not enhanced, there naturally arises the question of what channels are involved in the induced decay of the isomer.

An analysis of the spectra suggested several "new" components, some of them were obviously seen in the spectra stored during 1998 series of experiments, but the statistics was not enough to discuss them in papers [4, 5]. Figure 4 shows the best of such lines observed in the experiment reported here for E_γ = 210.6 keV. The line 210.3 keV was known as a member of the $K^\pi = 6^+$ band in ^{178}Hf, but it was not previously seen in spontaneous decay of the isomer [7]. Other transitions by this band were observed neither for the ^{178m_2}Hf decay previously nor in present measurement.

According to [7], very weak line of ^{172}Lu should be detected at E_γ = 210.28 keV, and it was really seen in the baseline spectrum. However, its intensity, being in agreement with [7], was fourfold lower than that in the spectrum taken "inbeam." Thus, the 210.6-keV line shown in Fig. 4 cannot be explained by a contribution from ^{172}Lu.

4. DISCUSSIONS AND CONCLUSION

The first reports [4, 5] of the great cross section for the decay of the ^{178m_2}Hf isomer induced by low-energy

Table 1. Comparison of the gamma emission from the target irradiated at the inbeam position with the baseline obtained without irradiation

E_γ, keV	Nucleus	With irradiation area	Baseline		Excess, counts
			area	norm. area*	
296.8	^{178}Hf	1692 (68)	14925 (201)	1685 (27)	7 (73)
302.9	^{133}Ba	6503 (103)	58052 (304)	6554 (64)	−51 (121)
323.9	^{172}Lu	1403 (71)	12891 (222)	1455 (28)	−52 (76)
325.5	^{178}Hf	17035 (146)	147952 (451)	16703 (148)	332 (208)**
356.0	^{133}Ba	22617 (180)	200333 (482)	Normalizing line	
372 + 373	^{172}Lu	2439 (84)	21860 (250)	2468 (90)	−29 (123)
377.5	^{172}Lu	3098 (75)	27445 (225)	3098 (36)	0 (83)
383.8	^{133}Ba	3225 (76)	28160 (261)	3179 (40)	46 (86)

* Normalized to the 356-keV line of ^{133}Ba. Statistical inaccuracy of normalization is included.

** Estimation of the effect: (2.0 ± 1.2)%.

Table 2. Comparison of gamma emission acquired from the target in the outbeam geometry with the baseline obtained without irradiation (normalization is identical to that in Table 1)

E_γ, keV	Nucleus	Outbeam area	Baseline		Excess, counts
			area	norm. area	
296.8	^{178}Hf	785 (52)	20826 (262)	832 (14)	−47 (54)
302.9	^{133}Ba	3021 (70)	75754 (352)	3028 (36)	−7 (79)
323.9	^{172}Lu	722 (49)	17737 (250)	709 (13)	13 (51)
325.5	^{178}Hf	7961 (103)	199062 (517)	7957 (88)	4 (135)
356.0	^{133}Ba	10408 (110)	260372 (551)	Normalizing line	
372 + 373	^{172}Lu	1258 (57)	29652 (284)	1185 (55)	73 (79)
377.5	^{172}Lu	1428 (51)	36429 (260)	1456 (19)	−28 (54)
383.8	^{133}Ba	1509 (52)	36928 (261)	1476 (19)	33 (55)

Table 3. Integrated cross section $\sigma\Gamma$ calculated from a 2% enhancement of the 325.5-keV ^{178m_2}Hf line under the assumption of different activation-energy values

E_x, keV	20	30	40	50	$K_{\alpha 1}$ (W)*	60	$K_{\beta 1}$ (W)*	70
$\sigma\Gamma$, cm^2 keV Flux with no filter	3.2×10^{-23}	5.4×10^{-23}	1.6×10^{-22}	3.4×10^{-22}	1.6×10^{-23}	3.9×10^{-22}	3.3×10^{-23}	1.1×10^{-21}
$\sigma\Gamma$, cm^2 keV Flux with 2.7-mm Al filter	3.5×10^{-22}	1.2×10^{-22}	2.4×10^{-22}**	4.5×10^{-22}	2.0×10^{-23}	4.7×10^{-22}	4.0×10^{-23}	1.3×10^{-21}

* Under the assumption that the natural width of the emission line is 50 eV.

** For a comparison with [5].

x-rays seems to be unexpected because it was not predicted by any model. The problem has not been resolved by the results of the experiment reported here. However, some illumination of the unexpected nature of the phenomenon has been realized, it is still instructive to examine the details.

Of prime importance is the fact that general phenomenology has been reproduced in accordance with [4, 5]. Table 1 shows that with the same type of small x-ray generator traditionally used in dental medicine enhancements of the order of 2% can be induced in the rate of spontaneous decay of the Hf isomer. As can be seen from Table 2, there is no comparable value of a spurious enhancement found when the empty target holder was irradiated while the ^{178m_2}Hf sample was

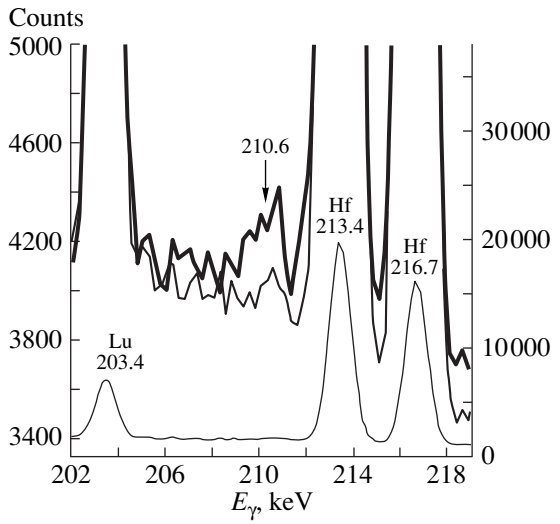

Fig. 4. Spectra obtained under the different conditions. From top to bottom: inbeam spectrum, baseline spectrum normalized to the previous one by the peak counts in the 213.4 line (left scale for both), and full range baseline spectrum (right scale). The FWHM values for the marked peaks are 1.10, 0.91, 1.06, and 1.04 keV from left to right, as given by the fit.

placed in the outbeam geometry. The excess counts in the 325.5-keV line are essentially zero, as can be seen as well in Fig. 3.

The yield of triggering events would equal the product of the number of isomeric atoms in the target, the spectral flux density from Fig. 2 at the appropriate energy, and the unknown integrated cross section, $\sigma\Gamma$, for the branch of the excitation of a *K*-mixing level that ends in a state other than that of the initial isomer. Since each quantity is known, except for the integrated cross section for the "triggering branch," the latter one can be obtained if the transition energy is estimated. Possible values of $\sigma\Gamma$ are summarized in Table 3. The specific value of $\sigma\Gamma$ is strongly dependent on the position of an intermediate level because of the strong variation of the x-ray flux with energy. Assuming the resonance band lies near the maxima of flux, one can derive $\sigma\Gamma \approx (2\text{–}3) \times 10^{-23}$ cm^2 keV. The emission lines of *W* were detected in the x-ray spectrum with resolution of 0.9 keV. The natural width is much smaller, and, in reality, the flux is respectively higher in the characteristic X-ray peaks.

For the case of isomeric ^{178}Hf, we have confirmed that the irradiation by photons with the energy of the order of 20–60 keV can induce the prompt release of the 2.446 MeV stored by the isomer into freely radiating states. This is an energy gain of about 60.

Further research is needed to provide greater precision to the measurements of the transition energy to the *K*-mixing level and to clarify properties of the cascade feeding the GSB. Such data will then facilitate a better understanding of these first evidences of the triggering of induced gamma emission from the 31-yr isomer of ^{178}Hf with very low energy photons through large integrated cross sections, $\sigma\Gamma \geq 2 \times 10^{-23}$ cm^2 keV.

ACKNOWLEDGMENTS

We are grateful to the US Air Force Office of Scientific Research's European Office of Aerospace Research and Development (EOARD) (contract no. F61708-98-W0027) and the US Air Force Office of Scientific Research (AFOSR contract no. F49620-99-1-0082) for support of this experiment; we also gratefully acknowledge the supportive efforts of our particular colleagues, students, and staff members, who assisted so generously in the collection and analysis of the data.

REFERENCES

1. C. B. Collins *et al.*, J. Appl. Phys. **53**, 4645 (1982).
2. C. B. Collins, C. D. Eberhard, J. W. Glesener, and J. A. Anderson, Phys. Rev. C **37**, 2267 (1988).
3. P. M. Walker *et al.*, Phys. Lett. B **408**, 42 (1997).
4. C. B. Collins *et al.*, Phys. Rev. Lett. **82**, 695 (1999).
5. C. B. Collins *et al.*, Laser Phys. **9**, 8 (1999).
6. S. A. Karamian, Invited Talk at LASERS'99 Conference, Quebec, Canada, 1999.
7. NNDC Online Data Service, Brookhaven National Laboratory, http://www.nndc.bnl.gov

Physics of Atomic Nuclei, Vol. 63, No. 12, 2000, pp. 2073–2078. From Yadernaya Fizika, Vol. 63, No. 12, 2000, pp. 2169–2174.

NUCLEI
Theory

Investigating the Hydrogen Atom in Crossed External Fields by the Method of Moments*

V. A. Gani[1), **] and V. M. Weinberg[***]

Institute of Theoretical and Experimental Physics, Bol'shaya Cheremushkinskaya ul. 25, Moscow, 117259 Russia

Received February 9, 2000; in final form, April 26, 2000

Abstract—Recurrence relations of perturbation theory for the hydrogen ground state are obtained. With the aid of these relations, polarizabilities in constant mutually perpendicular electric and magnetic fields are computed up to the 80th order of perturbation theory. The high-order asymptotic expression is compared with its semiclassical estimate. For the case of an arbitrary relative orientation of external fields, a general sixth-order formula is given. The energy and the width of the ground state are obtained by means of a perturbation-series summation. © *2000 MAIK "Nauka/Interperiodica".*

1. INTRODUCTION

The hydrogen atom in constant uniform electric and magnetic fields still remains the subject of theoretical investigations. For example, the authors of [1] developed a recurrent nonperturbative method for constructing a convergent double series representing the exact wave function of the hydrogen atom in a magnetic field. For a more extensive discussion of the problem, the reader is referred to the review article of Lisitsa [2].

The well-known technical problem of the impossibility of separating the variables only stimulates the application of new investigation methods, including perturbative ones. The method of moments, which was first used to treat perturbatively an anharmonic oscillator [3], does not require separating relevant variables. The recent application of this method to the Zeeman effect problem [4] allowed a check of the behavior of the high-order asymptotic expression for a perturbation series. Independently of [3], the method of moments was developed by Fernandez and Castro [5] in a form similar to that used in [4]. It was then applied to the hydrogen atom in parallel electric and magnetic fields [6]; later on, the Zeeman effect problem was considered for four sequences of hydrogen-atom states [7].

It seems even more important to apply it to the hydrogen atom in crossed electric ($\vec{\mathscr{E}}$) and magnetic ($\vec{\mathscr{H}}$) fields because only initial terms of power expansion in terms of $\vec{\mathscr{E}}$ and $\vec{\mathscr{H}}$ have hitherto been considered for this case [8–12]. As will be shown in the present study, the method of moments permits computing sufficiently high orders of this expansion.

The high-order asymptotic behavior can be obtained by using the imaginary-time method [13–15]. This asymptotic behavior is determined by the contribution of an extreme subbarrier classical trajectory to the atom-ionization probability [16, 17]. A pair of extreme paths replaces this trajectory at some value of the ratio of external fields, $\gamma = \mathscr{H}/\mathscr{E}$. The γ dependence of high-order terms in a perturbation series reflects this change of extreme trajectory and should be especially sharp for mutually perpendicular external fields. This is the case that we study here.

2. RECURRENT EVALUATION OF A PERTURBATION SERIES

Let us consider the ground state of the hydrogen atom placed in mutually perpendicular electric and magnetic fields. These fields are assumed to be constant and uniform. We restrict ourselves to the nonrelativistic approximation and neglect the electron spin. From the outset, we attempt to simplify numerical computations and to achieve a sufficiently high order of perturbation theory. For this purpose, we treat γ as a fixed parameter, replacing the double expansion in external fields by the single-variable series

$$\psi = \sum_{k=0}^{\infty} \mathscr{E}^k |k\rangle, \quad E = \sum_{j=0}^{\infty} E_{2j}^{\perp} \mathscr{E}^{2j}, \tag{1}$$

where the wave-function corrections $|k\rangle$ and hyperpolarizabilities $E_k^{\perp}$ depend on γ. We also introduce circular coordinates

$$x_{\pm} = x \pm iy;$$

after that, all relations given below will have real coefficients. In terms of these coordinates, the Hamiltonian

* This article was submitted by the authors in English.

1) Moscow State Engineering Physics Institute (Technical University), Kashirskoe sh. 31, Moscow, 115409 Russia.
** e-mail: gani@heron.itep.ru
*** e-mail: wein@vxitep.itep.ru

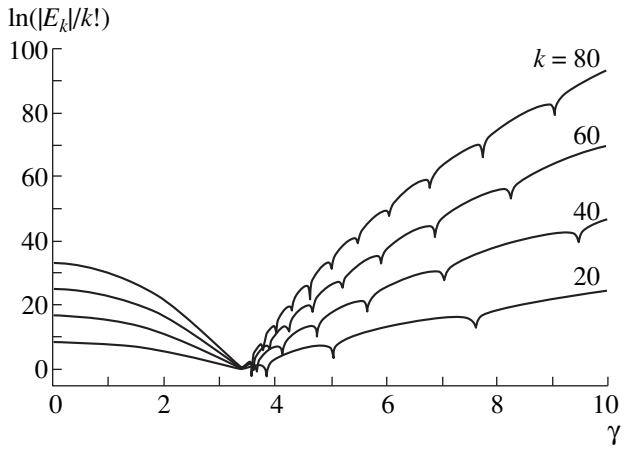

Fig. 1. Functions $f_k(\gamma) = \ln(|E_k^{\perp}|/k!)$ resulting from the recurrently computed hyperpolarizabilities.

of the problem in question has the form

$$\hat{H} = \hat{H}_0 + \mathscr{E}\hat{H}_1 + \mathscr{E}^2\hat{H}_2, \quad \hat{H}_0 = -\frac{1}{2}\Delta - \frac{1}{r},$$

$$\hat{H}_1 = x + \frac{\gamma}{2}\hat{L}_z = \frac{1}{2}(x_+ + x_-) + \frac{\gamma}{2}\left(x_+\frac{\partial}{\partial x_+} - x_-\frac{\partial}{\partial x_-}\right), \quad (2)$$

$$\hat{H}_2 = \frac{\gamma^2}{8}(x^2 + y^2) = \frac{\gamma^2}{8}x_+x_-.$$

We use atomic units. The electric and magnetic fields are measured in the units of $\mathscr{E}_{at} = m^2e^5/\hbar^4 = 5.142 \times 10^9$ V/cm and $\mathscr{H}_{at} = m^2e^3c/\hbar^3 = 2.35 \times 10^9$ G, respectively. The wave-function correction of order k satisfies the differential equation

$$(\hat{H}_0 - E_0)|k\rangle = -\hat{H}_1|k-1\rangle - \hat{H}_2|k-2\rangle + \sum_{j=1}^{[k/2]} E_{2j}^{\perp}|k-2j\rangle. \quad (3)$$

In just the same way as in other problems to which the method of moments was used [3, 4], it is easy to transform Eq. (3) into the algebraic relation between the moments of order k:

$$P_{\sigma\alpha\beta}^k = \langle 0|r^{\sigma-\alpha-\beta}x_+^{\alpha}x_-^{\beta}|k\rangle. \quad (4)$$

Multiplying (3) from the left by $\langle 0|r^{\sigma-\alpha-\beta}x_+^{\alpha}x_-^{\beta}$ and considering that the Hamiltonian is Hermitian, we obtain the recurrence relation

$$\frac{1}{2}(\sigma-\alpha-\beta)(\sigma+\alpha+\beta+1)P_{\sigma-2,\alpha\beta}^k + 2\alpha\beta P_{\sigma-2,\alpha-1,\beta-1}^k - \sigma P_{\sigma-1,\alpha\beta}^k = R_{\sigma\alpha\beta}^k, \quad (5)$$

where

$$R_{\sigma\alpha\beta}^k \equiv \frac{1}{2}[P_{\sigma+1,\alpha+1,\beta}^{k-1} + P_{\sigma+1,\alpha,\beta+1}^{k-1} + \gamma(\alpha-\beta)P_{\sigma\alpha\beta}^{k-1}] + \frac{\gamma^2}{8}P_{\sigma+2,\alpha+1,\beta+1}^{k-2} - \sum_{j=1}^{[k/2]} E_{2j}^{\perp}P_{\sigma\alpha\beta}^{k-2j}.$$

The right-hand side of relation (5) and hyperpolarizability $E_k^{\perp}$ depend only on the moments of preceding orders. As was usually done in the method of moments [3], the following orthogonality condition is accepted:

$$\langle 0|k\rangle = \delta_{0,k} \longrightarrow P_{0,0,0}^k = \delta_{0,k}. \quad (6)$$

An expression for hyperpolarizability arises from (5) at $\sigma = \alpha = \beta = 0$ and even k:

$$E_k^{\perp} = \frac{1}{2}(P_{1,1,0}^{k-1} + P_{1,0,1}^{k-1}) + \frac{\gamma^2}{8}P_{2,1,1}^{k-2}. \quad (7)$$

The closed system of recurrence relations (5)–(7) enables us to calculate, at least in principle, an arbitrary high order of the perturbation theory. The computation starts from

$$P_{\sigma\alpha\beta}^0 = \frac{(\sigma+2)!\alpha!}{2^{\sigma+1-\alpha}(2\alpha+1)!!}\delta_{\alpha\beta}.$$

The sequence of manipulations is similar to that used in [4] to compute Zeeman shift of a nondegenerate state. At every order k, only moments $P_{\sigma\alpha\beta}^k$ from the sector $\sigma \geq \alpha + \beta - 1$, $\alpha \geq 0$, $\beta \geq 0$ are necessary. They are evaluated by successively increasing of σ, α, and β values with the use of relation (5).

We have obtained hyperpolarizabilities in mutually perpendicular fields up to the 80th order of perturbation theory. This order is large enough to compare the dependence of these coefficients on γ (see Fig. 1), with the predictions following from semiclassical considerations. One can see from Fig. 1 that the function $f_k(\gamma) \equiv \ln(|E_k^{\perp}|/k!)$ has two features. It has a minimum at $\gamma \approx 3.4$ and a sequence of singular points to the right of this point. Note that the function $E_k^{\perp}(\gamma)$ changes its sign at every singular point of $f_k(\gamma)$.

3. HIGH-ORDER ASYMPTOTIC BEHAVIOR

It is well known [16] that the dispersion equation relates the asymptotic expression of high-order coefficients $E_k^{\perp}$ to the ionization probability of the atom, i.e., to the penetrability of the potential barrier. This relation is a consequence of the fact that the energy eigenvalue $E = E_0(\mathscr{E}^2) - (i/2)\Gamma(\mathscr{E}^2)$ has essential singularity at $\mathscr{E}^2 = 0$ and a cut along $\mathscr{E}^2 > 0$ semiaxis. (Similarly,

$E(\mathcal{H}^2)$ has essential singularity at $\mathcal{H} = 0$ and a cut along $\mathcal{H}^2 < 0$.)

To evaluate the ionization probability Γ, the imaginary-time method was previously developed [13–15]. The leading term of the asymptotic expression $\tilde{E}_k^{\perp}$ of the $E_k^{\perp}$ coefficients at $k \longrightarrow \infty$ is determined by the classical subbarrier path with extremal value of the abbreviated action. Time takes complex values during this subbarrier motion. There are two kinds of complex classical trajectories. As in the Stark effect case, the ionization may be induced by the electric field in the case of the stabilizing effect of the magnetic field. The path of this kind produces the asymptotic expression

$$\tilde{E}_k^{\perp}(\gamma) \sim k! a^k(\gamma), \quad k \text{ is even.} \tag{8}$$

This asymptotic expression is applicable at a moderate magnetic field for γ below some critical value γ_c. According to [18], $\gamma_c = 3.54$ for mutually perpendicular external fields. It is possible to penetrate through the barrier also at $\mathcal{H}^2 < 0$ as in the Zeeman effect problem. Subbarrier trajectories of this kind are responsible for the form of $\tilde{E}_k^{\perp}(\gamma)$ in the opposite case, $\gamma > \gamma_c$. This change of asymptotic expression explains the origin of the left minimum in Fig. 1.

To obtain an estimate for the function $a(\gamma)$ entering into $\tilde{E}_k^{\perp}$, we apply the results of [18, 19] and represent here some necessary expressions for the special case of mutually perpendicular external fields. For more general considerations related to arbitrary $\vec{\mathscr{E}}$ and $\vec{\mathcal{H}}$ mutual orientation, see [18].

The time τ of subbarrier motion satisfies the equation [19]

$$\tau^2 - (\tau\coth\tau - 1)^2 = \gamma^2, \tag{9}$$

which has a set of solutions $\tau_n = in\pi + \tau_n'$. The minimum value of the imaginary part of the subbarrier action is provided by τ_0 for $\gamma < \gamma_c$ and by a pair of solutions $\tau_{\pm 1}$ for $\gamma > \gamma_c$. In the region $\gamma < \gamma_c$, the energy half-width is

$$\Gamma(\mathscr{E}^2) = \frac{B(\gamma)}{\mathscr{E}}\exp\left[-\frac{2g(\gamma)}{3\mathscr{E}}\right],$$
$$g(\gamma) = \frac{3\tau}{2\gamma^3}(\gamma^2 - \sqrt{\tau^2 - \gamma^2}). \tag{10}$$

The dispersion relation in $\mathscr{E}^2$ then leads to

$$\tilde{E}_{2j}^{\perp} = -\frac{1}{2\pi}\int_0^{\infty}\frac{\Gamma(z)dz}{z^{j+1}} \sim (2j)! a^{2j}, \tag{11}$$

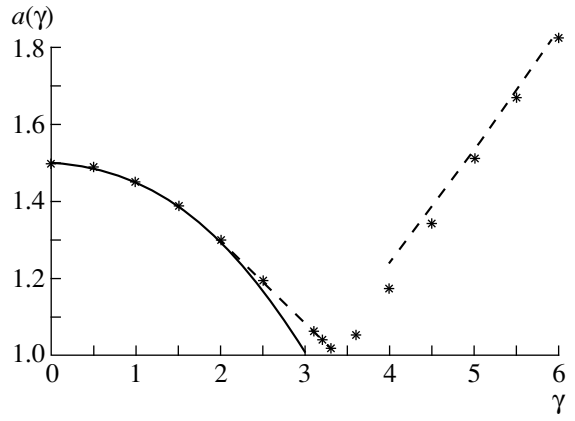

Fig. 2. Parameter $a(\gamma)$ of the perturbation-series asymptotic behavior. The solid line follows from the semiclassical estimate at $\gamma \ll 1$ [see (13)]; the same estimate for $\gamma \gg 1$ is shown by dashed lines [see (14) and (15)]. Values obtained numerically are denoted by asterisks.

where

$$a(\gamma) = \frac{3}{2g(\gamma)}. \tag{12}$$

The last equality is valid also in the region $\gamma > \gamma_c$, where $g(\gamma)$ and $a(\gamma)$ are complex functions. At $\gamma < \gamma_c$, the resulting approximate expressions for $a(\gamma)$ are

$$a(\gamma) = \frac{3}{2}\left(1 - \frac{1}{30}\gamma^2 - \frac{71}{2100}\gamma^4 + \ldots\right), \quad \gamma \ll 1; \tag{13}$$

$$a(\gamma) \simeq \frac{4\gamma^3}{(\gamma^2 - 1)^2(1 - 2e^{-\gamma^2 - 1})}, \quad \gamma \gg 1. \tag{14}$$

In the region $\gamma > \gamma_c$, another representation is applicable:

$$|a(\gamma)| = \frac{\gamma}{\pi}\left[1 - \frac{2}{\gamma^2} + \left(\frac{8\pi^2}{3} + 3\right)\frac{1}{\gamma^4} + \ldots\right]. \tag{15}$$

On the other hand, in the limit of large k, the following simple relation appropriate for numerical evaluation holds:

$$\ln|a(\gamma)| = \frac{d}{dk}\ln\frac{|E_k|}{k!}. \tag{16}$$

Evaluating $a(\gamma)$ above γ_c, we used smoothed function $E_k^{\perp}(\gamma)$ excluding the nodes vicinities. Figure 2 shows the function $a(\gamma)$ obtained numerically in such a manner as compared to expressions (13)–(15).

Now we turn to the region $\gamma > \gamma_c$. Two solutions of Eq. (9), τ_1 and τ_{-1}, lead to complex conjugate values of $g(\gamma)$. Substituting approximate τ_1 value into second expression (10), we obtain the phase of the function

$a(\gamma)$ in the form

$$\arg(a) = -\arg(g) = -\frac{\pi}{2} + \alpha(\gamma),$$

$$\alpha(\gamma) = \frac{2}{\gamma} - \frac{\pi^2 + 2}{3\gamma^3} + O(1/\gamma^5).$$

Finally, the sign-alternating asymptotic behavior arises:

$$\tilde{E}_{2j}^{\perp} = 2|B(\gamma)|(2j)!|a|^{2j+1} \times \cos\left[(2j+1)\left(-\frac{\pi}{2} + \alpha(\gamma)\right) + \beta(\gamma)\right] \sim (-1)^j (2j)!|a|^{2j+1} \sin[(2j+1)\alpha(\gamma) + \beta(\gamma)], \quad j \gg 1. \tag{17}$$

Here, $\beta(\gamma) = \arg(B)$ is the phase of the preexponential factor. Its relative contribution to the total phase decreases as $1/j$.

When the perturbation theory order $2j$ is fixed and γ increases, expression (17) changes its sign at every point where the argument of the sinus turns to zero. This could explain the singular points in Fig. 1 in terms of the asymptotic expression. But rather lengthy calculations are required to establish a detailed quantitative relationship between asymptotic expression (17) and exact $E_{2j}^{\perp}$ coefficients including node vicinities. A simple approximate expression for $\alpha(\gamma)$ is not enough for this aim.

4. CROSSED EXTERNAL FIELDS OF ARBITRARY MUTUAL ORIENTATION

For the general case of the ground-state-energy expansion in powers of crossed external fields, the term of the fourth power was known for a long time [9]:

$$E = -\frac{1}{2} + \sum_{j=1}^{\infty} E^{(2j)}, \quad E^{(2)} = -\frac{9}{4}\vec{\mathscr{E}}^2 + \frac{1}{4}\vec{\mathscr{H}}^2, \tag{18}$$

$$E^{(4)} = -\frac{3555}{64}\vec{\mathscr{E}}^4 + \frac{159}{32}\vec{\mathscr{E}}^2\vec{\mathscr{H}}^2 + \frac{10}{3}[\vec{\mathscr{H}} \times \vec{\mathscr{E}}]^2 - \frac{53}{192}\vec{\mathscr{H}}^4. \tag{19}$$

The value of $E^{(4)}$ is confirmed for mutually perpendicular fields in [12] and for parallel fields in [12, 17, 20]. The $E_4^{\perp}$ coefficient computed by means of recurrence relations (5)–(7) exactly agrees with (19). However, there is a numerical difference between our coefficient $E_6^{\perp}$ and the corresponding quantity from [12]. Therefore, the sixth order of the perturbation theory was analyzed in detail.

The magneto-electric susceptibilities, i.e., coefficients of the double series in powers of external fields, can be easily obtained from hyperpolarizabilities $E_k^{\perp}(\gamma)$. Thus, in the sixth order, taking into account that Stark and Zeeman coefficients are fixed, it is enough to choose four different γ values and to solve a set of four linear equations. As a result we obtain the representation

$$E_6^{\perp} = -\frac{1}{512}\left(2512779 - 521353\gamma^2 + \frac{953869}{27}\gamma^4 - \frac{5581}{9}\gamma^6\right) \equiv \sum_{j=0}^{3} \gamma_{6-2j,2j}^{\perp} (\mathscr{H}/\mathscr{E})^{2j}. \tag{20}$$

(The last identity introduces notation of [12].) Using the linear relation between expansions (1) and (18) and the known magneto-electric susceptibilities in parallel fields [20], it is easy to obtain the following term of series (18):

$$E^{(6)} = -\frac{2512779}{512}\vec{\mathscr{E}}^6 + \frac{254955}{512}\vec{\mathscr{E}}^4\vec{\mathscr{H}}^2 + \frac{133199}{256}\vec{\mathscr{E}}^2[\vec{\mathscr{H}} \times \vec{\mathscr{E}}]^2 - \frac{49195}{1536}\vec{\mathscr{E}}^2\vec{\mathscr{H}}^4 - \frac{255557}{6912}\vec{\mathscr{H}}^2[\vec{\mathscr{H}} \times \vec{\mathscr{E}}]^2 + \frac{5581}{4608}\vec{\mathscr{H}}^6. \tag{21}$$

Some next terms of series (18) can be obtained by the same procedure. Expressions (20) and (21) are convenient to check term by term the sixth-order correction. As follows from [12],

$$\gamma_{24}^{\perp[12]} = -\frac{1610197}{27648} \quad \text{and} \quad \gamma_{42}^{\perp[12]} = \frac{2417015}{1536}, \tag{22}$$

while the results of our computation are

$$\gamma_{24}^{\perp} = -\frac{953869}{13824} \quad \text{and} \quad \gamma_{42}^{\perp} = \frac{521353}{512}. \tag{23}$$

All other coefficients from [12] coincide with our respective results. We carried out an additional independent calculation by means of the method from [9] and obtained

$$\gamma_{24}^{\perp[9]} = -\frac{953869}{13824}. \tag{24}$$

Note that [9] contains complete correction of the sixth power in external fields for the case of parallel fields and only a part of it for the case of perpendicular fields. These "celebrated" sixth-order terms result as a by-product of fourth-order calculations in [9]. The agreement between high-order hyperpolarizabilities $E_k^{\perp}$ and their asymptotic $\tilde{E}_k^{\perp}$ confirms once again the correctness of recurrence relations (5)–(7).

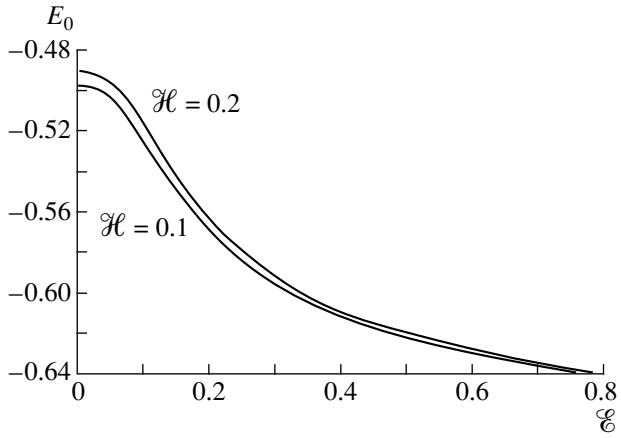

Fig. 3. Real part of the lowest energy eigenvalue of hydrogen atom placed in mutually perpendicular external fields.

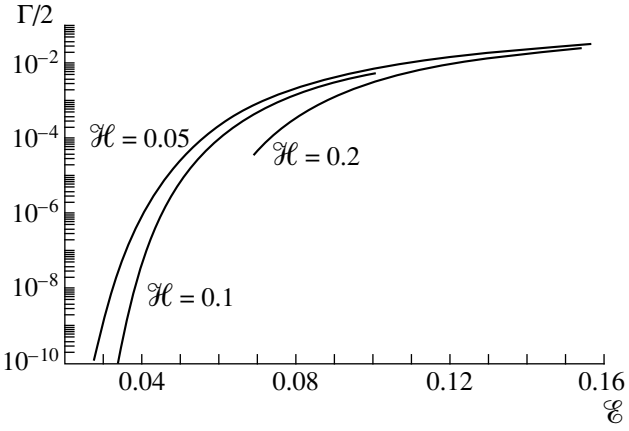

Fig. 4. Half-widths of the lowest hydrogen state in mutually perpendicular external fields.

5. ENERGY AND WIDTH CALCULATION

Summation of the obtained perturbation series was performed with the use of Hermite–Padé approximants, just as it was previously done for the case of Stark effect [21]. Let us recall that this method is based on employing the relation

$$A_L(x)E^2(x) + B_M(x)E(x) + C_N(x) = O(x^{L+M+N+2}), \quad (25)$$

where $x = \mathscr{E}^2$; $E(\mathscr{E}^2)$ is series (1); and $A_L(x)$, $B_M(x)$, and $C_N(x)$ are polynomials of the powers L, M, and N, respectively. Normalization $A_L(0) = 1$ is accepted. First, Eq. (25) is considered as an identity in x, and the resulting system of linear equations is solved for the unknown coefficients of polynomials A_L, B_M, and C_N. Then, Eq. (25) is solved as a quadratic equation for the sum of series $E(\mathscr{E}^2)$. This way, the branching of exact function $E(\mathscr{E}^2)$ at the point of its essential singularity $\mathscr{E}^2 = 0$ is approximately reproduced. In practice, successions of approximants $[L, L, L](\mathscr{E}^2)$ up to $L = 13$ were computed. As an example of their convergence, we note that the obtained energy eigenvalues have five exact decimal digits at $\mathscr{H} = 0.2$, $\mathscr{E} = 0.1$ and three exact decimal digits at $\mathscr{H} = 0.2$, $\mathscr{E} = 0.5$. The resultant ground-state energy and width are presented in Figs. 3 and 4. The magnetic field stabilizes the level diminishing its binding energy and width.

We give now some technical remarks. The energy convergence is worsened in the vicinity of the branching point, at $\mathscr{E} \sim 0.01$–0.07 for $\mathscr{H}$ from 0.05 to 0.2, respectively. At large electric fields, convergence is observed up to $\mathscr{E} \sim 1$. It is rather obvious that the precision of the final result may be increased and the range of fields for which the convergence takes place may be extended by increasing the order of employed approximants. Besides, it appears practically optimal if the maximal order of the approximants used is almost equal to the number of exact decimal digits of $E_k^{\perp}$ coefficients.

6. CONCLUSION

The problem considered above demonstrates once again the high efficiency and convenience of the method of moments. The resulting recurrence relations have allowed advance up to the 80th order of perturbation theory. The high-order asymptotic behavior was also analyzed. Basic parameters of this asymptotic expression are in good agreement with those previously obtained in the semiclassical approximation with the use of the imaginary-time method.

In the problem under consideration, the method of moments can also be applied to excited states as well just as it was previously used for the Zeeman effect case [4]. The most substantial points of this application are the following. The moments

$$P^k_{\sigma\alpha\beta} = \langle\tilde{0}|r^{\sigma-\alpha-\beta}x_+^\alpha x_-^\beta|k\rangle$$
$$\text{with} \quad |\tilde{0}\rangle = e^{im\phi - r/n} = \left(\frac{x_+}{x_-}\right)^{m/2} e^{-r/n} \quad (26)$$

allow consideration of an arbitrary hydrogen state. Note that bra $\langle\tilde{0}|$ in this definition is the nodeless exponential factor of the unperturbed wave function, rather than the unperturbed wave function. The degeneracy of each excited state should be taken into account from the very beginning, i.e., at the stage of $P^0_{\sigma\alpha\beta}$ computation. In the second approximation, a constraint excluding ambiguity of energy correction is introduced. This is enough to uniquely determine the mixing parameters inherited by the moments from the unperturbed wave function.

It is well known that very strong magnetic fields are created by some astrophysical objects. Pulsars possess

a magnetic field up to at least $\mathcal{H} \sim 10^3 \mathcal{H}_{at}$. In addition, magnetic white dwarfs with $\mathcal{H} \sim (0.2–0.5)\mathcal{H}_{at}$ are observed [22, 23]. An atom moving fast in vicinity of such an object is subjected in its rest frame to intense mutually perpendicular electric and magnetic fields. Quasistatic perpendicular fields are also present in the radio waves emitted by a pulsar. These fields may be strong enough near the surface of the radiating star. The possibility of the investigations of the neutron-star atmospheres in the ultraviolet and x-ray ranges of their absorption spectra is discussed in [23].

For astrophysical applications, the properties of hydrogen in crossed external fields were successfully computed in an adiabatic approach with a Landau level as the initial approximation [24]. However, avoided crossings of hydrogen levels give no way to use the adiabatic approximation below $\mathcal{H} \sim 100\mathcal{H}_{at}$. The perturbative approach described above seems to be more appropriate for moderately strong external fields.

ACKNOWLEDGMENTS

We would like to express our deep gratitude to V.S. Popov and A.E. Kudryavtsev for valuable comments. We are grateful to N.L. Manakov, S.I. Marmo, and V.D. Ovsyannikov for correspondence and discussion and to F.M. Fernandez, who drew our attention to the studies reported in [5–7]. Discussion with V.D. Mur is also gratefully acknowledged.

This work was supported in part by the Russian Foundation for Basic Research (project no. 98-02-17007). The work of V. A. Gani was supported by the INTAS (grant no. 96-0457) within the research program of the International Center for Fundamental Physics in Moscow.

REFERENCES

1. Yu. P. Kravchenko, M. A. Liberman, and B. Johansson, Phys. Rev. Lett. **77**, 619 (1996); Phys. Rev. A **54**, 287 (1996).
2. V. S. Lisitsa, Usp. Fiz. Nauk **153**, 379 (1987) [Sov. Phys. Usp. **30**, 927 (1987)].
3. J. P. Ader, Phys. Lett. A **97A**, 178 (1983).
4. V. M. Weinberg, V. A. Gani, and A. E. Kudryavtsev, Zh. Éksp. Teor. Fiz. **113**, 550 (1998) [JETP **86**, 305 (1998)].
5. F. M. Fernández and E. A. Castro, Int. J. Quantum Chem. **26**, 497 (1984).
6. F. M. Fernández and E. A. Castro, Int. J. Quantum Chem. **28**, 603 (1985).
7. F. M. Fernández and J. A. Morález, Phys. Rev. A **46**, 318 (1992).
8. Yu. N. Demkov, B. S. Monozon, and V. N. Ostrovsky, Zh. Éksp. Teor. Fiz. **57**, 1431 (1969) [Sov. Phys. JETP **30**, 775 (1969)].
9. P. Lambin, J. C. van Hay, and E. Kartheuser, Am. J. Phys. **46**, 1144 (1978).
10. E. A. Solov'ev, Zh. Éksp. Teor. Fiz. **85**, 109 (1983) [Sov. Phys. JETP **58**, 63 (1983)].
11. A. V. Turbiner, Zh. Éksp. Teor. Fiz. **84**, 1329 (1983) [Sov. Phys. JETP **57**, 770 (1983)]; Zh. Éksp. Teor. Fiz. **95**, 1152 (1989) [Sov. Phys. JETP **68**, 664 (1989)].
12. N. L. Manakov, S. I. Marmo, and V. D. Ovsyannikov, Zh. Éksp. Teor. Fiz. **91**, 404 (1986) [Sov. Phys. JETP **64**, 236 (1986)].
13. A. M. Perelomov, V. S. Popov, and M. V. Terent'ev, Zh. Éksp. Teor. Fiz. **50**, 1393 (1966) [Sov. Phys. JETP **23**, 924 (1966)]; Zh. Éksp. Teor. Fiz. **51**, 309 (1966) [Sov. Phys. JETP **24**, 207 (1967)].
14. A. M. Perelomov and V. S. Popov, Zh. Éksp. Teor. Fiz. **52**, 514 (1967) [Sov. Phys. JETP **25**, 336 (1967)].
15. V. S. Popov, V. P. Kuznetsov, and A. M. Perelomov, Zh. Éksp. Teor. Fiz. **53**, 331 (1967) [Sov. Phys. JETP **26**, 222 (1968)].
16. C. M. Bender and T. T. Wu, Phys. Rev. D **7**, 1620 (1973).
17. V. S. Popov and A. V. Sergeev, Pis'ma Zh. Éksp. Teor. Fiz. **63**, 398 (1996) [JETP Lett. **63**, 417 (1996)].
18. V. S. Popov and A. V. Sergeev, Zh. Éksp. Teor. Fiz. **113**, 2047 (1998) [JETP **86**, 1122 (1998)].
19. V. S. Popov, B. M. Karnakov, and V. D. Mur, Phys. Lett. A **229**, 306 (1997).
20. B. R. Johnson, K. F. Scheibner, and D. Farrelly, Phys. Rev. Lett. **51**, 2280 (1983).
21. V. M. Weinberg, V. D. Mur, V. S. Popov, and A. V. Sergeev, Zh. Éksp. Teor. Fiz. **93**, 450 (1987) [Sov. Phys. JETP **66**, 258 (1987)].
22. P. Fassbinder and W. Schweizer, Astron. Astrophys. **314**, 700 (1996); Phys. Rev. A **53**, 2135 (1996).
23. G. G. Pavlov *et al.*, in *The Lives of the Neutron Stars*, Ed. by M. Alpar, Ü. Kiziloğlu, and J. van Paradijus (Kluwer, Dordrecht, 1995), p. 71.
24. A. Y. Potekhin, J. Phys. B **27**, 1073 (1994); **31**, 49 (1998).

Physics of Atomic Nuclei, Vol. 63, No. 12, 2000, pp. 2079–2084. Translated from Yadernaya Fizika, Vol. 63, No. 12, 2000, pp. 2175–2180.

NUCLEI
Theory

Energies of Mass-Asymmetric Coulomb Systems

T. K. Rebane and A. V. Filinsky[1)]

Institute of Physics (Petrodvorets Branch), St. Petersburg State University, ul. Ul'yanovskaya 1, Petrodvorets, 198904 Russia

Received May 19, 1999; in final form, October 29, 1999

Abstract—It is found that particle-mass-symmetric and particle-mass-asymmetric Coulomb systems are adiabatically similar. Expressions are proposed for the mass dependence of upper and lower bounds on the energies of asymmetric systems, and an expression approximating these energies is given. The energies of the families of mesic molecules that are adiabatically similar to the mesic molecules $dp\mu$, $tp\mu$, and $td\mu$ are investigated with the aid of these expressions. *© 2000 MAIK "Nauka/Interperiodica".*

1. INTRODUCTION

In [1], precise variational calculations were performed for a large number of three-particle Coulomb systems symmetric in the masses of likely charged particles, and analytic formulas that describe accurately the energies of these systems were constructed on this basis. In the present study, we consider relations between the energies of mass-asymmetric three-particle systems, which have yet to receive adequate study.

The system of three particle having the unit charges of $q_1 = q_2 = \pm 1$ and $q_3 = \mp 1$ and masses m_1, m_2, and m_3 is described by the Hamiltonian

$$H(\mathbf{r}_1, \mathbf{r}_2, \mathbf{r}_3) = -(1/2)[\Delta_1/m_1 + \Delta_2/m_2 + \Delta_3/m_3] + 1/r_{12} - 1/r_{13} - 1/r_{23}. \quad (1)$$

For physical quantities, we use here the system of atomic units ($\hbar = m_e = |e| = 1$). The likely charged particles 1 and 2 are numbered in such a way that $m_1 \geq m_2$. The eigenvalue spectrum of the operator in (1) begins from $E(m_1, m_2, m_3)$, the ground-state energy of the system with a fixed center of mass.

2. UPPER BOUND ON ENERGY

An upper bound on the energy $E(m_1, m_2, m_3)$ of a system asymmetric in the masses of the likely charged particles 1 and 2 can be expressed in terms of the energy of its symmetric analog. Let us consider the operator

$$H(\mathbf{r}_1, \mathbf{r}_2, \mathbf{r}_3; \lambda) = -(1/4)[(\Delta_1 + \Delta_2)(1/m_1 + 1/m_2) + \lambda(\Delta_1 - \Delta_2)(1/m_1 - 1/m_2)] - \Delta_3/2m_3 + 1/r_{12} - 1/r_{13} - 1/r_{23}, \quad (2)$$

which depends on the parameter λ. We denote by $\varepsilon(\lambda)$ its lower eigenvalue. A comparison with (1) shows that the operator in (2) describes the system of particles with masses m_1, m_2, and m_3 at $\lambda = 1$ and the system of two particles 1 and 2 with identical masses equal to $2m_1m_2/(m_1 + m_2)$ at $\lambda = 0$. Hence, the eigenvalues of the operators in (1) and (2) satisfy the equalities

$$\varepsilon(0) = E(2m_1m_2/(m_1 + m_2), 2m_1m_2/(m_1 + m_2), m_3), \quad \varepsilon(1) = E(m_1, m_2, m_3). \quad (3)$$

The reversal of the sign of the parameter λ in (2) corresponds to the interchange of the numbers of particles 1 and 2. Since this does not change the energy of the system, $\varepsilon(\lambda)$ is an even function of λ,

$$\varepsilon(-\lambda) = \varepsilon(\lambda), \quad (4)$$

so that its derivative vanishes at the origin:

$$\varepsilon'(0) = 0. \quad (5)$$

Since the operator in (2) depends on λ linearly, the second derivative of its lowest eigenvalue $\varepsilon(\lambda)$ is nonpositive (see Appendix),

$$\varepsilon''(\lambda) \leq 0. \quad (6)$$

From (5) and (6), it follows that $\varepsilon'(\lambda) \leq 0$ for $\lambda \geq 0$. Hence, the function $\varepsilon(\lambda)$ decreases monotonically in the interval $0 \leq \lambda \leq 1$,

$$\varepsilon(0) \geq \varepsilon(\lambda) \geq \varepsilon(1). \quad (7)$$

Substituting the values of the function $\varepsilon(\lambda)$ at the points $\lambda = 1$ and 0 from (3) into (7), we arrive at

$$E(m_1, m_2, m_3) \leq E(2m_1m_2/(m_1 + m_2), 2m_1m_2/(m_1 + m_2), m_3). \quad (8)$$

This inequality expresses an upper bound on the energy of an asymmetric system involving likely charged particles of unequal masses in terms of the energy of the symmetric system in which the masses of these particles coincide.

3. HAMILTONIAN IN TERMS OF JACOBI COORDINATES

We introduce the scaled Jacobi coordinates

$$\mathbf{s} = [m_1m_2/(m_1 + m_2)](\mathbf{r}_2 - \mathbf{r}_1),$$
$$\mathbf{t} = [m_1m_2m_3/(m_1 + m_2 + m_3)]^{1/2} \times [\mathbf{r}_3 - (m_1\mathbf{r}_1 + m_2\mathbf{r}_2)/(m_1 + m_2)] \quad (9)$$

[1)] Admiral Makarov State Marine Academy, St. Petersburg, Russia.

and rewrite the Hamiltonian (1) of the system of particles with a fixed center of mass in terms of **s** and **t** as

$$H(\mathbf{s}, \mathbf{t}) = [m_1 m_2/(m_1 + m_2)]h(\mathbf{s}, \mathbf{t}), \quad (10)$$

where the operator $h(\mathbf{s}, \mathbf{t})$ is given by

$$\begin{aligned} h(\mathbf{s}, \mathbf{t}) \equiv &- \Delta_s/2 - \Delta_t/2 + 1/|\mathbf{s}| - 2x(m_1, m_2, m_3) \\ &\times [1/|\mathbf{t} + [x(m_1, m_2, m_3) + y(m_1, m_2, m_3)]\mathbf{s}| \\ &+ 1/|\mathbf{t} - [x(m_1, m_2, m_3) - y(m_1, m_2, m_3)]\mathbf{s}|] \end{aligned} \quad (11)$$

and where we have introduced the following two combinations of the particle masses:

$$\begin{aligned} &x(m_1, m_2, m_3) \\ &= [m_3(m_1 + m_2)^2/4m_1 m_2(m_1 + m_2 + m_3)]^{1/2}, \end{aligned} \quad (12)$$

$$\begin{aligned} &y(m_1, m_2, m_3) \\ &= [m_3(m_1 - m_2)^2/4m_1 m_2(m_1 + m_2 + m_3)]^{1/2}. \end{aligned} \quad (13)$$

We will refer to $h(\mathbf{s}, \mathbf{t})$ as the operator of the reduced energy of the system. Its eigenvalues η depend on the particle masses through the quantities x and y and are related to the eigenvalues of the Hamiltonian for the system with a fixed center of mass by the equation

$$\begin{aligned} &E(m_1, m_2, m_3) \\ &= [m_1 m_2/(m_1 + m_2)]\eta(x(m_1, m_2, m_3), y(m_1, m_2, m_3)). \end{aligned} \quad (14)$$

4. ADIABATIC APPROXIMATION

In [2], it was shown that the lowest energy value E_{ad} of a quantum-mechanical system in the adiabatic approximation coincides with its ground-state energy:

$$E_{ad}(m_1, m_2, m_3) \le E(m_1, m_2, m_3). \quad (15)$$

Going over to the adiabatic approximation, where we consider the coordinates **t** and **s** as, respectively, a fast and a slow one, we can represent an approximate eigenfunction of the reduced-energy operator (11) in the form

$$\Psi(\mathbf{t}; \mathbf{s}, x, y) = \psi(\mathbf{t}; \mathbf{s}, x, y)\chi(\mathbf{s}; x), \quad (16)$$

where ψ and χ are the wave functions for, respectively, the fast and the slow subsystem. The wave function ψ for the fast subsystem and the eigenvalue W of its adiabatic energy are determined by the equation

$$\begin{aligned} &\{-\Delta_t/2 - 2x(m_1, m_2, m_3) \\ &\times [1/|\mathbf{t} + [x(m_1, m_2, m_3) + y(m_1, m_2, m_3)]\mathbf{s}| \\ &+ 1/|\mathbf{t} - [x(m_1, m_2, m_3) - y(m_1, m_2, m_3)]\mathbf{s}|]\} \\ &\times \psi(\mathbf{t}; \mathbf{s}, x, y) = W(\mathbf{s}; x)\psi(\mathbf{t}; \mathbf{s}, x, y). \end{aligned} \quad (17)$$

This wave function is dependent on the coordinate **t** playing the role of a dynamical variable and parametrically on the coordinate **s** and the particle-mass combinations x and y. If the vector **s** is fixed, Eq. (17) assumes the form of the Schrödinger equation, in terms of the radius vector **t**, for a particle of charge –1 that moves in the field of two fixed Coulomb centers having the equal charges of $q = 2x(m_1, m_2, m_3)$. These centers are located at the points where the denominators of the fractions in the bracketed expressions on the left-hand side of (17) vanish—that is, at the points whose **t** coordinates are

$$\begin{aligned} \mathbf{t}_1 &= -[x(m_1, m_2, m_3) + y(m_1, m_2, m_3)]\mathbf{s}, \\ \mathbf{t}_2 &= [x(m_1, m_2, m_3) - y(m_1, m_2, m_3)]\mathbf{s}. \end{aligned}$$

They are separated by the distance $R = |\mathbf{t}_2 - \mathbf{t}_1| = 2sx(m_1, m_2, m_3)$. The eigenvalue W of the particle energy depends on the charges q of the centers and on the distance R between them; therefore, this eigenvalue is a function of the quantities s (the absolute value of the vector **s**) and x. At the same time, it is independent of y since a change in y implies parallel translation of the two centers at a fixed distance between them, in which case the particle energy W remains unaffected.

Since W is independent of y, the operator of the reduced energy of the slow subsystem $[-\Delta_s/2 + 1/|\mathbf{s}| + W]$ and its eigenfunction χ do not depend on y either. The function χ, together with the adiabatic reduced-energy levels η_{ad} of the total system, is determined from the equation

$$[-\Delta_s/2 + 1/|\mathbf{s}| + W(s; x)]\chi(\mathbf{s}; x) = \eta_{ad}(x)\chi(\mathbf{s}; x). \quad (18)$$

Since y does not appear in (18), the reduced-energy adiabatic levels depend on the particle masses only through the combination $x(m_1, m_2, m_3)$. Taking into account (14), we find that the adiabatic energy levels of the system are given by

$$\begin{aligned} &E_{ad}(m_1, m_2, m_3) \\ &= [m_1 m_2/(m_1 + m_2)]\eta_{ad}(x(m_1, m_2, m_3)). \end{aligned} \quad (19)$$

A systems of particles with masses m_1, m_2, and m_3 and a system of particles with masses m_1', m_2', and m_3' are referred to as adiabatically similar systems if they are characterized by the same value of x (12); that is,

$$x(m_1, m_2, m_3) = x(m_1', m_2', m_3'), \quad (20)$$

whence it follows that

$$\begin{aligned} &m_3(m_1 + m_2)^2/4m_1 m_2(m_1 + m_2 + m_3) \\ &= m_3'(m_1' + m_2')^2/4m_1' m_2'(m_1' + m_2' + m_3'). \end{aligned} \quad (21)$$

It can be seen from (18) that the ratio of the adiabatic energies of such systems is equal to the ratio of the reduced masses of likely charged particles,

$$\begin{aligned} &E_{ad}(m_1', m_2', m_3') : E_{ad}(m_1, m_2, m_3) \\ &= [m_1' m_2'/(m_1' + m_2')] : [m_1 m_2/(m_1 + m_2)]. \end{aligned} \quad (22)$$

This means that, for the system formed by particles with masses m_1, m_2, and m_3, $E_{ad}(m_1, m_2, m_3)$ determines the adiabatic value of the energy and, hence, a lower

Energies of asymmetric mesic molecules as estimated in terms of the energies of systems that are adiabatically similar to them and which represent, in each case, a symmetric mesic molecule involving nuclei of identical masses and a mesic molecule involving one fixed nucleus (see main body of the text) versus precise results (all energy values are given in atomic units)

Mesic molecules under consideration	Asymmetry parameter u	Energies of symmetric mesic molecules	Energies of mesic molecules with a fixed nucleus	Energies of mesic molecules under consideration	
				estimate on the basis of Eq. (28)	precise results from [4, 5]
$dp\mu$	0.1112615	−105.7065	−108.2807	−105.99	−106.01
$tp\mu$	0.2402140	−106.9404	−109.0532	−107.47	−107.49
$td\mu$	0.0396933	−111.3272	−112.2274	−111.36	−111.36

Note: Precise energy values from [4, 5] were rounded off to five significant decimal places.

bound on the precise energies [see the inequality in (15)] for the entire family of adiabatically similar systems, those that consist of particles whose masses m_1', m_2', and m_3' satisfy Eq. (21).

5. APPROXIMATE EXPRESSION FOR THE ENERGIES OF ADIABATICALLY SIMILAR SYSTEMS

Extending equality (22) from the adiabatic energies E_{ad} to the precise energies E of adiabatically similar systems, we arrive at the approximate relation

$$E(m_1', m_2', m_3') : E(m_1, m_2, m_3) \simeq [m_1'm_2'/(m_1' + m_2')] : [m_1m_2/(m_1 + m_2)]. \quad (23)$$

The form of the operator in (11) indicates that, for the systems under consideration, the measure of inaccuracy of this relation is controlled by the difference of $y(m_1', m_2', m_3')$ and $y(m_1, m_2, m_3)$. Under the condition $y(m_1', m_2', m_3') = y(m_1, m_2, m_3)$, the approximate relation (23) becomes exact.

6. ENERGIES OF THREE FAMILIES OF ADIABATICALLY SIMILAR MESIC MOLECULES

Let us apply relations (8), (22), and (23) to three families of systems that are adiabatically similar to the mesic molecules $dp\mu$, $tp\mu$, and $td\mu$.

Using the values of the muon, proton, deuteron, and triton masses ($m_\mu = 206.76826$, $m_p = 1836.1527$, $m_d = 3670.4830$, $m_t = 5496.9216$), we find that, for these molecules, x and y take the values

$$x(dp\mu) = 0.2017599,\ x(tp\mu) = 0.1911185,$$
$$x(td\mu) = 0.1515551,\ y(dp\mu) = 0.06729878,$$
$$y(tp\mu) = 0.09540891,\ y(td\mu) = 0.03019459.$$

The mesic molecules under consideration belong to three different families of adiabatically similar systems featuring the same third particle (muon, $m_3 = m_\mu$). The quantity x takes the same value for all members of a family, which differ by y values varying in the range $0 \le y < x$. The masses of the first two particles of family members are given by

$$m_1(x, y) = (1 + y^2 - x^2)m_3/[2x(x - y)],$$
$$m_2(x, y) = (1 + y^2 - x^2)m_3/[2x(x + y)]. \quad (24)$$

At $y = 0$, we have a symmetric mesic molecule featuring nuclei of identical masses, $m_1(x, 0) = m_2(x, 0) = (1 - x^2)m_3/2x^2$; at $y = x$, the system reduces to a molecule where an infinitely heavy (immobile) first particle generates the field for the remaining two (mobile) particles, the second particle having the mass $m_2(x, x) = (1 - x^2)m_3/4x^2$ and the charge identical to that of the first particle and a muon, which has an opposite charge.

Upper bounds on the energies of the family members were calculated according to (8). The required energies of symmetric systems with identical masses of the first two particles, $\bar{M} = 2m_1(x, y)m_2(x, y)/(m_1(x, y) + m_2(x, y))$, were calculated by the formula [1]

$$E(\bar{M}, \bar{M}, m_3) = [\bar{M}m_3/(2\bar{M} + m_3)] \sum_{k=0}^{12} C_k [m_3/(2\bar{M} + m_3)]^{k/2}, \quad (25)$$

where $C_0 = -1.20526924$, $C_1 = 0.641781090$, $C_2 = 0.285160388$, $C_3 = -0.177735530$, $C_4 = -0.259757745$, $C_5 = 2.38013126$, $C_6 = -21.1917686$, $C_7 = 113.523948$, $C_8 = -376.094845$, $C_9 = 777.364202$, $C_{10} = -978.197128$, $C_{11} = 687.774491$, and $C_{12} = -207.711422$.

For the members of the above families of mesic molecules, the adiabatic energy values (which coincide with lower bounds on the exact energies) were calculated by formulas (15) and (22) by using the adiabatic energies $E_{ad}(M, M, m)$ computed in [3] for the corresponding symmetric systems, the latter being interpolated in the form

$$E_{ad}(M, M, m_3) = \sum_{k=0}^{7} D_k [m/(2M + m_3)]^{1 + k/2}, \quad (26)$$

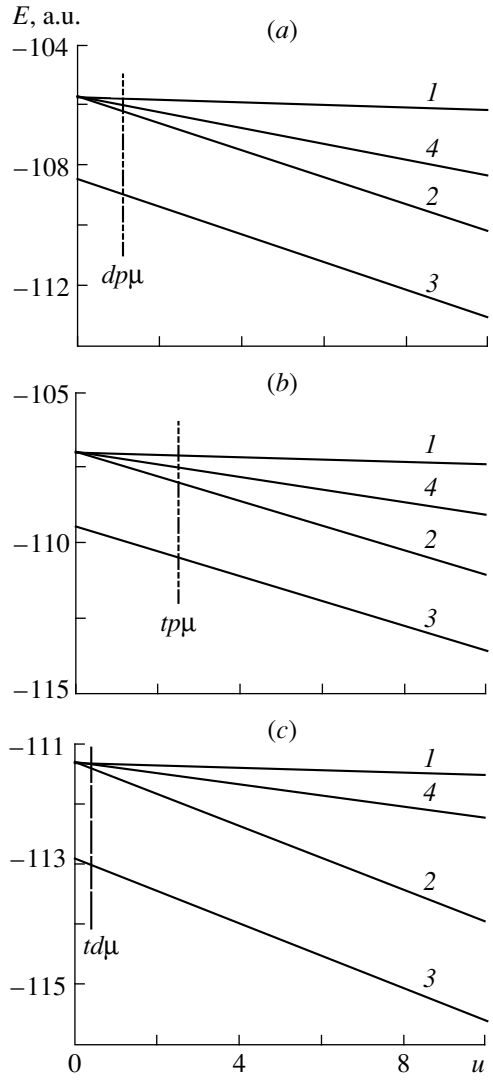

Fig. 1. Ground-state energies of the families of mesic molecules that are adiabatically similar to the (*a*) *dp*μ, (*b*) *tp*μ, and (*c*) *td*μ molecules versus the parameter $u = (m_1 - m_2)^2/(m_1 + m_2)^2$ of the mass asymmetry of likely charged particles. Vertical dashed lines in Figs. 1*a*, 1*b*, and 1*c* correspond to the mesic molecules *dp*μ, *tp*μ, and *td*μ, respectively. Solid curves represent (*1*) the upper bounds according to Eq. (8), (*2*) the estimates according to Eq. (23), (*3*) the adiabatic lower bounds according to Eq. (15), and (*4*) the results of a variational calculation.

where $D_0 = -1.205278$, $D_1 = 0.643267$, $D_2 = -0.499109$, $D_3 = 2.085603$, $D_4 = -27.07942$, $D_5 = 172.0880$, $D_6 = -543.8975$, and $D_7 = 674.7041$.

Taking into account relations (24), we find that the mass of particles 1 and 2 of the symmetric mesic molecule belonging to the family of adiabatically similar systems that is characterized by a given value of x is equal to

$$M = (1 - x^2)m_3/2x^2. \tag{27}$$

Setting $m_1' = m_2' = M$ and $m_3' = m_3 = m_\mu$ in (22) and taking into account (26), we find that, for the energies of the members of a family of adiabatically similar mesic molecules, expression (15) yields the adiabatic lower bound

$$E(m_1, m_2, m_\mu) \geq E_{\text{ad}}(m_1, m_2, m_\mu) = [2m_1m_2/(m_1 + m_2)]\sum_{k=0}^{7} D_k[m_\mu/(2M + m_\mu)]^{1+k/2}, \tag{28}$$

where m_1 and m_2 depend on x and y according to (24), while M is given by (27).

In addition to deriving the above upper and lower bounds on the energies of the systems considered here, we have also calculated the corresponding approximated values on the basis of (23).

The results of our calculations for the families of systems that are adiabatically similar to the mesic molecules *dp*μ, *tp*μ, and *td*μ are presented in Figs. 1*a*, 1*b*, and 1*c*, respectively, along with the variational values obtained for the corresponding energies by using a broad basis of Laguerre functions of the perimetric coordinates of the relevant particles. These results are in perfect agreement with those from [4, 5] for the mesic molecules *dp*μ, *tp*μ, and *td*μ.

From Fig. 1, we can see that the adiabatic lower bound on the energy as given by (15) lies 1.5 to 2.5 a.u. below the precise value. The approximation in (23), which relies on the exact value of the symmetric-molecule energy and which takes into account the property of adiabatic similarity, yields a more accurate lower bound on the energy.

Exact energy values for the members of the families of adiabatically similar mesic molecules lie between the lower bound in (23) and the upper bound in (8). Within five decimal places, the energy values calculated precisely for the mesic molecules *dp*μ, *tp*μ, and *td*μ agree with the arithmetic mean of the above bounds.

As can be seen from the figure, the precise energy values for the members of the families of adiabatically similar systems depend almost linearly on the parameter $u = (y/x)^2 = (m_1 - m_2)^2/(m_1 + m_2)^2$ (which characterizes the mass asymmetry of likely charged particles), and so do the estimates in (8), (15), and (23). This enables us to approximate the energies of adiabatically similar systems by the expression

$$E(m_1(x, y), m_2(x, y), m_3) \simeq (1 - u)E(m_1(x, 0), m_2(x, 0), m_3) + uE(m_1(x, x), m_2(x, x), m_3), \tag{29}$$

where the dependence of the particle masses on the parameters x and y is given by (24). By using the expression for the parameters x, y, and u in terms of the particle masses m_1, m_2, and m_3, we can recast the result presented in (29) in such a way as to obtain an approximate formula that relates the energy of an asymmetric mesic molecule involving particles of arbitrary masses

to the energies of two systems that are adiabatically similar to the system being considered and which represent a mesic molecule symmetric in the masses of the constituent nuclei and a mesic molecule featuring one infinitely heavy nucleus,

$$E(m_1, m_2, m_3) \simeq [4m_1m_2E(M, M, m_3) + (m_1 - m_2)^2E(\infty, m, m_3)]/(m_1 + m_2)^2, \quad (30)$$

where $M = 2m_1m_2/(m_1 + m_2) - (m_1 - m_2)^2m_3/2(m_1 + m_2)^2$ and $m = m_1m_2(m_1 + m_2 + m_3)/(m_1 + m_2)^2$.

This expression was used to estimate the energies of asymmetric mesic molecules. The values that are obtained in this way and which are displayed in the table demonstrate that the approximation in (30) is quite accurate.

6. CONCLUSION

The results presented in this study give sufficient ground to believe that the property of adiabatic similarity can be employed in calculating the energies of Coulomb mesic molecules that are asymmetric in the masses of likely charged particles. That the energy of the members of families of adiabatically similar systems is a nearly linear function of the mass-asymmetry parameter has enabled us to construct a highly accurate formula that expresses the energy of an asymmetric system in terms of the energy of a symmetric mesic molecule and the energy of a mesic molecule involving one infinitely heavy nucleus.

ACKNOWLEDGMENTS

This work was supported by the Russian Foundation for Basic Research (project no. 97-02-16126).

APPENDIX

The inequality in (6) follows from basic equations of perturbation theory. We now consider a quantum-mechanical system whose Hamiltonian depends linearly on a parameter λ; that is,

$$H(\lambda) = L + \lambda W, \quad (A.1)$$

where the operator L is independent of λ.

We will rely on perturbation theory, associating the operator in (A.1) with the Hamiltonian of the unperturbed system [$H^{(0)} = H(\lambda)$] and taking the operator

$$H(\lambda + \delta\lambda) = H(\lambda) + \delta\lambda W \quad (A.2)$$

for the total Hamiltonian of the perturbed system.

Here, we treat W and $\delta\lambda$ as the perturbation operator and the parameter of perturbation, respectively. For the sake of simplicity, we will omit below the dependence of the operators and of the wave functions on dynamical variables, retaining only their dependence on the parameters λ and $\delta\lambda$ (if any).

We assume that, at λ and $\delta\lambda$ values being considered, the ground state of the system at energy $\varepsilon(\lambda + \delta\lambda)$ is bound, so that the wave function $\Psi(\lambda + \delta\lambda)$ is normalized to unity. We expand the lowest eigenvalue $\varepsilon(\lambda + \delta\lambda)$ and the corresponding wave function $\Psi(\lambda + \delta\lambda)$ in a series in powers of the perturbation parameter,

$$\varepsilon(\lambda + \delta\lambda) = \varepsilon^{(0)}(\lambda) + \varepsilon^{(1)}(\lambda)\delta\lambda + \varepsilon^{(2)}(\lambda)(\delta\lambda)^2 + \ldots, \quad (A.3)$$

$$\Psi(\lambda + \delta\lambda) = \Psi^{(0)}(\lambda) + \Psi^{(1)}(\lambda)\delta\lambda + \Psi^{(2)}(\lambda)(\delta\lambda)^2 + \ldots . \quad (A.4)$$

Substituting expansions (A.3) and (A.4) into the equation

$$H(\lambda + \delta\lambda)\Psi(\lambda + \delta\lambda) = \varepsilon(\lambda + \delta\lambda)\Psi(\lambda + \delta\lambda) \quad (A.5)$$

of the relevant eigenvalue problem and equating the coefficient at each power of the parameter $\delta\lambda$ to zero, we arrive at an infinite set of perturbation-theory equations. The first three of these are given by

$$[H(\lambda) - \varepsilon^{(0)}(\lambda)]\Psi^{(0)}(\lambda) = 0, \quad (A.6)$$

$$[H(\lambda) - \varepsilon^{(0)}(\lambda)]\Psi^{(1)}(\lambda) + [W - \varepsilon^{(1)}(\lambda)]\Psi^{(0)}(\lambda) = 0, \quad (A.7)$$

$$[H(\lambda) - \varepsilon^{(0)}(\lambda)]\Psi^{(2)}(\lambda) + [W - \varepsilon^{(1)}(\lambda)]\Psi^{(1)}(\lambda) - \varepsilon^{(2)}(\lambda)\Psi^{(0)}(\lambda) = 0. \quad (A.8)$$

Multiplying Eq. (A.7) by $\Psi^{(1)}(\lambda)$ from the left and integrating the resulting product with respect to dynamical variables, we obtain

$$\langle\Psi^{(1)}(\lambda)|H(\lambda) - \varepsilon^{(0)}(\lambda)|\Psi^{(1)}(\lambda)\rangle + \langle\Psi^{(1)}(\lambda)|W - \varepsilon^{(1)}(\lambda)|\Psi^{(0)}(\lambda)\rangle = 0. \quad (A.9)$$

Since $\varepsilon^{(0)}(\lambda)$ is the lowest eigenvalue of the operator $H(\lambda)$, the operator $[H(\lambda) - \varepsilon^{(0)}(\lambda)]$ is positive definite. Therefore, the first term in (A.9) is nonnegative: it represents the expectation value of the positive-definite operator for the wave function $\Psi^{(1)}(\lambda)$. Hence, the second term on the left-hand side of (A.9) is nonpositive,

$$\langle\Psi^{(1)}(\lambda)|W - \varepsilon^{(1)}(\lambda)|\Psi^{(0)}(\lambda)\rangle \le 0. \quad (A.10)$$

Further, we multiply Eq. (A.9) by $\Psi^{(0)}(\lambda)$ from the left and integrate the resulting product with respect to dynamical variables. By virtue of Eq. (A.6) and the fact that the operator $H(\lambda)$ is self-conjugate, the contribution of the term involving the second-order correction function $\Psi^{(2)}(\lambda)$ vanishes. Considering that the unperturbed wave function is normalized by the condition $\langle\Psi^{(0)}(\lambda)|\Psi^{(0)}(\lambda)\rangle = 1$, we find that the second-order correction to the energy is given by

$$\varepsilon^{(2)}(\lambda) = \langle\Psi^{(1)}(\lambda)|W - \varepsilon^{(1)}(\lambda)|\Psi^{(0)}(\lambda)\rangle. \quad (A.11)$$

From the last two formulas, it follows that the second-order correction to the ground-state energy is nonpositive, $\varepsilon^{(2)}(\lambda) \leq 0$. Taking into account the expansion in (A.3) for the energy, we can say that the second derivative of the ground-state energy with respect to the parameter that enters linearly into the Hamiltonian is indeed nonpositive, $\varepsilon''(\lambda) \leq 0$.

REFERENCES

1. T. K. Rebane and A. V. Filinsky, Yad. Fiz. **60**, 1985 (1997) [Phys. At. Nucl. **60**, 1816 (1997)].
2. V. F. Brattsev, Dokl. Akad. Nauk SSSR **160**, 570 (1965) [Sov. Phys. Dokl. **10**, 44 (1965)].
3. D. S. Bystrov and T. K. Rebane, Khim. Fiz. **5**, 451 (1986).
4. S. I. Vinitskiĭ and L. I. Ponomarev, Fiz. Élem. Chastits At. Yadra **13**, 1336 (1982) [Sov. J. Part. Nucl. **13**, 557 (1982)].
5. I. V. Puzynin and S. I. Vinitsky, Muon Catal. Fusion **3**, 307 (1988).

Translated by O. Chernavskaya

Physics of Atomic Nuclei, Vol. 63, No. 12, 2000, pp. 2085–2090. Translated from Yadernaya Fizika, Vol. 63, No. 12, 2000, pp. 2181–2186.

NUCLEI
Theory

Approach to Studying Three-Body Processes

J. V. Mebonia, M. A. Abusini, P. J. Saralidze, K. I. Sulakadze, and G. É. Skhirtladze

Tbilisi State University, Tbilisi, Georgia

Received August 19, 1999; in final form, April 11, 2000

Abstract—An approach to studying three-body reactions that takes consistently into account the single-collision mechanism is discussed. Specific calculations are performed for elastic and quasielastic nucleon scattering by a deuteron. The ability of the proposed simple approach to account for a wide range of experimental data suggests that it can be applied to more complicated nuclear reactions. *© 2000 MAIK "Nauka/Interperiodica".*

1. INTRODUCTION

Investigation of three-body processes in nonrelativistic scattering theory furnishes important information about fundamental problems in nuclear physics. It is sufficient to mention that many serious difficulties inherent in general many-body problems arise even at the three-body level. We mean here the problem of deriving and solving correct equations. For this reason, not only did the advent of the set of Faddeev integral equations [1] give impetus to a vigorous development of the theory of three-body reactions proper, but it also inspired hopes for evolving a consistent approach to complicated processes.

However, a straightforward application of the Faddeev equations to three-body problems involves technical difficulties. For this reason, theorists usually resort to various approximate schemes. In particular, unitary schemes were proposed in [2–4]. However, these schemes did not become popular because they do not simplify calculations substantially. The method of straightforwardly summing the truncated Watson–Faddeev iteration series [5] also proved to be inefficient.

Two formally different unitary approaches to studying three-body reactions—the cutoff three-body impulse approximation (CTBIA) [6] and the unitarized three-body impulse approximation (UTBIA) [7]—were proposed by one of the present authors (J.V. Mebonia). Either approach is based on consistently taking into account the single-collision mechanism, but the specific implementations of this were different. A method for unitarizing the relevant amplitude on the basis of approximately solving the Faddeev equations in the *K*-matrix formalism was devised within the UTBIA.

Provided that the stringent constraints of the eikonal approximation are met and that the particles constituting the target nucleus are frozen, the differential elastic-scattering cross section calculated within the UTBIA coincides with the well-known Glauber–Sitenko formula [8, 9].

In the CTBIA, it is stated that, under certain conditions, the Faddeev equations can be solved in the *T*-matrix formalism by retaining only first-order terms. However, such terms would correspond to a single collision proper only if the incident particle (say, particle 1) does not interact simultaneously with the two particles forming the bound state (particles 2 and 3). These undesirable interactions can be eliminated by cutting off the Fourier transform of the radial wave function $\varphi(r)$ for the bound state: $G(q) \longrightarrow G(q, R)$, where

$$G(q, R) = \sqrt{2/\pi}\int_R^\infty r^2 dr\varphi(r)\frac{\sin(qr)}{qr}. \qquad (1)$$

The cutoff radius R must be greater than the de Broglie wavelength λ associated with the motion of particle 1 with respect to the (2, 3) system. It can be expressed in terms of the absolute value of the relevant momentum $\boldsymbol{\omega}$ as (see Fig. 1)

$$R = C/|\boldsymbol{\omega}|, \qquad (2)$$

where C is a constant that ensures fulfillment of the requirement $\lambda \le R$. The amplitude for three-body scattering within the CTBIA then assumes the form

$$M_{fi} = \hat{A}\left\langle \Phi_f \middle| \sum_{j=2,3} t_j \middle| \Phi_i \right\rangle, \qquad (3)$$

where t_j is the two-body scattering matrix for particles l and n ($j\,ln$ = 123, 231, 312); Φ_i and Φ_f are the asymptotic functions associated with the initial and the final state, respectively; and $\hat{A}$ is the operator of antisymmetrization with respect to identical particles.

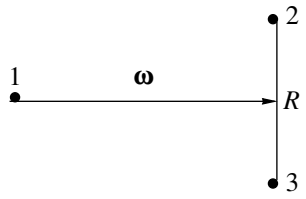

Fig. 1.

1063-7788/00/6312-2085$20.00

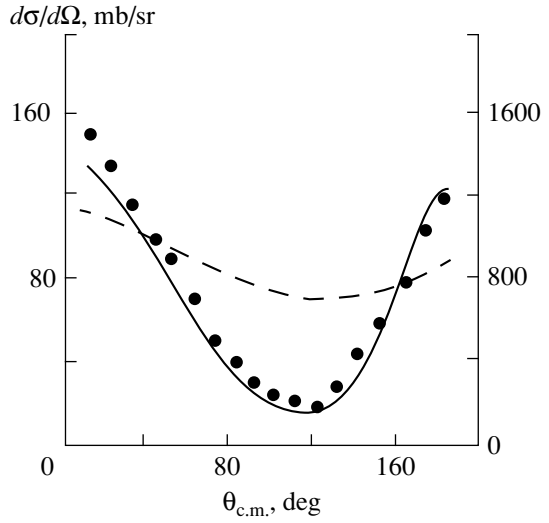

Fig. 2. Differential cross section for elastic *Nd* scattering as a function of the scattering angle $\theta_{c.m.}$ in the c.m. frame at the laboratory incident-neutron energy of E_n = 14.1 MeV. Presented in the figure are the results of the calculations performed (solid curve and left scale) with and (dashed curve and right scale) without a cutoff. The experimental data (left scale) were taken from [19].

This brings up the question of why the cutoff according to Eq. (1) leads to unitarization of the amplitude for single scattering. As early as 1973, Nakamura [10] showed that, in the expansion of the amplitude for three-body scattering in two-particle partial-wave amplitudes, three-particle unitarity is violated by partial-wave amplitudes associated with low orbital angular momenta. For this reason, it was proposed to introduce a cutoff in orbital space. In the semiclassical approximation, the orbital angular momentum, the linear momentum, and the radius vector are related as $L \sim Rk$. Therefore, a cutoff in orbital space at a given value of energy must be equivalent to a cutoff in coordinate space. For this reason, the CTBIA can be considered as a qualitative alternative to the UTBIA, because the latter has a firmer theoretical ground than the former. Nevertheless, the CTBIA proved to be an efficient scheme for treating various three-body processes [11–13]. Later on, the equivalence of the two approaches was proven in [14] for the example of nucleon–deuteron collisions.

The objective of the present study is to test the potential of the CTBIA by extending the analysis of three-body reactions to the cases of the elastic and quasielastic nucleon–deuteron scattering processes $d(N, N)d$ and $d(N, 2N)N$.

2. ELASTIC-SCATTERING PROCESS $d(N, N)d$

The advent of the Faddeev equations initiated intensive investigations into the physics of elastic *Nd* scattering [15–17]. The problem can be solved in a closed form for any realistic nucleon–nucleon (*NN*) potential. These potentials leading to the same results for the on-energy-shell amplitudes of nucleon–nucleon scattering may yield, however, different results for the off-energy-shell amplitudes. The off-energy-shell partial-wave amplitudes are required for solving the Faddeev equations at various energies. Owing to this, a comparison of such solutions obtained with a sufficiently high precision with experimental data may be helpful in choosing between various *NN* potentials. In this respect, valuable information comes not only from the differential cross sections but also from the so-called polarization asymmetry.

There is yet another important possibility associated with studying *Nd* scattering. Such studies make it possible to test various approximate methods for solving three-body problems in order to extend them to more complicated cases. This served as motivation for applying the CTBIA, the simplest unitary scheme, to elastic *Nd* scattering.

Formula (3) implies that the differential cross section for elastic *Nd* scattering in the c.m. frame can be represented in the form

$$\frac{d\sigma}{d\Omega} = (2\pi)^4 \frac{2m^2}{27} \sum_{\text{spins}} |M|^2, \tag{4}$$

where

$$M = \hat{A} \sum_{j=2,3} \int d\mathbf{q} \Psi_d^*(\mathbf{p}) t_j(\boldsymbol{\xi}, \boldsymbol{\eta}; \varepsilon) \Psi_d(\mathbf{p}_0), \tag{5}$$

$$\mathbf{p} = -\frac{\mathbf{k}}{2} - \mathbf{q}, \quad \mathbf{p}_0 = -\frac{\mathbf{k}_0}{2} - \mathbf{q},$$
$$\boldsymbol{\xi} = \mathbf{k} + \frac{\mathbf{q}}{2}, \quad \boldsymbol{\eta} = \mathbf{k}_0 - \frac{\mathbf{q}}{2}, \quad \varepsilon = \frac{3}{4m}(\mathbf{k}^2 - \mathbf{q}^2) - Q, \tag{6}$$

Ψ_d is the total deuteron wave function, m is the nucleon mass, Q is the deuteron binding energy, and $\mathbf{k}_0$ ($\mathbf{k}$) is the momentum of the incident nucleon in the initial (final) state. Summation in formula (4) is performed over the nucleon- and deuteron-spin projections prior to and after a collision event; explicitly, these spin projections, as well as the functions $G(p_0)$ and $G(p_0, R)$, appear after expanding Ψ_d and t_j in partial waves.

We use the system of units in which $\hbar = c = 1$. In our calculation, the two-nucleon off-energy-shell T matrix and the radial part of the deuteron wave function were constructed for the nonlocal separable Mongan potential [18].

We have calculated the differential cross section for elastic *Nd* scattering as a function of the scattering angle $\theta_{c.m.}$ The results of this calculation are displayed in Figs. 2 and 3, along with relevant experimental data at energies 14.1 and 22.7 MeV in the laboratory frame. The solid curve and the left scale show the results obtained within the CTBIA, whereas the dashed curve and the right scale correspond to similar calculations without a cutoff. Experimental data (left scale) were

taken from [19, 20]. In the calculations, we took into account the $^1S_0$, $^1P_1$, $^1D_2$, $^3S_1 + {}^3D_1$, $^3P_0$, $^3P_1$, $^3P_2 + {}^3F_2$, and $^3D_2$ two-nucleon states. However, the eventual results are dominated by the contribution of zero partial-wave amplitudes, since we restrict our consideration to sufficiently low energies.

As can easily be seen, the results that the cutoff-free impulse approximation, which is usually associated with the single-collision mechanism, yields for the differential cross section differ sizably from experimental data both in shape and in magnitude.

On the other hand, even the unitarization procedure as simple as the application of cutoff to the bound-state wave function improves considerably the agreement between the theoretical results and the experimental data. Nevertheless, some qualitative discrepancies still remain. This might have been expected because we use an approximate method for solving the problem. It is quite natural that rigorous calculations on the basis of the Faddeev equations adequately describe elastic *Nd* scattering.

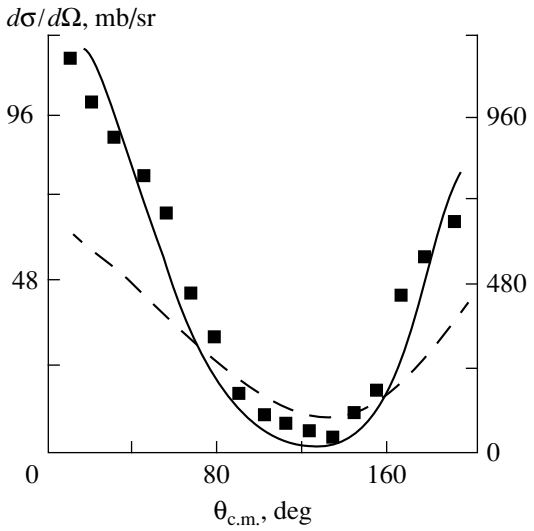

Fig. 3. As in Fig. 2, but for E_n = 22.7 MeV. The experimental data (left scale) were taken from [20].

3. QUASIELASTIC-SCATTERING REACTION $d(N, 2N)N$

All that was said in the preceding section about elastic *Nd* scattering remains in force for the quasielastic-scattering reaction $d(N, 2N)N$. Moreover, the latter reaction offers additional possibilities for studying a three-nucleon system in the region of the continuous spectrum. This allows one to obtain new information about the properties of the two-nucleon off-energy-shell amplitudes. In what follows, we show that, within the CTBIA, the matrix element for the quasielastic-scattering reaction $d(N, 2N)N$ can be expressed directly in terms of the half-off-energy-shell amplitudes for nucleon–nucleon scattering, a circumstance of paramount importance indeed, which renders the analysis of *NN* interactions clearer than the analysis of elastic *Nd* scattering, because, in the latter case, one deals with integrals involving the off-energy-shell *NN* amplitudes [see Eq. (5)] and not the amplitudes themselves. Finally, the reaction $d(N, 2N)N$ represents the simplest process from a wide class of quasielastic-scattering reactions. The majority of such reactions involve rather complex fragments, and the relevant matrix elements are expressed in terms of two-fragment off-energy-shell amplitudes, which are usually determined from experimental data on free fragment scattering. Such a determination is possible only if the difference between the off- and on-energy-shell amplitudes is disregarded or if two-fragment phenomenological potentials are used. It is conceivable that, at moderately low energies, a microscopic description of the interaction between the fragments as composite objects consisting of nucleons is essential. But prior to proceeding to study these reactions at the microscopic level, it is reasonable to test the method to be used by applying it to simpler processes like the reaction $d(N, 2N)N$.

We denote by $\mathbf{k}_0$ the laboratory momentum of the incident nucleon and by $\mathbf{k}_1$, $\mathbf{k}_2$, and $\mathbf{k}_3$ the momenta of the scattered nucleons. Usually, experiments of this type are performed in coplanar geometry, and the quantity subjected to investigation is the differential cross section as a function of the scattering angles of two final-state nucleons and the energy of one of these. The remaining kinematical quantities are determined from the law of energy–momentum conservation.

Within the CTBIA, the differential cross section for the reaction $d(N, 2N)N$ has the form

$$\frac{d^3\sigma}{d\Omega_1 d\Omega_2 dE_1} = \frac{8}{3}\pi^4 m^3 \frac{k_1 k_2^2}{k_0} \frac{\sum_{\text{spins}} |M|^2}{|2k_2 - k_0\cos(\theta_2) + k_1\cos(\theta_1 + \theta_2)|}, \tag{7}$$

where

$$M = \hat{A} \sum_{j=2,3} t_j(\boldsymbol{\xi}_j, \boldsymbol{\eta}_j; \varepsilon_j)\Psi_d(\mathbf{p}_j), \tag{8}$$

$$\boldsymbol{\xi}_j = \frac{1}{2}(\mathbf{k}_n - \mathbf{k}_l); \quad \boldsymbol{\eta}_j = \mathbf{k}_0 - \frac{1}{2}(\mathbf{k}_n + \mathbf{k}_l);$$
$$\varepsilon_j = \xi_j^2/4m; \quad \mathbf{p}_j = \mathbf{k}_n + \mathbf{k}_l - \mathbf{k}_0. \tag{9}$$

The rest of the notation and the computational procedure are identical to those in the preceding section.

Measurements are usually performed in such a way that the scattering angles are fixed, so that the differential cross section is determined as a function of the energy E_1 of one of the recorded nucleons. In recent years, however, measurements often determine the differential cross section as a function of the so-called arc

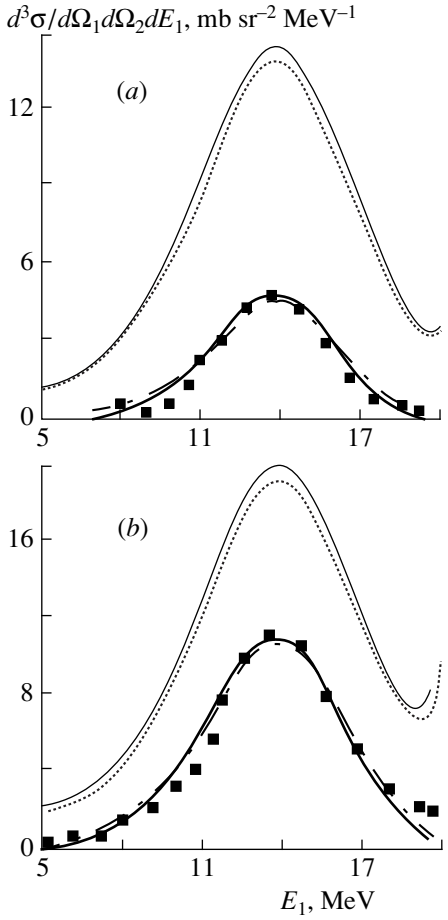

Fig. 4. Differential cross sections for the reactions (*a*) $d(p, 2p)n$ and (*b*) $d(p, pn)p$ as functions of the energy E_1 of a recorded proton at scattering angles of $\theta_1 = 42.5°$ and $\theta_2 = -42.5°$ and the incident-proton energy of $E_0 = 30$ MeV. Solid curves represent the results of the calculations that were performed (thick curves) with and (thin curves) without a cutoff and which take into account all phase shifts in each case. Dash-dotted and dotted curves correspond to similar calculations that were performed, respectively, with and without a cutoff and which take into account only the $\mathcal{S}$-wave phase shifts in each case. The experimental data were taken from (*a*) [25] and (*b*) [26].

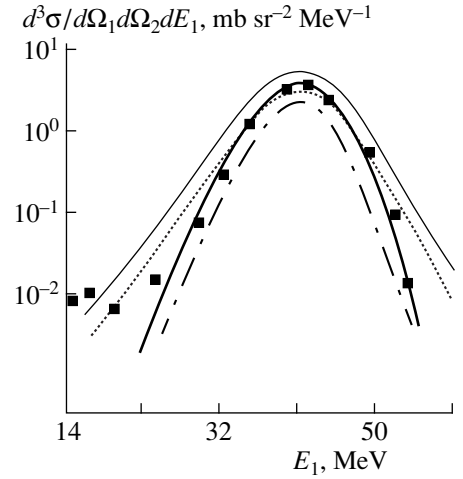

Fig. 5. As in Fig. 4*a*, but for $\theta_1 = 43.57°$, $\theta_2 = -43.57°$, and $E_0 = 85$ MeV. The experimental data were taken from [27].

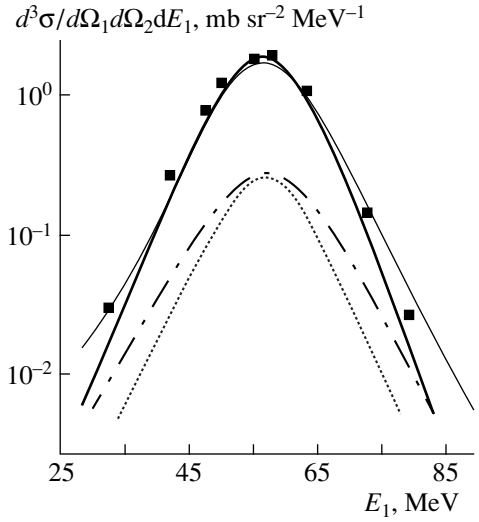

Fig. 6. As in Fig. 4*a*, but for $\theta_1 = 52°$, $\theta_2 = -40°$ and $E_0 = 156$ MeV. The experimental data were taken from [28].

length S [21–24], which is related to the energies of the final-state particles by the equation

$$dS = \sqrt{dE_1^2 + dE_2^2} \qquad (10)$$

and which is required to satisfy the condition $S = 0$ at $E_2 = 0$ and $E_1 \neq 0$.

A preliminary CTBIA analysis of the differential cross section for the reaction $d(N, 2N)N$ as a function of the energy E_1 was performed in [11–14]. Here, we pursue the analysis of this dependence (see Figs. 4–6) further, considering quite a wide range of incident-nucleon energies ($E_0 = 10$–160 MeV). Figures 7 and 8 display the differential cross section $\dfrac{d^3\sigma}{d\Omega_1 d\Omega_2 dS}$ as a function of S. Solid curves represent the results of the calculations that take into account all phase shifts (thick curves) with and (thin curves) without a cutoff, while dash-dotted and dotted curves correspond to analogous calculations taking into account only the $\mathcal{S}$-wave phases shifts. Experimental data were taken from [22, 25–28]. It can easily be seen that the introduction of the cutoff improves the agreement between the theoretical result and experimental data on the differential cross section both in magnitude and in shape. With increasing energy, the role of the cutoff becomes less pronounced, which primarily concerns the differential cross section. This must have been expected because, as the energy is increased, the wavelengths of the collid-

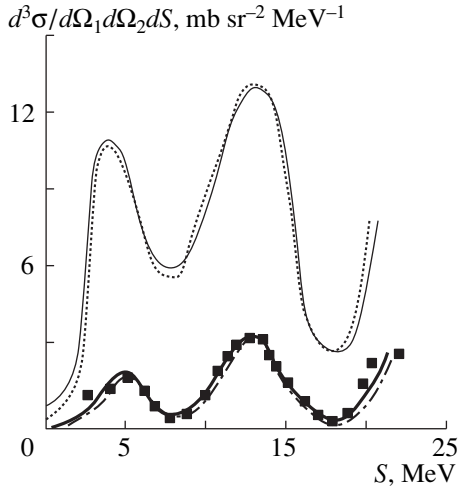

Fig. 7. Differential cross section for the reaction $d(p, 2p)n$ as a function of the arc length S at $\theta_1 = 52°$, $\theta_2 = -63°$, and $E_0 = 19$ MeV. The notation for the curves is identical to that in Fig. 4*a*. The experimental data were taken from [22].

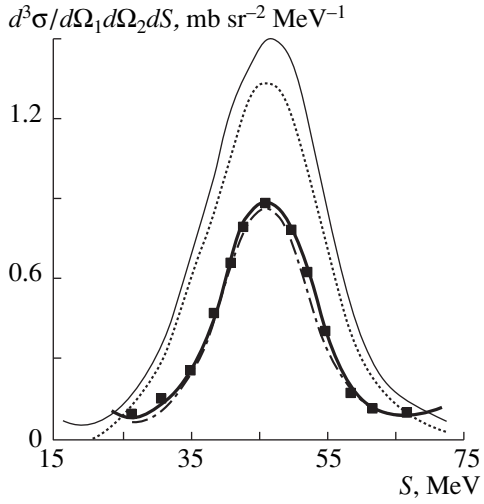

Fig. 8. As in Fig. 4*a*, but at $\theta_1 = 35.2°$, $\theta_2 = -35.2°$, and $E_0 = 65$ MeV. The experimental data were taken from [22].

ing particles decrease, and so is, according to Eqs. (1) and (2), the contribution associated with the discarded part of the bound-state wave function. It is interesting to note that, at sufficiently low energies, the cross sections for the reactions $d(p, 2p)n$ and $d(p, pn)p$ differ substantially even under identical kinematical conditions (see Figs. 4*a*, 4*b*). This can be explained as follows. The leading contribution to the differential cross section comes from the amplitude describing the interaction between the recorded particles. At low energies, the proton–neutron pair can be either in the $^1S_0$ or in the $^3S_1$ state, whereas the two protons can be only in the first of these two state—the second is forbidden by the Pauli exclusion principle. As a consequence, the maximum of the differential cross section for the reaction $d(p, pn)p$ is approximately twice as large as the maximum of the cross section for the reaction $d(p, 2p)n$. This difference is reproduced by the theoretical calculations only upon introducing the cutoff—that is, if the single-collision mechanism is consistently taken into consideration. With increasing energy, the contribution of other states increases, so that the difference between the proton–proton and the proton–neutron amplitudes gradually vanishes. Of particular interest is the dependence of the differential cross section for the reaction $d(p, 2p)n$ on the arc length S (Figs. 7, 8). What is worthy of note here above all is that both the magnitude of the cross section and the shape of the corresponding curve greatly depend on the incident-proton energy. For this reason, we eagerly expect new experimental results in this region at various energies and scattering angles.

Finally, we note that some degree of arbitrariness in choosing the cutoff parameter $C \geq 1$ was used to normalize the theoretical plots to experimental data. It turned out nonetheless that, in all cases considered here, the parameter C changed within 12% ($C = 1.20 \pm 0.15$).

The above results reveal that the single-collision mechanism, when consistently taken into account, has not yet exhausted its potential, which can be of use in studying complicated nuclear reactions. That the CTBIA, a simple unitary method, is capable of accounting for the experimental results considered here demonstrates the importance of respecting basic physical principles in constructing approximate methods.

REFERENCES

1. L. D. Faddeev, Zh. Éksp. Teor. Fiz. **39**, 1459 (1960) [Sov. Phys. JETP **12**, 1014 (1960)].
2. R. T. Cahill, Nucl. Phys. A **194**, 599 (1972).
3. K. L. Kowalski, Phys. Rev. D **5**, 39 (1972).
4. T. Sasakawa, Nucl. Phys. A **203**, 496 (1973).
5. J. M. Wallac, Phys. Rev. C **7**, 10 (1973).
6. J. V. Mebonia, Phys. Lett. A **48A**, 196 (1974).
7. J. V. Mebonia and T. I. Kvarackheliya, Phys. Lett. B **90B**, 17 (1980).
8. R. J. Glauber, Lect. Theor. Phys. **1**, 315 (1959).
9. A. G. Sitenko, Ukr. Fiz. Zh. (Russ. Ed.) **4**, 152 (1959).
10. H. Nakamura, Nucl. Phys. A **208**, 207 (1973).
11. T. I. Kvarackhelia and J. V. Mebonia, J. Phys. G **10**, 1677 (1984).
12. O. L. Bartaya and J. V. Meboniya, Yad. Fiz. **33**, 987 (1981) [Sov. J. Nucl. Phys. **33**, 521 (1981)].
13. V. Sh. Jikia, T. I. Kvaratskhelia, and J. V. Mebonia, Yad. Fiz. **58**, 30 (1995) [Phys. At. Nucl. **58**, 27 (1995)].
14. T. I. Kvaratskhelia and J. V. Mebonia, Soobshch. Akad. Nauk Gruz. SSR **136**, 53 (1989).
15. M. Sawada *et al.*, Phys. Rev. C **27**, 1932 (1983).
16. P. Doleschall, Nucl. Phys. A **220**, 491 (1974).

17. W. Klüge, R. Schlüfter, and W. Ebenhoh, Nucl. Phys. A **228**, 29 (1974).
18. Th. Mongan, Phys. Rev. **178**, 1957 (1968).
19. G. Rauprich *et al.*, Few-Body Syst. **5**, 67 (1988).
20. H. Witala and W. Glöckle, Nucl. Phys. A **528**, 48 (1991).
21. M. Karus *et al.*, Phys. Rev. C **31**, 1112 (1985).
22. J. Strate *et al.*, Nucl. Phys. A **501**, 51 (1989).
23. G. Rauprich *et al.*, Nucl. Phys. A **535**, 313 (1991).
24. J. Zejma *et al.*, Phys. Rev. C **55**, 42 (1997).
25. J. L. Durand, Phys. Rev. C **6**, 393 (1972).
26. J. L. Durand, Nucl. Phys. A **224**, 77 (1974).
27. V. K. Cheng, Nucl. Phys. A **225**, 397 (1974).
28. F. Takeutchi, Nucl. Phys. A **152**, 434 (1970).

Translated by R. Rogalyov

Physics of Atomic Nuclei, Vol. 63, No. 12, 2000, pp. 2091–2102. Translated from Yadernaya Fizika, Vol. 63, No. 12, 2000, pp. 2187–2198.

NUCLEI
Theory

Formation of Two Pions on Nuclei in $A(\gamma, \pi\pi N)B$ Reactions

I. V. Glavanakov

Institute of Nuclear Physics, Tomsk Polytechnic Institute, Tomsk, Russia

Received July 28, 1999; in final form, February 15, 2000

Abstract—A model is proposed for double pion photoproduction on nuclei that is accompanied by nucleon emission. Simple models that faithfully reproduce single-particle differential cross sections are used to describe photon interactions with intranuclear nucleons. The calculated cross sections for pion photoproduction on ^{12}C nuclei are compared with inclusive pion spectra measured in the second resonance region of photon energies. *© 2000 MAIK "Nauka/Interperiodica".*

1. INTRODUCTION

In recent years, much attention has been given to studying modifications to the properties of hadrons placed in a nuclear medium. The problem in question is of interest since the internal structure of hadrons and nonnucleonic degrees of freedom of the nucleus can play an important role in this phenomenon of nuclear physics [1, 2]. The question of modifications to the properties of nucleons, mesons, and nucleon resonances in a nucleus arises in studying (e, e') reactions [3], pion-production processes [4], vector-meson-production processes [5, 6], and other similar processes. Results obtained by measuring the total cross sections for photoabsorption on a proton and on C and Pb nuclei [7] exemplify data whose analysis leads to the assumption that the properties of hadrons suffer changes in a nucleus. In particular, virtually no evidence for the excitation of $N(1520)D_{13}$ and $N(1680)F_{15}$ resonances could be seen in the energy dependences of the cross sections for photoabsorption on nuclei. There are at least three possible reasons for this behavior of the cross section: (i) There exists a mechanism suppressing the photoexcitation of the above resonances in nuclei (modification of γN interaction in a nuclear medium). (ii) The masses and widths of resonances excited in a nuclear medium differ significantly from those in a vacuum. (iii) The dynamics of photon–nucleus interaction is such that it smooths the energy dependence of the cross sections.

It is obvious that a detailed analysis of individual reactions leading to photon absorption is the most efficient way toward solving this problem, but it is quite laborious. It can easily be verified that, at an energy of about 700 MeV, which corresponds to a cross-section maximum associated with the photoexcitation of the $N(1520)$ resonance, two processes—single and double pion photoproduction—nearly saturate the photoabsorption cross section. It can be expected that photon–nucleus interaction will be dominated by the processes of single and double quasifree pion photoproduction.

Single quasifree pion photoproduction has been studied for more than 20 years. As a result, a vast body of experimental data has been accumulated over this period of time, and theoretical models have been developed [8–12] that explain a major part of experimental results. As to investigation of double pion photoproduction, the second process under discussion, it is still in its infancy. There is only one experimental study, that which is reported in [13], where the inclusive spectrum of negative pions was measured in the energy region of interest. Only in recent years has double pion photoproduction on nuclei attracted the attention of theorists [14–16]: the inclusive total cross sections for pion photoproduction in $A(\gamma, \pi\pi)X$ reactions were studied in [14, 15], while the coherent production of pion pairs on nuclei was explored in [16]. Experimental data are available neither for total inclusive cross sections nor for coherent double pion photoproduction. Double pion photoproduction on complex nuclei that is accompanied by nucleon emission has been investigated neither theoretically nor experimentally.

Information about some isotopic channels of single and double quasifree pion photoproduction on nuclei in the photon-energy region of interest will be obtained in the near future from an experiment at the Tomsk synchrotron, where the yields of $\pi^0 p$ and $\pi^\pm p$ pairs originating from interactions between a beam of bremsstrahlung photons having an endpoint energy of 900 MeV and H, Li, C, and Al nuclei are being measured as functions of the secondary-proton energy and of the azimuthal angle of pion emission.

For double pion photoproduction on nuclei that is accompanied by nucleon emission, it is desirable to develop a model that could be used, together with a similar model for the production of single pions, to analyze experimental data in the second resonance region, and it is precisely the objective that is pursued in the present study.

The model proposed here to describe double pion production on nuclei is based on the impulse approximation, where the amplitude of photon interaction with

1063-7788/00/6312-2091$20.00

a nucleon bound in a nucleus is replaced by the amplitude of photon interaction with a free nucleon. Within this approach, which takes no account of intermediate-isobar interaction with a nucleus, it is possible to explain a significant part of experimental data on the cross sections for single pion production in the reaction $^{12}C(\gamma, \pi^- p)^{11}C$ in the $\Delta(1232)$ region [10–12]. Two manifestations of a nucleus are usually considered in its interaction with an isobar: (i) Because of the Pauli exclusion principle, intranuclear nucleons restrict the phase space of the nucleon formed in isobar decay, whereby the isobar width is reduced. (ii) The scattering of an isobar on intranuclear nucleons opens new channels of its decay, whereby the isobar width is increased. According to [17], these two mechanisms governing the changes in the isobar width compensate each other near the $\Delta(1232)$ pole. This is one of the possible reasons why quasifree pion production in the $\Delta(1232)$ region is satisfactorily described within the impulse approximation. That the degree to which the isobar width changes depends on the density of nuclear matter may be another reason for this. Because of the presence of two strongly interacting particles in the final state of $A(\gamma, \pi N)B$ reactions, the cross sections for these reactions are strongly suppressed by final-state interaction. It follows that pions are more efficiently produced at the nuclear periphery, where the modifying properties of nuclei are weaker. In the second resonance region, constraints associated with the Pauli exclusion principle are weaker for isobars of higher mass, $N(1520)$ and $N(1680)$; as a result, their widths prove to be somewhat greater than in a vacuum [17]. In the case of $A(\gamma, \pi\pi N)B$ reactions, however, pion production is superficial to a much greater extent, which validated the disregard of the interaction of intermediate isobars with the participant nucleus in the conceptual framework of the model (impulse approximation).

The ensuing exposition is organized as follows. Three different approximations of the amplitude for the elementary process $\gamma N \longrightarrow \pi\pi N$ that describe satisfactorily single-particle pion and proton spectra and the experimental azimuthal dependence of the charged-pion yield as determined in Tomsk are considered in Section 2. In Section 3, the $A(\gamma, \pi\pi N)B$ amplitude is represented as the sum of terms corresponding to quasifree, exchange, and quasielastic pion-production mechanisms. The last two mechanisms are dominant at low nucleon momenta. The problem of kinematically defining one-nucleon amplitudes is considered. Numerical results presented in Section 4 for pion-photoproduction cross sections are compared with experimental data.

2. PHOTOPRODUCTION OF TWO PIONS ON NUCLEONS

The production of two pions in photon interactions with nucleons occurs in six reactions

$$\text{(a) } \gamma p \longrightarrow \pi^+\pi^- p, \quad \text{(b) } \gamma p \longrightarrow \pi^+\pi^0 n,$$
$$\text{(c) } \gamma p \longrightarrow \pi^0\pi^0 p, \quad \text{(d) } \gamma n \longrightarrow \pi^+\pi^- n, \qquad (1)$$
$$\text{(e) } \gamma n \longrightarrow \pi^-\pi^0 p, \quad \text{(f) } \gamma n \longrightarrow \pi^0\pi^0 n.$$

The most vigorous experimental investigations into the photoproduction of two pions on a proton were conducted in the late 1960s by using bubble chambers. The cross sections for pion production on neutrons were measured in the 1970s. A comprehensive list of references to experimental studies performed by that time can be found in [18]. In recent years, the advent of high-current electron accelerators made it possible to continue investigating double pion photoproduction on a proton by new methods ensuring a 4π coverage of multiparticle events. Some of the results obtained in Mainz at a facility of this type (DAPHNE) are quoted in [18]. Measured total cross sections constitute the bulk of information about double pion photoproduction. Presently, the cross section for reaction (1a) have been measured to a high statistical precision. The cross sections for reactions (1b) and (1c) are known to a somewhat poorer precision of (2–4)%. The accuracy achieved in measuring the cross sections for reactions (1d) and (1e) occurring on a neutron and leading to the formation of charged particles in the final state is about 10%. There are no experimental data on reaction (1f).

Concurrently, the theoretical model of the process evolved, becoming ever more complicated, which is reflected in the growth of the number of Feynman diagrams taken into account in the calculations: from 5 in [19] to 67 in [20]. The model that was proposed in [20] for reaction (1a) and which includes the intermediate baryonic states N, $\Delta(1232)$, $N^*(1440)$, and $N^*(1520)$ and the ρ meson as a two-pion intermediate resonance was extended in [18] to other isotopic channels of the photoproduction of two pions.

A calculation of cross sections for particle–nucleus interactions in the impulse approximation involves considerable technical difficulties associated with the presence of multidimensional integrals. Such problems arise even in the analysis of single pion production in reactions like $A(\gamma, \pi N)B$. An increase in the number of final-state particles can render these problems next to insurmountable. For this reason, the model used to calculate the amplitudes for the reactions in (1) must be as simple as possible. Three comparatively simple model versions satisfactorily reproducing available experimental data will be considered here. Each of these is based on experimental results for the total cross sections.

Let us represent the differential cross section for the reaction $\gamma N \longrightarrow \pi\pi N$ in the form

$$d\sigma = (2\pi)^{-5}\delta^4(P_\gamma + P_{N_i} - P_{\pi_1} - P_{\pi_2} - P_N) \times \frac{1}{j}\frac{1}{4E_\gamma E_{N_i}}\overline{|M_{fi}|^2}\frac{d\mathbf{p}_{\pi_1}}{2E_{\pi_1}}\frac{d\mathbf{p}_{\pi_2}}{2E_{\pi_2}}\frac{d\mathbf{p}_N}{2E_N}, \qquad (2)$$

where $P_\gamma = (E_\gamma, \mathbf{p}_\gamma)$, $P_{N_i} = (E_{N_i}, \mathbf{p}_{N_i})$, and $P_N = (E_N, \mathbf{p}_N)$ are the 4-momenta of the incident photon, the initial-state nucleon, and the final-state nucleon, respectively; $P_{\pi_1} = (E_{\pi_1}, \mathbf{p}_{\pi_1})$ and $P_{\pi_2} = (E_{\pi_2}, \mathbf{p}_{\pi_2})$ are the 4-momenta of two final-state pions; j is the particle flux; and $\overline{|M_{fi}|^2}$ is the quantity obtained by averaging the squared modulus of the transition matrix element over the polarization states of the photon and of the initial-state nucleon and by summing the result over the polarization states of the final-state nucleon.

From an analysis of $\gamma p \longrightarrow \pi^+\pi^- p$ events recorded by a bubble chamber, it was deduced [21] that the distribution of these events with respect to the recoil-proton momentum $\mathbf{p}_N$ is satisfactorily described by the phase-space distribution normalized to the total cross section σ_{tot}. Therefore, the squared modulus of the matrix element (2) can be set to

$$\overline{|M_{fi}|^2} = (2\pi)^5 \times 4E_\gamma E_{N_i} j \frac{\sigma_{\text{tot}}}{S_{\text{tot}}}, \qquad (3)$$

where $S_{\text{tot}} = \dfrac{2\pi^2}{m_0}\displaystyle\int_{2m_\pi}^{m_0 - m_N} p_N^* p_\pi^{**} dm_{\pi\pi}$ is the total phase space of the reaction in question; m_N is the nucleon mass; m_π is the pion mass; $m_{\pi\pi}$ and m_0 are, respectively, the two-pion and the γN invariant mass; p_N^* is the nucleon momentum in the γN c.m. frame; and p_π^{**} is the pion momentum in the two-pion c.m. frame.

In the approximation specified by Eq. (3), the differential cross section with respect to the recoil-nucleon momentum and the direction of emission in the laboratory frame is given by

$$\frac{d^2\sigma}{dp_N d\Omega_N} = \pi \frac{p_N^2}{2E_N} \frac{p_\pi^{**}}{m_{\pi\pi}} \frac{\sigma_{\text{tot}}}{S_{\text{tot}}}. \qquad (4)$$

In Fig. 1, the recoil-proton-momentum distribution of $\gamma p \longrightarrow \pi^+\pi^- p$ events that was averaged over photon energies in the range 600–700 MeV and which was obtained on the basis of data presented in [21] is displayed for proton emission angles in the ranges 18°–24° and 38°–44°. The dashed curve in Fig. 1 represents the distribution of events that was calculated by averaging the differential cross section in (4) in relevant kinematical regions and by performing normalization to the total number of events recorded in the chosen photon-energy interval. As can be seen, the distribution of recoil protons is satisfactorily described in the approximation that is specified by Eq. (3) and which does not rely on any assumptions on the dynamics of the reaction $\gamma p \longrightarrow \pi^+\pi^- p$.

For charged-pion photoproduction on a proton, Fig. 2 shows the differential cross section measured in a beam of 730-MeV tagged photons from the synchrotron of Tokyo University [22] at the polar pion emission angle of $\theta_\pi = 40°$. The formation of positively charged pions that contributed to the experimental cross sections in Fig. 2*a* was accompanied by the emergence of charged particles. At the same time, no charged particles were found in recording pions that contributed to the data in Fig. 2*c*. It can therefore be conjectured that

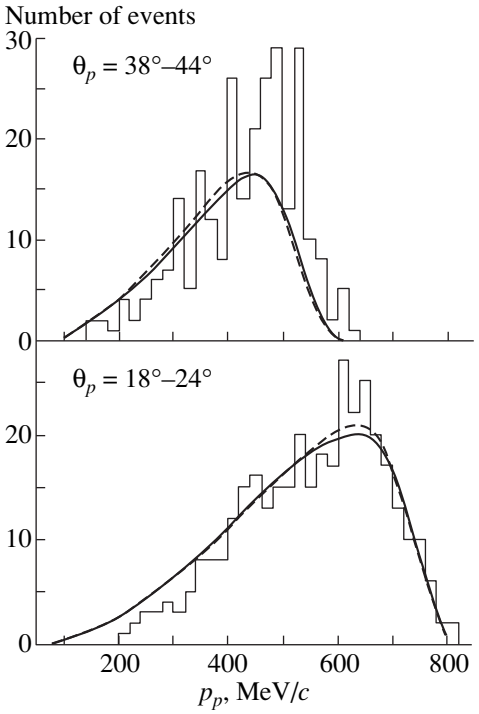

Fig. 1. Recoil-proton-momentum (p_p) distribution of $p(\gamma, \pi^+\pi^-)p$ events at E_γ = 600–700 MeV in two ranges of the recoil-proton emission angle (see main body of the text). The experimental distributions were obtained on the basis of data reported in [21].

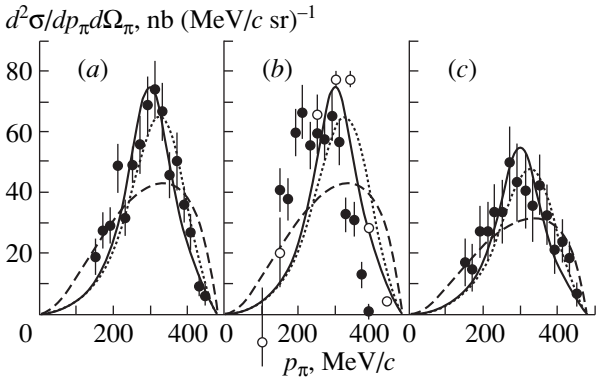

Fig. 2. Differential cross sections for charged-pion production in the reactions (*a*) $\gamma p \longrightarrow \pi^+$ + *charged particles*, (*b*) $\gamma p \longrightarrow \pi^-$ + *all the remaining particles*, and (*c*) $\gamma p \longrightarrow \pi^+$ + *neutral particles* as functions of the pion momentum p_π (E_γ = 730 MeV, θ_π = 40°). Points represent experimental data from (●) [22] and (○) [23] as quoted in [22].

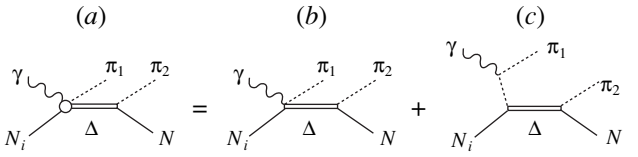

Fig. 3. Diagrams representing the isobaric mechanism of double pion photoproduction on a proton.

the data in Figs. 2*a* and 2*b* correspond, respectively, to positively and to negatively charged pions from the reaction $\gamma p \longrightarrow \pi^+\pi^- p$ and that the data in Fig. 2*c* correspond to positive pions from the reaction $\gamma p \longrightarrow \pi^+\pi^0 n$. The dashed curves in Fig. 2 represent the cross sections computed in the approximation specified by Eq. (3). It can be seen that, in contrast to the proton spectra, the pion spectra are not described by the phase-space distributions.

According to [19, 20], the production of two pions is dominated by the isobaric-reaction mechanism illustrated by the diagram in Fig. 3*a*. Taking this circumstance into account, we represent the expression for $\overline{|M_{fi}|^2}$ in the form

$$\overline{|M_{fi}|^2} = (2\pi)^5 \cdot 4E_\gamma E_{N_i} j \frac{B(m)}{2m}\frac{\sigma_{\text{tot}}}{S'}, \qquad (5)$$

where m is the invariant mass of the $\pi_2 N$ system; $B(m) = \dfrac{1}{\pi}\dfrac{\Gamma/2}{(m_\Delta - m)^2 + \Gamma^2/4}$ is the Breit–Wigner function describing the mass distribution of the delta isobar; $S' = \dfrac{2\pi^2}{m_0}\displaystyle\int_{m_\pi + m_N}^{m_0 - m_\pi} p^*_{\pi_1} p^{**}_{\pi_2}\frac{B(m)}{2m}dm$ is the convolution of the phase space of the cascade in Fig. 3*a* with the mass distribution of the isobar; m_Δ and Γ are the $\Delta(1232)$ mass and width, respectively; $p^*_{\pi_1}$ is the momentum of the first pion in the γN c.m. frame; and $p^{**}_{\pi_2}$ is the momentum of the second pion in the $\pi_2 N$ c.m. frame (for further details of the notation used here, see Fig. 3*a*).

In the approximation specified by Eq. (5), the dependence of the cross sections on the momenta of the pions π_1 and π_2 is given by

$$\frac{d^2\sigma}{dp_{\pi_1}d\Omega_{\pi_1}} = \pi\frac{p^2_{\pi_1}}{2E_{\pi_1}}\frac{p^{**}_{\pi_2}}{m}\frac{B(m)}{2m}\frac{\sigma_{\text{tot}}}{S'}, \qquad (6)$$

$$\frac{d^2\sigma}{dp_{\pi_2}d\Omega_{\pi_2}} = \frac{p^2_{\pi_2}}{2E_{\pi_2}}\frac{1}{4m' p'_{\pi_2}} \times\left[\arctan\left(\frac{m_1 - m_\Delta}{\Gamma/2}\right) - \arctan\left(\frac{m_2 - m_\Delta}{\Gamma/2}\right)\right]\frac{\sigma_{\text{tot}}}{S'}, \qquad (7)$$

where m' is the invariant mass of the $\pi_1 N$ system, p'_{π_2} is the momentum of the pion π_2 in the $\pi_1 N$ c.m. frame, and

$$m_1^2 = m_N^2 + m_\pi^2 + 2(E_N E_{\pi_2} + p_N p_{\pi_2}),$$
$$m_2^2 = m_N^2 + m_\pi^2 + 2(E_N E_{\pi_2} - p_N p_{\pi_2}).$$

For the scattered and the decay pion (π_1 and π_2 in Fig. 3, respectively), the momentum distributions calculated in the approximation specified by Eq. (5) are represented by, respectively, the solid and the dotted curves in Fig. 2. It can be seen that, within the experimental errors, the differential cross sections (6) and (7) satisfactorily reproduce experimental data. If, however, we focus on the high-momentum slope of the cross section, where the assumption that the recorded events are associated with double pion production is more justified, we can conclude that the differential cross section for the formation of positively charged pions in the reaction $\gamma p \longrightarrow \pi^+\pi^- p$ complies better with the decay-pion cross section (7) and that the cross section for negatively charged pions rather agrees with the scattered-pion cross section. The calculated cross sections for negatively charged pions are in better agreement with experimental data from [23]. The recoil-proton-momentum distribution of $\gamma p \longrightarrow \pi^+\pi^- p$ events that was calculated in the approximation specified by Eq. (5) and which is depicted by the solid curves in Fig. 1 differs only slightly from the results of the calculations in the approximation specified by Eq. (3).

The exclusive differential cross sections exhibit the highest sensitivity to reaction dynamics. Unfortunately, there are presently no experimental data on the exclusive cross sections for double pion photoproduction on a nucleon, so that the models used cannot be subjected to a detailed test on this basis. Information about the azimuthal angular correlation of protons and charged pions in the reaction $\gamma p \longrightarrow \pi^+\pi^- p$ was obtained from an experiment that studied the production of πp pairs on nuclei at the Tomsk synchrotron. For the reaction in question, this experiment measured, as a function of the azimuthal charged-pion emission angle ϕ_π, the differential yield $d^3Y/dE_p d\Omega_p d\Omega_\pi$, which is related to the cross section

$$\frac{d^3\sigma}{dE_p d\Omega_p d\Omega_\pi} = (2\pi)^{-5}\frac{1}{j}\frac{1}{4E_\gamma m_p}\overline{|M_{fi}|^2} \times\frac{p_p p_\pi^3}{8\left|(E_0 - E_p)p_\pi^2 - E_\pi \mathbf{p}_\pi\cdot(\mathbf{p}_0 - \mathbf{p}_p)\right|}, \qquad (8)$$

where E_0 and $\mathbf{p}_0$ are, respectively, the energy and the momentum of the γN system, by the equation

$$\frac{d^3Y}{dE_p d\Omega_p d\Omega_\pi} = \int dE_\gamma f(E_\gamma)\left(\frac{d^3\sigma_{\pi^+}}{dE_p d\Omega_p d\Omega_\pi} + \frac{d^3\sigma_{\pi^-}}{dE_p d\Omega_p d\Omega_\pi}\right). \qquad (9)$$

In expression (9), $f(E_\gamma)$ is the bremsstrahlung spectrum normalized by the condition

$$\int_0^{E_{\gamma\max}} f(E_\gamma)E_\gamma dE_\gamma = E_{\gamma\max},$$

where $E_{\gamma\max}$ is the maximal photon energy equal to 900 MeV. In the experiment, the azimuthal angle ϕ_π was varied in the interval 0°–40° with a step of 10°. The azimuthal angle of proton emission was kept at a constant value equal to π. At zero value of ϕ_π, the momenta of all particles participating in the reaction lie in the same plane. The polar angles of pion emission and of proton emission were chosen to be 61° and 41°, respectively. A polyethylene target was used in the experiment. The effect from hydrogen was determined from the difference of the yields from the reactions occurring on a polyethylene and on a carbon target. The differential cross section (8) for the scattered pions, that for the decay pions, and their sum are displayed in Figs. 4*a*, 4*b*, and 4*c*, respectively, as functions of the azimuthal pion emission angle at the proton kinetic energy of T_p = 140 MeV and the incident-proton energy of E_γ = 900 MeV. The cross sections calculated in the approximation specified by Eq. (3) and in the approximation specified by Eq. (5) are depicted by the dotted and by the dashed curves, respectively. The solid curves in Fig. 4 represent the results of the calculations based on the isobaric model proposed in [24]. This model takes into account the contribution of two dominant diagrams in Fig. 3: the contact diagram in Fig. 3*b* and the one-pion-exchange diagram in Fig. 3*c*. Within this model, the squared modulus of the transition matrix element is given by

$$\overline{|M_{fi}|^2} = (2\pi)^5 \cdot 4E_\gamma E_{N_i} j \frac{1}{4}\sum_\lambda \mathrm{tr}(m_\lambda m_\lambda^+)\frac{\sigma_{\mathrm{tot}}}{S''}, \quad (10)$$

where

$$m_\lambda = \frac{\mathbf{S}\left(\mathbf{p}_{\pi_2} - \frac{E_{\pi_2}}{m_\Delta}\mathbf{p}_\Delta\right)\mathbf{S}^+\left[\boldsymbol{\varepsilon}_\lambda + \frac{2\mathbf{p}_{\pi_1}\boldsymbol{\varepsilon}_\lambda}{(P_{\pi_1} - P_\gamma)^2 - m_\pi^2}(\mathbf{p}_{\pi_1} - \mathbf{p}_\gamma)\right]}{E_\Delta - E_{\Delta s} + i\Gamma/2}.$$

Here, λ and $\boldsymbol{\varepsilon}_\lambda$ are the photon polarization index and the photon polarization vector, respectively; E_Δ and $E_{\Delta s}$ are the delta-isobar energies in the intermediate state and on the mass shell, respectively; $\mathbf{p}_\Delta$ is the delta-isobar momentum; **S** is the operator connecting the spin-3/2 and spin-1/2 states [25]; the isobar mass m_Δ and width Γ were chosen in accordance with [26]; and the quantity S'' in (10) was determined in just the same way as the quantities S_{tot} and S' in (3) and (5), respectively—that is, by introducing a normalization of the cross section in (2) to the total cross section σ_{tot} measured experimentally.

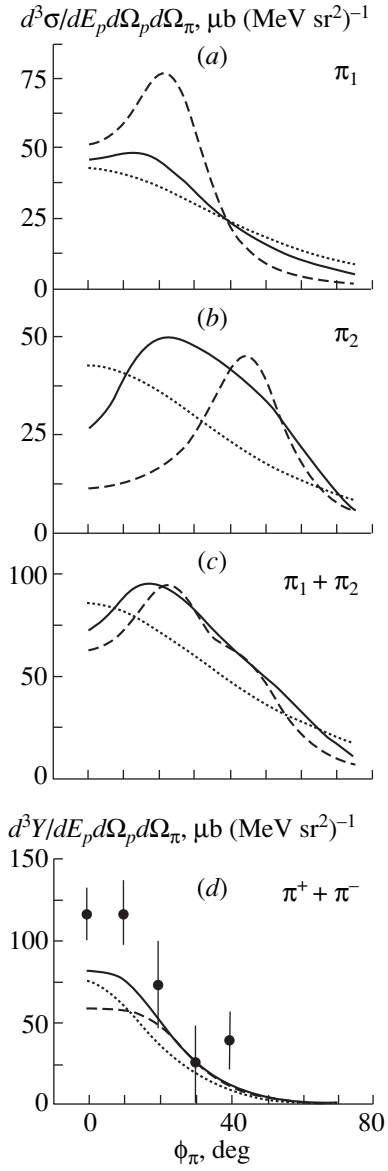

Fig. 4. Differential cross section for the reaction $\gamma p \longrightarrow \pi^+\pi^- p$ as a function of the azimuthal pion emission angle ϕ_π at the proton kinetic energy of T_p = 140 MeV and the incident-photon energy of E_γ = 900 MeV for (*a*) scattered, (*b*) decay, and (*c*) all product pions; (*d*) reaction yield as a function of the azimuthal pion emission angle ϕ_π at T_p = 160 ± 20 MeV. Points represent experimental data obtained in Tomsk.

It can be seen that the aforementioned three approximations for $\overline{|M_{fi}|^2}$ lead to markedly different dependences of the cross sections on the azimuthal angle. The cross sections for scattered and decay pions in the approximation specified by Eq. (5) differ considerably from those in the approximation specified by Eq. (10). However, the azimuthal dependence of the sum of the cross sections for two pions is weakly dependent on the model used. The results of the calculations for the azi-

muthal dependences of the differential reaction yields (9) (see Fig. 4*d*, where these results are presented along with experimental data obtained in Tomsk for protons of kinetic energy $T_p = 160 \pm 20$ MeV) show a similar degree of distinctions. Satisfactorily reproducing the shape of the experimental azimuthal dependence, the calculated yield falls short of the experimental data in absolute value.

3. $A(\gamma, \pi\pi N)B$ CROSS SECTION

The differential cross section for the production of two pions, π_1 and π_2, on a nucleus with the emission of a nucleon N,

$$\gamma + A \longrightarrow B + N + \pi_1 + \pi_2,$$

can be represented in the form

$$d\sigma = 2\pi\delta(E_\gamma + M_T - E_{\pi_1} - E_{\pi_2} - E_N - E_r) \times \overline{|T|^2}\frac{d\mathbf{p}_{\pi_1}}{(2\pi)^3}\frac{d\mathbf{p}_{\pi_2}}{(2\pi)^3}\frac{d\mathbf{p}_N}{(2\pi)^3}\frac{d\mathbf{p}_r}{(2\pi)^3},$$

where T is the matrix of the transition from the initial state involving a photon and a nucleus to the final state comprising two pions (π_1 and π_2), a nucleon, and a residual nucleus; ($\mathbf{p}_r$, E_r) is the 4-momentum of the residual nucleus; and M_T is the mass of the target nucleus.

The transition matrix T can be written as [27]

$$T = V_{\pi\pi A\gamma} + (V_{\pi\pi A} + V_{NB})(E + i\eta - H)^{-1}V_{\pi\pi A\gamma}, \quad (11)$$

where H is the Hamiltonian of the system, E is an eigenvalue of H, $V_{\pi\pi A\gamma}$ is the photon–nucleus interaction resulting in the production of two pions, $V_{\pi\pi A}$ is the interaction of the pions with the residual nuclear system, and V_{NB} is the interaction of the nucleon involved with the set of nucleons forming the nucleus B.

In the impulse approximation, the matrix element of the interaction $V_{\pi\pi A\gamma}$ has the form [28]

$$T_{\mathrm{IA}} = \int dx_1 \ldots dx_A \Psi_f^*(x_1, \ldots, x_A) \times \sum_{j=1}^{A} e^{i\mathbf{q}\cdot\mathbf{r}_j(j)} t_{\pi\pi N\gamma} \Psi_i(x_1, \ldots, x_A),$$

where x_j is the complete set of variables (spatial, spin, and isospin ones) of the jth nucleon; the integral sign denotes integration with respect to spatial variables and summation over spin and isospin variables; $t_{\pi\pi N\gamma}$ is the operator of pion photoproduction on a free nucleon; $\mathbf{q} = \mathbf{p}_\gamma - \mathbf{p}_{\pi_1} - \mathbf{p}_{\pi_2}$; $\Psi_i = \Psi_\alpha(x_1, \ldots, x_A)$ is the antisymmetric wave function of nucleus A in the state α; and Ψ_f is the wave function of the system consisting of the residual nucleus B and the knock-on nucleon.

Representing Ψ_f as the antisymmetrized product of the wave function $\varphi_n(x_1)$ of a free nucleon in the state n and the wave function $\Psi_\beta(x_2, \ldots, x_A)$ of the residual nucleus B in the state β and the multiparticle wave function of nucleus A as a linear combination of the products of the wave functions of the system formed by $A - 1$ nucleons and one more nucleon, we can recast the expression for the matrix element T_{IA} into the form [29]

$$T_{\mathrm{IA}} = T_{\mathrm{QF}} + T_{\mathrm{Ex}}, \quad (12)$$

where

$$T_{\mathrm{QF}} = \frac{\sqrt{A}}{(2\pi)^3}\sum_{n'}\langle n|t_{\pi\pi N\gamma}|n'\rangle\langle n', \beta|\alpha\rangle,$$

$$T_{\mathrm{Ex}} = \frac{\sqrt{A}}{(2\pi)^3}\sum_{\beta'}\langle\beta|t_{\pi\pi(A-1)\gamma}|\beta'\rangle\langle n, \beta'|\alpha\rangle.$$

Here, the $\sum$ sign denotes summation over spin and isospin states and integration with respect to the momentum of the relevant particle;

$$\langle n|t_{\pi\pi N\gamma}|n'\rangle = \int dx \varphi_n^*(x) e^{i\mathbf{q}\cdot\mathbf{r}} t_{\pi\pi N\gamma}\varphi_{n'}(x)$$

is the amplitude of pion production on a nucleon;

$$\langle\beta|t_{\pi\pi(A-1)\gamma}|\beta'\rangle = \int dx_1 \ldots dx_{A-1}\Psi_\beta^*(x_1, \ldots, x_{A-1}) \times \sum_{j=1}^{A-1} e^{i\mathbf{q}\cdot\mathbf{r}_j} t_{\pi\pi N\gamma}^{(j)} \Psi_{\beta'}(x_1, \ldots, x_{A-1})$$

is the amplitude of pion production on a nucleus formed by $A - 1$ nucleons; and

$$\langle n, \beta'|\alpha\rangle = \int dx_1 \ldots dx_A \varphi_n^*(x_1)\Psi_{\beta'}^*(x_2, \ldots, x_A)\Psi_\alpha(x_1, \ldots, x_A)$$

is an overlap integral that characterizes the probability of the virtual-decay process $A \longrightarrow (A - 1) + 1$.

Two pole diagrams—that which features a nucleon in a virtual state (Fig. 5*a*) and that which features an $(A - 1)$-nucleon nucleus in a virtual state (Fig. 5*b*)—correspond to two terms in (12) [10]. These terms represent, respectively, the amplitude of quasifree pion photoproduction and the exchange amplitude.

Let us consider the second term in the transition matrix as given by (11). For a first approximation, the mechanism of $A(\gamma, \pi\pi N)B$ reactions is determined by the dynamics of the nuclear system involved. In expression (11), we therefore disregard the interaction $V_{\pi\pi A}$. Under the assumption that the Green's function $(E + i\eta - H)^{-1}$ is diagonal in the intermediate states, the matrix element for the simplest intermediate state—that is, a state where there is only one virtual particle,

an excited nucleus A^* in our case—can be represented as [30]

$$T_{\mathrm{QE}} = \frac{1}{(2\pi)^3}\sum_{\alpha^*}\frac{\langle n, \beta|V_{NB}|\alpha^*\rangle\langle\alpha^*|t_{\pi\pi A\gamma}|\alpha\rangle}{E_N + E_B - E_{\alpha^*} + i\eta},$$

where $\langle\alpha^*|t_{\pi\pi A\gamma}|\alpha\rangle$ is the amplitude of partial pion photoproduction accompanied by the transition of the target nucleus to the α^* state, E_{α^*} is the energy of the nucleus in this state, and the $\sum$ sign denotes summation over discrete states of the nucleus and integration with respect to its momentum.

This expression is represented by the diagram in Fig. 5*c*; following the terminology adopted in [27], we will refer to the corresponding pion-production mechanism as a quasielastic mechanism.

Thus, the transition matrix T taken in the approximation described above appears to be the sum of three terms,

$$T = T_{\mathrm{QF}} + T_{\mathrm{Ex}} + T_{\mathrm{QE}}, \tag{13}$$

which correspond to the quasifree, the exchange, and the quasielastic mechanism of pion production in $A(\gamma, \pi\pi N)B$ relations.

In the resonance energy region, where the cross section shows sharp variations, it is of paramount importance to give a correct kinematical definition of the pion-photoproduction amplitude—to a great extent, what must be done for this reduces to taking correctly into account the Fermi motion of intranuclear nucleons and to considering that these nucleons are off the mass shell. We will proceed as follows. In the terms of the amplitude in the laboratory frame that correspond to the above three reaction mechanisms, the structures determining the kinematics of the amplitude for pion photoproduction on a nucleon in the plane-wave approximation are given by

$$\begin{aligned}
&(\mathrm{QF})\quad \int d\mathbf{r}_{A-1}\phi^*_{\mathbf{p}_N}e^{i\mathbf{q}\cdot\mathbf{r}_{A-1}}t_{\pi\pi N\gamma}(\hat{\mathbf{p}}_f, \hat{\mathbf{p}}_i)\Psi_\alpha(\mathbf{r}_{A-1}),\\
&(\mathrm{Ex})\quad \int d\mathbf{r}_{A-2}\Psi^*_{\beta'}(\mathbf{r}_{A-2})\\
&\times\exp\left(-i\frac{\mathbf{p}_r}{A-1}\mathbf{r}_{A-2}\right)e^{i\mathbf{q}\cdot\mathbf{r}_{A-2}}t_{\pi\pi N\gamma}(\hat{\mathbf{p}}_f, \hat{\mathbf{p}}_i)\\
&\quad\times\exp\left(-i\frac{\mathbf{p}_N}{A-1}\mathbf{r}_{A-2}\right)\Psi_\beta(\mathbf{r}_{A-2}),\\
&(\mathrm{QE})\quad \int d\mathbf{r}_{A-1}\Psi^*_{\alpha'}(\mathbf{r}_{A-1})\\
&\times\exp\left(-i\frac{\mathbf{p}_N+\mathbf{p}_r}{A}\mathbf{r}_{A-1}\right)e^{i\mathbf{q}\cdot\mathbf{r}_{A-1}}t_{\pi\pi N\gamma}(\hat{\mathbf{p}}_f, \hat{\mathbf{p}}_i)\Psi_\alpha(\mathbf{r}_{A-1}),
\end{aligned} \tag{14}$$

where $\mathbf{r}_{A-1}$ and $\mathbf{r}_{A-2}$ are the coordinates of the nucleons with respect to the centers of mass of the $(A-1)$-nucleon and the $(A-2)$-nucleon system, respectively;

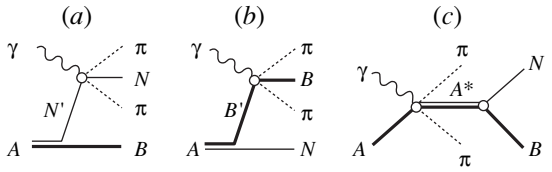

Fig. 5. Diagrams representing (*a*) the quasifree, (*b*) the exchange, and (*c*) the quasielastic mechanism of pair pion photoproduction on a nucleus.

$\Psi_\alpha(r)$ is the single-particle wave function of a bound nucleon in the state α; and $\hat{\mathbf{p}}_i$ and $\hat{\mathbf{p}}_f$ are the nucleon-momentum operators in, respectively, the initial and the final state (these operators appear in the amplitude $t_{\pi\pi N\gamma}$).

Substituting the bound-nucleon wave functions in the form of expansions in the eigenfunctions of the momentum operator into (14), we obtain

$$\begin{aligned}
&(\mathrm{QF})\quad t_{\pi\pi N\gamma}(\mathbf{p}_N, -\mathbf{p}_r)\Psi_\alpha(-\mathbf{p}_r),\\
&(\mathrm{Ex})\quad \int d\mathbf{p}\Psi^*_{\beta'}\left(\mathbf{q}\frac{A-2}{A-1}+\mathbf{p}\right)\\
&\times t_{\pi\pi N\gamma}\left(\mathbf{q}\frac{A-2}{A-1}+\mathbf{p}+\frac{\mathbf{p}_r}{A-1}, -\frac{\mathbf{p}_N}{A-1}+\mathbf{p}\right)\Psi_\beta(\mathbf{p}),
\end{aligned} \tag{15}$$

$$(\mathrm{QE})\quad \int d\mathbf{p}\Psi^*_{\alpha'}\left(\mathbf{q}\frac{A-1}{A}+\mathbf{p}\right)t_{\pi\pi N\gamma}(\mathbf{q}+\mathbf{p}, \mathbf{p})\Psi_\alpha(\mathbf{p}), \tag{16}$$

where $\Psi_\alpha(\mathbf{p})$ is bound-nucleon wave function in the momentum representation, while $t_{\pi\pi N\gamma}(\mathbf{p}_f, \mathbf{p}_i)$ is the amplitude for pion photoproduction on a nucleon ($\mathbf{p}_i$ and $\mathbf{p}_f$ are, respectively, the initial-state and the final-state momentum).

In expressions (15) and (16) for the exchange and the quasielastic mechanism, respectively, the one-nucleon amplitude is averaged over nucleon momenta with a weight appearing to be the transition density of the momentum distribution of intranuclear nucleons. Commonly, use is made here of the factorization approximation: the one-nucleon amplitude is factored outside the integral sign at the momentum value corresponding to the maximal transition density. In the oscillator model, the transition density

$$\Psi_{\alpha'}(\mathbf{p}' + \mathbf{p})\Psi_\alpha(\mathbf{p})$$

of the momentum distribution—generally, it depends on the initial and on the final state of the nucleon—is maximal at $\mathbf{p} = -\frac{1}{2}\mathbf{p}'$ for the majority of the transitions. In this case, which occurs quite frequently, the laboratory momenta of the initial- and final-state nucleons for the exchange and the quasielastic pion-production

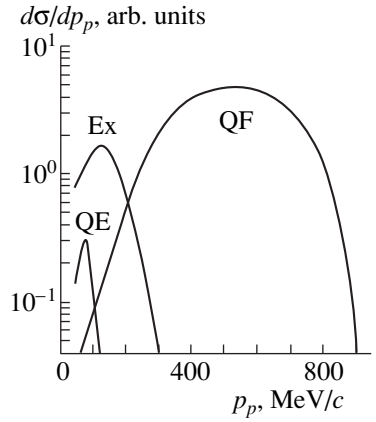

Fig. 6. Differential ross section for the reaction ^{4}He(γ, $\pi^+\pi^-$ p)^{3}H as a function of the proton momentum at the incident-photon energy of E_γ = 700 MeV. The curves labeled with the QF, Ex, and QE symbols represent results obtained by assuming the quasifree, the exchange, and the quasielastic reaction mechanism, respectively.

mechanism in the factorization approximation and for the quasifree mechanism are given by

$$\begin{aligned}
&\text{(QF)}\quad \mathbf{p}_i = -\mathbf{p}_r, \quad \mathbf{p}_f = \mathbf{p}_N,\\
&\text{(Ex)}\quad \mathbf{p}_i = -\mathbf{p}_N\frac{1}{A-1} - \frac{1}{2}\mathbf{q}\frac{A-2}{A-1},\\
&\qquad \mathbf{p}_f = \frac{1}{2}\mathbf{q}\frac{A-2}{A-1} + \mathbf{p}_r\frac{1}{A-1},\\
&\text{(QE)}\ \mathbf{p}_i = -\frac{1}{2}\mathbf{q}\frac{A-1}{A}, \quad \mathbf{p}_f = \frac{1}{2}\mathbf{q}\frac{A+1}{A}.
\end{aligned} \tag{17}$$

It is well known that the factorization approximation is quite satisfactory if the amplitude of the reaction occurring on a nucleon changes slowly in the region being considered. Otherwise, the exact expressions (15) and (16) must be used to calculate the amplitudes for the exchange and for the quasielastic mechanism.

The averaging of the amplitude for pion production on a free nucleon in (15) and (16) over the states of intranuclear nucleons smooths the energy dependence of the cross section for the reaction occurring on a nucleus. In view of this, the region dominated by the quasifree mechanism of pion photoproduction is more appropriate for experimentally studying in-medium changes in the properties of resonances because, there, the kinematics of final-state particles furnishes the vastest amount of information for determining the one-nucleon amplitude.

In order to specify kinematically the one-nucleon amplitude for the quasifree reaction mechanism, quantities that describe the state of the particles participating in reactions of the $N_i(\gamma, \pi\pi)N$ type are assigned the values of the analogous quantities for the corresponding reaction on a nucleus, $A(\gamma, \pi\pi N)B$. In the N_i rest frame, the photon energy E_γ^0 is given by

$$E_\gamma^0 = \frac{m_{\pi\pi N}^2 - m_{N_i}^2}{2m_{N_i}},$$

where m_{N_i} is the free-nucleon mass and $m_{\pi\pi N} = [(E_{\pi_1} + E_{\pi_2} + E_N)^2 - (\mathbf{p}_{\pi_1} + \mathbf{p}_{\pi_2} + \mathbf{p}_N)^2]^{1/2}$ is the invariant mass of the $\pi_1\pi_2N$ system. It is of importance that the active nucleon is taken to be off the mass shell. From (17) and from the conservation of energy at the vertex of the virtual decay $A \longrightarrow (A-1) + N_i$, it follows that

$$E_i = M_A - E_r, \quad m_i^2 = E_i^2 - \mathbf{p}_r^2 < m_{N_i}.$$

In this case, the energy and the momentum are conserved in the $N_i(\gamma, \pi\pi)N$ vertex as well. That the one-nucleon amplitude was kinematically defined in this way made it possible to describe satisfactorily the energy dependence of the cross section for quasifree single negative-pion photoproduction in the $\Delta(1232)$ region [31].

4. NUMERICAL RESULTS

From the numerical results displayed in Fig. 6, we deduce qualitative information about the kinematical regions where the reaction mechanisms corresponding to the three diagrams in Fig. 5 are operative. The contributions of the three amplitudes in (13) to the cross section for the reaction ^{4}He(γ, $\pi^+\pi^-p$)^{3}H are shown in Fig. 6 as functions of the proton momentum. The calculation that yielded these results was performed in the plane-wave approximation on the basis of expression (3) for the amplitude of the reaction $p(\gamma, \pi^+\pi^-)p$. The contribution from the two lowest excited states of the ^{4}He nucleus at 20.1 and 21.1 MeV (their quantum numbers are 0^+0 and 0^-0, respectively) were taken into account in calculating the amplitude for the quasielastic reaction mechanism. It was assumed that the configurations of these 0^+0 and 0^-0 states are $(1s)^{-1}(2s)$ and $(1s)^{-1}(1p)$. It can be seen that the quasifree pion-photoproduction mechanism is dominant for proton momenta exceeding the characteristic intranuclear-nucleon momentum of about 200 MeV/c. The exchange- and the quasielastic-mechanism contribution overlap in Fig. 6, but they are separated to a considerable extent in the dependence of the cross section on the invariant mass of the p^3H system; at the minimal excitation energy, these mechanisms can also be separated by studying the differential cross section with respect to the angle of divergence of the proton and the ^{3}H nucleus.

Figure 7 shows the inclusive spectra of negative pions that were formed in the interactions of photons having energies in the intervals 515–595, 595–675, and 675–755 MeV with ^{12}C nuclei and which were emitted

at an angle of 41° with respect to the photon-beam axis [13]. The relevant data come from the experiment that was performed at the synchrotron of Tokyo University. The experimental results are presented in the form of the dependence on the difference Δp of the momentum p_0 that follows from the kinematics of single pion production on a free nucleon and the momentum of the recorded pion. It is rather difficult to analyze these data since negatively charged pions can be formed in many processes at these energies. However, the contribution of some single-pion-production processes where the final nucleus occurs in a bound state can be disregarded because, under the kinematical conditions being considered, the minimal absolute value of the momentum transfer, $|\mathbf{p}_\gamma - \mathbf{p}_\pi|$, exceeds 300 MeV/$c$. For the same reason, it is legitimate to disregard the exchange and the quasielastic mechanism of single pion photoproduction accompanied by nucleon emission.

In the quasifree approximation, negative pions can be formed via single pion photoproduction in the reaction

$$^{12}\mathrm{C}(\gamma, \pi^- p)^{11}\mathrm{C} \tag{18}$$

and via three double-pion-photoproduction processes

$$^{12}\mathrm{C}(\gamma, \pi^-\pi^+ p)^{11}\mathrm{B}, \quad ^{12}\mathrm{C}(\gamma, \pi^-\pi^+ n)^{11}\mathrm{C}, \quad ^{12}\mathrm{C}(\gamma, \pi^-\pi^0 p)^{11}\mathrm{C}. \tag{19}$$

In Fig. 7, the curves labeled with the symbol π represent the cross section calculated for reaction (18) in the quasifree approximation with distorted waves, while the curves labeled with the symbol $\pi\pi$ correspond to the sum of the cross sections calculated for three double-pion-photoproduction reactions (19) within the approximation specified by Eq. (5). The final-state interaction was taken into account in the eikonal approximation. The potential that was proposed in [32] and which describes satisfactorily the effect of proton interaction with a residual nucleus in the single-pion-production process at energies in the $\Delta(1232)$ region [33] was taken here for the nucleon–nucleus optical potential. The pion wave function was distorted by the optical potential used in [34]. The states of intranuclear nucleons were described by oscillator wave functions characterized by the oscillator parameter equal to the charge radius of the ^{12}C nucleus.

The high-momentum section of the pion spectrum (small negative values of Δp) is satisfactorily described by the contribution from the single quasifree photoproduction of negatively charged pions. The contribution of double quasifree pion photoproduction faithfully reproduces the rate of the cross-section growth with Δp in the region $\Delta p > 100$ MeV/c. At the minimal photon energy, the absolute value of the cross section for the reactions in (19) around the maximum is nearly one-half as large as the experimental inclusive cross section. As the photon energy is increased, the agreement between the computed and measured cross sections is substantially improved. It is worth noting that the filling of the cross section minimum is more pronounced in the region where the cross sections for single and double photoproduction overlap. One of the possible reasons behind underestimating the experimental cross sections in this region of the pion spectra may be associated with the contribution of the coherent photoproduction of two pions on a carbon nucleus in the reaction $^{12}\mathrm{C}(\gamma, \pi^-\pi^+)^{12}\mathrm{C}$ [16]. In the same interval of pion momenta, it is natural to expect manifestations of the exchange and of the quasielastic mechanism of the reactions in (19).

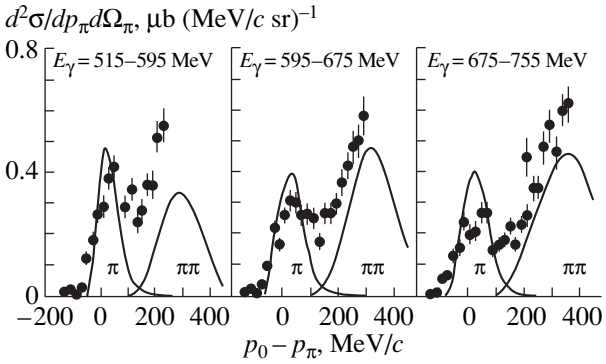

Fig. 7. Differential cross section for the reaction $^{12}\mathrm{C}(\gamma, \pi^-)X$ as a function of the difference of the momentum p_0 that follows from the kinematics of single pion production on a free nucleon and the recorded-pion momentum p_π ($\theta_\pi = 41°$). Experimental data were borrowed from [13].

In analyzing experimental results for the photoabsorption cross section, it is of interest to compare the total cross sections for single and double pion photoproduction on a proton with the total cross sections (integrated over the total phase space) for quasifree single and double pion photoproduction on a ^{12}C nucleus. This comparison makes it possible to assess a minimal degree of the changes that the energy dependence of the cross section for the reaction occurring on a nucleus may suffer within the impulse approximation. It can be expected that the contributions from other photoabsorption channels will provide a poorer description of the cross section for photon–nucleon interaction.

In Fig. 8*a*, the dashed and the dash-dotted curve represent the total cross sections for the reactions $p(\gamma, \pi^0)p$ and $p(\gamma, \pi^+)n$, respectively, as functions of the total c.m. energy $s^{1/2}$. These cross sections were obtained by integrating the experimental differential cross sections $d\sigma/d\Omega^*$ represented in the form of an expansion in powers of $\cos\theta_\pi^*$. The expansion coefficients were taken from [35]. The dotted curve corresponds to the sum of the total cross sections for the double-pion-photoproduction reactions $p(\gamma, \pi^+\pi^-)p$, $p(\gamma, \pi^+\pi^0)n$, and $p(\gamma, \pi^0\pi^0)p$ [18]. In Fig. 8*a*, the solid curve represents the sum of the total cross sections for single and double pion photoproduction on a proton as a function of energy. The same notation for the curves is used in

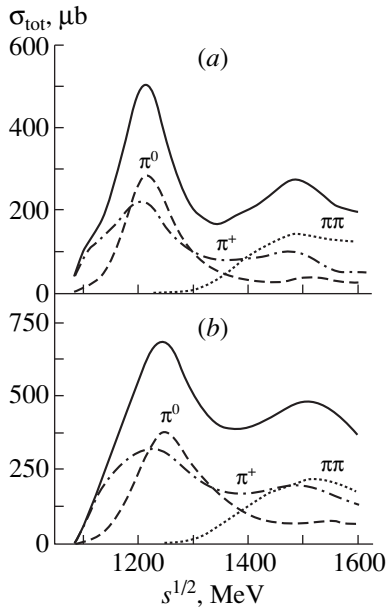

Fig. 8. (*a*) Cross sections for the reactions $p(\gamma, \pi^0)p$ and $p(\gamma, \pi^+)n$ and sum of the cross sections for double pion photoproduction in the reactions $p(\gamma, \pi^+\pi^-)p$, $p(\gamma, \pi^+\pi^0)n$, and $p(\gamma, \pi^0\pi^0)p$ and (*b*) cross section for single pion photoproduction in the reactions $^{12}C(\gamma, \pi^0 p)^{11}B$ and $^{12}C(\gamma, \pi^+ n)^{11}B$ and sum of the cross sections for double pion photoproduction in the reactions $^{12}C(\gamma, \pi^+\pi^- p)^{11}B$, $^{12}C(\gamma, \pi^+\pi^0 n)^{11}B$, and $^{12}C(\gamma, \pi^0\pi^0 p)^{11}B$ as functions of the total c.m. energy $s^{1/2}$.

Fig. 8*b* to depict the cross sections for single pion photoproduction in the reactions

$$^{12}C(\gamma, \pi^0 p)^{11}B, \quad ^{12}C(\gamma, \pi^+ n)^{11}B \tag{20}$$

and the sum of the cross sections for double pion photoproduction in the reactions

$$^{12}C(\gamma, \pi^+\pi^- p)^{11}B, \quad ^{12}C(\gamma, \pi^+\pi^0 n)^{11}B, \quad ^{12}C(\gamma, \pi^0\pi^0 p)^{11}B. \tag{21}$$

These cross sections were calculated in the quasifree approximation with distorted waves by using Eq. (5). In the quasifree approximation, reactions (20) and (21) proceed via photon interaction with the protons of the ^{12}C nucleus. The final-state interaction was taken into account in the eikonal approximation (the relevant details were described above in connection with interpreting the negative-pion spectra displayed in Fig. 7). The data in Figs. 8*a* and 8*b* are presented in the same form as the measured cross sections in [7]: the same photon energy in the laboratory frame for the reaction on a proton and for the reaction on a nucleus corresponds to a specific value of $s^{1/2}$.

In the energy range being considered, the energy dependence of the cross section for pion photoproduction on a free proton is governed by three factors: $\Delta(1232)$ excitation; a sharp growth of the cross section for double pion production—at $s^{1/2} \sim 1500$ MeV, this cross section reaches a maximum value; and the resonance contribution of $N(1520)$ to the cross section for all processes. Effects resulting from the fact that intranuclear nucleons are in a bound state are vividly exemplified by observables of the reactions $p(\gamma, \pi^0)p$ and $^{12}C(\gamma, \pi^0 p)^{11}B$: the cross-section maximum associated with the excitation of the $\Delta(1232)$ isobar is shifted to the region of higher energies with increasing width of the peak. Qualitatively similar changes in the cross section are observed in the $N(1520)$ region.

Final-state interaction has a pronounced effect on the energy dependence of the cross section. At a resonance photon energy, the mean energy of product pions does not have a resonance value with respect to the interaction with nucleons at rest. This leads to a shift of the maximum of the cross-section suppression to the region of higher photon energies. It follows that not only does the final-state interaction suppress the cross section in the $\Delta(1232)$ region by a factor greater than 3, but it also deforms considerably the energy dependence of the cross section. The latter effect is especially pronounced when one compares the cross sections for the production of positively charged pions in the reactions $p(\gamma, \pi^+)n$ and $^{12}C(\gamma, \pi^+ n)^{11}B$. In the $N(1520)$ region, the final-state interaction changes the relationship between the cross sections for single and double pion photoproduction. Because of the presence of two pions, the second process is more sensitive to nuclear-medium effects than the first one. The suppression of the cross section for double pion production because of pion interaction with the residual nucleus is enhanced when we approach the region where both pions reach the resonance energy with a high probability, in which case the cross-section maximum in the $N(1520)$ region becomes more pronounced.

By comparing the sum of the total cross sections for single and double pion production on a free proton with that for the analogous processes on a nucleus, we can conclude that, although the energy dependence of the cross section for the reaction occurring on a nucleus basically reproduces typical features of the cross section for the analogous reactions on a proton, the energy dependence of the former has a less pronounced structure. The cross-section minimum between the two resonance regions is filled sizably, but not to an extent sufficient for explaining the absence of a maximum in the energy dependence of the photoabsorption cross section at the position of the $N(1520)$ resonance. It should be borne in mind, however, that, with allowance for the isotopically symmetric reactions

$$^{12}C(\gamma, \pi^0 n)^{11}C, \quad ^{12}C(\gamma, \pi^- p)^{11}C;$$
$$^{12}C(\gamma, \pi^+\pi^- n)^{11}C, \quad ^{12}C(\gamma, \pi^-\pi^0 p)^{11}C,$$
$$^{12}C(\gamma, \pi^0\pi^0 n)^{11}C,$$

the cross sections displayed in Fig. 8*b* saturate only 30–40% of the photoabsorption cross section and that the

effect of $N(1520)$ excitation is somewhat smaller in photon–neutron interactions [18, 36].

A result that is qualitatively similar (to that described above) in what is concerned with the manifestations of the cross-section maximum at the position of the $N(1520)$ resonance was obtained in the semiclassical transport model used in [17] to explain the cross section for photoabsorption on ^{40}Ca. According to the estimates presented there, the isobar width increases in a nucleus by 20–40 MeV, which is one order of magnitude less than what is required for explaining the photoabsorption cross sections [37].

5. CONCLUSION

Reactions of the $A(\gamma, \pi\pi N)B$ type, which represent one of the main channels of photon absorption by a nucleus in the second resonance region of energies, have been analyzed. The reaction amplitude has been represented as the sum of the amplitude for quasifree pion production, the exchange amplitude, and the quasielastic amplitude. In the quasielastic process, the production of a pion pair is accompanied by the excitation of the nucleus, which further decays via the emission of a nucleon. The quasifree mechanism of pion production is dominant in the kinematical region where the proton momentum exceeds a value of about 200 MeV/c.

For the $N(\gamma, \pi\pi)N$ reactions, three models have been considered here. These are (i) the phase-space model, which satisfactorily reproduces the results of bubble-chamber measurements for recoil-proton-momentum distributions of events of the reaction $p(\gamma, \pi^+\pi^-)p$; (ii) the phase-space model embedded in the isobaric model—this approach makes it possible to describe the spectra of charged pions from the reactions $p(\gamma, \pi^+\pi^-)p$ and $p(\gamma, \pi^+\pi^0)n$ induced by a beam of tagged photons from the synchrotron of Tokyo University; and (iii) the isobaric model that takes into account the contribution of the contact diagram and the contribution of the pion-exchange diagram. For the shape of the azimuthal dependence of the yield from the reaction $p(\gamma, \pi^+\pi^-)p$, all these models provide results that are in satisfactory agreement with data obtained at the Tomsk synchrotron.

Within the model that takes into account single and double quasifree pion photoproduction, the spectra of negatively charged pions from photon interactions with a ^{12}C nucleus have been calculated in the second resonance region of energies. The results of the calculations satisfactorily reproduce the high-momentum contributions to the experimental inclusive pion spectrum, which are due to single pion production; the low-momentum spectrum is described at energies $E_\gamma > 600$ MeV. At low momenta, the calculated spectrum associated with double pion photoproduction falls slightly short of the experimental spectrum.

In order to clarify the nuclear-medium effect on the energy dependence of the cross section for pion photoproduction on nuclei, the energy dependence of the total cross sections for some isotopic channels through which the reactions $^{12}C(\gamma, \pi N)^{11}B$ and $^{12}C(\gamma, \pi\pi N)^{11}B$ proceed owing to prompt photon interactions with the protons of the ^{12}C nucleus has been calculated in the quasifree approximation. Together with the cross sections for isotopically symmetric channels for pion production, the cross sections for the above processes saturate 30 to 40% of the photoabsorption cross section. These results have been compared with the cross section for single and double pion production on a free proton. In addition to trivial broadening of resonance peaks, which is due to the Fermi motion of the nucleons, and a shift to the region of higher energies, a pronounced effect of the final-state interaction on the energy dependence of the cross section has been revealed. The final-state interaction deforms noticeably the energy dependence of the cross section in the $\Delta(1232)$ region and changes the relationship between the cross sections for single and for double pion production at the position of the $N(1520)$ resonance. The cross-section minimum between two resonance regions is partly filled. The majority of the factors listed above smooths the energy dependence of the cross sections for above-type reactions on a nucleus. Nonetheless, this provides no way to explain the absence of the maximum in the cross section for photoabsorption on ^{12}C in the $N(1520)$ region.

ACKNOWLEDGMENTS

This work was supported by the Russian Foundation for Basic Research (project no. 97-02-17765).

REFERENCES

1. P. J. Mulders, Phys. Rep. **185**, 83 (1990).
2. N. C. Mukhopadhyay and V. Vento, RPI Internal Report RPI-97, No. 117 (1997); nucl-th/9712073.
3. R. M. Sealock, K. L. Giovanetti, S. T. Thornton, *et al.*, Phys. Rev. Lett. **62**, 1350 (1989).
4. D. Pelte, nucl-ex/9902006.
5. Ye. S. Golubeva, L. A. Kondratyuk, and W. Cassing, Nucl. Phys. A **625**, 832 (1997).
6. S. H. Lee, nucl-th/9904007.
7. A. Deppman, N. Bianchi, E. De Sanctis, *et al.*, nucl-th/9809085.
8. A. I. Shebeko, Yad. Fiz. **14**, 1191 (1971) [Sov. J. Nucl. Phys. **14**, 664 (1971)].
9. J. M. Laget, Nucl. Phys. A **194**, 81 (1972).
10. I. V. Glavanakov, Yad. Fiz. **49**, 91 (1989) [Sov. J. Nucl. Phys. **49**, 58 (1989)].
11. C. Bennhold, X. Li, and L. E. Wright, Phys. Rev. C **48**, 816 (1993).
12. J. I. Johansson and H. S. Sherif, Nucl. Phys. A **575**, 477 (1994).
13. I. Arai, H. Fujii, S. Homma, *et al.*, J. Phys. Soc. Jpn. **45**, 1 (1978).

14. J. A. Gómez Tejedor, M. J. Vicente-Vacas, and E. Oset, Nucl. Phys. A **588**, 819 (1995).
15. M. Effenberger, A. Hombach, S. Teis, and U. Mosel, Nucl. Phys. A **614**, 501 (1997).
16. S. S. Kamalov and E. Oset, Nucl. Phys. A **625**, 873 (1997).
17. M. Effenberger and U. Mosel, nucl-th/9707010.
18. J. A. Gómez Tejedor and E. Oset, hep-ph/9506209.
19. L. Lüke and P. Söding, Springer Tracts Mod. Phys. **59**, 39 (1971).
20. J. A. Gómez Tejedor and E. Oset, Nucl. Phys. A **571**, 667 (1994).
21. P. Brinckmann and W. Mohr, Bonn-PI-1-111 (1970).
22. K. Maruyama, H. Fujii, S. Homma, *et al.*, J. Phys. Soc. Jpn. **46**, 1403 (1979).
23. S. Fukui, Y. Inagaki, S. Iwata, *et al.*, Nucl. Phys. B **81**, 378 (1974).
24. J. M. Laget, Phys. Rev. Lett. **41**, 89 (1978).
25. H. Sugawara and F. von Hippel, Phys. Rev. **172**, 1764 (1968).
26. I. Blomqvist and J. M. Laget, Nucl. Phys. A **280**, 405 (1977).
27. M. L. Goldberger and K. M. Watson, *Collision Theory* (Wiley, New York, 1964; Mir, Moscow, 1967).
28. M. Lax and H. Feshbach, Phys. Rev. **81**, 189 (1951).
29. I. V. Glavanakov, Vopr. At. Nauki Tekh., Ser. Obshch. Yad. Fiz. **1** (34), 94 (1986).
30. I. V. Glavanakov, Yad. Fiz. **50**, 1231 (1989) [Sov. J. Nucl. Phys. **50**, 767 (1989)].
31. I. V. Glavanakov, Yad. Fiz. **35**, 875 (1982) [Sov. J. Nucl. Phys. **35**, 509 (1982)].
32. C. J. Batty, Nucl. Phys. **23**, 562 (1961).
33. I. V. Glavanakov, Yad. Fiz. **31**, 342 (1980) [Sov. J. Nucl. Phys. **31**, 181 (1980)].
34. Y. Futami and J. Suzumura, Prog. Theor. Phys. **66**, 534 (1981).
35. H. Genzel, P. Joos, and W. Pfeil, *Photoproduction of Elementary Particles* (Springer-Verlag, New York, 1973).
36. F. X. Lee, C. Bennhold, S. S. Kamalov, and L. E. Wright, nucl-th/9806024.
37. L. A. Kondratyuk and Ye. S. Golubeva, Yad. Fiz. **61**, 951 (1998) [Phys. At. Nucl. **61**, 865 (1998)].

Translated by A. Isaakyan

Physics of Atomic Nuclei, Vol. 63, No. 12, 2000, pp. 2103–2110. From Yadernaya Fizika, Vol. 63, No. 12, 2000, pp. 2199–2206.

NUCLEI
Theory

Reactions $p(d, p)d$ and $p(d, p)pn$ as a Tool for Studying the Short-Range Internal Structure of the Deuteron*

V. P. Ladygin**
Joint Institute for Nuclear Research, Dubna, Moscow oblast, 141980 Russia
Received August 5, 1999; in final form, January 18, 2000

Abstract—In recent years, the deuteron structure at short distances has often been treated from the point of view of nonnucleonic degrees of freedom. In this study, measurements of *T*-odd polarization observables by using a tensorially polarized deuteron beam and a polarized proton target or a proton polarimeter are proposed as a means for seeking quark configurations inside the deuteron. © *2000 MAIK "Nauka/Interperiodica".*

1. INTRODUCTION

Recent experimental results concerning the structure of the deuteron led to the speculations that manifestations of the quark–gluon degrees of freedom are present even at relatively large distances between nucleons. Measurements of the cross section for the inclusive deuteron-breakup reaction $A(d, p)X$ on carbon with the proton emitted at zero angle [1] showed a relatively broad shoulder at internal nucleon momenta of $k \sim 0.35$ GeV/c in the deuteron defined in the light-cone dynamics [2–4]. This enhancement was observed later at different initial energies and for different A values of the target [5–7]. This shoulder could not be reproduced by calculations within relativistic impulse approximation (IA) by using the standard deuteron wave functions [8–10] or by including rescattering corrections [11]. The theoretical study of Kobushkin and Vizireva led to the possibility that there exists a $6q$ admixture in the deuteron wave function [12]. This $6q$ amplitude, arising from the S configurations of six quarks, must be added to the S component of the standard deuteron wave function with a relative phase χ. A fit to the experimental data [5] gave the probability of the $6q$ configuration about 4% and relative angle of $\chi \sim 82°$ and $\sim 61°$ for the Paris [8] and the Reid soft-core (RSC) [9] NN potential, respectively. An admixture of the $6q$ state of about 3.4% was introduced in [13] as well to describe the tail of the momentum spectrum for the reaction $^{12}C(d, p)X$ [5].

One of the important features of this hybrid wave function is that an additional $6q$ admixture masks the node of the NN S wave, and this is drastically reflected in the behavior of polarization observables. For instance, data obtained at Saclay for the tensor analyzing power T_{20} and the cross section in inclusive deuteron breakup at zero angle and at an initial energy of 2.1 GeV [7] were explained by the hybrid wave function with ~4% of the $|6q\rangle$ probability at 55° of the relative phase between $|6q\rangle$ and the S component from the RSC potential [9].

Recent measurements of the tensor analyzing power T_{20} for deuteron inclusive breakup at 0° that were performed in Saclay [7] and in Dubna [14–16] at different energies and for different targets showed the strong deviation from the IA predictions at $k \geq 0.2$ GeV/c. The behavior of the coefficient of polarization transfer from a vectorially polarized deuteron to a proton (κ_0) [17–19] also disagrees with the calculations using conventional deuteron wave functions at $k \geq 0.2$ GeV/c. On the other hand, both T_{20} and κ_0 data demonstrate some features of the IA like a weak dependence on the target mass number A and an approximate energy independence. A consideration of the mechanisms additional to the IA one [20, 21] cannot explain the experimental data.

The most intriguing feature of experimental data is that the tensor analyzing power T_{20} in deuteron inclusive breakup and backward elastic deuteron–proton scattering show, at high internal proton momenta, the same negative value of about –(0.3–0.4) [15, 16, 22], which is incompatible with the predictions using any reasonable nucleon–nucleon potential. Various attempts were undertaken to explain the T_{20} data by taking into account nonnucleonic degrees of freedom in the deuteron. An asymptotic negative limit on T_{20} was obtained within the QCD-motivated approach presented in [23] and based on the reduced-nuclear-amplitude method [24]. The results of calculations [20] with the hybrid deuteron wave function [25] made it possible to describe satisfactorily the T_{20} data up to $k \sim 1$ GeV/c [15]. Recently, the data on T_{20} and κ_0 in the $^{12}C(d, p)X$ reaction at 0° were reasonably reproduced within a model that incorporates multiple scattering and the Pauli exclusion principle at the quark level [26]. By additionally taking into account the exchanges of negative-parity nucleon resonances, Azhgirey and Yudin [27] were able to improve the agreement

* This article was submitted by the author in English.
** e-mail: ladygin@sunhe.jinr.ru

between the results of the calculations and experimental data on T_{20} in backward elastic dp scattering. The tensor analyzing power A_{yy} obtained for deuteron inclusive breakup up to proton transverse momenta of 600 MeV/c [28] also disagrees with the calculations within the hard-scattering model [29] using conventional deuteron wave functions. However, the sign of A_{yy} at high proton momenta at zero angle [14–16],[1)] as well as at an angle of about 90° in the deuteron rest frame [28], is identical to that predicted by the QCD-motivated approach used in [23].

These special features of experimental data and relatively successful attempts at describing them by considering nonnucleonic degrees of freedom stimulate possible efforts to measure additional polarization observables that are crucial to quark degrees of freedom in the deuteron.

In [30], it was proposed to study the deuteron structure at short distances by using a polarized proton target and a proton polarimeter. Here, investigation of T-odd polarization observables [31] in deuteron exclusive breakup in collinear geometry and backward elastic dp scattering is considered as a means for identifying the exotic 6q configurations inside the deuteron.

2. MATRIX ELEMENTS OF THE REACTIONS $dp \longrightarrow ppn$ AND $dp \longrightarrow pd$

In this section, we analyze the polarization effects in two processes: deuteron breakup in the strictly collinear geometry, $d + p \longrightarrow p(0°) + p(180°) + n$, and backward elastic deuteron–proton scattering, $d + p \longrightarrow p + d$, using the hybrid deuteron wave function with the complex 6q admixture.

This function can be presented in the momentum space in the following form:

$$\Phi_d(\mathbf{p}) = \frac{i}{\sqrt{2}}\frac{1}{\sqrt{4\pi}}\psi_p^{\alpha+}\Big[\Big(U(p)(\boldsymbol{\sigma}\cdot\boldsymbol{\xi}) - \frac{W(p)}{\sqrt{2}}(3(\hat{\mathbf{p}}\cdot\boldsymbol{\xi})(\boldsymbol{\sigma}\cdot\hat{\mathbf{p}}) - (\boldsymbol{\sigma}\cdot\boldsymbol{\xi}))\Big)\sigma_y\Big]_{\alpha\beta}\psi_n^{\beta+}, \quad (1)$$

where ψ_p and ψ_n are the proton and neutron spinors, respectively; $\boldsymbol{\xi}$ is the deuteron polarization vector defined in a standard manner:

$$\boldsymbol{\xi}_1 = -\frac{1}{\sqrt{2}}(1, i, 0), \quad \boldsymbol{\xi}_{-1} = \frac{1}{\sqrt{2}}(1, -i, 0), \quad \boldsymbol{\xi}_0 = (0, 0, 1); \quad (2)$$

$\mathbf{p}$ is the relative proton–neutron momentum inside the deuteron; and $\hat{\mathbf{p}} = \mathbf{p}/|\mathbf{p}|$ is the unit vector in the $\mathbf{p}$ direction. Here, S and D components are defined as

$$U(p) = u(p) + v_0(p)e^{i\chi}, \quad W(p) = w(p) + v_2(p)e^{i\chi}, \quad (3)$$

where $u(p)$ and $w(p)$ are S and D components of the standard deuteron wave function based on the NN potentials, and $v_0(p)e^{i\chi}$ and $v_2(p)e^{i\chi}$ are the complex 6q admixtures to the S and D components of the standard deuteron wave function, respectively.

Using parity conservation, time reversal invariance, and the Pauli exclusion principle, we can write the matrix of NN elastic scattering in terms of five independent complex amplitudes [32] (when isospin invariance is assumed):

$$M(\mathbf{k}', \mathbf{k}) = \frac{1}{2}((a+b) + (a-b)(\boldsymbol{\sigma}_1\cdot\mathbf{n})\cdot(\boldsymbol{\sigma}_2\cdot\mathbf{n}) + (c+d)(\boldsymbol{\sigma}_1\cdot\mathbf{m})\cdot(\boldsymbol{\sigma}_2\cdot\mathbf{m}) + (c-d)(\boldsymbol{\sigma}_1\cdot\mathbf{l})\cdot(\boldsymbol{\sigma}_2\cdot\mathbf{l}) + e((\boldsymbol{\sigma}_1+\boldsymbol{\sigma}_2)\cdot\mathbf{n})), \quad (4)$$

where a, b, c, d, and e are the scattering amplitudes; $\boldsymbol{\sigma}_1$ and $\boldsymbol{\sigma}_2$ are the Pauli 2×2 matrices; $\mathbf{k}$ and $\mathbf{k}'$ are the unit vectors in the directions of the incident and scattered particles, respectively; and center-of-mass basis vectors $\mathbf{n}$, $\mathbf{l}$, and $\mathbf{m}$ are defined as

$$\mathbf{n} = \frac{\mathbf{k}'\times\mathbf{k}}{|\mathbf{k}'\times\mathbf{k}|}, \quad \mathbf{l} = \frac{\mathbf{k}'+\mathbf{k}}{|\mathbf{k}'+\mathbf{k}|}, \quad \mathbf{m} = \frac{\mathbf{k}'-\mathbf{k}}{|\mathbf{k}'-\mathbf{k}|}. \quad (5)$$

However, at a zero angle there are only three independent amplitudes, and the matrix element (4) can be written as [32]

$$\mathcal{M}(0) = \frac{1}{2}(A + B(\boldsymbol{\sigma}_1\cdot\boldsymbol{\sigma}_2) + C(\boldsymbol{\sigma}_1\cdot\mathbf{k})(\boldsymbol{\sigma}_2\cdot\mathbf{k})), \quad (6)$$

where amplitudes A, B, and C are related to the amplitudes defined in [32] as follows:

$$A = a(0) + b(0), \quad B = c(0) + d(0), \quad C = -2d(0). \quad (7)$$

We consider deuteron breakup reaction in the special kinematics, i.e., with the emission of the spectator proton at zero angle, while the neutron interacts with the proton target and the products of this interaction go along the axis of the reaction.

Using both expressions (1) and (6), the matrix element of deuteron breakup process in collinear geometry can be written as [30]

$$\mathcal{M} = \frac{i}{2\sqrt{2}}\frac{1}{\sqrt{4\pi}}\psi_1^+\psi_2^+\Big[\Big(U(p)(\boldsymbol{\sigma}\cdot\boldsymbol{\xi}) - \frac{W(p)}{\sqrt{2}}(3(\hat{\mathbf{p}}\cdot\boldsymbol{\xi})(\boldsymbol{\sigma}\cdot\hat{\mathbf{p}}) - (\boldsymbol{\sigma}\cdot\boldsymbol{\xi}))\Big)\sigma_y\Big] \times (A + B(\boldsymbol{\sigma}_1\cdot\boldsymbol{\sigma}_2) + C(\boldsymbol{\sigma}_1\cdot\mathbf{k})(\boldsymbol{\sigma}_2\cdot\mathbf{k}))\psi_1^*\psi_2. \quad (8)$$

The matrix element of backward elastic dp scattering within the framework of one-nucleon exchange has

[1)] At zero emission angle, we have $A_{yy} = -T_{20}/\sqrt{2}$.

the following form:

$$\mathcal{M} = \frac{1}{8\pi}\psi_f^+\Big(U^*(p)(\boldsymbol{\sigma}_f\cdot\boldsymbol{\xi}_f^*) - \frac{W^*(p)}{\sqrt{2}}(3(\hat{\mathbf{p}}\cdot\boldsymbol{\xi}_f^*)(\boldsymbol{\sigma}_f\cdot\hat{\mathbf{p}}) - (\boldsymbol{\sigma}_f\cdot\boldsymbol{\xi}_f^*))\Big) \times\Big(U(p)(\boldsymbol{\sigma}_i\cdot\boldsymbol{\xi}_i) - \frac{W(p)}{\sqrt{2}}(3(\hat{\mathbf{p}}\cdot\boldsymbol{\xi}_i)(\boldsymbol{\sigma}_i\cdot\hat{\mathbf{p}}) - (\boldsymbol{\sigma}_i\cdot\boldsymbol{\xi}_i))\Big)\psi_i. \quad (9)$$

3. SIX-QUARK CONFIGURATIONS

In this section, we consider different models considering the quark (or baryon–baryon) degrees of freedom inside the deuteron.

In the hybrid model of the deuteron wave function [12], the $6q$ amplitude arising from the s^6 configurations of six quarks must be added to the S component of the standard deuteron wave function according to the expression

$$U(k) = \sqrt{1-\beta^2}u(k) + \beta v_0(k)e^{i\chi}, \quad (10)$$

where the parameter β and the phase χ represent the value of the $6q$ admixture in the deuteron and the degree of nonorthogonality between np and $6q$ components of the deuteron wave function, respectively.

The $6q$ admixture has the following form:

$$v_0(k) = I\sqrt{10}\cdot 2^{2/3}\left(\frac{2}{1+\sqrt{2}}\right)^6\left(\frac{2}{3\pi\omega}\right)^{3/4}e^{-k^2/3\omega}. \quad (11)$$

Here, factor $I \approx 0.332$ is the overlap factor of color spin–isospin wave functions, ω defines the root-mean-square radius of the $6q$ configuration $r^2 = 5/4\omega$, and k is internal momentum of a nucleon in the deuteron defined in the light-cone dynamics [2–4].

The parameters of the $6q$ admixture r, β, and χ were obtained in [33] from the fit of the experimental data on the momentum density of the nucleon in deuteron $\phi^2(k)$ [5], tensor analyzing power T_{20} [16], and polarization-transfer coefficient κ_0 [17–19] for inclusive deuteron breakup with the emission of the proton at a zero angle using standard deuteron wave functions [8–10]. The results of the fit are given in Table 1 and shown in Fig. 1 by the solid, dashed, and dotted curves for the RSC [9], Paris [8], and Bonn (version C) [10] deuteron wave functions, respectively. One can see the satisfactory description of the experimental data. The probability of the $6q$ admixture is found to be 3–4%. The relative phase is ~40° for the RSC [9], ~47° for the Paris [8], and 55° for the Bonn (C) deuteron wave function [10]. The radius is $r \sim 0.6$ fm for all used deuteron wave functions. The parameters are comparable with the results obtained in [7] using the RSC deuteron wave function [9].

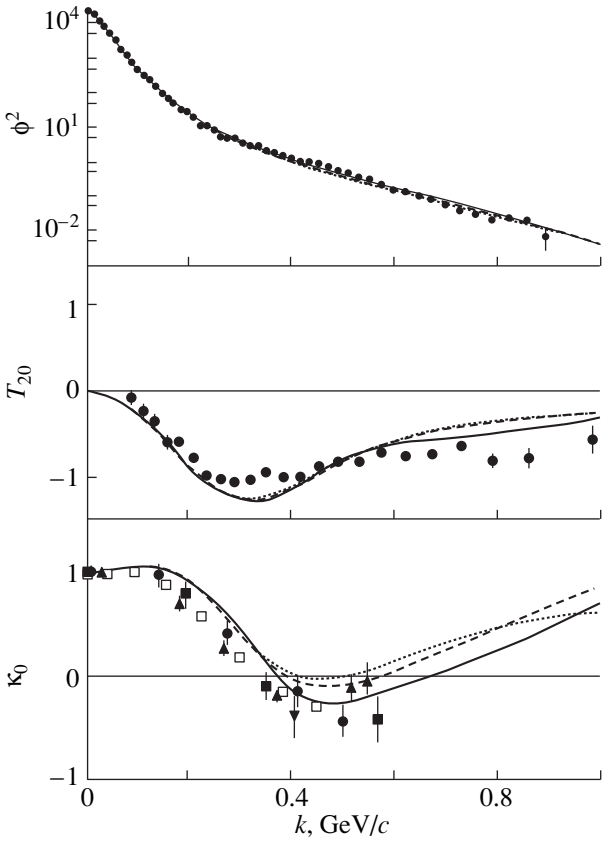

Fig. 1. Momentum density $\phi^2(k)$ [5], tensor analyzing power T_{20} [16], and polarization transfer coefficient κ_0 [17] (open squares), [18] (full triangles), and [19] (full circles and squares) versus internal momentum k in deuteron inclusive breakup with the emission of proton at 0°. Solid, dashed, and dotted curves correspond to calculations with hybrid wave function [12] using the RSC [9], Paris [8], and Bonn (C) [10] deuteron wave functions, respectively.

In [20, 25], the nonnucleonic degrees of freedom (NN^*, $NN\pi$, and higher components of the Fock space) were taken into account in the following way:

$$\Phi^2(\alpha, k_t) = (1-\beta^2)\phi_{NN}^2(\alpha, k_t)/(2\alpha(1-\alpha)) + \beta^2 G_d(\alpha, k_t), \quad (12)$$

where $\Phi^2(\alpha, k_t)$ is the distribution of constituents in the deuteron; $\phi_{NN}(\alpha, k_t)$ is the relativized standard deuteron wave function; $G_d(\alpha, k_t)$ is the distribution of NN^*, $NN\pi$, …, or $6q$ component in the deuteron. Parameter β^2 gives the probability of this nonnucleonic compo-

Table 1. Parameters of the $6q$ admixture in the hybrid model [12] for various standard deuteron wave functions [8–10]

DWF	β^2, %	χ, deg	r, fm
[8]	3.42 ± 0.09	47.2 ± 0.6	0.578 ± 0.009
[9]	4.07 ± 0.10	40.1 ± 0.6	0.590 ± 0.009
[10]	2.79 ± 0.09	55.1 ± 0.7	0.595 ± 0.010

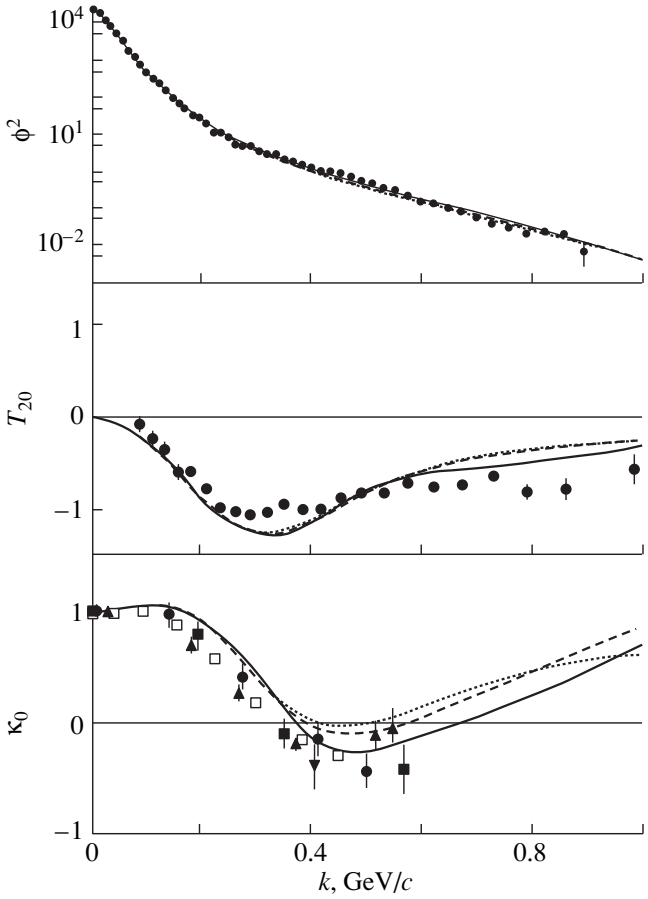

Fig. 2. Momentum density $\phi^2(k)$ [5], tensor analyzing power T_{20} [16], and polarization transfer coefficient κ_0 [17–19] versus internal momentum k in deuteron inclusive breakup with the emission of proton at 0°. Solid, dashed, and dotted curves correspond to calculations with the wave function adopted in [20, 25] using the RSC [9], Paris [8], and Bonn (C) [10] deuteron wave functions, respectively. The notation for the points is identical to that in Fig. 1.

nent. The relativistic form of the deuteron wave function $\phi_{NN}(\alpha, k_t)$ can be written according to [2–4] as

$$\phi_{NN}(\alpha, k_t) = \left(\frac{m_p^2 + k_t^2}{4\alpha(1-\alpha)}\right)^{1/4} \phi(k), \qquad (13)$$

where $\phi(k)$ is the standard deuteron wave function (for instance, [8–10]) and internal momentum k and longitudinal momentum fraction α are defined as [2–4]

$$k^2 = \frac{m_p^2 + k_t^2}{4\alpha(1-\alpha)} - m_p^2,$$
$$\alpha = \frac{k_\parallel + \sqrt{k_\parallel^2 + m_p^2}}{2\sqrt{k_\parallel^2 + m_p^2}}. \qquad (14)$$

Here, $k_\parallel$ is the longitudinal momentum in infinite momentum frame and m_p is the nucleon mass.

The expression for nonnucleonic component $G_d(\alpha, k_t)$ is written as [25]

$$G_d(\alpha, k_t) = b^2/(2\pi) G_1(\alpha) e^{-bk_t} \qquad (15)$$

with

$$G_1(\alpha) = \Gamma(A_2 + B_2 + 2)/(\Gamma(A_2 + 1)\Gamma(B_2 + 1)) \times \alpha^{A_2}(1-\alpha)^{B_2}, \qquad (16)$$

where $\Gamma(\ldots)$ denotes the Γ function. The parameter b is chosen to be 5 GeV/c. We assume that nonnucleonic component (15), (16) has the relative phase χ with the S wave of the standard deuteron wave function [20].

The results of the fit of the experimental data [5, 16–19] are given in Table 2 and shown in Fig. 2 by the solid, dashed, and dotted curves for RSC [9], Paris [8], and Bonn (C) [10] deuteron wave functions, respectively. The probability of the nonnucleonic component is found to be also ~3%. The relative phase χ between *NN* and nonnucleonic components is 40°–60°. The parameters A_2 and B_2 are found to be approximately the same for Paris [8], RSC [9], and Bonn (C) [10] deuteron wave functions. Note that all the used *NN* deuteron wave functions provide satisfactory agreement with the existing data; however, using the RSC deuteron wave function gives a better description of the polarization transfer coefficient κ_0.

Table 2. Parameters of the 6q admixture [20, 25] for various standard deuteron wave functions [8–10]

DWF	β_2, %	A_2	B_2	χ, deg
[8]	2.96 ± 0.18	10.0*	20.23 ± 0.42	47.0 ± 0.6
[9]	3.70 ± 0.43	10.0 ± 0.9	19.87 ± 2.72	40.2 ± 0.6
[10]	2.67 ± 0.19	10.0*	19.46 ± 0.48	54.6 ± 0.7

* This parameter is fixed.

4. *T*-ODD POLARIZATION EFFECTS

Let us define the general spin observable of the third order in terms of Pauli 2×2 spin matrices σ for protons and a set of spin operators S_λ for the spin-one particle for both reactions as [34]

$$C_{\alpha,\lambda,\beta,0} = \frac{\mathrm{tr}(\mathcal{M}\sigma_\alpha^p S_\lambda^d \mathcal{M}^+ \sigma_\beta^p)}{\mathrm{tr}(\mathcal{M}\mathcal{M}^+)}, \qquad (17)$$

where indices α and λ refer to the initial proton and deuteron polarization, and index β refers to the final proton, respectively.

We use a right-hand coordinate system, defined in accordance with Madison convention [35]. This system is specified by a set of three orthogonal vectors **L**, **N**, and **S**, where **L** is the unit vector along the momenta of the incident particle, **N** is taken to be orthogonal to **L**, and $\mathbf{S} = \mathbf{N} \times \mathbf{L}$.

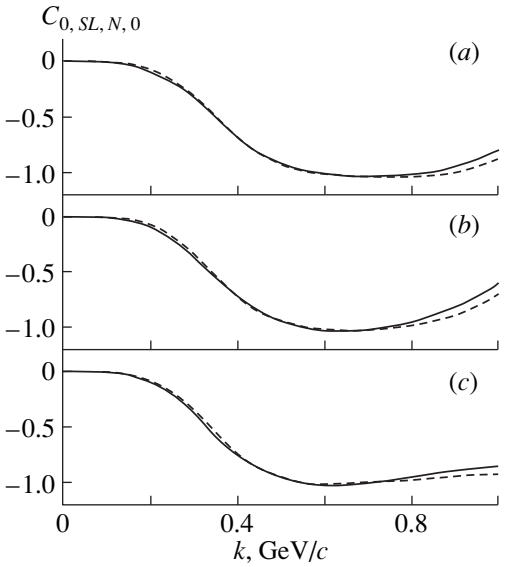

Fig. 3. Tensor-vector polarization transfer coefficient $C_{0, SL, N, 0}$ in deuteron exclusive breakup in the collinear geometry and backward elastic dp scattering using $6q$ admixture adopted in [12] (solid curves) and [20, 25] (dashed curves). The curves are obtained with the use of the (*a*) Paris [8], (*b*) RSC [9], and (*c*) Bonn (C) [10] deuteron wave functions.

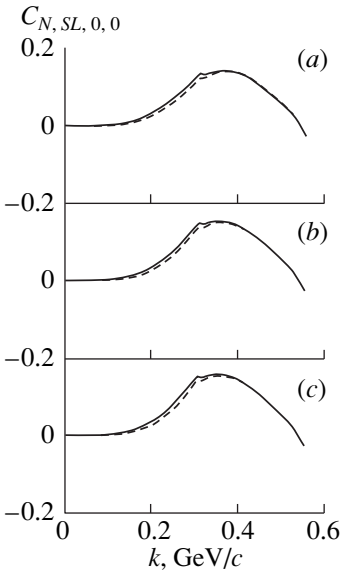

Fig. 4. Tensor-vector spin correlation parameter $C_{N, SL, 0, 0}$ in deuteron exclusive breakup in the collinear geometry at 2.1 GeV of the deuteron initial energy using $6q$ admixture adopted in [12] (solid curves) and [20, 25] (dashed curves). The curves are obtained with the use of the (*a*) Paris [8], (*b*) RSC [9], and (*c*) Bonn (C) [10] deuteron wave functions.

In this paper, we consider *T*-odd polarization observables, namely, tensor-vector spin correlations $C_{N, SL, 0, 0}$ due to tensor polarization of the beam and polarization of the initial proton and polarization transfer coefficient $C_{0, SL, N, 0}$ from tensor polarized deuteron to proton in the $dp \longrightarrow pd$ and $dp \longrightarrow p(0°) + p(180°) + n$ reactions. Note that such observables must be zero in the framework of one-nucleon exchange using standard deuteron wave functions; however, they do not vanish with the existing $6q$ admixture in the deuteron wave function.

Using the formulas for the matrix elements of the $p(d, p)pn$ and $p(d, p)d$ reactions (8) and (9), respectively, one can obtain the expression for the polarization transfer coefficient $C_{0, SL, N, 0}$:

$$C_{0, SL, N, 0} = \frac{3}{\sqrt{2}} \frac{w v_0 \sin\chi}{u^2 + w^2 + v_0^2 + 2uv_0\cos\chi}. \qquad (18)$$

One can see that $C_{0, SL, N, 0}$ does not depend on the initial energy and is defined only by the interference between the *D* wave of the standard deuteron wave function and $6q$ admixture. The results of the calculations with the use of Paris [8], RSC [9], and Bonn (C) [10] deuteron wave functions are presented in Figs. 3*a*, 3*b*, and 3*c* for two different models of the $6q$ admixture: [12] (solid curves) and [20, 25] (dashed curves). These two types of hybrid deuteron wave functions give quite similar behavior of the $C_{0, SL, N, 0}$ up to $k \sim 800$ MeV/c; however, they differ at higher momenta. Both models predict the smooth variation of the $C_{0, SL, N, 0}$ of about –1 at $k \sim 600$ MeV/c. The dependence on the used *NN* deuteron wave function occurs only at high k of about 900 MeV/c. Therefore, the observation of a large negative value of $C_{0, SL, N, 0}$ could indicate that quark degrees of freedom play quite an important role in the deuteron at large k.

Spin correlation parameter $C_{N, SL, 0, 0}$ due to tensor polarization of the beam and polarization of the initial

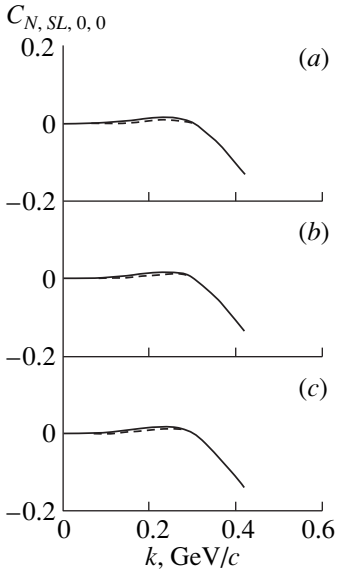

Fig. 5. As in Fig. 4, but for the collinear geometry at 1.25 GeV.

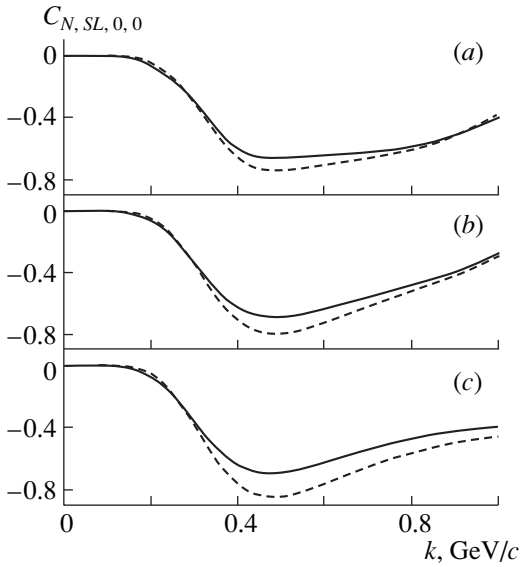

Fig. 6. Tensor-vector spin correlation parameter $C_{N, SL, 0, 0}$ in backward elastic deuteron–proton scattering using $6q$ admixture adopted in [12] (solid curves) and [20, 25] (dashed lines). The curves are obtained with the use of the (*a*) Paris [8], (*b*) RSC [9], and (*c*) Bonn (C) [10] deuteron wave functions.

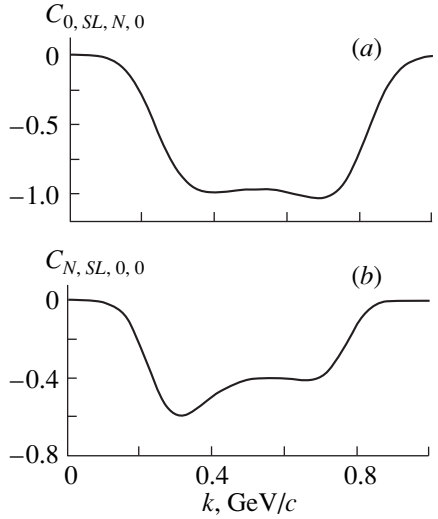

Fig. 7. (*a*) Tensor-vector polarization transfer coefficient $C_{0, SL, N, 0}$ in deuteron exclusive breakup in the collinear geometry and backward elastic *dp* scattering and (*b*) tensor-vector spin correlation parameter $C_{N, SL, 0, 0}$ in backward elastic deuteron–proton scattering using results of [39] and Paris deuteron wave function [8].

proton for the $dp \longrightarrow p(0°) + p(180°) + n$ process can be written as

$$C_{N, SL, 0, 0} = \frac{3}{\sqrt{2}} \frac{w v_0 \sin\chi}{u^2 + w^2 + v_0^2 + 2uv_0\cos\chi} A_{oonn}(0°), \quad (19)$$

where $A_{oonn}(0°)$ is spin correlation of elastic neutron–proton scattering at a zero angle for vertically polarized particles (see notation used in [32, 30]). Therefore, the behavior of $C_{N, SL, 0, 0}$ in the $dp \longrightarrow p(0°) + p(180°) + n$ reaction is defined by both the deuteron wave function and the *np* elementary amplitude, which is energy dependent. The calculations of $C_{N, SL, 0, 0}$ for the deuteron initial energy of 2.1 and 1.25 GeV using the results of phase-shift analysis performed in [36] are shown in Figs. 4 and 5, respectively. One can see that $C_{N, SL, 0, 0}$ is positive at 2.1 GeV up to $k \sim 550$ MeV/*c* and negative at 1.25 GeV at $k \sim 300$–400 MeV/*c*. The difference between the two models of $6q$ admixture shown by the solid [12] and dashed [20, 25] curves for (*a*) Paris [8], (*b*) RSC [9], and (*c*) Bonn (C) [10] deuteron wave functions is not dramatic at both energies.

Spin correlation parameter $C_{N, SL, 0, 0}$ in backward elastic deuteron–proton scattering is given by

$$C_{N, SL, 0, 0} = \frac{1}{\sqrt{2}} \frac{w v_0 \sin\chi((u + v_0\cos\chi - \sqrt{2}w)^2 + v_0^2\sin^2\chi)}{(u^2 + w^2 + v_0^2 + 2uv_0\cos\chi)^2}. \quad (20)$$

The behavior of this observable for different types of $6q$ admixture in the deuteron wave functions is shown in Fig. 6 for (*a*) Paris [8], (*b*) RSC [9], and (*c*) Bonn (C) [10] deuteron wave functions by the solid [12] and dashed [20, 25] curves. One can see that the spin correlation $C_{N, SL, 0, 0}$ has a small negative value at low *k*, then it approaches a minimum of –(0.7–0.8) at $k \sim 400$ MeV/*c*, and afterwards it goes smoothly to a zero for both models of $6q$ component. However, the use of deuteron wave functions with the $6q$ admixture adopted in [20, 25] gives systematically more negative value of spin correlation at internal momenta ≥300 MeV/*c*. The use of different *NN* potentials [8–10] (see Figs. 6*a*, 6*b*, and 6*c*, respectively) gives slightly different behavior of $C_{N, SL, 0, 0}$ for both models of $6q$ admixture. Nevertheless, one can conclude that the measurements of spin correlation $C_{N, SL, 0, 0}$ in backward elastic *dp* scattering can help to distinguish between these two models.

Note that nonorthogonality in the deuteron wave function results in the *T*-invariance violation, which contradicts the experiment. However, *NN* and $6q$ components can be orthogonalized following the procedure described in [37]. Such a procedure only slightly changes the probability of $6q$ admixture [37], but does not affect the behavior of the considered observables. For instance, the probability of $6q$ component changes from 2.96 to 3.31% and from 3.42 to 4.17% for the models [12] and [20, 25], respectively, in the case of the use of the Paris deuteron wave function [8].

The six-quark wave function of the deuteron has been calculated recently not only from s^6, but also from s^4p^2 configurations [38]. Such configurations are orthogonal to the usual *S* and *D* waves in the deuteron. Tensor analyzing power T_{20} and polarization transfer

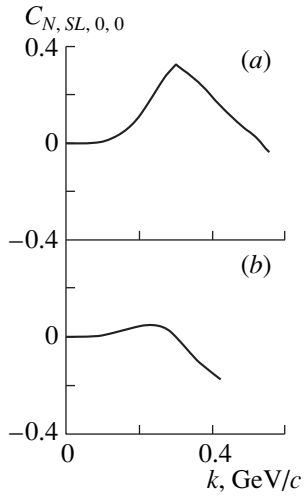

Fig. 8. Tensor-vector spin correlation parameter $C_{N, SL, 0, 0}$ in deuteron exclusive breakup in the collinear geometry at (*a*) 2.1 GeV and (*b*) at 1.25 GeV of the deuteron initial energy results of [39] and Paris deuteron wave function [8].

coefficient κ_0 in deuteron inclusive breakup at zero proton emission angle have been qualitatively reproduced at large internal momenta using the results of these calculations [39]. The probability of the *D* wave originated from s^4p^2 configurations was found to be about 0.5% (a small part of the total *D* wave probability ~6%). The results on the polarization transfer $C_{0, SL, N, 0}$ and spin correlation $C_{N, SL, 0, 0}$ in backward elastic *dp* scattering using the Paris deuteron wave function [8] and the 6*q* projection on *NN* component from [39] are given in Figs. 7*a* and 7*b*, respectively. The behavior of this observable differs significantly from the results shown in Figs. 3 and 6. This deviation is due to presence of *D* wave in the six-quark wave function. The results on tensor-vector spin correlation $C_{N, SL, 0, 0}$ in the reaction $dp \longrightarrow p(0°) + p(180°) + n$ at the initial deuteron energy of 2.1 and 1.25 GeV are shown in Figs. 8*a* and 8*b*, respectively. The behavior is qualitatively the same as shown in Figs. 4 and 5; however, the value of $C_{SL, N, 0, 0}$ at 2.1 GeV and $k \sim 300$ MeV/c is twice as much as that in the case of absence of *D* wave.

One of the interesting features of QCD consists in the possible existence of resonances in the dibaryon system corresponding to six-quark states with dominantly hidden color, i.e., the states orthogonal to the usual *np* states. The rich structure in the behavior of the tensor analyzing power T_{20} in backward elastic *dp* scattering [22, 40] can be an indication of such dibaryon resonances [41].

Of course, the mechanisms additional to one-nucleon exchange can contribute to $C_{N, SL, 0, 0}$ and $C_{0, SL, N, 0}$. However, the calculations taking into account such mechanisms [20] show that their contribution is small at large internal momenta. Thus, the observation of large values of $C_{N, SL, 0, 0}$ and $C_{0, SL, N, 0}$ at momenta higher than 600 MeV/c could be a rather clear indication of the exotic 6*q* configurations.

5. CONCLUSION

We have considered *T*-odd observables in deuteron exclusive breakup and backward elastic *dp* scattering, namely, tensor-vector polarization transfer coefficient $C_{0, SL, N, 0}$ and tensor-vector spin correlation $C_{N, SL, 0, 0}$. These observables, which are associated with the tensor polarization of the deuteron and the polarization of the proton, are sensitive to quark degrees of freedom in the deuteron and to their spin structure. The calculations give a sizable effect at large internal momenta, which could be measured with the existing experimental techniques.

Measurement of these observables could be performed at COSY at the Zero Degree Facility (ANKE) using an internal polarized target with the detection of two charged particles in case of deuteron breakup and with the detection of the fast proton in case of backward elastic *dp* scattering.

Such experiments could be also performed at the Laboratory for High Energies of the Joint Institute for Nuclear Research. The rotation of the primary deuteron spin could be provided by the magnetic field of the beam line upstream of the target or by the special spin-rotating magnet.

ACKNOWLEDGMENTS

I am indebted to Dr. N. B. Ladygina for critically revising this manuscript and for permanent help and support. I am also grateful to Prof. A.P. Kobushkin for helpful comments and discussions. I thank I.M. Sitnik for estimating the bending angle of the magnetic system upstream of the polarized target installed now at the Laboratory for High Energies of JINR.

REFERENCES

1. V. G. Ableev *et al.*, Nucl. Phys. A **393**, 491 (1983); Erratum: **411**, 541 (1983); Pis'ma Zh. Éksp. Teor. Fiz. **37**, 196 (1983) [JETP Lett. **37**, 233 (1983)].
2. P. A. M. Dirac, Rev. Mod. Phys. **21**, 392 (1949).
3. S. Weinberg, Phys. Rev. **150**, 1313 (1966).
4. L. L. Frankfurt and M. I. Strikman, Phys. Rep. **76**, 215 (1981).
5. V. G. Ableev *et al.*, Pis'ma Zh. Éksp. Teor. Fiz. **45**, 467 (1987) [JETP Lett. **45**, 596 (1987)]; JINR Rapid Commun., No. 1[52]-92, 10 (1992).
6. L. Anderson *et al.*, Phys. Rev. C **28**, 1224 (1983).
7. C. F. Perdrisat *et al.*, Phys. Rev. Lett. **59**, 2840 (1987); V. Punjabi *et al.*, Phys. Rev. C **39**, 608 (1989).
8. M. Lacombe *et al.*, Phys. Lett. B **101B**, 131 (1981).
9. R. V. Reid *et al.*, Ann. Phys. (N.Y.) **50**, 411 (1968).
10. R. Machleidt *et al.*, Phys. Rep. **149**, 1 (1987).

11. L. Bertocchi and A. Tekou, Nuovo Cimento A **21**, 223 (1974); L. Bertocchi and D. Treleani, Nuovo Cimento A **36**, 1 (1976).
12. A. P. Kobushkin and L. Vizireva, J. Phys. G **8**, 893 (1982).
13. M. A. Ignatenko and G. I. Lykasov, Yad. Fiz. **46**, 1080 (1987) [Sov. J. Nucl. Phys. **46**, 625 (1987)].
14. V. G. Ableev *et al.*, Pis'ma Zh. Éksp. Teor. Fiz. **47**, 558 (1988) [JETP Lett. **47**, 649 (1988)]; JINR Rapid Commun. 4[43]-90, 5 (1990).
15. T. Aono *et al.*, Phys. Rev. Lett. **74**, 4997 (1995).
16. L. S. Azhgirey *et al.*, Phys. Lett. B **387**, 37 (1996).
17. N. E. Cheung *et al.*, Phys. Lett. B **284**, 210 (1992).
18. A. A. Nomofilov *et al.*, Phys. Lett. B **325**, 327 (1994).
19. B. Kuehn *et al.*, Phys. Lett. B **334**, 298 (1994); L. S. Azhgirey *et al.*, JINR Rapid Commun., No. 3[77]-96, 23 (1996).
20. G. I. Lykasov and M. G. Dolidze, Z. Phys. A **336**, 339 (1990); G. I. Lykasov, Fiz. Élem. Chastits At. Yadra **24**, 140 (1993) [Phys. Part. Nucl. **24**, 59 (1993)].
21. C. F. Perdrisat and V. Punjabi, Phys. Rev. C **42**, 1899 (1990).
22. L. S. Azhgirey *et al.*, Phys. Lett. B **391**, 22 (1997); Yad. Fiz. **61**, 494 (1998) [Phys. At. Nucl. **61**, 432 (1998)].
23. A. P. Kobushkin, J. Phys. G **19**, 1993 (1993).
24. S. J. Brodsky and J. R. Hiller, Phys. Rev. C **28**, 475 (1983).
25. A. V. Efremov *et al.*, Yad. Fiz. **47**, 1364 (1988) [Sov. J. Nucl. Phys. **47**, 868 (1988)]; Z. Phys. A **338**, 247 (1991).
26. A. P. Kobushkin, Phys. Lett. B **421**, 53 (1998).
27. L. S. Azhgirey and N. P. Yudin, Preprint No. R1-99-157, OIYaF (Joint Institute for Nuclear Research, Dubna, 1999); Yad. Fiz. **63**, 2280 (2000) [Phys. At. Nucl. **63**, 2184 (2000)].
28. S. V. Afanasiev *et al.*, Phys. Lett. B **434**, 21 (1998); V. P. Ladygin *et al.*, Few-Body Syst., Suppl. **10**, 451 (1999); L. S. Azhgirey *et al.*, Preprint No. R1-98-199, OIYaF (Joint Institute for Nuclear Research, Dubna, 1998); Yad. Fiz. **62**, 1796 (1999) [Phys. At. Nucl. **62**, 1673 (1999)].
29. L. S. Azhgirey and N. P. Yudin, Yad. Fiz. **57**, 160 (1994) [Phys. At. Nucl. **57**, 151 (1994)].
30. V. P. Ladygin, Yad. Fiz. **60**, 1371 (1997) [Phys. At. Nucl. **60**, 1238 (1997)].
31. G. G. Ohlsen, Rep. Prog. Phys. **35**, 717 (1972).
32. J. Bystricky, F. Lehar, and P. Winternitz, J. Phys. (Paris) **39**, 1 (1978).
33. V. P. Ladygin, PhD Thesis (Dubna, 1998).
34. V. Ghazikhanian *et al*., Phys. Rev. C **43**, 1532 (1991).
35. *Proceedings of the Third International Symposium on Polarization Phenomena in Nuclear Reactions*, Ed. by H. H. Barschall and W. Haeberli (Madison, 1970).
36. R. A. Arndt *et al.*, Phys. Rev. C **50**, 2731 (1994); Code SAID-95.
37. V. V. Burov *et al.*, Preprint No. R2-81-621, OIYaF (Joint Institute for Nuclear Research, Dubna, 1981).
38. L. Ya. Glozman, V. G. Neudatchin, and I. T. Obukhovsky, Phys. Rev. C **48**, 389 (1993); L. Ya. Glozman and E. I. Kuchina, Phys. Rev. C **49**, 1149 (1994).
39. V. S. Gorovoj and I. T. Obukhovsky, in *Proceedings of the XII International Symposium on High Energy Physics Problems, Dubna, September 1994*, Ed. by A. M. Baldin and V. V. Burov (1997), JINR E1.2-97-79, Vol. 2, p. 189.
40. V. Punjabi *et al.*, Phys. Lett. B **350**, 178 (1995).
41. S. V. Afanasiev *et al.*, JINR Rapid Commun., No. 4[84]-97, 5 (1997).

Physics of Atomic Nuclei, Vol. 63, No. 12, 2000, pp. 2111–2114. Translated from Yadernaya Fizika, Vol. 63, No. 12, 2000, pp. 2207–2210.

ELEMENTARY PARTICLES AND FIELDS
Theory

Inclusive Features of Neutral Strange Particles in $\bar{p}A$ Interactions at 40 GeV/c

K. G. Akhobadze, T. S. Grigalashvili, L. D. Chikovani, E. Sh. Ioramashvili, L. A. Khizanishvili, E. S. Mailian, M. I. Nicoladze, and L. V. Shalamberidze

Institute of Physics, Georgian Academy of Sciences, ul. Tamarashvili 6, GE-380077 Tbilisi, Georgia

Received June 21, 1999

Abstract—Mean inclusive features of neutral strange particles produced in antiproton interactions with D, Li, C, S, Cu, and Pb nuclei at an incident momentum of 40 GeV/c are found as functions of the target mass number.

1. INTRODUCTION

Inclusive characteristics of neutral strange particles produced in antiproton interactions with nuclei at intermediate energies have not yet received adequate study. Such investigations remain topical at present. Our group has already analyzed the yields of neutral strange particles (K^0, Λ, $\bar{\Lambda}$) [1] and the associated multiplicities of charged particles [2] produced in antiproton–nucleus collisions at a momentum of 40 GeV/c. The present article reports on an investigation of inclusive features of neutral strange particles in antiproton collisions with D, Li, C, S, Cu, and Pb nuclei. A global analysis of the aforementioned issues would make it possible to obtain deeper insights into the dynamics of hadron–nucleus interactions.

In studying antiproton–proton collisions at a projectile momentum of 32 GeV/c, Bogolyubsky *et al.* [3] compared the momentum characteristics of antiproton–proton and proton–proton collisions at the same energy. It was shown that K_S^0 mesons produced in the annihilation channel have broader longitudinal-momentum distributions than those in the nonannihilation channel. On average, the kaon transverse momenta are somewhat higher in antiproton–proton than in proton–proton interactions.

In antiproton–proton collisions at c.m. energies of 200 and 900 GeV, the UA5 experiment [4] determined the mean transverse momenta $\langle p_\perp \rangle$ of neutral strange particles in the rapidity region $|y| \le 2$ for Λ hyperons and in the rapidity region $|y| \le 2.5$ for K_S^0 mesons. The mean values $\langle p_\perp \rangle_\Lambda$ appeared to be greater than $\langle p_\perp \rangle_{K^0}$ by a factor of 1.5 at 200 GeV and by a factor of about 1.2 at 900 GeV.

For $\bar{p}$Xe interactions at 200 GeV/c, the NA5 experiment [5] analyzed the rapidity and transverse-momentum distributions of K^0 mesons and Λ hyperons. A shift toward low rapidity values was found in the rapidity distribution of K^0 mesons. The leading-particle effect was observed for Λ hyperons in the nucleus-fragmentation region.

2. DESCRIPTION OF THE EXPERIMENT AND PROCEDURE FOR DATA PROCESSING

An experiment that employed a relativistic ionization streamer chamber (RISK) was performed at the Serpukhov accelerator U-70 with the aim of studying hadron–hadron and hadron–nucleus interactions under the conditions of 4π coverage. A 5-m streamer chamber that was placed in a magnetic field of strength 1.5 T and which made it possible to measure charged-particle momenta to within 10% served as a detector. An unseparated beam that contained π^-, K^-, and $\bar{p}$ particles in the proportion 98 : 1.7 : 0.3 traversed D, Li, C, S, Cu, and Pb nuclear targets of thickness less than 1% of the nuclear range that were arranged at a distance of 30 cm from one another to minimize systematic errors. Eleven targets featuring seven nuclear combinations—D, Li, C, S, Cu, CsI, and Pb—were installed in the chamber of fiducial volume $470 \times 93 \times 80$ cm^3. In fact, we analyzed six pure nuclear species, discarding data on CsI because of its complex composition. The targets were of nonidentical thicknesses, which were reduced in accordance with the growth of the cross section for the production of secondary particles with increasing mass number of the nucleus. Table 1 presents the parameters of the targets in the same order as they were positioned in the chamber.

Film data were viewed on a scanning table with a magnification of 1 : 4 : 5 with respect to the actual chamber dimensions. In scanning, we recorded all secondary two-prong stars (V^0 particles) whose total momentum was directed toward the interaction vertex. These events were further considered as candidates for strange particles. After double viewing, the detection efficiency was 99%.

Table 1. Parameters of targets

Number	Target	Thickness, mm	L_{abs}, %	L_{rad}, %
1	D	198	–	–
2	Pb	0.867	0.315	15.480
3	S	7.123	0.890	6.720
4	Pb	0.612	0.222	10.930
5	Li	16.500	0.840	1.060
6	Pb	0.819	0.298	14.630
7	CsI	1.666	0.283	8.820
8	Cu	1.416	0.641	9.880
9	C	7.040	0.939	2.570
10	CsI	3.315	0.563	16.980
11	Cu	0.978	0.443	6.820

The vertex coordinates and the V^0-particle tracks were measured and reconstructed within the chamber volume. The momentum vectors and the polar and azimuthal emission angles for products originating from V^0-particle decays were calculated on the basis of the results of the reconstruction.

The candidate events were then kinematically processed. This included calculating the coplanarity, the mass, the total momentum, the transverse momentum, the energy, the emission angle with respect to the primary-particle momentum, and the decay range for V^0 particles. Each V^0 event characterized by a deviation from coplanarity in excess of 6° at a root-mean-square error of about 2° was excluded from a further analysis. Such events were either two-prong inelastic interactions of neutral particles (NI) or three-body decays. After that, the V^0 events were identified by means of a least squares kinematical fit to four hypotheses (K_S^0, Λ, γ, $\bar{\Lambda}$) at three degrees of freedom (3*C* fit). Each two-prong event was taken to be unambiguously identified, provided that χ^2 did not exceed 11 for one of the hypotheses. The distributions in $p_\perp^\pi$, the transverse momenta of decay products in the rest frame with respect to the direction of the neutral-particle momentum in the laboratory frame, were used to separate ambiguously identified Λ/K_S^0 and $\bar{\Lambda}/K_S^0$ particles. Unseparated particles were associated with K_S^0 mesons if $p_\perp^\pi \geq 105$ MeV/*c* including the errors in the measurement of this momentum. Only unambiguously identified neutral strange particles were analyzed to determine their physical properties. More details on the selection and identification of the relevant events can be found in [1].

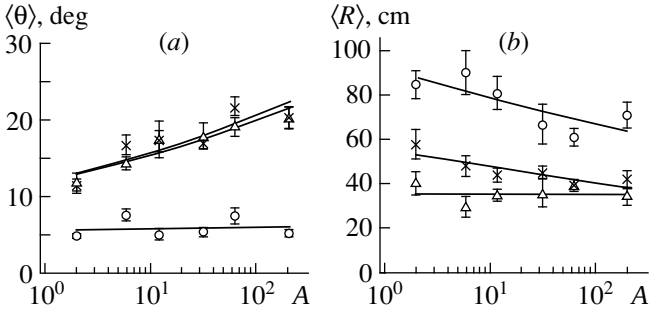

Fig. 1. (*a*) Mean emission angles $\langle\theta\rangle$ for K^0 mesons, Λ hyperons, and $\bar{\Lambda}$ hyperons and (*b*) their mean decay ranges versus the target mass number *A*. In both panels, data for K^0, Λ, and $\bar{\Lambda}$ are represented by crosses, open triangles, and open circles, respectively.

3. ANALYSIS OF EXPERIMENTAL DATA

In this article, the inclusive features of neutral strange particles as functions of the target mass number are presented for the reactions

$$\bar{p}A \longrightarrow K^0 + X, \quad (1)$$

$$\bar{p}A \longrightarrow \Lambda + X, \quad (2)$$

$$\bar{p}A \longrightarrow \bar{\Lambda} + X. \quad (3)$$

Figures 1*a* and 1*b* show the mean emission angles $\langle\theta\rangle$ for strange particles from reactions (1)–(3) with respect to the primary-particle momentum and their decay ranges $\langle R\rangle$ as functions of the target mass number *A*. It is obvious that $\langle\theta\rangle$ is independent of *A* for $\bar{\Lambda}$ hyperons and increases in nearly the same way for K^0 mesons and Λ hyperons. For deuteron targets, the mean emission angle for $\bar{\Lambda}$ hyperons is smaller than those for K^0 and Λ by a factor of about 2.5, and this difference increases with increasing atomic number. For D, Li, C, and S targets, the K^0 and Λ decay ranges differ, but they become indistinguishable within the measurement errors in the case of heavy target nuclei (Cu and Pb). With increasing *A*, the mean decay range is constant for Λ hyperons and decreases in nearly the same way for K^0 mesons and $\bar{\Lambda}$ hyperons.

As might have been expected, the mean decay range $\langle R\rangle$ of $\bar{\Lambda}$ antihyperons is sizably greater than the those for K^0 mesons and Λ hyperons (by factors of about 2 and 3, respectively). Since the decay range $L_0 = \beta\gamma c\tau_0$ depends not only on the lifetime, but also on the particle momentum, $\bar{\Lambda}$ hyperons that have β values in excess of 0.98 decay at distances of $R > 0.7$ m from the interaction vertex, and this explains the loss of $\bar{\Lambda}$ hyperons having momenta above 20–25 GeV/*c*. Lambda antihyperons that escape detection for this reason originate predominantly from the targets in the second half of the chamber in the downstream direction (C and Cu), and that is why their mean momenta are biased for the production processes on these targets.

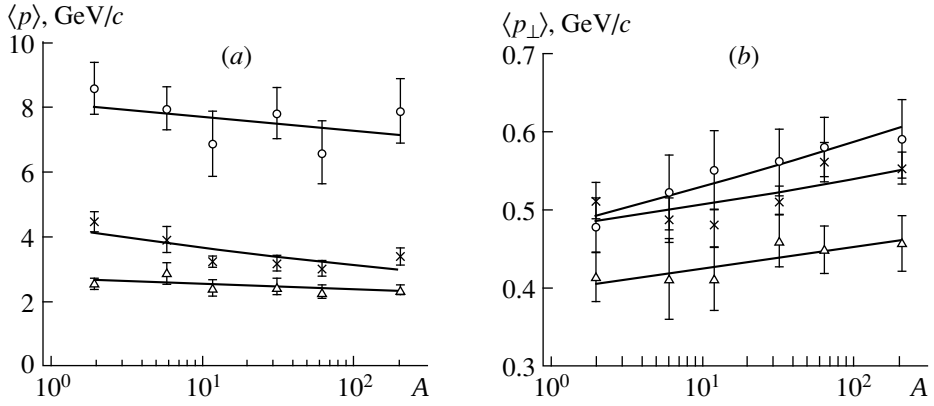

Fig. 2. (*a*) Mean momenta $\langle p \rangle$ and (*b*) mean transverse momenta $\langle p_\perp \rangle$ of (crosses) K^0 mesons, (open triangle) Λ hyperons, and (open circles) $\bar{\Lambda}$ hyperons versus the target mass number *A*.

Since measurements of short tracks after the ($\bar{p}$, π^+) decay resulted in significant errors (in order that $\Delta p/p \sim$ 10%, the length of such "energetic" tracks must exceed 1.5 m), these tracks were excluded from statistics. According to our estimate, their number was about 1.5% of all observed $\bar{\Lambda}$ hyperons.

Figures 2*a* and 2*b* display, respectively, the mean momenta $\langle p \rangle$ and the mean transverse momenta $\langle p_\perp \rangle$ of strange particles as functions of the mass number *A*. As was mentioned above, the mean momenta of $\bar{\Lambda}$ hyperons produced on C and Cu nuclei are somewhat underestimated. The mean momentum of K^0 mesons decreases with increasing target mass number, while the mean momentum of Λ hyperons remains constant.

A slight growth of the transverse momenta $\langle p_\perp \rangle$ with increasing target mass number is observed for almost all neutral strange particles.

The rapidity distributions are known to indicate the kinematical regions where the particles under study are produced. Figure 3 shows the mean laboratory rapidities $\langle y \rangle$ as functions of the target mass number. It is obvious that, in the interactions on deuterons, K^0 mesons and $\bar{\Lambda}$ hyperons are produced in the central rapidity region (the projectile-fragmentation region $\langle y \rangle_{K^0} = 2.27 \pm 0.07$ for kaons and $\langle y \rangle_{\bar{\Lambda}} = 2.24 \pm 0.10$ for lambda antihyperons), while Λ hyperons are produced in the target-fragmentation region ($\langle y \rangle_\Lambda = 1.39 \pm 0.05$). With increasing mass number, $\langle y \rangle$ values for K^0 mesons are shifted to the left, while those for $\bar{\Lambda}$ remain constant.

All the inclusive features studied above were fitted in terms of the power-law function aA^α. Table 2 shows the fitted parameter values and the corresponding values of χ^2/NDF.

4. DISCUSSION OF THE RESULTS

In [1, 2], our group analyzed data on the yields of neutral strange particles and on the associated multiplicities of charged particles in events leading to the production of neutral strange particles in $\bar{p}A$ interactions at 40 GeV/*c*. The results of those analyses suggest the development of an intranuclear cascade in reaction (2) and the suppression of such cascades in reactions (1) and (3). The present analysis confirms these conclusions.

A possible explanation of the decrease in the mean momentum $\langle p \rangle$ of K^0 mesons with increasing target mass number is that K^0 mesons, which are products of a primary interaction or annihilation, have time to undergo rescattering in the nucleus.

It is well known that Λ hyperons are predominantly produced in cascade processes, but the secondary interactions of annihilation kaons with intranuclear nucleons is an additional source of Λ hyperons in antiproton–nucleus collisions. Our analysis of the experimental data reveals that the mean momentum $\langle p \rangle$ of Λ hyper-

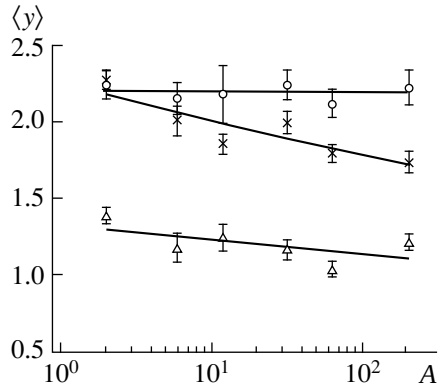

Fig. 3. Mean laboratory rapidities $\langle y \rangle$ of (crosses) K^0 mesons, (open triangle) Λ hyperons, and (open circles) $\bar{\Lambda}$ hyperons versus the target mass number *A*.

Table 2. Fitted values of the parameters in the power-law form aA^{α} used to parametrize the inclusive features of neutral strange particles

Particle	α	*a*	χ^2/NDF
	$\langle p \rangle$		
K^0	-0.07 ± 0.01	4.3 ± 0.4	2.9
Λ	-0.035 ± 0.007	2.8 ± 0.2	0.5
$\bar{\Lambda}$	-0.03 ± 0.01	8.2 ± 0.7	0.6
	$\langle p_\perp \rangle$		
K^0	0.027 ± 0.006	0.48 ± 0.02	1.1
Λ	0.027 ± 0.004	0.40 ± 0.01	0.2
$\bar{\Lambda}$	0.044 ± 0.003	0.48 ± 0.01	0.1
	$\langle y \rangle$		
K^0	-0.051 ± 0.007	2.3 ± 0.1	3.8
Λ	-0.034 ± 0.009	1.3 ± 0.1	3.6
$\bar{\Lambda}$	-0.001 ± 0.003	2.20 ± 0.05	0.3
	$\langle \theta \rangle$		
K^0	0.12 ± 0.01	12.0 ± 1.3	3.5
Λ	0.112 ± 0.008	11.9 ± 0.8	0.6
$\bar{\Lambda}$	0.02 ± 0.02	6.0 ± 1.0	3.8
	$\langle R \rangle$		
K^0	-0.069 ± 0.008	56.0 ± 4.0	1.6
Λ	-0.001 ± 0.010	36.0 ± 4.0	1.0
$\bar{\Lambda}$	-0.07 ± 0.01	92.0 ± 9.0	2.0

ons assumes a near-threshold value (about 2.5 GeV/*c*) owing to these two processes. As a consequence, $\langle p \rangle$ is virtually independent of *A*, in contrast to what occurs in $\pi^- A$ interactions, where the mean momentum $\langle p \rangle$ of Λ hyperons decreased from 4.5 to 2.3 GeV/*c* [6], because there occurred only cascade processes.

Because of a high production threshold, $\bar{\Lambda}$ antihyperons originate only from primary interactions with nuclei—they can be generated neither in cascade processes nor in the interactions of annihilation kaons within the target nucleus; as a result, the mean momentum of $\bar{\Lambda}$ hyperons is virtually independent of the target mass number.

All the aforesaid is confirmed by the results of the analysis of the mean rapidities $\langle y \rangle$ versus the target mass number *A* for neutral strange particles. For K^0 mesons, $\langle y \rangle$ is shifted from the projectile-fragmentation region to the target-fragmentation region. For Λ hyperons, $\langle y \rangle$ is always in the target-fragmentation region, while, for $\bar{\Lambda}$ hyperons, the mean rapidities are always in the projectile-fragmentation region and remain invariable with increasing target mass number.

5. CONCLUSIONS

To summarize the results obtained from our investigation of the mean inclusive features of neutral strange particles (K^0 mesons and Λ and $\bar{\Lambda}$ hyperons) produced in antiproton–nucleus interactions at an incident momentum of 40 GeV/*c*, we list here the changes that these features have been found to undergo in response to the increase in the mass number of the target nucleus.

(i) For K^0 mesons, the mean emission angle $\langle \theta \rangle$ increases, the mean decay range $\langle R \rangle$ decreases, the mean momentum $\langle p \rangle$ decreases, the mean transverse momentum $\langle p_\perp \rangle$ increases, and the mean rapidity $\langle y \rangle$ is shifted from the projectile-fragmentation region to the target-fragmentation region.

(ii) For Λ hyperons, the mean emission angle $\langle \theta \rangle$ increases, the mean decay range $\langle R \rangle$ and the mean momentum $\langle p \rangle$ both remain virtually constant, the mean transverse momentum $\langle p_\perp \rangle$ increases, and the mean rapidity $\langle y \rangle$ is always in the target-fragmentation region.

(iii) For $\bar{\Lambda}$ hyperons, the mean emission angle $\langle \theta \rangle$ remains unchanged, the mean decay range $\langle R \rangle$ and the mean momentum $\langle p \rangle$ decrease, the mean transverse momentum $\langle p_\perp \rangle$ increases, and the mean rapidity $\langle y \rangle$ is always in the projectile-fragmentation region.

ACKNOWLEDGMENTS

We are grateful to our collaborators in the RISC experiment, who participated in all its stages.

This work was supported by the Georgian Academy of Sciences (project no. 2.11).

REFERENCES

1. T. Grigalashvili *et al.*, Z. Phys. C (in press).
2. K. G. Akhobadze *et al.*, Yad. Fiz. **63**, 904 (2000) [Phys. At. Nucl. **63**, 834 (2000)].
3. M. Yu. Bogolyubskiĭ *et al.*, Yad. Fiz. **50**, 683 (1989) [Sov. J. Nucl. Phys. **50**, 424 (1989)].
4. R. E. Ansorge *et al.*, Nucl. Phys. B **328**, 36 (1989).
5. I. Derado *et al.*, Z. Phys. C **50**, 31 (1991).
6. K. G. Akhobadze *et al.*, Yad. Fiz. **61**, 245 (1998) [Phys. At. Nucl. **61**, 196 (1998)].

Translated by E. Kozlovskiĭ

Physics of Atomic Nuclei, Vol. 63, No. 12, 2000, pp. 2115–2122. Translated from Yadernaya Fizika, Vol. 63, No. 12, 2000, pp. 2211–2218.

ELEMENTARY PARTICLES AND FIELDS
Theory

Lienard–Wiechert Potentials and Synchrotron Radiation from a Relativistic Spinning Particle in Pseudoclassical Theory

S. A. Arakelyan, G. V. Grigoryan*, and R. P. Grigoryan**

Yerevan Physics Institute, ul. Brat'ev Alikhanian 2, AM-375036 Yerevan, Armenia

Received March 29, 1999; in final form, December 3, 1999

Abstract—For a relativistic spinning particle with an anomalous magnetic moment, Lienard–Wiechert potentials are constructed within the pseudoclassical approach. Some specific cases of the motion of a spinning particle are considered on the basis of general expressions obtained in this study for the Lienard–Wiechert potentials. In particular, the intensity of the synchrotron radiation from a transversely polarized particle moving along a circle at a constant speed is investigated as a function of the particle spin. In the specific case of particles having no anomalous magnetic moment and moving in an external uniform magnetic field, the resulting expressions coincide with familiar formulas from the quantum theory of radiation. The spin dependence of the polarization of synchrotron radiation is investigated. © *2000 MAIK "Nauka/Interperiodica".*

1. It is well known that theories of pointlike particles where particle spins are described even at the classical level can be constructed in terms of variables representing elements of a Grassmann algebra [1, 2]. Such theories, referred to as pseudoclassical theories, exemplify constrained gauge systems. A detailed account of methods for quantizing systems of this type can be found, for example, in [3–5]. That the spin in external fields can be consistently described even within classical theory by invoking Grassmann variables opens the possibility of studying spin effects in some physical processes on the basis of classical equations of motion. It should be noted that the spin can also be introduced in classical theories without resort to Grassmann variables, but all such theories do not lead, upon quantization, to the conventional Dirac equation (see the review article of Frydryszak [6] and references therein).

In the present study, the pseudoclassical approach is used to construct Lienard–Wiechert potentials for a relativistic spinning charged particle having an anomalous magnetic moment (AMM) and interacting with an electromagnetic field (a consistent pseudoclassical theory for the interaction of a spinning particle having an anomalous magnetic moment with an electromagnetic field was developed in [7–9]). Some specific cases of the motion of such a particle are considered here on the basis of general expressions that we obtain for the Lienard–Wiechert potentials. In particular, we derive general expressions that describe the spin dependence of the intensity and polarization of the synchrotron radiation from a transversely polarized particle moving along a circle at a constant speed. Our analysis is performed in the second-order approximation in Grassmann variables (first-order approximation in the spin). This corresponds to the inclusion of the spin in the semiclassical approximation. In the case where the particle being considered moves in a uniform external magnetic field, the formulas obtained here in this approximation (with allowance for the external-magnetic-field dependence of the effective particle mass) for particles having no anomalous magnetic moment coincide with the analogous formulas derived previously either in the semiclassical theory of radiation [10] or in the corresponding quantum theory [11]. We also investigate the spin dependence of synchrotron-radiation polarization.

It should be emphasized that a derivation of expressions describing the spin dependence of observables of the radiation from a relativistic particle is much more straightforward within the approach being discussed than within QED.

The ensuing exposition is organized as follows. In Section 2, an action functional is formulated within pseudoclassical theory that describes the interaction of a relativistic spinning particle having an anomalous magnetic moment with an electromagnetic field. We present there relevant equations of motion, introduce subsidiary gauge-fixing conditions, and derive general expressions for Lienard–Wiechert potentials. In Section 3, we consider the case of a spinning particle at rest with a precessing spin. In Section 4, we obtain formulas for the strengths of the electromagnetic field of the synchrotron radiation from a transversely polarized relativistic spinning particle moving along a circle at a constant speed and investigate the spin dependences of the intensity and the polarization of this radiation. The motion of such a particle in a uniform external magnetic field is investigated in detail.

2. Let us consider the action functional within a theory describing the interaction of a relativistic spinning

* e-mail: gagri@lx2.yerphi.am
** e-mail: rogri@lx2.yerphi.am

particle having an anomalous magnetic moment with an electromagnetic field in $D = 4$ space. We have [7–9]

$$S = \frac{1}{2}\int d\tau\Big[\frac{(\dot{x}^\mu)^2}{e} + em^2 - i(\xi_\mu\dot{\xi}^\mu - \xi_5\dot{\xi}_5) - 2g\dot{x}^\mu A_\mu - igMeF_{\mu\nu}\xi^\mu\xi^\nu + 4iGF_{\mu\nu}\dot{x}^\mu\xi^\nu\xi_5 - i\chi\Big(\frac{\xi_\mu\dot{x}^\mu}{e} + m\xi_5 + iGF_{\mu\nu}\xi^\mu\xi^\nu\xi_5\Big) - eG^2(F_{\mu\nu}\xi^\mu\xi^\nu)^2\Big] - \frac{1}{4}\int d^4z F_{\mu\nu}(z)F^{\mu\nu}(z), \quad (1)$$

where x^μ are the particle coordinates; ξ^μ are Grassmann variables describing spin degrees of freedom; ξ_5, e, and χ are auxiliary fields, e (χ and ξ_5) being an even element (odd elements) of the Grassmann algebra; A_μ is the 4-potential of the electromagnetic field; $F_{\mu\nu} = \partial_\mu A_\nu - \partial_\nu A_\mu$; g is the charge; G is the anomalous magnetic moment; $M = 1 + 2Gm/g$ is the total magnetic moment of the particle in units of the Bohr magneton; overdots denote differentiation with respect to the parameter τ along the particle trajectory; and the derivatives with respect to Grassmann variables are left-hand.

The action functional in Eq. (1) possesses three gauge symmetries: reparametrization and supergauge symmetries [8] and the gauge $U(1)$ symmetry of electromagnetic interactions. These symmetries correspond to the presence of three primary first-class constraints in the Hamiltonian formulation of the theory. The relevant degrees of freedom will be fixed below.

In order to derive expressions for the Lienard–Wiechert potentials, we write down explicitly the equations of motion for the electromagnetic field A_μ and for the fields e, ξ_5, and χ:

$$\frac{\delta S}{\delta A_\lambda(y)} = \partial_\mu F^{\mu\lambda}(y) - g\int d\tau\dot{x}^\lambda\delta(x(\tau)-y) + 2iG\int d\tau(\dot{x}^\mu\xi^\lambda - \dot{x}^\lambda\xi^\mu)\xi_5\partial_\mu\delta(x(\tau)-y) - igM\int d\tau e\xi^\mu\xi^\lambda\partial_\mu\delta(x(\tau)-y) - 2G^2\int d\tau eF_{\sigma\rho}\xi^\sigma\xi^\rho\xi^\mu\xi^\lambda\partial_\mu\delta(x(\tau)-y) + G\int d\tau\chi\xi^\mu\xi^\lambda\xi_5\partial_\mu\delta(x(\tau)-y) = 0, \quad (2)$$

$$\frac{\delta S}{\delta e} = -\frac{\dot{x}^2}{e^2} + m^2 - igMF_{\mu\nu}\xi^\mu\xi^\nu - G^2(F_{\mu\nu}\xi^\mu\xi^\nu)^2 + i\chi\frac{\xi_\mu\dot{x}^\mu}{e^2} = 0, \quad (3)$$

$$\frac{1}{i}\frac{\delta S}{\delta\chi} = \frac{\xi_\mu\dot{x}^\mu}{e} + m\xi_5 + iGF_{\mu\nu}\xi^\mu\xi^\nu\xi_5 = 0, \quad (4)$$

$$\frac{1}{i}\frac{\delta S}{\delta\xi_5} = 2\dot{\xi}_5 - 4GF_{\mu\nu}\dot{x}^\mu\xi^\nu + \chi(m + iGF_{\mu\nu}\xi^\mu\xi^\nu) = 0. \quad (5)$$

We fix one of the gauge degrees of freedom by imposing the constraint

$$\dot{x}^\mu\xi_\mu = 0. \quad (6)$$

By virtue of relation (4), it is equivalent to the condition $\xi_5 = 0$. By using this condition and considering that, from relation (6), it follows that the quartic terms in ξ_μ vanish, we find from Eqs. (3) and (5) that the auxiliary fields e and χ are given by

$$e = -\sqrt{\frac{\dot{x}^2}{m^2 - igMF_{\mu\nu}\xi^\mu\xi^\nu}}, \qquad \chi = \frac{4GF_{\mu\nu}\dot{x}^\mu\xi^\nu}{m + iGF_{\mu\nu}\xi^\mu\xi^\nu} = \frac{4GF_{\mu\nu}\dot{x}^\mu\xi^\nu}{m}\Big(1 - \frac{iG}{m}F_{\mu\nu}\xi^\mu\xi^\nu\Big). \quad (7)$$

(The sign of e is chosen in such a way that the energy is positive in the nonrelativistic limit.)

Substituting expression (7) for e and the condition $\xi_5 = 0$ into (2), we obtain the equation for the field A_μ in the form

$$(\partial_\mu\partial^\mu A^\lambda - \partial^\lambda\partial_\mu A^\mu)(y) = j^\lambda(y), \quad (8)$$

where $j^\lambda(y)$ is given by

$$j^\lambda(y) = g\int d\tau\dot{x}^\lambda\delta(x(\tau)-y) + \frac{igM}{m}\frac{\partial}{\partial y^\mu}\int d\tau\delta(x(\tau)-y)\sqrt{\dot{x}^2}\xi^\mu\xi^\lambda. \quad (9)$$

This equation can be further simplified as follows. We fix the remaining two gauges in the theory. For this, we choose the gauge condition for the field A_μ in the form $\partial_\mu A^\mu = 0$ and take the parameter τ for the proper time, whereby we fix, respectively, the $U(1)$ gauge freedom and the reparametrization freedom. In this case, $\dot{x}^2(\tau) = 1$. We note that Eq. (8) involves only second-order terms in ξ_μ. Since second-order terms in ξ will be proportional to $\hbar$ upon quantization, our consideration is equivalent to taking into account spin in the semiclassical approximation. With allowance for the above, Eq. (8) takes the form

$$\Box A^\mu = j^\mu, \quad (10)$$

where $\Box = \partial^\mu\partial_\mu$, and j^μ is given by relation (9) in which we have taken into account the condition $\dot{x}^2 = 1$. It is convenient to represent the current vector j^μ as the sum of two terms,

$$j^\mu(y) = g\int d\tau\dot{x}^\mu\delta(x(\tau)-y) + \frac{\partial}{\partial y^\nu}\int d\tau\delta(x(\tau)-y)p^{\nu\mu}(\tau), \quad (11)$$

where

$$p^{\mu\nu} = \frac{igM}{m}\xi^\mu\xi^\nu, \quad p^{\mu\nu} = -p^{\nu\mu}. \quad (12)$$

The first term in Eq. (11) corresponds to the current of a charged particle having no dipole moment, while the second term represents the contribution to the current from the dipole moment of a charged spinning particle.

It can easily be seen that, by virtue of relation (6), the particle electric dipole moment, which is related to q_μ by the equation $q_\mu = -p_{\mu\nu}\dot{x}^\nu$ (see, for example, [12]), vanishes,

$$q_\mu = -\frac{igM}{m}\xi_\mu(\dot{x}\xi) = 0, \tag{13}$$

as it must in the case of a pointlike particle. We will now show that, from the pseudoclassical expression (12) for $p^{\mu\nu}$, it follows that the particle magnetic moment is expected to be aligned with the spin vector. For this, we consider that the particle-magnetic-moment pseudovector m_μ is related to the dipole-moment tensor $p^{\mu\nu}$ by the equation [12]

$$m_\mu = -\frac{1}{2}\varepsilon_{\mu\nu\lambda\sigma}\dot{x}^\nu p^{\lambda\sigma}. \tag{14}$$

By using Eq. (1), we further express the particle 4-momentum $\mathcal{P}_\mu = (\tilde{\mathcal{E}}, \boldsymbol{\mathcal{P}})$ as

$$\mathcal{P}_\mu = \frac{\partial L}{\partial \dot{x}^\mu} + gA_\mu = \frac{\dot{x}_\mu}{e} + 2iGF_{\mu\nu}\xi^\nu\xi_5 - i\frac{\chi\xi_\mu}{2e}. \tag{15}$$

Using the gauge specified by Eq. (6), taking into account (7), and disregarding the quartic terms in ξ^4, we find from (15) (at $\dot{x}^2 = 1$) that

$$\begin{aligned}\dot{x}^\mu &= -\mathcal{P}^\mu/m_{\text{eff}} - \frac{2iG}{m^2}F_{\nu\lambda}\mathcal{P}^\nu\xi^\lambda\xi^\mu,\\ m_{\text{eff}} &= m - \frac{igM}{2m}F^{\mu\nu}\xi_\mu\xi_\nu.\end{aligned} \tag{16}$$

For the case being considered, the analog of the relation between the particle 4-momentum and the particle mass has the form $\mathcal{P}_\mu^2 - m_{\text{eff}}^2 = 0$. The signs on the right-hand side of the first equation in (16) are governed by the definition of the generalized momentum conjugate to the particle coordinate.

Substituting (12) and (16) into (14), we obtain

$$m_\mu = \frac{i}{2}\frac{gM}{m}\varepsilon_{\mu\nu\lambda\sigma}\frac{\mathcal{P}^\nu}{m}\xi^\lambda\xi^\sigma = \frac{gM}{m}\frac{W_\mu}{m} = M\frac{g}{2m}a_\mu, \tag{17}$$

where W_μ is the pseudoclassical analog of the Pauli–Lubanski vector and is given by (see [9])

$$W_\mu = \frac{i}{2}\varepsilon_{\mu\nu\lambda\sigma}\mathcal{P}^\nu\xi^\lambda\xi^\sigma, \tag{18}$$

while $a_\mu/2$ is a relativistic generalization of the pseudoclassical spin vector (upon a canonical quantization of the theory, the vector a_μ goes over to the polarization 4-vector of the spinning particle being considered). From (17), it follows that the vector of the magnetic moment of a particle is proportional to its polarization vector, the proportionality factor being equal to the total magnetic moment of the particle.

By using the identity (see, for example, [12])

$$p_{\mu\nu} = -(\delta_\mu^\alpha\delta_\nu^\beta - \delta_\mu^\beta\delta_\nu^\alpha)q_\alpha\dot{x}_\beta - \varepsilon_{\mu\nu\lambda\sigma}m^\lambda\dot{x}^\sigma \tag{19}$$

and taking into account Eqs. (13) and (17), we obtain the equality

$$p_{\mu\nu} = -\frac{gM}{m^2}\varepsilon_{\mu\nu\lambda\sigma}W^\lambda\dot{x}^\sigma, \tag{20}$$

which will be needed below.

A solution to Eq. (10) with the current represented in the form (11) was found in [12] in terms of retarded fields. This solution can be written as

$$\begin{aligned}A^\mu(y) = A^\mu_{\text{ret}}(y) &= \frac{1}{4\pi}\left[\frac{g\dot{x}^\mu}{\rho}\right]_{\tau=\tau_r}\\ &-\frac{1}{4\pi}\left\{\frac{1}{\rho}(\dot{p}^{\mu\nu}k_\nu - p^{\mu\nu}(\ddot{x}k)k_\nu) + \frac{1}{\rho^2}(p^{\mu\nu}k_\nu - p^{\mu\nu}\dot{x}_\nu)\right\}_{\tau=\tau_r},\end{aligned} \tag{21}$$

$$\begin{aligned}F^{\mu\nu}_{\text{ret}}(y) &= \frac{g}{4\pi}\left[\frac{2}{\rho}(k^{[\mu}\ddot{x}^{\nu]} - (\ddot{x}k)k^{[\mu}\dot{x}^{\nu]}) + \frac{2}{\rho^2}k^{[\mu}\dot{x}^{\nu]}\right]_{\tau=\tau_r}\\ &+\frac{1}{4\pi}\left\{\frac{2P_1^{[\mu\nu]}}{\rho} + \frac{2Q_1^{[\mu\nu]}}{\rho^2} + \frac{2R_1^{[\mu\nu]}}{\rho^3}\right\}_{\tau=\tau_r},\end{aligned} \tag{22}$$

where $R^\mu \equiv y^\mu - x^\mu(\tau)$, $R^\mu R_\mu = 0$, $\rho = \dot{x}^\nu R_\nu$, and $k_\mu = R_\mu/\rho$; all the quantities in (21) and (22) are taken at the time instant τ_r specified by the equation $t_0 = t_0(\tau_r) = t - R(t_0)$.[1)] The explicit expressions for the quantities appearing in (22) are

$$P_1^{\mu\nu} = \{\dot{p}^\mu{}_\alpha - 3(\ddot{x}k)\dot{p}^\mu{}_\alpha + 3(\ddot{x}k)^2 p^\mu{}_\alpha - (\dddot{x}k)p^\mu{}_\alpha\}k^\alpha k^\nu, \tag{23}$$

$$\begin{aligned}Q_1^{\mu\nu} &= \dot{p}^{\mu\nu} + 3\dot{p}^\mu{}_\alpha k^\alpha k^\nu - 4\dot{p}^\mu{}_\alpha k^{(\alpha}\dot{x}^{\nu)} - (\ddot{x}k)p^{\mu\nu}\\ &-6(\ddot{x}k)p^\mu{}_\alpha k^\alpha k^\nu + 6(\ddot{x}k)p^\mu{}_\alpha k^{(\alpha}\dot{x}^{\nu)} - 2p^\mu{}_\alpha k^{(\alpha}\ddot{x}^{\nu)},\end{aligned} \tag{24}$$

$$R_1^{\mu\nu} = p^{\mu\nu} + 3p^\mu{}_\alpha k^\alpha k^\nu - 6p^\mu{}_\alpha k^{(\alpha}\dot{x}^{\nu)} + 2p^\mu{}_\alpha\dot{x}^\alpha\dot{x}^\nu. \tag{25}$$

In Eqs. (21) and (22), the bracketed expressions correspond to the contributions of a charged particle to A_μ and $F_{\mu\nu}$ without allowing for its spin, whereas the braced expressions represent the contribution of the dipole moment of this particle.

Substituting the explicit expressions for the quantities $p^{\mu\nu}$ and x^μ and for their derivatives into (21)–(25), we obtain, within pseudoclassical theory, the Lienard–

[1)] Hereafter, brackets […] in the subscript denote a complete antisymmetrization—for example, $A_{[\alpha\beta\gamma]} = 1/3!\{A_{\alpha\beta\gamma} + A_{\beta\gamma\alpha} + A_{\gamma\alpha\beta} - A_{\beta\alpha\gamma} - A_{\alpha\gamma\beta} - A_{\gamma\beta\alpha}\}$; parentheses (…) denote a complete symmetrization—for example, $A_{(\alpha\beta\gamma)} = 1/3!\{A_{\alpha\beta\gamma} + A_{\beta\gamma\alpha} + A_{\gamma\alpha\beta} + A_{\beta\alpha\gamma} + A_{\alpha\gamma\beta} + A_{\gamma\beta\alpha}\}$.

Wiechert potentials in the general form and the corresponding strength tensor for the electromagnetic field created by a charged spinning particle.

3. In order to clarify the correspondence between the pseudoclassical expressions obtained here for the Lienard–Wiechert potentials and the well-known formulas for the strengths of the electric and magnetic fields of a charged particle having a magnetic moment, we consider, by way of example, the case of a particle at rest ($\dot{x}^i = 0$, $\dot{x}^\mu = \delta^\mu_0$) with a precessing spin.

From Eqs. (22)–(25), we can easily find that the strength tensor of the electromagnetic field created by a particle at rest is given by

$$F^{\mu\nu}_{\text{ret}}(y) = \left[\frac{g}{4\pi R^2}n^\mu\delta^\nu_0 + \frac{1}{4\pi R}\dot{p}^{\mu\beta}n_\beta n^\nu + \frac{1}{4\pi R^2}(\dot{p}^{\mu\nu} + 3\dot{p}^{\mu\beta}n_\beta n^\nu - 2\dot{p}^{\mu\beta}n_\beta\delta^\nu_0) + \frac{1}{4\pi R^3}(p^{\mu\nu} + 3p^{\mu\beta}n_\beta n^\nu - 3p^{\mu\beta}n_\beta\delta^\nu_0)\right]_{\tau=\tau_r} - [\mu \longleftrightarrow \nu]_{\tau=\tau_r}, \tag{26}$$

where $n^\mu = R^\mu/R = (1, \mathbf{n})$ and $R = R_0 = \sqrt{R_1^2 + R_2^2 + R_3^2}$ (for retarded fields, we have $R_0 = y_0 - x_0(\tau) > 0$). Formula (26) was obtained by considering that, in the rest frame, $p^{0i} = 0$, which immediately follows from (20). From (20) at $\mathbf{v} = 0$, we can also obtain

$$p_{ij} = -\frac{gM}{m^2}\varepsilon_{ijk0}W^k\dot{x}^0 = -\frac{gM}{m^2}\varepsilon_{ijk}W_k \tag{27}$$

($\varepsilon_{ijk} = -\varepsilon_{0ijk} = \varepsilon^{0ijk}$, $\varepsilon_{123} = 1$).

Considering that, in the particle rest frame, we have [13]

$$W_i = mS_i, \tag{28}$$

where S_i is the particle spin, we arrive at

$$p_{ij} = -\frac{gM}{m}\varepsilon_{ijk}S_k. \tag{29}$$

Accordingly, $\dot{p}_{ij}$ and $\ddot{p}_{ij}$ are given by

$$\dot{p}_{ij} = -\frac{gM}{m}\varepsilon_{ijk}\dot{S}_k, \quad \ddot{p}_{ij} = -\frac{gM}{m}\varepsilon_{ijk}\ddot{S}_k. \tag{30}$$

Let us now assume that the particle spin precesses about a certain axis at a constant angular velocity $\boldsymbol{\omega}$; that is,

$$\dot{S}_i = [\boldsymbol{\omega}\times\mathbf{S}]_i = \varepsilon_{ikl}\omega_k S_l. \tag{31}$$

Substituting (31) into (30), we obtain

$$\dot{p}_{ij} = -\frac{gM}{m}(\omega_i S_j - \omega_j S_i),$$
$$\ddot{p}_{ij} = -\frac{gM}{m}\{\omega_i[\boldsymbol{\omega}\times\mathbf{S}]_j - \omega_j[\boldsymbol{\omega}\times\mathbf{S}]_i\}. \tag{32}$$

By using (29) and (32) and the equality $p_{0i} = 0$, we find from (26) that the strengths of the electric and magnetic fields created by an immobile charged particle with a precessing spin are given by

$$E_i = F_{i0} = \frac{g}{4\pi R^2}n_i + \frac{gM}{4\pi mR}\{\omega_i([\boldsymbol{\omega}\times\mathbf{S}]\cdot\mathbf{n}) - (\boldsymbol{\omega}\cdot\mathbf{n})[\boldsymbol{\omega}\times\mathbf{S}]_i\} + \frac{gM}{4\pi mR^2}\{\omega_i(\mathbf{S}\cdot\mathbf{n}) - (\boldsymbol{\omega}\cdot\mathbf{n})S_i\}, \tag{33}$$

$$B_i = -\frac{1}{2}\varepsilon_{ikl}F_{kl} = \frac{gM}{4\pi mR^3}\{3(\mathbf{n}\cdot\mathbf{S})n_i - S_i\} - \frac{gM}{4\pi mR}\{[\boldsymbol{\omega}\times\mathbf{n}]_i([\boldsymbol{\omega}\times\mathbf{S}]\cdot\mathbf{n}) + (\boldsymbol{\omega}\cdot\mathbf{n})(\mathbf{n}\cdot\mathbf{S})\omega_i - (\boldsymbol{\omega}\cdot\mathbf{n})^2S_i\} + \frac{gM}{4\pi mR^2}\{2[\boldsymbol{\omega}\times\mathbf{S}]_i - 3[\boldsymbol{\omega}\times\mathbf{n}]_i(\mathbf{n}\cdot\mathbf{S}) + 3(\boldsymbol{\omega}\cdot\mathbf{n})[\mathbf{S}\times\mathbf{n}]_i\}. \tag{34}$$

From these formulas, we can easily obtain expressions for the strengths of the electric and magnetic fields of an immobile particle having a fixed magnetic-moment vector. The results are

$$E_i = \frac{g}{4\pi R^2}n_i, \quad B_i = \frac{gM}{4\pi mR^3}\{3(\mathbf{n}\cdot\mathbf{S})n_i - S_i\}. \tag{35}$$

Expressions (33)–(35) coincide with the corresponding expressions for the fields generated by a particle having the charge g and the total magnetic-moment vector $\boldsymbol{\mu} = \frac{gM}{m}\mathbf{S}$ (see, for example, [14, 15]).

4. In this section, we obtain expressions for the strengths of the electromagnetic field of the synchrotron radiation generated by a relativistic spinning particle moving along a circle at a constant speed, as well as for the power and polarizations of this radiation. This is done for the case of a transverse particle polarization (the vector of the particle spin is orthogonal to the plane of its rotation). The problem is of interest for testing the possibility of determining particle polarization in cyclic accelerators on the basis of measured observables of synchrotron radiation.

It is well known that the radiation field is controlled by those terms in expression (22) that are proportional to $1/\rho$; that is,

$$F^{\mu\nu}_{\text{rad}}(y) = \left[\frac{g}{4\pi\rho}\frac{2}{}(k^{[\mu}\ddot{x}^{\nu]} - (\ddot{x}k)k^{[\mu}\dot{x}^{\nu]}) + \frac{1}{4\pi}\frac{2P_1^{[\mu\nu]}}{\rho}\right]_{\tau=\tau_r}, \tag{36}$$

where $P_1^{\mu\nu}$ is given by (23).

Let us now transform expression (36) with allowance for the relations

$$\begin{aligned} \dot{x}^\mu &= \gamma(1, \mathbf{v}), \\ \rho &= \gamma(R - (\mathbf{v}\cdot\mathbf{R})) = \gamma R(1 - (\mathbf{v}\cdot\mathbf{n})), \\ \gamma &= 1/\sqrt{1-\mathbf{v}^2}, \\ \ddot{x}^\mu &= (\gamma^4(\mathbf{v}\cdot\mathbf{a}), \gamma^2\mathbf{a} + \gamma^4\mathbf{v}(\mathbf{v}\cdot\mathbf{a})), \\ k^\alpha &= \left(\frac{R}{\rho}, \frac{\mathbf{R}}{\rho}\right) = \frac{R}{\rho}n^\alpha, \\ \dddot{x}^\mu &= (\dot{a}^0, \gamma^3\mathbf{b} + 3\gamma^5(\mathbf{v}\cdot\mathbf{a})\mathbf{a} + \dot{a}^0\mathbf{v}), \\ \dot{a}^0 &= \gamma^5[(\mathbf{v},\mathbf{b}) + \mathbf{a}^2] + 4\gamma^7(\mathbf{v}\cdot\mathbf{a})^2, \end{aligned} \tag{37}$$

where $\mathbf{v} \equiv (v^i) = dx^i/dt$ is the particle 3-velocity, $\mathbf{a} = d\mathbf{v}/dt$, $\mathbf{b} = d\mathbf{a}/dt$, and $dt/d\tau = (1-\mathbf{v}^2)^{-1/2} = \gamma$.

Upon substituting expressions (37) into the first term in (36), we arrive at the well-known formula for the strength E_i^{ch} of the electric field of the radiation from a charged spinless particle:

$$\begin{aligned} E_i^{\mathrm{ch}} &= \frac{g}{4\pi R(1-(\mathbf{v}\cdot\mathbf{n}))^3} \\ &\times[(n_i - v_i)(\mathbf{a}\cdot\mathbf{n}) - a_i(1-(\mathbf{v}\cdot\mathbf{n}))]. \end{aligned} \tag{38}$$

In order to transform the spin component $P_1^{\mu\nu}$ of the tensor $F_{\mathrm{rad}}^{\mu\nu}$ [$P_1^{\mu\nu}$ contains $p^{\mu\nu}$, which is related to W^μ by Eq. (20)], we make use of the equation that relates W_μ and the vector $\mathbf{S} \equiv (S_i)$ of the particle spin in the rest frame and which has the form [9, 13]

$$\begin{aligned} \frac{W_\mu}{m} &= \left(\frac{(\mathscr{P}^D\cdot\mathbf{S})}{m}, S_i + \frac{\mathscr{P}_i^D(\mathscr{P}^D\cdot\mathbf{S})}{m(\mathscr{E}+m)}\right) \\ &= \left(\gamma(\mathbf{v}\cdot\mathbf{S}), S_i + \gamma^2\frac{v_i(\mathbf{v}\cdot\mathbf{S})}{\gamma+1}\right), \end{aligned} \tag{39}$$

where $\mathscr{P}_\mu^D = -\mathscr{P}_\mu = (\mathscr{E}, \mathscr{P}^D)$ stands for the physical particle 4-momentum and where the second equality has been written in the approximation linear in $\mathbf{S}$.

Using Eq. (20) and taking into account Eq. (39), we arrive at

$$p_{0i} = -\frac{gM}{m^2}\varepsilon_{0ijk}W^j\dot{x}^k = -\gamma\frac{gM}{m}\varepsilon_{ijk}S_jv_k, \tag{40}$$

$$\begin{aligned} p_{ij} &= -\frac{gM}{m^2}\varepsilon_{ij\mu\nu}W^\mu\dot{x}^\nu \\ &= -\frac{gM}{m}\varepsilon_{ijk}\left[\gamma S_k - \frac{\gamma^2}{\gamma+1}(\mathbf{v}\cdot\mathbf{S})v_k\right]. \end{aligned} \tag{41}$$

In the case of a transversely polarized particle moving along a circle at a constant speed (the particle spin is aligned with the external magnetic field; see Fig. 1)—this is precisely the case that is considered here—we have

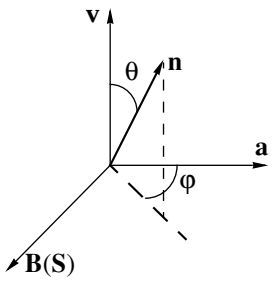

Fig. 1. Reference frame for specifying angles in considering angular features of radiation.

$$\begin{aligned} (\mathbf{v}\cdot\mathbf{a}) = (\mathbf{S}\cdot\mathbf{v}) = (\mathbf{S}\cdot\mathbf{a}) = (\mathbf{S}\cdot\mathbf{b}) = 0, \\ \dot{\mathbf{S}} = 0, \quad \dot{\gamma} = 0, \quad \mathbf{b} = -\omega^2\mathbf{v}, \end{aligned} \tag{42}$$

where ω is the angular velocity of particle rotation. Taking into account these equalities, we recast expression (41) into the form

$$p_{ij} = -\frac{gM}{m}\gamma\varepsilon_{ijk}S_k. \tag{43}$$

Using (40) and (43) and taking into account (42), we obtain

$$\begin{aligned} \dot{p}_{0i} &= -\frac{gM}{m}\gamma^2\varepsilon_{ijk}S_ja_k, \\ \ddot{p}_{0i} &= -\frac{gM}{m}\gamma^3\varepsilon_{ijk}S_jb_k = \frac{gM}{m}\omega^2\gamma^3\varepsilon_{ijk}S_jv_k, \\ \dot{p}^{ij} &= \ddot{p}^{ij} = 0. \end{aligned} \tag{44}$$

With the aid of the explicit expression (23) for $P_1^{\mu\nu}$, the contributions that the dipole moment of a particle makes to the strengths $\mathbf{E}^{\mathrm{rad}}$ and $\mathbf{B}^{\mathrm{rad}}$ of the electromagnetic field of the radiation generated by this particle can be represented as

$$\begin{aligned} E_i^{\mathrm{dip}} &= -\frac{1}{4\pi\rho}(T_{0j}k^jk_i - T_{i\mu}k^\mu k_0) \\ &= -\frac{R^2}{4\pi\rho^3}(T_{0j}(\delta_{ij} - n_in_j) + T_{ij}n_j), \\ E_i^{\mathrm{rad}} &= E_i^{\mathrm{ch}} + E_i^{\mathrm{dip}}, \quad \mathbf{B}^{\mathrm{rad}} = [\mathbf{n}\times\mathbf{E}^{\mathrm{rad}}], \end{aligned} \tag{45}$$

where

$$T_{\mu\nu} = \ddot{p}_{\mu\nu} - 3(\dot{x}k)\dot{p}_{\mu\nu} + 3(\dot{x}k)^2p_{\mu\nu} - (\ddot{x}k)p_{\mu\nu}. \tag{46}$$

From (37) and (42), we obtain

$$\dot{x}^\mu = (0, \gamma^2a^i), \quad \ddot{x}^\mu = (0, \gamma^3b^i) = (0, -\gamma^3\omega^2v^i). \tag{47}$$

Taking into account (40), (43), (44), and (47), we find from (46) that

$$T_{0i} = -\frac{gM}{m}\gamma^3\varepsilon_{ijk}S_j\left[\frac{3(\mathbf{a}\cdot\mathbf{n})a_k}{1-(\mathbf{n}\cdot\mathbf{v})} + \frac{3v_k(\mathbf{a}\cdot\mathbf{n})^2}{(1-(\mathbf{n}\cdot\mathbf{v}))^2} - \frac{\omega^2 v_k}{1-(\mathbf{n}\cdot\mathbf{v})}\right], \quad (48)$$

$$T_{ij} = -\frac{gM}{m}\gamma^3\varepsilon_{ijk}S_k\left[\frac{3(\mathbf{a}\cdot\mathbf{n})^2}{(1-(\mathbf{n}\cdot\mathbf{v}))^2} - \frac{\omega^2(\mathbf{n}\cdot\mathbf{v})}{1-(\mathbf{n}\cdot\mathbf{v})}\right]. \quad (49)$$

In the case of the motion of a transversely polarized particle along a circle at a constant speed, we also have, in addition to the equalities in (42), the obvious relations

$$\varepsilon_{ijk}S_j v_k = [\mathbf{S}\times\mathbf{v}]_i = -\frac{S_B}{\omega}a_i, \qquad \varepsilon_{ijk}S_j a_k = [\mathbf{S}\times\mathbf{a}]_i = S_B\omega v_i, \quad (50)$$

where S_B is the spin-vector projection onto the direction of the external magnetic field **B**. Taking these relations into account, we can recast expression (48) into the form

$$T_{0i} = -\frac{gM}{m}\gamma^3\left[\frac{\omega a_i}{1-(\mathbf{n}\cdot\mathbf{v})} + \frac{3(\mathbf{a}\cdot\mathbf{n})\omega v_i}{1-(\mathbf{n}\cdot\mathbf{v})} - \frac{3(\mathbf{a}\cdot\mathbf{n})^2 a_i}{\omega(1-(\mathbf{n}\cdot\mathbf{v}))^2}\right]S_B. \quad (51)$$

Substituting (51) and (49) into (45), we obtain

$$E_i^{\mathrm{dip}} = \frac{gM}{4m\pi R(1-(\mathbf{n}\cdot\mathbf{v}))^3} \times\left\{\left(\frac{3(\mathbf{a}\cdot\mathbf{n})^2}{(1-(\mathbf{n}\cdot\mathbf{v}))^2} - \frac{\omega^2(\mathbf{n}\cdot\mathbf{v})}{1-(\mathbf{n}\cdot\mathbf{v})}\right)[\mathbf{n}\times\mathbf{S}]_i + \left[\frac{\omega a_j}{1-(\mathbf{n}\cdot\mathbf{v})} + \frac{3(\mathbf{a}\cdot\mathbf{n})\omega v_j}{1-(\mathbf{n}\cdot\mathbf{v})} - \frac{3(\mathbf{a}\cdot\mathbf{n})^2 a_j}{\omega(1-(\mathbf{n}\cdot\mathbf{v}))^2}\right]S_B(\delta_{ij}-n_in_j)\right\}. \quad (52)$$

Using relations (38) and (52) and the equality

$$[\mathbf{n}\times\mathbf{S}]_i = \frac{S_B}{\omega v^2}((\mathbf{v}\cdot\mathbf{n})a_i - (\mathbf{a}\cdot\mathbf{n})v_i), \quad (53)$$

which is obtained with allowance for (42) and (50), we can represent the energy of the synchrotron radiation emitted by a particle into a solid-angle element $d\Omega$ per unit of "particle time" (at the radiation instant) t_0 as

$$\frac{dI}{dt_0 d\Omega} = \left(\frac{g}{4\pi}\right)^2\frac{a^2}{(1-v\cos\theta)^5}\left[(1-v\cos\theta)^2 - (1-v^2)\sin^2\theta\cos^2\varphi - 2\frac{M}{m}\omega S_B\sin^2\theta\sin^2\varphi\right], \quad (54)$$

where θ and φ are angles that specify the direction of the vector **n** in the coordinate frame determined by the vectors **v**, **a**, and **B**(**S**) (see Fig. 1).

Integrating expression (54) over the solid angle, we find that the radiation power is given by

$$\frac{dI}{dt_0} = \frac{g^2}{4\pi}\frac{2a^2}{3(1-v^2)^2}\left[1-\frac{M}{m}\frac{\omega S_B}{1-v^2}\right]. \quad (55)$$

In order to compare this expression with the analogous expression obtained in the quantum theory of radiation, we consider that, for the case of a uniform external magnetic field, the effective particle mass, which is given by (16), takes the simple form

$$m_{\mathrm{eff}} = m - \frac{i}{2}\frac{gM}{m}F_{ij}\xi_i\xi_j = m - \frac{1}{2}F_{ij}p_{ij}. \quad (56)$$

The right-hand equality in (56) is written with allowance for Eq. (12). Substituting the expression for p_{ij} from (43) into (56), we find that, in the first order in the spin, m_{eff} is given by

$$m_{\mathrm{eff}} = m - \gamma\frac{gM}{m}B_iS_i. \quad (57)$$

With the aid of (16), the expression for $\mathcal{P}_\mu^D$ in the case of above-type motion in an external magnetic field can be reduced to the form

$$(\mathcal{P}_\mu^D)^2 = m_{\mathrm{eff}}^2, \quad \mathcal{E} = \gamma m_{\mathrm{eff}} + 2G\gamma^2 v^2(\mathbf{B}\cdot\mathbf{S}), \qquad \boldsymbol{\mathcal{P}}^D = \gamma m_{\mathrm{eff}}\mathbf{v} + 2G\gamma^2(\mathbf{B}\cdot\mathbf{S})\mathbf{v}. \quad (58)$$

By means of expression (57) and the expression for $\mathcal{E}$ from (58), we find in the first order in the spin (for $\gamma \gg 1$) that

$$\gamma^n = \left(\frac{\mathcal{E}}{m}\right)^n\left(1 + n\frac{g}{m^2}\frac{\mathcal{E}}{m}BS_B\right) = \left(\frac{\mathcal{E}}{m}\right)^n\left[1 + \frac{n}{m}\left(\frac{\mathcal{E}}{m}\right)^2 S_B\omega\right]. \quad (59)$$

In deriving the last equality, we have made use of the relation $gB = m\omega\gamma$. Further taking into account (59), we can recast (55) into the form

$$\frac{dI}{dt_0} = \frac{g^2}{4\pi}\frac{2a^2}{3}\left(\frac{\mathcal{E}}{m}\right)^4\left[1 + \frac{4-M}{m}S_B\omega\left(\frac{\mathcal{E}}{m}\right)^2\right]. \quad (60)$$

Considering that $S = \frac{1}{2}\zeta$, where $\zeta = \pm 1$ is the spin component along the magnetic field, we find that, in the absence of an anomalous magnetic moment ($M = 1$), formula (60) (in the first approximation in the spin) coincides with the analogous formulas obtained in the semiclassical ([10]) or in the quantum ([11]) theory of radiation. Thus, formula (60) appears to be a generalization of the formula for the synchrotron-radiation intensity in the first order in the spin to the case where

the particle in question possesses an anomalous magnetic moment.

As in [16], we will investigate the polarization properties of synchrotron radiation by decomposing the electric-field strength $\mathbf{E}^{\mathrm{rad}}$ into two components aligned with two mutually orthogonal unit vectors $\mathbf{e} = \mathbf{a}/a$ and $[\mathbf{n} \times \mathbf{e}]$:

$$\mathbf{E}^{\mathrm{rad}} = E_1 \mathbf{e} + E_2 [\mathbf{n} \times \mathbf{e}]. \tag{61}$$

This choice of unit vectors is reasonable when use is made (with the aim of describing radiation from fast particles) of the reference frame in Fig. 2 for specifying the relevant angles. This reference frame is convenient because the dominant contribution comes from small angles β and ψ of about $1/\gamma$, since the angle between the vectors **n** and **v** is about $1/\gamma$. As was indicated in [16], the representation of $\mathbf{E}^{\mathrm{rad}}$ in the form (61) is disadvantageous in that the right-hand side of Eq. (61) is not orthogonal to the vector **n**, but this uncertainty is about $1/\gamma$, so that the decomposition in (61) can be used to compute leading terms (to a precision of $1/\gamma$). From Eqs. (38) and (52), we find, according to the decomposition in (61), that E_1 and E_2 are given by

$$E_1 = \frac{ga}{\pi R(\mu^2 + \psi^2)^3} \times \left[(\psi^2 - \mu^2) + \frac{M}{m} S_B \omega \frac{4\beta^2(\mu^2 - 5\psi^2)}{(\mu^2 + \psi^2)^2} \right]_{\tau = \tau_r}, \tag{62}$$

$$E_2 = -\frac{2ga}{\pi R(\mu^2 + \psi^2)^3} \times \left[\beta\psi - \frac{M}{m} S_B \omega \frac{4\beta\psi(2\mu^2 - \psi^2)}{(\mu^2 + \psi^2)^2} \right]_{\tau = \tau_r}, \tag{63}$$

where $\mu^2 = \gamma^{-2} + \beta^2$.

Taking into account Eq. (59), we represent the expression for μ^2 in the form

$$\mu^2 = \beta^2 + \left(\frac{m}{\mathscr{E}}\right)^2 - \frac{2}{m} S_B \omega = \mu_0^2 - \frac{2}{m} S_B \omega, \qquad \mu_0^2 = \beta^2 + \left(\frac{m}{\mathscr{E}}\right)^2. \tag{64}$$

Further substituting the expression for μ^2 into (62) and (63), we find in the first order in the spin that

$$E_1 = \frac{ga}{\pi R(\mu_0^2 + \psi^2)^3} \left\{ (\psi^2 - \mu_0^2) + \frac{4}{m} S_B \omega \left[\frac{2\psi^2 - \mu_0^2}{\mu_0^2 + \psi^2} + \frac{M\beta^2(\mu_0^2 - 5\psi^2)}{(\mu_0^2 + \psi^2)^2} \right] \right\}_{\tau = \tau_r}, \tag{65}$$

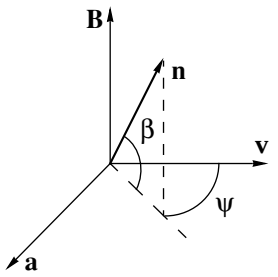

Fig. 2. Reference frame for specifying angles in describing radiation from fast particles.

$$E_2 = -\frac{2ga\beta\psi}{\pi R(\mu_0^2 + \psi^2)^3} \left\{ 1 - \frac{S_B \omega}{m} \times \left[\frac{2(\mu_0^2 - 5\psi^2)}{(\mu_0^2 + \psi^2)^2} + \frac{4(M-1)(2\mu_0^2 - \psi^2)}{(\mu_0^2 + \psi^2)^2} \right] \right\}_{\tau = \tau_r}. \tag{66}$$

At $\mu_0^2 - \psi^2 = 0$, it follows from (65) and (66) that

$$E_1 = \frac{ga}{4\pi R \mu_0^6} \frac{S_B \omega}{m} \left(1 - \frac{2M\beta^2}{\mu_0^2} \right)_{\tau = \tau_r}, \tag{67}$$

$$E_2 = -\frac{ga\beta\psi}{4\pi R \mu_0^6} \left(1 + \frac{(3-M) S_B \omega}{m \mu_0^2} \right)_{\tau = \tau_r}. \tag{68}$$

From the above formulas, it can be seen that, in the (**a**, **v**) plane ($\beta = 0$), there is radiation (proportional to the spin) in the direction $\psi = m/\mathscr{E}$, in contrast to what we have in the case of a spinless particle.

ACKNOWLEDGMENTS

We are grateful to I.V. Tyutin and A. Airapetyan for enlightening discussions on the problems considered here.

This work was supported in part by grants nos. 96-538 and 93-1038 from INTAS and the joint grant no. 95-0829 from INTAS and the Russian Foundation for Basic Research.

REFERENCES

1. F. A. Berezin and M. S. Marinov, Ann. Phys. (N.Y.) **104**, 336 (1977).
2. R. Casalbuoni, Nuovo Cimento A **33**, 115 (1976).
3. P. A. M. Dirac, *Lectures on Quantum Mechanics* (Yeshiva Univ., New York, 1964).
4. D. V. Gitman and I. V. Tyutin, *Canonical Quantization of Constrained Fields* (Nauka, Moscow, 1986).
5. M. Henneaux and C. Teitelboim, *Quantization of Gauge Systems* (Princeton Univ. Press, Princeton, 1992).
6. A. Frydryszak, hep-th/9601020.
7. A. A. Zheltukhin, Teor. Mat. Fiz. **65**, 151 (1985).

8. D. Gitman and A. Saa, Class. Quantum Grav. **10**, 1447 (1993).
9. G. V. Grigoryan and R. P. Grigoryan, Yad. Fiz. **58**, 1146 (1995) [Phys. At. Nucl. **58**, 1072 (1995)].
10. I. M. Ternov and V. A. Bordovitsyn, Vestn. Mosk. Univ., Ser. 3: Fiz., Astron. **24**, 69 (1983).
11. I. M. Ternov, V. G. Bagrov, and R. A. Rzaev, Zh. Éksp. Teor. Fiz. **46**, 374 (1964) [Sov. Phys. JETP **19**, 255 (1964)]; *Synchrotron Radiation*, Ed. by A. A. Sokolov and I. M. Ternov (Nauka, Moscow, 1966).
12. J. R. Ellis, J. Math. Phys. **7**, 1185 (1965).
13. G. V. Grigoryan and R. P. Grigoryan, Zh. Éksp. Teor. Fiz. **103**, 3 (1993) [JETP **76**, 1 (1993)].
14. V. V. Batygin and I. N. Toptygin, *Problems in Electrodynamics* (Nauka, Moscow, 1970; Academic, London, 1964).
15. V. A. Bordovitsyn, N. N. Byzov, G. K. Razina, and V. Ya. Épp, Izv. Vyssh. Uchebn. Zaved., Fiz., No. 5, 12 (1978).
16. V. N. Baĭer, V. M. Katkov, and V. S. Fadin, *Radiation from Relativistic Electrons* (Atomizdat, Moscow, 1973); V. N. Baier, V. M. Katkov, and V. M. Strakhovenko, *Electromagnetic Processes at High Energies in Oriented Single Crystals* (World Sci., Singapore, 1998).

Translated by A. Isaakyan

Physics of Atomic Nuclei, Vol. 63, No. 12, 2000, pp. 2123–2144. From Yadernaya Fizika, Vol. 63, No. 12, 2000, pp. 2219–2240.

ELEMENTARY PARTICLES AND FIELDS
Theory

Semileptonic Decays of the B_c Meson*

V. V. Kiselev, A. K. Likhoded, and A. I. Onishchenko[1)]

Institute for High Energy Physics, Protvino, Moscow oblast, 142284 Russia

Received September 1, 1999; in final form, February 1, 2000

Abstract—The semileptonic decays of the B_c meson into heavy quarkonia $J/\psi(\eta_c)$ and a pair of leptons are investigated on the basis of three-point sum rules of QCD and nonrelativistic QCD (NRQCD). Calculations of analytic expressions for the spectral densities of QCD and NRQCD correlation functions with allowance for Coulomb-like α_s/v terms are presented. At recoil momenta close to zero, generalized relations due to the spin symmetry of NRQCD are derived for the $B_c \longrightarrow J/\psi(\eta_c)l\nu_l$ form factors, with l denoting one of the leptons (e, μ, or τ). This allows one to express all NRQCD form factors in terms of a single universal quantity, an analog of the Isgur–Wise function at the maximal lepton-pair invariant mass. The gluon-condensate corrections to three-point functions are calculated both in full QCD in the Borel transform scheme and in NRQCD in the moment scheme. This enlarges the parametric-stability region of the sum-rule method, thereby rendering the results of the approach more reliable. Numerical estimates of the widths for the transitions $B_c \longrightarrow J/\psi(\eta_c)l\nu_l$ are presented. © *2000 MAIK "Nauka/Interperiodica".*

1. INTRODUCTION

In [1], the CDF collaboration reported on the first experimental observation of the B_c meson, a heavy quarkonium with a mixed heavy flavor [1]. This meson is similar to the families of the charmonium $\bar{c}c$ and the bottomonium $\bar{b}b$ in what is concerned with its spectroscopic properties: two heavy quarks move nonrelativistically, since the confinement scale, determining the presence of light degrees of freedom (sea of gluons and quarks), is suppressed with respect to the heavy-quark masses m_Q, and Coulomb-like exchanges result in transfers about $\alpha_s m_Q^2$, which is again much less than the heavy-quark mass. Therefore, the nonrelativistic picture of binding the quarks leads to the well-known arrangement of system levels, which is very similar to those in the families mentioned above. The calculations of the $\bar{b}c$ mass spectrum were reviewed in [2, 3]. We expect

$$M_{B_c} = 6.25 \pm 0.03 \text{ GeV},$$

whereas the measurement yielded

$$M_{B_c}^{\exp} = 6.40 \pm 0.39 \pm 0.13 \text{ GeV}.$$

There is a significant difference in the mechanisms that govern the production of the heavy quarkonia $\bar{c}c$, $\bar{b}b$, and B_c. To bind the $\bar{b}$ and c quarks, one has to produce four heavy quarks in flavor-conserving interactions,[2)] which allows one to use perturbative QCD, since the virtualities are determined by the scale of the heavy-quark mass. Thus, we see that the production of B_c is relatively suppressed, $\sigma(B_c)/\sigma(\bar{b}b) \sim 10^{-3}$, because of an additional heavy-quark pair in final states. Basic special features of production mechanisms appear owing to higher orders of QCD even in the leading approximation: the fragmentation regime at high transverse momenta much greater than the quark masses and a strong role of nonfragmentation contributions at $p_T \sim m_Q$, which admit a precise perturbative calculation; a negligible contribution of the octet mechanism [4] because there is no enhancement due to a lower order in α_s. The predictions for the cross sections and distributions of B_c in various interactions are discussed in [5], where we see good agreement with the CDF measurements [1].

In contrast to $\bar{c}c$ and $\bar{b}b$ states decaying owing to the annihilation into light quarks and gluons, the B_c meson is a long-lived particle, since it decays owing to weak interaction. The lifetime and various modes of decays were analyzed within (a) potential models [6], (b) technique of operator-product expansion in the effective theory of nonrelativistic QCD (NRQCD) [7] by considering the series in both a small relative velocity v of heavy quarks inside the meson and the inverse heavy-quark mass [8], and (c) QCD sum rules [9, 10] applied to the three-point correlation functions [11–13]. The results of potential models and NRQCD are in agreement with each other. Thus, we expect that the total lifetime is

$$\tau_{B_c} = 0.55 \pm 0.15 \text{ ps},$$

which agrees, within the errors, with the experimental value given by CDF [1]:

$$\tau_{B_c}^{\exp} = 0.46^{+0.18}_{-0.16} \pm 0.03 \text{ ps}.$$

* This article was submitted by the authors in English.

1) Institute of Theoretical and Experimental Physics, Bol'shaya Cheremushkinskaya ul. 25, Moscow, 117259 Russia.

2) We do not consider the production in weak interactions.

1063-7788/00/6312-2123$20.00

Further, a consideration of exclusive B_c decays within QCD sum rules showed that the role of Coulomb corrections to the bare-quark-loop results could be very important to reach the agreement with the other approaches mentioned [13]. This requires evaluating α_s/v corrections in NRQCD, which possesses spin symmetry providing some relations between the exclusive form factors. For semileptonic decays, such a relation was derived in [14]. Note that the CDF collaboration observed 20 $B_c^+ \longrightarrow J/\psi e^+(\mu^+)\nu$ events, so that a consistent calculation of semileptonic decay modes is of interest. For theoretical reviews on B_c-meson physics, the reader is referred to [15].

In this study, we perform a detailed analysis of semileptonic B_c decays within QCD and NRQCD sum rules. We recalculate the double spectral densities available previously in [11] in full QCD for the massless leptons and add the analytic expressions for the form factors necessary in evaluation of decays to massive leptons and P-wave levels of quarkonium with different quark masses. We analyze the NRQCD sum rules for the three-point correlation functions for the first time. We derive generalized relations between the NRQCD form factors, which extends the consideration in [14], because we explore a soft limit of recoil momentum close to zero, wherein the velocities of initial and final heavy quarkonia $v_{1,2}$ are not equal to each other, when their product tends to zero, in contrast to the hard limit $v_1 = v_2$. The spin symmetry relations between the form factors are conserved after taking into account the Coulomb α_s/v corrections, which can be written down in covariant form. We investigate numerical estimates in the sum-rule schemes of spectral-density moments and Borel transform and show an important role of the Coulomb corrections. Next, we perform the calculation of gluon condensate contribution to the three-point sum rules of both full QCD and NRQCD for the case of three massive quarks, for the first time.

The QCD sum rules of three-point correlation functions are considered in Section 2, where the spectral densities are calculated in the bare quark-loop approximation and with allowance for the Coulomb corrections, and the gluon-condensate term in the Borel transform scheme is presented. Section 3 is devoted to the NRQCD sum rules for recoil close to zero. The spin symmetry relations are derived, and the gluon condensate is taken into account in the scheme of moments. The numerical results are summarized in Section 4. Appendices A and B contain technical details of evaluation of decay widths for the massive leptons and gluon condensate in full QCD, respectively.

2. THREE-POINT QCD SUM RULES

In this article, we will use the approach of three-point QCD sum rules [9, 10] to study form factors and decay rates for the transitions $B_c^+ \longrightarrow J/\psi(\eta_c) l^+\nu_l$, where l denotes one of the leptons e, μ, or τ. This procedure is similar to that of two-point sum rules, and information from the latter on the coupling of mesons to their currents is required in order to extract the values of the form factors. Thus, in our work, we will use the meson couplings, defined by the equations

$$\langle 0|\bar{q}_1 i\gamma_5 q_2|P(p)\rangle = \frac{f_P M_P^2}{m_1 + m_2} \tag{1}$$

and

$$\langle 0|\bar{q}_1 \gamma_\mu q_2|V(p,\epsilon)\rangle = i\epsilon_\mu M_V f_V, \tag{2}$$

where P and V represent the scalar and vector mesons with desired flavor quantum numbers, respectively, and m_1 and m_2 are the quark masses. Now we would like to describe the method used.

2.1. Description of the Method

As we have already said, for the calculation of hadronic matrix elements relevant to the semileptonic B_c decays into the pseudoscalar and vector mesons in the framework of QCD, we explore the QCD sum-rule method. The hadronic matrix elements for the transition $B_c^+ \longrightarrow J/\psi(\eta_c) l^+\nu_l$ can be written down as follows:

$$\langle \eta_c(p_2)|V_\mu|B_c(p_1)\rangle = f_+(p_1 + p_2)_\mu + f_- q_\mu, \tag{3}$$

$$\frac{1}{i}\langle J/\psi(p_2)|V_\mu|B_c(p_1)\rangle = iF_V \epsilon_{\mu\nu\alpha\beta}\epsilon^{*\nu}(p_1 + p_2)^\alpha q^\beta, \tag{4}$$

$$\begin{aligned}\frac{1}{i}\langle J/\psi(p_2)|A_\mu|B_c(p_1)\rangle &= F_0^A \epsilon_\mu^* \\ &+ F_+^A(\epsilon^* \cdot p_1)(p_1 + p_2)_\mu + F_-^A(\epsilon^* \cdot p_1) q_\mu,\end{aligned} \tag{5}$$

where $q_\mu = (p_1 - p_2)_\mu$, $\epsilon^\mu = \epsilon^\mu(p_2)$ is the polarization vector of the J/ψ meson, and V_μ and A_μ are the flavor-changing vector and axial electroweak currents. The form factors $f_\pm$, F_V, F_0^A, and $F_\pm^A$ are functions of q^2 only. It should be noted that by virtue of transversality of the lepton current $l_\mu = l\gamma_\mu(1 + \gamma_5)\nu_l$ in the limit $m_l \longrightarrow 0$, the probabilities of semileptonic decays into $e^+\nu_e$ and $\mu^+\nu_\mu$ are independent of f_- and F_-^A. Thus, in calculation of these particular decay modes of B_c meson, these form factors can be consistently neglected [6, 11, 13]. However, since the calculation of both semileptonic decay modes, including e, μ, or τ, and some hadronic decays, stands among the goals of this paper, we will present the results for the complete set of form factors given in (3)–(5).

Following the standard procedure for the evaluation of form factors in the framework of QCD sum rules, we

consider the three-point functions

$$\Pi_\mu(p_1, p_2, q^2) = i^2\int dxdy e^{i(p_2\cdot x - p_1\cdot y)} \times\langle 0|T\{\bar{q}_1(x)\gamma_5 q_2(x), V_\mu(0), \bar{b}(y)\gamma_5 c(y)\}|0\rangle, \quad (6)$$

$$\Pi^{V,A}_{\mu\nu}(p_1, p_2, q^2) = i^2\int dxdy e^{i(p_2\cdot x - p_1\cdot y)} \times\langle 0|T\{\bar{q}_1(x)\gamma_\mu q_2(x), J^{V,A}_\mu(0), \bar{b}(y)\gamma_5 c(y)\}|0\rangle, \quad (7)$$

where $\bar{q}_1(x)\gamma_5 q_2(x)$ and $\bar{q}_1(x)\gamma_\mu q_2(x)$ are interpolating currents for states with the quantum numbers of η_c and J/ψ, respectively, and $J^{V,A}_\mu$ are the currents V_μ and A_μ of relevance to the various cases.

The Lorentz structures in the correlation functions can be written down as

$$\Pi_\mu = \Pi_+(p_1 + p_2)_\mu + \Pi_- q_\mu, \quad (8)$$

$$\Pi^V_{\mu\nu} = i\Pi_V \epsilon_{\mu\nu\alpha\beta} p_2^\alpha p_1^\beta, \quad (9)$$

$$\Pi^A_{\mu\nu} = \Pi^A_0 g_{\mu\nu} + \Pi^A_1 p_{2,\mu} p_{1,\nu} + \Pi^A_2 p_{1,\mu} p_{1,\nu} + \Pi^A_3 p_{2,\mu} p_{2,\nu} + \Pi^A_4 p_{1,\mu} p_{2,\nu}. \quad (10)$$

The form factors $f_\pm$, F_V, F^A_0, and $F^A_\pm$ will be determined, respectively, from the amplitudes $\Pi_\pm$, Π_V, Π^A_0, and $\Pi^A_\pm = \frac{1}{2}(\Pi^A_1 \pm \Pi^A_2)$. In (8)–(10) the scalar amplitudes Π_i are the functions of kinematical invariants, i.e., $\Pi_i = \Pi_i(p_1^2, p_2^2, q^2)$.

To calculate the QCD expression for the three-point correlation functions, we employ the operator product expansion (OPE) for the *T*-ordered product of currents in (6) and (7). The vacuum correlations of heavy quarks are related to their contribution to the gluon operators. For example, for the $\langle\bar{Q}Q\rangle$ and $\langle\bar{Q}GQ\rangle$ condensates, the heavy-quark expansion gives

$$\langle\bar{Q}Q\rangle = -\frac{1}{12m_Q}\frac{\alpha_s}{\pi}\langle G^2\rangle - \frac{1}{360m_Q^3}\frac{\alpha_s}{\pi}\langle G^3\rangle + \ldots,$$

$$\langle\bar{Q}GQ\rangle = \frac{m_Q}{2}\log(m_Q^2)\frac{\alpha_s}{\pi}\langle G^2\rangle - \frac{1}{12m_Q}\frac{\alpha_s}{\pi}\langle G^3\rangle + \ldots.$$

Then, in the lowest order for the energy dimension of operators, the only nonperturbative correction comes from the gluon condensate:

$$\Pi_i(p_1^2, p_2^2, q^2) = \Pi_i^{\text{pert}}(p_1^2, p_2^2, q^2) + \Pi_i^{G^2}(p_1^2, p_2^2, q^2)\left\langle\frac{\alpha_s}{\pi}G^2\right\rangle. \quad (11)$$

The leading QCD term is a triangle quark loop diagram, for which we can write down the double dispersion representation at $q^2 \le 0$:

$$\Pi_i^{\text{pert}}(p_1^2, p_2^2, q^2) = -\frac{1}{(2\pi)^2}\int\frac{\rho_i^{\text{pert}}(s_1, s_2, Q^2)}{(s_1 - p_1^2)(s_2 - p_2^2)}ds_1 ds_2 + \text{subtractions}, \quad (12)$$

where $Q^2 = -q^2 \ge 0$. The integration region in (12) is determined by the condition

$$-1 < \frac{2s_1s_2 + (s_1 + s_2 - q^2)(m_b^2 - m_c^2 - s_1)}{\lambda^{1/2}(s_1, s_2, q^2)\lambda^{1/2}(m_c^2, s_1, m_b^2)} < 1 \quad (13)$$

and

$$\lambda(x_1, x_2, x_3) = (x_1 + x_2 - x_3)^2 - 4x_1x_2.$$

The calculation of spectral densities $\rho_i^{\text{pert}}(s_1, s_2, Q^2)$ and gluon-condensate contribution to (11) will be considered in the next sections. Now let us proceed with the physical part of three-point sum rules. The connection to hadrons in the framework of QCD sum rules is obtained by matching the resulting QCD expressions of current correlation functions with the spectral representation, derived from the double dispersion relation at $q^2 \le 0$:

$$\Pi_i(p_1^2, p_2^2, q^2) = -\frac{1}{(2\pi)^2}\int\frac{\rho_i^{\text{phys}}(s_1, s_2, Q^2)}{(s_1 - p_1^2)(s_2 - p_2^2)}ds_1 ds_2 + \text{subtractions}. \quad (14)$$

Assuming that the dispersion relation (14) is well convergent, the physical spectral functions are generally saturated by the lowest hadronic states plus a continuum starting at some effective thresholds s_1^{th} and s_2^{th}:

$$\rho_i^{\text{phys}}(s_1, s_2, Q^2) = \rho_i^{\text{res}}(s_1, s_2, Q^2) + \theta(s_1 - s_1^{\text{th}})\theta(s_2 - s_2^{\text{th}})\rho_i^{\text{cont}}(s_1, s_2, Q^2), \quad (15)$$

where

$$\rho_i^{\text{res}}(s_1, s_2, Q^2) = \langle 0|\bar{c}\gamma_\mu(\gamma_5)c|J/\psi(\eta_c)\rangle \times\langle J/\psi(\eta_c)|F_i(Q^2)|B_c\rangle\langle B_c|\bar{b}\gamma_5 c|0\rangle(2\pi)^2\delta(s_1 - M_1^2) \times\delta(s_2 - M_2^2) + \text{higher state contributions}, \quad (16)$$

and $M_{1,2}$ denote the masses of quarkonia in the initial and final states. The continuum of higher states is modeled by the perturbative absorptive part of Π_i, i.e., by ρ_i. Then, the expressions for the form factors F_i can be derived by equating the representations for the three-point functions Π_i in (11) and (14), which means the formulation of sum rules.

2.2. Calculating the Spectral Densities

In this section, we present the analytic expressions to one-loop approximation for the perturbative spectral functions. We have recalculated their values, already available in the literature [11]. Among new results there are the expressions for ρ_-, ρ_-^A, and $\rho_\pm^{\prime A}$, where $\rho_\pm^{\prime A}$ are spectral functions, which come from the double dispersion representation of $\Pi_\pm^{\prime A} = \frac{1}{2}(\Pi_3^A \pm \Pi_4^A)$. These spectral densities are not required for the purposes of this paper, but they will be useful for calculation of form factors for the transition of the B_c meson into a scalar meson.[3)] The procedure of evaluating the spectral functions involves the standard use of Cutkosky rules [16]. There is, however, one subtle point in using these rules. At $Q^2 > 0$, there is no problem in applying the Cutkosky rules in order to determine $\rho_i(s_1, s_2, Q^2)$ and the limits of integration with respect to s_1 and s_2. At $Q^2 < 0$, which is the physical region, non-Landau-type singularities appear [17, 18], which makes the determination of spectral functions quite complicated. In our case, we restrict the region of integration in s_1 and s_2 by s_1^{th} and s_2^{th}, so that at moderate values of Q^2 the non-Landau singularities do not contribute to the values of spectral functions. For spectral densities $\rho_i(s_1, s_2, Q^2)$, we have the expressions

$$\begin{aligned}\rho_+(s_1, s_2, Q^2) &= \frac{3}{2k^{3/2}}\Bigg\{\frac{k}{2}(\Delta_1 + \Delta_2)\\ &- k[m_3(m_3 - m_1) + m_3(m_3 - m_2)]\\ &- [2(s_2\Delta_1 + s_1\Delta_2) - u(\Delta_1 + \Delta_2)]\\ &\times\left[m_3^2 - \frac{u}{2} + m_1m_2 - m_2m_3 - m_1m_3\right]\Bigg\},\end{aligned} \tag{17}$$

$$\begin{aligned}\rho_-(s_1, s_2, Q^2) &= -\frac{3}{2k^{3/2}}\Bigg\{\frac{k}{2}(\Delta_1 - \Delta_2)\\ &- k[m_3(m_3 - m_1) - m_3(m_3 - m_2)]\\ &+ [2(s_2\Delta_1 - s_1\Delta_2) + u(\Delta_1 - \Delta_2)]\\ &\times\left[m_3^2 - \frac{u}{2} + m_1m_2 - m_2m_3 - m_1m_3\right]\Bigg\},\end{aligned} \tag{18}$$

$$\begin{aligned}\rho_V(s_1, s_2, Q^2) &= \frac{3}{k^{3/2}}\{(2s_1\Delta_2 - u\Delta_1)(m_3 - m_2)\\ &+ (2s_2\Delta_1 - u\Delta_2)(m_3 - m_1) + m_3k\},\end{aligned} \tag{19}$$

$$\begin{aligned}&\rho_0^A(s_1, s_2, Q^2)\\ &= \frac{3}{k^{1/2}}\Bigg\{(m_1 - m_3)\left[m_3^2 + \frac{1}{k}(s_1\Delta_2^2 + s_2\Delta_1^2 - u\Delta_1\Delta_2)\right]\\ &- m_2\left(m_3^2 - \frac{\Delta_1}{2}\right) - m_1\left(m_3^2 - \frac{\Delta_2}{2}\right)\\ &+ m_3\left[m_3^2 - \frac{1}{2}(\Delta_1 + \Delta_2 - u) + m_1m_2\right]\Bigg\},\end{aligned} \tag{20}$$

$$\begin{aligned}&\rho_+^A(s_1, s_2, Q^2)\\ &= \frac{3}{2k^{3/2}}\Bigg\{m_1[2s_2\Delta_1 - u\Delta_1 + 4\Delta_1\Delta_2 + 2\Delta_2^2]\\ &+ m_1m_3^2[4s_2 - 2u] + m_2[2s_1\Delta_2 - u\Delta_1]\\ &- m_3[2(3s_2\Delta_1 + s_1\Delta_2) - u(3\Delta_2 + \Delta_1) + k\\ &+ 4\Delta_1\Delta_2 + 2\Delta_2^2 + m_3^2(4s_2 - 2u)]\\ &+ \frac{6}{k}(m_1 - m_3)[4s_1s_2\Delta_1\Delta_2 - u(2s_2\Delta_1\Delta_2\\ &+ s_1\Delta_2^2 + s_2\Delta_1^2) + 2s_2(s_1\Delta_2^2 + s_2\Delta_1^2)]\Bigg\},\end{aligned} \tag{21}$$

$$\begin{aligned}\rho_-^A(s_1, s_2, Q^2) &= -\frac{3}{2k^{5/2}}\{kum_3(2m_1m_3 - 2m_3^2 + u)\\ &+ 12(m_1 - m_3)s_2^2\Delta_1^2 + k\Delta_2[(m_1 + m_3)u\\ &- 2s_1(m_2 - m_3)] + 2\Delta_2^2(k + 3us_1)(m_1 - m_3)\\ &+ \Delta_1[ku(m_2 - m_3) + 2\Delta_2(k - 3u^2)(m_1 - m_3)]\\ &+ 2s_2(m_1 - m_3)[2km_3^2 - k\Delta_1 + 3u\Delta_1^2 - 6u\Delta_1\Delta_2]\\ &- 2s_1s_2(km_3 - 3\Delta_2^2(m_1 - m_3))\},\end{aligned} \tag{22}$$

$$\begin{aligned}\rho_+^{\prime A}(s_1, s_2, Q^2) &= -\frac{3}{2k^{5/2}}\{-2(m_1 - m_3)[(k - 3us_2)\Delta_1^2\\ &+ 6s_1^2\Delta_2^2] + ku(m_1 - m_3)(2m_3^2 + \Delta_2) + ku^2m_3\\ &+ \Delta_1[ku(2m_1 - m_2 - 3m_3)\\ &- 2(m_1 - m_3)(ks_2 - k\Delta_2 + 3u^2\Delta_2)]\\ &- 2s_1[(m_1 - m_3)(2km_3^2 - 6u\Delta_1\Delta_2 - 3u\Delta_2^2)\\ &+ 2s_2(km_3 + 3m_1\Delta_1^2 - 3m_3\Delta_1^2)\\ &+ k\Delta_2(2m_1 - m_2 - 3m_3)]\},\end{aligned} \tag{23}$$

[3)] The meson at the *P*-wave level, for which $\langle 0|\bar{q}_1\gamma_\mu q_2|P(p)\rangle = if_P p_\mu$, where $P(p)$ denotes the scalar *P*-wave meson under consideration, and $m_1 \neq m_2$.

$$\rho'^{A}_{-}(s_1, s_2, Q^2) = \frac{3}{2k^{5/2}}\{2(m_1 - m_3)[(k + 3us_2)\Delta_1^2 + 6s_1^2\Delta_2^2] + ku(m_1 - m_3)(2m_3^2 + \Delta_2) + ku^2 m_3 + \Delta_1[ku(-2m_1 - m_2 + m_3) - 2(m_1 - m_3)(ks_2 - k\Delta_2 + 3u^2\Delta_2)] + 2s_1[(m_1 - m_3)(2km_3^2 - 6u\Delta_1\Delta_2 + 3u\Delta_2^2) - 2s_2(km_3 - 3m_1\Delta_1^2 + 3m_3\Delta_1^2) + k\Delta_2(2m_1 + m_2 - m_3)]\}. \quad (24)$$

Here, $k = (s_1 + s_2 + Q^2)^2 - 4s_1s_2$, $u = s_1 + s_2 + Q^2$, $\Delta_1 = s_1 - m_1^2 + m_3^2$, and $\Delta_2 = s_2 - m_2^2 + m_3^2$; m_1, m_2, and m_3 are the masses of quark flavors relevant to the various decays (see prescriptions in Fig. 1).

We neglect hard $O(\alpha_s/\pi)$ corrections to the triangle diagrams, as they are not available yet. Nevertheless, we expect that their contributions are quite small (~10%); bearing in mind the accuracy of QCD sum rules, we therefore conclude that the correction will not drastically change our results.

In expressions (12), the integration with respect to s_1 and s_2 is performed in the near-threshold region, where instead of α_s, the expansion should be done in the parameters $(\alpha_s/v_{13(23)})$, with $v_{13(23)}$ meaning the relative velocities of quarks in $b\bar{c}$ and $c\bar{c}$ systems. For the heavy quarkonia, where the quark velocities are small, these corrections take an essential role (as in the case for two-point sum rules [19, 20]). The α_s/v corrections, caused by the Coulomb-like interaction of quarks, are related to the ladder diagrams shown in Fig. 2. It is well known that, numerically, the Born value of the spectral density is doubled or tripled upon taking into account these corrections in two-point sum rules [21, 22].

Now, let us comment on the effect of these corrections in the case of three-point sum rules [13]. Consider, for example, the three-point function $\Pi_\mu(p_1, p_2, q)$ at $q^2 = q^2_{\max}$, where $q^2_{\max}$ is the maximum invariant mass of the lepton pair in the decay $B_c \longrightarrow \eta_c l\nu_l$. Introduce the notation $p_1 \equiv (m_b + m_c + E_1, \mathbf{0})$ and $p_2 \equiv (2m_c + E_2, \mathbf{0})$. At $s_1 = M_1^2$ and $s_2 = M_2^2$, we have $E_1 \ll (m_b + m_c)$ and $E_2 \ll 2m_c$. In this kinematics, the quark velocities are small, and, thus, the diagram in Fig. 2 may be considered in the nonrelativistic approximation. We will use the Coulomb gauge, in which the ladder diagrams with the Coulomb-like gluon exchange are dominant. The gluon propagator then has the form

$$D^{\mu\nu} = i\delta^{\mu 0}\delta^{\nu 0}/\mathbf{k}^2. \quad (25)$$

In this approximation, the nonrelativistic potential of heavy-quark interaction in the momentum representation is given by

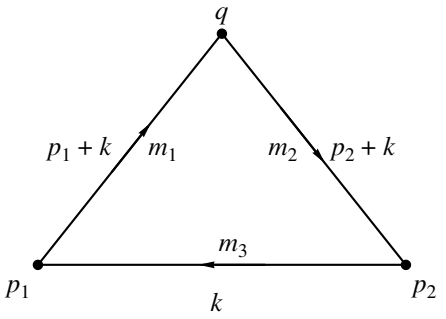

Fig. 1. The triangle diagram giving the leading perturbative term in the OPE expansion of the three-point function.

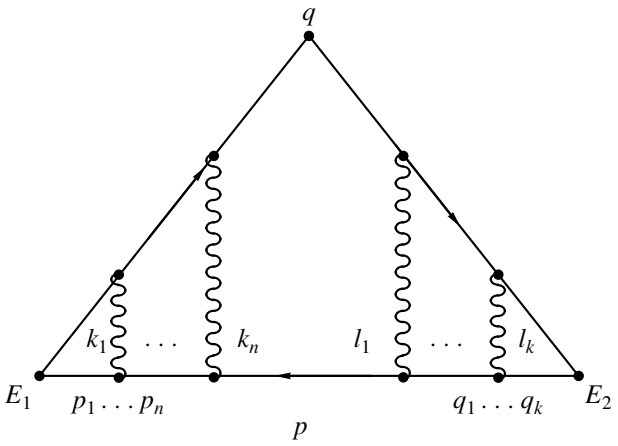

Fig. 2. The ladder diagram of the Coulomb-like quark interaction.

$$\tilde{V}(\mathbf{k}) = -\frac{4}{3}\alpha_s(\mathbf{k}^2)\frac{4\pi}{\mathbf{k}^2}, \quad \alpha_s(\mathbf{k}^2) = \frac{4\pi}{b_0 \ln(\mathbf{k}^2/\Lambda^2)},$$

$$b_0 = 11 - \frac{2}{3}n_f, \quad \Lambda = \Lambda_{\overline{MS}}\exp\left[\frac{1}{b_0}\left(\frac{31}{6} - \frac{5}{9}n_f\right)\right],$$

with n_f being the number of flavors, while the fermionic propagators, corresponding to either a particle or an antiparticle, have the following forms:

$$S_F(k + p_i) = \frac{i(1 + \gamma_0)/2}{E_i + k^0 - \frac{|\mathbf{k}|^2}{2m} + i0},$$

$$S_F(p) = \frac{-i(1 - \gamma_0)/2}{-k^0 - \frac{|\mathbf{k}|^2}{2m} + i0}.$$

The notation concerning Fig. 2 is given by

$$k_i = p_{i+1} - p_i, \quad l_i = q_i - q_{i-1}, \quad p_{n+1} \equiv q_0 \equiv p.$$

Integration with respect to p_i^0, p^0, and q_i^0 by means of residues yields the expression

$$\Pi_\mu(E_1, E_2, q) = 2N_c g_{\mu 0} \times \sum_{n=1}^{\infty} \prod_{i=1}^{n} \frac{d\mathbf{p}_i}{(2\pi)^3 \left(\frac{|\mathbf{p}_i|^2}{2\mu_1} - E_1 - i0 \right)} \tilde{V}((\mathbf{p}_{i+1} - \mathbf{p}_i)^2) \times \frac{1}{\frac{|\mathbf{p}|^2}{2\mu_1} - E_1 - i0} \frac{1}{\frac{|\mathbf{p}|^2}{2\mu_2} - E_2 - i0} \times \sum_{k=1}^{\infty} \prod_{j=1}^{k} \frac{d\mathbf{q}_j}{(2\pi)^3 \left(\frac{|\mathbf{q}_j|^2}{2\mu_2} - E_2 - i0 \right)} \tilde{V}((\mathbf{q}_j - \mathbf{q}_{j-1})^2) \frac{d\mathbf{p}}{(2\pi)^3}, \quad (26)$$

$$\tilde{V}((\mathbf{p}_{n+1} - \mathbf{p}_n)^2) \equiv \tilde{V}((\mathbf{p} - \mathbf{p}_n)^2),$$
$$\tilde{V}((\mathbf{q}_1 - \mathbf{q}_0)^2) = \tilde{V}((\mathbf{q}_1 - \mathbf{p})^2),$$

where N_c denotes the number of colors, and μ_1 and μ_2 are the reduced masses of the $b\bar{c}$ and $c\bar{c}$ systems, respectively. This three-point function may be expressed in terms of the Green's functions for the relative motion of heavy quarks in the $b\bar{c}$ and $c\bar{c}$ systems in the Coulomb field, $G_E^{(i)}(\mathbf{x}, \mathbf{y})$:

$$G_E^{(i)}(\mathbf{x}, \mathbf{y}) = \sum_{n=1}^{\infty} \left(\prod_{k=1}^{n} \int \frac{d\mathbf{p}_k}{(2\pi)^3 \left(\frac{|\mathbf{p}_k|^2}{2\mu_i} - E_i - i0 \right)} \right) \times \prod_{k=1}^{n-1} \tilde{V}((\mathbf{p}_k - \mathbf{p}_{k+1})^2) e^{i\mathbf{p}_1 \cdot \mathbf{x} - i\mathbf{p}_n \cdot \mathbf{y}}. \quad (27)$$

Comparing expressions (26) and (27), we find

$$\Pi_\mu(E_1, E_2, q_{\max}^2) = 2N_c g_{\mu 0} \int G_{E_1}^{(1)}(\mathbf{x} = 0, \mathbf{p}) G_{E_2}^{(2)}(\mathbf{p}, \mathbf{y} = 0) \frac{d\mathbf{p}}{(2\pi)^3} = 2N_c g_{\mu 0} \int G_{E_1}^{(1)}(0, z) G_{E_2}^{(2)}(z, 0) d^3 z. \quad (28)$$

For the Green's function, we use the representation

$$G_E(\mathbf{x}, \mathbf{y}) = \sum_{l,m} \left(\sum_{n=l+1}^{\infty} \frac{\Psi_{nlm}(\mathbf{x}) \Psi_{nlm}^*(\mathbf{y})}{E_{nl} - E - i0} + \int \frac{dk}{(2\pi)} \frac{\Psi_{klm}(\mathbf{x}) \Psi_{klm}^*(\mathbf{y})}{k - E - i0} \right). \quad (29)$$

Provided $\mathbf{x} = 0$, only the terms with $l = 0$ are retained in the sum. For the spectral density we then have

$$\rho_\mu(E_1, E_2, q_{\max}^2) = -2N_c g_{\mu 0} \Psi_1^C(0) \Psi_2^C(0) \times \int \tilde{\Psi}_{1E_1}^C(\mathbf{p}) \tilde{\Psi}_{2E_2}^C(\mathbf{p}) \frac{d\mathbf{p}}{(2\pi)^3}, \quad (30)$$

where Ψ_i^C are the Coulomb wave functions for the $b\bar{c}$ or $c\bar{c}$ systems. An analogous expression can also be derived in the Born approximation:

$$\rho_\mu^B(E_1, E_2, q_{\max}^2) = -2N_c g_{\mu 0} \Psi_1^f(0) \Psi_2^f(0) \int \tilde{\Psi}_{1E_1}^f(\mathbf{p}) \tilde{\Psi}_{2E_2}^f(\mathbf{p}) \frac{d\mathbf{p}}{(2\pi)^3}. \quad (31)$$

Here, Ψ_i^f stands for the function of free quark motion. Since the continuous-spectrum Coulomb functions have the same normalization as the free states, we obtain the approximation

$$\rho_\mu(E_1, E_2, q_{\max}^2) \approx \rho_\mu^B(E_1, E_2, q_{\max}^2) \frac{\Psi_1^C(0) \Psi_2^C(0)}{\Psi_1^f(0) \Psi_2^f(0)} \equiv \rho_\mu^B(E_1, E_2, q_{\max}^2) \mathbf{C}, \quad (32)$$

$$\mathbf{C} = \left\{ \frac{4\pi\alpha_s}{3v_{13}} \left[1 - \exp\left(-\frac{4\pi\alpha_s}{3v_{13}} \right)^{-1} \right] \times \frac{4\pi\alpha_s}{3v_{23}} \left[1 - \exp\left(-\frac{4\pi\alpha_s}{3v_{23}} \right)^{-1} \right] \right\}^{1/2}, \quad (33)$$

where v_{13} and v_{23} are relative velocities in the $b\bar{c}$ and $c\bar{c}$ systems, respectively. For them, we have the following expressions:

$$v_{13} = \sqrt{1 - \frac{4m_1 m_3}{p_1^2 - (m_1 - m_3)^2}}, \quad (34)$$

$$v_{23} = \sqrt{1 - \frac{4m_2 m_3}{p_2^2 - (m_2 - m_3)^2}}. \quad (35)$$

Equation (32) is exact for the identical quarkonia in the initial and final states of transition under consideration. However, if the reduced masses are different, then the overlapping of Coulomb functions can deviate from unity, which breaks the exact validity of (32). From a pessimistic viewpoint, this relation can serve as an estimate of the upper bound on the form factor at zero recoil. In reality, this boundary is practically saturated, which means that in sum rules at low momenta inside the quarkonia, i.e., in the region of physical resonances, the most essential effect comes from the normalization factor **C**, determined by the Coulomb function at the origin. The latter renormalizes the coupling constant at

the quark–meson vertex from the bare value to the "dressed" one. After that, the motion of heavy quarks in the triangle loop is very close to that of free quarks.

In accordance with (8) for the Lorentz decomposition of $\rho_\mu(p_1, p_2, q^2)$, we have

$$\rho_\mu(p_1, p_2, q^2) = (p_1 + p_2)_\mu \rho_+(q^2) + q_\mu \rho_-(q^2). \quad (36)$$

As we have seen, the nonrelativistic expression of $\rho_\mu(E_1, E_2, q^2_{\max})$ is proportional to the vector $g_{\mu 0}$, which allows us to isolate the evident combination of form factors $f_\pm$. The relations between the form factors appearing in NRQCD at a recoil momentum close to zero will be considered below. Here, we stress only that we have

$$\rho_+(q^2_{\max}) = \rho^{\mathrm{B}}_+(q^2_{\max})\mathbf{C}, \quad (37)$$

where the factor $\mathbf{C}$ has been specified in (33).

In the case of $B_c \longrightarrow J/\psi l \nu_l$ transition, one can easily obtain an analogous result for $\rho^A_0(q^2)$ (note that the form factor $F^A_0 \sim \rho^A_0$ gives the dominant contribution to the width of this decay [14]). In the nonrelativistic approximation, we have

$$\rho^A_0(q^2_{\max}) = \rho^{A,\mathrm{B}}_0(q^2_{\max})\mathbf{C}. \quad (38)$$

To conclude this section, note that the derivation of formulas (37) and (38) is purely formal, since the spectral densities are not specified at $q^2_{\max}$ (one can easily show $\rho^{\mathrm{B}}_i(q^2)$ to be singular in this point). Therefore, the resultant relations are valid only for q^2 approaching $q^2_{\max}$. Unfortunately, this derivation does not give the q^2 dependence of the factor $\mathbf{C}$. But we suppose that $\mathbf{C}$ does not crucially affect the pole behavior of the form factors. Therefore, the resultant widths of transitions can be treated as the saturated upper bounds in the QCD sum rules.

2.3. Gluon-Condensate Contribution

In this subsection, we will discuss the calculation of Borel transformed Wilson coefficient of the gluon-condensate operator for the three-point sum rules with arbitrary masses. The technique used is the same as in [18] with some modifications to simplify the resulting expression. As was noted in [18], this method does not allow for the subtraction of continuum contributions, which, however, only change our results a little, as the total contribution of the gluon condensate to the three-point sum rule is small by itself (≤10%), and, thus, its continuum portion is small too. The form of the obtained expression does not permit us to use the same argument as in [18] to argue over the absence of those contributions at all. Their argument was based on an expectation that the typical continuum contribution can show up as incomplete Γ functions in the resulting expression and the absence of them in the final answer leads authors of [18] to the conclusion that such contributions are actually absent in the processes they considered.

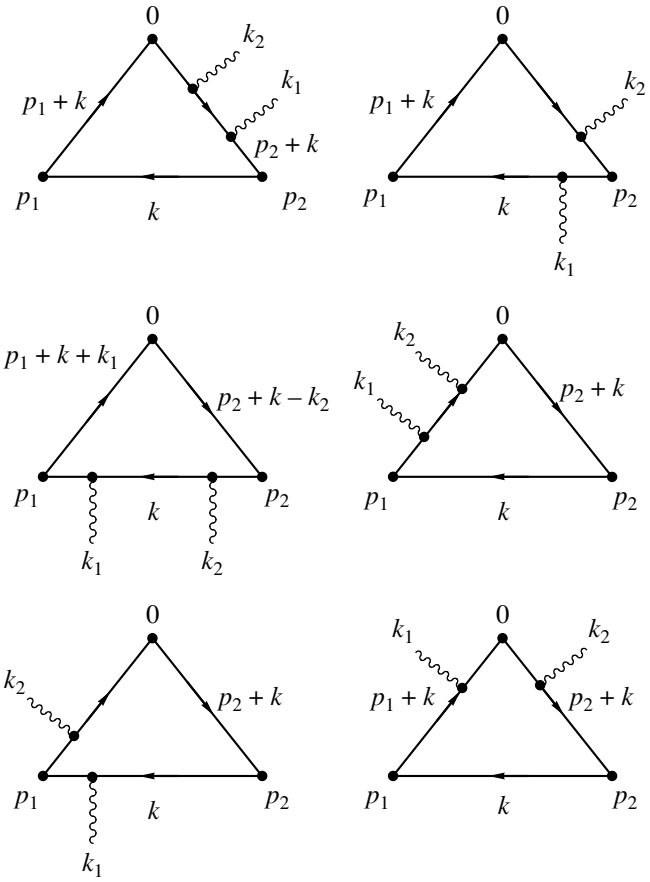

Fig. 3. The gluon-condensate contribution to three-point QCD sum rules. The directions of p_1, k_1, and k_2 momenta are incoming, and that of p_2 is outgoing.

The gluon condensate contribution to three-point sum rules is given by diagrams depicted in Fig. 3. For calculations, we have used the Fock–Schwinger fixed-point gauge [20, 23]:

$$x^\mu A^a_\mu(x) = 0, \quad (39)$$

where A^a_μ ($a = \{1, 2, \ldots, 8\}$) is the gluon field.

In the evaluation of the diagrams in Fig. 3, we encounter integrals of the type[4)]

$$I_{\mu_1\mu_2\ldots\mu_n}(a, b, c) = \int \frac{d^4k}{(2\pi)^4} \times \frac{k_{\mu_1}k_{\mu_2}\ldots k_{\mu_n}}{[k^2 - m_3^2]^a[(p_1 + k)^2 - m_1^2]^b[(p_2 + k)^2 - m_2^2]^c}. \quad (40)$$

[4)]Since the diagrams under consideration do not have UV divergences, there is no need for a dimensional regularization.

Continuing to Euclidean spacetime and employing the Schwinger representation for propagators

$$\frac{1}{[p^2+m^2]^a} = \frac{1}{\Gamma(a)}\int_0^\infty d\alpha\alpha^{a-1}e^{-\alpha(p^2+m^2)}, \qquad (41)$$

we find the following expression for the scalar integral ($n = 0$):

$$I_0(a,b,c) = \frac{(-1)^{a+b+c}i}{\Gamma(a)\Gamma(b)\Gamma(c)} \times\int_0^\infty\int_0^\infty\int_0^\infty d\alpha d\beta d\gamma\alpha^{a-1}\beta^{b-1}\gamma^{c-1} \qquad (42)$$
$$\times\int\frac{d^4k}{(2\pi)^4}e^{-\alpha(k^2+m_3^2)-\beta(s_1+k^2+2p_1\cdot k+m_1^2)-\gamma(s_2+k^2+2p_2\cdot k+m_2^2)}.$$

This representation proves to be very convenient for applying the Borel transformation with

$$\hat{B}_{p^2}(M^2)e^{-\alpha p^2} = \delta(1-\alpha M^2). \qquad (43)$$

We then have

$$\hat{I}_0(a,b,c) = \frac{(-1)^{a+b+c}i}{\Gamma(a)\Gamma(b)\Gamma(c)\cdot 16\pi^2}(M_{cc}^2)^{2-a-c} \times(M_{bc}^2)^{2-a-b}U_0(a+b+c-4,1-c-b), \qquad (44)$$

$$\hat{I}_\mu(a,b,c) = \frac{(-1)^{a+b+c+1}i}{\Gamma(a)\Gamma(b)\Gamma(c)\cdot 16\pi^2}\left(\frac{p_{1\mu}}{M_{bc}^2}+\frac{p_{2\mu}}{M_{cc}^2}\right) \times(M_{cc}^2)^{3-a-c}(M_{bc}^2)^{3-a-b}U_0(a+b+c-5,1-c-b), \qquad (45)$$

$$\hat{I}_{\mu\nu}(a,b,c) = \frac{(-1)^{a+b+c}i}{\Gamma(a)\Gamma(b)\Gamma(c)\cdot 16\pi^2}\left(\frac{p_{1\mu}}{M_{bc}^2}+\frac{p_{2\mu}}{M_{cc}^2}\right) \times\left(\frac{p_{1\nu}}{M_{bc}^2}+\frac{p_{2\nu}}{M_{cc}^2}\right)(M_{cc}^2)^{4-a-c}(M_{bc}^2)^{4-a-b} \times U_0(a+b+c-6,1-c-b) + \frac{g_{\mu\nu}}{2}\frac{(-1)^{a+b+c+1}i}{\Gamma(a)\Gamma(b)\Gamma(c)\cdot 16\pi^2}(M_{cc}^2)^{3-a-c}(M_{bc}^2)^{3-a-b} \times U_0(a+b+c-6,2-c-b), \qquad (46)$$

where M_{bc}^2 and M_{cc}^2 are the Borel parameters in the s_1 and s_2 channels, respectively. Here, we have introduced the $U_0(a, b)$ function, which is given by the expression

$$U_0(a,b) = \int_0^\infty dy(y+M_{bc}^2+M_{cc}^2)^a y^b \times\exp\left[-\frac{B_{-1}}{y}-B_0-B_1y\right], \qquad (47)$$

where

$$B_{-1} = \frac{1}{M_{cc}^2M_{bc}^2}(m_2^2M_{bc}^4+m_1^2M_{cc}^4 + M_{cc}^2M_{bc}^2(m_1^2+m_2^2-Q^2)),$$
$$B_0 = \frac{1}{M_{bc}^2M_{cc}^2}(M_{cc}^2(m_1^2+m_3^2)+M_{bc}^2(m_2^2+m_3^2)), \qquad (48)$$
$$B_1 = \frac{m_3^2}{M_{bc}^2M_{cc}^2}.$$

One can then express the results of calculation for any diagram in Fig. 3 through $\hat{I}_0(a, b, c)$, $\hat{I}_\mu(a, b, c)$, and $\hat{I}_{\mu\nu}(a, b, c)$ and their derivatives with respect to the Borel parameters, using the partial fractioning of the integrand expression together with the following relation:

$$\hat{B}_{p_1^2}(M_{bc}^2)\hat{B}_{p_2^2}(M_{cc}^2)[p_1^2]^m[p_2^2]^n I_{\mu_1\mu_2\ldots\mu_n}(a,b,c) = [M_{bc}^2]^m[M_{cc}^2]^n\frac{d^m}{d(M_{bc}^2)^m}\frac{d^n}{d(M_{cc}^2)^n} \times[M_{bc}^2]^m[M_{cc}^2]^n\hat{I}_{\mu_1\mu_2\ldots\mu_n}(a,b,c). \qquad (49)$$

The obtained expression can be further written down in terms of three quantities $\hat{I}_0(1, 1, 1)$, $\hat{I}_\mu(1, 1, 1)$, and $\hat{I}_{\mu\nu}(1, 1, 1)$ and their derivatives with respect to the Borel parameters and quark masses by means of

$$\hat{I}_{\mu_1\mu_2\ldots\mu_n}(a,b,c) = \frac{1}{\Gamma(a)\Gamma(b)\Gamma(c)}\frac{d^{a-1}}{d(m_3^2)^{a-1}} \times\frac{d^{b-1}}{d(m_1^2)^{b-1}}\frac{d^{c-1}}{d(m_2^2)^{c-1}}\hat{I}_{\mu_1\mu_2\ldots\mu_n}(1,1,1). \qquad (50)$$

However, contrary to the case discussed in [18], in such calculations values of parameters a and b will arise for which the $U_0(a, b)$ function has no analytic expression (it is connected to nonzero m_3 mass in our case). The analytic approximations for $U_0(a, b)$ at these values of parameters lead to very cumbersome expressions. The search for the most compact form of the final answer leads to the conclusion that the best decision in this case is to express the result in terms of the $U_0(a, b)$ function at different values of its parameters. For this

purpose, we have used the following transformation properties of $U_0(a, b)$:

$$\frac{dU_0(a,b)}{dM_{bc}^2} = aU_0(a-1,b) - \left(\frac{m_2^2}{M_{cc}^2} - \frac{m_1^2 M_{cc}^2}{M_{bc}^4}\right)U_0(a,b-1) + \frac{m_1^2+m_3^2}{M_{bc}^4}U_0(a,b) + \frac{m_3^2}{M_{bc}^4 M_{cc}^2}U_0(a,b+1), \quad (51)$$

$$\frac{dU_0(a,b)}{dM_{cc}^2} = aU_0(a-1,b) - \left(\frac{m_1^2}{M_{bc}^2} - \frac{m_2^2 M_{bc}^2}{M_{cc}^4}\right)U_0(a,b-1) + \frac{m_2^2+m_3^2}{M_{cc}^4}U_0(a,b) + \frac{m_3^2}{M_{bc}^2 M_{cc}^4}U_0(a,b+1). \quad (52)$$

In Appendix B, we have presented an analytic expression, obtained in this way, for the Wilson coefficient of the gluon-condensate operator, contributing to the $\Pi_1 = \Pi_+ + \Pi_-$ amplitude. One can see that, even in this form, the obtained results are very cumbersome. Thus, we have realized the gluon-condensate corrections as C++ codes, where the functions $U_0(a, b)$ are evaluated numerically. Analytic approximations that can be made for the $U_0(a, b)$ functions are discussed in Appendix B.

In Fig. 4, we have shown the effect of gluon condensate on the $f_1(0)$ form factor in the Borel transformed three-point sum rules.

We can draw the conclusion that the calculation of gluon-condensate term in full QCD sum rules allows one to enlarge the stability region in the parameter space for the form factors, which indicates the reliability of the sum-rule technique.

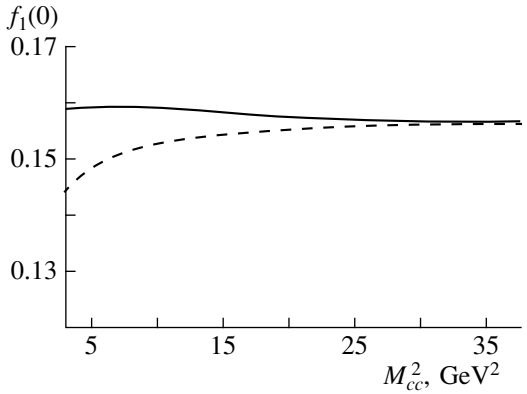

Fig. 4. The gluon-condensate contribution to the $f_1(0)$ form factor in the Borel transformed sum rules at fixed $M_{bc}^2 = 70$ GeV^2. The dashed curve represents the bare-quark-loop results, and the solid curve is the form factor including the gluon-condensate term at $\left\langle \frac{\alpha_s}{\pi} G^2 \right\rangle = 10^{-2}$ GeV^4.

3. THREE-POINT NRQCD SUM RULES

The formulation of sum rules in NRQCD follows the same lines as in QCD; the only difference is the Lagrangian, describing strong interactions of heavy quarks.

3.1. Symmetry of Form Factors in NRQCD and One-Loop Approximation

At the recoil momentum close to zero, the heavy quarks in both the initial and final states have small relative velocities, so that the dynamics of heavy quarks is essentially nonrelativistic. This allows us to use the NRQCD approximation in the study of mesonic form factors. As in the case of heavy quark effective theory (HQET), the expansion in the small relative velocities to the leading order leads to various relations between the different form factors. Solving these relations results in the introduction of a universal form factor (an analog of the Isgur–Wise function) at $q^2 \longrightarrow q^2_{\max}$.

In this subsection, we consider the limit

$$v_1^\mu \neq v_2^\mu, \quad w = v_1 \cdot v_2 \longrightarrow 1, \quad (53)$$

where $v_{1,2}^\mu = p_{1,2}^\mu / \sqrt{p_{1,2}^2}$ are the four-velocities of heavy quarkonia in the initial and final states. The study of region (53) is reasonable enough, because in the rest frame of the B_c meson ($p_1^\mu = (\sqrt{p_1^2}, \mathbf{0})$, the four-velocities differ only by a small value $|\mathbf{p}_2|$ ($p_2^\mu = (\sqrt{p_2^2}, \mathbf{p}_2)$), whereas their scalar product w deviates from unity only due to a term proportional to the square of $|\mathbf{p}_2|$: $w = \sqrt{1 + \frac{|\mathbf{p}_2|^2}{p_2^2}} \sim 1 + \frac{1}{2}\frac{|\mathbf{p}_2|^2}{p_2^2}$. Thus, in the linear approximation at $|\mathbf{p}_2| \longrightarrow 0$, relations (53) are valid and take place.

Here, we would like to note that (53) generalizes the investigation of [14], where the case of $v_1 = v_2$ was considered. This condition severely restricts the relations of spin symmetry for the form factors, and, as a consequence, it provides a single connection between the form factors.

As can be seen in Fig. 1, since the antiquark line with the mass m_3 is common to the heavy quarkonia, the four-velocity of an antiquark can be written down as a linear combination of four-velocities v_1 and v_2:

$$\tilde{v}_3^\mu = a v_1^\mu + b v_2^\mu. \quad (54)$$

In the leading order of NRQCD for the kinematical invariants, determining the spin structure of quark propagators in the limit $w \longrightarrow 1$, we have the following expressions:

$$\begin{aligned} p_1^2 &\longrightarrow (m_1 + m_3)^2 = \mathcal{M}_1^2, \\ p_2^2 &\longrightarrow (m_2 + m_3)^2 = \mathcal{M}_2^2, \\ \Delta_1 &\longrightarrow 2m_3\mathcal{M}_1, \\ \Delta_2 &\longrightarrow 2m_3\mathcal{M}_2, \\ u &\longrightarrow 2\mathcal{M}_1\mathcal{M}_2 \cdot w, \\ \lambda(p_1^2, p_2^2, q^2) &\longrightarrow 4\mathcal{M}_1^2\mathcal{M}_2^2(w^2 - 1). \end{aligned} \tag{55}$$

In this kinematics, it is an easy task to show that in (54) $a = b = -\frac{1}{2}$, i.e.,

$$\tilde{v}_3^\mu = -\frac{1}{2}(v_1 + v_2)^\mu. \tag{56}$$

Applying momentum conservation at the vertices in Fig. 1, we derive the following formulas for the four-velocities of quarks with the masses m_1 and m_2:

$$\tilde{v}_1^\mu = v_1^\mu + \frac{m_3}{2m_1}(v_1 - v_2)^\mu, \tag{57}$$

$$\tilde{v}_2^\mu = v_2^\mu + \frac{m_3}{2m_2}(v_2 - v_1)^\mu, \tag{58}$$

and in the limit $w \longrightarrow 1$, we have $\tilde{v}_1^2 = \tilde{v}_2^2 = 1$, as it should be.

After these definitions have been made, it is straightforward to write down the transition form factor for the current $J_\mu = \bar{Q}_1\Gamma_\mu Q_2$ with the spin structure $\Gamma_\mu = \{\gamma_\mu, \gamma_5\gamma_\mu\}$

$$\begin{aligned} \langle H_{Q_1\bar{Q}_3}|J_\mu|H_{Q_2\bar{Q}_3}\rangle &= \mathrm{tr}\Big[\Gamma_\mu\frac{1}{2}(1 + \tilde{v}_1^\mu\gamma_\mu) \\ \times\Gamma_1\frac{1}{2}(1 + \tilde{v}_3^\nu\gamma_\nu)\Gamma_2\frac{1}{2}(1 + \tilde{v}_2^\lambda\gamma_\lambda)\Big]&h(m_1, m_2, m_3), \end{aligned} \tag{59}$$

where Γ_1 determines the spin state in the heavy quarkonium $Q_1\bar{Q}_3$ (in our case it is pseudoscalar, so that $\Gamma_1 = \gamma_5$), and Γ_2 determines the spin wave function of quarkonium in the final state: $\Gamma_2 = \{\gamma_5, \epsilon^\mu\gamma_\mu\}$ for the pseudoscalar and vector states, respectively ($H = P, V$). The quantity h is a universal function at $w \longrightarrow 1$, independent of the quarkonium spin state. So, for the form factors discussed in our paper we have

$$\langle P_{Q_1\bar{Q}_3}|\bar{Q}_1\gamma^\mu Q_3|P_{Q_2\bar{Q}_3}\rangle = (c_1^P \cdot v_1^\mu + c_2^P \cdot v_2^\mu)h, \tag{60}$$

$$\langle P_{Q_1\bar{Q}_3}|\bar{Q}_1\gamma^\mu Q_3|V_{Q_2\bar{Q}_3}\rangle = ic_V \cdot \epsilon^{\mu\nu\alpha\beta}\epsilon_\nu v_{1\alpha}v_{2\beta} \cdot h, \tag{61}$$

$$\begin{aligned} &\langle P_{Q_1\bar{Q}_3}|\bar{Q}_1\gamma_5\gamma^\mu Q_3|V_{Q_2\bar{Q}_3}\rangle \\ &= (c_\epsilon \cdot \epsilon^\mu + c_1 \cdot v_1^\mu(\epsilon \cdot v_1) + c_2 \cdot v_2^\mu(\epsilon \cdot v_1))h, \end{aligned} \tag{62}$$

where

$$\begin{aligned} c_\epsilon &= -2, \\ c_1 &= -\frac{m_3(3m_1 + m_3)}{4m_1m_2}, \\ c_2 &= \frac{1}{4m_1m_2}(4m_1m_2 + m_1m_3 + 2m_2m_3 + m_3^2), \\ c_V &= -\frac{1}{2m_1m_2}(2m_1m_2 + m_1m_3 + m_2m_3), \\ c_1^P &= 1 + \frac{m_3}{2m_1} - \frac{m_3}{2m_2}, \\ c_2^P &= 1 - \frac{m_3}{2m_1} + \frac{m_3}{2m_2}. \end{aligned} \tag{63}$$

For the form factors in NRQCD, we then have the following symmetry relations:

$$\begin{aligned} f_+(c_1^P \cdot \mathcal{M}_2 - c_2^P \cdot \mathcal{M}_1) - f_-(c_1^P \cdot \mathcal{M}_2 + c_2^P \cdot \mathcal{M}_1) &= 0, \\ F_0^A \cdot c_V - 2c_\epsilon \cdot F_V\mathcal{M}_1\mathcal{M}_2 &= 0, \\ F_0^A(c_1 + c_2) - c_\epsilon \cdot \mathcal{M}_1(F_+^A(\mathcal{M}_1 + \mathcal{M}_2) & \\ + F_-^A(\mathcal{M}_1 - \mathcal{M}_2)) &= 0, \\ F_0^A c_1^P + c_\epsilon \cdot \mathcal{M}_1(f_+ + f_-) &= 0. \end{aligned} \tag{64}$$

Thus, we can claim that, in the approximation of NRQCD, the form factors of weak currents responsible for the transitions between two heavy quarkonium states are given in terms of the single form factor, say, F_0^A. An exception is observed for the form factors F_+^A and F_-^A, since a definite value is only taken by their linear combination $F_+^A(\mathcal{M}_1 + \mathcal{M}_2) + F_-^A(\mathcal{M}_1 - \mathcal{M}_2)$. This fact has a simple physical explanation. Indeed, the polarization of vector quarkonium ϵ^μ has two components: the longitudinal term ϵ_L^μ and transverse one ϵ_T^μ (i.e., $(\epsilon_T \cdot v_1) = 0$). The quantity ϵ_L^μ can be decomposed in terms of v_1^μ and v_2^μ:

$$\epsilon^\mu = \alpha\epsilon_L^\mu + \beta\epsilon_T^\mu, \quad \alpha^2 + \beta^2 = 1, \tag{65}$$

where

$$\begin{aligned} \epsilon_L^\mu &= \frac{1}{\sqrt{s_2k}}(-2s_2p_1^\mu + up_2^\mu) \longrightarrow \frac{1}{\sqrt{w^2 - 1}}(-v_1^\mu + wv_2^\mu), \\ \alpha &= -\frac{2\sqrt{s_2}}{\sqrt{k}}(\epsilon_L \cdot p_1) \longrightarrow -\frac{1}{\sqrt{w^2 - 1}}(\epsilon \cdot v_1). \end{aligned} \tag{66}$$

From (66), one can see that the decomposition of polarization vector ϵ into the longitudinal and transverse parts in NRQCD is singular in the limit $w \longrightarrow 1$:

$$\epsilon^\mu = -\frac{1}{w^2-1}(-v_1^\mu + w v_2^\mu)(\epsilon \cdot v_1) + \beta \cdot \epsilon_T^\mu. \quad (67)$$

It means that the introduction into the form factor F_0^A of an additional term $\Delta F_0^A = (w^2-1)\delta h$, which vanishes at $w \longrightarrow 1$ and, thus, is not under control in NRQCD, leads to a finite correction for the form factors F_+^A and F_-^A. This correction is canceled in the special linear combination of form factors presented in (64).

In the case of $v_1 = v_2$, we reproduce the single relation between form factors F_0^A and $f_\pm$, as it was obtained earlier in [14].

Thus, we have obtained the generalized relations due to the spin symmetry of NRQCD Lagrangian for the case $v_1 \neq v_2$ in the limit where the invariant mass of lepton pair takes its maximum value, i.e., at a recoil momentum close to zero.

In the one-loop approximation for the three-point NRQCD sum rules, i.e., in the calculation of bare-quark loop, the symmetry relations (64) already take place for the double spectral densities ρ_j^{NR} in the limit $|\mathbf{p}_2| \longrightarrow 0$. We have checked that the spectral densities of the full QCD in the NRQCD limit $w \longrightarrow 1$ satisfy the symmetry relations (64).

It is easily seen that in this approximation

$$\rho_0^{A,\,NR} = -\frac{6m_1m_2m_3}{|\mathbf{p}_2|(m_1+m_3)}. \quad (68)$$

When integrating over the resonance region, we must take into account that

$$\frac{|\omega_2 - \omega_1 m_{13}/m_{23}|m_2}{|\mathbf{p}_2|\sqrt{2\omega_1 m_{13}}} \leq 1, \quad (69)$$

so we see that, in the limit $|\mathbf{p}_2| \longrightarrow 0$, the integration region tends to a single point. Here, $p_1 = (m_1 + m_3 + \omega_1, \mathbf{0})$, $p_2 = (m_2 + m_3 + \omega_2, \mathbf{p}_2)$, and $m_{ij} = \dfrac{m_i m_j}{m_i + m_j}$ is the reduced mass of system $Q_i\bar{Q}_j$.

After the substitutions of variables $\omega_1 = \dfrac{k^2}{2m_{13}}$ and $x = \left(\omega_2 - \dfrac{k^2}{2m_{23}}\right)\dfrac{m_2}{|\mathbf{p}_2|k}$ in the limit $|\mathbf{p}_2| \longrightarrow 0$ for the correlation function $\Pi_0^{A,\,NR}$, we have the expression

$$\Pi_0^{A,\,NR} = -\frac{1}{(2\pi)^2}\int \frac{d\tilde{\omega}_1 d\tilde{\omega}_2}{(\tilde{\omega}_1 - \omega_1)(\tilde{\omega}_2 - \omega_2)}\rho_0^{A,\,NR}$$
$$= \frac{3}{\pi^2}\int_0^{k_{th}} \frac{k^2 dk}{\left(\omega_1 - \dfrac{k^2}{2m_{13}}\right)\left(\omega_2 - \dfrac{k^2}{2m_{23}}\right)}, \quad (70)$$

where k_{th} denotes the resonance region boundary. In the method of moments in NRQCD sum rules, we set $\omega_1 = -(m_1 + m_3) + q_1$ and $\omega_2 = -(m_2 + m_3) + q_2$, so that in the limit $q_{1,2} \longrightarrow 0$ we have

$$\frac{1}{n!}\frac{1}{m!}\frac{d^{n+m}}{dq_1^n dq_2^m}\Pi_0^{A,\,NR} = \Pi_0^{A,\,NR}[n,m]$$
$$= \frac{3}{\pi^2}\int_0^{k_{th}} \frac{k^2 dk}{\left(\mathcal{M}_1 + \dfrac{k^2}{2m_{13}}\right)^{n+1}\left(\mathcal{M}_2 + \dfrac{k^2}{2m_{23}}\right)^{m+1}}. \quad (71)$$

In the hadronic part of NRQCD sum rules in the limit $|\mathbf{p}_2| \longrightarrow 0$, we model the resonance contribution using the following representation:

$$\Pi_0^{A,\,res} = \sum_{i,j}\frac{f_i^{Q_1\bar{Q}_3}M_{1,i}^2}{(m_1+m_3)M_{1,i}^2}\frac{f_j^{Q_2\bar{Q}_3}M_{2,j}}{M_{2,j}^2}F_{0,ij}^A$$
$$\times \sum_{l,m}\left(\frac{q_1^2}{M_{1,i}^2}\right)^l\left(\frac{q_2^2}{M_{2,j}^2}\right)^m. \quad (72)$$

Saturating the p_1^2 and p_2^2 channels by ground states of mesons under consideration for the $F_{0,1S\to 1S}^A$ form factor, we have

$$F_{0,1S\to 1S}^A = \frac{\Pi_0^{A,\,NR}[n,m](m_1+m_3)}{f_{1S}^{Q_1\bar{Q}_3}M_{1,1S}^2 f_{1S}^{Q_2\bar{Q}_3}M_{2,1S}^2}M_{1,1S}^n M_{2,1S}^m. \quad (73)$$

In the next subsection, we will proceed with the gluon-condensate contribution to NRQCD sum rules.

3.2. Contribution of the Gluon Condensate

Following a general formalism for the calculation of gluon-condensate contribution in the Fock–Schwinger gauge [20, 23], we have considered diagrams depicted in Fig. 3. In our calculations, we have used the NRQCD approximation and analyzed the limit where the invariant mass of the lepton pair takes its maximum value. Here, we would like to note that the spin structure, in the leading order of relative velocity of heavy quarks, does not change, in comparison with the bare-loop result for the nonrelativistic quarks. Thus, we can conclude that in this approximation the symmetries of

NRQCD Lagrangian lead to a universal Wilson coefficient for the gluon-condensate operator. As a consequence, relations (64) remain valid.

Below, we perform calculations for the form factor $F_0^A(p_1^2, p_2^2, q^2)$ in the limit $q^2 \longrightarrow q^2_{\max}$. The contribution of gluon condensate to the corresponding correlation function is given by the expression

$$\Delta F_0^{G^2} = \left\langle \frac{\alpha_s}{\pi} G^2_{\mu\nu} \right\rangle \frac{\pi}{48}[3R_0 - R_2], \tag{74}$$

where

$$R_0 = -\frac{1}{\pi^2 i}\int \frac{k^2 dk dk_0}{P_3(k, k_0)P_1(k, k_0, \omega_1)P_2(k, k_0, \omega_2)} R_g,$$
$$R_2 = -\frac{1}{\pi^2 i}\int \frac{k^4 dk dk_0}{P_3(k, k_0)P_1(k, k_0, \omega_1)P_2(k, k_0, \omega_2)} R_k. \tag{75}$$

In these expressions, the inverse propagators are

$$P_1(k, k_0, \omega_1) = \omega_1 + k_0 - \frac{k^2}{2m_1},$$
$$P_2(k, k_0, \omega_2) = \omega_2 + k_0 - \frac{k^2}{2m_2}, \tag{76}$$
$$P_3(k, k_0) = -k_0 - \frac{k^2}{2m_3}.$$

The functions R_g and R_k are symmetric under the permutation of indices 1 and 2 and are given by

$$R_g = -\frac{1}{m_1}\left[\frac{1}{P_3} + \frac{1}{P_1}\right]\frac{1}{P_1^2} - \frac{1}{m_2}\left[\frac{1}{P_3} + \frac{1}{P_1}\right]\frac{1}{P_2^2},$$
$$R_k = \frac{3}{m_1^2}\frac{1}{P_1^4} + \frac{3}{m_2^2}\frac{1}{P_2^4} + \frac{3}{m_1^2}\frac{1}{P_1^3 P_3} + \frac{3}{m_2^2}\frac{1}{P_2^3 P_3}$$
$$+ \frac{1}{m_1 m_3}\frac{1}{P_1^2 P_3^2} + \frac{1}{m_2 m_3}\frac{1}{P_2^2 P_3^2} - \frac{1}{m_3^2}\frac{1}{P_3^4} - \frac{1}{m_1 m_3}\frac{1}{P_1 P_3^3} \tag{77}$$
$$- \frac{1}{m_2 m_3}\frac{1}{P_2 P_3^3} - \frac{1}{m_1 m_2}\frac{1}{P_1 P_2 P_3^2} - \frac{1}{m_1 m_2}\frac{1}{P_1^2 P_2^2}.$$

Let us note that, in the calculation of the diagrams in Fig. 3, we have used the following vertex for the interaction of a heavy quark with a gluon:

$$L^v_{\text{int}} = -g_s \bar{h}_v v_\mu A^\mu h_v, \tag{78}$$

where $A_\mu = A^a_\mu \frac{\lambda^a}{2}$ and its Fourier transform in Fock–Schwinger gauge has the form

$$A^a_\mu(k_g) = -\frac{i}{2} G^a_{\mu\nu}(0)\frac{\partial}{\partial k_g}(2\pi)^4 \delta(k_g). \tag{79}$$

After two differentiations of the nonrelativistic propagators

$$\frac{1}{P(p, m_Q)} = \frac{1}{pv + \dfrac{p^2}{2m_Q}}, \tag{80}$$

two types of contributions to the gluon-condensate correction appear. The first is equal to

$$v_\mu v_\nu \alpha_s G^a_{\mu\alpha} G^a_{\nu\beta} \cdot g^{\alpha\beta} \longrightarrow \langle \alpha_s G^2_{\mu\nu} \rangle \frac{3}{12}, \tag{81}$$

and it leads to the term with R_0. The second expression

$$v_\mu v_\nu \alpha_s G^a_{\mu\alpha} G^a_{\nu\beta} k^\alpha k^\beta \longrightarrow \langle \alpha_s G^2_{\mu\nu} \rangle \frac{k^2 - (v \cdot k)^2}{12}$$
$$= -\langle \alpha_s G^2_{\mu\nu} \rangle \frac{|\mathbf{k}|^2}{12} \tag{82}$$

leads to the term with R_2, which is of the same order in the relative velocity of heavy quarks as R_0, but it is suppressed numerically in the region of moderate numbers for the momenta of spectral densities, where the nonperturbative contributions (condensates) of higher dimension operators are not essential.

It is easy to show that the contributions of R_0 and R_2 can be obtained by the differentiation of two basic integrals:

$$E_0 = -\frac{1}{\pi^2 i}\int_0^\infty \frac{k^2 dk dk_0}{P_1 P_2 P_3} = \frac{2m_{13} \cdot 2m_{23}}{k_{13} + k_{23}},$$
$$E_2 = -\frac{1}{\pi^2 i}\int_0^\infty \frac{k^4 dk dk_0}{P_1 P_2 P_3} \tag{83}$$
$$= -\frac{2m_{13} \cdot 2m_{23}}{k_{13} + k_{23}}(k_{13}^2 + k_{13}k_{23} + k_{23}^2),$$

where $k_{13} = \sqrt{-2m_{13}\omega_1}$ and $k_{23} = \sqrt{-2m_{23}\omega_2}$. For R_0 and R_2, we then have

$$R_0 = \hat{R}_g \cdot E_0,$$
$$R_2 = \hat{R}_k \cdot E_2,$$

where operators $\hat{R}_g$ and $\hat{R}_k$ can be obtained from R_g and R_k in (77) after the substitutions

$$\frac{1}{P_1^n} \longrightarrow \frac{(-1)^n}{n!}\frac{\partial^n}{\partial \omega_1^n},$$
$$\frac{1}{P_2^m} \longrightarrow \frac{(-1)^m}{m!}\frac{\partial^m}{\partial \omega_2^m},$$

$$\frac{1}{P_3^l} \longrightarrow \frac{(-1)^l}{l!}\left[\frac{\partial}{\partial\omega_1} + \frac{\partial}{\partial\omega_2}\right]^l.$$

As a result, we have

$$R_0 = \left\{\frac{1}{6m_1}\frac{\partial^3}{\partial\omega_1^3} + \frac{1}{6m_2}\frac{\partial^3}{\partial\omega_2^3} + \frac{1}{2m_1}\left(\frac{\partial^3}{\partial\omega_1^3} + \frac{\partial^3}{\partial\omega_1^2\partial\omega_2}\right) + \frac{1}{2m_2}\left(\frac{\partial^3}{\partial\omega_2^3} + \frac{\partial^3}{\partial\omega_2^2\partial\omega_1}\right)\right\}\frac{2m_{13}2m_{23}}{k_{13}+k_{23}}, \quad (84)$$

$$R_2 = \left\{\frac{3}{4!m_1^2}\frac{\partial^4}{\partial\omega_1^4} + \frac{3}{4!m_2^2}\frac{\partial^4}{\partial\omega_2^4} + \frac{3}{3!m_1^2}\left(\frac{\partial^4}{\partial\omega_1^4} + \frac{\partial^4}{\partial\omega_1^3\partial\omega_2}\right) + \frac{1}{3!m_2^2}\left(\frac{\partial^4}{\partial\omega_2^4} + \frac{\partial^4}{\partial\omega_2^3\partial\omega_1}\right) + \frac{1}{4m_1m_3}\left(\frac{\partial^4}{\partial\omega_1^4} + 2\frac{\partial^4}{\partial\omega_1^3\partial\omega_2} + \frac{\partial^4}{\partial\omega_1^2\partial\omega_2^2}\right) + \frac{1}{4m_2m_3}\left(\frac{\partial^4}{\partial\omega_2^4} + 2\frac{\partial^4}{\partial\omega_2^3\partial\omega_1} + \frac{\partial^4}{\partial\omega_1^2\partial\omega_2^2}\right) - \frac{1}{4!m_3^2}\left(\frac{\partial^4}{\partial\omega_1^4} + 4\frac{\partial^4}{\partial\omega_1^3\partial\omega_2} + 6\frac{\partial^4}{\partial\omega_1^2\partial\omega_2^2} + 4\frac{\partial^4}{\partial\omega_1\partial\omega_2^3} + \frac{\partial^4}{\partial\omega_2^4}\right) \quad (85)$$

$$- \frac{1}{3!m_1m_3}\left(\frac{\partial^4}{\partial\omega_1^4} + 3\frac{\partial^4}{\partial\omega_1^3\partial\omega_2} + 3\frac{\partial^4}{\partial\omega_1^2\partial\omega_2^2} + \frac{\partial^4}{\partial\omega_1\partial\omega_2^3}\right) - \frac{1}{3!m_2m_3}\left(\frac{\partial^4}{\partial\omega_2^4} + 3\frac{\partial^4}{\partial\omega_2^3\partial\omega_1} + 3\frac{\partial^4}{\partial\omega_1^2\partial\omega_2^2} + \frac{\partial^4}{\partial\omega_2\partial\omega_1^3}\right) - \frac{1}{2m_1m_2}\left(\frac{\partial^4}{\partial\omega_1^3\partial\omega_2} + 2\frac{\partial^4}{\partial\omega_1^2\partial\omega_2^2} + \frac{\partial^4}{\partial\omega_1\partial\omega_2^3}\right) - \frac{1}{4m_1m_2}\left(\frac{\partial^4}{\partial\omega_1^2\partial\omega_2^2}\right)\left\{\left(-\frac{2m_{13}2m_{23}}{m_{13}+m_{23}}\right)(k_{13}^2 + k_{13}k_{23} + k_{23}^2).\right.$$

Equations (74), (84), and (85) represent the most compact analytic expression for the contribution of gluon condensate to the form factor F_0^A, whereas performing the differentiations leads to very cumbersome expressions.

In the moment scheme of sum rules, we suppose

$$\omega_1 = -(m_1 + m_3) + q_1,$$
$$\omega_2 = -(m_2 + m_3) + q_2$$

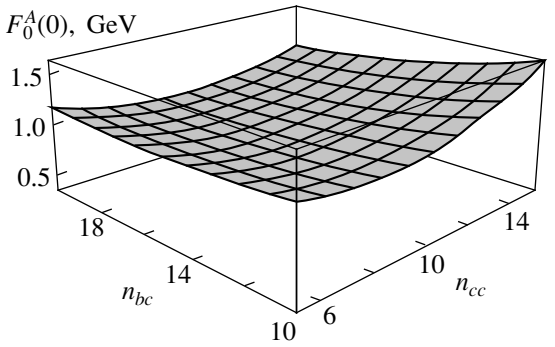

Fig. 5. The QCD sum-rule results in the moment scheme for the $F_0^A(0)$ form factor in the bare approximation.

and expand $\Delta F_0^{G^2}$ in a series in $\{q_1, q_2\}$ at the point $\{0, 0\}$, which allows us to determine $\Delta F_0^{G^2}[n, m] = \frac{1}{n!}\frac{1}{m!}\frac{d^{n+m}}{dq_1^n dq_2^m}\Delta F_0^{G^2}$. Further analysis has been performed numerically with the help of MATHEMATICA.

To conclude, we have calculated the contribution of gluon condensate to the three-point sum rules for heavy quarkonia in the leading order of relative velocity of heavy quarks and in the first order of α_s. Due to the symmetry of NRQCD in the limit where the invariant mass of the lepton pair takes its maximum value, i.e., at a recoil momentum close to zero, the Wilson coefficient for the form factor F_0^A is universal in the sense that it determines the contributions of gluon condensate to other form factors, in accordance with relations (64).

4. NUMERICAL RESULTS ON THE FORM FACTORS

First, we evaluate the form factors in the scheme of spectral density moments. This scheme is not strongly sensitive to the values of threshold energies determining the region of resonance contribution. In the QCD sum rule calculations, we set (in GeV)

$$\begin{aligned} k_{\text{th}}(\bar{b}c) &= 1.5, \\ k_{\text{th}}(\bar{c}c) &= 1.2, \\ m_b &= 4.6, \\ m_c &= 1.4, \end{aligned} \quad (86)$$

where k_{th} is the momentum of quark motion in the rest frame of quarkonium. The chosen values of threshold momenta correspond to the minimal energy of heavy-meson pairs in specified channels.

The typical behavior of form factors in the moment scheme of QCD sum rules is presented in Fig. 5.

Table 1. Form factors for B_c^+ decay into heavy quarkonia at $q^2 = 0$ in the bare-quark-loop approximation with allowance for the Coulomb correction

Approximation	f_+	f_-	F_V, GeV^{-1}	F_0^A, GeV	F_+^A, GeV^{-1}	F_-^A, GeV^{-1}
Bare	0.10	−0.057	0.016	0.90	−0.011	0.018
Coulomb	0.66	−0.36	0.11	5.9	−0.074	0.12

The evaluation of the Coulomb corrections strongly depends on the appropriate set of α_s for the quarkonia under consideration. The corresponding scale of gluon virtuality is determined by quite a low value close to the average momentum transfer in the system. So, the expected α_s is about 0.5. To decrease the uncertainty, we consider the contribution of the Coulomb rescattering in the two-point sum rules giving the leptonic constants of heavy quarkonia. These sum rules are quite sensitive to the value of the strong-coupling constant, as the perturbative contribution depends on it linearly. The observed value for the charmonium, $f_{J/\psi} \approx 410$ MeV, can be obtained in this technique at $\alpha_s^{\mathrm{C}}(\bar{c}c) = 0.6$. The value $f_{B_c} = 385$ MeV, as it is predicted in QCD sum rules [22], gives $\alpha_s^{\mathrm{C}}(\bar{b}c) = 0.45$. We present the results of the Coulomb enhancement for the form factors in Table 1.

The result after the introduction of the Coulomb correction is shown in Fig. 6. Such large corrections to the form factors should not lead to confusion, as they resulted from the fair account of the Coulomb corrections both for the bare-quark-loop diagram and for the meson-coupling constant.

Working in the same scheme for the case of NRQCD sum rules, we have plotted in Fig. 7 the value of $F^A_{0,\,1S\to 1S}$ at fixed $n_{cc} = 4$ with the following values of the parameters:[5)]

$$k_{\mathrm{th}} = 1.3\ \mathrm{GeV},$$
$$m_b = 4.6\ \mathrm{GeV},$$
$$m_c = 1.4\ \mathrm{GeV}.$$
$$\left\langle \frac{\alpha_s}{\pi} G^2_{\mu\nu} \right\rangle = 1.7 \times 10^{-2}\ \mathrm{GeV}^4.$$

Further, in (72) we can take into account the dominant subleading term, which is the contribution by the $2S \longrightarrow 2S$ transition. In this case, one could expect that the form factor is not suppressed in comparison with the contribution by the $1S \longrightarrow 2S$ transition, since in the potential picture the latter decay has to be neglected because the overlapping between the wave functions at zero recoil is close to zero for the states with the different quantum numbers.[6)] Thus, we can easily modify the relation (73) due to the second transition and justify the value of $F^A_{0,\,2S\to 2S}$ to reach the stability of $F^A_{0,\,1S\to 1S}$ at low values of moment numbers. We find $F^A_{0,\,2S\to 2S}/F^A_{0,\,1S\to 1S} \approx 3.7$ and present the behavior of the form factor F_0^A at zero recoil in Fig. 8.

As can be seen in these figures, the gluon contribution, while varying the moment number in the region of bound $\bar{c}c$ states, plays an important role, because it allows us to extend the stability region for the form factor F_0^A up to three times (from $n < 5$ to $n < 15$) and thus the reliability of sum-rule predictions. Let us also note that, in the scheme of saturation for the hadronic part of sum rules by the ground states in both variables s_1 and s_2, the allowance for the gluon condensate leads to the 20% reduction for the value of form factor F_0^A.

The analysis of the dependence on the moment number n_{bc} in the region of bound states $\bar{b}c$ at fixed n_{cc} shows that the contribution of gluon condensate in this case does not affect the character of this dependence. This may be explained by the fact that the Coulomb corrections to the Wilson coefficient of gluon operator $G^2_{\mu\nu}$ play an essential role.[7)] The summation of α_s/v terms for $\bar{b}c$ may give a sizable effect, contrary to the situation with the $\bar{c}c$ system, where the relative velocity of heavy quarks is not too small.

In the scheme of the Borel transformation for QCD sum rules, we find a strong dependence on the thresholds of continuum contribution. We think that this dependence reflects the influence of contributions coming from the excited states. So, the choice of k_{th} values in the same region as in the scheme of spectral-density moments results in form factors which are approximately 50% greater than the predictions in the

[5)]The evaluation of the $\Delta F_0^{G^2}[n_{cc}, n_{bc}]$ dependence in a broad range of $[n_{cc}, n_{bc}]$ takes too much calculation time, so we restrict ourselves by showing the results in Figs. 7 and 8 for the fixed $n_{cc} = 4$.

[6)]The corresponding estimates were performed in [24], where the $1S \longrightarrow 2S$ transition is suppressed with respect to $1S \longrightarrow 1S$ as 1/25.

[7)]At present, there is an analytic calculation of initial six moments for the Wilson coefficient of gluon condensate in the second order of α_s [26]. In this region, the influence of gluon condensate on the sum-rule results is negligibly small for the heavy quarkonia, containing the b quark, which does not allow one to draw definite conclusions on the role of such α_s corrections.

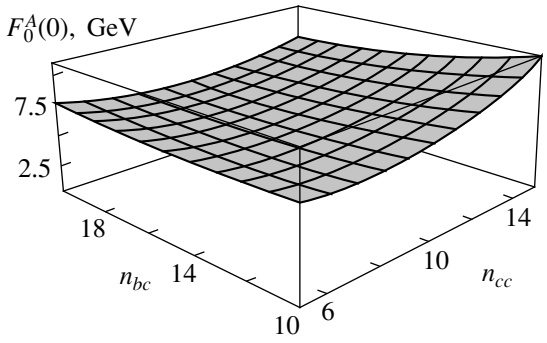

Fig. 6. The QCD sum-rule results in the moment scheme for the $F_0^A(0)$ form factor with allowance for the Coulomb corrections.

moments scheme, where the higher excitations numerically are not essential. In this case, we can explore the ideology of finite-energy sum rules [25], wherein the choice of interval for the quark–hadron duality, expressed by means of sum rules, allows one to isolate the contribution of basic states only. So, if we set

$$\begin{aligned} k_{\text{th}}(\bar{b}c) &= 1.2\ \text{GeV}, \\ k_{\text{th}}(\bar{c}c) &= 0.9\ \text{GeV}, \end{aligned} \tag{87}$$

then the region of the lowest bound states is taken into account in both channels of initial and final states, and the Borel transform scheme leads to results that are very close to those of the moment scheme. The dependence of calculated values on the Borel parameters is presented in Figs. 9 and 10, in the bare and Coulomb approximations, respectively.

As for the dependence of form factors on q^2, the consideration of bare-quark-loop term shows that, say, for $F_0^A(q^2)$, it can be approximated by the pole function

$$F_0^A(q^2) = \frac{F_0^A(0)}{1 - q^2/M_{\text{pole}}^2}, \tag{88}$$

with $M_{\text{pole}} \approx 4.5$ GeV. The latter is in good agreement with the value given in [12]. However, we believe that the pole mass can change after the inclusion of α_s corrections.[8)] From the naive meson dominance model, we expect that $M_{\text{pole}} \approx 6.3$–$6.5$ GeV.

We have calculated the total widths of semileptonic decays in the region of $M_{\text{pole}} = 4.5$–6.5 GeV, which result in the 30% variation of predictions for the modes with the massless leptons and more sizable dependence for the modes with the τ lepton (see Table 2).

To compare with other estimates, we calculate the width of $\bar{b} \longrightarrow \bar{c}e^+\nu_e$ transition as the sum of decays into the pseudoscalar and vector states and find[9)]

[8)]In HQET, the slope of Isgur–Wise function acquires a valuable correction due to the α_s term.

[9)]For normalization of the calculated branching ratios, we used the total B_c width obtained in the framework of the OPE approach [8].

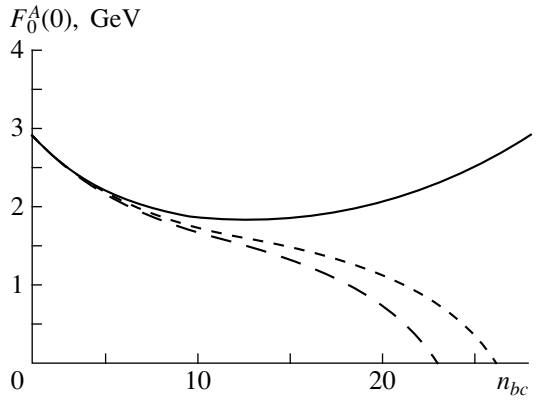

Fig. 7. The NRQCD sum-rule results for the $F_0^A(0)$ form factor. The solid curve represents the bare-quark-loop contribution, the short dashed curve is the result obtained by taking into account the gluon-condensate term R_0 only, and the long dashed curve is the form factor including the full expression for the gluon condensate.

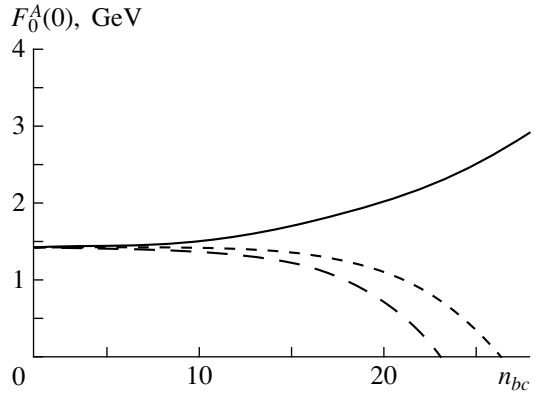

Fig. 8. The NRQCD sum-rule results for the $F_0^A(0)$ form factor. The contribution of $2S \longrightarrow 2S$ transition has been taken into account. The notation is the same as in Fig. 7.

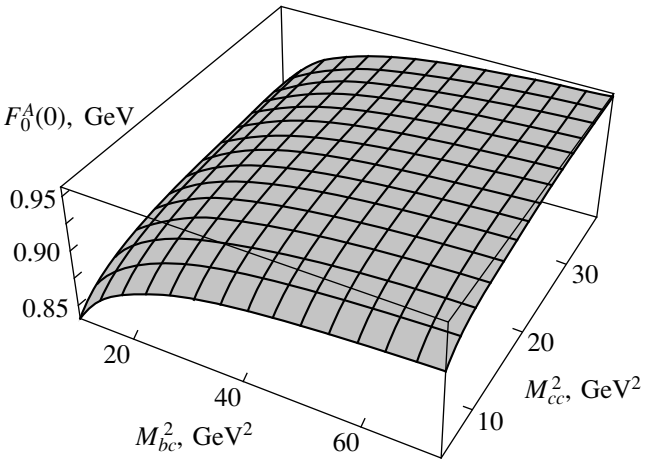

Fig. 9. The Borel transformed sum-rule results for the $F_0^A(0)$ form factor in the bare approximation of QCD.

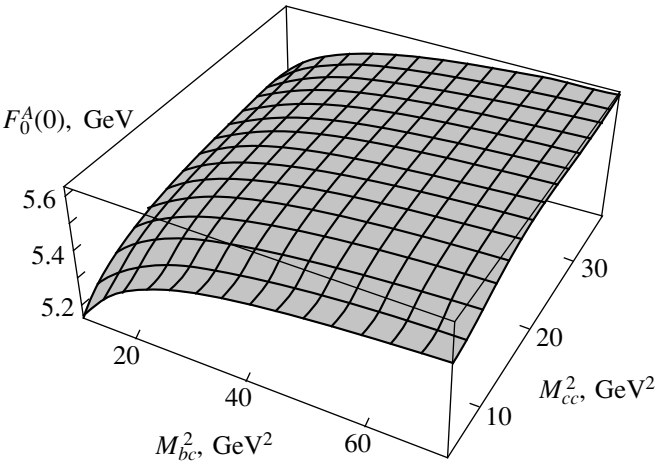

Fig. 10. The Borel transformed sum-rule results for the $F_0^A(0)$ form factor with allowance for the Coulomb corrections.

$\mathrm{Br}(B_c^+ \longrightarrow c\bar{c}e^+\nu_e) \approx (3.4 \pm 0.6)\%$, which is in good agreement with the value obtained in potential models [6] and in OPE calculations [8], where the following estimate was obtained: $\mathrm{Br}(B_c^+ \longrightarrow c\bar{c}e^+\nu_e) \approx 3.8\%$. As for our estimates for exclusive decay channels, they also agree with the results obtained previously in the framework of potential models [6].

In the results presented, we have supposed the quark mixing matrix element $|V_{bc}| = 0.040$.

As for the hadronic decays, in the approach of factorization [27], we assume that the width of transition $B_c^+ \longrightarrow J/\psi(\eta_c) + \textit{light hadrons}$ can be calculated with the same form factors after the introduction of QCD corrections, which can be easily written down as the factor $H = N_c a_1^2$. The factor a_1 represents the hard α_s corrections to the four-fermion weak interaction. Numerically, we set $a_1 = 1.2$, which yields $H \approx 4.3$. So, we find

$$\mathrm{Br}[B_c^+ \longrightarrow J/\psi + \text{light hadrons}] = (11 \pm 2)\%, \quad (89)$$

Table 2. Width with respect to B_c^+ decay into heavy quarkonia and leptonic pair and branching fractions calculated at $\tau_{B_c} = 0.55$ ps

Mode	Γ, 10^{-15} GeV	Br, %
$\eta_c e^+\nu_e$	11 ± 1	0.9 ± 0.1
$\eta_c \tau^+\nu_\tau$	3.3 ± 0.9	0.27 ± 0.07
$J/\psi e^+\nu_e$	28 ± 5	2.5 ± 0.5
$J/\psi \tau^+\nu_\tau$	7 ± 2	0.60 ± 0.15

$$\mathrm{Br}[B_c^+ \longrightarrow \eta_c + \text{light hadrons}] = (4.0 \pm 0.5)\%. \quad (90)$$

Neglecting the decays $\bar{b} \longrightarrow \bar{c}c\bar{s}$, which are suppressed by both the small phase space and the negative Pauli interference of decay product with the charmed quark in the initial state [8], we evaluate the branching fraction of beauty decays in the total width of B_c as

$$\mathrm{Br}[B_c^+ \longrightarrow \bar{c}c + X] = (23 \pm 5)\%,$$

which is in agreement with the estimates in other approaches [6, 8], where this value is equal to 25%.

5. CONCLUSIONS

We have calculated the semileptonic decays of B_c meson in the framework of sum rules in QCD and NRQCD. We have extended the previous evaluations in QCD to the case of massive leptons: the complete set of double spectral densities in the bare-quark-loop approximation have been presented. The analysis in the sum-rule schemes of density moments and Borel transform has been performed, and consistent results have been obtained.

We have taken into account the gluon-condensate contribution for the form factors of semileptonic transitions between the heavy quarkonia in the Borel transform sum rules of QCD, wherein the analytic expressions for the case of three nonzero masses of quarks have been presented.

We have considered the soft limit on the form factors in NRQCD at a recoil momentum close to zero, which has allowed one to derive the generalized relations due to the spin symmetry of the effective Lagrangian. The relations have shown good agreement with the numerical estimates in full QCD, which means that the corrections in both the relative velocities of heavy quarks inside the quarkonia and the inverse heavy-quark masses are small within the accuracy of the method. Next, we have presented the analytic results on the gluon-condensate term in the NRQCD sum rules within the moments scheme.

In both the QCD and NRQCD sum rules, the account of the gluon condensate has allowed one to enforce the reliability of predictions, since the region of physical stability for the form factors evaluated was significantly expanded in comparison with the leading-order calculations of bare-quark-loop contribution.

Next, we have investigated the role played by the Coulomb α_s/v corrections for the semileptonic transitions between the heavy quarkonia. We have shown that, as in the case of two-point sum rules, the three-point spectral densities are enhanced due to the Coulomb renormalization of quark–meson vertices.

The complete analysis shows that the numerical estimates of various branching fractions,

$$\mathrm{Br}[B_c^+ \longrightarrow J/\psi l^+ \nu_l] = (2.5 \pm 0.5)\%,$$

$$\mathrm{Br}[B_c^+ \longrightarrow \bar{c}c + X] = (23 \pm 5)\%,$$

agree with the results obtained in the framework of potential models and OPE in NRQCD. More detailed results are presented in tables.

Thus, we draw the conclusion that at present the theoretical predictions on the semileptonic decays of B_c meson give consistent and reliable results.

ACKNOWLEDGMENTS

We are grateful to Prof. A. Wagner and the members of the DESY Theory Group for their kind hospitality during the visit to DESY, where this article was written, and to Prof. S.S. Gershtein for discussions. We also thank Prof. A. Ali for reading this manuscript and for enlightening comments.

This work was supported in part by the Russian Foundation for Basic Research (RFBR), project nos. 99-02-16558 and 00-15-96575. The work of A.I. Onishchenko was supported in part by grants from the International Center for Fundamental Physics in Moscow and the International Science Foundation and by a joint grant (no. 95I1300) from INTAS and RFBR.

APPENDIX A

Semileptonic Decay Width

In this Appendix, we present the derivation of exclusive semileptonic widths for the B_c-meson decays into the J/ψ and η_c mesons with allowance for lepton masses.

The exclusive semileptonic width Γ_{SL} for the decay $B_c \longrightarrow J/\psi(\eta_c) l \bar{\nu}_l$, where $l = e$, μ, or τ, can be written down in the form [28]

$$\Gamma_{\mathrm{SL}} = \frac{1}{(2\pi)^3}\frac{G_{\mathrm{F}}^2 |V_{bc}|^2}{M_{B_c}}\int d^4q \int d\tau_l L^{\alpha\beta} W_{\alpha\beta}, \qquad (A.1)$$

where $d^4q = 2\pi|\mathbf{q}|dq^2 dq_0$, $d\tau_l = |\mathbf{p}_l| d\Omega_l/(16\pi^2\sqrt{q^2})$ is the leptonic-pair phase space, $d\Omega_l$ is the solid angle of charged lepton l, $|\mathbf{p}_l| = \sqrt{q^2}\,\Phi_l/2$ is its momentum in the dilepton center-of-mass system, and $\Phi_l \equiv \sqrt{1 - 2\lambda_+ + \lambda_-^2}$, with $\lambda_\pm \equiv (m_l^2 \pm m_{\nu_l}^2)/q^2$. The tensors $L^{\alpha\beta}$ and $W_{\alpha\beta}$ in (A.1) are given by

$$L^{\alpha\beta} = \frac{1}{4}\sum_{\text{spins}} (\bar{l} O^\alpha \nu_l)(\bar{\nu}_l O^\beta l)$$
$$= 2[p_l^\alpha p_{\nu_l}^\beta + p_l^\beta p_{\nu_l}^\alpha - g^{\alpha\beta}(p_l \cdot p_{\nu_l}) + i\epsilon^{\alpha\beta\gamma\delta} p_{l\gamma} p_{\nu_l\delta}], \qquad (A.2)$$

$$W_{\alpha\beta} = \int \frac{d^3\mathbf{p}_2}{2E_2}\delta^4(p_1 - p_2 - q)\tilde{W}_{\alpha\beta}$$
$$= \theta(E_2)\delta(M_1^2 - 2M_1 \cdot q_0 + q^2 - M_2^2)\tilde{W}_{\alpha\beta}\big|_{p_2 = p_1 - q}, \qquad (A.3)$$

where

$$\tilde{W}_{\alpha\beta} = (f_+(t)(p_1 + p_2)_\alpha + f_-(t)q_\alpha) \times (f_+(t)(p_1 + p_2)_\beta + f_-(t)q_\beta) \qquad (A.4)$$

for the pseudoscalar particle in the final state, and

$$\tilde{W}_{\alpha\beta} = -(iF_0^4 g_{\alpha e} + iF_+^A p_{1e}(p_1 + p_2)_\alpha + iF_-^A p_{1e} q_\alpha$$
$$- F_V \epsilon_{\alpha eij}(p_1 + p_2)^i q^j)(iF_0^A + iF_+^A p_{1k}(p_1 + p_2)_\beta \qquad (A.5)$$
$$+ iF_-^A p_{1k} q_\beta + F_V \epsilon_{\beta kmn}(p_1 + p_2)^m q^n)\left(\sum_{\text{polarizations}} \epsilon^e \epsilon^{*k}\right)$$

for the vector meson in the final state with the polarization ϵ_μ, where

$$\sum_{\text{polarizations}} \epsilon^e \epsilon^{*k} = \frac{p_2^e p_2^k}{M_2^2} - g^{ek}, \qquad (A.6)$$

and M_2 is the mass of final-state meson (J/ψ or η_c).

The integral over the leptonic phase space in (A.1) is given by

$$\int d\tau_l L^{\alpha\beta} = \frac{1}{4\pi}\frac{|\mathbf{p}_l|}{\sqrt{q^2}}\langle L^{\alpha\beta}\rangle, \qquad (A.7)$$

with

$$\langle L^{\alpha\beta}\rangle = \frac{1}{4\pi}\int d\Omega_l L^{\alpha\beta}$$
$$= \frac{2}{3}\left\{(1 + \lambda_1)(q^\alpha q^\beta - g^{\alpha\beta} q^2) + \frac{3}{2}\lambda_2 g^{\alpha\beta} q^2\right\}, \qquad (A.8)$$

where $\lambda_1 \equiv \lambda_+ - 2\lambda_-^2$ and $\lambda_2 \equiv \lambda_+ - \lambda_-^2$. Introducing the dimensionless kinematical variable $t \equiv q^2/m_b^2$ and integrating with respect to q_0, the semileptonic width takes the following form:

$$\Gamma_{\mathrm{SL}} = \frac{1}{64\pi^3}\frac{G_{\mathrm{F}}^2 |V_{bc}|^2 m_b^2}{M_1^2} \times \int_{t_{\min}}^{t_{\max}} dt \Phi_l(t)|\mathbf{q}|\langle L^{\alpha\beta}\rangle \tilde{W}_{\alpha\beta}, \qquad (A.9)$$

where

$$|\mathbf{q}| = \frac{1}{2M_1}\sqrt{(M_1^2 + m_b^2 t - M_2^2)^2 - 4m_b^2 M_1^2 t}.$$

In (A.9), the limits of integration are given by $t_{\min} = \frac{m_l^2}{m_b^2}$ and $t_{\max} = \frac{1}{m_b^2}(M_1 - M_2)^2$.

Calculation of $\langle L^{\alpha\beta}\rangle \tilde{W}_{\alpha\beta}$ yields the expressions

$$\begin{aligned}\langle L^{\alpha\beta}\rangle \tilde{W}_{\alpha\beta} &= \frac{1}{3}\{3t^2 f_-^2(t)\lambda_2 m_b^4 + 6t f_-(t) f_+(t)(M_1^2 - M_2^2)\lambda_2 m_b^2 \\ &+ f_+^2(t)[t^2(2\lambda_1 - 3\lambda_2 + 2)m_b^4 - 2t(M_1^2 + M_2^2)(2\lambda_1 \\ &- 3\lambda_2 + 2)m_b^2 + 2(M_1^2 - M_2^2)^2(\lambda_1 + 1)]\}\end{aligned}$$

for the pseudoscalar meson in the final state, and

$$\begin{aligned}\langle L^{\alpha\beta}\rangle \tilde{W}_{\alpha\beta} &= \frac{1}{12M_2}\{2[t^2(\lambda_1 + 1)m_b^4 - 2t((1 + \lambda_1)M_1^2 \\ &- 5(1 + \lambda_1)M_2^2 + 9M_2^2\lambda_2)m_b^2 + (M_1^2 - M_2^2)^2(1 \\ &+ \lambda_1)](F_0^A)^2 - 2[t^2 m_b^4 - 2t(M_1^2 + M_2^2)m_b^2 \\ &+ (M_1^2 - M_2^2)^2][F_+^A(2(1 + \lambda_1)tm_b^2 - 3t\lambda_2 m_b^2 \\ &- 2(1 + \lambda_1)M_1^2 + 2(1 + \lambda_1)M_2^2) - 3tF_-^A m_b^2\lambda_2]F_0^A \\ &+ (t^2 m_b^4 - 2t(M_1^2 + M_2^2)m_b^2 + (M_1^2 - M_2^2)^2) \\ &\times [(2t^2 m_b^4 + 2t^2\lambda_1 m_b^4 - 3t^2\lambda_2 m_b^4 - 4(1 + \lambda_1)tM_1^2 m_b^2 \\ &- 4(1 + \lambda_1)tM_2^2 m_b^2 + 6tM_1^2\lambda_2 m_b^2 + 6tM_2^2\lambda_2 m_b^2 \\ &+ 2(1 + \lambda_1)M_1^4 + 2(1 + \lambda_1)M_2^4 - 4(1 + \lambda_1)M_1^2 M_2^2) \\ &\times (F_+^A)^2 + 6tF_-^A F_+^A\lambda_2 m_b^2(M_1^2 - M_2^2) + tm_b^2(3t(F_-^A)^2 \\ &\times \lambda_2 m_b^2 + 16(1 + \lambda_1)(F_V)^2 M_2^2 - 24\lambda_2 M_2^2(F_V)^2)]\}\end{aligned}$$

for the vector meson in the final state.

APPENDIX B

Gluon-Condensate Contribution to QCD Sum Rules

In this appendix, we illustrate the kind of expressions that arise for the gluon-condensate contribution to the form factors $F^i(t)$ in the framework of Borel transformed three-point sum rules in the case of the $f_1(t) = f_+(t) + f_-(t)$ form factor.

Following the algorithm described in Subsection 2.3, for $\Pi_1^{\langle G^2\rangle}$, we have the expression

$$\begin{aligned}\Pi_1^{\langle G^2\rangle} &= C_1^{(-1,-2)}U_0(-1,-2) + C_1^{(-1,-1)}U_0(-1,-1) \\ &+ \sum_{i=-4}^{0} C_1^{(0,i)}U_0(0,i) + \sum_{i=-5}^{-1} C_1^{(1,i)}U_0(1,i) \\ &+ \sum_{i=-6}^{0} C_1^{(2,i)}U_0(2,i) + \sum_{i=-6}^{0} C_1^{(3,i)}U_0(3,i),\end{aligned} \tag{B.1}$$

where

$$C_1^{(-1,-2)} = -\frac{M_{bc}^2 + M_{cc}^2}{12M_{bc}^2}, \tag{B.2}$$

$$C_1^{(-1,-1)} = -\frac{1}{12M_{bc}^2}, \tag{B.3}$$

$$\begin{aligned}C_1^{(0,-4)} &= \frac{1}{48M_{bc}^6 M_{cc}^4}(M_{bc}^{10}(6m_2^2 + m_3^2) + 8m_2^2 M_{bc}^8 M_{cc}^2 \\ &+ (-5m_1^2 + 5m_2^2 + m_3^2)M_{bc}^6 M_{cc}^4 + (-7m_1^2 + 3m_2^2 \\ &+ 2m_1(m_2 - m_3))M_{bc}^4 M_{cc}^6 - 4m_1^2 M_{bc}^2 M_{cc}^8 - 2m_1^2 M_{cc}^{10}),\end{aligned} \tag{B.4}$$

$$\begin{aligned}C_1^{(0,-3)} &= \frac{1}{48M_{bc}^6 M_{cc}^4}((m_1^2 - 2m_1m_3 - 2m_3^2)M_{cc}^8 \\ &+ (6m_2^2 + 4M_{cc}^2)M_{bc}^8 - (2m_1^2 + 2m_2^2 + 6m_2m_3 + 2m_3^2 \\ &+ 2m_1(-5m_2 + m_3) - 11M_{cc}^2 - 2Q^2)M_{bc}^6 M_{cc}^2 \\ &+ (m_1^2 - m_2^2 + 2m_1(m_2 - 5m_3) - 2m_2m_3 + 2m_3^2 \\ &+ 5M_{cc}^2 + Q^2)M_{bc}^4 M_{cc}^6 + (-7m_1^2 + 4m_1m_2 - 2m_2^2 \\ &- 10m_1m_3 - 8m_2m_3 + 2m_3^2 + 12M_{cc}^2 + 2Q^2)M_{bc}^4 M_{cc}^4),\end{aligned} \tag{B.5}$$

$$\begin{aligned}C_1^{(0,-2)} &= \frac{1}{48M_{bc}^6 M_{cc}^4}((3m_1^2 - 2m_1m_3 - 2m_3^2)M_{cc}^6 \\ &+ (m_2^2 - 5m_3^2 + 9M_{cc}^2)M_{bc}^6 + (-4m_1^2 - 7m_2^2 \\ &+ 2m_1(6m_2 - 5m_3) - 8m_2m_3 - 13m_3^2 + 16M_{cc}^2 \\ &+ 4Q^2)M_{bc}^4 M_{cc}^2 - (5m_1^2 - 4m_1(m_2 - 4m_3) \\ &+ 2(m_2^2 + 2m_2m_3 + m_3^2 - M_{cc}^2 - Q^2)M_{bc}^2 M_{cc}^4),\end{aligned} \tag{B.6}$$

$$\begin{aligned}C_1^{(0,-1)} &= \frac{1}{48M_{bc}^6 M_{cc}^4}(-2m_3^2 M_{cc}^4 + (-6m_3^2 + 5M_{cc}^2)M_{bc}^4 \\ &+ (-m_1^2 + 2m_1m_2 - m_2^2 + 4m_2m_3 \\ &- 16m_3^2 + M_{cc}^2 + Q^2)M_{bc}^2 M_{cc}^2),\end{aligned} \tag{B.7}$$

$$C_1^{(0,0)} = \frac{m_3^2(M_{bc}^2 + M_{cc}^2)}{48M_{bc}^6 M_{cc}^4}, \tag{B.8}$$

$$C_1^{(1,-5)} = -\frac{1}{48M_{bc}^8 M_{cc}^6}(m_2^2 M_{bc}^4 - m_1^2 M_{cc}^4)$$
$$\times((5m_2^2 + m_3^2)M_{bc}^8 - m_3^2 M_{bc}^6 M_{cc}^2$$
$$-(4m_1^2 + 3m_2^2)M_{bc}^4 M_{cc}^4 + 2m_1(m_2 - m_3)M_{bc}^2 M_{cc}^6$$
$$+ 2m_1^2 M_{cc}^8), \tag{B.9}$$

$$C_1^{(1,-4)} = \frac{1}{48M_{bc}^8 M_{cc}^6}(m_1^2(3m_1^2 + 2m_1m_3 + 6m_3^2)M_{cc}^{10}$$
$$+(-2m_2^4 - 7m_2^2M_{cc}^2 + m_3^2M_{cc}^2)M_{bc}^{10} + (8m_2^4 + 4m_2^3m_3$$
$$+3m_2^2m_3^2 + 2m_2m_3^3 + m_1^2(4m_2^2 + m_3^2) - 2m_1(4m_2^3$$
$$-3m_2^2m_3 + m_2m_3^2 - m_3^3) - 11m_2^2M_{cc}^2 - 3m_3^2M_{cc}^2$$
$$-4m_2^2Q^2 - m_3^2Q^2)M_{bc}^8M_{cc}^2 - (3m_1^4 + 6m_2^2m_3^2$$
$$+m_1^3(-6m_2 + 4m_3) + 2m_1(m_2^2m_3 + 2m_2M_{cc}^2$$
$$-2m_3M_{cc}^2) + m_1^2(10m_2^2 + 2m_2m_3 + 2m_3^2 - 8M_{cc}^2$$
$$-3Q^2))M_{bc}^4M_{cc}^6 + (4m_1m_2^2m_3 + m_1^2(9m_2^2 + 16M_{cc}^2)$$
$$+m_2^2(2m_2^2 + 4m_2M_{cc} - 3m_2m_3 - 4m_3^2 - M_{cc}^2 - 2Q^2))$$
$$\times M_{bc}^6M_{cc}^4 - m_1(6m_1^3 + 4m_1^2m_3 + 2m_3^2(-m_2 + m_3)$$
$$+m_1(m_2^2 + 2m_2m_3 - 4m_3^2 + 5M_{cc}^2 - Q^2))M_{bc}^2M_{cc}^8), \tag{B.10}$$

$$C_1^{(1,-3)} = \frac{1}{48M_{bc}^8 M_{cc}^6}(2m_3(m_1^3 + 5m_1^2m_3 + 2m_3^3)M_{cc}^8$$
$$+(m_3^4 + m_2^2(9m_3^2 - 4M_{cc}^2) + 8m_2m_3M_{cc}^2 - 3m_3^2M_{cc}^2$$
$$-11M_{cc}^4)M_{bc}^8 + (2m_2^4 + 10m_2^2m_3^2 + m_3^4 + 7m_2^2M_{cc}^2$$
$$+18m_2m_3M_{cc}^2 + 2m_3^2M_{cc}^2 - 20M_{cc}^4 - 4m_1(m_2 - m_3)$$
$$\times(m_2^2 + 2M_{cc}^2) + m_1^2(2m_2^2 + 5M_{cc}^2) - 2m_2^2Q^2$$
$$-5M_{cc}^2Q^2)M_{bc}^6M_{cc}^2 + (-7m_2^2m_3^2 - 4m_3^4$$
$$+4m_2^2M_{cc}^2 + 10m_2m_3M_{cc}^2 - 7M_{cc}^4 + 2m_1^2(2m_2m_3$$
$$-m_3^2 + 5M_{cc}^2) + m_1(6m_2^3 - 6m_3^3 - 2m_2^2m_3 + 4m_2m_3^2$$
$$+4m_2M_{cc}^2 + 10m_3M_{cc}^2) + 2m_3^2Q^2 - 4M_{cc}^2Q^2)M_{bc}^2M_{cc}^6$$
$$+(m_1^4 - 2m_1^3(m_2 - 4m_3) + 10m_3^2M_{cc}^2 + 2m_1m_3(m_2^2$$
$$+m_2m_3 + m_3^2 - M_{cc}^2 - Q^2) + m_1^2(m_2^2$$
$$+2m_2m_3 + 7M_{cc}^2 - Q^2)M_{cc}^8), \tag{B.11}$$

$$C_1^{(1,-2)} = \frac{1}{48M_{bc}^8 M_{cc}^6}(m_3^2(3m_1^2 - 2m_1m_3 + 6m_3^2)M_{cc}^6$$
$$+(14m_2m_3M_{cc}^2 + (16m_3^2 - 13M_{cc}^2)M_{cc}^2$$
$$+m_2^2(4m_3^2 + M_{cc}^2))M_{bc}^6 + (-5m_2^2m_3^2 - 2m_2m_3^3$$
$$-2m_3^4 + 4m_2^2M_{cc}^2 + 8m_2m_3M_{cc}^2 + 32m_3^2M_{cc}^2 - 8M_{cc}^4$$
$$+m_1^2(-3m_3^2 + 4M_{cc}^2) + 2m_1(3m_2m_3^2 - 2m_3^3$$
$$-2m_2M_{cc}^2 + 6m_3M_{cc}^2) + 3m_3^2Q^2 - 4M_{cc}^2Q^2)M_{bc}^4M_{cc}^2$$
$$-(2m_1^3m_3 + m_1^2(-4m_2m_3 + 4m_3^2 + M_{cc}^2)$$
$$+m_3^2(m_2^2 + 2m_2m_3 + 4m_3^2 - 7M_{cc}^2 - Q^2)$$
$$+2m_1m_3(m_2^2 - m_2m_3 + 3m_3^2 - 2M_{cc}^2 - Q^2))M_{bc}^2M_{cc}^4), \tag{B.12}$$

$$C_1^{(1,-1)} = -\frac{1}{48M_{bc}^8 M_{cc}^6}(2m_1m_3^3M_{cc}^4 + (4m_3^4$$
$$-17m_3^2M_{cc}^2 + M_{cc}^4)M_{bc}^4 + 2m_3^2(m_1^2 - 2m_1m_2$$
$$+m_2^2 + 2m_1m_3 + 4m_3^2 - 6M_{cc}^2 - Q^2)), \tag{B.13}$$

$$C_1^{(2,-6)} = \frac{(M_{bc}^2 - M_{cc}^2)(m_2^2M_{bc}^4 - m_1^2M_{cc}^4)^3}{96M_{bc}^{10}M_{cc}^8}, \tag{B.14}$$

$$C_1^{(2,-5)} = -\frac{1}{96M_{bc}^8 M_{cc}^6}(m_2^2M_{bc}^4 - m_1^2M_{cc}^4)$$
$$\times((m_2^2 + 2m_3^2)M_{bc}^6 + 7m_1^2M_{bc}^2M_{cc}^4 + m_2^2(m_1^2$$
$$-2m_1m_2 + m_2^2 + 2m_1m_3 + 2m_2m_3 + 3M_{cc}^2$$
$$-Q^2)M_{bc}^4 - m_1^2(m_1^2 - 2m_1m_2 + m_2^2 + 2m_1m_3$$
$$+2m_2m_3 + 7M_{cc}^2 - Q^2)M_{cc}^4), \tag{B.15}$$

$$C_1^{(2,-4)} = \frac{1}{96M_{bc}^{10}M_{cc}^8}(-3m_1^4m_3^2M_{cc}^{10} + m_1^3(6m_2M_{bc}^2$$
$$-6m_3M_{bc}^2 + m_1m_3^2 - 2m_1M_{cc}^2 - 4m_3M_{cc}^2)M_{bc}^2M_{cc}^8$$
$$-(12m_2^3m_3M_{cc}^2 + 4m_2m_3^3M_{cc}^2 - 12m_2^2M_{cc}^4 - 4m_3^2M_{cc}^4$$
$$+m_2^4(3m_3^2 + 4M_{cc}^2))M_{bc}^{10} + 2m_1(-3m_2^3M_{bc}^2$$
$$+4m_1m_2m_3M_{cc}^2 - 8m_1M_{cc}^4 + m_2^2(3m_3M_{bc}^2 - m_1m_3^2$$
$$+3m_1M_{cc}^2 + 2m_3M_{cc}^2))M_{bc}^6M_{cc}^4 + 2m_1^2(-4m_2(m_1$$
$$-2m_3)M_{cc}^2 + m_2^2(m_3^2 + 3M_{cc}^2) + (3m_1^2 + 6m_1m_3$$
$$+2M_{cc}^2 - 3Q^2)M_{cc}^2)M_{bc}^4M_{cc}^6 + m_2^2(m_2^2(m_3^2 - 4M_{cc}^2)$$
$$\tag{B.16}$$

$$+4m_2(m_1-4m_3)M_{cc}^2+2(-2m_1^2-4m_1m_3+3M_{cc}^2+2Q^2)M_{cc}^2)M_{bc}^8M_{cc}^2),$$

$$C_1^{(2,-3)}=\frac{1}{48M_{bc}^8M_{cc}^6}(m_1(9m_3M_{bc}^2-m_1m_3^2+m_2(-9M_{bc}^2-4m_1m_3+4m_3^2)+4m_1M_{cc}^2)M_{bc}^2M_{cc}^4-(2m_2^3m_3+9m_2^2m_3^2+m_3^4+10m_2m_3M_{cc}^2-10M_{cc}^4)M_{bc}^6+(m_2^4m_3^2+2m_2^3m_3^3-3m_2^2m_3^2M_{cc}^2-3m_2^2M_{cc}^4-14m_2m_3M_{cc}^4+9M_{cc}^6+m_1^2(m_2^2m_3^2+2m_3^2M_{cc}^2-3M_{cc}^4)+2m_1(-m_2^3m_3^2+m_2^2m_3^3+m_2^2m_3M_{cc}^2-2m_2m_3^2M_{cc}^2+m_2M_{cc}^4-3m_3M_{cc}^4)-m_2^2m_3^2Q^2-2m_3^2M_{cc}^2Q^2+3M_{cc}^4Q^2)M_{bc}^4+m_1(m_1^3m_3^2+3(m_2-m_3)m_3^2M_{bc}^2+m_1^2(3m_2M_{bc}^2-3m_3M_{bc}^2-2m_2m_3^2+2m_3^3-2m_3M_{cc}^2)+m_1m_3^2(m_2^2+2m_2m_3-3M_{cc}^2-Q^2))M_{cc}^4),$$ (B.17)

$$C_1^{(2,-2)}=\frac{1}{96M_{bc}^{10}M_{cc}^8}(3m_1^2m_3^4M_{cc}^6+m_1m_3^2M_{bc}^2M_{cc}^4(6m_2M_{bc}^2-6m_3M_{bc}^2+m_1m_3^2-2m_1M_{cc}^2+4m_3M_{cc}^2)+M_{bc}^6(3m_2^2m_3^4+8m_2m_3(m_3^2-M_{cc}^2)M_{cc}^2+4M_{cc}^4(-11m_3^2+2M_{cc}^2))+M_{bc}^4m_3M_{cc}^2(-8m_2(m_1-2m_3)m_3M_{cc}^2+m_2^2(m_3^3+6m_3M_{cc}^2)-2M_{cc}^2(-3m_1^2m_3-6m_1m_3^2+2m_1M_{cc}^2+20m_3M_{cc}^2+3m_3Q^2))),$$ (B.18)

$$C_1^{(2,-1)}=\frac{1}{96M_{bc}^8M_{cc}^6}m_3^2(M_{bc}^2(4m_2m_3+15m_3^2-16M_{cc}^2)+m_3(-m_1^2m_3+2m_1(m_2m_3-m_3^2+2M_{cc}^2)+m_3(-m_2^2-2m_2m_3+13M_{cc}^2+Q^2))),$$ (B.19)

$$C_1^{(2,0)}=-\frac{m_3^4(M_{bc}^2(m_3^2-4M_{cc}^2)+m_3^2M_{cc}^2)}{96M_{bc}^{10}M_{cc}^8},$$ (B.20)

$$C_1^{(3,-6)}=\frac{(M_{bc}^4m_2^2-m_1^2M_{cc}^4)^3}{96M_{bc}^{10}M_{cc}^8},$$ (B.21)

$$C_1^{(3,-5)}=\frac{1}{96M_{bc}^8M_{cc}^8}(M_{bc}^4m_2^2-m_1^2M_{cc}^4)\times(M_{bc}^4m_2^2(2m_2m_3+M_{cc}^2)-m_1^2M_{cc}^4(2m_2m_3+7M_{cc}^2)),$$ (B.22)

$$C_1^{(3,-4)}=-\frac{1}{96M_{bc}^{10}M_{cc}^8}(-3m_1^4m_3^2M_{cc}^8+M_{bc}^8m_2^2(m_2^2m_3^2-8m_2m_3M_{cc}+2M_{cc}^4)+2M_{bc}^4m_1^2M_{cc}^4(m_2^2m_3^2+6m_2m_3M_{cc}^2+3M_{cc}^4)),$$ (B.23)

$$C_1^{(3,-3)}=\frac{1}{48M_{bc}^8M_{cc}^8}(m_1^2m_3^2M_{cc}^4(-2m_2m_3+M_{cc}^2)+M_{bc}^4(-2m_2^3m_3^3+2m_2^2m_3^2M_{cc}^2+6m_2m_3M_{cc}^4-3M_{cc}^6)),$$ (B.24)

$$C_1^{(3,-2)}=-\frac{m_3^2(3m_1^2m_3^2M_{cc}^4+M_{bc}^4(m_2^2m_3^2+12m_2m_3M_{cc}^2-18M_{cc}^4))}{96M_{bc}^{10}M_{cc}^8},$$ (B.25)

$$C_1^{(3,-1)}=\frac{m_3^4(2m_2M-3m_2^2-9M_{cc}^2)}{96M_{bc}^8M_{cc}^8},$$ (B.26)

$$C_1^{(3,0)}=\frac{m_3^6}{96M_{bc}^{10}M_{cc}^8}.$$ (B.27)

For functions $U_0(a, b)$, we have the expressions

$$U_0(a,b)=\sum_{n=1+b}^{1+a+b}2C_{n-b-1}^a\exp[-B_0]\times(M_{bc}^2+M_{cc}^2)^{a+b+1-n}\left(\frac{B_{-1}}{B_1}\right)^{n/2}K_{-n}[2\sqrt{B_{-1}B_1}]$$

for $a \geq 0$. Here, $K_n[z]$ is the modified Bessel function of the second order. In the case of $U_0(-1, -2)$ and $U_0(-1, -1)$, we have failed to obtain exact analytic expressions, so we present their analytic approximations:

$$U_0(-1,-2)=\frac{\exp[-B_0]}{2v^3B_{-1}B_1}\left\{2\exp\left[-\sqrt{\frac{B_{-1}}{B_1}}\right]B_1v^2+2\exp[-B_{-1}^{1/2}B_1^{3/2}]\sqrt{B_{-1}B_1}v^2+\exp[-B_{-1}^{1/2}B_1^{3/2}]\times B_{-1}^{3/2}B_1^{1/2}(2+vB_1)v-2v^2B_{-1}B_1^2\times\left(\exp\left[\frac{B_{-1}}{v}\right]\Gamma\left(0,\frac{B_{-1}}{v}+\sqrt{\frac{B_{-1}}{B_1}}\right)+\Gamma(0,B_{-1}^{1/2}B_1^{3/2})\right)\right.$$

$$- 2\nu B_{-1}B_1\left(\exp\left[\frac{B_{-1}}{\nu}\right]\Gamma\left(0, \frac{B_{-1}}{\nu} + \sqrt{\frac{B_{-1}}{B_1}}\right)\right. \quad \text{(B.28)}$$

$$\left. + \Gamma(0, B_{-1}^{1/2}B_1^{3/2}) - \exp[\nu B_1]\Gamma(0, B_{-1}^{1/2}B_1^{3/2} + \nu B_1)\right)$$

$$- \nu^2 B_{-1}\exp[B_{-1}^{1/2}B_1^{3/2}] - B_{-1}^2 B_1(\nu^2 B_1^2\Gamma(0, B_{-1}^{1/2}B_1^{3/2})$$

$$+ 2\nu B_1\Gamma(0, B_{-1}^{1/2}B_1^{3/2}) + 2\Gamma(0, B_{-1}^{1/2}B_1^{3/2})$$

$$\left. - 2\exp[\nu B_1]\Gamma(0, B_{-1}^{1/2}B_1^{3/2} + \nu B_1))\right\},$$

$$U_0(-1,-1) = \frac{-\exp[B_0]}{\nu^2}\left\{\left(\exp\frac{B_{-1}}{\nu}\Gamma\left(0, \frac{B_{-1}}{\nu} + \sqrt{\frac{B_{-1}}{B_1}}\right)\right.\right.$$

$$+ \Gamma(0, B_{-1}^{1/2}B_1^{3/2}) - \exp(\nu B_1)\Gamma(0, B_{-1}^{1/2}B_1^{3/2} + \nu B_1)$$

$$\left. + \nu\left(\exp\frac{B_{-1}}{\nu}\Gamma\left(0, \frac{B_{-1}}{\nu} + \sqrt{\frac{B_{-1}}{B_1}}\right) - \Gamma\left(0, \sqrt{\frac{B_{-1}}{B_1}}\right)\right)B_1\right) \quad \text{(B.29)}$$

$$- \sqrt{\frac{B_{-1}}{B_1}}\nu\exp[-B_{-1}^{1/2}B_1^{3/2}] + B_{-1}(\nu B_1\Gamma(0, B_{-1}^{1/2}B_1^{3/2})$$

$$\left.\left. + \Gamma(0, B_{-1}^{1/2}B_1^{3/2}) - \exp[\nu B_1]\Gamma(0, B_{-1}^{1/2}B_1^{3/2} + \nu B_1))\right\},\right.$$

where $\nu = M_{bc}^2 + M_{cc}^2$ and $\Gamma(a, z)$ is the incomplete gamma function, which is given by the integral $\Gamma(a, z) = \int_z^\infty t^{a-1}e^{-t}dt$.

REFERENCES

1. CDF Collab. (F. Abe *et al.*), Phys. Rev. Lett. **81**, 2432 (1998); Phys. Rev. D **59**, 112004 (1998).
2. E. Eichten and C. Quigg, Phys. Rev. D **49**, 5845 (1994).
3. S. S. Gershtein *et al.*, Phys. Rev. D **51**, 3613 (1995).
4. E. Braaten, S. Fleming, and T. Ch. Yuan, Annu. Rev. Nucl. Part. Sci. **46**, 197 (1996).
5. C.-H. Chang and Y.-Q. Chen, Phys. Rev. D **46**, 3845 (1992); **50**, 6013 (1994); E. Braaten, K. Cheung, and T. C. Yuan, Phys. Rev. D **48**, 4230 (1993); V. V. Kiselev, A. K. Likhoded, and M. V. Shevlyagin, Z. Phys. C **63**, 77 (1994); T. C. Yuan, Phys. Rev. D **50**, 5664 (1994); K. Cheung and T. C. Yuan, Phys. Rev. D **53**, 3591 (1996); A. V. Berezhnoy, A. K. Likhoded, and M. V. Shevlyagin, Phys. Lett. B **342**, 351 (1995); K. Kolodziej, A. Leike, and R. Rückl, Phys. Lett. B **348**, 219 (1995); A. V. Berezhnoy, V. V. Kiselev, and A. K. Likhoded, Phys. Lett. B **381**, 341 (1996); A. V. Berezhnoy, V. V. Kiselev, and A. K. Likhoded, Z. Phys. A **356**, 89 (1996); A. V. Berezhnoy, A. K. Likhoded, and M. V. Shevlyagin, Yad. Fiz. **58**, 730 (1995) [Phys. At. Nucl. **58**, 672 (1995)]; A. V. Berezhnoy, A. K. Likhoded, and O. P. Yuschenko, Yad. Fiz. **59**, 742 (1996) [Phys. At. Nucl. **59**, 709 (1996)]; C.-H. Chang *et al.*, Phys. Lett. B **364**, 78 (1995); K. Kolodziej, A. Leike, and R. Rückl, Phys. Lett. B **355**, 337 (1995); A. V. Berezhnoy, V. V. Kiselev, and A. K. Likhoded, Z. Phys. A **356**, 79 (1996); A. V. Berezhnoy, V. V. Kiselev, A. K. Likhoded, and A. I. Onishchenko, Yad. Fiz. **60**, 1889 (1997) [Phys. At. Nucl. **60**, 1729 (1997)].
6. V. V. Kiselev, Mod. Phys. Lett. A **10**, 1049 (1995); V. V. Kiselev, Int. J. Mod. Phys. A **9**, 4987 (1994); V. V. Kiselev, A. K. Likhoded, and A. V. Tkabladze, Yad. Fiz. **56** (5), 128 (1993) [Phys. At. Nucl. **56**, 643 (1993)]; V. V. Kiselev and A. V. Tkabladze, Yad. Fiz. **48**, 536 (1988) [Sov. J. Nucl. Phys. **48**, 341 (1988)]; G. R. Dzhibuti and Sh. M. Esakiya, Yad. Fiz. **50**, 1065 (1989) [Sov. J. Nucl. Phys. **50**, 664 (1989)]; Yad. Fiz. **51**, 1681 (1990) [Sov. J. Nucl. Phys. **51**, 1061 (1990)]; C.-H. Chang and Y.-Q. Chen, Phys. Rev. D **49**, 3399 (1994); M. Lusignoli and M. Masetti, Z. Phys. C **51**, 549 (1991); V. V. Kiselev, Phys. Lett. B **372**, 326 (1996); Preprint No. 96-41 (Institute for High Energy Physics, Protvino, 1996); hep-ph/9605451; A. Yu. Anisimov, P. Yu. Kulikov, I. M. Narodetsky, and K. A. Ter-Martirosian, Preprint No. APCTP-98-21, 1998; hep-ph/9809249; A. Yu. Anisimov *et al.*, Phys. Lett. B **452**, 452 (1999).
7. G. T. Bodwin, E. Braaten, and G. P. Lepage, Phys. Rev. D **51**, 1125 (1995); T. Mannel and G. A. Schuller, Z. Phys. C **67**, 159 (1995).
8. M. Beneke and G. Buchalla, Phys. Rev. D **53**, 4991 (1996); I. Bigi, Phys. Lett. B **371**, 105 (1996).
9. M. A. Shifman, A. I. Vainshtein, and V. I. Zakharov, Nucl. Phys. B **147**, 385 (1979).
10. L. J. Reinders, H. R. Rubinstein, and S. Yazaki, Phys. Rep. **127**, 1 (1985).
11. P. Colangelo, G. Nardulli, and N. Paver, Z. Phys. C **57**, 43 (1993).
12. E. Bagan *et al.*, Z. Phys. C **64**, 57 (1994).
13. V. V. Kiselev and A. V. Tkabladze, Phys. Rev. D **48**, 5208 (1993).
14. E. Jenkins, M. Luke, A. V. Manohar, and M. J. Savage, Nucl. Phys. B **390**, 463 (1993).
15. S. S. Gershtein, V. V. Kiselev, A. K. Likhoded, *et al.*, Talk given at 4th International Workshop on Progress in Heavy Quark Physics, Rostock, Germany, 1997: IHEP 98-22; hep-ph/9803433; S. S. Gershtein, V. V. Kiselev, A. K. Likhoded, and A. V. Tkabladze, Usp. Fiz. Nauk **165**, 3 (1995) [Phys. Usp. **38**, 1 (1995)].
16. R. E. Cutkosky, J. Math. Phys. **1**, 429 (1960).
17. P. Ball, V. M. Braun, and H. G. Dosch, Phys. Rev. D **44**, 3567 (1991).
18. P. Ball, Phys. Rev. D **48**, 3190 (1993).
19. V. A. Novikov *et al.*, Phys. Rep. **41**, 1 (1978).
20. J. Schwinger, Phys. Rev. **82**, 664 (1951); J. Schwinger, *Particles, Sources and Fields* (Addison-Wesley, Reading, 1973), Vols. 1, 2.
21. S. S. Grigorian, Preprint No. 88-7 (Institute for High Energy Physics, Protvino, 1988).
22. S. Narison, Phys. Lett. B **210**, 238 (1988); V. V. Kiselev and A. V. Tkabladze, Yad. Fiz. **50**, 1714 (1989) [Sov. J. Nucl. Phys. **50**, 1063 (1989)]; T. M. Aliev and O. Yilmaz, Nuovo Cimento A **105**, 827 (1992); S. Reinshagen and R. Rückl, Preprints CERN-TH.6879/93, MPI-Ph/93-88, 1993; M. Chabab, Phys. Lett. B **325**, 205 (1994); V. V. Ki-

selev, Int. J. Mod. Phys. A **11**, 3689 (1996); Nucl. Phys. B **406**, 340 (1993).

23. V. A. Fock, Sov. Phys. Usp. **12**, 404 (1937); V. A. Fock, *Works on Quantum Field Theory* (Leningr. Gos. Univ., Leningrad, 1957), p. 150.
24. See the paper by C.-H. Chang and Y.-Q. Chen in [6].
25. R. Shankar, Phys. Rev. D **15**, 755 (1977); R. G. Moorhose, M. R. Pennington, and G. G. Ross, Nucl. Phys. B **124**, 285 (1977); K. G. Chetyrkin and N. V. Krasnikov, Nucl. Phys. B **119**, 174 (1977); K. G. Chetyrkin, N. V. Krasnikov, and A. N. Tavkhelidze, Phys. Lett. B **76B**, 83 (1978); N. V. Krasnikov, A. A. Pivovarov, and N. N. Tavkhelidze, Z. Phys. C **19**, 301 (1983); N. V. Krasnikov and A. A. Pivovarov, Phys. Lett. B **112B**, 397 (1982); A. L. Kataev, N. V. Krasnikov, and A. A. Pivovarov, Phys. Lett. B **123B**, 93 (1983); S. G. Gorishny, A. L. Kataev, and S. A. Larin, Phys. Lett. B **135B**, 457 (1984); E. G. Floratos, S. Narison, and E. de Rafael, Nucl. Phys. B **155**, 115 (1979); R. A. Bertlmann, G. Launer, and E. de Rafael, Nucl. Phys. B **250**, 61 (1985).
26. P. A. Baikov, K. G. Chetyrkin, V. A. Ilin, *et al.*, Phys. Lett. B **263**, 481 (1991); D. J. Broadhurst, P. A. Baikov, V. A. Iliyn, *et al.*, Phys. Lett. B **329**, 103 (1994).
27. M. Dugan and B. Grinstein, Phys. Lett. B **255**, 583 (1991); M. A. Shifman, Nucl. Phys. B **388**, 346 (1992); B. Blok and M. Shifman, Nucl. Phys. B **389**, 534 (1993).
28. I. I. Bigi, N. G. Uraltsev, and A. I. Vainshtein, Phys. Lett. B **247**, 293 (1992); I. I. Bigi, M. A. Shifman, N. G. Uraltsev, and A. I. Vainshtein, Phys. Rev. Lett. **71**, 496 (1993); Int. J. Mod. Phys. A **9**, 2467 (1994); A. V. Manohar and M. B. Wise, Phys. Rev. D **49**, 1310 (1994); B. Block, L. Koyrach, M. A. Shifman, and A. I. Vainshtein, Phys. Rev. D **49**, 3356 (1994); T. Mannel, Nucl. Phys. B **413**, 396 (1994).

Physics of Atomic Nuclei, Vol. 63, No. 12, 2000, pp. 2145–2156. From Yadernaya Fizika, Vol. 63, No. 12, 2000, pp. 2241–2252.

ELEMENTARY PARTICLES AND FIELDS
Theory

Light-Front Quark Model and Analysis of the Spectrum of Photons from Inclusive $B \longrightarrow X_s\gamma$ Decays*

P. Yu. Kulikov and I. M. Narodetskiĭ

Institute of Theoretical and Experimental Physics, Bol'shaya Cheremushkinskaya ul. 25, Moscow, 117259 Russia

Received January 21, 2000

Abstract—The electroweak-decay width $\Gamma(B \longrightarrow X_s\gamma)$ is investigated in a light-front (LF) constituent quark model. A new partonlike formula is derived that establishes a simple relation between $\Gamma(B \longrightarrow X_s\gamma)$ and the $b \longrightarrow s\gamma$ decay width. A treatment of the b quark as an on-mass-shell particle and the inclusion of effects that arise from the transverse motion of the b quark in the B meson are basic features of this approach. Adopting different b-quark LF distribution functions, both phenomenological ones and those that are derived from constituent quark models, and neglecting perturbative corrections, we compute the photon energy spectra and the moments of the shape function. It is shown that the LF approach can be matched completely with a heavy-quark expansion (HQE), provided that the constituent b-quark mass is redefined in a way similar to that used in HQE to define the pole mass of the b quark. In this way, the correction to first order in $1/m_b$ can be eliminated from the total width in agreement with the general statement of HQE. We also show that the photon energy spectra calculated in the LF approach agree well with those obtained in the model of Altarelli *et al.*, provided that the same distribution function is used as an input in both cases. Despite the simplicity of the model, our results are in fairly good agreement both with HQE predictions and with available experimental data. © *2000 MAIK "Nauka/Interperiodica".*

1. INTRODUCTION

In the Standard Model (SM), rare B-meson decays are induced by one-loop W-boson- or up-quark-exchange diagrams. In particular, the flavor-changing neutral-current decay $b \longrightarrow s\gamma$ may proceed via the electroweak penguin diagram [1] where the quark emits and reabsorbs a W boson, thus changing the flavor twice, and a photon is radiated from either the W boson or one of the charged-quark lines. Penguin decays became increasingly appreciated in recent years. They give insight into the SM because these decays can be used to determine various elements of the Cabibbo–Kobayashi–Maskawa (CKM) matrix that enter into the SM Lagrangian. In particular, the penguin transitions $b \longrightarrow s\gamma$ and $b \longrightarrow d\gamma$ are sensitive to $|V_{ts}|$ and $|V_{td}|$, respectively, which will be very difficult to measure in top decay. In addition, penguin decays may be quite sensitive to new physics [2].

At present, b-quark decays are under investigation with high-statistics samples from the following three colliders: the CESR at Cornell, which produces $B\bar{B}$ pairs at the $\Upsilon(4S)$ resonance just above the $e^+e^- \longrightarrow B\bar{B}$ threshold; the LEP collider at CERN, which produces $b\bar{b}$ pairs in Z^0 decays; and the Tevatron at FNAL, which produces $b\bar{b}$ pairs in $p\bar{p}$ collisions. For the review of various aspects of these machines, the reader is referred to [3]. Presently, the B-meson factories that are under consideration at SLAC (BaBar) and KEK (Belle) and the upgraded B factory at CESR (CLEO III collaboration) will drastically change the experimental situation concerning rare B decays in the near future. With an expected high luminosity, radiative B decay will no longer be rare events. An experimental error in the inclusive mode $b \longrightarrow s\gamma$ below 10% is possible. This is also a motivation for increasing the accuracy of theoretical predictions.

The existence of loop decays was first confirmed experimentally by an observation of an electromagnetic penguin in the exclusive mode $B \longrightarrow K^*\gamma$ by the CLEO II collaboration [4]. The branching ratio found for the decay $B \longrightarrow X_s\gamma$ by the CLEO collaboration in 1994 is [5]

$$\begin{aligned}&\mathrm{Br}(B \longrightarrow X_s\gamma)\\ &= (2.32 \pm 0.57(\mathrm{stat.}) \pm 0.35(\mathrm{syst.})) \times 10^{-4},\end{aligned} \tag{1}$$

and the very recent preliminary updated data from CLEO yield [6]

$$\begin{aligned}&\mathrm{Br}(B \longrightarrow X_s\gamma)\\ &= (3.15 \pm 0.80(\mathrm{stat.}) \pm 0.72(\mathrm{syst.})) \times 10^{-4}.\end{aligned} \tag{2}$$

The ALEPH measurement of the corresponding branching ratio for B hadrons (mesons and baryons) produced in Z^0 decays yields [7]

$$\mathrm{Br}(B \longrightarrow X_s\gamma) = (3.11 \pm 0.80 \pm 0.72) \times 10^{-4}. \tag{3}$$

* This article was submitted by the authors in English.

Note that the measurements by CLEO and ALEPH were quite different and should not be expected to give identical results. The experimental results presented above were obtained by measuring the high-energy section of the photon spectrum and by extrapolating it to the total rate. This requires the theoretical understanding of the photon spectrum.

Processes of the $B \longrightarrow X_s\gamma$ type are expected to be dominated by the two-body decays such as $B \longrightarrow K^*(892)\gamma$ and by final states with soft-gluon emission that kinematically resemble two-body decays. In this case, the photon energy in the B-meson rest frame has a spectrum that peaks approximately at half of the B-meson mass. In contrast, charged-current-initiated radiative b decays, such as $b \longrightarrow cW^*\gamma$ and $b \longrightarrow uW^*\gamma$ (where W^* is a virtual W boson), produce photons with a spectrum resembling that from bremsstrahlung and, hence, of much lower energy. The experimental results for the inclusive decay rate were obtained by measuring the high-energy section of the photon spectrum,

$$\mathrm{Br}(B \longrightarrow X_s\gamma)(E_\gamma^{\min}) = \int_{E_\gamma^{\min}}^{E_\gamma^{\max}} \frac{d\mathrm{Br}}{dE_\gamma} dE_\gamma, \qquad (4)$$

with the present experimental cut of $E_\gamma^{\min} \sim 2.1$ GeV by CLEO collaboration [8] and the extrapolation to the total rate. To determine the total branching ratio for $B \longrightarrow X_s\gamma$ from such a measurement, one must know theoretically the fraction R of the $B \longrightarrow X_s\gamma$ events with photon energies above $E_\gamma^{\min}$. Therefore, the study of the photon spectrum from the weak radiative decay $B \longrightarrow X_s\gamma$ is important for understanding the possible accuracy that can be attained in the prediction of the total rate in the presence of an experimental cut on the photon energy E_γ. Gross features of the spectrum, such as the average photon energy, may be used to measure the fundamental heavy-quark-expansion (HQE) parameters determining the quark pole mass and the kinetic energy [9, 10].

The experimental results given above have been solely based on the ACM model [11, 12]. This model treats the heavy hadron as a bound state of the heavy quark and a spectator, with a certain momentum distribution $\Phi(p^2)$. The photon energy spectrum from the decay of the B meson at rest is then given by

$$\frac{d\Gamma(B \longrightarrow X_s\gamma)}{dE_\gamma} = \int_0^{p_{\max}} dp\, p^2 \Phi(p^2) \frac{d\Gamma(b \longrightarrow s\gamma)}{dE_\gamma}(E_\gamma, m_f(p^2)). \qquad (5)$$

Here, $d\Gamma(b \longrightarrow s\gamma)/dE_\gamma$ is the photon energy spectrum from the in-flight decay of the b quark with floating mass $m_f(p^2) = M_B - \sqrt{p^2 + m_{\mathrm{sp}}^2}$, where m_{sp} is the mass of the spectator quark, and $p_{\max}$ is the maximally allowed value of p. Distribution $\Phi(p^2)$ is usually assumed to have the Gaussian form determined by a nonperturbative parameter, p_{F},

$$\Phi(p^2) = \frac{4}{\sqrt{\pi} p_{\mathrm{F}}^3} \exp\left(-\frac{p^2}{p_{\mathrm{F}}^2}\right), \qquad (6)$$

with the wave-function normalization

$$\int_0^\infty \Phi(p^2) p^2 dp = 1.$$

Based on calculation of [13] for the photon energy spectrum and adopting the Fermi motion model of [12], CLEO used the value $R = 85$–94% [8] to determine $\mathrm{Br}(B \longrightarrow X_s\gamma)$ from the measured partial branching ratio.

In contrast to the exclusive decays, the inclusive decay modes are theoretically simpler, because no specific model is needed to describe the final hadronic states. Assuming the quark–hadron duality and the fact that the b quark is heavy as compared to the characteristic low-energy scale Λ_{QCD} of the strong interactions, the inclusive $B \longrightarrow X_s\gamma$ decay rate was traditionally calculated in a systematic QCD-based expansion [14] in powers of Λ/m_b:

$$\mathrm{Br}(B \longrightarrow X_s\gamma) = \mathrm{Br}(b \longrightarrow s\gamma) + \mathbb{O}\left(\frac{1}{m_b^2}\right). \qquad (7)$$

This formula is known under the name of HQE. The free quark decay width including the QCD perturbative corrections from the real and virtual gluons emerges as the leading term in this expansion. The nonperturvative corrections are suppressed by the factor Λ^2/m_b^2.[1)] The fact that there are no first-order corrections is based on a particular definition of m_b [16] that can be regarded as a nonperturbative generalization of the pole mass.

In the free-quark approximation neglecting the radiative corrections, the spectrum of photons is a monochromatic line:

$$\frac{d\Gamma(b \longrightarrow s\gamma)}{dE_\gamma} = \Gamma(b \longrightarrow s\gamma)\delta\left(E_\gamma - \frac{m_b}{2}\right). \qquad (8)$$

For energy E_γ not too close to its maximal value, the photon spectrum $d\Gamma(b \longrightarrow s\gamma)/dE_\gamma$ has a perturbative expansion in the strong interaction coupling constant α_s, and the first (α_s independent) term of the expansion

[1)] In addition, the nonperturbative contributions from $c\bar{c}$ intermediate states were found which scale like $1/m_c^2$ and enlarge the branching ratio by ≈3% [15].

is given by (8). This expansion is known at the order of α_s [10]. The $\alpha_s^2\beta_0$ contributions, where $\beta_0 = 11 - 2n_f/3$ is the one-loop β function, have been recently computed [17]. However, near the end point, the energy released for a light quark system is not of the order $\mathbb{O}(m_b)$ but of the order of $\bar{\Lambda} = M_B - m_b \sim \Lambda_{\rm QCD}$. Thus, the expansion parameter is no longer $1/m_b^2$, but rather $1/m_b\bar{\Lambda} \sim \mathbb{O}$ (1 GeV), and the operator product expansion breaks down. The divergent series in the effective theory corresponding to the nonperturbative effect due to the soft interactions of the b quark with the light constituents have to be resumed. This so-called "Fermi motion" can be included in the heavy-quark expansion by summing an infinite set of leading-twist contributions into a shape function $F(x)$ [18], where a scaling variable is defined as

$$x = \frac{2E_\gamma - m_b}{\bar{\Lambda}}, \quad \text{with} \quad \bar{\Lambda} = M_B - m_b + \mathbb{O}(1/m_b). \tag{9}$$

This is quite similar to what happens for the structure function in deep-inelastic scattering in the region, where the Bjorken variable $x_{\rm B} \longrightarrow 1$. A model-independent determination of the shape function in the effective theory is not possible at present; however, it may be possible to solve this problem by using lattice QCD [19]. An ansatz for the shape function constrained by the information on its few first moments has been recently used in [20] including the next-to-leading (NLO) perturbative QCD corrections.

In this paper, we consider the light-front (LF) approach to calculation for the photon energy spectra from inclusive $B \longrightarrow X_s\gamma$ decay. This approach was originally suggested for the inclusive semileptonic transitions [21–24] and has been recently refined in [25]. The corresponding ansatz from [25] reduces to a specific choice of the input LF distribution function $|\psi(\xi, p_\perp^2)|^2$, which represents the probability that the b quark carries a LF fraction ξ and a transverse momentum squared $p_\perp^2 = |\mathbf{p}_\perp|^2$. As a result, a new partonlike formula for the width of inclusive semileptonic $b \longrightarrow c, u$ decays has been derived [25], which is similar to the formula obtained by Bjorken *et al.* [26] in the case of infinitely heavy b and c quarks.

Some of the dynamical features of this model get obscured by the integration over the lepton energy. They are better manifested in the spectrum of the photons in the radiative $B \longrightarrow X_s\gamma$ transitions. In this paper, we extend the work of [25] to compute the nonperturbative corrections to the photon spectrum and the inclusive rate $B \longrightarrow X_s\gamma$.[2)] We attempt to take into account the B-meson wave function effects on the photon energy and the invariant mass distributions of the hadrons recoiling against the photon. We will compare the photon spectra $d\Gamma/dE_\gamma$ calculated in the LF and ACM approaches and will show that the discrepancy between the two is very small.

The paper is organized as follows. In Section 2, we collect the main facts concerning the calculation of the $\mathrm{Br}(b \longrightarrow s\gamma)$ in QCD. In Section 3, we derive the partonic formula for the photon energy spectra from $B \longrightarrow X_s\gamma$. In Section 4, we consider the ansätze for the distribution function $f(x, p_\perp^2)$. In Section 5, we discuss the choice of the b-quark mass in our approach. The numerical results for the photon energy spectra and the moments are presented in Section 6, where we also present the comparison of our results with those obtained in the ACM model. In Section 7, we discuss the invariant mass spectra and the calculation of $\mathrm{Br}(B \longrightarrow K^*\gamma)$ in our approach. Finally, Section 8 contains our conclusions.

2. PERTURBATIVE TREATMENT OF $\Gamma(b \longrightarrow s\gamma)$ IN QCD

In this section, we just briefly recall the main points of the calculation of the $b \longrightarrow s\gamma$ decay in QCD (for general discussion see [28]).

At high energy scale $\mu \sim M_W$, the $b \longrightarrow s\gamma$ quark decay is governed by an electroweak penguin diagram. To obtain an effective low-energy theory relevant for scales $\mu \sim m_b$, heavy degrees of freedom related to W and Z^0 bosons and t quark must be integrated out to obtain an effective coupling for the pointlike interactions of initial and final particles. After the integration, the effective Lagrangian for $b \longrightarrow s$ penguin decays takes the form

$$\mathcal{L}_{\rm eff} = \frac{4G_{\rm F}}{\sqrt{2}} V_{tb}V_{ts}^* \sum_1^{10} C_i(\mu)O_i(\mu), \tag{10}$$

where O_i are current–current ($i = 1, 2$), gluonic penguin ($i = 3, \ldots, 6$), and electroweak penguin ($i = 7, \ldots, 10$) operators. In (10), $G_{\rm F}$ is the Fermi constant and V_{ij} are the elements of the CKM matrix. The effects of the heavy degrees of freedom are hidden in the effective gauge coupling constants, running quark masses, and the Wilson coefficients C_i describing the effective strength of the local operators O_i in (10). The coefficients C_i at $\mu \sim M_W$ serve in leading order as initial conditions to the renormalization group evolution from μ_W down to μ_b. An explicit form of the operators O_i in (10) can be found, e.g., in [28]. The operators relevant for leading approximation are the electroweak penguin

$$O_{7\gamma} = \frac{e}{32\pi^2}\bar{m}_b(\mu)\bar{s}_\alpha\sigma_{\mu\nu}(1+\gamma_5)b_\alpha F_{\mu\nu} \tag{11}$$

and the gluonic penguin

$$O_{8G} = \frac{g_s}{32\pi^2}\bar{m}_b(\mu)\bar{s}_\alpha\sigma_{\mu\nu}(1+\gamma_5)T^a_{\alpha\beta}b_\beta G^a_{\mu\nu}, \tag{12}$$

[2)] A preview of this work can be found in [27].

where e and g_s are the electromagnetic and strong coupling constants, and $F_{\mu\nu}$ and $G^a_{\mu\nu}$ denote the electromagnetic and the gluonic field strength tensor, respectively. The contribution of other operators O_3, …, O_6 can be neglected to an excellent approximation. Wilson coefficients of these operators originate from operator mixing only and are numerically small.

Technically, the calculations are performed at a high-energy scale $\mu_W \sim \mathcal{O}(M_W)$ at which the full theory is matched with the effective five-quark theory and then is evolved to a low-energy scale $\mu \sim \mu_b$ using renormalization group equations. At $\mu_W \sim M_W$, the contribution of the matrix element of $O_{7\gamma}$ to the $b \longrightarrow s\gamma$ decay width has the form[3)]

$$\Gamma_0 = \Gamma(b \longrightarrow s\gamma) = \frac{\alpha G_F^2}{32\pi^4}|V_{tb}V_{ts}|^2 c_{7\gamma}^2(\mu_W)\overline{m}_b(\mu_W)^2 m_b^3. \quad (13)$$

The factor m_b^3 in (13) originates from the two–body phase space. In HQE, m_b is usually associated with the b-quark pole mass $m_{b,\,\mathrm{pole}}$. For $\mu_b \sim m_b$, one has

$$m_b^2(\mu_b) = m_{b,\,\mathrm{pole}}^2\left(1 - \frac{8}{3}\frac{\alpha_s(\mu_b)}{\pi}\right). \quad (14)$$

This difference does not enter the leading approximation. The basic functions $c_{7\gamma}(M_W) = C_{7\gamma}^{(0)}(x_t)$ and $c_{8G}(M_W) = C_{8G}^{(0)}(x_t)$, $x_t = m_t^2/M_W^2$ were calculated by many authors, in particular, by Inami and Lim [29]. Their explicit form is

$$C_{7\gamma}^{(0)}(M_W) = x_t^2\frac{3x_t - 2}{4(x_t-1)^4}\ln x_t + \frac{8x_t^3 + 5x_t^2 - 7x_t}{24(1-x_t)^3}, \quad (15)$$

$$C_{8G}^{(0)}(M_W) = \frac{-3x_t^2}{4(x-1)^4}\ln x_t + \frac{-x_t^3 + 5x_t^2 + 2x_t}{8(x_t-1)^3}. \quad (16)$$

For $m_t = 170$ GeV, $C_{7\gamma}^{(0)} = -0.193$, and $C_{8G}^{(0)} = -0.096$.

Expressions (15) and (16) do not include QCD correction. The evolution of (10) down to μ_b mixes the operators

$$C_i(\mu_b) = \sum_j U(\mu_b, \mu_W)C_j(M_W). \quad (17)$$

In particular, $\Gamma(b \longrightarrow s\gamma)$ in the leading order is again given by (13) in which $c_{7\gamma}(\mu_b)$ is replaced by "effective coefficient" $C_{7\gamma}^{(0)\mathrm{eff}}(\mu_b)$ [30]

$$c_{7\gamma}(\mu_b) \longrightarrow C_{7\gamma}^{(0)\mathrm{eff}}(\mu_b) = \eta^{16/25}C_{7\gamma}^{(0)}(M_W) + \frac{8}{3}(\eta^{14/25} - \eta^{16/25})C_{8G}^{(0)}(M_W) + C_2^{(0)}(M_W)\sum_1^8 h_i\eta^{a_i} \quad (18)$$

with $C_2^{(0)}(M_W) = 1$ and $\eta = \alpha(\mu_W)/\alpha(\mu_b)$. The "magic numbers" h_i and a_i are given, e.g., in Table 23 from [28]. The scale μ_b enters into (18) only through η.

For $m_t = 170$ GeV, $C_{8G}^{(0)}(\mu_W) = -0.096$. Then, using

$$\alpha_s(\mu_b) = \frac{\alpha_s(M_Z)}{1 - \beta_0\dfrac{\alpha_s(M_Z)}{2\pi}\ln\dfrac{M_Z}{\mu_b}} \quad (19)$$

with $\mu_b = 5$ GeV and $\alpha_s(M_Z) = 0.118$, one obtains $C_{7\gamma}^{(0)\mathrm{eff}}(\mu_b) = 0.695C_{7\gamma}^{(0)}(\mu_W) + 0.085C_{8G}^{(0)}(\mu_W) - 0.158C_2^{(0)}(\mu_W) = -0.3$. In the absence of QCD corrections, we would have $\eta = 1$ and $C_{7\gamma}^{(0)\mathrm{eff}}(\mu_b) = C_{7\gamma}^{(0)}(\mu_W)$. Therefore, the leading QCD corrections cause the large QCD enhancement of the $B \longrightarrow X_s\gamma$ rate [31].

The predictions for $\mathrm{Br}(B \longrightarrow X_s\gamma)$ are usually obtained by normalizing the result to that for the semileptonic rate, thereby eliminating the uncertainties due to the CKM matrix elements and the factor m_b^5. In the leading approximation, one obtains

$$\frac{\Gamma(B \longrightarrow X_s\gamma)}{\Gamma(B \longrightarrow X_c\bar{\nu}_e)} \approx \frac{\Gamma(b \longrightarrow s\gamma)}{\Gamma(b \longrightarrow c\bar{\nu}_e)} = R_{\mathrm{quark}}, \quad (20)$$

where

$$R_{\mathrm{quark}} = \frac{|V_{ts}^*V_{tb}|^2}{|V_{cb}|^2}\frac{6\alpha_{\mathrm{QED}}}{\pi g(\rho)}|C_{7\gamma}^{(0)\mathrm{eff}}(\mu_b)|^2\left(1 - \frac{\delta_{\mathrm{SL}}}{m_b^2} + \frac{\delta_{\mathrm{RAD}}}{m_b^2}\right), \quad (21)$$

$g(\rho) = 1 - 8\rho + 8\rho^2 - \rho^4 - 12\rho^2\ln\rho$ is the phase space factor in the semileptonic $b \longrightarrow ce\bar{\nu}$ decay, and $\rho = m_{c,\,\mathrm{pole}}^2/m_{b,\,\mathrm{pole}}^2$. The last factor in (21) parametrizes the nonperturbative corrections in HQE to the semileptonic and radiative decay rates [9]

$$\delta_{\mathrm{SL}} = \frac{1}{2}\lambda_1 + \left(\frac{3}{2} - \frac{6(1-\rho)^4}{f(\rho)}\right)\lambda_2, \qquad \delta_{\mathrm{RAD}} = \frac{\lambda_1}{2} - \frac{9\lambda_2}{2}, \quad (22)$$

where λ_1 and λ_2 parametrize the matrix elements of the kinetic and chromomagnetic operators, respectively, which appear in the effective Lagrangian of HQE at the order of $1/m_b$. The value of λ_2 is known from B^*–B

[3)] The strange quark mass will be neglected throughout this paper; it only enters the final results quadratically as m_s^2/m_b^2.

splitting, $\lambda_2 = 0.12$ GeV^2. The value of λ_1 is controversial, fortunately it cancels on the right-hand side of (22). The two nonperturbative corrections in (22) both are of a few percent and tend to cancel each other. Therefore, the total nonperturbative correction in (22) is much smaller than the accuracy of the perturbative calculation of R_{quark}. The final result of the leading-order analysis is [30]

$$\text{Br}(B \longrightarrow X_s\gamma) = (2.8 \pm 0.8) \times 10^{-4}, \quad (23)$$

where uncertainty reflects mainly the scale ambiguity μ_b.

The NLO corrections include the α_s corrections to $C_{7\gamma}^{(0)\text{eff}}$ [32] and the α_s corrections originating from one-loop matrix elements $\langle s\gamma|O_{7\gamma}|b\rangle$ and $\langle s\gamma|O_{8G}|b\rangle$ and two-loop matrix elements $\langle s\gamma|O_i|b\rangle$ of the remaining operators (see Eq. (21) of [32]). A part of NLO corrections originates from the bremsstrahlung corrections. For an updated review of NLO calculation, see [20]. All the theoretical predictions with allowance of the NLO QCD corrections in the SM fall in the range

$$\text{Br}(B \longrightarrow X_s\gamma) = (3.3 \pm 0.3) \times 10^{-4}; \quad (24)$$

i.e., the LO result is shifted by about 20%, and the present theoretical uncertainty is reduced to about 10%. This theoretical result is in good agreement with updated experimental data (2) and (3).

3. THE PARTON FORMULAS

As a preliminary, we briefly discuss a derivation of the inclusive photon energy spectrum for the $B \longrightarrow X_s\gamma$ decays in the context of the LF approach of [25]. Similar to the ACM model, the LF quark model treats the beauty meson as consisting of the heavy b quark plus a spectator quark. Both quarks have fixed masses, m_b and m_{sp}, though. This is at variance with the ACM model that has been introduced in order to avoid the notion of the heavy quark mass at all.

To calculate the $B \longrightarrow X_s\gamma$ decay width, we use the approach of [25] which assumes that the sum over all possible strange final states X_s can be modeled by the decay width of an on-shell b quark into an on-shell c quark weighted with the b-quark distribution function $f(\xi, p_\perp^2)$. Going through the intermediate steps (for the details, see [25]), we obtain the partial decay width of the inclusive $B \longrightarrow X_s\gamma$ decay in the form

$$d\Gamma = 4x_0\Gamma_0 \int \frac{d^2p_\perp d\xi}{\xi} f(\xi, p_\perp^2) d\tau, \quad (25)$$

where

$$x_0 = m_b/M_B. \quad (26)$$

In our phenomenological consideration, we associate m_b with the constituent b-quark mass (see below). The normalization of $f(\xi, p_\perp^2)$ in (25) is as follows:

$$\pi \int_0^1 d\xi \int_0^\infty dp_\perp^2 f(\xi, p_\perp^2) = 1, \quad (27)$$

where the factor $1/\xi$ comes from the normalization of the $B \longrightarrow b\bar{d}$ vertex [33]. The phase space factor $d\tau$ is given by

$$d\tau = \delta[(p_b - q)^2] E_\gamma dE_\gamma. \quad (28)$$

We choose the z axis as being parallel to the 3-vector $\mathbf{q}$, so that $q_+ = 2E_\gamma$, $q_- = 0$, where $q_\pm = q_0 \pm q_z$, then $d\tau$ takes the form

$$d\tau = \delta\left(m_b^2 - \frac{p_\perp^2 + m_b^2}{p_b^+}\right) E_\gamma dE_\gamma. \quad (29)$$

In the first approximation, we neglect $p_\perp^2$ in the argument of the δ function. Then, in terms of the scaling variable

$$y = 2E_\gamma/M_B, \quad (30)$$

the photon spectrum $d\Gamma/dy$ in $B \longrightarrow X_s\gamma$ takes the simple form

$$\frac{1}{\Gamma_0}\frac{d\Gamma(B \longrightarrow X_s\gamma)}{dy} = R_{\text{LF}}(y), \quad (31)$$

where

$$R_{\text{LF}}(y) = \frac{1}{x_0} y \tilde{f}(y), \quad (32)$$

and

$$\tilde{f}(\xi) = \pi \int_0^\infty dp_\perp^2 f(\xi, p_\perp^2). \quad (33)$$

Equivalently, one can write the spectrum in the standard QCD form [34]

$$\frac{1}{\Gamma_0}\frac{d\Gamma}{dE} = \frac{2}{\bar{\Lambda}} F(x), \quad (34)$$

where

$$x = \frac{2E_\gamma - m_b}{\bar{\Lambda}} = \frac{y - x_0}{1 - x_0}, \quad (35)$$

and x_0 is defined by (26). Therefore, the specific choice adopted for $\tilde{f}(\xi)$ corresponds to the following particular form of the QCD shape function

$$F(x) = (\Lambda/M_B x_0) y \tilde{f}(y). \quad (36)$$

Note that if one uses the infinite momentum frame prescription [21, 22] $p_b = \xi P_B$, i.e., $m_b^2(\xi) = \xi^2 M_B^2$, then one easily derives from (25) and (29) that $d\Gamma \propto E_\gamma^3 \tilde{f}(y) dE_\gamma$ [35].

We take into account now the transverse motion of the b quark, i.e., the term $p_\perp^2$ in (29), to find a little more complicated expression for $R_{\rm LF}(y)$ [25]

$$R_{\rm LF}(y) = 2m_b\pi\int_y^1 f(\xi, p_\perp^{*2})d\xi, \qquad (37)$$

where the integration limits follow from the condition $p_\perp^{*2} \geq 0$, with

$$p_\perp^{*2} = p_\perp^{*2}(\xi, E) = m_b^2(\xi/y - 1). \qquad (38)$$

In this case, the shape of the spectrum is obtained by direct integration of the distribution function $f(\xi, p_\perp^2)$. We will see below that the difference between $R_{\rm LF}(y)$ given by (32) and (37) is very small.

In the free-quark approximation,

$$f(\xi, p_\perp^2) = \delta(\xi - \xi_0)\delta(p_\perp^2), \qquad (39)$$

the total inclusive width $\Gamma(B \longrightarrow X_s\gamma)$ of the B meson is the same as the radiative width $\Gamma(b \longrightarrow s\gamma)$, and the spectrum of photons is monochromatic [see (8)]. Due to the heavy-quark motion, the δ function in (8) is transformed into a finite width peak. This effect is solely responsible for the filling in of the windows between $m_b/2$ and the kinematical boundary in the B-meson decay, $E_{\max} = M_B/2$.[4)] Expressions in (32) and (37) exhibit a pronounced peak, which is rather asymmetric. It is a gratifying feature of the LF model, since it is in qualitative agreement with both findings in QCD and experimental data. The perturbative corrections arising from gluon bremsstrahlung and one-loop effects [13] also lead to a nontrivial photon spectrum at the partonic level. Since our primary object here is to discuss nonperturbative effects due to the Fermi motion, we will implicitly ignore perturbative gluon emission throughout our analysis. In this case, the parton matrix element squared is a constant and can be taken out of the integral in (25).

4. ANSÄTZE FOR THE LF HEAVY-QUARK DISTRIBUTION

Since we do not have an explicit representation for the B-meson Fock expansion in QCD, we shall proceed by making an ansatz for the momentum representation of the wave function. This is a model-dependent enterprise, but it has close equivalence in studies of $B \longrightarrow X_s\gamma$ by using the ACM model. In what follows, we will adopt both a phenomenological LF wave function and the LF functions corresponding to the various equal time (ET) quark-model wave functions. As to the phenomenological ansatz, we use a model first proposed in [36] and also employed in [22, 24] to take into account the bound state effects in B-meson decays. It is written in the Lorentz-invariant form

$$\psi(|\mathbf{p}|) = \mathcal{N}\exp\left(-\frac{\lambda}{2}v_b v_{\rm sp}\right) = \mathcal{N}\exp\left(-\frac{\lambda}{2}\frac{\varepsilon_p}{m_{\rm sp}}\right), \quad (40)$$

where v_b and $v_{\rm sp}$ are the 4-velocities of the b quark and the spectator quark, respectively, and $\varepsilon_p = \sqrt{|\mathbf{p}|^2 + m_{\rm sp}^2}$ is the energy of the spectator. We use the normalization condition

$$\int_0^\infty p^2 dp \frac{\psi^2(|\mathbf{p}|)}{2\varepsilon_p} = 1; \qquad (41)$$

in this case,

$$\mathcal{N}^2 = \frac{2\lambda}{m_{\rm sp}^2 K_1(\lambda)}, \qquad (42)$$

where $K_1(\lambda)$ is the Macdonald function. The function $\Phi(p^2) = \psi^2(|\mathbf{p}|)/2\varepsilon_p$ represents a momentum distribution of the spectator quark in the rest frame of B meson. We go over from ET to LF momenta by leaving the transverse momenta unchanged and letting

$$p_{iz} = \frac{1}{2}(p_i^+ - p_i^-) = \frac{1}{2}\left(p_i^+ - \frac{p_{i\perp}^2 + m_i^2}{p_i^+}\right) \qquad (43)$$

for both the b quark ($i = b$) and the spectator quark ($i =$ sp). The longitudinal LF momentum fractions ξ_i are defined as

$$\xi_{\rm sp} = \frac{p_{\rm sp}^+}{P_B^+}, \quad \xi_b = \frac{p_b^+}{P_B^+}, \qquad (44)$$

with $p_b^+ + p_{\rm sp}^+ = P_B^+$. In the rest frame of B meson, $P_B^+ = M_B$. Then, for the distribution function

$$f(\xi, p_\perp^2) = \frac{1}{8\pi}\frac{\psi^2(\xi, p_\perp^2)}{1 - \xi} \qquad (45)$$

($\xi = \xi_b$), normalized according to (27), one obtains

$$f(\xi, p_\perp^2) = \frac{\mathcal{N}^2}{8\pi(1-\xi)} \times \exp\left[-\frac{\lambda}{2}\left(\frac{1-\xi}{\xi_0} + \frac{\xi_0}{1-\xi}\left(1 + \frac{p_\perp^2}{m_{\rm sp}^2}\right)\right)\right], \qquad (46)$$

where $\xi_0 = m_{\rm sp}/M_B$. Function (46) is sharply peaked at $p_\perp^2 = 0$, $\xi = \xi_0$. In what follows, we will refer to the LF wave function of (46) as the case A.

[4)] The true endpoint is actually located at $[M_B^2 - (m_K + m_\pi)^2]/2M_B \approx 2.60$ GeV, i.e., slightly below $M_B/2 \approx 2.64$ GeV.

Table 1. Values of the parameters c_i (in units of $\mathrm{GeV}^{-3/2}$) and α_i (in units of GeV^{-2}) in (48) for the analytic parametrization of the B-meson wave function corresponding to AL1 and DSR potentials (the wave function is normalized by the condition $\int_0^\infty \psi^2(p)p^2dp = 1$)

Model	α_1	α_2	α_3	α_4	c_1	c_2	c_3	c_4
AL1	4.979	2.184	0.638	0.097	4.845	1.839	0.128	0.097
DSR	5.294	2.022	0.758	0.233	1.448	2.303	0.650	0.067

A priori, there is no relation between the ET momentum distribution $\Phi(p^2)$ of a constituent quark model and LF wave function $\psi(x, p_\perp^2)$. However, the mapping between the variables described above converts a normalized solution of the ET equation of motion into a normalized solution of the different-looking LF equation [37]. Because the ET function depends on the relative momentum, it is more convenient to use the quark–antiquark rest frame instead of the B-meson rest frame. Recall that these two frames are different in the LF formalism. As a result, one obtains the LF wave function in the form

$$\psi(\xi, p_\perp^2) = (\partial p_z/\partial\xi)\Phi(p_\perp^2 + p_z^2(\xi, p_\perp^2)). \quad (47)$$

The explicit form of this function is given by formulas (10) of [24]. It is wave functions made kinematically relativistic in this manner that were used in the recent calculation of the B_c lifetime [38]. We calculate the photon energy spectra using the three representative LF wave functions corresponding to the nonrelativistic ISGW2 [39], AL1 [40], and relativized DSR [41] constituent quark models. The ISGW2 equal-time function corresponds to the Gaussian distribution $\Phi(p^2)$ of (6) conventionally employed in the ACM model with $p_F = 0.43$ GeV. For AL1 and DSR models, we use simple analytic parametrizations of the ET wave functions [42]

$$\psi(p) = \sum c_i \exp(-\alpha_i p^2). \quad (48)$$

The parameters c_i and α_i are listed in Table 1. The main difference between the ET wave functions of these models lies in the behavior at a high value of the internal momentum (for further discussion see [38]). We believe that the spread of results obtained for these distribution functions is a fair representation of model dependence resulting from the inclusion of Fermi motion.

5. CHOICE OF m_b

Having specified the nonperturbative aspects of our calculations, we proceed to present numerical results for the photon spectrum in the $B \longrightarrow X_s\gamma$ decay. In this section, we analyze the sensitivity of the calculated spectra and the energy moments to the choice of the B-meson radial functions. We will calculate the photon energy spectra using both expressions (32) and (37) and using the four distribution functions $f(\xi, p_\perp^2)$ determined in the previous section. In the case A, we take $m_b = 4.8$ GeV, $m_{sp} = 0.3$ GeV, and $\lambda = 2$ as reference values. These values are motivated by a study of the $b \longrightarrow c$ decays [24]. For the models B to D, we use the constituent quark masses listed in Table 2.

The choice of m_b in our approach deserves some comments. The numerical calculations using the constituent b-quark masses show large deviations of the $\Gamma(B \longrightarrow X_s\gamma)$ from the free decay rate $\Gamma_0 \propto m_b^3$ (≈10% for the cases B to D, see Table 2). This points to the appearance of the linear $1/m_b$ corrections to the free quark limit. The reason is that the constituent quark models usually employ the b-quark masses that are 300–400 MeV higher than the pole b-quark mass. This fact seems to be a subtlety in applying the constituent quark model to calculate the nonperturbative corrections to the $B \longrightarrow X_s\gamma$ inclusive rate. To overcome the uncertainties induced by the mass of the constituent b quark, we use a simple phenomenological recipe that considerably improves the situation. Notice that, as in the ACM model [34], $1/m_b$ corrections can be absorbed into the definition of the b-quark mass. We introduce

$$\tilde{m}_b = m_b + \delta m_b \quad (49)$$

by imposing the condition $\bar{y}(\tilde{m}_b) = x_0$, where

$$\bar{y} = \int_0^1 y R_{LF}(y)dy. \quad (50)$$

Table 2. Values of the constituent quark mass m_b and m_{sp} (in GeV) for the models A to D [also indicated are the values of $\tilde{m}_b$ as defined by the HQET condition $\langle x\rangle = 0$); m_b^{ACM} are the average values of the floating mass $m_f(p^2)$]

Model	A	B	C	D
m_b	4.80	5.20	5.227	5.074
m_{sp}	0.30	0.33	0.315	0.221
$\tilde{m}_b$ [a)]	4.76	4.72	4.76	4.68
$\tilde{m}_b$ [b)]	4.73	4.68	4.73	4.60
m_b^{ACM}	4.73	4.68	4.73	4.60

Note: Cases [a)] and [b)] correspond to $R_{LF}(y)$ given by (32) and (37), respectively.

Table 3. Integrated photon spectra R_{LF} and R_{ACM} calculated with the use of (32) (case [a)]) and (37) (case [b)]) for the wave-function models A to D [the integrated spectra R_{ACM} were calculated by using Eq. (55)]

Model	A	B	C	D
$R_{LF}(m_b)$[a)]	0.9	0.9	0.9	0.9
$R_{LF}(m_b)$[b)]	0.973	0.900	0.905	0.899
$R_{LF}(\tilde{m}_b)$[a)]	0.995	0.994	0.995	0.99
$R_{LF}(\tilde{m}_b)$[b)]	0.987	0.986	0.989	0.974
$R_{ACM}(m_b^{ACM})$	1.008	1.005	1.008	1.003

Table 4. Energy moments $\bar{y}^n$, n = 1, 2, 3, and HQE moments $\langle x^2\rangle$ and $\langle x^3\rangle$ for cases A to D [the LF photon energy spectra were calculated by using Eq. (32); the scaling variables x and y are defined in Eqs. (9) and (30), respectively]

Model	A	B	C	D
$\bar{y}(m_b)$	0.889	0.822	0.831	0.823
$\bar{y}(\tilde{m}_b)$	0.897	0.888	0.897	0.877
$\bar{y}^2(m_b)$	0.806	0.744	0.758	0.740
$\bar{y}^2(\tilde{m}_b)$	0.813	0.797	0.812	0.783
$\bar{y}^3(m_b)$	0.733	0.676	0.693	0.670
$\bar{y}^3(\tilde{m}_b)$	0.739	0.718	0.737	0.705
$\langle x^2\rangle$	0.390	0.313	0.316	0.493
$\langle -x^3\rangle$	0.377	0.155	0.195	0.415

Table 5. Energy moments $\bar{y}^n$, n = 1, 2, 3, and HQE moments $\langle x^2\rangle$ and $\langle x^3\rangle$ for cases A to D [the LF photon energy spectra were calculated by using Eq. (37); the scaling variables x and y are defined in Eqs. (9) and (30), respectively]

Model	A	B	C	D
$\bar{y}(m_b)$	0.873	0.806	0.818	0.795
$\bar{y}(\tilde{m}_b)$	0.885	0.873	0.885	0.851
$\bar{y}^2(m_b)$	0.787	0.726	0.742	0.709
$\bar{y}^2(\tilde{m}_b)$	0.798	0.778	0.796	0.751
$\bar{y}^3(m_b)$	0.712	0.655	0.676	0.636
$\bar{y}^3(\tilde{m}_b)$	0.722	0.695	0.718	0.669
$\langle x^2\rangle$	0.378	0.295	0.302	0.456
$\langle -x^3\rangle$	0.348	0.130	0.176	0.348

This condition coincides with that used in HQE to define the pole mass of the b quark. As a result, the correction to first order in $1/m_b$ will be eliminated from the total width in agreement with the general statement of HQE.[5)]

To illustrate our arguments, we consider the exactly solvable case of the photon spectrum of (32) with the distribution function given by (46). In this case, we have

$$\tilde{f}(\xi) = \frac{2}{\lambda\xi_0 K_1(\lambda)}\exp\left[-\frac{\lambda}{2}\left(\frac{\xi_0}{1-\xi}+\frac{1-\xi}{\xi_0}\right)\right], \quad (51)$$

and simple analytic expressions for $R_{LF} = \int_0^1 R_{LF}(y)dy$ and $\bar{y}$ have the form

$$R_{FL} = \frac{1}{x_0}(1-\xi_0\kappa_2),$$
$$\bar{y} = \frac{1}{x_0}(1-2\xi_0\kappa_2+\xi_0^2\kappa_3), \quad (52)$$

where $\kappa_n = K_n(\lambda)/K_1(\lambda)$. The $1/M_B$ correction to R_{LF} can be included into the definition of $\tilde{m}_b$. Indeed, neglecting ξ_0^2 and letting $\tilde{m}_b \approx (1-\xi_0\kappa_2)M_B$, one obtains $R_{LF} = 1 + \mathbb{O}(1/M_B^2)$. The B-meson mass can be eliminated in favor of the b-quark mass, so we have the desired result in the form

$$R_{LF} = 1 + \mathbb{O}(1/m_b^2). \quad (53)$$

For the models B to D, we have no analytic results. However, the numerical effect of introducing $\tilde{m}_b$ is the same (see Table 3). We have calculated numerically the values of $\tilde{m}_b$ in different models using both (32) and (37) for $R_{LF}(y)$. Although $\tilde{m}_b$ depends on the assumed shape of distribution, this dependence is marginal: the uncertainty on $\tilde{m}_b$ is between 4.6 and 4.7 GeV depending on the choice of $f(\xi, p_\perp^2)$ (see Table 2). These values are consistent with the b-quark pole mass $m_{b,\,pole} = 4.8 \pm 0.15$ GeV [43].

6. PHOTON ENERGY SPECTRA AND THE ENERGY MOMENTS

We study first the photon spectra using (32) and (37). Our results for the integrated photon spectra and energy moments are presented in Fig. 1 and in Tables 3–5. The different curves in Fig. 1 correspond to the models A to D. For each case, we show separately the spectra calculated from (32) and (37) by using the corresponding

[5)] In this way, the bound-state effects are largely compensated by the shift in the b-quark mass.

values of $\tilde{m}_b$ and the photon energy spectra calculated in the ACM model (see below). The influence of the various choices of the distribution function and the b-quark mass can be seen from Table 3, where we show both $R_{\rm LF}(m_b)$, $R_{\rm LF}(\tilde{m}_b)$ and analogous quantities $R_{\rm ACM}$ for the ACM model. In Tables 4 and 5, we show the average photon energy $\bar{y}$ normalized to $M_B/2$, and the moments $\bar{y}^2$ and $\bar{y}^3$. We present the results obtained using both (32) (Table 4) and (37) (Table 5). The replacement $m_b \longrightarrow \tilde{m}_b$ modifies the predictions for the total rate and the moments $\bar{y}$ and $\bar{y}^2$ by about 8–9% for the models B–D, while it changes the corresponding quantities by less than 1.5% for the model A. Our final results for the integrated photon spectra $R_{\rm LF}(\tilde{m}_b)$ agree well with the corresponding OPE prediction [9] $R_{\rm OPE} = 1 + \delta_{\rm RAD}$, where $\delta_{\rm RAD}$ has been defined in (22). For $\lambda_1 = -0.3 \pm 0.2$ GeV^2 and $\lambda_2 = 0.12 \pm 0.02$ GeV^2, $R_{\rm OPE}$ changes the free quark result by a few percent, $R_{\rm OPE} = 0.975 \pm 0.005$. Note also that the sensitivity of $R_{\rm LF}$ to the functional form chosen for the distribution function is small. This behavior agrees again with that based on the global quark–hadron duality that ensures insensitivity of even partially integrated quantities to the bound state effects. Note that the effect of the transverse momentum is considerably smaller than the model-dependent uncertainty.

The dependence of the energy moments $\bar{y}^n$ on m_b is rather weak, in contrast to that of the QCD moments of the shape function

$$\langle x^n \rangle = \int\limits_{-2M_B/\bar{\Lambda}}^{1} x^n F(x)\,dx, \qquad (54)$$

which are very sensitive to the difference between M_B and m_b. In particular, change of the b-quark mass from m_b to $\tilde{m}_b$ modifies $\langle x^2 \rangle$ and $\langle x^3 \rangle$ drastically. Note that the resulting values of $\langle x^2 \rangle$ and $\langle x^3 \rangle$ are still considerably model dependent. Our predictions for $\langle x^2 \rangle$ are relatively small, although in agreement (for the model D) with the result of [20] and compatible with the results obtained from the QCD sum rules; $\langle x^2 \rangle \approx 0.5$. This means that the LF ansatz can be made consistent with the QCD description, provided the spectator quark is relativistic. This conclusion agrees with the similar conclusion obtained in the ACM model in [34].

In order to compare our results with those derived in the ACM model, we have calculated the inclusive $B \longrightarrow X_s\gamma$ photon spectra in a simplified ACM model [34] assuming the monochromatic distribution (8) for the free b quark. In this case, one easily obtains

$$\frac{d\Gamma_{\rm ACM}}{dE_\gamma} \sim \Gamma_0 \int\limits_{p_0^2(\varepsilon)}^{\infty} dp^2 \Phi(p^2)\left(m_b^f(p^2)\right)^3, \qquad (55)$$

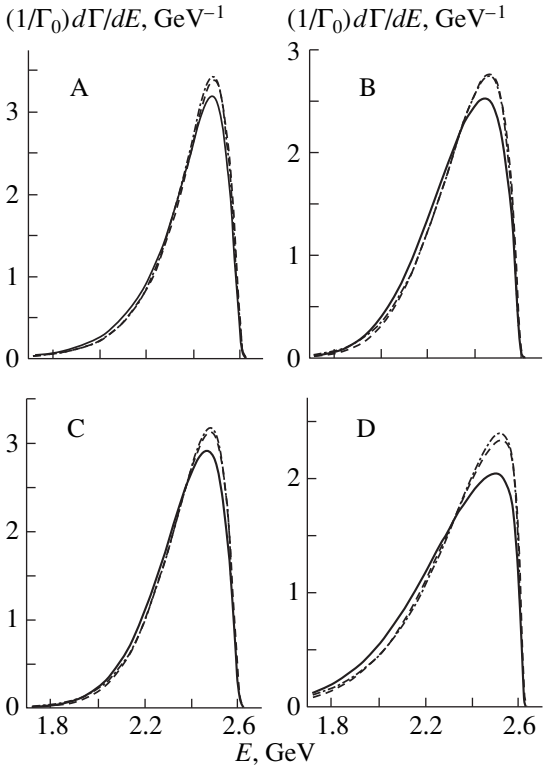

Fig. 1. Theoretical predictions for the photon energy spectrum using the LF quark models described in the text. Each plot shows the spectra calculated by using the b-quark masses $\tilde{m}_b$ from (32) (solid lines) and (37) (dashed lines). The dash-dotted lines show the photon energy spectra calculated in the ACM model. The curves A to D show the results for the corresponding models.

where m_b^f is the floating b-quark mass and

$$p_0^2(\varepsilon) = \frac{1}{4}\left(\frac{m_{\rm sp}^2}{\varepsilon} - \varepsilon\right)^2, \quad \varepsilon = M_B(1-y). \qquad (56)$$

We have used the momentum distributions $\Phi(p^2)$ of the spectator quark for the models A to D. In all cases, we have found that the spectra calculated in ACM and LF parton models are almost identical. This is not surprising because we have checked numerically that the quark masses $\tilde{m}_b$ defined using the LF models practically coincide with the values of the floating b-quark mass m_b^f averaged over the distribution $\Phi(p^2)$ (see Table 2). The integrated energy spectra $R_{\rm ACM}$ for the models A to D are presented in Table 3. They coincide with $R_{\rm LF}$ within a percent accuracy. The energy moments for the ACM model are shown in Table 6.

Although in this paper we do not consider perturbative corrections, it is instructive to compare theoretical predictions for the Doppler shifted spectrum $dB/dE_{\rm lab}$ in the laboratory frame with the CLEO data. To perform a fit to the data, we rebin the boosted photon spectra in the same energy intervals as used by CLEO and,

for each choice of the distribution function, adjust the overall normalization to provide the best fit to the data. The results are reported in Table 7, and the best fits are displayed in Fig. 2. All fits have $\chi^2/n_{\rm dof} \ll 1$, indicating the present accuracy of experiment. Averaging over the models, we obtain

$$\begin{aligned}&\mathrm{Br}(B \longrightarrow X_s\gamma)\\ &= (2.5 \pm 0.5(\mathrm{exp.}) \pm 0.3(\mathrm{model})) \times 10^{-4},\end{aligned} \tag{57}$$

where the last error originates from the model dependence. This result is consistent with both the updated CLEO value (2), and the recent reanalysis [20] $\mathrm{Br}(B \longrightarrow X_s\gamma) = (2.62 \pm 0.60(\mathrm{exp.})^{+0.37}_{-0.30}(\mathrm{theor.})) \times 10^{-4}$ of the GLEO data.

7. INVARIANT-MASS SPECTRUM

In addition to the photon energy spectrum, the invariant hadronic mass distribution in radiative B decays can be studied. The invariant mass M_H of the hadronic final state is related to the scaling variable y by $M_H^2 = M_B^2(1-y)$. Therefore, the theoretical results for the photon spectrum can be translated into predictions for the hadronic mass spectrum. The X_s mass distribution from the reconstruction analysis of CLEO inclusive data shows a clear K^* peak followed by a dip which is expected since the next excited-kaon resonance is $K_1(1270)$. A broad enhancement at and above $K_1(1270)$ is observed; this is also expected since many resonance states exist in this region. The present experimental statistics are insufficient to identify any of the individual resonances beyond $K^*(892)$. Combining the exclusive and inclusive measurements, CLEO determines

$$\begin{aligned}R_{K^*(892)} &= \frac{\mathrm{Br}(B \longrightarrow K^*(892))}{\mathrm{Br}(B \longrightarrow X_s\gamma)}\\ &= (18.1 \pm 6.8)\%.\end{aligned} \tag{58}$$

Figure 3 shows the invariant mass distribution of the hadrons recoiling against the photon for the models A–D. Our predictions for hadronic mass spectra must be understood in the sense of quark–hadron duality. The true hadronic mass spectrum for low $M_H^2 \propto M_{K^*}^2$ has a resonance structure that looks rather different from our predictions. A realistic model for the hadronic mass

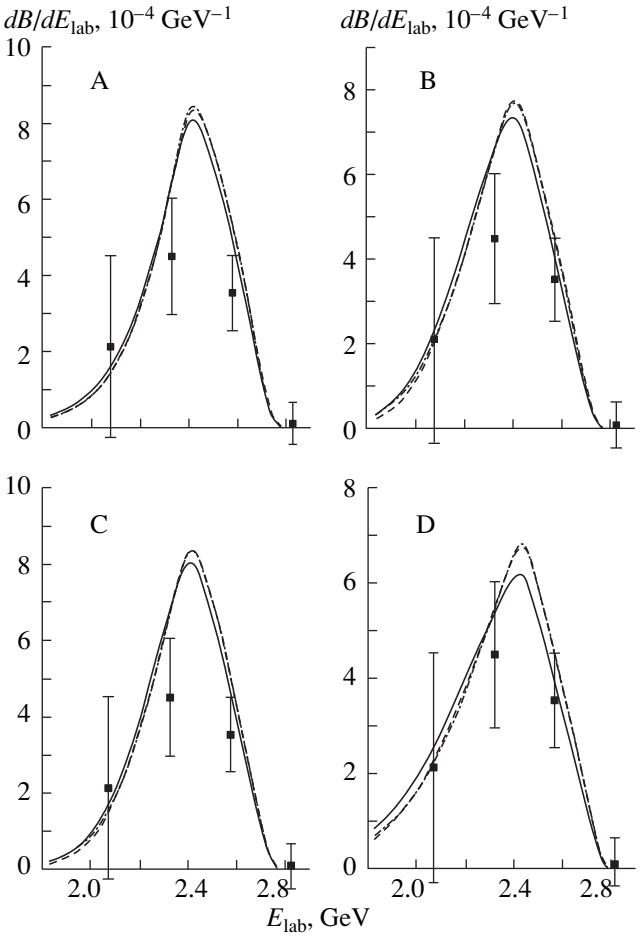

Fig. 2. Theoretical predictions for the photon energy spectrum in the laboratory frame for the different distribution functions $f(\xi, p_\perp^2)$ and the corresponding $\tilde{m}_b$. The notation is the same as in Fig. 1. The experimental data are the CLEO results [46]. Both the left-hand plot and the right-hand plot show the results of the best fit reported in Table 7.

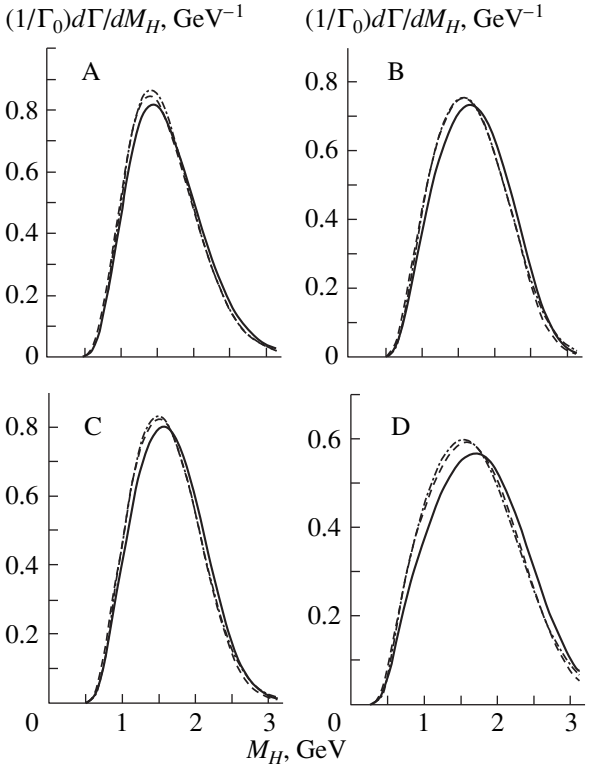

Fig. 3. Comparison of the theoretical predictions for the invariant hadronic mass spectrum for the LF and ACM models. The notation is identical to that in Fig. 1.

Table 6. Energy moments $\bar{y}^n$, $n = 1, 2, 3$, and HQE moments $\langle x^2\rangle$ and $\langle x^3\rangle$ for cases A to D [the photon energy spectra were calculated by using Eq. (55); the scaling variables x and y are defined in Eqs. (9) and (30), respectively]

Model	A	B	C	D
$\bar{y}$	0.903	0.894	0.901	0.883
$\bar{y}^2$	0.817	0.800	0.813	0.786
$\bar{y}^3$	0.743	0.718	0.737	0.706
$\langle x^2\rangle$	0.355	0.308	0.317	0.489
$\langle -x^3\rangle$	0.289	0.141	0.206	0.427

Table 7. Branching ratios $\mathrm{Br}(B \longrightarrow X_s\gamma)$ obtained from a fit to the CLEO data and partial fractions $R_{K^*(892)}$

Model	A	B	C	D
$\Gamma_0/\Gamma_B \times 10^4$	2.54	2.59	2.50	2.91
$R_{K^*(892)}$ [a)]	0.192	0.158	0.174	0.218
$R_{K^*(892)}$ [b)]	0.168	0.131	0.149	0.181

Note: Cases [a)] and [b)] correspond to $R_{\mathrm{LF}}(y)$ given by Eqs. (32) and (37), respectively.

spectrum consists of a single peak located at the mass $K^*(892)$ followed by a continuum (above a threshold value M_{th}) which is given by the inclusive spectrum and is dual to a large number of overlapping resonances. In Table 7, we show the ratios $R_{K^*(892)}$ obtained by the integration of the inclusive spectrum in the range $M_H \le M_{\mathrm{th}}$. The result crucially depends on the choice of M_{th}; we use a value of $M_{\mathrm{th}} = 1.15$ GeV adopted in [20]. Averaging over the different model predictions, we obtain $R_{K^*(892)} = 0.157^{+0.24}_{-0.44}$. This result agrees with both experimental data and theoretical estimates based on QCD sum rules [44] and lattice QCD calculation [45].

8. CONCLUSION

We have derived a new parton formula that establishes a simple relation between the electroweak decay rate $\Gamma(B \longrightarrow X_s\gamma)$ and the rate of free b-quark decay. The main features of our approach are the treatment of the b quark as an on-mass-shell particle and the inclusion of the effects arising from the b-quark transverse motion in the B meson. Formulas (32) and (37) present our main result. Using various b-quark distribution functions, we have calculated the photon energy spectra and the corrections to the free decay rate. We have shown that the decay width has no corrections linear to $1/m_b$ only if it is expressed not in terms of the constituent quark mass, but in terms of a mass $\tilde{m}_b$ which is defined in the way similar to that used in the HQE to define $m_{b,\,\mathrm{pole}}$. In this way, one avoids an otherwise large (and model-dependent) correction of order $1/m_b$, but at the expense of introducing the shift in the constituent quark mass which substantially compensates the bound state effects. A summary of our results presented in Tables 3–5 shows a fairly good agreement with both the QCD results and the available experimental data. We have also found that the photon energy spectra calculated in our LF partonlike approach agree well with the spectra obtained in the ACM model, provided the same ET distribution function $\Phi(p^2)$ is used as input in both cases. Finally, we note that it would be interesting to check whether the effective values of the b-quark mass $\tilde{m}_b$ are approximately the same for different channels ($b \longrightarrow c$ vs. $b \longrightarrow u$ or $b \longrightarrow s$) and for different beauty hadrons. This work is in progress, and the results will be reported elsewhere.

ACKNOWLEDGMENTS

This work was supported in part by the INTAS (grant no. 96-155).

REFERENCES

1. J. Ellis *et al.*, Nucl. Phys. B **131**, 285 (1977); T. Inami and C. S. Lim, Prog. Theor. Phys. **65**, 297 (1981); Erratum: **65**, 1772 (1981); B. A. Campbell and P. J. O'Donnell, Phys. Rev. D **25**, 1989 (1982); N. G. Deshpande and G. Eilam, Phys. Rev. D **26**, 2463 (1982).
2. A. Masiero, in *Proceedings of 8th Symposium on Heavy Flavour, Southampton, UK, 1999*.
3. K. Lingel, T. Skwarnicki, and J. G. Smith, Annu. Rev. Nucl. Part. Sci. **48**, 253 (1998).
4. CLEO Collab. (R. Ammar, S. Ball, P. Barnes, *et al.*), Phys. Rev. Lett. **71**, 674 (1993).
5. CLEO Collab. (M. S. Alam, I. J. Kim, Z. Ling, *et al.*), Phys. Rev. Lett. **74**, 2885 (1995).
6. T. Skwarnicki, Talk presented at XXIX International Conference on High Energy Physics, Vancouver, BC, Canada, 1998, No. 702.
7. ALEPH Collab. (R. Barate *et al.*), Phys. Lett. B **429**, 169 (1998).
8. CLEO Collab. (S. Ahmed *et al.*), hep-ex/9908022.
9. A. F. Falk, M. Luke, and M. Savage, Phys. Rev. D **49**, 3367 (1994).
10. A. Kapustin and Z. Ligeti, Phys. Lett. B **355**, 318 (1995).
11. A. Ali and E. Pietarinen, Nucl. Phys. B **154**, 512 (1979).
12. G. Altarelli, N. Cabibbo, G. Corbo, *et al.*, Nucl. Phys. B **202**, 512 (1982).
13. A. Ali and C. Greub, Z. Phys. C **49**, 431 (1991); **60**, 433 (1993); Phys. Lett. B **259**, 182 (1991); **287**, 191 (1992); **361**, 146 (1995); N. Pott, Phys. Rev. D **54**, 938 (1996).
14. J. Chay, H. Georgy, and B. Grinstein, Phys. Lett. B **247**, 399 (1990); I. I. Bigi, N. G. Uraltsev, and A. I. Vainshtein, Phys. Lett. B **293**, 430 (1992); Erratum: **297**, 477 (1993); I. I. Bigi, M. Shifman, N. G. Uraltsev, and A. I. Vainshtein, Phys. Rev. Lett. **71**, 496 (1993); A. V. Manohar and M. B. Wise, Phys. Rev. D **49**, 1310 (1994).

15. M. B. Voloshin, Phys. Lett. B **397**, 295 (1997); A. Khodjamirian, R. Rückl, G. Stoll, and D. Wyler, Phys. Lett. B **402**, 167 (1997); Z. Ligeti, L. Randall, and M. B. Wise, Phys. Lett. B **402**, 178 (1997); A. K. Grant, A. G. Morgan, S. Nussinov, and R. D. Peccei, Phys. Rev. D **56**, 3151 (1997); G. Buchalla, G. Isidori, and S. J. Rey, Nucl. Phys. B **511**, 594 (1998).
16. A. F. Falk, M. Neubert, and M. Luke, Nucl. Phys. B **388**, 363 (1993); M. Neubert, Phys. Rev. D **46**, 3914 (1992).
17. Z. Ligeti, M. Luke, A. V. Manohar, and M. B. Wise, Phys. Rev. D **60**, 034019 (1999).
18. M. Neubert, Phys. Rev. D **49**, 3392 (1994); **49**, 4623 (1994); T. Mannel and M. Neubert, Phys. Rev. D **50**, 2037 (1994); I. I. Bigi, M. A. Shifman, N. G. Uraltsev, and A. I. Vainshtein, Int. J. Mod. Phys. A **9**, 2467 (1994); R. D. Dikeman, M. A. Shifman, and N. G. Uraltsev, Int. J. Mod. Phys. A **11**, 571 (1996).
19. U. Aglietti *et al.*, Phys. Lett. B **441**, 371 (1998).
20. A. L. Kagan and M. Neubert, Eur. Phys. J. C **7**, 5 (1999).
21. C. H. Jin, M. F. Palmer, and E. A. Paschos, Phys. Lett. B **329**, 364 (1994); C. H. Jin and E. A. Paschos, in *Proceedings of the International Symposium on Heavy Flavor and Electroweak Theory, Beijing, China, 1995*, Ed. by C. H. Chang and C. S. Huang (World Sci., Singapore, 1996), p. 132.
22. V. L. Morgunov and K. A. Ter-Martirosyan, Yad. Fiz. **59**, 1279 (1996) [Phys. At. Nucl. **59**, 1221 (1996)].
23. K. Y. Lee and J. K. Kim, Phys. Lett. B **377**, 153 (1996).
24. I. L. Grach, I. M. Narodetskii, S. Simula, and K. A. Ter-Martirosyan, Nucl. Phys. B **502**, 227 (1997).
25. S. Ya. Kotkovsky, I. M. Narodetskii, S. Simula, and K. A. Ter-Martirosyan, Phys. Rev. D **60**, 114 024 (1999).
26. J. Bjorken, I. Dunietz, and M. Taron, Nucl. Phys. B **371**, 111 (1992).
27. Y.-Y. Keum, P. Yu. Kulikov, I. M. Narodetskii, and H. S. Song, Phys. Lett. B **471**, 72 (1999).
28. A. Buras, hep-ph/9806471.
29. T. Inami and C. S. Lim, Prog. Theor. Phys. **65**, 297 (1981); Erratum: **65**, 1772 (1981).
30. A. J. Buras, M. Misiak, M. Münz, and S. Pokorski, Nucl. Phys. B **431**, 374 (1994).
31. S. Bertolini, F. Borzumati, and A. Masiero, Phys. Rev. Lett. **59**, 180 (1987); N. G. Deshpande, P. Lo, J. Trampetic, *et al.*, Phys. Rev. Lett. **59**, 183 (1987).
32. K. Chetyrkin, M. Misiak, and M. Münz, Phys. Lett. B **400**, 206 (1997); Erratum: **425**, 414 (1998).
33. N. B. Demchuck, I. L. Grach, I. M. Narodetskii, and S. Simula, Phys. At. Nucl. **59**, 2152 (1996).
34. I. Bigi, M. Shifman, N. Uraltsev, and A. Vainshtein, Phys. Lett. B **328**, 431 (1994).
35. C. H. Jin, Eur. Phys. J. C **11**, 335 (1999).
36. A. Dubin and A. Kaidalov, Yad. Fiz. **56** (2), 164 (1993) [Phys. At. Nucl. **56**, 237 (1993)].
37. F. Coester, Prog. Part. Nucl. Phys. **29**, 1 (1992).
38. A. Anisimov, I. M. Narodetskii, C. Semay, and B. Silvestre-Brac, Phys. Lett. B **452**, 129 (1999).
39. D. Scora and N. Isgur, Phys. Rev. D **52**, 2783 (1995).
40. B. Silvestre-Brac and C. Semay, Z. Phys. C **61**, 271 (1994); Few-Body Syst. **20**, 1 (1996).
41. B. Silvestre-Brac and C. Semay, Nucl. Phys. A **618**, 455 (1997).
42. C. Semay and B. Silvestre-Brac, private communication.
43. N. Neubert, Phys. Rep. **245**, 259 (1994).
44. A. Ali, V. M. Braun, and H. Z. Simma, Z. Phys. C **63**, 437 (1994).
45. L. Del Debbio, J. M. Flynn, L. Lellouch, and J. Nieves, Phys. Lett. B **416**, 392 (1998).
46. S. Glenn, quoted in [20].

Physics of Atomic Nuclei, Vol. 63, No. 12, 2000, pp. 2157–2172. From Yadernaya Fizika, Vol. 63, No. 12, 2000, pp. 2253–2268.

ELEMENTARY PARTICLES AND FIELDS
Theory

Nonforward Color-Octet Kernel of the Balitsky–Fadin–Kuraev–Lipatov Equation*

V. S. Fadin and D. A. Gorbachev*****

Budker Institute of Nuclear Physics, Siberian Division, Russian Academy of Sciences, pr. Akademika Lavrentieva 11, Novosibirsk, 630090 Russia, and Novosibirsk State University, Novosibirsk, Russia

Received February 11, 2000

Abstract—The contribution to the kernel of the nonforward Balitsky–Fadin–Kuraev–Lipatov equation from two-gluon production is calculated for the case of the antisymmetric color-octet state of two Reggeized gluons in the t channel. The one-gluon contribution to the kernel in the one-loop approximation is also obtained by using the one-loop expression for the effective vertex of the one-gluon production in Reggeon–Reggeon collisions. An explicit form of the total kernel is presented. *© 2000 MAIK "Nauka/Interperiodica".*

1. INTRODUCTION

The most common basis for describing processes at small values of $x = Q^2/s$ (Q^2 is a typical virtuality and $\sqrt{s}$ is the c. m. s. energy) within perturbative QCD is the Balitsky–Fadin–Kuraev–Lipatov (BFKL) equation [1], originally derived in the leading-logarithm approximation (LLA), which means resummation of all terms of the type $[\alpha_s \ln s]^n$ [$\alpha_s = g^2/(4\pi)$ is the QCD coupling constant]. The calculation of radiative corrections to the kernel of this equation took many years of hard work [2–7]. Recently, the kernel was obtained in the next-to-leading approximation (NLA) [8] for the case of forward scattering—that is, for zero momentum transfer ($t = 0$) and the vacuum quantum numbers in the t channel. In the $\overline{MS}$ renormalization scheme with a reasonable scale setting, corrections appear to be large. At present, this problem is being widely discussed in the literature [9]. In this situation, it is very important to be sure that both the basic hypotheses used and the calculations performed in deriving the equation are correct.

It should be recalled that the derivation of the BFKL equation (in the NLA, as well as in the LLA) is based on one of the remarkable properties of QCD—gluon Reggeization [10], which was proved in the LLA [1, 11]. In the NLA, this property was only checked in the first three orders of perturbation theory [6]. Since gluon Reggeization forms a basis for deriving the BFKL equation, it is clear that more powerful tests are necessary.

As for the calculations of radiative corrections to the kernel, they are very complicated, and only some of them has been independently performed [7] or checked [12]. Therefore, the calculations must be carefully verified.

Both goals—a stringent test of gluon Reggeization and an examination of the calculations—can be solved simultaneously by the check of the bootstrap equations [13, 14] appearing as the requirement of the compatibility of gluon Reggeization with s-channel unitarity. In fact, the BFKL equation is the equation for the Green's function of two Reggeized gluons. In the color-singlet state, these Reggeized gluons create a Pomeron. Self-consistency requires that, in the antisymmetric color-octet state, the two Reggeized gluons reproduce a Reggeized gluon itself (bootstrap condition). The above statements are valid in the NLA, as well as in the LLA. Along with the stringent test of gluon Reggeization, the check of the bootstrap equations provides a global test of the calculations of the NLA kernel, because these equations contain almost all quantities appearing in the calculations.

In the BFKL approach, amplitudes of high-energy processes are expressed in terms of the aforementioned Green's function and impact factors of scattered particles, which are defined by Reggeon–particle scattering amplitudes. The nonforward impact factors for gluon [15] and quark [16] scattering were recently calculated in the NLA, and fulfillment of the bootstrap conditions for them was demonstrated [15–17] for both helicity-conserving and helicity-nonconserving parts, in an arbitrary spacetime dimension $D = 4 + 2\epsilon$.

The quark contribution to the nonforward BFKL kernel was also calculated [18], and fulfillment of the bootstrap conditions for the kernel in the part associated with this contribution was explicitly demonstrated in the NLA [18, 19], in an arbitrary spacetime dimension as well. Only one (but the most complicated) bootstrap condition remains unchecked—for the gluon part of the kernel. In this study, we calculate the gluon contribution to the nonforward color-octet kernel of the BFKL equation.

* This article was submitted by the authors in English.

** e-mail: fadin@imp.nsk.su
*** e-mail: gorbachev@inp.nsk.su

1063-7788/00/6312-2157$20.00 © 2000 MAIK "Nauka/Interperiodica"

The significance of the nonforward octet kernel is not exhausted by the check of the bootstrap condition. The kernel of the nonforward BFKL equation for an arbitrary color state in the t channel is expressed in terms of the gluon Regge trajectory and the part related to real particle production in Reggeon–Reggeon scattering ("real" part, for brevity). The trajectory is known [4] and enters into the kernel in the universal (not depending on a color state) way [13]. The "real" part includes contributions from one-gluon, two-gluon, and quark–antiquark pair production. The last two contributions can be separated (for an arbitrary color state in the t channel) in two pieces, one of which being determined by the color-octet state. Therefore, the color-octet piece enters (with some group coefficient) into kernels for other color states—in particular, for the color-singlet state (Pomeron channel). In the Pomeron channel, the nonforward BFKL equation can be used directly to describe experimental data. Evidently, the applicability range of this equation is much wider than the forward-case one.

The ensuing exposition is organized as follows. In Section 2, we present a general form of the gluon contribution to the kernel and an explicit form of the gluon piece of the gluon trajectory. In Section 3, we derive the gluon part of the contribution to the kernel from one-gluon production. In Section 4, we consider two-gluon production in collision of two Reggeized gluons. The contribution of this process to the kernel and the result for the total gluon contribution to the kernel are presented in Sections 5 and 6, respectively.

2. DEFINITIONS AND BASIC EQUATIONS

In the BFKL approach, the high-energy-scattering amplitudes are expressed in terms of the impact factors Φ of the scattering particles and of the Green's function G for the scattering of Reggeized gluons [13]. Considering the Green's function, we can take, without any loss of generality, masses of the colliding particles with momenta p_A and p_B equal to zero: $p_A^2 = p_B^2 = 0$ ($p_A + p_B)^2 = 2(p_A p_B) = s$. As usual, in an analysis of high-energy processes, we use the Sudakov decomposition for particle momenta. The Mellin transform of the Green's function with the initial momenta of the Reggeized gluons in the s channel $q_1 \simeq \beta p_A + q_{1\perp}$ and $-q_2 \simeq \alpha p_B - q_{2\perp}$ and the momentum transfer $q \simeq q_\perp$ obeys the equation [13]

$$\omega G_\omega^{(\mathcal{R})}(\mathbf{q}_1, \mathbf{q}_2, \mathbf{q}) = \mathbf{q}_1^2 \mathbf{q}_1'^2 \delta^{(D-2)}(\mathbf{q}_1 - \mathbf{q}_2) + \int \frac{d^{D-2} r}{\mathbf{r}^2 \mathbf{r}'^2} \mathcal{H}^{(\mathcal{R})}(\mathbf{q}_1, \mathbf{r}; \mathbf{q}) G_\omega^{(\mathcal{R})}(\mathbf{r}, \mathbf{q}_2; \mathbf{q}), \tag{1}$$

where $\mathcal{R}$ denotes the representation of the color group in the t channel. The transverse momenta are spacelike and we use the bold font for them. Here and below, we use for brevity $v' \equiv v - q$ for any v. The spacetime dimension $D = 4 + 2\epsilon$ is taken different from 4 to regularize the infrared divergences. We use the normalization adopted in [13].

The nonforward kernel, as well as the forward one, is given by the sum of the "virtual" part, defined by the gluon trajectory $j(t) = 1 + \omega(t)$, and the "real" part $\mathcal{H}_r^{(\mathcal{R})}$, related to the real particle production in the Reggeon–Reggeon collisions

$$\mathcal{H}^{(\mathcal{R})}(\mathbf{q}_1, \mathbf{q}_2; \mathbf{q}) = [\omega(-\mathbf{q}_1^2) + \omega(-\mathbf{q}_1'^2)] \times \mathbf{q}_1^2 \mathbf{q}_1'^2 \delta^{(D-2)}(\mathbf{q}_1 - \mathbf{q}_2) + \mathcal{H}_r^{(\mathcal{R})}(\mathbf{q}_1, \mathbf{q}_2; \mathbf{q}). \tag{2}$$

As is seen from (2), the gluon trajectory enters the equation in the universal (independent from $\mathcal{R}$) way. In the one-loop approximation (LLA), the trajectory is purely gluonic:

$$\omega^{(1)}(t) = \frac{g^2 N t}{2(2\pi)^{D-1}} \int \frac{d^{D-2} q_1}{\mathbf{q}_1^2 \mathbf{q}_1'^2}, \tag{3}$$

where $t = q^2 = -\mathbf{q}^2$, and N is the number of colors ($N = 3$ in QCD). In the NLA, the trajectory was calculated in [4]. Since the quark contribution to the nonforward kernel was already considered [18], we present here the two-loop gluon contribution:

$$\omega_G^{(2)}(t) = \frac{g^2 t}{(2\pi)^{D-1}} \times \int \frac{d^{(D-2)} q_1}{\mathbf{q}_1^2 \mathbf{q}_1'^2} [F_G(\mathbf{q}_1, \mathbf{q}) - 2F_G(\mathbf{q}_1, \mathbf{q}_1)], \tag{4}$$

where

$$F_G(\mathbf{q}_1, \mathbf{q}) = -\frac{g^2 N^2 \mathbf{q}^2}{4(2\pi)^{D-1}} \int \frac{d^{(D-2)} q_2}{\mathbf{q}_2^2 (\mathbf{q}_2 - \mathbf{q})^2} \left[\ln\left(\frac{\mathbf{q}^2}{(\mathbf{q}_1 - \mathbf{q}_2)^2} \right) - 2\psi(D-3) - \psi\left(3 - \frac{D}{2}\right) + 2\psi\left(\frac{D}{2} - 2\right) + \psi(1) + \frac{2}{(D-3)(D-4)} + \frac{D-2}{4(D-1)(D-3)} \right]; \tag{5}$$

$$\psi(x) = \frac{\Gamma'(x)}{\Gamma(x)},$$

and $\Gamma(x)$ is the Euler gamma function. In Eqs. (3)–(5) and below, g is the bare coupling constant related to the renormalized coupling g_μ in the $\overline{MS}$ scheme by the relation

$$g = g_\mu \mu^{-\epsilon} \left[1 + \left(\frac{11}{3} - \frac{2}{3} \frac{n_f}{N} \right) \frac{\bar{g}_\mu^2}{2\epsilon} \right], \tag{6}$$

where n_f is the number of the quark flavors,

$$\bar{g}_\mu^2 = \frac{g_\mu^2 N\Gamma(1-\epsilon)}{(4\pi)^{2+\epsilon}}. \quad (7)$$

Let us stress that in this paper we will systematically use the perturbative expansion in terms of the bare coupling g.

The "real" part for the nonforward case in the LLA is [1, 21]

$$\mathcal{K}_r^{(\mathcal{R})\mathrm{B}}(\mathbf{q}_1, \mathbf{q}_2; \mathbf{q}) = \frac{g^2 c_R}{(2\pi)^{D-1}}\left(\frac{\mathbf{q}_1^2\mathbf{q}_2'^2 + \mathbf{q}_2^2\mathbf{q}_1'^2}{(\mathbf{q}_1-\mathbf{q}_2)^2} - \mathbf{q}^2\right), \quad (8)$$

where the superscript B means the LLA (Born) approximation and the color group coefficients c_R for the singlet ($R = 1$) and octet ($R = 8$) cases are

$$c_1 = N, \quad c_8 = \frac{N}{2}. \quad (9)$$

In the NLA, the "real" part of the kernel can be presented as [13]

$$\begin{aligned}\mathcal{K}_r^{(\mathcal{R})}&(\mathbf{q}_1, \mathbf{q}_2; \mathbf{q}) \\ &= \int_0^\infty \frac{ds_{RR}}{(2\pi)^D}\mathrm{Im}\,\mathcal{A}_{RR}^{(\mathcal{R})}(q_1, q_2; \mathbf{q})\theta(s_\Lambda - s_{RR}) \\ &- \frac{1}{2}\int\frac{d^{D-2}r}{\mathbf{r}^2\mathbf{r}'^2}\mathcal{K}_r^{(\mathcal{R})\mathrm{B}}(\mathbf{q}_1, \mathbf{r}; \mathbf{q})\mathcal{K}_r^{(\mathcal{R})\mathrm{B}}(\mathbf{r}, \mathbf{q}_2; \mathbf{q}) \\ &\times \ln\left(\frac{s_\Lambda^2}{(\mathbf{r}-\mathbf{q}_1)^2(\mathbf{r}-\mathbf{q}_2)^2}\right).\end{aligned} \quad (10)$$

Here, $\mathcal{A}_{RR}^{(\mathcal{R})}(q_1, q_2; \mathbf{q})$ is the scattering amplitude of the Reggeons with the initial momenta $q_1 = \beta p_A + q_{1\perp}$ and $-q_2 = \alpha p_B - q_{2\perp}$ at the momentum transfer $q = q_\perp$ and the representation $\mathcal{R}$ of the color group in the t channel, and $s_{RR} = (q_1 - q_2)^2 = s\alpha\beta - (\mathbf{q}_1 - \mathbf{q}_2)^2$ is the squared invariant mass of the Reggeons. The s_{RR}-channel imaginary part $\mathrm{Im}\,\mathcal{A}_{RR}^{(\mathcal{R})}(q_1, q_2; \mathbf{q})$ is expressed in terms of the effective vertices for the production of particles in the Reggeon–Reggeon collisions [13]. The second term on the right-hand side of Eq. (10) serves for the subtraction of the contribution of the large s_{RR} region in the first term, in order to avoid a double counting of this region in the BFKL equation. The intermediate parameter s_Λ in (10) must be taken tending to infinity. At large s_{RR}, only the contribution of the two-gluon production does survive in the first integral, so that the dependence of s_Λ disappears in (10) due to the factorization property of the two-gluon production vertex [13].

The remarkable properties of the kernel are

$$\begin{aligned}\mathcal{K}_r^{(\mathcal{R})}(\mathbf{0}, \mathbf{q}_2; \mathbf{q}) &= \mathcal{K}_r^{(\mathcal{R})}(\mathbf{q}_1, \mathbf{0}; \mathbf{q}) \\ = \mathcal{K}_r^{(\mathcal{R})}(\mathbf{q}, \mathbf{q}_2; \mathbf{q}) &= \mathcal{K}_r^{(\mathcal{R})}(\mathbf{q}_1, \mathbf{q}; \mathbf{q}) = 0\end{aligned} \quad (11)$$

and

$$\begin{aligned}\mathcal{K}_r^{(\mathcal{R})}(\mathbf{q}_1, \mathbf{q}_2; \mathbf{q}) &= \mathcal{K}_r^{(\mathcal{R})}(\mathbf{q}_1', \mathbf{q}_2'; -\mathbf{q}) \\ &= \mathcal{K}_r^{(\mathcal{R})}(-\mathbf{q}_2, -\mathbf{q}_1; -\mathbf{q}).\end{aligned} \quad (12)$$

The properties in (11) mean that the kernel turns into zero at zero transverse momenta of the Reggeons and follow from the gauge invariance; expressions (11) are the consequences of the symmetry of the imaginary part of the Reggeon–Reggeon scattering amplitude (see below (13)).

Using the operator $\hat{\mathcal{P}}_\mathcal{R}$ for the projection of the two-gluon color states in the t channel on the irreducible representation $\mathcal{R}$ of the color group, we can represent the imaginary part of the Reggeon–Reggeon scattering amplitude entering (10) in the form

$$\begin{aligned}\mathrm{Im}\,\mathcal{A}_{RR}^{(\mathcal{R})}(q_1, q_2; \mathbf{q}) &= \frac{\langle c_1c_1'|\hat{\mathcal{P}}_\mathcal{R}|c_2c_2'\rangle}{2n_\mathcal{R}} \\ \times\sum_{\{f\}}\int\gamma_{c_1c_2}^{\{f\}}(q_1, q_2)&(\gamma_{c_1'c_2'}^{\{f\}}(q_1', q_2'))^* d\rho_f.\end{aligned} \quad (13)$$

Here, $n_\mathcal{R}$ is the number of independent states in the representation $\mathcal{R}$, the sum $\{f\}$ is performed over all states f which are produced in the Reggeon–Reggeon collisions and over all discrete quantum numbers of these states. $\gamma_{c_1c_2}^{\{f\}}(q_1, q_2)$ is the effective vertex for the production of the state f, and $d\rho_f$ is the phase space element for this state,

$$\begin{aligned}d\rho_f &= \frac{1}{n!}(2\pi)^D\delta^{(D)}\left(q_1 - q_2 - \sum_{i\in f}k_i\right) \\ &\times\prod_{i\in f}\frac{d^{D-1}k_i}{(2\pi)^{D-1}\cdot 2\epsilon_i},\end{aligned} \quad (14)$$

where n is the number of identical particles in the state f. In the LLA, only the one-gluon production does contribute in (13), and Eq. (10) gives for the kernel its LLA value (8); in the NLA, the contributing states include also the two-gluon and the quark–antiquark states. The normalization of the corresponding vertices is defined in [13].

The most interesting representations $\mathcal{R}$ are the color singlet (Pomeron channel) and the antisymmetric color octet (gluon channel). We have for the singlet case

$$\langle c_1c_1'|\hat{\mathcal{P}}_1|c_2c_2'\rangle = \frac{\delta_{c_1c_1'}\delta_{c_2c_2'}}{N^2-1}, \quad n_1 = 1, \quad (15)$$

and for the octet case

$$\langle c_1 c_1' | \hat{\mathcal{P}}_8 | c_2 c_2' \rangle = \frac{f_{c_1 c_1' c} f_{c_2 c_2' c}}{N}, \quad n_8 = N^2 - 1, \quad (16)$$

where f_{abc} are the structure constants of the color group.

3. THE ONE-GLUON CONTRIBUTION TO THE KERNEL

The gluon contribution to the Reggeon–Reggeon–gluon (RRG) vertex was calculated in [3]. Recall that the complicated analytic structure [20, 3] of the vertex is irrelevant in the NLA, where only the real parts of the production amplitudes do contribute (only these parts interfere with the LLA amplitudes, which are real). Recall also that, in the NLA, the vertex depends on the energy scale s_R used in the Regge factors. In (10) and (13), it was assumed that $s_R = \mathbf{k}^2$, where k is the produced gluon momentum. Neglecting the imaginary part, we have for the gluon contribution to the RRG vertex with this choice of s_R [21]

$$\begin{aligned}\gamma^G_{c_1 c_2}(q_1, q_2) &= g T^d_{c_1 c_2} e^*_\mu(k) \Bigg\{ C^\mu(q_2, q_1) \\ &\times \left[1 + \frac{2g^2 N \Gamma(1-\epsilon)}{(4\pi)^{2+\epsilon}} (f_1^{(G)} + f_2^{(G)}) \right] \\ &+ \left(\frac{p_A}{(kp_A)} - \frac{p_B}{(kp_B)} \right)_\mu \frac{g^2 N \Gamma(1-\epsilon)}{(4\pi)^{2+\epsilon}} \\ &\times [f_3^{(G)} - (2\mathbf{k}^2 - \mathbf{q}_1^2 - \mathbf{q}_2^2) f_2^{(G)}] \Bigg\}. \end{aligned} \quad (17)$$

Here, d is the color index of the product gluon, $e^\mu(k)$ is its polarization vector, $T^d_{c_1 c_2} = -i f_{d c_1 c_2}$ are the matrix elements of the color-group generator in the adjoint representation, $k = q_1 - q_2$,

$$\begin{aligned} C(q_2, q_1) &= -q_{1\perp} - q_{2\perp} + (q_1 - q_{1\perp}) \left(1 - \frac{2\mathbf{q}_1^2}{\mathbf{k}^2} \right) \\ &+ (q_2 - q_{2\perp}) \left(1 - \frac{2\mathbf{q}_2^2}{\mathbf{k}^2} \right), \end{aligned} \quad (18)$$

$$\begin{aligned} 2 f_1^{(G)} &= \frac{11}{6} \frac{(\mathbf{q}_1^2 + \mathbf{q}_2^2)}{(\mathbf{q}_1^2 - \mathbf{q}_2^2)} \ln\left(\frac{\mathbf{q}_1^2}{\mathbf{q}_2^2} \right) - \frac{1}{2} \ln^2\left(\frac{\mathbf{q}_1^2}{\mathbf{q}_2^2} \right) \\ &- (\mathbf{k}^2)^\epsilon \left(\frac{1}{\epsilon^2} - 3\zeta(2) + 2\epsilon\zeta(3) \right), \end{aligned} \quad (19)$$

$$2 f_2^{(G)} = \frac{\mathbf{k}^2}{3(\mathbf{q}_1^2 - \mathbf{q}_2^2)^2} \left[\mathbf{q}_1^2 + \mathbf{q}_2^2 - 2 \frac{\mathbf{q}_1^2 \mathbf{q}_2^2}{(\mathbf{q}_1^2 - \mathbf{q}_2^2)} \ln\left(\frac{\mathbf{q}_1^2}{\mathbf{q}_2^2} \right) \right],$$

$$f_3^{(G)} = \frac{11}{3} \frac{\mathbf{q}_1^2 \mathbf{q}_2^2}{(\mathbf{q}_1^2 - \mathbf{q}_2^2)} \ln\left(\frac{\mathbf{q}_1^2}{\mathbf{q}_2^2} \right) + \frac{k^2}{6},$$

where $\zeta(n)$ is a Riemann zeta function. Note that the one-loop contribution to the RRG vertex is not known for arbitrary ϵ. Therefore, Eqs. (19), contrary to all the preceding formulas, are valid only in the limit $\epsilon \longrightarrow 0$. The only term of these equations which remains unexpanded in ϵ is $(\mathbf{k}^2)^\epsilon$. For this term, the expansion is not performed because the RRG vertex is singular at $\mathbf{k}^2 = 0$, and in subsequent integrations of its contribution to the kernel the region $\epsilon |\ln(\mathbf{k}^2)| \sim 1$ does contribute. In (19), all terms are retained, which gives, after these integrations, contributions nonvanishing in the limit $\epsilon \longrightarrow 0$.

The vertex (17) is explicitly invariant under the gauge transformation

$$e^\mu(k) \longrightarrow e^\mu(k) + k^\mu \chi, \quad (20)$$

so that we can use the relation

$$\sum_\lambda e^{*(\lambda)}_\mu(k) e^{(\lambda)}_\nu(k) = -g_{\mu\nu}. \quad (21)$$

Substituting (17) into (13) and using (21) for the sum over polarizations and the relations

$$\begin{aligned} \delta_{c_1 c_1'} \delta_{c_2 c_2'} T^d_{c_1 c_2} (T^d_{c_1' c_2'})^* &= N(N^2 - 1), \\ f_{c_1 c_1' c} f_{c_2 c_2' c} T^d_{c_1 c_2} (T^d_{c_1' c_2'})^* &= N^2 (N^2 - 1)/2 \end{aligned} \quad (22)$$

for the sum over color indices, with the help of Eqs. (18), (19), and (14)–(16), we obtain from (10) the gluon part of the contribution to the kernel from the one-gluon production in Reggeon–Reggeon collisions:

$$\begin{aligned} \mathcal{H}^{G(\mathcal{R})}_{RRG}(\mathbf{q}_1, \mathbf{q}_2; \mathbf{q}) &= \frac{g^2 c_{\mathcal{R}}}{(2\pi)^{D-1}} \Bigg\{ \left(\frac{\mathbf{q}_1^2 \mathbf{q}_2'^2 + \mathbf{q}_1'^2 \mathbf{q}_2^2}{\mathbf{k}^2} - \mathbf{q}^2 \right) \\ &\times \left(\frac{1}{2} + \frac{g^2 N \Gamma(1-\epsilon)}{2(4\pi)^{2+\epsilon}} \left[-(\mathbf{k}^2)^\epsilon \left(\frac{2}{\epsilon^2} - \pi^2 + 4\epsilon\zeta(3) \right) \right. \right. \\ &\left. \left. - \ln^2\left(\frac{\mathbf{q}_1^2}{\mathbf{q}_2^2} \right) \right] \right) + \frac{g^2 N \Gamma(1-\epsilon)}{6(4\pi)^{2+\epsilon}} \left(\left[\frac{\mathbf{q}_1'^2 - \mathbf{q}_2'^2}{\mathbf{q}_1^2 - \mathbf{q}_2^2} \right. \right. \\ &\left. \left. - \frac{\mathbf{k}^2}{(\mathbf{q}_1^2 - \mathbf{q}_2^2)^2} (\mathbf{q}_1^2 + \mathbf{q}_2^2 + 4\mathbf{q}_1' \cdot \mathbf{q}_2' - 2\mathbf{q}^2) \right] \right. \\ &\times \left[\frac{2\mathbf{q}_1^2 \mathbf{q}_2^2}{\mathbf{q}_1^2 - \mathbf{q}_2^2} \ln\left(\frac{\mathbf{q}_1^2}{\mathbf{q}_2^2} \right) - \mathbf{q}_1^2 - \mathbf{q}_2^2 \right] + 11 \left[\frac{2\mathbf{q}_1^2 \mathbf{q}_2^2}{\mathbf{q}_1^2 - \mathbf{q}_2^2} \right. \end{aligned} \quad (23)$$

$$+\frac{\mathbf{q}_1^2\mathbf{q}_2'^2-\mathbf{q}_1'^2\mathbf{q}_2^2}{\mathbf{k}^2}-\frac{\mathbf{q}_1^2+\mathbf{q}_2^2}{\mathbf{q}_1^2-\mathbf{q}_2^2}\mathbf{q}^2\Bigg]\ln\left(\frac{\mathbf{q}_1^2}{\mathbf{q}_2^2}\right)-2\mathbf{q}_1'\cdot\mathbf{q}_2'\Bigg)\Bigg\}$$

$$+\frac{g^2c_{\mathcal{R}}}{(2\pi)^{D-1}}\{\mathbf{q}_i\longleftrightarrow\mathbf{q}_i'\}.$$

The symmetry properties (12) of $\mathcal{H}_{RRG}^{G(\mathcal{R})}(\mathbf{q}_1, \mathbf{q}_2; \mathbf{q})$ are evident from (23). The properties in (11) are not so evident, but can be easily checked.

4. THE TWO-GLUON PRODUCTION

Let us consider the production of two gluons with momenta k_1 and k_2 in collisions of two Reggeons with momenta q_1 and $-q_2$. We will use the Sudakov parametrization for the product-gluon momenta:

$$\begin{gathered}k_i = \beta_i p_A + \alpha_i p_B + k_{i\perp},\\ s\alpha_i\beta_i = -k_{i\perp}^2 = \mathbf{k}_i^2,\quad i = 1, 2,\\ \beta_1+\beta_2=\beta,\quad \alpha_1+\alpha_2=\alpha,\\ k_{1\perp}+k_{2\perp}=q_{1\perp}-q_{2\perp},\end{gathered}\tag{24}$$

and the notation

$$k = k_1 + k_2 = q_1 - q_2,\tag{25}$$

so that $s_{RR} = k^2$. For the effective vertex of the two-gluon production in the Reggeon–Reggeon collision, we have

$$\begin{gathered}\gamma_{c_1c_2}^{GG}(q_1, q_2) = g^2 e_{\alpha_1}^*(k_1)e_{\alpha_2}^*(k_2)\\ \times[T_{c_1j}^{d_1}T_{jc_2}^{d_2}A^{\alpha_1\alpha_2}(k_1, k_2)+T_{c_1j}^{d_2}T_{jc_2}^{d_1}A^{\alpha_2\alpha_1}(k_2, k_1)],\end{gathered}\tag{26}$$

where d_i are the color indices of the produced gluons, and $e^\mu(k_i)$ are their polarization vectors. The tensor $A^{\alpha_1\alpha_2}(k_1, k_2)$ obtained in [2] satisfies the transversality conditions

$$k_1^{\alpha_1}A_{\alpha_1\alpha_2}(k_1, k_2) = k_2^{\alpha_2}A_{\alpha_1\alpha_2}(k_1, k_2) = 0.\tag{27}$$

Due to these conditions, the two terms in (26) are separately invariant with respect to independent gauge transformations of the gluon polarization vectors

$$e^\alpha(k_i)\longrightarrow e^\alpha(k_i)+k_i^\alpha\chi_i,\tag{28}$$

so that we can use different gauges for each of the produced gluons and for each of the terms. Choosing

$$\begin{aligned}e_\alpha(k_1)k_1^\alpha &= e_\alpha(k_1)p_1^\alpha = 0,\\ e_\alpha(k_2)k_2^\alpha &= e_\alpha(k_2)p_2^\alpha = 0,\end{aligned}\tag{29}$$

we can present the polarization vectors as

$$\begin{aligned}e(k_1) &= e_\perp(k_1)-\frac{(k_1e_\perp(k_1))}{k_1p_1}p_1,\\ e(k_2) &= e_\perp(k_2)-\frac{(k_2e_\perp(k_2))}{k_2p_2}p_2,\end{aligned}\tag{30}$$

and their convolution with the tensor $A^{\alpha_1\alpha_2}(k_1, k_2)$ as

$$\begin{gathered}e_{\alpha_1}^*(k_1)e_{\alpha_2}^*(k_2)A^{\alpha_1\alpha_2}(k_1, k_2)\\ \equiv 4e_{\perp\alpha_1}^*(k_1)e_{\perp\alpha_2}^*(k_2)c^{\alpha_1\alpha_2}(k_1, k_2).\end{gathered}\tag{31}$$

The tensor $c^{\mu\nu}(k_1, k_2)$ in the transverse space was defined in [6]. It can be presented in the form

$$\begin{gathered}c^{\mu\nu}(k_1, k_2) = \frac{(q_1-k_1)_\perp^\mu(q_1-k_1)_\perp^\nu}{\tilde t_1}\\ -\frac{(q_1-k_1)_\perp^\mu}{k^2}\left(k_1-\frac{\beta_1}{\beta_2}k_2\right)_\perp^\nu+\left(k_2-\frac{\alpha_2}{\alpha_1}k_1\right)_\perp^\mu\frac{(q_1-k_1)_\perp^\nu}{k^2}\\ +\frac{k_{1\perp}^\mu k_{1\perp}^\nu}{k^2}\frac{t_2}{s\alpha_1\beta}+\frac{k_{2\perp}^\mu k_{2\perp}^\nu}{k^2}\frac{t_1}{s\alpha\beta_2}\\ -\frac{k_{1\perp}^\mu k_{2\perp}^\nu}{k^2}\left(1+\frac{\tilde t_1}{s\alpha_1\beta_2}\right)+\frac{k_{2\perp}^\mu k_{1\perp}^\nu}{k^2}-\frac{1}{2}g_\perp^{\mu\nu}\left(1+\frac{\tilde t_1}{k^2}\right.\\ \left.+\frac{s\alpha_1\beta_2}{\tilde t_1}-\frac{s\alpha_2\beta_1}{k^2}+\frac{s\alpha_1\beta_2}{k^2}-\frac{\alpha_2t_1}{\alpha k^2}-\frac{\beta_1t_2}{\beta k^2}\right),\end{gathered}\tag{32}$$

where the notation

$$t_i = q_{i\perp}^2,\quad i = 1, 2;\quad \tilde t_1 = (q_1-k_1)^2\tag{33}$$

is used, and $g_\perp^{\mu\nu}$ is the metric tensor in the transverse plane,

$$g_\perp^{\mu\nu} = g^{\mu\nu}-\frac{p_A^\mu p_B^\nu+p_B^\mu p_A^\nu}{(p_Ap_B)}.\tag{34}$$

Since different gauges are used for each of the produced gluons, to obtain the contribution of the second term in (26) one has to change not only $k_1\longleftrightarrow k_2$ in the contribution of the first term, but also the gauges $e(k)p_1 = 0\longleftrightarrow e(k)p_2 = 0$, so that

$$\begin{gathered}e_{\alpha_1}^*(k_1)e_{\alpha_2}^*(k_2)A^{\alpha_2\alpha_1}(k_2, k_1)\\ = 4e_{\perp\alpha_1}^*(k_1)e_{\perp\alpha_2}^*(k_2)\Omega^{\alpha_1\beta_1}(k_1)\Omega^{\alpha_2\beta_2}(k_2)c_{\beta_2\beta_1}(k_2, k_1),\end{gathered}\tag{35}$$

where

$$\Omega^{\alpha\beta}(k) = g_\perp^{\alpha\beta}-2\frac{k_\perp^\alpha k_\perp^\beta}{k_\perp^2}.\tag{36}$$

In order to calculate the two-gluon contribution to the imaginary part of the Reggeon–Reggeon scattering amplitude (13) entering Eq. (10) for the kernel, we need

to sum over gluon polarizations and color indices. The first sum can be obtained using the relation

$$\sum_{\lambda}(e_{\perp}^{\alpha(\lambda)}(k))^{*}e_{\perp}^{\beta(\lambda)}(k) = -g_{\perp}^{\alpha\beta}, \tag{37}$$

and the second, for the most interesting singlet and octet representations, with the help of

$$\begin{aligned}
&\delta_{c_1c_1'}\delta_{c_2c_2'}T^{d_1}_{c_1i}T^{d_2}_{ic_2}T^{d_1}_{c_1'j}T^{d_2}_{jc_2'} = N^2(N^2-1),\\
&\delta_{c_1c_1'}\delta_{c_2c_2'}T^{d_1}_{c_1i}T^{d_2}_{ic_2}T^{d_2}_{c_1'j}T^{d_1}_{jc_2'} = \frac{N^2(N^2-1)}{2},\\
&f_{c_1c_1'c}f_{c_2c_2'c}T^{d_1}_{c_1i}T^{d_2}_{ic_2}T^{d_1}_{c_1'j}T^{d_2}_{jc_2'} = \frac{N^3(N^2-1)}{4},\\
&f_{c_1c_1'c}f_{c_2c_2'c}T^{d_1}_{c_1i}T^{d_2}_{ic_2}T^{d_2}_{c_1'j}T^{d_1}_{jc_2'} = 0.
\end{aligned} \tag{38}$$

Using these formulas, we obtain

$$\begin{aligned}
&\frac{\langle c_1c_1'|\hat{\mathcal{P}}_{\mathcal{R}}|c_2c_2'\rangle}{2n_{\mathcal{R}}}\sum_{GG}\gamma^{GG}_{c_1c_2}(q_1,q_2)(\gamma^{GG}_{c_1'c_2'}(q_1',q_2'))^{*}\\
&= 8g^4N^2[(a_Rc^{\alpha_1\alpha_2}(k_1,k_2)c'_{\alpha_1\alpha_2}(k_1,k_2)\\
&+ b_Rc_{\alpha_1\alpha_2}(k_1,k_2)c'_{\beta_2\beta_1}(k_2,k_1)\Omega^{\alpha_1\beta_1}(k_1)\Omega^{\alpha_2\beta_2}(k_2))\\
&+ (k_1\longleftrightarrow k_2)],
\end{aligned} \tag{39}$$

where $c'_{\alpha_1\alpha_2}(k_1,k_2)$ is obtained from $c_{\alpha_1\alpha_2}(k_1,k_2)$ by the substitution $q_i \longrightarrow q_i'$ and the coefficients a_R and b_R for the singlet ($R = 1$) and octet ($R = 8$) representations are

$$a_0 = 1, \quad b_0 = \frac{1}{2}; \quad a_8 = \frac{1}{4}, \quad b_8 = 0. \tag{40}$$

Evidently the term $(k_1 \longleftrightarrow k_2)$ in (39) gives the same contribution to the kernel as the preceding terms, so that in the following only these terms will be considered and their contribution to the kernel will be doubled.

To perform in Eqs. (10) and (13) the integration over longitudinal components of the produced gluon momenta, we will use the variable $x \equiv \beta_1/\beta$, so that

$$x_1 = x, \quad x_2 = 1-x, \quad x_i = \frac{\beta_i}{\beta}, \quad i = 1,2. \tag{41}$$

The alternative choice is y, with

$$y_2 = y, \quad y_1 = 1-y, \quad y_i = \frac{\alpha_i}{\alpha}, \quad i = 1,2. \tag{42}$$

The variables x and y are connected by the relations

$$y = \frac{x\mathbf{k}_2^2}{x\mathbf{k}_2^2+(1-x)\mathbf{k}_1^2}, \quad x = \frac{y\mathbf{k}_1^2}{y\mathbf{k}_1^2+(1-y)\mathbf{k}_2^2}, \tag{43}$$

which are inverse to each other. Recall that the vector sign is used for the transverse components. The integration measure in (10) and (13) with allowance for (14) has the same form for both choices:

$$\begin{aligned}
\frac{dk^2}{2\pi}d\rho_{GG} &= \frac{dx}{4x(1-x)}\frac{d^{D-2}k_1}{(2\pi)^{(D-1)}}\\
&= \frac{dy}{4y(1-y)}\frac{d^{D-2}k_2}{(2\pi)^{(D-1)}},\\
1 \ge x \ge 0, &\quad 1 \ge y \ge 0.
\end{aligned} \tag{44}$$

Note that

$$\mathbf{k}_1+\mathbf{k}_2 = \mathbf{k} = \mathbf{q}_1-\mathbf{q}_2 = \mathbf{q}_1'-\mathbf{q}_2' \tag{45}$$

is fixed.

The important symmetry properties of the convolutions

$$f_a(k_1,k_2) = c^{\alpha_1\alpha_2}(k_1,k_2)c'_{\alpha_1\alpha_2}(k_1,k_2) \tag{46}$$

and

$$\begin{aligned}
&f_b(k_1,k_2)\\
&= c_{\alpha_1\alpha_2}(k_1,k_2)c'_{\beta_2\beta_1}(k_2,k_1)\Omega^{\alpha_1\beta_1}(k_1)\Omega^{\alpha_2\beta_2}(k_2)
\end{aligned} \tag{47}$$

entering (39) are their invariance with respect to the "left–right" transformation

$$\begin{aligned}
&\mathbf{k}_1 \longleftrightarrow \mathbf{k}_2, \quad \alpha_1 \longleftrightarrow \beta_2, \quad \alpha_2 \longleftrightarrow \beta_1,\\
&\mathbf{q}_1 \longleftrightarrow -\mathbf{q}_2, \quad \mathbf{q}_1' \longleftrightarrow -\mathbf{q}_2'.
\end{aligned} \tag{48}$$

This invariance follows from the transformation law for the tensor $c^{\mu\nu}(k_1,k_2)$. It is easily seen from (32) that this tensor reduces $c^{\nu\mu}(k_1,k_2)$ under transformation (48). In terms of the variables $\mathbf{k}_i$, x, and y, this transformation is represented as

$$\mathbf{k}_1 \longleftrightarrow \mathbf{k}_2, \ x \longleftrightarrow y, \ \mathbf{q}_1 \longleftrightarrow -\mathbf{q}_2, \ \mathbf{q}_1' \longleftrightarrow -\mathbf{q}_2'. \tag{49}$$

One can check by a direct inspection that the tensor $c^{\mu\nu}(k_1,k_2)$ (32) is equal to zero when the transverse momentum of one the Reggeons is zero, $\mathbf{q}_1 = \mathbf{0}$ or $\mathbf{q}_2 = \mathbf{0}$. This guarantees another important property of the functions $f_a(k_1,k_2)$ and $f_b(k_1,k_2)$—they vanish at zero transverse momenta of the Reggeons [compare with (11)].

Let us adopt the first choice $(x, \mathbf{k}_1)$ of variables for the integration in Eqs. (10) and (13). The two-gluon contribution to the kernel is then represented in the form

$$\begin{aligned}
&\mathcal{H}^{(\mathcal{R})}_{RRGG}(\mathbf{q}_1,\mathbf{q}_2;\mathbf{q}) = \frac{4g^2N^2}{(2\pi)^{D-1}}\int\frac{d^{D-2}k_1}{(2\pi)^{(D-1)}}\\
&\times\int_0^1\frac{dx\theta(s_\Lambda-k^2)}{x(1-x)}[a_Rf_a(k_1,k_2)+b_Rf_b(k_1,k_2)]\\
&-\frac{1}{2}\int\frac{d^{D-2}r}{\mathbf{r}^2\mathbf{r}'^2}\mathcal{H}_r^{(\mathcal{R})\mathrm{B}}(\mathbf{q}_1,\mathbf{r};\mathbf{q})\mathcal{H}_r^{(\mathcal{R})\mathrm{B}}(\mathbf{r},\mathbf{q}_2;\mathbf{q})\\
&\times\ln\left(\frac{s_\Lambda^2}{(\mathbf{r}-\mathbf{q}_1)^2(\mathbf{r}-\mathbf{q}_2)^2}\right),
\end{aligned} \tag{50}$$

where the group coefficients a_R and b_R are defined in (40) and the functions $f_a(k_1, k_2)$ and $f_b(k_1, k_2)$ in (46) and (47), respectively. The functions must be expressed in terms of x and $\mathbf{k}_1$. It can be done by using (41) and the relations

$$k^2 = \frac{((1-x)\mathbf{k}_1 - x\mathbf{k}_2)^2}{x(1-x)},$$

$$\tilde{t}_1 = -\frac{1}{x}((1-x)\mathbf{k}_1^2 + x(\mathbf{k}_1 - \mathbf{q}_1)^2), \qquad (51)$$

$$\mathbf{k}_1 + \mathbf{k}_2 = \mathbf{k}, \quad t_i = \mathbf{q}_i^2, \quad \alpha_i = \frac{\mathbf{k}_i^2}{s\beta_i}, \quad i = 1, 2.$$

To understand the behavior of the functions $f_a(k_1, k_2)$ and $f_b(k_1, k_2)$ in the integration region of (50), it is convenient to express the tensor $c^{\mu\nu}(k_1, k_2)$ in (32) in terms of x and $\mathbf{k}_1$. After this, it is not difficult to show that, for any x in the interval [0, 1], the tensor decreases in proportion to $1/\mathbf{k}_1^2$, so that the integration over $\mathbf{k}_1$ is well convergent in the ultraviolet region. As for the x behavior at fixed $\mathbf{k}_1$, it is easy to see that in the limit $x \longrightarrow 0$ the tensor $c^{\alpha_1\alpha_2}(k_1, k_2)$ tends to zero, whereas at $x \longrightarrow 1$ the tensor has a finite value. It means that the function $f_b(k_1, k_2)$ [see (47)] turns to zero both at $x = 0$ and $x = 1$, so that performing the integration of the term with $f_b(k_1, k_2)$ in (50) we can ignore the restrictions on the integration region imposed by $\theta(s_\Lambda - k^2)$. Recall that the parameter s_Λ must be taken tending to infinity, therefore, due to the convergence of the integral over $\mathbf{k}_1$ in the ultraviolet region, the restrictions have the form

$$1 - \frac{\mathbf{k}_2^2}{s_\Lambda} \geq x \geq \frac{\mathbf{k}_1^2}{s_\Lambda}. \qquad (52)$$

From the discussion above, it is clear that the restriction from below does not play any role, but the upper limit is important for the integration of $f_a(k_1, k_2)$ in (50).

The limit $x \longrightarrow 1$ corresponds to the multi-Regge limit of large relative rapidities of the produced gluons, so that the value of $f_a(k_1, k_2)$ at this limit is related to the LLA kernel $\mathcal{K}_r^{(\mathcal{R})\mathrm{B}}$. Indeed, by using (41) and (51), we find from (32) that

$$c^{\mu\nu}(k_1, k_2)\big|_{x=1} = \frac{-1}{(\mathbf{q}_1 - \mathbf{k}_1)^2}\left[q_1 - k_1 + \frac{(\mathbf{q}_1 - \mathbf{k}_1)^2}{\mathbf{k}_1^2}k_1\right]_\perp^\mu \times \left[q_1 - k_1 - \frac{(\mathbf{q}_1 - \mathbf{k}_1)^2}{\mathbf{k}_2^2}k_2\right]_\perp^\nu. \qquad (53)$$

This result and Eqs. (30), (31), and (18) give us the relation

$$e_\mu^*(k_1)e_\nu^*(k_2)A^{\mu\nu}(k_1, k_2)\big|_{x=1} = -\frac{e_\mu^*(k_1)C^\mu(q_1 - k_1, q_1)e_\nu^*(k_2)C^\nu(q_2, q_1 - k_1)}{(\mathbf{q}_1 - \mathbf{k}_1)^2}, \qquad (54)$$

which means that in the multi-Regge limit, the vertex for the two-gluon production is expressed in terms of the one-gluon production vertices. For the function $f_a(k_1, k_2)$ (46), we obtain from (53), using (8),

$$\left(\frac{2g^2c_R}{(2\pi)^{D-1}}\right)^2 f_a(k_1, k_2)\big|_{x=1} = \frac{1}{(\mathbf{q}_1 - \mathbf{k}_1)^2(\mathbf{q}_1' - \mathbf{k}_1)^2} \times \mathcal{K}_r^{(\mathcal{R})\mathrm{B}}(\mathbf{q}_1, \mathbf{q}_1 - \mathbf{k}_1; \mathbf{q})\mathcal{K}_r^{(\mathcal{R})\mathrm{B}}(\mathbf{q}_1 - \mathbf{k}_1, \mathbf{q}_2; \mathbf{q}).$$

Therefore, the subtraction term in (50) can be written as

$$-\frac{1}{2}\int\frac{d^{D-2}r}{\mathbf{r}^2\mathbf{r}'^2}\mathcal{K}_r^{(\mathcal{R})\mathrm{B}}(\mathbf{q}_1, \mathbf{r}; \mathbf{q})\mathcal{K}_r^{(\mathcal{R})\mathrm{B}}(\mathbf{r}, \mathbf{q}_2; \mathbf{q}) \times \ln\left(\frac{s_\Lambda^2}{(\mathbf{r} - \mathbf{q}_1)^2(\mathbf{r} - \mathbf{q}_2)^2}\right) = -\frac{1}{2}\left(\frac{2g^2c_R}{(2\pi)^{D-1}}\right)^2 \times \int d^{D-2}k_1 \int\limits_{\mathbf{k}_1^2/s_\Lambda}^{1-\mathbf{k}_2^2/s_\Lambda} \frac{dx}{x(1-x)} f_a(k_1, k_2)\big|_{x=1}. \qquad (55)$$

Taking into account that $c_R^2 = N^2a_R$ [compare (9) and (40)], we obtain that the two-gluon contribution to the kernel can be presented as

$$\mathcal{K}_{RRGG}^{(\mathcal{R})}(\mathbf{q}_1, \mathbf{q}_2; \mathbf{q}) = \frac{4g^4N^2}{(2\pi)^{D-1}}\int_0^1\frac{dx}{x(1-x)} \times \int\frac{d^{2+2\epsilon}k_1}{(2\pi)^{D-1}}\{a_R[f_a(k_1, k_2) - x(f_a(k_1, k_2)\big|_{x=1})] + b_R f_b(k_1, k_2)\} + \frac{2g^4N^2}{(2\pi)^{D-1}} \times \int\frac{d^{2+2\epsilon}k_1}{(2\pi)^{D-1}}a_R f_a(k_1, k_2)\big|_{x=1}\ln\left(\frac{k_1^2}{k_2^2}\right). \qquad (56)$$

Recall that, from general arguments, the kernel must be symmetric [see (12)] with respect to the substitutions $\mathbf{q}_i \longleftrightarrow \mathbf{q}_i'$, $i = 1, 2$, and $\mathbf{q}_1 \longleftrightarrow -\mathbf{q}_2$, $\mathbf{q}_1' \longleftrightarrow -\mathbf{q}_2'$ (note that at both of them $\mathbf{q}$ changes its sign). The symmetries of the two-gluon contribution to the kernel can be explicitly demonstrated using representation (50). First of all, it is easy to show with the help of expression (8) for the Born kernel that the subtraction term is symmetric under these substitutions. After this, the symme-

try of the total contribution under the first transformation follows from the evident invariance of the convolutions in (46) and (47) under this transformation. The symmetry under the second transformation follows from the invariance of these convolutions as well as the integration measure [see (44)] with respect to the "left–right" transformation given by (48) and (49). Turning to (56), we see that the contribution of $f_b(k_1, k_2)$ is symmetric with respect to both transformations. As for the terms with $f_a(k_1, k_2)$, the last of them gives the contribution antisymmetric under the substitution $\mathbf{q}_1 \longleftrightarrow -\mathbf{q}_2$, $\mathbf{q}_1' \longleftrightarrow -\mathbf{q}_2'$. Therefore, this term can be omitted together with antisymmetric contributions from the remaining terms. So, the total contribution of all three terms with $f_a(k_1, k_2)$ can be obtained by integration of the first term with respect to x from zero to $1-\delta$ at arbitrary small δ with subsequent omission of terms proportional to $\ln\delta$ and terms antisymmetric under the substitution $\mathbf{q}_1 \longleftrightarrow -\mathbf{q}_2$, $\mathbf{q}_1' \longleftrightarrow -\mathbf{q}_2'$.

5. THE TWO-GLUON CONTRIBUTION TO THE OCTET KERNEL

Up to now, our results could be used for any color representation $\mathcal{R}$. Starting from this point, we will consider only the case of the gluon channel (antisymmetric octet representation). In this case, only the function $f_a(k_1, k_2)$ does contribute to the kernel. From the discussion at the end of the preceding section, it follows that the two-gluon contribution to the octet kernel can be presented as

$$\mathcal{K}^{(8)}_{RRGG}(\mathbf{q}_1, \mathbf{q}_2; \mathbf{q}) = \frac{g^4 N^2}{(2\pi)^{D-1}}\hat{\mathcal{S}} \times \int_0^1 \frac{dx}{(1-x)_+}\int \frac{d^{2+2\epsilon}k_1}{(2\pi)^{D-1}}\frac{f_a(k_1, k_2)}{x}, \tag{57}$$

where $\hat{\mathcal{S}}$ denotes the operator of symmetrization with respect to the substitution $\mathbf{q}_1 \longleftrightarrow -\mathbf{q}_2$, $\mathbf{q}_1' \longleftrightarrow -\mathbf{q}_2'$ and $(1-x)_+$ means the subtraction

$$\int_0^1 \frac{dx}{(1-x)_+} f(x) \equiv \int_0^1 \frac{dx}{(1-x)}[f(x) - f(1)]. \tag{58}$$

According to (46), the function $f_a(k_1, k_2)$ is determined by the convolution of the tensor $c^{\mu\nu}(k_1, k_2)$ given by (32) with the tensor $c'_{\mu\nu}(k_1, k_2)$ given by the same formula with the substitution $q_i \longrightarrow q_i' \equiv q_i - q$. We obtain (details of the calculation are given in Appendix A)

$$\begin{aligned} f_a(k_1, k_2) = \Bigg\{ \frac{1+\epsilon}{k^2}\Bigg[\frac{x^2(1-x)}{\Sigma}\mathbf{q}_1'^2\Big(\mathbf{q}_1\cdot\mathbf{\Lambda} + (1-2x)(1-x)\frac{\mathbf{q}_1^2(\mathbf{\Lambda}\cdot\mathbf{k})}{\Sigma}\Big) + \frac{(\mathbf{q}_1'\cdot\mathbf{\Lambda})(\mathbf{q}_1\cdot\mathbf{\Lambda})}{k^2}\Bigg] \\ + \frac{x(1-x)\mathbf{q}_1'^2}{k^2\Sigma}\left(\frac{x(1-x)\mathbf{q}_1^2}{2k^2\Sigma}k_\perp^\mu k_\perp^\nu - \frac{k_\perp^\mu q_{1\perp}^\nu}{k^2}\right) \\ \times(2(1+\epsilon)\Lambda_\mu\Lambda_\nu + \mathbf{\Lambda}^2 g^\perp_{\mu\nu}) + \frac{x^2\mathbf{q}_1'^2\mathbf{q}_2^2}{4\mathbf{k}_1^2\Sigma} + \frac{x\mathbf{q}_1'^2\mathbf{q}_2^2}{4(1-x)\mathbf{k}_1^2k^2} \\ + \left(\frac{x(1-x)}{\Sigma}\right)^2\frac{\mathbf{q}_1'^2\mathbf{q}_1^2}{2}\left(\frac{1+\epsilon}{2} - (3+2\epsilon)x(1-x)\right) \\ - \frac{x(1-x)\mathbf{q}_1'^2}{2k^2\Sigma}[(1-x)((1+\epsilon)(2(\mathbf{k}_1\cdot\mathbf{q}_1) - x\mathbf{q}_1^2) \\ - \epsilon x(\mathbf{k}^2 - \mathbf{q}_2^2)) - (1+\epsilon)\mathbf{k}_2^2 + 2\mathbf{q}_2^2] + \frac{x\mathbf{q}_1^2\mathbf{q}^2}{4\tilde{t}_1\mathbf{k}_1^2} \\ - (\mathbf{q}_1\cdot\mathbf{q})(1-x)\frac{(\mathbf{q}_1'^2 - 2(\mathbf{k}_1\cdot\mathbf{q}_1'))}{\tilde{t}_1\tilde{t}_1'} + \frac{(1+\epsilon)(1-x)^2}{4} \\ \times\frac{(\mathbf{q}_1'^2 - 2(\mathbf{k}_1\cdot\mathbf{q}_1'))(\mathbf{q}_1^2 - 2(\mathbf{k}_1\cdot\mathbf{q}_1))}{\tilde{t}_1\tilde{t}_1'} \\ + \frac{1}{k^2\tilde{t}_1}\Bigg[2((\mathbf{q}_1\cdot\mathbf{q}_2)(\mathbf{k}_1\cdot\mathbf{q}_1') - (\mathbf{q}_1'\cdot\mathbf{q}_2)(\mathbf{k}_1\cdot\mathbf{q}_1)) \\ + x\mathbf{q}_2'^2\mathbf{q}_1^2 - x\mathbf{k}^2(\mathbf{q}_1\cdot\mathbf{q}) + \mathbf{q}_1^2(\mathbf{q}_1'\cdot\mathbf{q}) \\ - \mathbf{q}_1'^2\mathbf{q}_2^2\frac{(1-x)\mathbf{k}_1^2}{\Sigma} + \frac{1+\epsilon}{2}(1-x) \\ \times\Bigg\{(\mathbf{q}_1^2 - 2(\mathbf{k}_1\cdot\mathbf{q}_1))(\mathbf{q}_1'^2(1-x) - 2(\mathbf{q}_1'\cdot\mathbf{\Lambda})) \\ + \frac{\mathbf{k}_1^2\mathbf{k}_2^2\mathbf{q}_1'^2}{\Sigma}\Bigg\}\Bigg] + \frac{(\mathbf{q}^2)^2}{8\tilde{t}_1\tilde{t}_1'} + \frac{x\mathbf{q}_1^2\mathbf{q}^2\mathbf{k}^2}{4k^2\tilde{t}_1\mathbf{k}_1^2} - \frac{x\mathbf{q}_1'^2(\mathbf{q}_2^2)^2}{4k^2\Sigma\tilde{t}_1} \\ - \frac{x\mathbf{q}_2'^2(\mathbf{q}_1^2)^2}{4k^2\tilde{t}_1\mathbf{k}_1^2} + \frac{x\mathbf{q}_2^2(\mathbf{q}_1^2(\mathbf{q}_1'\cdot\mathbf{k}_1) - \mathbf{q}_1'^2(\mathbf{q}_1\cdot\mathbf{k}_1))}{2(1-x)k^2\tilde{t}_1\mathbf{k}_1^2} \\ - \frac{\mathbf{q}_2^2(\mathbf{q}_1'\cdot\mathbf{q})}{2(1-x)k^2\tilde{t}_1}\Bigg\} + \{\mathbf{q}_i \longleftrightarrow \mathbf{q}_i'\}, \end{aligned} \tag{59}$$

where $\tilde{t}_1'$ is obtained from $\tilde{t}_1$ (51) by the substitution $\mathbf{q}_1 \longrightarrow \mathbf{q}_1'$

$$\mathbf{\Lambda} = ((1-x)k_1 - xk_2)_\perp, \qquad \Sigma = \mathbf{\Lambda}^2 + x(1-x)\mathbf{k}^2. \tag{60}$$

Unfortunately, integral (57) cannot be expressed in terms of elementary functions (and dilogarithms) at arbitrary ϵ. Therefore, we present the result (see details of the integration in Appendix B) in a "combined" form, leaving untouched the terms in $f_a(k_1, k_2)$ which cannot be integrated in elementary functions:

$$\mathcal{H}^{(8)}_{RRGG}(\mathbf{q}_1, \mathbf{q}_2; \mathbf{q}) = \frac{4g^4N^2\Gamma(1-\epsilon)}{(4\pi)^D\pi^{1+\epsilon}}\frac{\Gamma^2(1+\epsilon)}{\Gamma(1+2\epsilon)}$$
$$\times\left\{\frac{(\mathbf{k}^2)^{\epsilon-1}}{4\epsilon}\left[(\mathbf{q}_1'^2\mathbf{q}_2^2+\mathbf{q}_2'^2\mathbf{q}_1^2)\left(\frac{1}{\epsilon}+\psi(1)+\psi(1+\epsilon)\right.\right.\right.$$
$$\left.\left.-2\psi(1+2\epsilon)-\frac{11+7\epsilon}{2(1+2\epsilon)(3+2\epsilon)}\right)-\frac{\mathbf{q}^2\mathbf{k}^2}{\epsilon}\right]$$
$$+\frac{(\mathbf{q}^2)^{\epsilon+1}}{4\epsilon}\left(-\frac{1}{\epsilon}+\psi(1)-\psi(1-\epsilon)+2\psi(1+\epsilon)\right.$$
$$\left.-2\psi(1+2\epsilon)-\frac{11+7\epsilon}{2(1+2\epsilon)(3+2\epsilon)}\right)$$
$$-\frac{11+7\epsilon}{4\epsilon(1+2\epsilon)(3+2\epsilon)}\mathbf{q}_1^2\mathbf{q}_2^2\frac{(\mathbf{q}_1^2)^\epsilon-(\mathbf{q}_2^2)^\epsilon}{\mathbf{q}_1^2-\mathbf{q}_2^2}$$
$$+\frac{\mathbf{q}^2}{\epsilon(1+2\epsilon)}\frac{(\mathbf{q}_1^2)^{\epsilon+1}-(\mathbf{q}_2^2)^{\epsilon+1}}{\mathbf{q}_1^2-\mathbf{q}_2^2}+\frac{\mathbf{q}^2}{4\epsilon}\left(\frac{1}{2\epsilon}-\psi(1+\epsilon)\right.$$
$$\left.+\psi(1+2\epsilon)\right)((\mathbf{q}_1^2)^\epsilon+(\mathbf{q}_2^2)^\epsilon)+\frac{1}{8\epsilon(1+2\epsilon)(3+2\epsilon)} \quad (61)$$
$$\times\left[(2(1+\epsilon)\mathbf{q}_1^2\mathbf{q}_2^2((\mathbf{q}_1^2)^\epsilon-(\mathbf{q}_2^2)^\epsilon)-\epsilon(\mathbf{q}_1^2+\mathbf{q}_2^2)\right.$$
$$\times((\mathbf{q}_1^2)^{\epsilon+1}-(\mathbf{q}_2^2)^{\epsilon+1}))\left(\frac{\mathbf{k}^2}{(\mathbf{q}_1^2-\mathbf{q}_2^2)^3}(\mathbf{q}_1^2+\mathbf{q}_2^2+2\mathbf{q}_1'^2\right.$$
$$\left.+2\mathbf{q}_2'^2-2\mathbf{k}^2-2\mathbf{q}^2)-\frac{\mathbf{q}_1'^2-\mathbf{q}_2'^2}{(\mathbf{q}_1^2-\mathbf{q}_2^2)^2}\right)$$
$$+\frac{(\mathbf{q}_1^2)^{\epsilon+1}-(\mathbf{q}_2^2)^{\epsilon+1}}{(\mathbf{q}_1^2-\mathbf{q}_2^2)}(\epsilon(\mathbf{q}_1'^2+\mathbf{q}_2'^2-\mathbf{k}^2)$$
$$\left.-2(1+\epsilon)\mathbf{q}^2)\right]+\frac{\Gamma(1+2\epsilon)}{4\Gamma^2(1+\epsilon)}I(\mathbf{q}_1, \mathbf{q}_2; \mathbf{q})\Bigg\}$$
$$+\frac{4g^4N^2}{(4\pi)^D\pi^{1+\epsilon}}\Gamma(1-\epsilon)\frac{\Gamma^2(1+\epsilon)}{\Gamma(1+2\epsilon)}$$
$$\times\{\mathbf{q}_1\longleftrightarrow\mathbf{q}_1', \mathbf{q}_2\longleftrightarrow\mathbf{q}_2'\},$$

where

$$I(\mathbf{q}_1, \mathbf{q}_2; \mathbf{q}) = 4\hat{\mathcal{P}}\int_0^1\frac{dx}{x(1-x)_+}\int\frac{d^{2+2\epsilon}k_1}{\pi^{1+\epsilon}\Gamma(1-\epsilon)}$$
$$\times\left(\frac{x\mathbf{q}_2^2}{2\tilde{\mathbf{\Lambda}^2t_1}}\left[\frac{x(\mathbf{q}_1^2(\mathbf{k}_1\cdot\mathbf{q}_1')-\mathbf{q}_1'^2(\mathbf{k}_1\cdot\mathbf{q}_1))}{\mathbf{k}_1^2}-(\mathbf{q}\cdot\mathbf{q}_1')\right]\right.$$
$$\left.-\frac{x^2(1-x)}{4\tilde{\mathbf{\Lambda}^2t_1}}\left[\frac{\mathbf{q}_1'^2\mathbf{q}_2^4}{\Sigma}+\frac{\mathbf{q}_1^4\mathbf{q}_2'^2-\mathbf{q}_1^2\mathbf{q}^2\mathbf{k}^2}{\mathbf{k}_1^2}\right]\right) \quad (62)$$
$$-\frac{\Gamma^2(\epsilon)}{\Gamma(2\epsilon)}\frac{(\mathbf{k}^2)^{\epsilon-1}}{2\epsilon}(\mathbf{q}_1^2\mathbf{q}_2'^2+\mathbf{q}_2^2\mathbf{q}_1'^2-\mathbf{q}^2\mathbf{k}^2)$$
$$-\frac{(\mathbf{q}^2)^2}{4}\frac{1}{\pi^{1+\epsilon}\Gamma(1-\epsilon)}\int\frac{d^{2+2\epsilon}l}{(\mathbf{q}_1-\mathbf{l})^2(\mathbf{q}_1'-\mathbf{l})^2}$$
$$\times\ln\left(\frac{\mathbf{l}^2(\mathbf{l}-\mathbf{k})^2}{\mathbf{q}^4}\right).$$

The first of the symmetries in (12) of the two-gluon contribution is explicit in (61); the second is also easily seen. The properties in (11) are not so evident. It takes some work to demonstrate their existence. In particular, one has to calculate the function $I(\mathbf{q}_1, \mathbf{q}_2; \mathbf{q})$ at $\mathbf{q}_2 = 0$ and $\mathbf{q}_2' = 0$. It is not too easy, but possible (for details, see Appendix C), so that we have checked the fulfillment of (11) for the two-gluon contribution at arbitrary ϵ.

In the limit $\epsilon \longrightarrow 0$, we obtain

$$\mathcal{H}^{(8)}_{RRGG}(\mathbf{q}_1, \mathbf{q}_2; \mathbf{q}) = \frac{g^4N^2\Gamma(1-\epsilon)}{(4\pi)^D\pi^{1+\epsilon}}$$
$$\times\left\{(\mathbf{k}^2)^{\epsilon-1}(\mathbf{q}_1'^2\mathbf{q}_2^2+\mathbf{q}_2'^2\mathbf{q}_1^2-\mathbf{q}^2\mathbf{k}^2)\left[\frac{1}{\epsilon^2}-\frac{11}{6\epsilon}+\frac{67}{18}\right.\right.$$
$$\left.-4\zeta(2)+\epsilon\left(-\frac{202}{27}+9\zeta(3)+\frac{11}{6}\zeta(2)\right)\right]$$
$$+\mathbf{q}^2\left[\frac{1}{2}\left(\frac{1}{\epsilon}+\ln\mathbf{q}^2\right)\ln\left(\frac{\mathbf{q}_1^2\mathbf{q}_2^2}{\mathbf{q}^4}\right)-2\zeta(2)\right.$$
$$+\frac{11}{6}\left(\ln\left(\frac{\mathbf{q}_1^2\mathbf{q}_2^2}{\mathbf{k}^2\mathbf{q}^2}\right)+\frac{(\mathbf{q}_1^2+\mathbf{q}_2^2)}{(\mathbf{q}_1^2-\mathbf{q}_2^2)}\ln\left(\frac{\mathbf{q}_1^2}{\mathbf{q}_2^2}\right)\right) \quad (63)$$
$$\left.+\frac{1}{4}\ln^2\left(\frac{\mathbf{q}_1^2}{\mathbf{q}^2}\right)+\frac{1}{4}\ln^2\left(\frac{\mathbf{q}_2^2}{\mathbf{q}^2}\right)\right]+\frac{\mathbf{q}_1\cdot\mathbf{q}_2}{3}-\frac{11}{6}(\mathbf{q}_1^2+\mathbf{q}_2^2)$$
$$-\frac{1}{6}\left(11-\frac{\mathbf{k}^2}{(\mathbf{q}_1^2-\mathbf{q}_2^2)^2}(\mathbf{q}_1^2+\mathbf{q}_2^2+4(\mathbf{q}_1'\cdot\mathbf{q}_2')-2\mathbf{q}^2)\right.$$
$$\left.+\frac{\mathbf{q}_1'^2-\mathbf{q}_2'^2}{(\mathbf{q}_1^2-\mathbf{q}_2^2)}\right)\left(\frac{2\mathbf{q}_1^2\mathbf{q}_2^2}{(\mathbf{q}_1^2-\mathbf{q}_2^2)}\ln\left(\frac{\mathbf{q}_1^2}{\mathbf{q}_2^2}\right)-\mathbf{q}_1^2-\mathbf{q}_2^2\right)$$

$$+ I(\mathbf{q}_1, \mathbf{q}_2; \mathbf{q})\Bigg\} + \frac{g^4 N^2 \Gamma(1-\epsilon)}{(4\pi)^D \pi^{1+\epsilon}} \{\mathbf{q}_i \longleftrightarrow \mathbf{q}_i'\}.$$

In this limit, the function $I(\mathbf{q}_1, \mathbf{q}_2; \mathbf{q})$ takes the form

$$I(\mathbf{q}_1, \mathbf{q}_2; \mathbf{q}) = \frac{1}{2}\int_0^1 \frac{dx}{(\mathbf{q}_1(1-x) + \mathbf{q}_2 x)^2}$$
$$\times \ln\left(\frac{\mathbf{q}_1^2(1-x) + \mathbf{q}_2^2 x}{\mathbf{k}^2 x(1-x)}\right)\Bigg[\mathbf{q}^2(\mathbf{k}^2 - \mathbf{q}_1^2 - \mathbf{q}_2^2) + 2\mathbf{q}_1^2\mathbf{q}_2^2$$
$$- \mathbf{q}_1^2\mathbf{q}_2'^2 - \mathbf{q}_2^2\mathbf{q}_1'^2 + \frac{\mathbf{q}_1^2\mathbf{q}_2'^2 - \mathbf{q}_2^2\mathbf{q}_1'^2}{\mathbf{k}^2}(\mathbf{q}_1^2 - \mathbf{q}_2^2)\Bigg]$$
$$+ \frac{\mathbf{q}^2}{2}\left(4\zeta(2) - \frac{1}{2}\ln^2\left(\frac{\mathbf{q}_1^2}{\mathbf{q}_2^2}\right)\right) - \frac{\mathbf{q}_1^2\mathbf{q}_2'^2 - \mathbf{q}_2^2\mathbf{q}_1'^2}{4\mathbf{k}^2}$$
$$\times \ln\left(\frac{\mathbf{q}_1^2}{\mathbf{q}_2^2}\right)\ln\left(\frac{\mathbf{q}_1^2\mathbf{q}_2^2}{\mathbf{k}^4}\right) - \frac{\mathbf{q}^2}{4}\Bigg[\left(\frac{1}{\epsilon} + \ln\mathbf{q}^2\right)\ln\left(\frac{\mathbf{q}_1^2\mathbf{q}_2^2\mathbf{q}_1'^2\mathbf{q}_2'^2}{\mathbf{q}^8}\right)$$
$$+ \frac{1}{2}\ln^2\left(\frac{\mathbf{q}_1^2}{\mathbf{q}_1'^2}\right) + \frac{1}{2}\ln^2\left(\frac{\mathbf{q}_2^2}{\mathbf{q}_2'^2}\right)\Bigg]. \tag{64}$$

The integral in (64) can be presented in another form:

$$\int_0^1 \frac{dx}{(\mathbf{q}_1(1-x) + \mathbf{q}_2 x)^2}\ln\left(\frac{\mathbf{q}_1^2(1-x) + \mathbf{q}_2^2 x}{\mathbf{k}^2 x(1-x)}\right)$$
$$= \int_0^\infty \frac{dz}{z + \mathbf{k}^2}\frac{1}{\sqrt{(\mathbf{q}_1^2 + \mathbf{q}_2^2 + z)^2 - 4\mathbf{q}_1^2\mathbf{q}_2^2}} \tag{65}$$
$$\times \ln\left(\frac{\mathbf{q}_1^2 + \mathbf{q}_2^2 + z + \sqrt{(\mathbf{q}_1^2 + \mathbf{q}_2^2 + z)^2 - 4\mathbf{q}_1^2\mathbf{q}_2^2}}{\mathbf{q}_1^2 + \mathbf{q}_2^2 + z - \sqrt{(\mathbf{q}_1^2 + \mathbf{q}_2^2 + z)^2 - 4\mathbf{q}_1^2\mathbf{q}_2^2}}\right).$$

It is also possible to express the integral in (64) in terms of dilogarithms, but this expression is not too convenient:

$$\int_0^1 \frac{dx}{(\mathbf{q}_1(1-x) + \mathbf{q}_2 x)^2}\ln\left(\frac{\mathbf{q}_1^2(1-x) + \mathbf{q}_2^2 x}{\mathbf{k}^2 x(1-x)}\right)$$
$$= -\frac{2}{|\mathbf{q}_1||\mathbf{q}_2|\sin\phi}\Bigg[\ln\rho\,\arctan\frac{\rho\sin\phi}{(1-\rho\cos\phi)} \tag{66}$$
$$+ \mathrm{Im}\,(L(\rho\exp i\phi))\Bigg],$$

where ϕ is the angle between $\mathbf{q}_1$ and $\mathbf{q}_2$,

$$\rho = \min\left(\frac{|\mathbf{q}_1|}{|\mathbf{q}_2|}, \frac{|\mathbf{q}_2|}{|\mathbf{q}_1|}\right), \quad L(z) = \int_0^1 \frac{dt}{t}\ln(1-t). \tag{67}$$

6. THE NONFORWARD OCTET BFKL KERNEL

The general form of the kernel (for arbitrary representation $\mathcal{R}$ of the color group in the t channel) is given by Eq. (2). The "virtual" part is universal (does not depend on $\mathcal{R}$) and is determined by the gluon Regge trajectory, which is given by Eqs. (3)–(5). (Recall that in this paper we consider pure gluodynamics.) The quark part of the kernel was considered in [18]. The "real" part, related to real particle production in Reggeon–Reggeon collisions, in the NLA is given by the one-gluon and two-gluon contributions considered in Section 3 and Section 5, respectively. Since the radiative corrections to the effective vertex of the one-gluon production are known only in the limit $\epsilon \longrightarrow 0$, the total "real" part of the kernel can be obtained only in this limit. It is given by the sum of (23) and (63). After powerful cancellations (in particular, between the terms with singularities $1/\epsilon^2$ and all terms with $(\mathbf{q}_1^2 - \mathbf{q}_2^2)$ in denominators), we obtain

$$\mathcal{H}_r^{G(8)}(\mathbf{q}_1, \mathbf{q}_2; \mathbf{q}) = \frac{g^2 N}{2(2\pi)^{D-1}}\Bigg\{\left(\frac{\mathbf{q}_1^2\mathbf{q}_2'^2 + \mathbf{q}_1'^2\mathbf{q}_2^2}{\mathbf{k}^2} - \mathbf{q}^2\right)$$
$$\times\Bigg[\frac{1}{2} + \frac{g^2 N\Gamma(1-\epsilon)(\mathbf{k}^2)^\epsilon}{(4\pi)^{2+\epsilon}}\Bigg(-\frac{11}{6\epsilon} + \frac{67}{18} - \zeta(2)$$
$$+ \epsilon\left(-\frac{202}{27} + 7\zeta(3) + \frac{11}{6}\zeta(2)\right)\Bigg)\Bigg] + \frac{g^2 N\Gamma(1-\epsilon)}{(4\pi)^{2+\epsilon}}$$
$$\times\Bigg[\mathbf{q}^2\left(\frac{11}{6}\ln\left(\frac{\mathbf{q}_1^2\mathbf{q}_2^2}{\mathbf{q}^2\mathbf{k}^2}\right) + \frac{1}{4}\ln\left(\frac{\mathbf{q}_1^2}{\mathbf{q}^2}\right)\ln\left(\frac{\mathbf{q}_1'^2}{\mathbf{q}^2}\right)\right.$$
$$\left. + \frac{1}{4}\ln\left(\frac{\mathbf{q}_2^2}{\mathbf{q}^2}\right)\ln\left(\frac{\mathbf{q}_2'^2}{\mathbf{q}^2}\right) + \frac{1}{4}\ln^2\left(\frac{\mathbf{q}_1^2}{\mathbf{q}_2^2}\right)\right)$$
$$- \frac{\mathbf{q}_1^2\mathbf{q}_2'^2 + \mathbf{q}_2^2\mathbf{q}_1'^2}{2\mathbf{k}^2}\ln^2\left(\frac{\mathbf{q}_1^2}{\mathbf{q}_2^2}\right) + \frac{\mathbf{q}_1^2\mathbf{q}_2'^2 - \mathbf{q}_2^2\mathbf{q}_1'^2}{\mathbf{k}^2}$$
$$\times\ln\left(\frac{\mathbf{q}_1^2}{\mathbf{q}_2^2}\right)\left(\frac{11}{6} - \frac{1}{4}\ln\left(\frac{\mathbf{q}_1^2\mathbf{q}_2^2}{\mathbf{k}^4}\right)\right) + \frac{1}{2}\Bigg[\mathbf{q}^2(\mathbf{k}^2 - \mathbf{q}_1^2 - \mathbf{q}_2^2)$$
$$+ 2\mathbf{q}_1^2\mathbf{q}_2^2 - \mathbf{q}_1^2\mathbf{q}_2'^2 - \mathbf{q}_2^2\mathbf{q}_1'^2 + \frac{\mathbf{q}_1^2\mathbf{q}_2'^2 - \mathbf{q}_2^2\mathbf{q}_1'^2}{\mathbf{k}^2}(\mathbf{q}_1^2 - \mathbf{q}_2^2)\Bigg]$$
$$\times\int_0^1 \frac{dx}{(\mathbf{q}_1(1-x) + \mathbf{q}_2 x)^2}\ln\left(\frac{\mathbf{q}_1^2(1-x) + \mathbf{q}_2^2 x}{\mathbf{k}^2 x(1-x)}\right)\Bigg]\Bigg\}$$
$$+ \frac{g^2 N}{2(2\pi)^{D-1}}\{\mathbf{q}_i \longleftrightarrow \mathbf{q}_i'\}. \tag{68}$$

After cancellation of the terms ~$1/\epsilon^2$, the leading singularity of the kernel is $1/\epsilon$. It turns again into ~$1/\epsilon^2$ after subsequent integrations of the kernel because of the singular behavior of the kernel at $\mathbf{k}^2 = 0$. The additional singularity arises from the region of small $\mathbf{k}^2$, where $\epsilon|\ln\mathbf{k}^2| \sim 1$. Therefore, we have not expanded in ϵ the term $(\mathbf{k}^2)^\epsilon$. The terms ~ϵ are taken into account in the coefficient of the expression divergent at $\mathbf{k}^2 = 0$ in order to conserve all nonvanishing contributions in the limit $\epsilon \longrightarrow 0$ after the integrations.

The symmetries (12) of the kernel are easily seen. The first of them is explicit in (68). To notice the second, it is sufficient to change $x \longleftrightarrow (1-x)$ in the integral in (68).

In order to check that the kernel (68) vanishes at zero transverse momenta of the Reggeons (11), one needs to know the behavior of the integral in (68). A suitable representation for this purpose is given in (65). From this representation, one can see that singularities of the integral at zero transverse momenta of the Reggeons are no more than logarithmic. Verifying Eq. (11) therefore involves no more problems.

In conclusion, let us note that in [17] the octet kernel was obtained using as a basis the bootstrap relation and a specific ansatz to solve it. Our results disagree with the results obtained in [17]. To see the disagreement, it is sufficient to observe that the kernel obtained in [17] is expressed in terms of elementary functions. We conclude that the ansatz used in [17] is not correct.

ACKNOWLEDGMENTS

This work was supported by the Russian Foundation for Basic Research.

APPENDIX A

In this appendix, we present the details of the calculation of the convolution $f_a(k_1, k_2)$ (46).

It is suitable to represent the tensor $c^{\mu\nu}(k_1, k_2)$ in the form

$$c^{\mu\nu}(k_1, k_2) = l_1^{\mu\nu} + l_2^{\mu\nu} + l_3^{\mu\nu}, \tag{A.1}$$

where

$$l_1^{\mu\nu} = -\frac{x\mathbf{q}_1^2}{k^2}\left[\frac{k_{2\perp}^\mu k_{2\perp}^\nu}{\Sigma} + \frac{k_{1\perp}^\mu((1-x)k_1 - k_2)_\perp^\nu}{(1-x)\mathbf{k}_1^2} + \frac{g_\perp^{\mu\nu}}{2}\frac{(1-x)}{\Sigma}\left(\frac{\Sigma}{1-x} - \frac{\mathbf{k}_1^2}{x}\right)\right], \tag{A.2}$$

$$l_2^{\mu\nu} = \frac{1}{k^2}\left[-\frac{q_{1\perp}^\mu \Lambda_\perp^\nu}{1-x} + \left(k - \frac{x\mathbf{k}^2}{\mathbf{k}_1^2}k_1\right)_\perp^\mu q_{1\perp}^\nu - \frac{2x}{\mathbf{k}_1^2}k_{1\perp}^\mu\left(\frac{\mathbf{q}_1\cdot\mathbf{k}_1}{1-x}k_2 - (\mathbf{q}_1\cdot\mathbf{k})k_1\right)_\perp^\nu - (\mathbf{q}_1\cdot\mathbf{\Lambda})g_\perp^{\mu\nu}\right], \tag{A.3}$$

$$l_3^{\mu\nu} = -\frac{xk_{1\perp}^\mu(q_1-k_1)_\perp^\nu}{\mathbf{k}_1^2} + \frac{(q_1-k_1)_\perp^\mu(q_1-k_1)_\perp^\nu}{\tilde{t}_1} + \frac{g_\perp^{\mu\nu}}{2}\frac{(1-x)}{\tilde{t}_1}(\mathbf{q}_1^2 - 2\mathbf{k}_1\cdot\mathbf{q}_1). \tag{A.4}$$

Analogous decomposition is made for the tensor $c'_{\mu\nu}(k_1, k_2)$ obtained from $c_{\mu\nu}(k_1, k_2)$ by the substitution $\mathbf{q}_i \longleftrightarrow \mathbf{q}'_i$, $i = 1, 2$, and we denote as $l'_{n\mu\nu}$ $(n = 1, 2, 3)$ the tensors $l_{n\mu\nu}$ after this substitution.

The calculation of the products $l_n^{\mu\nu}l'_{n'\mu\nu}$ is significantly simpler than the calculation of the whole convolution $f_a(k_1, k_2)$ (46), though still rather tedious. The results are

$$l_1^{\mu\nu}l'_{1\mu\nu} = \frac{x^2\mathbf{q}_1'^2\mathbf{q}_1^2}{k^4}\left\{-k^2\left(\frac{\mathbf{k}_1\cdot\mathbf{k}_2}{\mathbf{k}_1^2\Sigma} + \frac{1-x}{x\Sigma} - \frac{1}{x(1-x)\mathbf{k}_1^2}\right) + \frac{1+\epsilon}{2}\left[\frac{1-x}{\Sigma}k^2\left(1 - 2x + \frac{2\mathbf{\Lambda}\cdot\mathbf{k}}{k^2}\right)\right]^2\right\}, \tag{A.5}$$

$$l_2^{\mu\nu}l'_{1\mu\nu} = \frac{x\mathbf{q}_1'^2}{2k^4}\left\{-2(1+\epsilon)(1-x)\left(1 - 2x + \frac{2\mathbf{\Lambda}\cdot\mathbf{k}}{k^2}\right)\times\frac{(\mathbf{q}_1\cdot\mathbf{\Lambda})k^2}{\Sigma} - k^2(\mathbf{q}_1\cdot\mathbf{k}_1)\left(\frac{xk^2}{\mathbf{k}_1^2\Sigma} - \frac{1-x}{\Sigma} - \frac{1-3x+x^2}{(1-x)\mathbf{k}_1^2}\right) + k^2(\mathbf{q}_1\cdot\mathbf{k})\left(\frac{1-2x}{\Sigma} - \frac{2}{\mathbf{k}_1^2}\right)\right\}, \tag{A.6}$$

$$l_3^{\mu\nu}l'_{1\mu\nu} = \frac{x\mathbf{q}_1'^2}{2k^2}\left\{(1+\epsilon)(1-x)^2\frac{k^2}{\Sigma\tilde{t}_1}(\mathbf{q}_1^2 - 2\mathbf{k}_1\cdot\mathbf{q}_1)\left(1 - 2x + \frac{2\mathbf{\Lambda}\cdot\mathbf{k}}{k^2}\right) - \frac{1}{2(1-x)\mathbf{k}_1^2\tilde{t}_1}\times[\mathbf{q}_1^2(\mathbf{q}_2^2 + (1-x)(\mathbf{q}_1^2 - \mathbf{k}^2)) - 2(1-x)k^2(\mathbf{q}_1^2 - \mathbf{k}_1\cdot\mathbf{q}_1)] - \frac{\mathbf{q}_2^2}{2\Sigma\tilde{t}_1}[\mathbf{q}_2^2 - 4(1-x)(\mathbf{q}_1^2 - 2\mathbf{k}_1\cdot\mathbf{q}_1)] - \frac{4(1-x)^2\mathbf{q}_1^2 - \mathbf{q}_2^2}{2x(1-x)\tilde{t}_1} + \frac{x\mathbf{k}^2(2\mathbf{q}_1\cdot\mathbf{k}_2 - \mathbf{k}^2)}{2\mathbf{k}_1^2\Sigma}\right\}. \tag{A.7}$$

$$+\frac{1}{\Sigma}\Big[(1-x)(\mathbf{q}_1^2-\mathbf{k}_1\cdot\mathbf{q}_1)+\frac{1-2x}{2}(\mathbf{q}_2^2-\mathbf{k}^2)\Big]$$
$$+\frac{1}{2(1-x)\mathbf{k}_1^2}(-2(1-3x+x^2)(\mathbf{q}_1\cdot\mathbf{k}_1)$$
$$+(1-x)\mathbf{k}^2+x\mathbf{q}_2^2-2\mathbf{q}_1^2)\Big\},$$

$$l_2^{\mu\nu}l'_{2\mu\nu}=\frac{x(1-x)}{k^2}\Bigg[\frac{\mathbf{q}_1\cdot\mathbf{q}'_1}{2}\left(\frac{1}{(1-x)^2}+\frac{\mathbf{k}^2}{\mathbf{k}_1^2}\right)$$
$$-\frac{(\mathbf{q}_1\cdot\mathbf{k}_1)(\mathbf{q}'_1\cdot\mathbf{\Lambda})}{(1-x)\mathbf{k}_1^2}\Bigg]+(1+\epsilon)\frac{(\mathbf{q}_1\cdot\mathbf{\Lambda})(\mathbf{q}'_1\cdot\mathbf{\Lambda})}{k^4} \quad (A.8)$$
$$+\{\mathbf{q}_1\longleftrightarrow\mathbf{q}'_1\},$$

$$l_3^{\mu\nu}l'_{3\mu\nu}=x^2\frac{\mathbf{q}_1\cdot\mathbf{q}'_1}{2\mathbf{k}_1^2}-\frac{\mathbf{q}^2(\mathbf{q}_1\cdot\mathbf{q}'_1)}{4\tilde{t}_1\tilde{t}'_1}+\frac{(1+\epsilon)(1-x)^2}{4}$$
$$\times\frac{(\mathbf{q}_1^2-2\mathbf{k}_1\cdot\mathbf{q}_1)}{\tilde{t}_1}\frac{(\mathbf{q}_1'^2-2\mathbf{k}_1\cdot\mathbf{q}'_1)}{\tilde{t}'_1}-\frac{x(1-x)}{2\mathbf{k}_1^2}$$
$$\times\frac{(\mathbf{q}_1'^2-2(\mathbf{k}_1\cdot\mathbf{q}'_1))(\mathbf{k}_1\cdot\mathbf{q}_1)}{\tilde{t}'_1}-\frac{\mathbf{q}_1'^2-2\mathbf{k}_1\cdot\mathbf{q}'_1}{2\tilde{t}_1\tilde{t}'_1} \quad (A.9)$$
$$\times\Big[(1-2x)(\mathbf{q}_1\cdot\mathbf{q})+\frac{2x(\mathbf{k}_1\cdot\mathbf{q}_1)}{\mathbf{k}_1^2}\mathbf{q}\cdot(\mathbf{q}_1-\mathbf{k}_1)\Big]$$
$$+\{\mathbf{q}_1\longleftrightarrow\mathbf{q}'_1,\mathbf{q}\longrightarrow-\mathbf{q}\},$$

$$l_3^{\mu\nu}l'_{2\mu\nu}=-(1+\epsilon)(1-x)(\mathbf{q}_1^2-2\mathbf{k}_1\cdot\mathbf{q}_1)\frac{\mathbf{q}'_1\cdot\mathbf{\Lambda}}{k^2\tilde{t}_1}$$
$$+x(1-x)\frac{\mathbf{q}'_1\cdot\mathbf{k}_1}{2\mathbf{k}_1^2\tilde{t}_1}(\mathbf{q}_1^2-2\mathbf{k}_1\cdot\mathbf{q}_1)$$
$$+\frac{x}{k^2\mathbf{k}_1^2}[(\mathbf{k}_1\cdot\mathbf{q}_1)(\mathbf{q}'_1\cdot\mathbf{\Lambda})-((\mathbf{q}'_1\cdot\mathbf{k}_1)(\mathbf{q}_1\cdot\mathbf{k})$$
$$-(\mathbf{q}_1\cdot\mathbf{k}_1)(\mathbf{q}'_1\cdot\mathbf{k}))]-\frac{x^2(\mathbf{q}_1\cdot\mathbf{q}'_1)}{2\mathbf{k}_1^2}-\frac{x(\mathbf{q}_1\cdot\mathbf{q}'_1)}{2(1-x)k^2}$$
$$-\frac{x(\mathbf{q}_1\cdot\mathbf{q}'_1)}{2\tilde{t}_1\tilde{k}_1^2}(\mathbf{q}_1^2-\mathbf{q}_1\cdot\mathbf{k}_1)$$
$$+\frac{\mathbf{q}_1^2(\mathbf{q}'_1\cdot\mathbf{k}_1)-(\mathbf{k}_1\cdot\mathbf{q}_1)(\mathbf{q}'_1\cdot\mathbf{q}_1)}{k^2\tilde{t}_1}$$
$$\times\Big[2+\frac{x}{2\mathbf{k}_1^2}\left(\frac{\mathbf{q}_1^2+\mathbf{k}^2}{1-x}-k^2\right)\Big]+\frac{x\mathbf{q}_1^2}{4(1-x)\tilde{t}_1\mathbf{k}_1^2k^2} \quad (A.10)$$
$$\times[(\mathbf{q}_1\cdot\mathbf{q}'_1)(\mathbf{q}_1^2+(2x-1)\mathbf{k}^2)-2x(\mathbf{q}'_1\cdot\mathbf{k})\mathbf{q}_1^2]$$
$$+\frac{1}{4(1-x)\tilde{t}_1k^2}\{(\mathbf{q}_1\cdot\mathbf{q}'_1)[\mathbf{q}_1^2(3-4x)-(1-2x)^2\mathbf{k}^2]$$
$$-\mathbf{q}_1^2(\mathbf{q}'_1\cdot\mathbf{k})\cdot2(1+4x(1-x))+4(\mathbf{q}_1\cdot\mathbf{q}'_1)(\mathbf{q}_1\cdot\mathbf{k})\}$$
$$+\frac{x}{4(1-x)\mathbf{k}_1^2k^2}[2\mathbf{q}_1^2(\mathbf{q}'_1\cdot\mathbf{\Lambda})+(\mathbf{q}_1\cdot\mathbf{q}'_1)(\mathbf{q}_1^2+\mathbf{k}^2)]$$
$$-x(1-x)\frac{(\mathbf{q}_1\cdot\mathbf{q}'_1)\mathbf{k}^2}{2k^2\mathbf{k}_1^2}+[(\mathbf{k}_1\cdot\mathbf{q}_1)(\mathbf{q}'_1\cdot\mathbf{k})$$
$$-(\mathbf{q}'_1\cdot\mathbf{k}_1)(\mathbf{q}_1\cdot\mathbf{k})]\left(\frac{2}{k^2\tilde{t}_1}+\frac{x\mathbf{q}_1^2}{(1-x)\mathbf{k}_1^2\tilde{t}_1k^2}\right).$$

With the aid of Eqs. (A.1)–(A.10) and the equations obtained from them by the substitution $\mathbf{q}_i\longleftrightarrow\mathbf{q}'_i$, we come to (59).

APPENDIX B

In this appendix, we present the details of the calculation of the integrals in (57) with $f_a(k_1, k_2)$ given by (59). First, let us recall the notation used:

$$\mathbf{k}=\mathbf{k}_1+\mathbf{k}_2=\mathbf{q}_1-\mathbf{q}_2,$$
$$\mathbf{\Lambda}=(1-x)\mathbf{k}_1-x\mathbf{k}_2,\quad\mathbf{q}'_i=\mathbf{q}_i-\mathbf{q},\quad i=1,2;$$
$$k^2=\frac{((1-x)\mathbf{k}_1-x\mathbf{k}_2)^2}{x(1-x)},\ \Sigma=\mathbf{\Lambda}^2+x(1-x)\mathbf{k}^2, \quad (B.1)$$
$$\tilde{t}_1=-\frac{1}{x}((1-x)\mathbf{k}_1^2+x(\mathbf{k}_1-\mathbf{q}_1)^2),$$

and $\tilde{t}'_1$ is obtained from $\tilde{t}_1$ by the substitution $\mathbf{q}_1\longrightarrow\mathbf{q}'_1$.

It is easy to see that

$$J_0=\int_0^1\frac{dx}{x(1-x)}\int\frac{d^{2+2\epsilon}k_1}{\pi^{1+\epsilon}\Gamma(1-\epsilon)}\Bigg\{\frac{1+\epsilon}{k^2}\Bigg[\frac{x^2(1-x)}{\Sigma}$$
$$\times\mathbf{q}_1'^2\left(\mathbf{q}_1\cdot\mathbf{\Lambda}+(1-2x)(1-x)\frac{\mathbf{q}_1^2(\mathbf{\Lambda}\cdot\mathbf{k})}{\Sigma}\right)$$
$$+\frac{(\mathbf{q}'_1\cdot\mathbf{\Lambda})(\mathbf{q}_1\cdot\mathbf{\Lambda})}{k^2}\Bigg]+\frac{x(1-x)\mathbf{q}_1'^2}{k^2\Sigma} \quad (B.2)$$
$$\times\left(\frac{x(1-x)\mathbf{q}_1^2}{2k^2\Sigma}k_\perp^\mu k_\perp^\nu-\frac{k_\perp^\mu q_{1\perp}^\nu}{k^2}\right)$$
$$\times(2(1+\epsilon)\Lambda_\mu\Lambda_\nu+\mathbf{\Lambda}^2g_{\mu\nu}^\perp)\Bigg\}=0.$$

The zero appears as a result of the integration with respect to $\mathbf{k}_1$ (or, equivalently, with respect to $\mathbf{\Lambda}$). The first two terms here give zero due to parity, the third vanishes due to the dimensional regularization, and the remaining terms vanish due to the isotropy of the transverse space leading to the replacement $2(1+\epsilon)\Lambda_\mu\Lambda_\nu \longrightarrow -\mathbf{\Lambda}^2 g^{\perp}_{\mu\nu}$ after the angular integration.

The calculation of the contributions of terms with the denominators Σ, Σ^2, $k^2\Sigma$, and $k^2\mathbf{k}^2$ is straightforward. We obtain, using usual Feynman parametrization if necessary,

$$I_\Sigma = \int\frac{d^{2+2\epsilon}k_1}{\pi^{1+\epsilon}\Gamma(1-\epsilon)}\frac{1}{\Sigma} = \frac{-1}{\epsilon}[x(1-x)\mathbf{k}^2]^\epsilon,$$

$$I_{\Sigma^2} = \int\frac{d^{2+2\epsilon}k_1}{\pi^{1+\epsilon}\Gamma(1-\epsilon)}\frac{1}{\Sigma^2} = [x(1-x)\mathbf{k}^2]^{\epsilon-1},$$

$$I_{\Lambda^2\Sigma} = \int\frac{d^{2+2\epsilon}k_1}{\pi^{1+\epsilon}\Gamma(1-\epsilon)}\frac{1}{\mathbf{\Lambda}^2\Sigma} = \frac{1}{\epsilon}[x(1-x)\mathbf{k}^2]^{\epsilon-1}, \tag{B.3}$$

$$I_{\Lambda^2 k_1^2} = \int\frac{d^{2+2\epsilon}k_1}{\pi^{1+\epsilon}\Gamma(1-\epsilon)}\frac{1}{\mathbf{\Lambda}^2\mathbf{k}_1^2} = \frac{\Gamma^2(\epsilon)}{\Gamma(2\epsilon)}[x^2\mathbf{k}^2]^{\epsilon-1}.$$

The subsequent integration of these terms with respect to x can be done without difficulties.

The integrals of the terms with the denominators $\mathbf{k}_1^2\Sigma$ and $\mathbf{k}_1^2\tilde{t}_1$ with respect to $\mathbf{k}_1$ cannot be expressed in terms of elementary functions at arbitrary ϵ. Nevertheless, these terms do not create problems. For such terms, it is convenient to make integration with respect to $\mathbf{k}_1$,

$$I_{k_1^2\Sigma} = \int\frac{d^{2+2\epsilon}k_1}{\pi^{1+\epsilon}\Gamma(1-\epsilon)}\frac{1}{\mathbf{k}_1^2\Sigma} = (\mathbf{k}^2)^{\epsilon-1}\int_0^1\frac{dz}{(xz(1-xz))^{1-\epsilon}},$$

$$I_{k_1^2 t_1} = \int\frac{d^{2+2\epsilon}k_1}{\pi^{1+\epsilon}\Gamma(1-\epsilon)}\frac{1}{\mathbf{k}_1^2\tilde{t}_1} \tag{B.4}$$

$$= -x(\mathbf{q}_1^2)^{\epsilon-1}\int_0^1\frac{dz}{(xz(1-xz))^{1-\epsilon}},$$

then to introduce the variable $y = xz$ instead of z and to change the order of the integrations with respect to x and y. After that, the integrals can be easily calculated.

This way, we obtain

$$J_1 = \int_0^1\frac{dx}{x(1-x)_+}\int\frac{d^{2+2\epsilon}k_1}{\pi^{1+\epsilon}\Gamma(1-\epsilon)}\left\{\frac{x^2\mathbf{q}_1'^2\mathbf{q}_2^2}{4\mathbf{k}_1^2\Sigma}\right.$$

$$+\frac{x\mathbf{q}_1'^2\mathbf{q}_2^2}{4(1-x)\mathbf{k}_1^2k^2}+\frac{x\mathbf{q}_1'^2\mathbf{q}_2^2}{4(1-x)\mathbf{k}_1^2k^2}+\left(\frac{x(1-x)}{\Sigma}\right)^2\frac{\mathbf{q}_1'^2\mathbf{q}_1^2}{2}$$

$$\times\left(\frac{1+\epsilon}{2}-(3+2\epsilon)x(1-x)\right)-\frac{x(1-x)\mathbf{q}_1'^2}{2k^2\Sigma} \tag{B.5}$$

$$\times[(1-x)((1+\epsilon)(2(\mathbf{k}_1\cdot\mathbf{q}_1)-x\mathbf{q}_1^2)-\epsilon x(\mathbf{k}^2-\mathbf{q}_2^2))$$

$$\left.-(1+\epsilon)\mathbf{k}_2^2+2\mathbf{q}_2^2]\right\} = \frac{\Gamma^2(1+\epsilon)}{\Gamma(1+2\epsilon)}\frac{\mathbf{q}_1'^2\mathbf{q}_2^2}{2\epsilon\mathbf{k}^2}(\mathbf{k}^2)^\epsilon\left\{\psi(1)\right.$$

$$\left.+\psi(\epsilon)-2\psi(2\epsilon)-\frac{11+7\epsilon}{2(1+2\epsilon)(3+2\epsilon)}\right\},$$

$$J_2 = \int_0^1\frac{dx}{x(1-x)_+}\int\frac{d^{2+2\epsilon}k_1}{\pi^{1+\epsilon}\Gamma(1-\epsilon)}\frac{x\mathbf{q}_1^2\mathbf{q}^2}{4\tilde{t}_1\mathbf{k}_1^2} \tag{B.6}$$

$$= -\frac{\Gamma^2(\epsilon)}{4\Gamma(2\epsilon)}(\mathbf{q}_1^2)^\epsilon\mathbf{q}^2[\psi(\epsilon)-\psi(2\epsilon)].$$

The integrals with $\tilde{t}_1\tilde{t}_1'$ in denominators can be calculated with the help of the trick used in [18]. Let us consider in (59) the first such term. It can be represented as

$$-(\mathbf{q}_1\cdot\mathbf{q})(1-x)\frac{\mathbf{q}_1'^2-2(\mathbf{k}_1\cdot\mathbf{q}_1')}{\tilde{t}_1\tilde{t}_1'} \tag{B.7}$$

$$= (\mathbf{q}_1\cdot\mathbf{q})(1-x)\left[\frac{1}{\tilde{t}_1}+\frac{\mathbf{k}_1^2}{x\tilde{t}_1\tilde{t}_1'}\right].$$

The first term on the right-hand side can be integrated with respect to k_1 and then with respect to x. For the second, it seems more convenient to begin with the integration with respect to x in (57), getting

$$\int_0^1\frac{dx}{x(1-x)}(\mathbf{q}_1\cdot\mathbf{q})(1-x)\frac{\mathbf{k}_1^2}{x\tilde{t}_1\tilde{t}_1'} \tag{B.8}$$

$$= \frac{\mathbf{q}_1\cdot\mathbf{q}}{(\mathbf{q}_1'-\mathbf{k}_1)^2-(\mathbf{q}_1-\mathbf{k}_1)^2}\ln\frac{(\mathbf{q}_1'-\mathbf{k}_1)^2}{(\mathbf{q}_1-\mathbf{k}_1)^2}.$$

With the help of the representation

$$\frac{1}{(\mathbf{q}_1'-\mathbf{k}_1)^2-(\mathbf{q}_1-\mathbf{k}_1)^2}\ln\frac{(\mathbf{q}_1'-\mathbf{k}_1)^2}{(\mathbf{q}_1-\mathbf{k}_1)^2} \tag{B.9}$$

$$= \int_0^1 dz\frac{1}{z(\mathbf{q}_1'-\mathbf{k}_1)^2+(1-z)(\mathbf{q}_1-\mathbf{k}_1)^2},$$

the integration with respect to k_1 and the subsequent

integration with respect to z become trivial and give

$$J_3 = -\int_0^1 \frac{dx}{x(1-x)_+}\int \frac{d^{2+2\epsilon}k_1}{\pi^{1+\epsilon}\Gamma(1-\epsilon)}(\mathbf{q}_1\cdot\mathbf{q})(1-x) \times \frac{\mathbf{q}_1'^2 - 2(\mathbf{k}_1\cdot\mathbf{q}_1')}{\tilde{t}_1\tilde{t}_1'} = -\frac{\Gamma^2(1+\epsilon)}{\Gamma(1+2\epsilon)}\frac{(\mathbf{q}_1\cdot\mathbf{q})}{\epsilon(1+2\epsilon)} \times [(\mathbf{q}^2)^\epsilon - (\mathbf{q}_1^2)^\epsilon]. \quad \text{(B.10)}$$

Analogously, we obtain

$$J_4 = \int_0^1 \frac{dx}{x(1-x)}\int \frac{d^{2+2\epsilon}k_1}{\pi^{1+\epsilon}\Gamma(1-\epsilon)}\frac{(1+\epsilon)(1-x)^2}{4} \times \frac{(\mathbf{q}_1'^2 - 2(\mathbf{k}_1\cdot\mathbf{q}_1'))(\mathbf{q}_1^2 - 2(\mathbf{k}_1\cdot\mathbf{q}_1))}{\tilde{t}_1\tilde{t}_1'} \quad \text{(B.11)}$$

$$= -\frac{\Gamma^2(1+\epsilon)}{\Gamma(1+2\epsilon)}\frac{(1+\epsilon)}{8\epsilon}\frac{((\mathbf{q}_1'^2)^{1+\epsilon} + (\mathbf{q}_1^2)^{1+\epsilon} - (\mathbf{q}^2)^{1+\epsilon})}{(1+2\epsilon)(3+2\epsilon)}.$$

The terms in $f_a(k_1, k_2)$ with the denominator $k^2\tilde{t}_1$ and with x^n in numerators at natural n can be calculated by performing the integration with respect to $\mathbf{k}_1$ at fixed Feynman parameter z and then making the change of variable $y = xz$:

$$\int_0^1 \frac{dx}{x(1-x)}\int \frac{d^{2+2\epsilon}k_1}{\pi^{1+\epsilon}\Gamma(1-\epsilon)}\frac{x^n}{k^2\tilde{t}_1} = -\int_0^1 dx\int_0^1 dz \frac{x^{n+1}}{\{xz[x(1-z)\mathbf{q}_2^2 + (1-x)\mathbf{q}_1^2]\}^{1-\epsilon}} \quad \text{(B.12)}$$

$$= -\int_0^1 dy y^{\epsilon-1}\int_y^1 dx \frac{x^n}{[x(\mathbf{q}_2^2 - \mathbf{q}_1^2) + \mathbf{q}_1^2 - y\mathbf{q}_2^2]^{1-\epsilon}}.$$

The change of variable $y = xz$ has been performed in the last equality. This integral can now be calculated integrating first with respect to x and then with respect to y. The complete calculation for all such terms in (59) is long, but straightforward. The integration of the terms

$$\frac{1}{k^2\tilde{t}_1}\left[-\mathbf{q}_1'^2\mathbf{q}_2^2\frac{(1-x)\mathbf{k}_1^2}{\Sigma} + \frac{1+\epsilon}{2}(1-x)\frac{\mathbf{k}_1^2\mathbf{k}_2^2\mathbf{q}_1'^2}{\Sigma}\right]$$

can be done quite analogously, since under transformation (49) they acquire the form of the terms discussed above. In this way, we obtain

$$\int_0^1 \frac{dx}{x(1-x)}\int \frac{d^{2+2\epsilon}k_1}{\pi^{1+\epsilon}\Gamma(1-\epsilon)}\frac{1}{k^2\tilde{t}_1}[2((\mathbf{q}_1\cdot\mathbf{q}_2)(\mathbf{k}_1\cdot\mathbf{q}_1') - (\mathbf{q}_1'\cdot\mathbf{q}_2)(\mathbf{k}_1\cdot\mathbf{q}_1)) + x\mathbf{q}_2'^2\mathbf{q}_1^2 - x\mathbf{k}^2(\mathbf{q}_1\cdot\mathbf{q}) + \mathbf{q}_1^2(\mathbf{q}_1'\cdot\mathbf{q}) - \mathbf{q}_1'^2\mathbf{q}_2^2\frac{(1-x)\mathbf{k}_1^2}{\Sigma}\Big] = \frac{\Gamma(\epsilon)\Gamma(1+\epsilon)}{2\Gamma(2+2\epsilon)} \quad \text{(B.13)}$$

$$\times\left[\mathbf{q}_1'^2(\mathbf{q}_1^2)^\epsilon + \frac{(\mathbf{q}^2 - \mathbf{q}_1^2)}{(\mathbf{q}_1^2 - \mathbf{q}_2^2)}((\mathbf{q}_1^2)^\epsilon(\mathbf{q}_1^2 + \mathbf{q}_2^2) - 2(\mathbf{q}_2^2)^{1+\epsilon})\right],$$

$$\int_0^1 \frac{dx}{x(1-x)}\int \frac{d^{2+2\epsilon}k_1}{\pi^{1+\epsilon}\Gamma(1-\epsilon)}\frac{(1+\epsilon)}{2}\frac{(1-x)}{k^2\tilde{t}_1} \times\left\{(\mathbf{q}_1^2 - 2\mathbf{k}_1\cdot\mathbf{q}_1)(\mathbf{q}_1'^2(1-x) - 2\mathbf{q}_1'\cdot\mathbf{\Lambda}) + \frac{\mathbf{k}_1^2\mathbf{k}_2^2\mathbf{q}_1'^2}{\Sigma}\right\}$$

$$= \frac{\Gamma(\epsilon)\Gamma(2+\epsilon)}{4\Gamma(4+2\epsilon)}\Big[(2(1+\epsilon)\mathbf{q}_1^2\mathbf{q}_2^2((\mathbf{q}_1^2)^\epsilon - (\mathbf{q}_2^2)^\epsilon) - \epsilon(\mathbf{q}_1^2 + \mathbf{q}_2^2)((\mathbf{q}_1^2)^{\epsilon+1} - (\mathbf{q}_2^2)^{\epsilon+1}))\left(\frac{\mathbf{k}^2}{(\mathbf{q}_1^2 - \mathbf{q}_2^2)^3}\right. \quad \text{(B.14)}$$

$$\times(\mathbf{q}_1^2 + \mathbf{q}_2^2 + 2\mathbf{q}_1'^2 + 2\mathbf{q}_2'^2 - 2\mathbf{k}^2 - 2\mathbf{q}^2) - \frac{\mathbf{q}_1'^2 - \mathbf{q}_2'^2}{(\mathbf{q}_1^2 - \mathbf{q}_2^2)^2}\Big) + \frac{((\mathbf{q}_1^2)^{\epsilon+1} - (\mathbf{q}_2^2)^{\epsilon+1})}{(\mathbf{q}_1^2 - \mathbf{q}_2^2)}(\epsilon(\mathbf{q}_1'^2 + \mathbf{q}_2'^2 - \mathbf{k}^2) - 2(1+\epsilon)(\mathbf{q}^2 - \mathbf{q}_1^2))\Big].$$

All the calculations discussed before were done exactly at arbitrary ϵ. This cannot be done for the remaining terms. They contribute into the function $I(\mathbf{q}_1, \mathbf{q}_2; \mathbf{q})$ [see (62)]. We have used the following equality:

$$\int_0^1 \frac{dx}{x(1-x)_+}\int \frac{d^{2+2\epsilon}k_1}{\pi^{1+\epsilon}\Gamma(1-\epsilon)}\frac{(\mathbf{q}^2)^2}{8\tilde{t}_1\tilde{t}_1'} = -\frac{\Gamma^2(\epsilon)}{\Gamma(2\epsilon)}\frac{(\mathbf{q}^2)^{1+\epsilon}}{16}\Big[\frac{2}{\epsilon} - 2\psi(1) + 2\psi(1-\epsilon) - 4\psi(1+\epsilon) + 4\psi(1+2\epsilon)\Big] \quad \text{(B.15)}$$

$$-\frac{(\mathbf{q}^2)^2}{8}\int \frac{d^{2+2\epsilon}k_1}{\pi^{1+\epsilon}\Gamma(1-\epsilon)}\frac{\ln(\mathbf{l}^2/\mathbf{q}^2)}{(\mathbf{q}_1 - \mathbf{l})^2(\mathbf{q}_1' - \mathbf{l})^2}.$$

This equality can be obtained performing the integration with respect to x first, using the representation

(B.9) and the integral

$$\int \frac{d^{2+2\epsilon}l}{\pi^{1+\epsilon}\Gamma(1-\epsilon)}\frac{\ln(\mathbf{l}^2/\mathbf{q}^2)}{\mathbf{l}^2(\mathbf{q}-\mathbf{l})^2} = -\frac{\Gamma^2(\epsilon)}{2\Gamma(2\epsilon)}\frac{(\mathbf{q}^2)^\epsilon}{\mathbf{q}^2} \times\left[\frac{1}{\epsilon} - 2(\psi(1)-\psi(1-\epsilon)+\psi(1+\epsilon)-\psi(1+2\epsilon))\right]. \quad \text{(B.16)}$$

The last integral can be easily obtained with the help of the generalized Feynman parametrization.

Using the integrals calculated above, we come to the representation (61) for the two-gluon contribution to the kernel.

In the limit $\epsilon \longrightarrow 0$, the expression (64) for $I(\mathbf{q}_1, \mathbf{q}_2; \mathbf{q})$ was obtained by performing the integration with respect to $\mathbf{k}$ in (62) first. We have

$$\int \frac{d^{2+2\epsilon}k_1}{\pi^{1+\epsilon}\Gamma(1-\epsilon)}\frac{1}{k^2\tilde{t}_1\mathbf{k}_1^2} \simeq -\frac{1-x}{\mathbf{q}_1^2\mathbf{k}^2}\left\{\frac{\Gamma^2(\epsilon)}{\Gamma(2\epsilon)}x^{2\epsilon-1}(\mathbf{k}^2)^\epsilon + \frac{(\mathbf{q}_1^2-\mathbf{q}_2^2)}{(\mathbf{q}_1^2(1-x)+\mathbf{q}_2^2x)}\left[\ln(x(\mathbf{q}_1^2(1-x)+\mathbf{q}_2^2x)^2 + \frac{2-(\mathbf{q}_1^2(1-x))^\epsilon}{\epsilon}\right] - \frac{2\mathbf{k}(\mathbf{q}_1(1-x)+\mathbf{q}_2x)}{(\mathbf{q}_1(1-x)+\mathbf{q}_2x)^2} \times\left[\ln\frac{\mathbf{q}_1^2(\mathbf{q}_1^2(1-x)+\mathbf{q}_2^2x)}{x\mathbf{k}^2} + \frac{1-(\mathbf{q}_1^2(1-x))^\epsilon}{\epsilon}\right]\right\}, \quad \text{(B.17)}$$

$$\int \frac{d^{2+2\epsilon}k_1}{\pi^{1+\epsilon}\Gamma(1-\epsilon)}\frac{\mathbf{k}_1}{k^2\tilde{t}_1\mathbf{k}_1^2} \simeq -x(1-x) \times\left\{\frac{\mathbf{q}_1}{\mathbf{q}_1^2(\mathbf{q}_1(1-x)+\mathbf{q}_2x)^2}\left[\ln\frac{\mathbf{q}_1^2(\mathbf{q}_1^2(1-x)+\mathbf{q}_2^2x)}{x\mathbf{k}^2} + \frac{1-(\mathbf{q}_1^2(1-x))^\epsilon}{\epsilon}\right] + \frac{\mathbf{k}}{x\mathbf{k}^2}\left[\frac{1}{(\mathbf{q}_1^2(1-x)+\mathbf{q}_2^2x)} \times\left(\ln\frac{x(\mathbf{q}_1^2(1-x)+\mathbf{q}_2^2x)^2}{\mathbf{q}_1^2(1-x)} + \frac{1}{\epsilon}\right) - \frac{1}{(\mathbf{q}_1(1-x)+\mathbf{q}_2x)^2}\ln\frac{\mathbf{q}_1^2(1-x)+\mathbf{q}_2^2x}{x(1-x)\mathbf{k}^2}\right]\right\}, \quad \text{(B.18)}$$

$$\int \frac{d^{2+2\epsilon}l}{\pi^{1+\epsilon}\Gamma(1-\epsilon)}\frac{\ln(\mathbf{l}^2/\mathbf{q}^2)}{(\mathbf{q}_1-\mathbf{l})^2(\mathbf{q}_1'-\mathbf{l})^2} \simeq \frac{1}{\mathbf{q}^2}\left[\left(\frac{1}{\epsilon}+\ln\mathbf{q}^2\right)\ln\left(\frac{\mathbf{q}_1^2\mathbf{q}_1'^2}{(\mathbf{q}^2)^2}\right) + \frac{1}{2}\ln^2\left(\frac{\mathbf{q}_1^2}{\mathbf{q}_1'^2}\right)\right]. \quad \text{(B.19)}$$

The integrals (B.17) and (B.18) are calculated for arbitrary small $\mathbf{k}^2$ and for x arbitrarily close to zero or unity.

The approximate form (64) for $I(\mathbf{q}_1, \mathbf{q}_2; \mathbf{q})$ can be obtained using (B.17)–(B.19) and the relation

$$\int_0^1 \frac{xdx}{(\mathbf{q}_1(1-x)-\mathbf{q}_2x)^2}\ln\left(\frac{\mathbf{q}_1^2(1-x)+\mathbf{q}_2^2x}{\mathbf{k}^2x(1-x)}\right) = \frac{\mathbf{k}^2+\mathbf{q}_1^2-\mathbf{q}_2^2}{2\mathbf{k}^2}\int_0^1\frac{dx}{(\mathbf{q}_1(1-x)-\mathbf{q}_2x)^2} \times\ln\left(\frac{\mathbf{q}_1^2(1-x)+\mathbf{q}_2^2x}{\mathbf{k}^2x(1-x)}\right) - \frac{1}{2\mathbf{k}^2}\left(L\left(1-\frac{\mathbf{q}_1^2}{\mathbf{q}_2^2}\right)-L\left(1-\frac{\mathbf{q}_2^2}{\mathbf{q}_1^2}\right)\right) - \frac{1}{4\mathbf{k}^2}\ln\left(\frac{\mathbf{q}_1^2\mathbf{q}_2^2}{\mathbf{k}^4}\right). \quad \text{(B.20)}$$

APPENDIX C

Due to the symmetries (12) of the kernel in (61), it is sufficient to show that the kernel vanishes at zero transverse momentum of one of the Reggeons, say, at $\mathbf{q}_2 = 0$. But even in this special case, integration in (62) cannot be performed in terms of elementary functions. Fortunately, expression (62) can be simplified at $\mathbf{q}_2 = 0$ and represented as

$$I(\mathbf{q}_1, \mathbf{q}_2; \mathbf{q})\big|_{\mathbf{q}_2=0} = -\frac{\Gamma^2(\epsilon)}{2\Gamma(2\epsilon)}\mathbf{q}^2(\mathbf{k}^2)^\epsilon[\psi(1)+\psi(\epsilon) - 2\psi(2\epsilon)] - \frac{(\mathbf{q}^2)^2}{4}\frac{1}{\pi^{1+\epsilon}\Gamma(1-\epsilon)} \times\int\frac{d^{2+2\epsilon}l}{\mathbf{l}^2(\mathbf{l}-\mathbf{q})^2}\ln\left(\frac{\mathbf{l}^2(\mathbf{l}-\mathbf{k})^2}{\mathbf{q}^4}\right). \quad \text{(C.1)}$$

Note, that at $\mathbf{q}_2 = 0$, we have $\mathbf{q}_2' = -\mathbf{q}$ and $\mathbf{q}_1' = \mathbf{k} - \mathbf{q}$.

Evidently, the integral term in (C.1) rules out, for the piece of the kernel (61) that does not change under the substitution $\mathbf{q}_i \longleftrightarrow \mathbf{q}_i'$, the possibility of vanishing alone at $\mathbf{q}_2 = \mathbf{0}$. Therefore, we need to calculate $I'(\mathbf{q}_1, \mathbf{q}_2; \mathbf{q}) \equiv I(\mathbf{q}_1', \mathbf{q}_2'; -\mathbf{q})$ at $\mathbf{q}_2 = \mathbf{0}$. This function can also be simplified. Note that, as in the preceding case, simplifications cannot be done for separate terms in (62) and are possible only due to the definite combination of them. We obtain

$$I(\mathbf{q}_1', \mathbf{q}_2'; -\mathbf{q})\big|_{\mathbf{q}_2=0} = \frac{\Gamma^2(\epsilon)}{2\Gamma(2\epsilon)}\mathbf{q}^2[(\mathbf{q}_1'^2)^\epsilon(\psi(\epsilon)-\psi(2\epsilon))$$

$$-(\mathbf{k}^2)^{\epsilon}(\psi(1)-\psi(2\epsilon))-(\mathbf{q}^2)^{\epsilon}(\psi(1)-\psi(1-\epsilon)$$
$$+2\psi(\epsilon)-2\psi(2\epsilon))]-\frac{(\mathbf{q}^2)^2}{4}\frac{1}{\pi^{1+\epsilon}\Gamma(1-\epsilon)} \quad \text{(C.2)}$$
$$\times\int\frac{d^{2+2\epsilon}l}{\mathbf{l}^2(\mathbf{l}-\mathbf{q})^2}\ln\left(\frac{\mathbf{l}^2}{(\mathbf{l}-\mathbf{k})^2}\right).$$

In the sum of (C.1) and (C.2), the terms with $\ln(\mathbf{l}-\mathbf{k})^2$ cancel each other; after that, the integrals can be calculated and we obtain

$$(I(\mathbf{q}_1,\mathbf{q}_2;\mathbf{q})+I(\mathbf{q}_1',\mathbf{q}_2';-\mathbf{q}))\big|_{\mathbf{q}_2=0}$$
$$=\frac{\Gamma^2(\epsilon)}{2\Gamma(2\epsilon)}\mathbf{q}^2[(\mathbf{q}_1'^2)^{\epsilon}(\psi(\epsilon)-\psi(2\epsilon))-(\mathbf{k}^2)^{\epsilon}(2\psi(1) \quad \text{(C.3)}$$
$$+\psi(\epsilon)-3\psi(2\epsilon))-(\mathbf{q}^2)^{\epsilon}(2\psi(1)$$
$$-2\psi(1-\epsilon)+3\psi(\epsilon)-3\psi(2\epsilon))].$$

With this result, it is a simple task to show that the kernel (61) vanishes at $\mathbf{q}_2 = 0$ [and, due to the symmetries in (12), at zero transverse momentum of any of the Reggeons].

REFERENCES

1. V. S. Fadin, E. A. Kuraev, and L. N. Lipatov, Phys. Lett. B **60B**, 50 (1975); E. A. Kuraev, L. N. Lipatov, and V. S. Fadin, Zh. Éksp. Teor. Fiz. **71**, 840 (1976) [Sov. Phys. JETP **44**, 443 (1976)]; Zh. Éksp. Teor. Fiz. **72**, 377 (1977) [Sov. Phys. JETP **45**, 199 (1977)]; Ya. Ya. Balitskii and L. N. Lipatov, Yad. Fiz. **28**, 1597 (1978) [Sov. J. Nucl. Phys. **28**, 822 (1978)].
2. L. N. Lipatov and V. S. Fadin, Pis'ma Zh. Éksp. Teor. Fiz. **49**, 311 (1989) [JETP Lett. **49**, 352 (1989)]; Yad. Fiz. **50**, 1141 (1989) [Sov. J. Nucl. Phys. **50**, 712 (1989)].
3. V. S. Fadin and L. N. Lipatov, Nucl. Phys. B **406**, 259 (1993); V. S. Fadin, R. Fiore, and M. I. Kotsky, Phys. Lett. B **389**, 737 (1996).
4. V. S. Fadin, Pis'ma Zh. Éksp. Teor. Fiz. **61**, 342 (1995) [JETP Lett. **61**, 346 (1995)]; V. S. Fadin, R. Fiore, and A. Quartarolo, Phys. Rev. D **53**, 2729 (1996); M. I. Kotsky and V. S. Fadin, Yad. Fiz. **59**, 1080 (1996) [Phys. At. Nucl. **59**, 1035 (1996)]; V. S. Fadin, R. Fiore, and M. I. Kotsky, Phys. Lett. B **359**, 181 (1995); Phys. Lett. B **387**, 593 (1996).
5. V. S. Fadin and R. Fiore, Phys. Lett. B **294**, 286 (1992); V. S. Fadin, R. Fiore, and A. Quartarolo, Phys. Rev. D **50**, 5893, 2265 (1994).
6. V. S. Fadin and L. N. Lipatov, Nucl. Phys. B **477**, 767 (1996); V. S. Fadin, M. I. Kotsky, and L. N. Lipatov, Phys. Lett. B **415**, 97 (1997); Yad. Fiz. **61**, 716 (1998) [Phys. At. Nucl. **61**, 641 (1998)].
7. S. Catani, M. Ciafaloni, and F. Hautmann, Phys. Lett. B **242**, 97 (1990); Nucl. Phys. B **366**, 135 (1991); G. Camici and M. Ciafaloni, Phys. Lett. B **386**, 341 (1996); Nucl. Phys. B **496**, 305 (1997); V. S. Fadin, R. Fiore, A. Flachi, and M. I. Kotsky, Phys. Lett. B **422**, 287 (1998); Yad. Fiz. **62**, 1066 (1999) [Phys. At. Nucl. **62**, 999 (1999)].
8. V. S. Fadin and L. N. Lipatov, Phys. Lett. B **429**, 127 (1998); M. Ciafaloni and G. Camici, Phys. Lett. B **430**, 349 (1998).
9. D. A. Ross, Phys. Lett. B **431**, 161 (1998); Yu. V. Kovchegov and A. H. Mueller, Phys. Lett. B **439**, 423 (1998); J. Blümlein, V. Ravindran, W. L. van Neerven, and A. Vogt, Preprint DESY-98-036; hep-ph/9806368; E. M. Levin, Preprint TAUP 2501-98 (1998); hep-ph/9806228; N. Armesto, J. Bartels, and M. A. Braun, Phys. Lett. B **442**, 459 (1998); G. P. Salam, hep-ph/9806482; M. Ciafaloni and D. Colferai, Phys. Lett. B **452**, 372 (1999); M. Ciafaloni, D. Colferai, and G. P. Salam, Preprint DFF-338-5-99 (1999); hep-ph/9905566; R. S. Thorne, Preprint OUTP-9902P (1999); hep-ph/9901331; S. J. Brodsky, V. S. Fadin, V. T. Kim, *et al.*, Preprint SLAC-PUB-8037; IITAP-98-010; hep-ph/9901229.
10. M. T. Grisaru, H. J. Schnitzer, and H. S. Tsao, Phys. Rev. Lett. **30**, 811 (1973); Phys. Rev. D **8**, 4498 (1973); L. N. Lipatov, Yad. Fiz. **23**, 642 (1976) [Sov. J. Nucl. Phys. **23**, 338 (1976)].
11. Ya. Ya. Balitskii, L. N. Lipatov, and V. S. Fadin, in *Proceedings of Leningrad Winter School, Physics of Elementary Particles, Leningrad, 1979*, p. 109.
12. J. Blümlein, V. Ravindran, and W. L. van Neerven, Phys. Rev. D **58**, 091502 (1998); V. Del Duca and C. R. Schmidt, Phys. Rev. D **59**, 074004 (1999).
13. V. S. Fadin and R. Fiore, Phys. Lett. B **440**, 359 (1998).
14. M. Braun, hep-ph/9901447.
15. V. S. Fadin, R. Fiore, M. I. Kotsky, and A. Papa, Preprint BUDKERINP/99-61 (Novosibirsk, 1999); UNICAL-TH 99/3 (1999); hep-ph/9908264.
16. V. S. Fadin, R. Fiore, M. I. Kotsky, and A. Papa, Preprint BUDKERINP/99-62 (Novosibirsk, 1999); UNICAL-TH 99/4 (1999); hep-ph/9908265.
17. M. Braun and G.P. Vacca, Phys. Lett. B **454**, 319 (1999).
18. V. S. Fadin, R. Fiore, and A. Papa, Phys. Rev. D **60**, 074025 (1999).
19. M. Braun and G. P. Vacca, hep-ph/9910432.
20. J. Bartels, Nucl. Phys. B **175**, 365 (1980).
21. V. S. Fadin, Preprint BUDKERINP 98–55 (Novosibirsk, 1998); hep-ph/9807528; in *Proceedings of the International Conference "LISHEP'98," Rio de Janeiro, 1998* (in press).

Physics of Atomic Nuclei, Vol. 63, No. 12, 2000, pp. 2173–2183. From Yadernaya Fizika, Vol. 63, No. 12, 2000, pp. 2269–2179.

ELEMENTARY PARTICLES AND FIELDS
Theory

Strong-Coupling Constant in Coordinate Space*

A. M. Badalian

Institute of Theoretical and Experimental Physics, Bol'shaya Cheremushkinskaya ul. 25, Moscow, 117959 Russia

Received April 27, 2000

Abstract—The coordinate-space behavior of (vector) strong-coupling constant in the background field $\alpha_B(r)$ is compared with that in standard perturbation theory $\alpha_V(r)$. The numerically calculated two-loop coupling constant $\alpha_B(r)$ is shown to exceed $\alpha_V(r)$ by 1–5% at very small distances, $r \lesssim 0.02$ fm, and to be in agreement with lattice measurements of the static potential. At large distances, $\alpha_B(r)$ approaches the freezing value at $r \gtrsim 0.5$ fm. An analytic form of $\alpha_B(r)$ is proposed that approximates $\alpha_B(r)$ with a precision $\lesssim 2\%$ in the region $r \gtrsim 0.5$ fm.

1. INTRODUCTION

Precise knowledge of the static potential between heavy quarks is very important in quarkonium physics because this potential determines the spectrum and the wave functions of the $Q\bar{Q}$ system. Usually, fundamental quarkonium properties are calculated in coordinate space, where we need to know both perturbative and nonperturbative contributions to the static potential. As is well established now [1], the nonperturbative potential $V_{NP}(r)$ has a linear behavior beginning from rather small distances, $r \gtrsim 0.2$ fm, and, at smaller distances, the exact form of $V_{NP}(r)$ is not very important in quarkonium physics since $V_{NP}(r)$ is much smaller than the perturbative part of interaction. Still, there is the point of view that, at small distances, the linear potential $\sigma_0 r$ also exists, with σ_0 being approximately equal to the asymptotic value of the string tension σ (see [2] and references therein).

The situation with the perturbative static potential, $V_P(r)$, is much more uncertain. In perturbation theory, $V_P(r)$ is known only at small distances, $r \ll \Lambda_R^{-1}$, where Λ_R is QCD constant in coordinate space which is significantly larger than $\Lambda_{\overline{MS}}$ in $\overline{MS}$ renormalization scheme [3] (see also Section 3):

$$\Lambda_R^{(n_f)} = \Lambda_{\overline{MS}}^{(n_f)} \exp\left(\frac{a_1}{2\beta_0} + \gamma_E\right);$$

for the number of flavors $n_f = 4$, $\Lambda_R^{(4)} = 2.536\Lambda_{\overline{MS}}^{(4)} \approx 710 \pm 100$ MeV if the conventional two-loop value of $\Lambda_{\overline{MS}}^{(4)} = 280 \pm 40$ MeV is used [4]. Therefore, the perturbative static potential calculated recently in the two-loop approximation [5, 6] is, in strict sense, defined only in the region $r \ll 0.3$ fm $= \Lambda_R^{-1}$, while the sizes of quarkonium states below the open-charm or the open-beauty threshold are much larger and change from 0.2 to 1 fm in bottomonium and from 0.4 to 1 fm in charmonium.

A precise determination of the strong-coupling constant at relatively large distances (or at small momenta in momentum space) cannot be performed within standard perturbation theory; therefore, a large variety of potentials were used in phenomenological calculations of quarkonium properties. Among the most popular potentials, we shortly discuss here only QCD-motivated potentials.

(i) For the Cornell potential [7]

$$V_{\text{Corn}}(r) = -\frac{4}{3}\frac{\alpha}{r} + \sigma r + C,$$

the running coupling constant $\alpha_s(r)$ is taken to be a constant over the entire region $r \geq 0$; yet, this potential gives an excellent description of the $Q\bar{Q}$ spectrum with only one drawback: the wave function at the origin, $\psi(0)$; and therefore the leptonic widths for the Cornell potential are found to be larger than in the case where the asymptotic-freedom behavior of $\alpha_s(r)$ is taken into account [8]. As a whole, one can conclude that the freezing phenomenon of the strong-coupling constant is extremely important in quarkonium physics.

(ii) For the Richardson potential defined in momentum space as [9]

$$V_{\text{Rich}}(q) = -\frac{4}{3}\frac{4\pi}{\beta_0}\frac{1}{q^2\ln(1 + q^2/\Lambda^2)};$$

$$V_{\text{Rich}}(q) \approx -\frac{4}{3}\frac{4\pi}{\beta_0}\frac{1}{q^2}\frac{\Lambda^2}{q^2} \quad (q^2 \ll \Lambda^2),$$

the nonperturbative part ($\sim 1/q^4$) corresponds to the linear potential σr, and it can be subtracted, so that the

* This article was submitted by the authors in English.

perturbative coupling constant, $\alpha_{\text{Rich}}(q)$, can be defined as

$$\alpha_{\text{Rich}}(q) = \frac{4\pi}{\beta_0}\left[\frac{1}{\ln(1+q^2/\Lambda^2)} - \frac{\Lambda^2}{q^2}\right]. \quad (1)$$

This coupling constant is finite at $q = 0$: $\alpha_{\text{Rich}}(q = 0) = 2\pi/\beta_0$—that is, it has a freezing property—and has the correct asymptotic behavior at high momenta, $q^2 \gg \Lambda^2$,

$$\alpha_{\text{Rich}}(q \longrightarrow \infty) = \frac{4\pi}{\beta_0}\left(\ln\frac{q^2}{\Lambda^2}\right)^{-1}.$$

However, the nonperturbative part of the Richardson potential is a Lorentz vector by definition, while, as is now established in QCD, the linear potential must be a Lorentz scalar [10, 11].

(iii) In the calculations of meson properties by Godfrey and Isgur [12], the dependence of $\alpha_s(q)$ on q was defined phenomenologically: $\alpha_s(q)$ was represented as the sum of exponentials and had also the property of freezing—in particular, at low momenta

$$\alpha_s(q \longrightarrow 0) \longrightarrow \text{const} = 0.60.$$

(iv) In [8], the asymptotic-freedom behavior of $\alpha_s(r)$ at small r and the freezing of $\alpha_s(r)$ at $r \geq r_0$ were taken into account, which resulted in a good description of the quarkonium spectra and leptonic widths.

(v) In lattice calculations of the static potential [13, 14], it was observed that, at distances $r \gtrsim 0.2$ fm, the strong-coupling constant, taken as a constant, reproduces lattice measurements with a good accuracy.

Thus, one can conclude that, in phenomenological calculations and in lattice QCD, two important properties of the strong-coupling constant are needed: the asymptotic-freedom behavior at small r and the freezing of $\alpha_s(r)$ at relatively large distances.

On the fundamental level, the freezing phenomenon was predicted in the framework of background field theory (BFTh) in [15], where the static potential in vacuum background fields was considered. Later, this approach was applied to the process $e^+e^- \longrightarrow$ *hadrons* [16], where it was shown that the presence of a background field results in the appearance of the background mass m_B, so that the strong-coupling constant in this case depends on the combination $(q^2 + m_B^2)$ instead of q^2 dependence in perturbation theory. The value of m_B was found to be defined by the hybrid excitations [17], and the value of $m_B \approx 1.0$–1.1 GeV was also extracted from fine-structure splittings in charmonium [18] and bottomonium [19].

Similar ideas were discussed in [20, 21], where the freezing of $\alpha_s(q^2)$ was considered as a natural consequence of a picture where the gluon acquires an effective dynamical mass m_g. In [20, 21], it was suggested (not deduced as in [16]) that $\alpha_s(q^2)$ depends on the combination $(q^2 + 4m_g^2)$, i.e., the doubled effective gluon mass, $2m_g$, plays a role of the background mass. In recent calculations of dynamical gluon masses (which depend on chosen quantum numbers) in [22], the lowest gluon mass $m_g = 0.53$ GeV was calculated, so that $2m_g = 1.06$ GeV. This number is in surprising agreement with $m_B \approx 1.0$ GeV obtained in [17–19].

In the framework of perturbation theory, an analytic effective coupling constant was constructed with the use of an "analytization" procedure [23]. This analytic $\alpha_{\text{an}}(q)$ is finite in the infrared limit and the value of $\alpha_{\text{an}}(q = 0)$ was found to be $4\pi/\beta_0$. In this approach, one-loop and two-loop expressions of $\alpha_s(q)$ are modified, but they do not contain any background mass. Note also that the freezing value of $\alpha_{\text{an}}(q = 0) = 4\pi/\beta_0$ is about three times larger than the freezing values predicted in [16, 18] and this significant difference can give rise to different predictions of some observed experimental values.

The theoretical formula describing the behavior of the strong-coupling constant in the background field, denoted as $\alpha_B(q)$, was deduced in [16] at large momenta, $q^2 \gtrsim m_B^2$, and to find the behavior of $\alpha_B(q)$ at smaller momenta, $q^2 \lesssim m_B^2$, an interpolation of this expression (valid at $q^2 \gtrsim m_B^2$) was used. Therefore, the precise number of the freezing coupling constant value, $\alpha_B(q = 0)$, is not still theoretically fixed in BFTh. To get this number, phenomenological analysis and lattice measurements of static potential at small separations can be very useful. Recently, lattice data on the static potential in the range $0.04 \leq r \leq 0.4$ fm were published in [24], and from the analysis of these data the background mass m_B can be estimated.

Our paper is mostly concentrated on the properties of $\tilde{\alpha}_B(r)$ in BFTh with a preliminary discussion of the two-loop coupling constant in momentum and coordinate spaces in perturbation theory, and also on the approximations to $\tilde{\alpha}_B(r)$ at large and small distances.

2. TWO-LOOP $\alpha_V(q)$ IN MOMENTUM SPACE

The perturbative potential $V_P(q)$ can be used to define a vector coupling constant $\alpha_V(q)$:

$$V_P(q) = -4\pi C_F\frac{\alpha_V(q)}{q^2}, \quad (2)$$

where $q^2 \equiv \mathbf{q}^2$. The coupling constant, expressed through $\alpha_{\overline{MS}}(\mu)$ in the renormalization scheme $\overline{MS}$, was recently calculated in the two-loop approximation [5, 6]:

$$\alpha_V(q) = \alpha_s(\mu)\left\{1 + C_1\frac{\alpha_s(\mu)}{4\pi} + C_2\left(\frac{\alpha_s(\mu)}{4\pi}\right)^2\right\}. \quad (3)$$

Here, $\alpha_s(\mu) \equiv \alpha_{\overline{MS}}(\mu)$ and

$$C_1 = a_1 + \beta_0 y,$$
$$C_2 = a_2 + \beta_0^2 y^2 + (\beta_1 + 2\beta_0 a_1) y, \quad (4)$$

and in (4), the variable y is

$$y = \ln(\mu^2/q^2). \quad (5)$$

The constants a_1 and a_2 are given by

$$a_1 = \frac{31}{3} - \frac{10}{9} n_f,$$
$$a_2 = 9\left[\frac{4343}{162} + 4\pi^2 - \frac{\pi^4}{4} + \frac{22}{3}\zeta(3)\right] - \frac{3}{2} n_f \left(\frac{1798}{81} + \frac{56}{3}\zeta(3)\right) - \frac{1}{2} C_F n_f \left(\frac{55}{3} - 16\zeta(3)\right) + \frac{100}{81} n_f^2. \quad (6)$$

In (6), C_F is the Casimir operator of the $SU(N)$ group. In particular, in the quenched approximation ($n_f = 0$) where the lattice measurements exist [24],

$$a_1 = 31/3, \quad a_2 = 456.74884\ldots. \quad (7)$$

In (6), $\zeta(3) = 1.202057$ denotes the Riemann ζ function. On the other hand, if the definition of β^V function is used,

$$\beta^V = \mu^2 \frac{\partial \alpha_V(\mu)}{\partial \mu^2} = -4\pi \sum_{n=0}^{\infty} \beta_n^V \left(\frac{\alpha_V(\mu)}{4\pi}\right)^{n+2}, \quad (8)$$

then with the help of expression (3) the coefficients of the QCD β^V function, β_n^V ($n = 0, 1, 2$), can be found [6]:

$$\beta_0^V = \beta_0, \ \beta_1^V = \beta_1, \ \beta_2^V = \beta_2 - a_1\beta_1 + \beta_0(a_2 - a_1^2). \quad (9)$$

Here, $\beta_n \equiv \beta_n^{\overline{MS}}$, and for $n_f = 0$, we have

$$\beta_0 = 11, \quad \beta_1 = 102, \quad \beta_2 = 2857/2.$$

Correspondingly, for the vector coupling constant $\beta_0^V = 11$, $\beta_1^V = 102$ are the renormalization scheme (RS) invariants, and the coefficient

$$\beta_2^V = 4224.1817\ldots \quad (10)$$

appears to be about three times larger than $\beta_2^{\overline{MS}}$.

The value of $\Lambda_{\overline{MS}}^{(0)}$ was recently calculated with a good accuracy in the finite-size lattice technique [25] ($n_f = 0$):

$$\Lambda_{\overline{MS}}^{(0)} = \frac{0.602(48)}{r_0}, \quad (11)$$

where r_0 denotes the Sommer scale. With the use of expression (3), QCD constant $\Lambda_V^{(n_f)}$, defining the running vector coupling constant $\alpha_V(q)$, can be expressed through $\Lambda_{\overline{MS}}^{(n_f)}$ [3]:

$$\Lambda_V^{(n_f)} = \Lambda_{\overline{MS}}^{(n_f)} \exp(a_1/2\beta_0); \quad (12)$$

or in the case $n_f = 0$

$$\Lambda_V^{(0)} = 1.5995 \Lambda_{\overline{MS}}^{(0)} = \frac{0.963(77)}{r_0}. \quad (13)$$

If r_0 is taken to be $r_0 = 0.5$ fm ≈ 2.54 GeV^{-1} as in [25], then

$$\Lambda_{\overline{MS}}^{(0)} = 237 \pm 19 \text{ MeV}, \quad \Lambda_V^{(0)} = 379 \pm 30 \text{ MeV}. \quad (14)$$

In our calculations below (see Section 6), we will use the following values:

$$\Lambda_{\overline{MS}}^{(0)} = 240.7 \text{ MeV}, \quad \Lambda_V^{(0)} = 385 \text{ MeV}, \quad (15)$$

which satisfy relation (13).

Since Λ_V and the coefficients β_n^V are known, the running vector coupling constant $\alpha_V(q)$ can be also written in the form

$$\alpha_V(q) = \frac{4\pi}{\beta_0 \tilde{y}} \left\{1 - \frac{\beta_1}{\beta_0^2} \frac{\ln \tilde{y}}{\tilde{y}} + \frac{\beta_1^2}{\beta_0^4 \tilde{y}^2} \left[\ln^2 \tilde{y} - \ln \tilde{y} + \frac{\beta_0 \beta_2^V}{\beta_1^2}\right]\right\}, \quad (16)$$

where β_2^V is given by number (10) and

$$\tilde{y} = \ln(q^2/\Lambda_V^2). \quad (17)$$

Note that, in (16), the small correction coming from the last term, $(4\pi/\tilde{y}^3)(\beta_2^V/\beta_0^4)$, is about three times larger than that in the $\overline{MS}$ renormalization scheme.

3. TWO-LOOP $\tilde{\alpha}_V(r)$ IN COORDINATE SPACE

The vector coupling constant in coordinate space, $\tilde{\alpha}_V(r)$, is also defined through the static potential:

$$V_P(r) = -C_F \frac{\tilde{\alpha}_V(r)}{r}. \quad (18)$$

By introducing the Fourier transform $V_P(q)$,

$$V_P(r) = \frac{1}{(2\pi)^3} \int V_P(q) e^{i\mathbf{q}\cdot\mathbf{r}} d\mathbf{q}, \quad (19)$$

it can be shown that $\tilde{\alpha}_V(r)$ and $\alpha_V(q)$, given by (3) or (16), satisfy the relation

$$\tilde{\alpha}_V(r) = \frac{2}{\pi}\int \alpha_V(q)\frac{\sin(qr)}{q}dq = \frac{2}{\pi}\int \alpha_V(y)\frac{\sin x}{x}dx, \quad y(x) = \ln\frac{\mu^2 r^2}{x^2}. \tag{20}$$

The integral in (20) can be analytically calculated if $\alpha_V(q)$ is taken in the two-loop approximation as in (3) (see Appendix), and the following expression for $\tilde{\alpha}_V(r)$ was obtained in [6, 26] ($\mu = 1/r$):

$$\tilde{\alpha}_V(r) = \alpha_{\overline{MS}}\left(\frac{1}{r}\right)\left\{1 + A_1\frac{\alpha_{\overline{MS}}(1/r)}{4\pi} + A_2\left(\frac{\alpha_{\overline{MS}}(1/r)}{4\pi}\right)^2\right\}. \tag{21}$$

Here, the coefficients A_1 and A_2 are the following constants:

$$A_1 = a_1 + 2\gamma_E\beta_0, \quad A_2 = a_2 + \beta_0^2\left(\frac{\pi^3}{3} + 4\gamma_E^2\right) + 2\gamma_E(\beta_1 + 2\beta_0 a_1). \tag{22}$$

Then, with the use of expansion (21), the coefficients of the two-loop β^R function in coordinate space can be calculated [26]:

$$\beta^R = \mu^2\frac{\partial\tilde{\alpha}_V(\mu)}{\partial\mu^2} = -4\pi\sum_{n=0}^{\infty}\beta_n^R\left(\frac{\tilde{\alpha}_V(\mu)}{4\pi}\right)^{n+2}, \tag{23}$$

with the following result: $\beta_0^R = \beta_0^V = \beta_0$, $\beta_1^R = \beta_1^V = \beta_1$. They are RS invariants, while

$$\beta_2^R = \beta_2^{\overline{MS}} - A_1\beta_1 + \beta_0(A_2 - A_1^2). \tag{24}$$

In the quenched approximation ($n_f = 0$), we have β_n^R = 8602.9962…, A_1 = 23.032079…, and A_2 = 1396.27376…. The coefficient β_2^R appears to be about two times larger than β_2^V in (10) and about six times larger than $\beta_2^{\overline{MS}}$. It means that the three-loop corrections to the coupling constant in coordinate space are significantly larger than in the $\overline{MS}$ renormalization scheme.

QCD constant $\Lambda_R^{(n_f)}$ defining the running coupling constant $\tilde{\alpha}_V(r)$ in coordinate space can be expressed through $\Lambda_{\overline{MS}}^{(n_f)}$ [3, 24] and turns out to be large:

$$\Lambda_R^{(n_f)} = \Lambda_{\overline{MS}}^{(n_f)}\exp\left(\frac{a_1}{2\beta_0} + \gamma_E\right). \tag{25}$$

From here (for $n_f = 0$ and $n_f = 4$), $\Lambda_R^{(0)}$ and $\Lambda_R^{(4)}$ are about 2.5–2.8 times larger than $\Lambda_{\overline{MS}}$:

$$\Lambda_R^{(0)} = 2.8488\Lambda_{\overline{MS}}^{(0)}, \quad \Lambda_R^{(4)} = 2.5359\Lambda_{\overline{MS}}^{(4)}. \tag{26}$$

If $\Lambda_{\overline{MS}}^{(0)} = 240.7$ MeV is taken as in [25], then in coordinate space the QCD constant is

$$\Lambda_R^{(0)} = 686 \text{ MeV}. \tag{27}$$

4. $\alpha_B(q)$ IN BACKGROUND-FIELD THEORY

The properties of the coupling constants in momentum and in coordinate spaces have been discussed above in the framework of perturbation theory, which is applicable only at large momenta, $q \gg \Lambda_V$, or at small distances, $\Lambda_R r \ll 1$. At smaller q^2, the influence of vacuum background fields on the interaction becomes important, and, as a result, the vector coupling constant is modified [15, 16]. The static potential $V_B(q)$ in the presence of background fields can be written just as $V_P(q)$ in (2):

$$V_B(q) = -4\pi C_F\frac{\alpha_B(q)}{q^2}. \tag{28}$$

It is important that $V_B(q)$ does not include a purely confining (scalar) contribution and takes into account only the influence of background fields on the perturbative (vector) part of interaction. In this respect, $V_B(q)$ essentially differs from the Richardson potential discussed in the Introduction and takes into account an interference of perturbative and nonperturbative effects at small distances.

As is shown in [16], the strong-coupling constant in the presence of a background field, denoted in (28) as $\alpha_B(q)$, depends on the combination $(q^2 + m_B^2)$, where m_B is a background mass. This mass can in general depend on a considered channel and in the case of static potential m_B is defined by the lowest hybrid excitation [16, 17] with $m_B \approx 1.0$ GeV. Just this value of m_B was extracted from fine-structure analysis of charmonium and bottomonium in [18, 19].

In [16, 27], it was deduced that in BFTh the strong-coupling constant $\alpha_B(q)$ at large momenta can be obtained as a generalization of the perturbative expression with q^2 replaced by the combination $(q^2 + m_B^2)$. Then the generalization of expansion (3) in momentum space can be written in the following way:

$$\alpha_B(q) = \alpha_B^{\overline{MS}}(\tilde{\mu})\left\{1 + B_1\frac{\alpha_B^{\overline{MS}}(\tilde{\mu})}{4\pi} + B_2\left(\frac{\alpha_B^{\overline{MS}}(\tilde{\mu})}{4\pi}\right)^2\right\}, \tag{29}$$

with

$$B_1 = a_1 + \beta_0 t, \quad B_2 = a_2 + \beta_0^2 t^2 + (\beta_1 + 2\beta_0 a_1)t. \tag{30}$$

Here, the variable t is

$$t = \ln\frac{\tilde{\mu}^2}{q^2 + m_B^2}, \quad \tilde{\mu}^2 = \mu^2 + m_B^2 \geq m_B^2. \tag{31}$$

In (30), the coefficients a_1 and a_2 are the same as in (6), and the running coupling constant $\alpha_B^{\overline{MS}}(\tilde{\mu})$ in the $\overline{MS}$ renormalization scheme now depends on $t_{\overline{MS}}$:

$$t_{\overline{MS}}(\mu) = \ln\frac{\mu^2 + m_B^2}{\Lambda_{\overline{MS}}^2} = \ln\frac{\tilde{\mu}^2}{\Lambda_{\overline{MS}}^2}, \tag{32}$$

$$\alpha_B^{\overline{MS}}(\tilde{\mu}) = \frac{4\pi}{\beta_0 t_{\overline{MS}}}\left\{1 - \frac{\beta_1}{\beta_0^2}\frac{\ln t_{\overline{MS}}}{t_{\overline{MS}}} + \ldots\right\}. \tag{33}$$

In (32), it was also assumed that in BFTh $\Lambda_B^{\overline{MS}}$ coincides with $\Lambda_{\overline{MS}}$ in perturbative theory. If $m_B = 0$, then expression (29) reduces to expression (2); therefore, in BFTh the values of β_n^V coefficients [for the coupling constant $\alpha_B(q)$] turn out to be the same as in perturbative theory, and the running coupling constant $\alpha_B(q)$ can be written as

$$\alpha_B(q) = \frac{4\pi}{\beta_0 t_B}\left\{1 - \frac{\beta_1}{\beta_0^2}\frac{\ln t_B}{t_B} + \frac{\beta_1^2}{\beta_0^4 t_B^2}\left[\ln^2 t_B - \ln t_B - 1 + \frac{\beta_0\beta_2^V}{\beta_1^2}\right]\right\}. \tag{34}$$

The only difference between (34) and (16) is that the variable $\tilde{y}$ is replaced by

$$t_B = \ln\frac{q^2 + m_B^2}{\Lambda_V^2} \quad (\Lambda_B^V = \Lambda_V). \tag{35}$$

Here, some remarks about QCD constants $\Lambda_B^{\overline{MS}}$ and Λ_B^V in BFTh are needed.

In the region of very large momenta,

$$q \gg \Lambda_B^{\overline{MS}} \quad \text{or} \quad q \gg \Lambda_B^V, \quad \text{and} \quad q \gg m_B, \tag{36}$$

and $\alpha_B(q)$ in (34) and $\alpha_B^{\overline{MS}}(q)$ in (33) coincide with perturbative expressions. Therefore, for $n_f = 5$, QCD constants Λ_V and Λ_B^V in (35) coincide:

$$\Lambda_B^V(n_f = 5) = \Lambda_V(n_f = 5), \quad \Lambda_B^{\overline{MS}}(n_f = 5) = \Lambda_{\overline{MS}}(n_f = 5). \tag{37}$$

As is shown in [18], for $n_f = 4$, $\Lambda_B^{\overline{MS}}$ and $\Lambda_{\overline{MS}}^{(4)}$ also coincide within 1–2 MeV accuracy and even for $n_f = 3$, $\Lambda_B^{\overline{MS}}$ is only by about 15–20 MeV larger than $\Lambda_{\overline{MS}}^{(3)}$; i.e., they coincide within the theoretical and experimental errors. Therefore we assume here that, in the quenched approximation, we have

$$\Lambda_B^{\overline{MS}} \approx \Lambda_{\overline{MS}}^{(0)}(n_f = 0). \tag{38}$$

It is essential that in (35) there exists a region of $q^2 \sim m_B^2$ where the condition $q^2 \gg \Lambda_V^2$ is still satisfied but the influence of background mass m_B under the logarithm becomes important. For example, if $q = m_B = 1.0$ GeV and $\Lambda_B^V = \Lambda_V = 380$ MeV, then $q^2/\Lambda_V^2 = 7$. This region can be called a preasymptotic one. In (29), $\alpha_B(q)$ was defined at $q \gtrsim m_B$. However, the coupling constant $\alpha_B(q)$ was not defined at small q^2: $0 \leq q^2 \lesssim \Lambda_V^2$. It was only obtained in [15, 16] that $\alpha_B(q)$ freezes at $q = 0$ at some value $\alpha_B(0)$ but the exact number of $\alpha_B(q = 0)$ was not calculated. Our main assumption here will be made about $\alpha_B(q)$ behavior at small momenta: the analytic two-loop expression (29) or (34) for $\alpha_B(q)$ is assumed to be valid over all range of momenta $q \geq 0$; i.e., expression (34) (obtained for $q^2 \gtrsim m_B^2$) is extrapolated to the region of small q^2: $m_B^2 \gtrsim q^2 \geq 0$.

This assumption has a pronounced effect on the behavior of the static potential in coordinate space and needs a special check, in particular, by comparison of the theoretical formula for $V_B(r)$ with lattice measurements. Therefore, the existing lattice data on the static potential at small and average distances appear to be of great importance for checking different theoretical concepts about the freezing of the strong-coupling constant.

5. $\tilde{\alpha}_B(r)$ IN COORDINATE SPACE

The strong-coupling constant $\tilde{\alpha}_B(r)$ in coordinate space in BFTh can be defined through the static potential as in (18):

$$V_B(r) = -C_F\frac{\tilde{\alpha}_B(r)}{r}, \tag{39}$$

and with the help of the Fourier transform it can be connected with $\alpha_B(q)$ in momentum space, as in (20),

$$\tilde{\alpha}_B(r) = \frac{2}{\pi}\int_0^\infty dq\frac{\sin(qr)}{q}\alpha_B(q) = \frac{2}{\pi}\int_0^\infty dq\frac{\sin x}{x}\alpha_B(x). \tag{40}$$

On the right-hand side of (40), $\alpha_B(x)$ depends on the variable

$$\tilde{t}(x) = \ln\frac{(\mu^2 + m_B^2)r^2}{x^2 + m_B^2 r^2}$$

instead of the $y(x)$ dependence in (20).

In the two-loop approximation [with the use of representation (29)], $\tilde{\alpha}_B(r)$ can be calculated:

$$\tilde{\alpha}_B(r) = \alpha_B^{\overline{MS}}\left(\mu = \frac{1}{r}\right) \times\left\{1 + \tilde{B}_1(r)\frac{\alpha_B^{\overline{MS}}(\mu = 1/r)}{4\pi} + \tilde{B}_2(r)\left[\frac{\alpha_B^{\overline{MS}}(\mu = 1/r)}{4\pi}\right]^2\right\}. \quad (41)$$

In contrast to the coefficients A_1 and A_2 in (21), now in (41) $\tilde{B}_1(r)$ and $\tilde{B}_2(r)$ depend on the variable r, if the renormalization scale $\mu = 1/r$ is chosen. In a general case, we have

$$\tilde{B}_1(r) = a_1 + 2\gamma_1(r)\beta_0,$$
$$\tilde{B}_2(r) = a_2 + 2\gamma_1(r)(\beta_1 + 2\beta_0 a_1) + \beta_0^2\gamma_2(r). \quad (42)$$

Here, the functions $\gamma_n(r)$ ($n = 1, 2$) are defined by the integrals ($\mu = 1/r$)

$$\gamma_n(r) = \frac{2}{\pi}\int dx\frac{\sin x}{x}\tilde{t}^n(x) \quad (43)$$

with

$$\tilde{t}(x) = \ln\frac{1 + m_B^2r^2}{x^2 + m_B^2r^2}. \quad (44)$$

The function $\gamma_1(r)$ (calculated analytically in the Appendix) can be written in two different forms:

$$\gamma_1(r) = \frac{1}{2}\ln\frac{1 + m_B^2r^2}{m_B^2r^2} + \mathrm{Ei}(-m_Br)$$
$$= \frac{1}{2}\ln(1 + m_B^2r^2) + \gamma_E + \sum_{k=1}^{\infty}\frac{(-m_Br)^k}{k!k}, \quad (45)$$

$$\gamma_1(r) = \ln\frac{1 + m_B^2r^2}{m_B^2r^2} + e^{-m_Br}\left[-\frac{1}{m_Br} + \frac{1}{(m_Br)^2}\right] + O\left(\frac{1}{(m_Br)^3}\right), \quad (46)$$
$$\text{if} \quad m_Br \gg 1.$$

Here, γ_E is the Euler constant. To find $\gamma_1(r)$ at small r, it is convenient to use expression (45), from which it is evident that $\gamma_1(r \longrightarrow 0) \longrightarrow \gamma_E$ and with the lowest correction taken into account $\gamma_1(r)$ is

$$\gamma_1(r \longrightarrow 0) = \gamma_E - m_Br. \quad (47)$$

The behavior of $\gamma_1(r)$ at large distances can be found from (46),

$$\gamma_1(m_Br \gg 1) = \frac{1}{m_B^2r^2} - \frac{e^{-m_Br}}{m_Br} \longrightarrow 0, \quad \text{if} \quad r \longrightarrow \infty. \quad (48)$$

Thus, the function $\gamma_1(r)$ is a decreasing function of r, and in the range $0 \le r < \infty$ it changes from $\gamma_1(0) = \gamma_E$ to $\gamma_1(\infty) = 0$:

$$\gamma_E \ge \gamma_1(r) \ge 0. \quad (49)$$

If one defines, as in perturbation theory, QCD constants Λ_B^R in coordinate space in terms of Λ_B^V in momentum space from representation (29),

$$\Lambda_B^R = \Lambda_V\exp(\gamma_1(r)), \quad (50)$$

then, Λ_B^R depends now on the distance r and only at very small r coincides with the perturbative Λ_R [28]:

$$\Lambda_B^R(r \longrightarrow 0) = \Lambda_R = \Lambda_V e^{\gamma_E}(r \longrightarrow 0, \gamma_1(r) \longrightarrow \gamma_E). \quad (51)$$

At large distances ($r \longrightarrow \infty$) $\gamma_1(r) \longrightarrow 0$; therefore, Λ_B^R coincides with QCD constant Λ_V in momentum space:

$$\Lambda_B^R(r \longrightarrow \infty) = \Lambda_V. \quad (52)$$

At the average distances, the values of $\Lambda_B^R(r)$ lie between Λ_R and Λ_V: $\Lambda_V < \Lambda_B^R < \Lambda_R$.

The second function $\gamma_2(r)$ in (42) is given by the expression (see Appendix)

$$\gamma_2(r, \mu = 1/r) = \ln^2(1 + m_B^2r^2) + 4\ln(1 + m_B^2r^2)\left(\gamma_E + \sum_{k=1}^{\infty}\frac{(-m_Br)^k}{k!k}\right) + \xi_2(r)$$
$$= \left[\ln\left(\frac{1 + m_B^2r^2}{m_B^2r^2}\right)\right]^2 + 4\ln\left(\frac{1 + m_B^2r^2}{m_B^2r^2}\right)\mathrm{Ei}(-m_Br) + \tilde{\xi}_2(r). \quad (53)$$

Here, the function $\xi_2(r)$ is defined by the integral

$$\xi_2(r) = \frac{2}{\pi}\int dx\frac{\sin x}{x}\ln^2(x^2 + m_B^2r^2), \quad (54)$$

while

$$\tilde{\xi}_2(r) = \frac{2}{\pi}\int dx\frac{\sin x}{x}\ln^2\left(1 + \frac{x^2}{m_B^2r^2}\right). \quad (55)$$

The function $\xi_2(r)$ and therefore $\gamma_2(r)$ can be analytically calculated only at small and large distances:

$$\gamma_2(r \longrightarrow 0) \longrightarrow \xi_2(r \longrightarrow 0) = 4\gamma_E^2 + \pi^2/3 = 4.622580. \quad (56)$$

At large distances, as seen from expression (54) (see also Appendix),

$$\tilde{\xi}_2(r \longrightarrow \infty) \longrightarrow 0, \quad \gamma_2(r \longrightarrow \infty) \longrightarrow 0; \quad (57)$$

therefore, expression (42) at large distances simplifies,

$$\tilde{B}_2(r \longrightarrow \infty) \longrightarrow a_2. \quad (58)$$

It is important to stress here that the dependence $\gamma_1(r)$ on r is quite pronounced even at rather small distances; e.g., if $m_B = 1.0$ GeV and $r = 0.1$ GeV$^{-1} = 0.02$ fm, then the correction to the function

$$\gamma_1(r) = \gamma_E - m_B r \quad (59)$$

coming from the second term is about 20%, and it grows for larger distances.

6. RUNNING COUPLING CONSTANT IN BFTh

The functions $\tilde{B}_1(r)$ and $\tilde{B}_2(r)$ in expansion (41) define the coefficients of β^{BR} function in BFTh:

$$\beta^{BR} = \tilde{\mu}^2 \frac{\partial \tilde{\alpha}_B(\tilde{\mu})}{\partial \tilde{\mu}^2} = -4\pi \sum_{n=0}^{\infty} \beta_n^{BR} \left(\frac{\tilde{\alpha}_B(\tilde{\mu})}{4\pi}\right)^{n+2}, \quad (60)$$

where β_0 and β_1 are RS invariants, while β_2^{BR} is RS dependent,

$$\beta_2^{BR} = \beta_2^{\overline{MS}} - \beta_1 \tilde{B}_1(r) - \beta_0[\tilde{B}_2(r) - \tilde{B}_1^2(r)], \quad (61)$$

and has different limits at small and large distances. At small $r(m_B r \ll 1)$ coefficient $\beta_2^{BR} \longrightarrow \beta_2^R$, given by (24), and at large distances, $r \longrightarrow \infty$, it approaches β_2^V—the coefficient of the vector coupling constant in momentum space:

$$\beta_2^{BR}(r \longrightarrow \infty) \longrightarrow \beta_2^V. \quad (62)$$

Therefore, at large distances, the running coupling constant can be approximated by the simple expression

$$\tilde{\alpha}_B(r \longrightarrow \infty) = \frac{4\pi}{\beta_0 t_0}\left\{1 - \frac{\beta_1}{\beta_0^2}\frac{\ln t_0}{t_0}\right\}, \quad (63)$$

where under the logarithm the variable t_0 is a number,

$$t_0 = \ln(m_B^2/\Lambda_V^2), \quad (64)$$

and QCD constant is equal to Λ_V. From the comparison of (64) and (34), one can easily get that the freezing values in coordinate and momentum spaces coincide:

$$\tilde{\alpha}_B(r \longrightarrow \infty) = \alpha_B(q = 0, \Lambda = \Lambda_V). \quad (65)$$

7. OUR CALCULATIONS

The running coupling constant $\tilde{\alpha}_B(r)$ can be numerically calculated. To this end, it is convenient to use for $\alpha_B(q)$ expression (34) in integral (40). Also, the last term in (34), proportional to $\tilde{t}^{-3}$, will be neglected here for two reasons. First, its contribution to the coupling constant is less than 1–5% over all region $q^2 \geq 0$; the second reason is that two-loop expression used here,

$$\alpha_B^{(2)}(q) = \frac{4\pi}{\beta_0 t_B}\left\{1 - \frac{\beta_1}{\beta_0^2}\frac{\ln t_B}{t_B}\right\}, \quad (66)$$

with

$$t_B = \ln\frac{q^2 + m_B^2}{\Lambda_V^2}, \quad (67)$$

contains only RS invariant coefficients β_0 and β_1. If $n_f = 0$ in (67), $\Lambda_V = 385$ MeV will be taken.

In the same approximation, $\tilde{\alpha}_B^{(2)}(r)$ in (40) can be written as

$$\tilde{\alpha}_B^{(2)}(r) = \frac{8}{\beta_0}\int_0^{\infty} dx \frac{\sin x}{x}\frac{1}{t(x)}\left\{1 - \frac{\beta_1}{\beta_0^2}\frac{\ln t(x)}{t(x)}\right\}, \quad t(x) = \ln\frac{x^2 + m_B^2 r^2}{\Lambda_V^2 r^2}. \quad (68)$$

This integral was numerically calculated in the quenched approximation ($n_f = 0$), and the coupling constant $\tilde{\alpha}_B^{(2)}(r)$ is shown by the dotted curve in the figure over the range $0 \leq r \leq 1$ fm, along with two different approximate curves.

(1) The "exact" $\tilde{\alpha}_B^{(2)}(r)$, given by integral (68) with $m_B = 1.0$ GeV, is compared to α_V in perturbation theory, which was discussed in Section 3. In the two-loop approximation, $\alpha_V(q = 1/r, \Lambda = \Lambda_R)$ is given by the expression

$$\alpha_V^{(2)}\left(q = \frac{1}{r}, \Lambda_R\right) = \frac{4\pi}{\beta_0 y(r)}\left\{1 - \frac{\beta_1}{\beta_0^2}\frac{\ln y(r)}{y(r)}\right\} \quad (69)$$

with

$$y(r) \equiv y\left(q = \frac{1}{r}\right) = \ln\frac{1}{r^2\Lambda_R^2}. \quad (70)$$

The behavior of $\alpha_V^{(2)}(q = 1/r, \Lambda_R)$ is shown by the dash-dotted curve in the figure. The values of $\alpha_V^{(2)}(q = 1/r, \Lambda_R)$ are also given in Table 1.

From our calculations presented in Table 1, one can see that the perturbative $\alpha_V^{(2)}(q = 1/r, \Lambda_R)$ at small dis-

Table 1. Comparison of two-loop $\tilde{\alpha}_B^{(2)}(r)$ in background-field theory with $\alpha_V^{(2)}(q = 1/r, \Lambda_R)$ in perturbation theory (Λ_R = 686 MeV, $\Lambda_{\overline{MS}}$ = 240.7 MeV) at small distances

r, fm	$\tilde{\alpha}_B^{(2)}(r)$*	$\alpha_V^{(2)}(q = 1/r, \Lambda_R)$**	r, fm	$\tilde{\alpha}_B^{(2)}(r)$*	$\alpha_V^{(2)}(q = 1/r, \Lambda_R)$
0.002	0.09641	0.09235	0.0355	0.19881	0.19433
0.004	0.11095	0.10505	0.041	0.20851	0.20794
0.006	0.12159	0.12089			
0.008	0.13032	0.12212	0.049	0.22036	0.22636
0.012	0.14455	0.13521	0.057	0.23108	0.24549
0.016	0.15640	0.14653	0.063	0.23844	0.26053
0.020	0.16657	0.15688	0.069	0.245321	0.27635
0.024	0.17573	0.16665	0.077	0.25394	0.29894
0.030	0.18797	0.18067	0.087	0.26386	0.33026

* The values of $\tilde{\alpha}_B(r)$ were found by calculating the integral in (68) with m_B = 1.0 GeV and Λ_V = 0.385 GeV.

** The approximate $\alpha_V(q = 1/r, \Lambda_R)$ is defined by Eq. (69), Λ_R = 0.686 GeV.

tances, $r \lesssim 0.04$ fm, is systematically smaller, by about 1–4%, than the "exact" coupling constant $\tilde{\alpha}_B^{(2)}(r)$ in BFTh. This fact takes place even at very small distances; e.g., at r = 0.002 fm the perturbative coupling constant $\alpha_V^{(2)}$ is still smaller than $\tilde{\alpha}_B^{(2)}(r)$ by about 4%. However, this result is virtually independent of m_B, because at such small distances the influence of the background mass is immaterial.

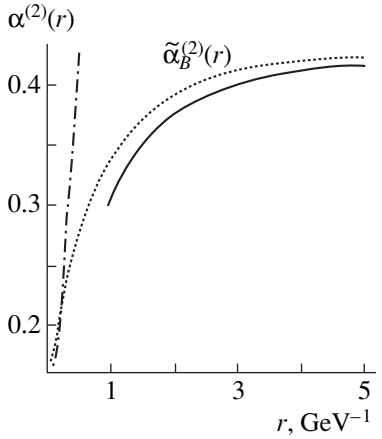

Two-loop strong-coupling constant in coordinate space as a function of the distance r in the quenched approximation (n_f = 0). The three curves represent perturbative $\alpha_V^{(2)}(q = 1/r, \Lambda_R)$ with Λ_R = 686 MeV (dash-dotted curve); the strong-coupling constant in BFTh $\tilde{\alpha}_B^{(2)}(r)$, defined by the integral in (68) with m_B = 1.0 GeV and Λ_V = 385 MeV (dotted curve); and $\alpha_B^{(2)}(q = 1/r, \Lambda_V = 385$ MeV) with m_B = 1.0 GeV (solid curve).

To explain this fact, it is convenient to consider the one-loop approximation when

$$\tilde{\alpha}_B^{(1)}(r) = \frac{8}{\beta_0}\int_0^\infty dx \frac{\sin x}{x}\left[\ln\left(\frac{x^2 + m_B^2 r^2}{\Lambda_V^2 r^2}\right)\right]^{-1}. \quad (71)$$

For $r \longrightarrow 0$, it is usually assumed [28] that this integral reduces to the one-loop perturbative expression:

$$\tilde{\alpha}_V^{(1)}(r) = \frac{4\pi}{\beta_0}\left(\ln\frac{1}{\Lambda_R^2 r^2}\right)^{-1}. \quad (72)$$

However, it is possible to use the expansion of the function $t^{-1}(x)$ [where $t(x)$ is given in (68)] at $r \longrightarrow 0$:

$$t^{-1}(x) = -\frac{1}{2\ln(\Lambda_V r)} \times\left\{1 + \frac{\ln(x^2 + m_B^2 r^2)}{2\ln(\Lambda_V r)} + \frac{\ln^2(x^2 + m_B^2 r^2)}{(2\ln(\Lambda_V r))^2}\right\}, \quad (73)$$

and term $(m_B^2 r^2)$ can be neglected under the logarithm. Then, $\tilde{\alpha}_B^{(1)}(r)$ in (71) can be calculated analytically:

$$\tilde{\alpha}_B^{(1)}(r) = \frac{4\pi}{\beta_0(-2\ln(\Lambda_V r))}\left\{1 - \gamma_E\frac{1}{\ln(\Lambda_V r)} + \frac{4\gamma_E^2 + \pi^2/3}{(2\ln(\Lambda_V r))^2}\right\} \cong \frac{4\pi}{\beta_0}\left\{\ln\frac{1}{\Lambda_R^2 r^2} - \frac{\pi^2}{3(-2\ln(\Lambda_V r))}\right\}^{-1}, \quad (74)$$

where $\Lambda_R = \Lambda_V \exp\gamma_E$. From (73), one can see that this expression does not actually depend on the background mass m_B and in the limit $r \longrightarrow 0$ it goes over to perturbative one-loop coupling constant (72). However, the

contribution of the second (small) term in the denominator remains important up to very small distances: at $r = 0.02$ fm this correction is 3%, and at $r_0 = 2 \times 10^{-4}$ fm this correction is still 1.4%. The importance of higher order corrections is a characteristic feature of the coupling constant in coordinate space.

(2) In our calculations, the background and perturbative coupling constants coincide at the point $r_1 \approx 0.04$ fm (see Table 1), and at $r > r_1$, the perturbative $\alpha_V^{(2)}(q = 1/r, \Lambda_R)$ becomes larger than $\tilde{\alpha}_B^{(2)}(r)$. This result of ours is in agreement with a similar observation in lattice measurements of the short-distance static potential [24]. In [24], it was observed that the absolute value of the lattice static potential is larger than the two-loop perturbative potential up to the separation $r_L \approx 0.12 r_0 \approx 0.06$ fm ($r_0 = 0.5$ fm). This value of r_L turns out to be rather close to our point $r_1 = 0.04$ fm discussed above. Here, it is worth to noting that the value of r_L in lattice data can depend on the chosen normalization condition and on the nonperturbative contribution to the static potential and therefore can slightly differ from the point r_1 where perturbative and background coupling constants are equal.

At larger distances, $0.1 > r > 0.04$ fm, the perturbative coupling constant becomes larger than $\tilde{\alpha}_B^{(2)}(r)$, being about 25% larger at the point $r \approx 0.09$ fm (see Table 1 and figure).

Thus, one can conclude that the perturbative two-loop coupling constant (70) with $\Lambda = \Lambda_R$ has the accuracy $\lesssim 5\%$ at the distances $r \lesssim 0.06$ fm and is significantly different at larger distances.

3. At large distances, $r \gtrsim 0.2$ fm, another approximation to $\tilde{\alpha}_B^{(2)}(r)$ can be used. To get this approximation, we have taken into account that at large distances QCD constant Λ is close to the value Λ_V and $\tilde{\alpha}_B(r)$ freezes if $r \longrightarrow \infty$. Therefore, the two-loop approximation to $\tilde{\alpha}_B^{(2)}(r)$ can be chosen as

$$\alpha_B^{(2)}\left(q = \frac{1}{r}, \Lambda_B = \Lambda_V\right) = \frac{4\pi}{\beta_0 t_B(r)}\left\{1 - \frac{\beta_1}{\beta_0^2}\frac{\ln t_B(r)}{t_B(r)}\right\}, \quad (75)$$

where

$$t(r) = \ln\frac{1 + m_B^2 r^2}{\Lambda_V^2 r^2}. \quad (76)$$

The comparison of the approximate coupling constant $\alpha_B^{(2)}(q = 1/r, \Lambda_V)$ and the "exact" coupling constant $\tilde{\alpha}_B^{(2)}(r)$ is illustrated by the numbers given in Table 2; see also solid and dotted curves in the figure. From Table 2, one can see that the approximate coupling constant is very close to $\tilde{\alpha}_B^{(2)}(r)$ at the distances $r > 0.4$ fm, remaining a bit smaller than $\tilde{\alpha}_B^{(2)}(r)$ over the entire region. The difference between them is 3.2, 2.3, and 1.6%, respectively, at the distances 0.5, 0.7, and 1.0 fm. Still the approximate expression (74), given in the analytic form, is very simple and can be useful in phenomenological calculations.

Table 2. Comparison of $\tilde{\alpha}_B(r)$ with the approximate coupling constant $\alpha_B(q = 1/r, \Lambda_V)$ at large distances

r, fm	"Exact" $\tilde{\alpha}_B(r)$*	$\alpha_B(q = 1/r, \Lambda_V)$** $\Lambda = \Lambda_V = 385$ MeV, $m_B = 1.0$ GeV
0.2	0.3367	0.3030
0.3	0.3710	0.3489
0.4	0.3914	0.3754
0.5	0.4041	0.3911
0.54	0.4077	0.3956
0.6	0.4121	0.4009
0.7	0.4171	0.4073
0.8	0.4204	0.4117
0.9	0.4225	0.4148
1.0	0.4238	0.4172
$r \longrightarrow \infty$	0.42756	0.42756

* The values of $\tilde{\alpha}_B^{(2)}(r)$ were found by calculating the integral in (68) with $m_B = 1.0$ GeV.

** The approximate coupling constant $\alpha_B(q = 1/r, \Lambda_V)$ is defined by Eq. (66).

It is also important that both coupling constants have the same freezing value (63), which is determined only by the background mass m_B since QCD constant Λ_V is supposed to be known. To define m_B, the lattice static potential, as well as fine-structure splittings, can be used [18, 19].

8. CONCLUSIONS

In our study, we have investigated the properties of the strong-coupling constant $\tilde{\alpha}_B(r)$ in BFTh, which was numerically calculated in the quenched approximation ($n_f = 0$).

It was found that at small distances two-loop $\tilde{\alpha}_B(r)$ is systematically 1–4% larger than a perturbative constant up to very small distances, $r \sim 10^{-4}$ fm. This property does not depend on the value of background mass m_B, playing a role of a regulator, and is a characteristic feature of the coupling constant in coordinate space. This result is in good agreement with lattice data on the static potential over small distances [24].

At average distances, $0.06 \lesssim r \lesssim 0.2$ fm, it turns out that there is no way to define QCD constant Λ in coor-

dinate space as a constant. As a function of the distance r, it changes in the range $\Lambda_R(r \longrightarrow 0) \geq \Lambda(r) \geq \Lambda_V(r \longrightarrow \infty)$, where $\Lambda_V = \Lambda_{\overline{MS}} \exp(a_1/2\beta_0)$ ($\Lambda_V^{(0)} \approx 1.6\Lambda_{\overline{MS}}^{(0)}$ for $n_f = 0$).

At large distances, $r \gtrsim 0.4$ fm, $\tilde{\alpha}_B(r)$ approaches fast the freezing value $\tilde{\alpha}_B(r \longrightarrow \infty)$, being only 3% smaller than $\tilde{\alpha}_B(r \longrightarrow \infty)$ at $r = 0.5$ fm. The freezing value in BFTh is fully defined by the background mass m_B since QCD constant Λ_V is supposed to be known (from lattice data or from experiment). The value of $m_B = 1.0$ GeV, taken here from fine-structure analysis in charmonium and bottomonium, gives $\tilde{\alpha}_B(r \longrightarrow \infty) = \alpha_B(q = 0) = 0.428$, which is very close to the values used in quarkonium phenomenology.

ACKNOWLEDGMENTS

This work was supported in part by RFBR–DFG (grant no. 96-02-00088g).

APPENDIX

To derive the coefficients A_1 and A_2 in expansion (21) of perturbative coupling constant $\tilde{\alpha}_V(r)$, one needs to calculate the integrals

$$J_n(\mu) = \frac{2}{\pi}\int_0^\infty \frac{dx}{x}\sin x\left(\ln\frac{\mu^2 r^2}{x^2}\right)^n \quad (n = 0, 1, 2). \quad \text{(A.1)}$$

Those integrals can be found in [29]:

$$J_0 = 1,$$
$$J_1(\mu, r) = [\ln(\mu^2 r^2) + 2\gamma_E], \quad \text{(A.2)}$$
$$J_2(\mu, r) = [\ln^2(\mu^2 r^2) + 4\gamma_E \ln(\mu^2 r^2) + 4\gamma_E^2 + \pi^2/3].$$

By taking the renormalization scale $\mu = 1/r$ in (A.2), one gets

$$J_1 = 2\gamma_E,$$
$$J_2 = 4\gamma_E^2 + \pi^2/3; \quad \text{(A.3)}$$

i.e., J_0, J_1, and J_2 turn out to be constants. With the use of (A.3), one can obtain the explicit expansions (22) for the coefficients A_1 and A_2 in (21).

In BFTh instead of integrals $J_n(\mu)$, given by (A.1), one needs to calculate the integrals

$$\eta_n(r, \mu) = \frac{2}{\pi}\int_0^\infty dx \frac{\sin x}{x}\left[\ln\frac{\mu^2 r^2 + m_B^2 r^2}{x^2 + m_B^2 r^2}\right]^n \quad \text{(A.4)}$$
$$(n = 0, 1, 2).$$

If $n = 0$, then $\eta_0 = J_0 = 1$. The function $\eta_1(r, \mu)$ (for $n = 1$) can be found by considering [29] that the integral

$$\xi_1(x) = \frac{2}{\pi}\int_0^\infty dx \frac{\sin x}{x}\ln(m_B^2 r^2 + x^2)$$
$$= \ln(m_B^2 r^2) - 2\,\mathrm{Ei}(-m_B r) \equiv -2\gamma(r), \quad \text{(A.5)}$$
$$\text{since} \quad \mathrm{Ei}(-x) = \gamma_E + \ln(-x) + \sum_{k=1}^\infty \frac{x^k}{k!k}.$$

Here, γ_E is the Euler constant, and

$$\gamma(r) = \gamma_E + \sum_{k=1}^\infty \frac{(-m_B r)^k}{k!k}. \quad \text{(A.6)}$$

Then, we have

$$\eta_1(r, \mu) = \ln(\mu^2 r^2 + m_B^2 r^2) + \gamma(r); \quad \text{(A.7)}$$

choosing $\mu = 1/r$, one obtains expression (45) for $\gamma_1(r)$:

$$\gamma_1(r) \equiv \frac{1}{2}\eta_1\left(r, \mu = \frac{1}{r}\right) = \frac{1}{2}\ln(1 + m_B^2 r^2) + \gamma(r). \quad \text{(A.8)}$$

In the case of $n = 2$, the integral (A.4),

$$\eta_2(r, \mu) = \frac{2}{\pi}\int_0^\infty dx \frac{\sin x}{x}\{[\ln(\mu^2 r^2 + m_B^2 r^2)]^2 \quad \text{(A.9)}$$
$$- 2\ln(\mu^2 r^2 + m_B^2 r^2)\ln(x^2 + m_B^2 r^2) + \ln^2(x^2 + m_B^2 r^2)\},$$

can be reduced to the expression

$$\eta_2(r, \mu) = \ln^2(\mu^2 r^2 + m_B^2 r^2)$$
$$+ 4\gamma(r)\ln(\mu^2 r^2 + m_B^2 r^2) + \xi_2(r), \quad \text{(A.10)}$$

where the function $\xi_2(r)$,

$$\xi_2(r) = \frac{2}{\pi}\int_0^\infty dx \frac{\sin x}{x}\ln^2(x^2 + m_B^2 r^2), \quad \text{(A.11)}$$

was not found in an analytic form. To get (A.9), expression (A.5) for $\xi_1(r)$ was used. Then choosing again in (A.9) the renormalization scale $\mu = 1/r$, one obtains

$$\eta_2\left(r, \mu = \frac{1}{r}\right) = \ln^2(1 + m_B^2 r^2)$$
$$+ 4\gamma\ln(1 + m_B^2 r^2) + \xi_2(r). \quad \text{(A.12)}$$

It was shown (see Section 5) that, in the perturbative limit, $m_B \longrightarrow 0$, $r \longrightarrow 0$, the $\gamma(r)$ and $\xi_2(r)$ functions have the following limits:

$$\gamma(r) \longrightarrow \gamma_E,$$
$$\xi_2(r) \longrightarrow 4\gamma_E^2 + \pi^2/3; \quad \text{(A.13)}$$

therefore, in this case the function $\gamma_2(r)$ in (42) is given by

$$\gamma_2(r) \equiv \eta_2\left(r, \mu = \frac{1}{r}\right) \longrightarrow 4\gamma_E^2 + \frac{\pi^2}{3} \quad (A.14)$$
$$(r \longrightarrow 0, m_B = 0).$$

REFERENCES

1. K. G. Wilson, Phys. Rev. D **10**, 2445 (1974); M. Greutz, *Quarks, Gluons, and Lattices* (Cambridge Univ. Press, Cambridge, 1983).
2. M. N. Chernodub, F. V. Gubarev, M. I. Polikarpov, and V. I. Zakharov, hep-ph/0003006; submitted to Phys. Lett.
3. A. Billoire, Phys. Lett. B **104B**, 472 (1981).
4. Particle Data Group, Eur. Phys. J. C **3**, 81 (1998).
5. M. Peter, Phys. Rev. Lett. **78**, 602 (1997); M. Jezábek, M. Peter, and Y. Sumino, Phys. Lett. B **428**, 352 (1998).
6. Y. Schröder, Phys. Lett. B **447**, 321 (1999).
7. E. Eichten *et al.*, Phys. Rev. Lett. **34**, 369 (1975).
8. A. M. Badalian and V. P. Yurov, Yad. Fiz. **51**, 1368 (1990) [Sov. J. Nucl. Phys. **51**, 869 (1990)]; Yad. Fiz. **56** (12), 239 (1993) [Phys. At. Nucl. **56**, 1760 (1993)].
9. J. Richardson, Phys. Lett. B **82B**, 272 (1979).
10. W. Buchmüller, Phys. Lett. B **112B**, 479 (1982).
11. Yu. A. Simonov, Yad. Fiz. **60**, 2252 (1999) [Phys. At. Nucl. **60**, 2069 (1999)]; hep-ph/9704301.
12. S. Godfrey and N. Isgur, Phys. Rev. D **32**, 189 (1985).
13. S. P. Booth *et al.*, Phys. Lett. B **294**, 385 (1992).
14. G. S. Bali and K. Schilling, Phys. Rev. D **47**, 661 (1993).
15. Yu. A. Simonov, Pis'ma Zh. Éksp. Teor. Fiz. **57**, 513 (1993) [JETP Lett. **57**, 525 (1993)]; Yad. Fiz. **58**, 113 (1995) [Phys. At. Nucl. **58**, 107 (1995)].
16. A. M. Badalian and Yu. A. Simonov, Yad. Fiz. **60**, 714 (1997) [Phys. At. Nucl. **60**, 630 (1997)].
17. Yu. A. Simonov, in *QCD and Topics Physics, Lectures at the XVII International School of Physics, Lisbon, 1999*; hep-ph/9911237.
18. A. M. Badalian and V. L. Morgunov, Phys. Rev. D **60**, 116008 (1999).
19. A. M. Badalian and B. G. L. Bakker, hep-ph/0004021.
20. J. M. Cornwall, Phys. Rev. D **26**, 1453 (1982); G. Parisi and R. Petronzio, Phys. Lett. B **94B**, 51 (1980).
21. A. C. Mattingly and P. M. Stevenson, Phys. Rev. D **49**, 437 (1994).
22. A. B. Kaidalov and Yu. A. Simonov, Yad. Fiz. **63**, 1507 (2000) [Phys. At. Nucl. **63**, 1428 (2000)]; hep-ph/9912434; hep-ph/9911291; Phys. Lett. B **477**, 163 (2000).
23. D. V. Shirkov and I. L. Solovtsov, Phys. Rev. Lett. **79**, 1209 (1997).
24. G. S. Bali, hep-ph/9905387; Phys. Lett. B **460**, 170 (1999).
25. S. Capitani, M. Luscher, R. Sommer, and H. Witting, Nucl. Phys. B **544**, 669 (1999).
26. M. Melles, hep-ph/0001295.
27. Yu. A. Simonov, Lect. Notes Phys. **479**, 139 (1996).
28. W. Lucha, F. Schöberl, and D. Gromes, Phys. Rep. **200**, 127 (1991).
29. I. S. Gradshteyn and I. M. Ryzhik, *Table of Integrals, Series, and Products* (Nauka, Moscow, 1971; Academic, New York, 1980).

Physics of Atomic Nuclei, Vol. 63, No. 12, 2000, pp. 2184–2196. Translated from Yadernaya Fizika, Vol. 63, No. 12, 2000, pp. 2280–2292.

ELEMENTARY PARTICLES AND FIELDS
Theory

Spin Effects in Backward Deuteron Scattering and Baryonic Degrees of Freedom in the Deuteron

L. S. Azhgirey* and N. P. Yudin[1)]

Joint Institute for Nuclear Research, Dubna, Moscow oblast, 141980 Russia

Received June 9, 1999; in final form, December 27, 1999

Abstract—The effect of the baryon-resonance admixture to the deuteron wave function on the momentum dependences of the differential cross section, the tensor analyzing power T_{20}, and the polarization-transfer coefficient κ_0 for backward elastic deuteron–proton scattering at high energies is investigated. The reaction in question is assumed to proceed predominantly through nucleon and nucleon-resonance exchanges. The formalism used in this study is based on light-front dynamics. The effect of various parameters of the problem on the results of the calculations is analyzed, and it is shown that, even at a 1% level of the total admixture of nucleon resonances to the deuteron wave function, a description of experimental data that is superior to that within the one-nucleon-exchange approximation can be achieved by appropriately choosing the contributions of various resonances. For qualitative agreement between the results of the calculations and experimental data to be attained, it is sufficient to take into account the contributions of the lightest negative-parity baryon resonances. Upon taking into account baryon exchanges, results computed for observables with different deuteron wave functions show a smaller scatter than analogous results obtained within the one-nucleon-exchange approximation. © *2000 MAIK "Nauka/Interperiodica".*

1. INTRODUCTION

Among intermediate-energy-physics problems of current interest, that of establishing the degrees of freedom that are operative in processes occurring at sufficiently small distances between hadrons (about 0.3–0.6 fm) attracts particular attention. Here, questions that are of prime importance for developing intermediate-energy physics include the following: Is it necessary at such distances to go over from effective hadronic degrees of freedom, which are widely used, for example, to describe nucleon–nucleon interactions, to fundamental quark–gluon degrees of freedom? What kind of dynamics is associated with one degree of freedom or another at such distances?

It is obvious that answers to these questions and some other questions of similar character cannot be obtained immediately—it is sufficient to recall the long way of development of nuclear physics and of the physics of nucleon–nucleon scattering. In the present study, we will attempt to clarify the above questions by analyzing the effect of a baryon-resonance admixture in the deuteron wave function on the characteristics of backward elastic deuteron–proton scattering.

The problem of isobaric states in the deuteron has been discussed for more than two decades. A number of reviews articles (see [1, 2]) and many original studies have been devoted to the subject. It could be thought that the most reliable information about the small-distance structure of the deuteron would come from applying electromagnetic probes to it. In particular, such investigations resulted in establishing the existence of meson-exchange currents in the deuteron [3] and in drawing the conclusion that it is necessary to take into account nucleon isobaric states in dealing with such probes [4]. As the time passed, it became clear, however, that the problem of resonances in the deuteron is very involved and that it can be solved only on the basis of additional experimental information accumulated by using both electromagnetic and hadronic probes. Proton–deuteron scattering into the backward hemisphere (in the c.m. frame) is one of the most appropriate reactions for studying the small-distance structure of the deuteron.

Available experimental data on the differential cross section for this process [5–12] show the following special features: (i) The differential angular distribution has an ascending character as the c.m. scattering angle approaches 180°. (ii) At a fixed angle, the differential cross section decreases fast with increasing incident-proton (incident-deuteron) energy. (iii) The cross section as a function of energy has a plateau at proton kinetic energies in the range 0.3–0.7 GeV (for backward elastic deuteron–proton scattering, this approximately corresponds to primary deuteron momenta in the range 1.6–2.6 GeV/c). To a great extent, these features gave impetus to the original discussion of isobaric states in the deuteron.

A radically new step in the investigation of deuteron–proton scattering was associated with the analysis of the polarization characteristics of this reaction. In particular, the tensor analyzing power T_{20} for backward

* e-mail: azhgirey@cv.jinr.ru
[1)] Moscow State University, Vorob'evy gory, Moscow, 119899 Russia.

elastic deuteron–proton scattering at primary deuteron momenta between 1.1 and 3.9 GeV/c and between 3.5 and 6.5 GeV/c was measured in Saclay [13, 14] and in Dubna [15], respectively; in addition, the coefficient κ_0 of polarization transfer from the vectorially polarized deuteron to the forward emitted proton was measured for the reaction ^{1}H(d, p)X at 3.5 GeV/c [16] and for the reaction ^{12}C(d, p)X in the deuteron-momentum range from 6 to 9 GeV/c [17–19].

A theoretical analysis of backward deuteron–proton scattering in the energy region under investigation is rather complicated, since it involves some unresolved dynamical problems of relativistic nuclear physics. Presently, these questions have not yet been clarified completely, and one has to rely on more or less reasonable approximations. If it is assumed that deuteron–proton scattering is dominated by effective hadronic degrees of freedom, the u-channel pole mechanism involving the transfer of a nucleon (in general, a baryon) from the deuteron to the proton (see the diagram in Fig. 1 below) appears to be the simplest and most natural reaction mechanism. A covariant treatment of this diagram on the basis of the Bethe–Salpeter equation [20, 21] leads to results that do not differ very strongly from those obtained within old-fashioned approaches that relied on a direct use of the deuteron wave function. It is necessary in this case that a right value of the internal nucleon momentum k (that allowing for relativistic kinematics) be substituted into the wave function. A result that is common to such calculations of backward deuteron–proton scattering is that they lead to a noticeable quantitative (and even qualitative in the case of the tensor analyzing power T_{20}) discrepancy with experimental data. It also appeared that the required behavior of T_{20} could be obtained by assuming a P-wave admixture in the deuteron ground state [22]. However, the antinucleon P wave that arises automatically in solving the Bethe–Salpeter equation is overly small to explain the observed internal-momentum dependence of the analyzing power T_{20}. A further complication of the mechanism of deuteron–proton scattering within the covariant field-theoretical formalism does not seem reasonable since this would involve introducing poorly defined form factors.

In view of this, the formalism of relativistic quantum mechanics—in particular, its version in the form of light-front dynamics, which realizes the Poincaré group in the basis of a few particles promptly interacting with one another (that is, through an instantaneous potential) [23, 24]—has recently become a popular means for analysis of deuteron–proton processes. This conceptual framework seems quite appealing for the following reasons. Based on calculations in terms of wave functions, it is formally similar to nonrelativistic theory; in addition, it enables one to test the accuracy in solving the scattering problem. Despite this, analyses within relativistic quantum mechanics that make use of a complicated mechanism taking into account, among other things, resonance exchanges, delta-isobar excitations, and rescattering processes do not lead to reasonable agreement with experimental data [25].

In analyzing backward deuteron–proton scattering, we attempt here to revive the u-channel pole diagram within light-front dynamics. Basically, the arguments that motivated our attempt are the following: (i) As was indicated above, the features of this process that are calculated here significantly depend on those internal-momentum values that are substituted into the deuteron wave functions. It will be shown below that the method of light-front dynamics opens new possibilities here. (ii) Although the framework being discussed is very attractive, a situation where some constraints are imposed on the scattering angles cannot be described in terms of relativistic quantum mechanics without invoking very strong hypotheses. Indeed, it seems highly improbable that an exact nonperturbative description can be effectively reduced to a scheme within relativistic quantum mechanics such that the operator associated with the spin of the system being considered ceases to depend on interaction [26]. (iii) Previous calculations of resonance-contribution effects assumed values for the resonance admixture to the deuteron wave function that are hardly justifiable. As is currently discussed, a nucleon-resonance admixture can arise in the deuteron wave function either via the meson mechanism [2] or via the formation of the s^4p^2 six-quark configuration [27, 28]. However, neither mechanism can be quantified precisely. It is especially important to emphasize this because it was found in recent years that the mesonic origin of nucleon–nucleon interaction is not universal even at low energies [29].

The main objective that is pursued in the present study and which is suggested by the aforesaid is twofold. First, we want to calculate spin effects in backward deuteron–proton scattering within a somewhat modified formalism of light-front dynamics. Second, we will try find out—without microscopically computing the resonance admixture in the deuteron wave function—whether it is possible in principle to attain, at reasonable phenomenological values of this admixture, at least qualitative agreement between the calculated and the measured values of the analyzing power T_{20} for backward elastic deuteron–proton scattering. An implicit hypothesis here is that it is this scattering process that must be the main source of information about the admixture of, say, the P wave in the deuteron wave function.

2. DESCRIPTION OF THE FORMALISM

2.1. Baryon Exchange within Light-Front Dynamics

In accordance with the comments presented in the Introduction, we will use methods of quantum field theory and consider that backward elastic deuteron–proton scattering at incident-deuteron momenta about 5 GeV/c is dominated by the exchange mechanism illustrated in Fig. 1. In addition to nucleon exchange, exchange of nucleon resonances also occurs.

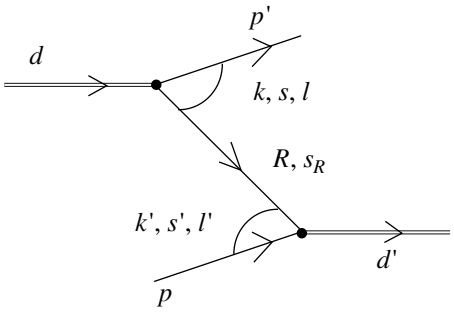

Fig. 1. One-nucleon-exchange diagram for backward elastic deuteron–proton scattering.

The covariant form of the amplitude associated with this diagram requires introducing a large number of unknown form factors in the deuteron vertices [30] and nontrivial propagators for particles of spin $s = 3/2, 5/2, \ldots$ [31]. Even in the particular case of only one diagram, it is therefore necessary to simplify radically the description of the process. It is of paramount importance that the formalism used be relativistically invariant since, under the kinematical conditions being considered, even the particles transferred in the process are essentially relativistic. In our opinion, light-front dynamics combines the requirements of simplicity and relativistic invariance in the most natural way [32].

Within light-front dynamics, the invariant amplitude $\mathcal{M}_{fi}$ corresponding to the diagram in Fig. 1 can be approximately represented as the sum over poles associated with the exchanges of a nucleon and of its excited states; that is,

$$\mathcal{M}_{fi} = \sum_R \frac{\mathcal{M}(d \longrightarrow p'R)\mathcal{M}(pR \longrightarrow d')}{2R^+(R^- - R^-_{\rm on})}, \qquad (1)$$

where $\mathcal{M}(d \longrightarrow p'R)$ and $\mathcal{M}(pR \longrightarrow d')$ are, respectively, the deuteron-breakup and the deuteron-formation amplitude; R is the index labeling resonances (including nucleon); R^+ and R^- are, respectively, the "plus" and the "minus" components of the resonance 4-momentum,

$$R^\pm = \frac{1}{\sqrt{2}}(R^0 \pm R^3), \qquad (2)$$

R^0 and R^3 being, respectively, the zeroth (energy) and the third component of the momentum R^μ; and $R^-_{\rm on}$ is the minus on-mass-shell component,

$$R^-_{\rm on} = \frac{M_R^2 + R_T^2}{2R^+}. \qquad (3)$$

Here, R_T is the R^μ component orthogonal to the z axis, while M_R is the resonance mass. In the Feynman diagram technique, which is equivalent in this case to the technique of time-ordered diagrams, we have

$$R^- = d^- - p'^-. \qquad (4)$$

Expression (1) is approximate in that the spin part of the resonance propagator is taken on the mass shell, as is usually done [33]. On one hand, this makes it possible to go over from vertices to wave functions; on the other hand, the propagator here proves to be noncovariant, so that relativistic invariance is violated. In order to restore covariance, it is necessary to add a contact part to the propagator [34]. This results in that the numerator of the propagator also involves the component R^- rather than $R^-_{\rm on}$. We believe that, in the approximation used here, the above violations of relativistic invariance are minimal.

By using the variable

$$x = p'^+/d^+, \qquad (5)$$

we can recast Eq. (1) into the form

$$\mathcal{M}_{fi} = \frac{1}{1-x}\sum_R \frac{\mathcal{M}(d \longrightarrow p'R)\mathcal{M}(pR \longrightarrow d')}{M_d^2 - M_{NT}^2/x - M_{RT}^2/(1-x)}, \qquad (6)$$

where

$$M_{NT}^2 = M_N^2 + R_T^2, \quad M_{RT}^2 = M_R^2 + R_T^2,$$

M_N and M_d being, respectively, the nucleon and the deuteron mass.

In light-front dynamics, the quantity

$$\frac{\mathcal{M}(d \longrightarrow Rp')}{M_d^2 - M^2(x, R_T)} = \varphi_d^{NR}(x, k_{RT}, \mu, \mu_R), \qquad (7)$$

where μ and μ_R are the projections of, respectively, the nucleon and the resonance spin onto the quantization axis, plays the role of the wave function in the NR channel. In (7), we have used the new variable k_{RT} defined as

$$k_{RT} = (1-x)p'_T - xR_T, \qquad (8)$$

where the subscript T labels the momentum component transverse with respect to the z axis.

The wave function in (7) is normalized by the condition

$$\sum_R \int \left|\varphi_d^{NR}\right|^2 d\tau_R = 1, \qquad (9)$$

where the integration measure $d\tau_R$ has the form

$$d\tau_R = \frac{dx d\mathbf{k}_T^R}{(2\pi)^3 \cdot 2x(1-x)}. \qquad (10)$$

In terms of the light-front-dynamics wave functions $\varphi_d^{NR}(x, \mathbf{k}_T^R)$, the amplitude in (6) can be represented in the form

$$\mathcal{M}_{fi} = \frac{1}{1-x}\sum_R \varphi_d^{NR}(x, k_{RT}, \mu', \mu_R)\varphi_d^{NR*}(x', k'_{RT}, \mu, \mu_R) \times \left(M_d^2 - \frac{M_N^2 + k_{RT}^2}{x'} - \frac{M_R^2 + k_{RT}^2}{1-x'}\right), \qquad (11)$$

where the quantity

$$x' = p^+/d'^+ \tag{12}$$

corresponds to the kinematics of a deuteron emitted from the lower vertex of the diagram in Fig. 1.

For the sake of convenience, we further go over from the variables x and k_{RT} to the momentum variables $k_R = (k_{RT}, k_R^3)$, where k_R^3 is determined by the relations

$$x = \frac{E_N(k_R) + k_R^3}{E_N(k_R) + E_R(k_R)}, \tag{13}$$

$$E_{N,R} = \sqrt{M_{N,R}^2 + k_R^2}. \tag{14}$$

In terms of the new variables, the amplitude $\mathcal{M}_{fi}$ assumes the form

$$\mathcal{M}_{fi} = \frac{1}{1-x}\sum_R \varphi_d^{NR}(k_R, \mu', \mu_R) \times \varphi_d^{NR*}(k_R', \mu, \mu_R)\Delta M^2(k_R'), \tag{15}$$

where

$$\Delta M^2(k_R') = M_d^2 - M^2(k_R'),$$

$$M^2(k_R') = \frac{M_N^2 + k_{RT}^2}{x'} + \frac{M_R^2 + k_{RT}^2}{1-x'} = [E_N(k_R') + E_R(k_R')]^2.$$

The normalization condition for the functions φ_d^{NR} then takes the form

$$\sum_{R\mu\mu_R}\int\left|\varphi_d^{NR}(k_R, \mu, \mu_R)\right|^2 \frac{d^3k_R}{(2\pi)^3 \cdot 2\mu_{NR}(k_R)} = 1, \tag{16}$$

where

$$\mu_{NR}(k_R) = \frac{E_N(k_R)E_R(k_R)}{E_N(k_R) + E_R(k_R)}.$$

In the ensuing analysis of polarization observables expressed in terms of the *S*- and *D*-wave components of the deuteron wave function, it is necessary to use the orbital angular momenta and the spin moments. In the *LS* representation of light-front dynamics, there arise some difficulties, since the spin operator depends, in general, on the interaction. In view of this, we further adopt the approximation in which the wave function used is identified, in each of the *NR* channels, with the two-body wave function in the relativistic quantum mechanics of the light front [24, 35, 36]. Within this theory, the spin operator of free particles is taken for the spin operator S, and the wave function $\varphi_d^{NR}(k_R, \mu, \mu_R)$ can be represented in the form

$$\varphi_d^{NR}(k_R, \mu, \mu_R) = \sum_{ls}\varphi_{ls}^{NR}(k_R)\left\langle \frac{1}{2}\nu s_R \nu_R \middle| sm_s\right\rangle \times \langle lms m_s|1M\rangle [R^+(k_R)]_{\mu\nu}[R^+(-k_R)]_{\mu_R\nu_R}Y_{lm}(n_R), \tag{17}$$

where n_R specifies the proton-emission direction and where the Melosh matrices $R^+(k_R)$ [37] are the D functions of the spatial rotation through the Melosh angle, which can be found from the explicit form of the Melosh matrix in the *NN* channel,

$$R^+(k_T) = \frac{M + E_N(k) + k^3 - i\epsilon_{rs}k_{Tr}\sigma_s}{\sqrt{2[E_N(k) + M][E_N(k) + k^3]}}. \tag{18}$$

Here, σ_s stands for the Pauli matrices; $r, s = 1, 2$; and ϵ_{rs} is the unit antisymmetric tensor normalized by the condition $\epsilon_{12} = -\epsilon_{21} = 1$.

The problem of calculating the amplitude for the diagram in Fig. 1 in terms of the deuteron wave functions in various channels can in principle be solved with the aid of Eqs. (15)–(17). Hence, the problem of determining the spin characteristics of backward elastic deuteron–proton scattering can also be solved at the model level.

So far, our consideration has been quite general. Let us now specify the direction of the z axis. Since the effective Lagrangian of the degrees of freedom being considered must be Lorentz invariant (in particular, invariant under rotations), the z axis can be chosen arbitrarily in general. However, the use of light-front-dynamics wave functions of relativistic quantum mechanics that are subjected to a constraint on angles instead of covariant vertices and the disregard of contact diagrams generally lead to violation of rotational invariance, so that the choice of the direction of the z axis becomes significant. A general consideration of this question is beyond the scope of the present article. Therefore, we only mention that it is common practice to align the z axis with the beam direction. This prescription is adopted, for example, in the theory of deep-inelastic scattering [38]. We will follow this tradition. A comparison with experimental data can serve as a criterion of correctness of this choice of direction [39]. Our choice leads to $x \neq x'$ and, hence, to $k_R \neq k_R'$. In the case of backward elastic deuteron–proton scattering, we have

$$xx' = (M_N/M_d)^2. \tag{19}$$

When the z-axis direction is chosen in this way, we do not need to take into account Melosh matrices—in the case of backward scattering, all transverse components of the momenta vanish, so that there are no Melosh rotations.

2.2. Differential Cross Section for Backward Elastic Deuteron–Proton Scattering

The differential cross section $d\sigma/d\Omega$ for backward elastic deuteron–proton scattering in the c.m. frame is given by

$$\frac{d\sigma}{d\Omega} = \frac{1}{6(8\pi)^2 s}\mathrm{tr}\{\mathcal{M}_{fi}\mathcal{M}_{fi}^{+}\}, \tag{20}$$

where s is the square of the total c.m. energy, $\mathcal{M}_{fi}$ is the amplitude for the process, and the trace symbol tr implies summation over the spin variables of the initial and of the final state. After some simple, but cumbersome calculations, we arrive at

$$\mathrm{tr}\{\mathcal{M}_{fi}\mathcal{M}_{fi}^{+}\} = \frac{1}{(1-x)^2}\sum_{\kappa_s RR'} B_{\kappa_s}^{RR'}(k_R, k_{R'}) \times B_{\kappa_s}^{RR'*}(k'_R, k'_{R'})\Delta M_R^2(k'_R)\Delta M_R^2(k'_{R'}), \tag{21}$$

where

$$B_{\kappa_s}^{RR'}(k_R, k_{R'}) = \sum_{lsl's'} b_{\kappa_s}^{RR'}(ls; l's')\phi_{ls}(k_R)\phi_{l's'}^{*}(k_{R'}), \tag{22}$$

$$b_{\kappa_s}^{RR'}(ls; l's') = (-1)^{s_{R'}+1/2}\frac{3}{4\pi}\hat{l}\hat{l}'\hat{s}\hat{s}'\langle l0l'0|\kappa_s 0\rangle \times \begin{Bmatrix} l & s & 1 \\ s' & l' & \kappa_s \end{Bmatrix}\begin{Bmatrix} s_R & s & 1/2 \\ s' & s_{R'} & \kappa_s \end{Bmatrix}. \tag{23}$$

Here, $\boldsymbol{\kappa}_s = \mathbf{s} + \mathbf{s}'$, $\hat{l} = \sqrt{2l+1}$, $\begin{Bmatrix} l & s & 1 \\ s' & l' & \kappa_s \end{Bmatrix}$ are Wigner $6j$ coefficients, and $\langle l0l'0|\kappa_s 0\rangle$ are Clebsch–Gordan coefficients. In deriving Eq. (21), we have made use of the relation

$$\sum_{M\mu}\varphi_M(k, \mu, \mu_R)\varphi_M^{*}(k, \mu, \mu_{R'}) = \delta_{\mu_R\mu_{R'}}\sum_{\kappa_s}(-1)^{s_{R'}-\mu_R}\langle s_R\mu_R s_{R'}-\mu_{R'}|\kappa_s q_s\rangle B_{\kappa_s}^{RR'}(k_R, k_{R'}), \tag{24}$$

where M is the projection of the deuteron spin onto the quantization axis (onto the z axis in our case).

If we restrict our consideration to the nucleon channel, it can be found from Eq. (20) that, in the one-nucleon-exchange approximation, the differential cross section has the form [40]

$$\frac{d\sigma}{d\Omega} = \frac{3}{(64\pi^2)^2 s}\left[\frac{M_d^2 - M^2(k'_N)}{1-x}\right]^2 \times [\phi_0^2(k) + \phi_2^2(k)][\phi_0^2(k') + \phi_2^2(k')]. \tag{25}$$

It is interesting to note that this expression is symmetric under the interchange of the primed and unprimed variables x and k. This means that the differential cross section for backward elastic deuteron–proton scattering as given by (25) is invariant under the reversal of the z-axis direction.

2.3. Tensor Analyzing Power for Backward Elastic Deuteron–Proton Scattering

The tensor analyzing power T_{20} is given by

$$T_{20} = \frac{\mathrm{tr}\{\mathcal{M}t_{20}\mathcal{M}^{+}\}}{\mathrm{tr}\{\mathcal{M}\mathcal{M}^{+}\}}, \tag{26}$$

where the standard spin–tensor

$$\langle 1M|t_{20}|1M'\rangle = (-1)^{1-M'}\langle 1M1-M|20\rangle \tag{27}$$

is chosen for the spin operator T_{20}.

Substituting expression (15) for the amplitude into (26) and taking into account (17), we obtain

$$T_{20} = \frac{\sum_{\kappa_s RR'}\Delta M^2(k'_R)\Delta M^2(k'_{R'})A_{\kappa_s}(k_R, k_{R'})B_{\kappa_s}^{*}(k'_R, k'_{R'})}{\sum_{\kappa_s RR'}\Delta M^2(k'_R)\Delta M^2(k'_{R'})B_{\kappa_s}(k_R, k_{R'})B_{\kappa_s}^{*}(k'_R, k'_{R'})}, \tag{28}$$

where

$$A_{\kappa_s}(k_R, k_{R'}) = \sum_{lsl's'} a_{\kappa_s}^{RR'}(ls; l's')\phi_{ls}(k_R)\phi_{l's'}^{*}(k_{R'}), \tag{29}$$

$$a_{\kappa_s}^{RR'}(ls; l's') = (-1)^{l'+\kappa_s+s-s_{R'}+1/2}\frac{3}{4\pi}\hat{s}\hat{s}'\hat{l}\hat{l}' \times \begin{Bmatrix} s_R & s & 1/2 \\ s' & s'_R & \kappa_s \end{Bmatrix}\sum_{\kappa_l q_l}\langle l0l'0|\kappa_l 0\rangle\langle\kappa_l 0\kappa_s 0|20\rangle \times \hat{\kappa}_l\begin{Bmatrix} l & \kappa_l & l' \\ 1 & 2 & 1 \\ s & \kappa_s & s' \end{Bmatrix}. \tag{30}$$

Here, $\kappa_l = l + l'$, $\begin{Bmatrix} l & \kappa_l & l' \\ 1 & 2 & 1 \\ s & \kappa_s & s' \end{Bmatrix}$ are Wigner $9j$ coefficients, and the expression for $B_{\kappa_s}(k_R, k_{R'})$ is given above [see Eq. (22)].

Formula (28) determines the components of the tensor analyzing power T_{20} with the z axis directed along the beam. In a number of experiments, however, the polarization of the deuteron beam was specified with

respect to the y axis that is orthogonal to the beam. It can easily be seen that the tensor analyzing power T_{20}^R with respect to this y axis is related to the above quantity T_{20} by a simple equation. (Only the "20" component of the density matrix is nonzero for a tensorially polarized deuteron beam.) Indeed, the spin–tensors t_{2q}^R specified with respect to the y axis and the spin–tensors t_{2q} specified with respect to the z axis are related by the equation

$$t_{2q}^R = Rt_{2q}R^{-1} = \sum_{q'} D_{q'q}^2(R)t_{2q'}, \tag{31}$$

where R is the rotation from the z axis to the y axis about the x axis and $D_{q'q}(R)$ are matrices of an irreducible representation of the group of rotations. In terms of the Euler angles, we have

$$R = \left(\frac{\pi}{2}, 0, 0\right). \tag{32}$$

From Eqs. (31) and (32), we obtain

$$T_{20}^R = T_{20}/2.$$

If we take into account only the nucleon channel in expression (28) and set $k = k'$, there arises the well-known formula (see, for example, [41])

$$T_{20} = \frac{\sqrt{8}u(k)w(k) - w^2(k)}{\sqrt{2}[u^2(k) + w^2(k)]}, \tag{33}$$

where $u(k)$ and $w(k)$ are the radial wave functions corresponding to the S- and the D-wave deuteron state.

2.4. Polarization-Transfer Coefficient in Backward Elastic Deuteron–Proton Scattering

The coefficient of polarization transfer from the vectorially polarized deuteron to the proton, κ_0, is given by [42]

$$\kappa_0 = \frac{\mathrm{tr}\{2J_y^p \mathcal{M} J_y^d \mathcal{M}^+\}}{\mathrm{tr}\{\mathcal{M}\mathcal{M}^+\}}, \tag{34}$$

where J_y^p and J_y^d are the y components of the proton and the neutron spin operator, respectively. In order to determine κ_0, we first calculate the quantity

$$\frac{\mathrm{tr}\{t_{1q}^p \mathcal{M} t_{1q}^d \mathcal{M}^+\}}{\mathrm{tr}\{\mathcal{M}\mathcal{M}^+\}}, \tag{35}$$

where t_{1q}^p and t_{1q}^d are the standard spin–tensors for the final proton and the initial deuteron, respectively. By using the simple, albeit cumbersome, relation

$$\sum_{MM'} \varphi_M(k_R, \mu, \mu_R)(-1)^{1-M'}\langle 1M1 - M'|\kappa q\rangle$$

$$\times \varphi_{M'}^*(k_{R'}, \mu', \mu_{R'}) = \frac{3}{\sqrt{4\pi}}\sum_g (-1)^{l'}\hat{g}\hat{\kappa}_s\hat{\kappa}_{s'}\hat{s}\hat{s}'\hat{l}\hat{l}' \times$$

$$\times \langle l0l'0|\kappa_l 0\rangle\langle \kappa_l q_l g m_g|1q\rangle\langle \kappa_{s'} q_{s'} \kappa_s q_s|g m_g\rangle \tag{36}$$

$$\times \begin{Bmatrix} 1/2 & \kappa_{s'} & 1/2 \\ s & g & s' \\ s_R & \kappa_s & s_{R'} \end{Bmatrix} \begin{Bmatrix} l & \kappa_l & l' \\ 1 & 1 & 1 \\ s & g & s' \end{Bmatrix} \langle \mu|t_{\kappa_{s'}q_{s'}}|\mu'\rangle\langle \mu_R|t_{\kappa_s q_s}|\mu_{R'}\rangle$$

$$\times Y_{\kappa_l q_l}(n)\phi_{ls}(k_R)\phi_{l's'}^*(k_{R'}),$$

we find for backward scattering that

$$\frac{\mathrm{tr}\{t_{1q'}^p \mathcal{M} t_{1q}^d \mathcal{M}^+\}}{\mathrm{tr}\{\mathcal{M}\mathcal{M}^+\}} \tag{37}$$

$$= \delta_{q'q}\frac{\sum_{\kappa_s RR'} P_{\kappa_s q}^{RR'}(k_R, k_{R'})B_{\kappa_s}^{RR'}(k'_R, k'_{R'})\Delta M^2(k'_R)\Delta M^2(k'_{R'})}{\sum_{\kappa_s RR'} B_{\kappa_s}^{RR'}(k_R, k_{R'})B_{\kappa_s}^{RR'*}(k'_R, k'_{R'})\Delta M^2(k'_R)\Delta M^2(k'_{R'})},$$

where the quantities $B_{\kappa_s}^{RR'}(k'_R, k'_{R'})$ are determined by Eq. (22) and

$$P_{\kappa_s q}^{RR'}(k_R, k_{R'}) = \frac{3\sqrt{3}}{4\pi}\sum_{ll'ss'g\kappa_s\kappa_l} (-1)^{l'}\hat{g}\hat{\kappa}_s\hat{s}\hat{s}'\hat{l}\hat{l}'\langle l0l'0|\kappa_l 0\rangle$$

$$\times \langle \kappa_l 0 g q|1q\rangle\langle 1q\kappa_s 0|gq\rangle \begin{Bmatrix} 1/2 & 1 & 1/2 \\ s & g & s' \\ s_R & \kappa_s & s_{R'} \end{Bmatrix} \tag{38}$$

$$\times \begin{Bmatrix} l & \kappa_l & l' \\ 1 & 1 & 1 \\ s & g & s' \end{Bmatrix} \phi_{ls}(k_R)\phi_{l's'}^*(k_{R'}).$$

Here, $q = \pm 1, 0$ are the spherical indices of the polarization vector,

$$P^x = \frac{1}{\sqrt{2}}(P^{-1} - P^{+1}),$$

$$P^y = \frac{i}{\sqrt{2}}(P^{-1} + P^{+1}),$$

$$P^z = P^0,$$

and $\hat{g} = \sqrt{2g+1}$, g taking the minimal values in the intervals $|s - s'| \le g \le s + s'$, $|1 - \kappa_s| \le g \le 1 + \kappa_s$, and $|\kappa_l - \kappa| \le g \le \kappa_l + \kappa$.

Returning to the definition of the coefficient κ_0 in Eq. (34), we note that

$$J_y^p = \frac{i}{2}(t_{11}^p + t_{1-1}^p),$$

$$J_y^d = i(t_{11}^d + t_{1-1}^d).$$

With the aid of Eq. (37), we then obtain

$$\frac{\langle 2J_{z'}^p \mathcal{M} J_{z'}^d \mathcal{M}^+ \rangle}{\langle \mathcal{M}\mathcal{M}^+ \rangle} = -\frac{1}{2}\left\{ \frac{\langle t_{11}^p \mathcal{M} t_{11}^d \mathcal{M}^+ \rangle}{\langle \mathcal{M}\mathcal{M}^+ \rangle} + \frac{\langle t_{1-1}^p \mathcal{M} t_{1-1}^d \mathcal{M}^+ \rangle}{\langle \mathcal{M}\mathcal{M}^+ \rangle} \right\}. \quad (39)$$

If we again restrict our consideration to nucleon exchange and set $k = k'$, the result is

$$\frac{\langle 2J_{z'}^p \mathcal{M} J_{z'}^d \mathcal{M}^+ \rangle}{\langle \mathcal{M}\mathcal{M}^+ \rangle} = \frac{1}{3}\frac{u^2(k) - w^2(k) - u(k)w(k)/\sqrt{2}}{u^2(k) + w^2(k)}. \quad (40)$$

This expression differs from that which is used most often only by a trivial normalization factor.

3. RESULTS OF THE CALCULATIONS AND DISCUSSION

We begin the discussion of our results by analyzing the potential of the pole diagram in Fig. 1 in the one-nucleon-exchange approximation of the present version of light-front dynamics (that is, we take into account, for the time being, only nucleonic degrees of freedom).

For backward elastic deuteron–proton scattering, the differential cross section $(d\sigma(180°)/d\Omega)_{\text{c.m.}}$ calculated with the deuteron wave functions for the Paris potential [43], the Reid soft-core potential [44], the *A* and *B* versions of the Bonn potential [45], and the Moscow potential [46] (curves *1*, *2*, *3*, *4*, and 5, respectively) is displayed in Fig. 2*a* as a function of the incident-deuteron momentum in the laboratory frame. Also shown in this figure are experimental data from [5–12] {the angular distributions that were obtained in [5, 9] near the angle of $\theta_{\text{c.m.}} = 180°$ were extrapolated to this angle on the basis of the dependence $(d\sigma(\theta)/d\Omega)_{\text{c.m.}} = \sum_{i=0}^{3} a_i |\cos\theta|^i$}.

From Fig. 2*a*, it can be seen that the results of the calculations with the different wave functions differ quite sizably. The figure also shows that the pole diagram does not describe the plateau in the range 2–2.5 GeV/*c*. However, this feature in the energy dependence of the differential cross section for elastic deuteron–proton scattering can be explained with the aid of the triangle diagram, whereby the cross section for deuteron–proton scattering is expressed in terms of the cross section for the process $NN \longrightarrow d\pi$, the latter being of a resonance character in the above energy region [47–49]. By taking into account relativistic effects and the *D*-wave admixture in the deuteron wave function, it was possible to improve additionally the description of experimental data [50].

The tensor analyzing power T_{20} and the polarization-transfer coefficient κ_0 calculated with the same deuteron wave functions are displayed in Figs. 2*b* and 2*c*, respectively. It is important to emphasize here that the discrepancy between the results of the calculations and experimental data cannot be removed within the one-nucleon-exchange model—in particular, it was shown by Punjabi *et al*. [14] that, within this model, the correlation between the T_{20} and κ_0 values associated with the same *k* value represents a circle on the (T_{20}, κ_0) plane, whereas the experimental form of this correlation is helical. A recent phenomenological analysis revealed that the description of experimental data can be somewhat improved by additionally taking into account absorption effects [51].

In order to calculate directly the analyzing power T_{20} and the polarization-transfer coefficient κ_0 within our approach, it is necessary to know the nucleon wave function of the deuteron; the wave functions $\phi_{ls}(k_R)$; the relation between the functions $\phi_{ls}(k_R)$ that are associated with the same resonance, but which correspond to different *s* values; and, finally, the magnitude of the admixture of baryon resonances to the deuteron wave function. We will now discuss the choice of these parameters in some detail.

3.1. *Wave Functions* $\phi_{ls}(k_R)$

In a consistent treatment, these functions are derived by solving the dynamical problem of a resonance admixture in the deuteron. Since we do not aim here at precisely describing experimental data, we approximate them by oscillator functions, which were successfully used to calculate nuclear hadronic systems localized in space. Specifically, we set

$$\phi_{ls}(k_R) = C_R k_R^l \exp(-\alpha_R k_R^2), \quad (41)$$

where C_R is a normalization factor and α_R is a parameter that characterizes the spatial localization of the resonance. It is natural to assume that the radius of the resonance distribution in the *NR* channels must be smaller than the deuteron radius (that is, the radius of the *NN* channel). This follows, in particular, from the uncertainty relation—the resonance formed in the central region of the deuteron cannot travel a distance greater than $1/\Delta M_R$, where $\Delta M_R = M_R - M_N$. From the same considerations, it follows that the heavier the resonance, the smaller the spatial region where it must be localized. In order to avoid increasing the number of parameters, we approximated the oscillator radius $r_{Rj} = 1/\sqrt{\alpha_{Rj}}$ as

$$r_{Rj} = r_0 \sqrt{\frac{M_{R1} - M_N}{M_{Rj} - M_N}}, \quad (42)$$

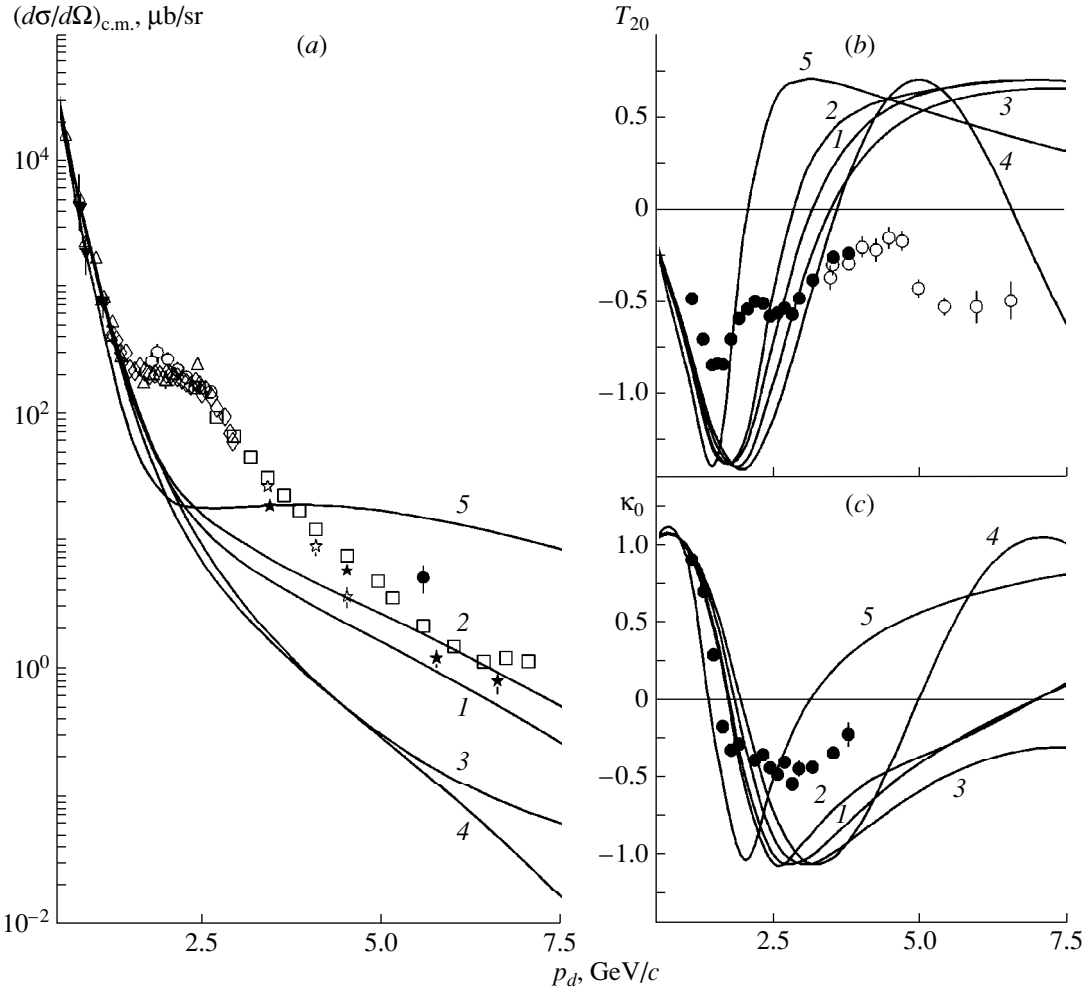

Fig. 2. Differential cross section $(d\sigma/d\Omega)_{\text{c.m.}}$, tensor analyzing power T_{20}, and polarization-transfer coefficient κ_0 for backward elastic deuteron–proton scattering versus the incident-deuteron momentum p_d that were calculated in the one-nucleon-exchange approximation with the deuteron wave functions for (curve *1*) the Paris potential [43], (curve *2*) Reid soft-core potential [44], (curve *3*) version *A* and (curve *4*) version *B* of the Bonn potential [45], and (curve *5*) the Moscow potential [46]. Experimental data were borrowed from (open stars) [5], (closed inverted triangles) [6], (closed circles) [7], (open circles) [8], (closed stars) [9], (open triangles) [10], (open diamonds) [11], and (open squares) [12] for (*a*) the differential cross section; from (closed circles) [14] and (open circles) [15] for (*b*) the tensor analyzing power T_{20}; and from (closed circles) [14] for (*c*) the polarization-transfer coefficient k_0.

where M_{R1} is the mass of the $N(1440)$ resonance and r_0 is a parameter common to all resonances.

3.2. Magnitude of Resonance Admixtures

As was indicated above, mechanisms that can be responsible for the emergence of resonance admixtures in the deuteron wave function are not discussed here. Both conceivable mechanisms mentioned in the Introduction predict the magnitude of the admixture at a level of a few tenths of a percent to a few percent. At the stage of choosing other parameter values, we fixed the total magnitude of the admixture at 2%. As will be seen below, this choice is not crucial—a qualitative description of data can be attained with a value of about 1% or even with a somewhat smaller value.

3.3. Relation between the Functions $\phi_{ls}(k_R)$ Corresponding to Different s Values

In the general case of the exchange of a spin-s_R baryon, two states, that of spin $s_R - 1/2$ and that of spin $s_R + 1/2$, arise in the *NR* channel. The possible values of the orbital angular momentum are determined by the parity of the exchanged baryon resonance. Since the functions $\phi_{ls}^{NR}(k_R)$ that we use were not derived by solving the dynamical problem, the relations between the functions that describe *NR* states and which are characterized by different *s* values are determined by the quality of the description of data.

3.4. Wave Function of the NN Channel

As was shown above, the results of the calculations in the one-nucleon-exchange approximation depend on

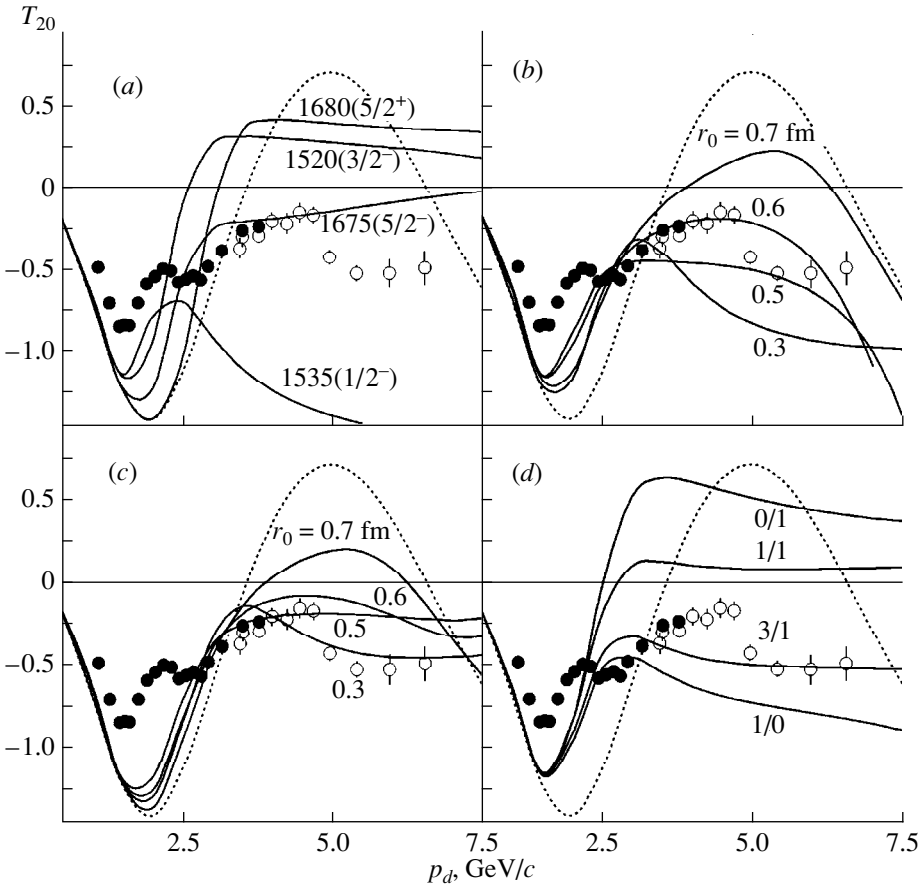

Fig. 3. Tensor analyzing power T_{20} for backward elastic deuteron–proton scattering versus the incident-deuteron momentum p_d according to the calculations in which the deuteron wave function is assumed to include a 2% admixture of (*a*) one of the baryon resonances $N(1520, 3/2^-)$, $N(1535, 1/2^-)$, $N(1675, 5/2^-)$, and $N(1680, 5/2^+)$ at $r_0 = 0.4$ fm; (b) the negative-parity baryon resonances $N(1520)$, $N(1535)$, $N(1650)$, and $N(1675)$ at various values of r_0 (indicated in the figure); (*c*) all known resonances from $N(1520)$ to $N(2600)$ at various values of r_0 (indicated in the figure) under the assumption that a nonvanishing contribution comes only from the wave function ϕ_{ls}^{NR} corresponding to the lower channel spin of the possible two values; and (*d*) the negative-parity resonances $N(1520)$, $N(1535)$, $N(1650)$, and $N(1675)$ at $r_0 = 0.4$ fm and various values of the wave-function ratio $\phi_{ls_{\min}}/\phi_{ls_{\max}}$ (indicated in the figure). The dotted curves were computed in the one-nucleon-exchange approximation. The displayed experimental data are identical to those in Fig. 2*b*.

the form of the *NN*-channel wave function. In choosing parameter values, the deuteron wave function for the *B* version of the Bonn potential [45] was used for the *NN*-channel wave function. The eventual results were obtained for all wave functions with which we performed the calculations in the one-nucleon-exchange approximation.

As can be seen from Fig. 2, the data on the tensor analyzing power T_{20} show the most specific type of momentum dependence; moreover, this spin observable has been presently measured up to the highest values of the internal momentum k. For this reason, the baryon-resonance contributions have been analyzed predominantly on the basis of a comparison of the results of the calculations precisely with these data.

As a typical illustration, the calculated analyzing power T_{20} as a function of the incident-deuteron momentum p_d is shown in Fig. 3*a* for the cases where the deuteron wave function contains a 2% admixture of only one of the baryon resonances $N(1520, 3/2^-)$, $N(1535, 1/2^-)$, $N(1675, 5/2^-)$, and $N(1680, 5/2^+)$ (indicated in parentheses here are the baryon mass, spin, and parity). At a fixed magnitude of the resonance admixture, the resonance-contribution effect on the behavior of T_{20} as a function of momentum depends on the parameter r_0 and on the relationship between the absolute values and phases of the wave functions ϕ_{ls}^{NR} corresponding to the different spin values of $s = s_R \pm 1/2$. The curves in Fig. 3*a* were computed at $r_0 = 0.4$ fm under the assumption that a nonvanishing contribution

comes only from the function for which the channel spin takes the lower value of the possible two.

As can be seen from this figure, the reversal of the sign of the analyzing power T_{20} in the region $p_d \geq 0.4$ GeV/c is the most spectacular effect of taking into account the contributions of $1/2^-$ resonances [$N(1535)$ and $N(1650)$]. If, in addition, we include $3/2^-$ resonances, the minimum in the analyzing power T_{20} calculated in the one-nucleon-exchange approximation with the deuteron wave function for version B of the Bonn potential (dotted curve) is slightly filled; concurrently, the T_{20} values are reduced in the momentum region $p_d \geq 0.4$ GeV/c. The contributions of the even-parity baryons alone have a smaller effect on the behavior of T_{20}. As might have been expected, the inclusion of the $N(1440)$ and $N(1710)$ resonances, which have the nucleon quantum numbers, does not change the shape of $T_{20}(p_d)$.

For the analyzing power $T_{20}(p_d)$ as a function of the incident-deuteron momentum at various values of r_0, the results of taking into account the total contribution of the 2% admixture of the negative-parity resonances $N(1520)$, $N(1535)$, $N(1650)$, and $N(1675)$ to the deuteron wave function are shown in Fig. 3*b* under the above assumption that a nonvanishing contribution comes only from the function ϕ_{ls}^{NR} for which the channel spin takes the lower value of the possible two. It can be seen from this figure that the inclusion of the additional contribution from negative-parity resonances changes substantially the result obtained within the one-nucleon-exchange approximation by taking into account only the NN-channel wave function for version B of the Bonn potential. Of course, it can hardly be expected that all details of the experimental dependence $T_{20}(p_d)$ will be reproduced by using only one pole diagram and quite a trivial form of the wave functions ϕ_{ls}^{NR}. Nonetheless, it can be seen that, even with these functions at r_0 values from the region 0.3–0.5 fm, we have achieved a better description of the data than within the one-nucleon-exchange approximation.

Since there are no obvious reasons for taking into account only the admixture of negative-parity resonances, it is of interest to explore the implications of including the exchanges of both negative- and positive-parity baryons. For the analyzing power T_{20}, the results of taking into account the total contribution to the deuteron wave function from the 2% admixture of all known resonances from $N(1520)$ to $N(2600)$ are shown in Fig. 3*c* for various values of r_0. Here, we again assumed that a nonvanishing contribution comes only from the function ϕ_{ls}^{NR} corresponding to the lower value of the channel spin. As can be seen from Fig. 3*c*, the inclusion of the exchanges of all resonances again improves the description of the experimental data on T_{20} in relation to the description in one-nucleon-exchange approximation with the deuteron wave function for version B of the Bonn potential. An optimal value of the parameter r_0 has not yet been chosen among those that were used in the calculations.

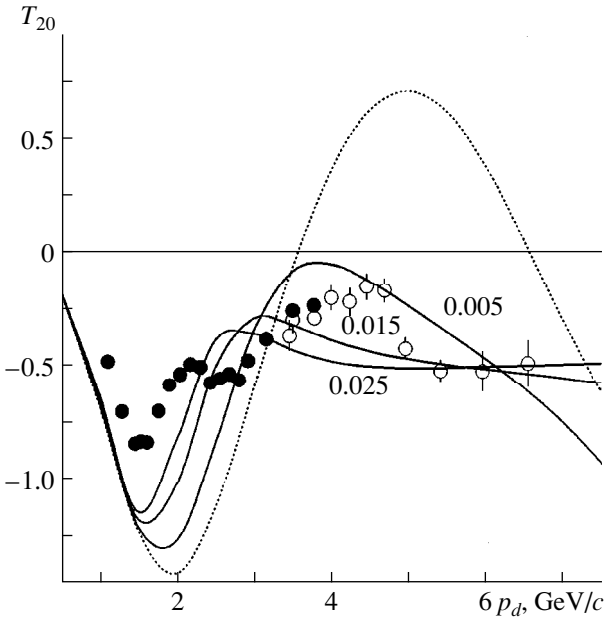

Fig. 4. Tensor analyzing power T_{20} for backward elastic deuteron–proton scattering versus the incident-deuteron momentum p_d according to calculations performed at various values of the total admixture (numbers on the curves) of the negative-parity resonances $N(1520)$, $N(1535)$, $N(1650)$, and $N(1675)$ to the deuteron wave function at $r_0 = 0.4$ fm and under the assumption that a nonvanishing contribution comes only from the wave function ϕ_{ls}^{NR} corresponding to lower channel spin of the possible two values. The dotted curve was computed in the one-nucleon-exchange approximation. The displayed experimental data are identical to those in Fig. 2*b*.

For the analyzing power T_{20} as a function of the incident-deuteron momentum, Fig. 3*d* illustrates the effect of variations in the wave-function ratio $\phi_{ls_{\min}}/\phi_{ls_{\max}}$ on the results of the calculations. In the calculations, we have taken into account the contributions of the negative-parity resonances $N(1520)$, $N(1535)$, $N(1650)$, and $N(1675)$ and set the parameter r_0 to 0.4 fm. As can be seen from this figure, the best agreement with the experimental data on T_{20} is achieved in the case where the contribution of the functions corresponding to the smaller value of the possible two channel spins exceeds the contribution of the functions corresponding to the higher spin value. In the calculations mentioned so far, the sign of the function $\phi_{ls_{\max}}$ was always taken to be identical to the sign of the function $\phi_{ls_{\min}}$. It is obvious that, in the case where the contribution of the functions corresponding to the smaller value of the channel spin exceeds the contribution of the functions corresponding to its higher value, the reversal of the relative sign is not

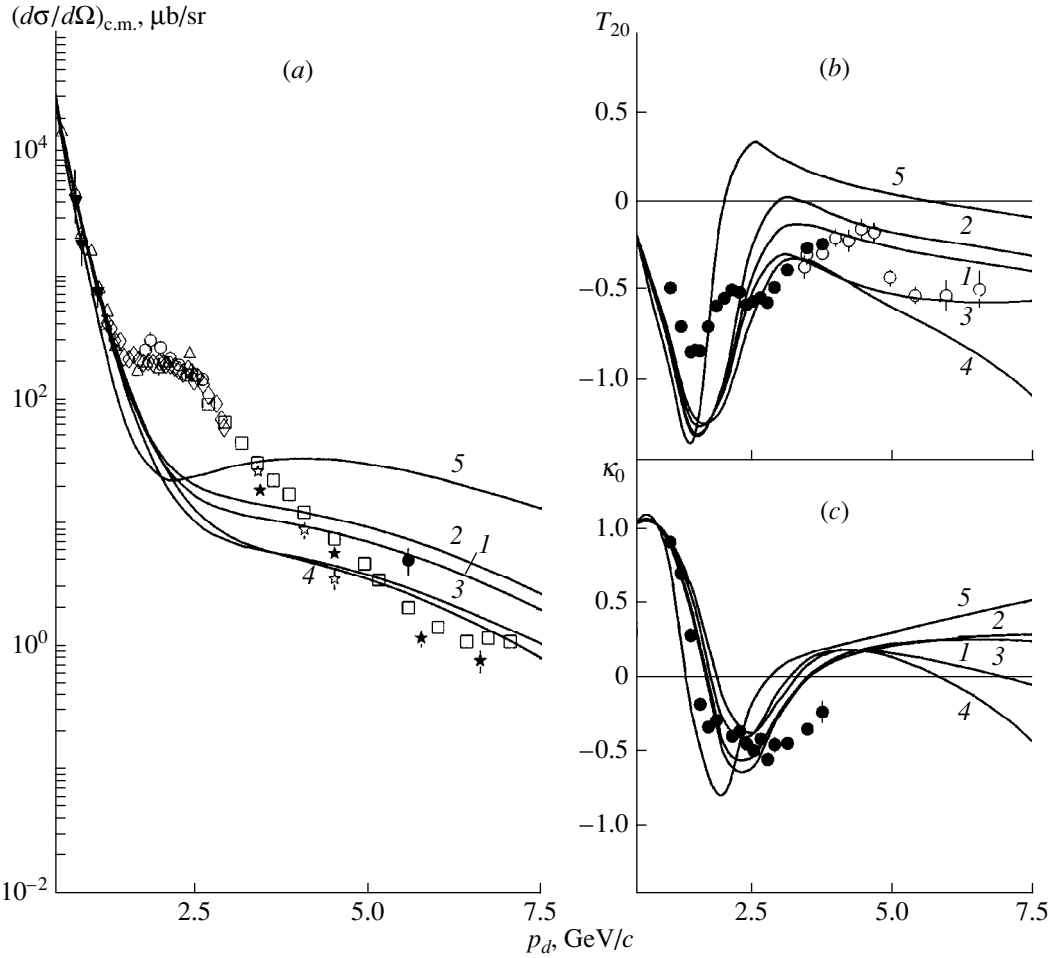

Fig. 5. Differential cross section $(d\sigma/d\Omega)_{\text{c.m.}}$, tensor analyzing power T_{20}, and polarization-transfer coefficient κ_0 for backward elastic deuteron–proton scattering versus the incident-deuteron momentum p_d that were calculated in the one-baryon-exchange approximation with the deuteron wave functions for (curve *1*) the Paris potential [43], (curve *2*) the Reid soft-core potential [44], versions (curve *3*) *A* and (curve *4*) *B* of the Bonn potential [45], and (curve *5*) the Moscow potential [46]. In the calculations, we took into account the contribution of a 1% admixture of the negative-parity resonances *N*(1520), *N*(1535), *N*(1650), and *N*(1675) to the deuteron wave function at $r_0 = 0.4$ fm and assumed that a nonvanishing contribution comes only from the wave function ϕ_{ls}^{NR} corresponding to the lower channel spin of the possible two values. The displayed experimental data are identical to those in Fig. 2.

expected to affect significantly the results of the calculations.

Figure 4 illustrates the effect that the change in the magnitude of the baryon-resonance admixture to the deuteron wave function can have on the quality of description of the data on T_{20}. In the calculations, we have taken into account the contributions of the negative-parity resonances *N*(1520), *N*(1535), *N*(1650), and *N*(1675) and set the wave-function ratio $\phi_{ls_{\min}}/\phi_{ls_{\max}}$ to 3/1 and the parameter r_0 to 0.4 fm. It can be seen that, at high p_d values, qualitative agreement with experimental data can be achieved at a relatively small magnitude of the admixture (about 0.5%).

Finally, Fig. 5 presents the momentum dependences of the differential cross section $[d\sigma(180°)/d\Omega)]_{\text{c.m.}}$, the tensor analyzing power T_{20}, and the polarization-transfer coefficient κ_0 calculated on the basis of the proposed approach. These calculations have been performed with the deuteron wave functions for the Paris potential [43], the Reid soft-core potential [44], versions *A* and *B* of the Bonn potential [45], and the Moscow potential [46] (curves *1*, *2*, *3*, *4*, and *5*, respectively). Also shown are available experimental data. In the calculations, which have been performed under the assumption that a nonvanishing contribution comes only from the functions ϕ_{ls}^{NR} corresponding to the lower value of the channel spin, we have taken into account the total effect of the 1% admixture of the negative-parity resonances *N*(1520), *N*(1535), *N*(1650), and *N*(1675) to the deuteron wave function and set $r_0 = 0.4$ fm. A comparison of these results with those calculated within the one-nucleon-exchange approximation (see Fig. 2) shows

that the inclusion of baryon-resonance exchanges, in addition to one-nucleon exchange, improves the description of data in the region of high p_d values. It is interesting to note that, upon taking into account baryon exchanges in calculating the observables considered in the present study, the values predicted for these observables with the different deuteron wave functions show a smaller scatter.

Let us briefly discuss the possible uncertainties that are associated with the approximations made in deriving the formulas used in our calculations. We begin by considering contact terms in the propagators. In instantaneous-form dynamics, a covariant field propagator reduces to the sum of particle and antiparticle propagators only for spinless and spin-1/2 particles. For example, the vector-particle propagator cannot be represented as the sum of particle and antiparticle propagators—it is necessary to add a contact term [34]. In light-front dynamics, covariant propagators possess this property for spin-1/2 particles as well [33]. As long as the field-theory formalism is used, there is no problem here—one can merely use a covariant propagator. But once quantities of the wave-function type are introduced, the problem of a contact part arises, since it cannot be included in a wave function. At present, the question of contact terms has received virtually no study. Following common practice, we simply disregard the contact part since this is a purely spin effect, which is usually insignificant.

The second question concerns the choice of the *z*-axis direction. In light-front dynamics, field theory must be in general invariant under rotations, but it is not straightforward to demonstrate this explicitly. Moreover, mechanisms that restore invariance under rotations (for example, excitations associated with rotations of new degrees of freedom) for the manifestly noninvariant original variables $p^{\pm} = (p^0 \pm p^3)/\sqrt{2}$ have not yet been disclosed. Usually, a formal way that consists in introducing additional degrees of freedom (orientation of the light hyperplane) is adopted in solving the problem of invariance under rotations [30, 39], but this significantly complicates the formalism. In our case, the results may depend on the choice of the *z*-axis direction. In all probability, however, the relevant uncertainty is insignificant (as is suggested both by the results of our calculations and by the results presented by Karmanov [39], who studied the spectrum of forward emitted protons in the deuteron-breakup reaction). It was indicated above that, in the case of backward elastic deuteron–proton scattering, the differential cross section associated with nucleon exchange is indeed independent of the reversal of the *z*-axis direction. Estimates show that uncertainties in other observables do not exceed the scatter of the results of the calculations performed with the different deuteron wave functions. A more comprehensive analysis of these questions will be performed elsewhere.

4. CONCLUSIONS

We have investigated quantitatively the effect of the baryon-resonance admixture to the deuteron ground state on the differential cross section $[d\sigma(180°)/d\Omega]_{\text{c.m.}}$, the tensor analyzing power T_{20}, and the polarization-transfer coefficient κ_0 for backward elastic deuteron–proton scattering. It has been assumed that, everywhere, with the exception of the region of intermediate momentum values between 1.6 and 2.6 GeV/*c*, the process predominantly proceeds via the transfer of a baryon (exchange of a nucleon and nucleon resonances). The formalism corresponding to this mechanism has been realized within light-front dynamics. The basic results of the present study can be summarized as follows:

(i) General formulas for the differential cross section $[d\sigma(180°)/d\Omega]_{\text{c.m.}}$, the tensor analyzing power T_{20}, and the polarization-transfer coefficient κ_0 have been obtained with allowance for admixtures of arbitrary resonances.

(ii) Predictions for these observables have been analyzed within the semiphenomenological approach that consists in choosing the wave functions for various *NR* channels and phase relations between them.

(iii) The effect of various parameters of the problem on the results of the calculations have been investigated, and it has been shown that, even at a 1% level of the nucleon-resonance admixture to the deuteron wave function, a description of experimental data that is superior to that within the one-nucleon-exchange approximation can be achieved by appropriately choosing the contributions of various resonances.

(iv) In order to fit the results of the calculations to experimental data, it has been sufficient to take into account the contributions of the lightest negative-parity baryon resonances, but the addition of the contributions from other resonances, including those of positive parity, has not led to a noticeable mismatch with data.

(v) Qualitatively, the contribution of negative-parity resonances slightly fills the deep minimum in the momentum dependence of the tensor analyzing power T_{20} calculated within the one-nucleon-exchange approximation and strongly diminishes this analyzing power at deuteron-momentum values not less than 3.5 GeV/*c*, thereby reducing the discrepancy between the theoretical and experimental results.

(vi) It has been established that, for the observables considered in the present study, a transition from one set of the deuteron wave functions used to another leads to a smaller scatter of the results when the baryon exchange is taken into account than when it is disregarded.

ACKNOWLEDGMENTS

We are grateful to Yu.N. Uzikov and E.A. Strokovsky for attention to this study and stimulating discussions.

REFERENCES

1. L. S. Kisslinger, *Mesons in Nuclei*, Ed. by M. Rho and D. H. Wilkinson (North-Holland, Amsterdam, 1979), p. 261, and references therein.
2. H. J. Weber and H. Arenhovel, Phys. Rep. **36**, 277 (1978).
3. O. O. Riska, Phys. Rep. **181**, 207 (1989).
4. R. Dymarz and F. C. Khanna, Nucl. Phys. A **516**, 549 (1990).
5. E. Coleman *et al.*, Phys. Rev. Lett. **16**, 761 (1966).
6. K. Kurod *et al.*, Nucl. Phys. **88**, 33 (1966).
7. Yu. D. Bayukov *et al.*, Yad. Fiz. **5**, 237 (1966) [Sov. J. Nucl. Phys. **5**, 167 (1966)].
8. V. I. Komarov *et al.*, Yad. Fiz. **16**, 234 (1972) [Sov. J. Nucl. Phys. **16**, 129 (1973)].
9. L. Dubal *et al.*, Phys. Rev. D **9**, 597 (1974).
10. P. C. Gugelot *et al.*, Phys. Scr. **10**, 252 (1974).
11. B. E. Bonner *et al.*, Phys. Rev. Lett. **39**, 1253 (1977).
12. P. Berthet *et al.*, J. Phys. G **8**, L111 (1982).
13. J. Arvieux *et al.*, Phys. Rev. Lett. **50**, 19 (1983); Nucl. Phys. A **431**, 613 (1984).
14. V. Punjabi *et al.*, Phys. Lett. B **350**, 178 (1995).
15. L. S. Azhgirey *et al.*, Phys. Lett. B **391**, 22 (1997); L. S. Azhgirey *et al.*, Yad. Fiz. **61**, 494 (1998) [Phys. At. Nucl. **61**, 432 (1998)].
16. E. Cheung *et al.*, Phys. Lett. B **284**, 210 (1992).
17. A. A. Nomofilov *et al.*, Phys. Lett. B **325**, 327 (1994).
18. B. Kuehn *et al.*, Phys. Lett. B **334**, 298 (1994).
19. L. S. Azhgirey *et al.*, JINR Rapid Commun., No. 3[77]-96, 23 (1996).
20. B. D. Keister and J. A. Tjon, Phys. Rev. C **26**, 578 (1982).
21. L. Kaptari *et al.*, Phys. Lett. B **351**, 400 (1995).
22. F. Gross, Phys. Rev. D **10**, 223 (1974); W. W. Buck and F. Gross, Phys. Rev. D **20**, 2361 (1979); F. Gross *et al.*, in *Proceedings of the XV European Few-Body Conference, Peniscola, 1995*, Ed. by R. Guardiola, Few-Body Syst., Suppl. **8**, 269 (1996); V. Punjabi and C. F. Perdrisat, in *Proceedings of the 3rd International Symposium "Dubna Deuteron-95," Dubna, 1996*, p. 304.
23. B. L. G. Bakker, L. A. Kondratyuk, and M. V. Terent'ev, Nucl. Phys. B **158**, 497 (1979).
24. Z.-J. Cao and B. D. Keister, Phys. Rev. C **42**, 2295 (1990).
25. Yu. N. Uzikov, Fiz. Élem. Chastits At. Yadra **29**, 1405 (1998) [Phys. Part. Nucl. **29**, 583 (1998)].
26. L. A. Kondratyuk and M. V. Terent'ev, Yad. Fiz. **31**, 1087 (1980) [Sov. J. Nucl. Phys. **31**, 561 (1980)].
27. L. Ya. Glozman, V. G. Neudatchin, and I. T. Obukhovsky, Phys. Rev. C **48**, 389 (1993).
28. V. S. Gorovoj and I. T. Obukhovsky, in *Proceedings of the 12th International Seminar on High Energy Physics Problems, Dubna, 1994* (in press); A. P. Kobushkin, A. I. Syamtomov, and L. Ya. Glozman, Yad. Fiz. **59**, 833 (1996) [Phys. At. Nucl. **59**, 795 (1996)].
29. V. I. Kukulin, in *Proceedings of the PNPI Winter School in Theoretical Physics, Gatchina, 1999* (in press).
30. J. Carbonell *et al.*, Phys. Rep. **300**, 215 (1998).
31. R. M. Davidson, N. C. Muchopodhay, and R. S. Wittman, Phys. Rev. D **43**, 71 (1991).
32. P. Dirac, Rev. Mod. Phys. **21**, 392 (1949).
33. G. P. Lepage and S. T. Brodsky, Phys. Rev. D **22**, 2157 (1980).
34. S. Weinberg, Phys. Rev. B **133**, 1318 (1964).
35. P. L. Chung *et al.*, Phys. Rev. C **37**, 2000 (1988).
36. W. N. Polyzou, Ann. Phys. (N.Y.) **193**, 367 (1989).
37. H. J. Melosh, Phys. Rev. D **9**, 1095 (1974).
38. R. P. Bickerstaft and A. W. Thomas, J. Phys. G **15**, 1523 (1989).
39. V. A. Karmanov, Pis'ma Zh. Éksp. Teor. Fiz. **42**, 116 (1985) [JETP Lett. **42**, 142 (1985)].
40. L. A. Kondratyuk and L. V. Shevchenko, Yad. Fiz. **29**, 792 (1979) [Sov. J. Nucl. Phys. **29**, 408 (1979)].
41. S. S. Vasan, Phys. Rev. D **8**, 4092 (1973).
42. G. G. Ohlsen, Rep. Prog. Phys. **35**, 717 (1972).
43. M. Lacombe *et al.*, Phys. Rev. C **21**, 861 (1980); Phys. Lett. B **101B**, 139 (1981).
44. R. V. Reid, Jr., Ann. Phys. (N.Y.) **50,** 411 (1968); G. Alberi *et al.*, Phys. Rev. Lett. **34**, 503 (1975).
45. R. Machleidt *et al.*, Phys. Rep. **149**, 1 (1987).
46. V. M. Krasnopol'sky *et al.*, Phys. Lett. B **165B**, 7 (1985).
47. T. Yao, Phys. Rev. B **134**, 454 (1964).
48. N. S. Craigie and C. Wilkin, Nucl. Phys. B **14**, 477 (1969).
49. G. W. Barry, Ann. Phys. (N.Y.) **73**, 482 (1972).
50. V. M. Kolybasov and N. Ya. Smorodinskaya, Yad. Fiz. **17**, 1211 (1973) [Sov. J. Nucl. Phys. **17**, 630 (1973)].
51. M. Tanifuji, S. Ishikawa, and Y. Iseri, Phys. Rev. C **57**, 2493 (1998).

Translated by A. Isaakyan

Physics of Atomic Nuclei, Vol. 63, No. 12, 2000, pp. 2197–2200. From Yadernaya Fizika, Vol. 63, No. 12, 2000, pp. 2293–2296.

NANP-99*

Higgs Boson Emission in Very Rare Decays of an Extra Vector Boson**

G. A. Kozlov

Joint Institute for Nuclear Research, Dubna, Moscow oblast, 141980 Russia

Received September 27, 1999

Abstract—We explore the phenomenological structure of E_6-inspired grand unified group with the gauge group $SU(3)_c \times SU(2)_L \times U(1)_Y \times U(1)$, the emphasis being laid upon its implications for Higgs boson observation. In particular, we discuss the probability for the mass eigenstate Z_2 to decay into a Higgs particle and a bound state composed of heavy quarks. Constraints on and relations between the Z_2 and Higgs masses are presented. © *2000 MAIK "Nauka/Interperiodica".*

1. INTRODUCTION

Very rare decay processes provide sensitive tests of new theories and an important testing ground for the Standard Model (SM). The field of very rare decays is diverse and active since it offers a rich potential for major discoveries. Theoretical interest in an extra neutral vector boson Z' has been mainly motivated by an experimental observation of possible deviations from SM predictions for the decay of the SM Z boson into $\bar{c}c$ and $\bar{b}b$ quark pairs (R_c and R_b ratios) [1]. The deviations may be considered as one of the indications of new physics beyond the SM. The promising explanation of the observed phenomena is implied in the extra-Z' models (see references [7–16] in [2]). New gauge bosons can be detected at future high-energy colliders—namely, Large Hadron Collider (LHC) at CERN, which can test the nature and structure of many theoretical models at a scale of 1 TeV, at least. Theoretical predictions of new neutral or charged gauge bosons come from various extensions of the SM [3]. New extra bosons naturally appear in the Grand Unification Theory (GUT) models [3]. A simple and well-known version among the extensions of the SM is the minimal one, which is aimed at unifying interactions, the E_6 GUT model [3]. Since the breakdown of E_6 GUT into the SM is accompanied by at least one extra $U(1)$ group [$E_6 \longrightarrow SU(3)_c \times SU(2)_L \times U(1)_Y \times U(1)$], there may exist a heavy neutral boson Z', which can mix with the ordinary Z boson. There are two new gauge bosons appearing in E_6 GUT models [3], where only one originates from the $SO(10)$ subgroup,

$$E_6 \supset SO(10) \times U(1)_\Psi,$$

$$SO(10) \supset SU(5) \times U(1)_\chi,$$

$$SU(5) \supset SU(3)_c \times SU(2)_L \times U(1)_Y,$$

while the Z' boson is a composition of Z_Ψ and Z_χ components mixed with a free angle θ [3]:

$$Z' = Z_\Psi \cos\theta - Z_\chi \sin\theta.$$

In order to seek Z' at LHC, it is important to know as much as possible about its decay modes both in standard sectors of the Drell–Yan (DY) type and in the (super)rare ones. Other channels can provide important information about the Z'-boson couplings. If we go beyond the SM, there are several possibilities for some quark bound-state resonances $B \equiv \{\bar{Q}Q\}$ to be produced via particle interplay accompanied by Higgs boson (H) emission. It is known that the Z boson is not yet an exact mass eigenstate, but that it turns out to be mixed with Z'. In the Z–Z' mixing scheme, the mass eigenstates Z_1 and Z_2 are rotated with respect to the basis formed by Z and Z',

$$\begin{pmatrix} Z_1 \\ Z_2 \end{pmatrix} = \begin{pmatrix} \cos\kappa & \sin\kappa \\ -\sin\kappa & \cos\kappa \end{pmatrix} \begin{pmatrix} Z \\ Z' \end{pmatrix},$$

through the mixing angle κ,

$$\kappa = \arctan\left(\frac{M_Z^2 - M_{Z_1}^2}{M_{Z_2}^2 - M_Z^2}\right)^{1/2},$$

with M_{Z_1} and M_{Z_2} being the masses for the mass eigenstates Z_1 and Z_2, respectively.

We study a possible extra Z_2 state and its interpretations that have direct implications for new physics at

* This section completes the publication of the Proceedings of the Second International Conference on Nonaccelerator New Physics (NANP) held at the Joint Institute for Nuclear Research (JINR, Dubna, Russia) between June 28 and July 3, 1999. For the main part of these proceedings, the reader is referred to Phys. At. Nucl. 63, 621–1303 (2000).

** This article was submitted by the author in English.

LHC. Our interest is in Z_2 production and possible pair production process $Z_2(W, Z)$ with Z_2 decay into pairs of heavy quarks leading to $\bar{Q}Q$ and $\bar{Q}Q(W, Z)$ events at LHC with $\bar{Q}Q$ invariant mass peaked at an $O(0.4\ \text{TeV})$ mass. If the Z_2 state is sufficiently heavy for producing an H boson, one can determine the effective coupling for Z_2–H interaction. Since H bosons are coupled to Z_2 and quarks, this opens the possibility of finding these Higgs bosons as products originating from the decays of the Z_2 mass eigenstate. We are to estimate the ratio of the partial decay widths Γ,

$$R(Z_2 \longrightarrow H\{\bar{Q}Q\}_{s=1}/\bar{Q}Q) \equiv \frac{\Gamma(Z_2 \longrightarrow H\{\bar{Q}Q\}_{s=1})}{\Gamma(Z_2 \longrightarrow \bar{Q}Q)}, \quad (1)$$

where $\{\bar{Q}Q\}_{s=1}$ stands for a spin-1 quark–antiquark bound state. Among the possible decays, the process $Z_2 \longrightarrow H\{\bar{Q}Q\}_{s=1}$ is of great interest, since it is almost kinematically allowed, even for the Z_2 mass as low as 0.5 TeV. The main backgrounds to Z_2 decays via Higgs boson emission will depend on the precise secondary modes of the decay of the product Higgs boson. In fact, background branches are most important if the Higgs boson decays primarily to leptons or quarks (with the exception of t quarks), as will be the case for a sufficiently light Higgs boson. Model calculations of the decays of the SM Z boson via Higgs boson emission to onia were performed in [4]. The rates of (super)rare decays $Z_2 \longrightarrow H\{\bar{Q}Q\}_{s=1}$ could be used as a check of the theory or to extract some of the parameters of the theory that are hard to reach through other processes.

2. DESCRIPTION OF THE FORMALISM

To analyze the effects of the Z_2 state within the model under consideration, we focus on the Z_2 couplings. The interactions of the mass eigenstates Z_i ($i > 1$) with heavy quarks are described by the Lagrangian density

$$-L_{Z_iQ} = g_Z \sum_{i=1}^{\infty} \sum_{Q} \bar{Q}(g_{V_i} - g_{A_i}\gamma_5)\gamma^\mu Q Z_{i_\mu}, \quad (2)$$

where one of the sums is taken over all heavy quarks Q, g_Z is presented as the SM coupling $g/\sqrt{1-s_W^2}$ ($s_W \equiv \sin\theta_W$), Z_{1_μ} is taken to mean the SM Z-boson field, and Z_i with $i \geq 2$ are additional Z states in the weak-eigenstate basis. We will consider the model featuring only one light Z_2 mass eigenstate. The vector and the axial-vector couplings g_{V_i} and g_{A_i} ($i = 1, 2$) in (2) are defined as

$$g_{V_1} = g_V \cos\kappa + g'_V \alpha \sin\kappa, \qquad g_{A_1} = g_A \cos\kappa + g'_A \alpha \sin\kappa, \quad (3)$$

$$g_{V_2} = \alpha g'_V \cos\kappa - g_V \sin\kappa, \qquad g_{A_2} = \alpha g'_A \cos\kappa - g_A \sin\kappa, \quad (4)$$

where

$$g_V = \frac{1}{2}T_{3L} - s_W^2 e_Q, \quad g_A = \frac{1}{2}T_{3L},$$

T_{3L} and e_Q being the third component of the weak isospin and the electric charge, respectively. Both g'_V and g'_A in (3) and (4) represent the chiral properties of the Z'-boson interplay with quarks and the relative strengths of these interactions:

$$-L_{Z'Q} = g'_Z \sum_Q \bar{Q}(g'_V - g'_A\gamma_5)\gamma^\mu Q Z'_\mu. \quad (5)$$

For GUT models, the free parameter g'_Z in (5) is related to α in (3) and (4) as $\alpha \equiv (g'_Z/g_Z) = \sqrt{(5/3)\omega}\, s_W$ [5], where ω depends on the symmetry-breaking pattern and the fermion sector of the model, but it is usually taken to be $\omega \sim 2/3$–1. The choice of $\alpha \simeq 0.62$ provides the equality of both g_Z and g'_Z on the scale of the mass of the unification $M_X \simeq M_{\text{GUT}}$ into E_6. Neglecting some differences in the renormalization-group evolution of both g_Z and g'_Z, one can deal with α at energies $\sim M_{Z'} \sim M_{Z_2} \sim O(1\ \text{TeV})$.

Suppose that the Z_2 state can be produced at LHC via the subprocess $\bar{q}q \longrightarrow Z_2$ and that, in the approximation of a small Z_2 width, the cross section

$$\sigma(\bar{q}q \longrightarrow Z_2) = K(M_{Z_2})\frac{2\pi G_F M_{Z_1}^2}{3\sqrt{2}}(g_{V_2}^2 + g_{A_2}^2)\delta(s - M_{Z_2}^2)$$

is dependent both on M_{Z_2} and on κ. Here, G_F is the Fermi constant, and the factor K reflects the higher order QCD process [6],

$$K(M_{Z_2}) = 1 + \frac{\alpha_s(M_{Z_2}^2)}{2\pi}\frac{4}{3}\left(1 + \frac{4}{3}\pi^2\right).$$

Note that the two-loop value is $\alpha_s(M_{Z_2}^2) \sim 0.1$ at $\Lambda_{\text{QCD}} = 200$ MeV for $M_{Z_2} < 2m_t$ (five flavors) and $M_{Z_2} > 2m_t$ (six flavors), m_t being the top-quark mass [2].

The partial width with respect to Z_2 decays into quarks is determined by the couplings g_{V_2} and g_{A_2} (4)—namely, we have (the number of colors, $N_c = 3$, is

taken into account)

$$\Gamma(Z_2 \longrightarrow \bar{Q}Q) = \frac{2G_F M_Z^2}{\sqrt{2}\pi} C(M_{Z_2}^2) \times M_{Z_2}(1-4r_q)^{1/2}[g_{V_2}^2(1+2r_q) + g_{A_2}^2(1-4r_q)]. \quad (6)$$

Here, $r_q \equiv m^2/M_{Z_2}^2$; M_Z and m are the masses of the Z boson and a quark, respectively; and the C factor is defined by the running strong coupling constant α_s as

$$C(\mu^2) = 1 + \frac{\alpha_s(\mu^2)}{\pi} + 1.409\frac{\alpha_s^2(\mu^2)}{\pi^2} - 12.77\frac{\alpha_s^3(\mu^2)}{\pi^3}$$

with an arbitrary scale μ. The interactions of the Z_2 state with quarks are expressed in terms of three parameters x, y^u, and y^d [1], where the labels u and d mean, respectively, the up and the down types of quarks:

$$2g_{V_2}^u = x + y^u, \quad -2g_{A_2}^u = -x + y^u,$$
$$2g_{V_2}^d = x + y^d, \quad -2g_{A_2}^d = -x + y^d.$$

3. RESULTS

The $\{\bar{Q}Q\}_{s=1}$ bound state with a 4-momentum Q_μ and a mass m_B may be produced in the decay of a Z_2 state via the emission of an H boson with a 4-momentum k_μ in the heavy-quark-loop scheme. The decay amplitude is given by [7]

$$A(k, Q) = \int d^4q \mathrm{tr}\left\{\Gamma_Q(q)\sum_{i=1}^{3} T_i(q, k; Q)\right\}, \quad (7)$$

where $\Gamma_Q(q_\mu)$ is the vertex function for the spin-1 quark bound state—it depends on the relative momentum q_μ of $\bar{Q}$ and Q—while T_i stand for the rest of the total matrix element. In fact, T_i in (7) carry the dependence of the interplay of H with heavy quarks (i = 1, 2) and the interplay of the Z_2 state with the H boson (i = 3) via the couplings $g_H = m/\langle H\rangle_0$ and $g_{Z_2H} = 2M_{Z_2}^2/\langle H\rangle_0$, respectively, where $\langle H\rangle_0$ stands for the vacuum expectation value of H. Generally, $\Gamma_Q(q_\mu)$ is constructed [8] in terms of the quark and antiquark spinors $u(Q_\mu)$ and $v(\bar{Q}_\mu)$ in a given spin configuration accompanied by the covariant confinement-type wave function $\phi_Q(q^2; \beta)$ containing the model parameter β [9]:

$$\Gamma_Q(q_\mu) = \bar{u}(Q_\mu)\frac{\delta_i^j}{\sqrt{3}}U_{\alpha\beta}\phi_Q(q^2; \beta)v(\bar{Q}_\mu). \quad (8)$$

Here, the symmetric rank-2 spinors $U_{\alpha\beta}$ obey the standard Bargmann–Wigner equations [10] $(\not{Q} - m_B)_\alpha^{\alpha'} U_{\alpha'\beta} = 0$.

Table 1. Values of $R(Z_2 \longrightarrow H\{\bar{b}b\}_{s=1}/\bar{b}b) \times 10^{10}$ for various embedding scales M_{Z_2} and Higgs boson masses m_H via the ratio $x_H = (m_H/M_{Z_2})^2$

M_{Z_2}, TeV	x_H					
	0	0.2	0.4	0.6	0.8	0.9
0.2	2.60	2.00	1.40	0.90	0.43	0.21
0.3	1.20	0.90	0.62	0.40	0.19	0.09
0.5	0.42	0.32	0.23	0.15	0.07	0.03
0.7	0.21	0.16	0.11	0.07	0.04	0.02

Table 2. Values of $R(Z_2 \longrightarrow H\{\bar{t}t\}_{s=1}/\bar{t}t) \times 10^9$ for various embedding scales M_{Z_2} and Higgs boson masses m_H via the ratio $x_H = (m_H/M_{Z_2})^2$

M_{Z_2}, TeV	x_H								
	0	0.05	0.10	0.15	0.20	0.25	0.30	0.35	0.40
0.6	1.00	0.81	0.61	0.49					
0.8	0.33	0.30	0.26	0.22	0.18	0.10	0.06		
1.0	0.17	0.15	0.14	0.12	0.11	0.09	0.07	0.05	0.02
1.2	0.11	0.10	0.09	0.08	0.07	0.06	0.05	0.04	0.03

The width with respect to the decay $Z_2 \longrightarrow H\{\bar{Q}Q\}_{s=1}$ is given by

$$\Gamma(Z_2 \longrightarrow H\{\bar{Q}Q\}_{s=1}) = \frac{g_Z^2 g_{V_2}^2 M_{Z_2}^3 N_c \cos^2\vartheta x_\beta^2 \sqrt{\lambda(1, x_H, x_B)}}{\pi^3(1-x_B)\langle H\rangle_0^2} \times (1-6x_\beta/x_B)\left\{\frac{1}{4d_0}\left[\frac{1}{3}(1-x_H)\left(1-5\frac{x_\beta}{d_0}\right) + \frac{5}{12}x_B\left(1+\frac{8x_\beta}{5d_0}\right) + \frac{1}{4}x_B - 5x_\beta - \frac{1}{3}(x_H-x_B)^2\left(1+4\frac{x_\beta}{d_0}\right)\right] + \frac{1-6x_\beta/x_B}{1-x_B}\right\}, \quad (9)$$

where $x_B \simeq (2m/M_{Z_2})^2$; $x_H \equiv (m_H/M_{Z_2})^2$; $x_\beta \equiv \beta/M_{Z_2}^2$; $d_0 \simeq \frac{1}{2}(1 + x_H - x_B)$; and $\cos\vartheta \equiv (\epsilon \cdot \epsilon_{Z_2})$, ϵ^μ and $\epsilon_{Z_2}^\mu$ being the polarization 4-vectors of the B and Z_2 states, respectively. The total relative width $R(Z_2 \longrightarrow H\{\bar{b}b\}_{s=1}/\bar{b}b)$ (1) derived from (6) and (9) in the case where B is composed of $\bar{b}b$, but for a DY type of $\bar{b}b$ normalization, is presented in Table 1 as a function of the H boson mass m_H via the ratio x_H.

For the sake of definiteness, we have considered the four values of M_{Z_2} = 0.2, 0.3, 0.5, and 0.7 TeV. As can be seen, the distribution is very steeply peaked toward low H-boson masses and drops to zero at the high-mass end. In fact, we can render the results valid for any masses by merely rescaling the ratios $x_{H,B,\beta}$. To be understood precisely, one has to note the following: first, the B state is treated relativistically [see Eq. (8)] and, in the case of zero binding energy, $m_B \simeq 2m$; second, gluon corrections to the process have not been included. For a heavy B state such as $\{\bar{b}b\}_{s=1}$ or $\{\bar{t}t\}_{s=1}$ (e.g., superheavy toponium bound via a Higgs boson [11]), either approximation should be accepted. The estimates of $R(Z_2 \longrightarrow H\{\bar{t}t\}_{s=1}/\bar{t}t)$ for M_{Z_2} = 0.6, 0.8, 1.0, and 1.2 TeV are presented in Table 2.

For a light spin-1 B state (heavier Higgs boson), the results can only be taken as a guide of an order of magnitude of the rates.

4. CONCLUSION

We investigated the Z_2 mass eigenstate of the simplest E_6-inspired GUT model and explored implications for the production and detection of Higgs bosons accompanied by spin-1 heavy hadrons. It should be emphasized that (super)rare decays $Z_2 \longrightarrow H\{\bar{Q}Q\}_{s=1}$ provide complementary information about potential new interactions. These decay processes are sensitive to new vector and axial-vector couplings g_{V_2} and g_{A_2}. The physically constrained nature of the model implies that predictions need only be explored as functions of a few parameters. In this paper, we have chosen these parameters to be (i) the mass of the Z_2 eigenstate, M_{Z_2}; (ii) the mass of the Higgs boson, m_H; and (iii) the mass of the heavy quark m; and (iv) the model parameter β [7]. The present electroweak experiments lead to the lower mass bound for the Z_2 boson on the order of 1 TeV [12]. The Z_2 boson with $M_{Z_2} \sim O(1\ \text{TeV})$ should be explored at future colliders such as LHC.

The possible existence of the Z' does open the possibility of an additional source of Higgs boson detection—namely, the production of a large number of Z' bosons followed by the decays $Z' \longrightarrow H\{\bar{Q}Q\}_{s=1}$. In particular, the lightest Higgs boson ($m_H < 120$ GeV) that is predicted by the minimal supersymmetric extension of the SM should generally be observable among Z' decays. The active program of this investigation has a major advancement in testing Z' (super)rare physics within new physics outside of the SM.

REFERENCES

1. G. Altarelli *et al.*, Phys. Lett. B **375**, 292 (1996).
2. V. Barger, K. Cheung, and P. Langacker, Phys. Lett. B **381**, 226 (1996).
3. J. L. Hewett and T. Rizzo, Phys. Rep. **183**, 193 (1989).
4. B. Guberina *et al.*, Nucl. Phys. B **174**, 317 (1980).
5. R. W. Robinett and J. L. Rosner, Phys. Rev. D **25**, 3036 (1982); P. Langacker, R. W. Robinett, and J. L. Rosner, Phys. Rev. D **30**, 1470 (1984); P. Langacker and M. Luo, Phys. Rev. D **45**, 278 (1992).
6. V. Barger and R. J. N. Philips, *Collider Physics* (Addison-Wesley, Redwood City, 1987).
7. G. A. Kozlov, Nuovo Cimento A (in press).
8. G. A. Kozlov, Int. J. Mod. Phys. A **7**, 1935 (1992).
9. S. Ishida, Prog. Theor. Phys. **46**, 1570, 1950 (1971); S. Ishida and M. Oda, Prog. Theor. Phys. **89**, 1033 (1993).
10. V. Bargmann and E. Wigner, Proc. Am. Acad. Sci. **34**, 211 (1948).
11. H. Inazawa and T. Morii, Phys. Lett. B **247**, 107 (1990); K. Hagiwara, K. Kato, A. D. Martin, and C.-K. Ng, Nucl. Phys. B **344**, 1 (1990).
12. Gi-Chol Cho, K. Hagiwara, and Y. Umeda, Nucl. Phys. B **531**, 65 (1998).

Physics of Atomic Nuclei, Vol. 63, No. 12, 2000, pp. 2201–2204. From Yadernaya Fizika, Vol. 63, No. 12, 2000, pp. 2297–2300.

New Limit on the Half-Life of ^{78}Kr with Respect to the 2*K*(2ν)-Capture Decay Mode*

Ju. M. Gavriljuk, V. V. Kuzminov, N. Ya. Osetrova, and S. S. Ratkevich[1)]**

Institute for Nuclear Research, Russian Academy of Sciences, pr. Shestidesyatiletiya Oktyabrya 7a, Moscow, 117312 Russia

Received October 13, 1999

Abstract—The features of data accumulated for 1817 h in an experimental search for the 2*K*(2ν)-capture mode of ^{78}Kr decay are discussed. A new limit on the half-life for this decay is found: $T_{1/2} \geq 2.3 \times 10^{20}$ yr (at a 90% C.L.). © *2000 MAIK "Nauka/Interperiodica".*

1. INTRODUCTION

The first result on the 2*K*(2ν)-capture mode of ^{78}Kr decay was presented in [1, 2]. The limit derived from the data collected for 254.2 h was given by $T_{1/2} \geq 0.9 \times 10^{20}$ yr (at a 90% C.L.). The known theoretical predictions for the half-life with respect to the capture reaction ^{78}Kr(2*e*, 2ν)^{78}Se are 3.7×10^{21} [3], 3.7×10^{22} [4], and 6.2×10^{23} yr [5]. The corresponding half-life values for the 2*K*(2ν)-capture decay mode are 4.7×10^{21}, 4.7×10^{22}, and 7.9×10^{23} yr if one considers that 2*K*-electron capture accounts for 78.6% in the total number of 2*e* captures for ^{78}Kr [6]. The method used in [1, 2] allows one to reach a sensitivity level of up to 10^{22} yr for the half-life and to test some theoretical models. The results of the next step of measurement are presented here.

2. EXPERIMENTAL SETUP

Our measurements were performed with aid of a multiwire wall-less proportional counter (MWPC) by using a krypton sample enriched in ^{78}Kr. The main features of the counter and measurement conditions were described elsewhere [1, 2]. The MWPC comprises a central main counter (MC) and a surrounding protection ring counter (RC) in the same body. A common anode-wire signal (PAC) from the RC and PC1 and PC2 signals from both ends of the MC anode are read out from the MWPC. A scheme with a signal readout from two sides of the MC anode allows one to determine the relative event coordinate β along the anode [β = 100 × PC1/(PC1 + PC2)] and to eliminate events that do not correspond to the selected working length. A shaping amplifier with an integration and differentiation shaping time of 26 μs was used to amplify the PC1 and PC2 pulses to have a sufficiently high energy resolution. The parameter $f = 1000 \times$ P12/(PC1 + PC2) was used to obtain information about the pulse rise time and the pulse front features. P12 signals are output pulses of the additional shaping amplifier that amplified the summary signal (PC1 + PC2) with shaping times of 1.5 μs. The parameter *f* depends on the energy space distribution of the event in the MC volume.

The *K*-shell double vacancy of the daughter ^{78}Se** isotope appears as a result of the capture reaction ^{78}Kr 2*K*(2ν) ^{78}Se. The total energy released is $2K_{ab}$ = 25.3 keV, where K_{ab} is the binding energy of the *K* electrons in the Se nucleus. One can find that the total probability for Se** to emit one or two characteristic x rays is 0.837 under the assumption that this double-vacancy deexcitation is equivalent to the sum of deexcitations of two single vacancies. A characteristic x ray ($E_{K_\alpha} \cong$ 11.2 keV, $E_{K_\beta} \cong 12.5$ keV) has a sufficiently long path length in krypton. Two pointlike energy releases with total energy $2K_{ab}$ (total energy of the absorption peak) will appear if the x ray is absorbed in the MC working volume. One part is the x-ray energy release, while the other is the release of the Auger electron cascade energy accompanied by the characteristic *L*-shell x-ray energy. The x rays may leave the MC volume. A one- or a two-point event would be detected in this case (escape peak). All single-electron-background events, such as those due to Compton electrons or inner β-decay electrons, will have one-point energy releases. A multipoint-event pulse P12 would represent a sequence of short pulses with a different time overlap. The number of pulses in the burst corresponds to the number of local regions where total ionization is distributed. The amplitude and the duration of each pulse in a burst depend on a local track length, orientation, and distance from the MC anode. The ADCs used to record the PAC, PC1, PC2, and P12 signals are triggered with the input-pulse-amplitude maximum. The P12 signal triggering will be done for the first amplitude maximum, which corresponds to the energy released in the nearest anode region. The peaks corresponding to one-point amplitudes P12 for the total energy of a fixed event appear in

* This article was submitted by the authors in English.

** e-mail: kuzminov@neutr.novoch.ru

1) Kharkov State University, pl. Svobody 4, Kharkov, 310077 Ukraine.

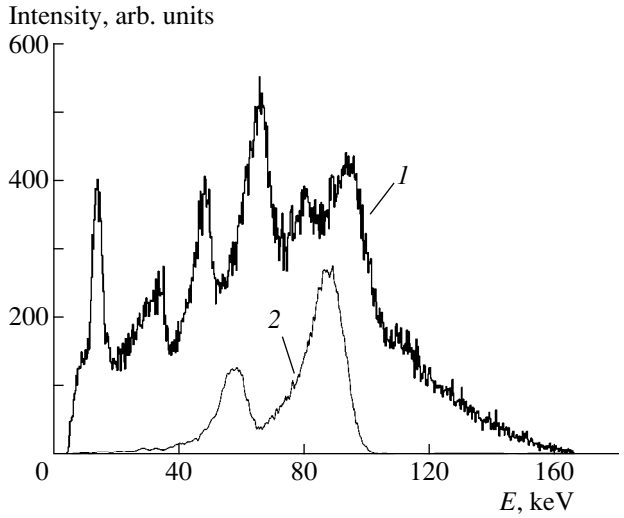

Fig. 1. Energy spectra of (*1*) the background and (*2*) the ^{109}Cd source of (PC1 + PC2) signals for type-1 events from the MWPC filled with pure xenon up to 4.8 atm.

the event-number distribution with respect to the parameter f (f distribution). Events with energy released only in the MC and in the MC and RC simultaneously are referred to as "type-1" and "type-2" events, respectively.

3. RESULTS

Krypton enriched in ^{78}Kr to 94% was used to seek the ^{78}Kr($2K$, 2ν)^{78}Se capture mode. It contains an admixture of natural β-radioactive ^{85}Kr ($T_{1/2}$ = 10.7 yr, $E_{\beta max}$ = 670 keV) with the volume activity of 0.14 Bq/l.

Our measurements were performed in the underground laboratory of the Baksan Neutrino Observatory of the Institute for Nuclear Research (Russian Academy of Sciences, Moscow) at a depth of 4900 mwe. The MWPC was placed in a low-background shield: 15 cm of lead, 8 cm of borated polyethylene, and 11 cm of copper.

The intrinsic background of the MWPC filled up to 4.8 atm with pure xenon without radioactive contamination was measured preliminary. The background energy spectrum collected for 973.9 h and conveniently scaled spectrum of a ^{109}Cd source (E_γ = 88 keV) are shown in Fig. 1 (curves *1* and *2*, respectively). The spectra consist of (PC1 + PC2) signals from type-1 events. Curve *2* has a peak at E_γ = 88 keV and a xenon escape peak at $E = E_\gamma - E_{\mathrm{Xe}K_\alpha}$ = 88 – 29.8 = 58.2 keV. The peak at 88 keV is not symmetric because of the radiation scattered in the counter wall. The energy resolution for the 88-keV γ line is equal to 13.7%.

The background spectrum has some features. The main peaks correspond to the energy values of 16, 35, 50, 68, 82, and 92 keV. In the energy region 35–68 keV, there are initial peaks accompanied by the escape peaks. The background counting rate in the energy range 20–100 keV is 91 h^{-1}.

Energy spectra of (PC1 + PC2) signals from type-1 and type-2 events for the ^{109}Cd calibration source and the krypton filling are shown in Fig. 2*a* (curves *1* and *2*, respectively).

One can see the 88-keV peak in the spectrum represented by curve *1*. This spectrum was multiplied by a factor of 0.5 for a convenient comparison. The energy resolution is 10.8% for this peak. The highest energy peak on curve *2* is the krypton escape peak at $E = E_\gamma - E_{\mathrm{Kr}K_\alpha}$ = 88 – 12.6 = 75.4 keV. It appears in type-2 events because of absorption in the RC of krypton characteristic radiation from the MC. The escape peak in the spectrum represented by curve *1* is on the left slope of the total absorption peak. The source radiation scattered in the counter body wall lies in this region too. The f distributions corresponding to this spectra are

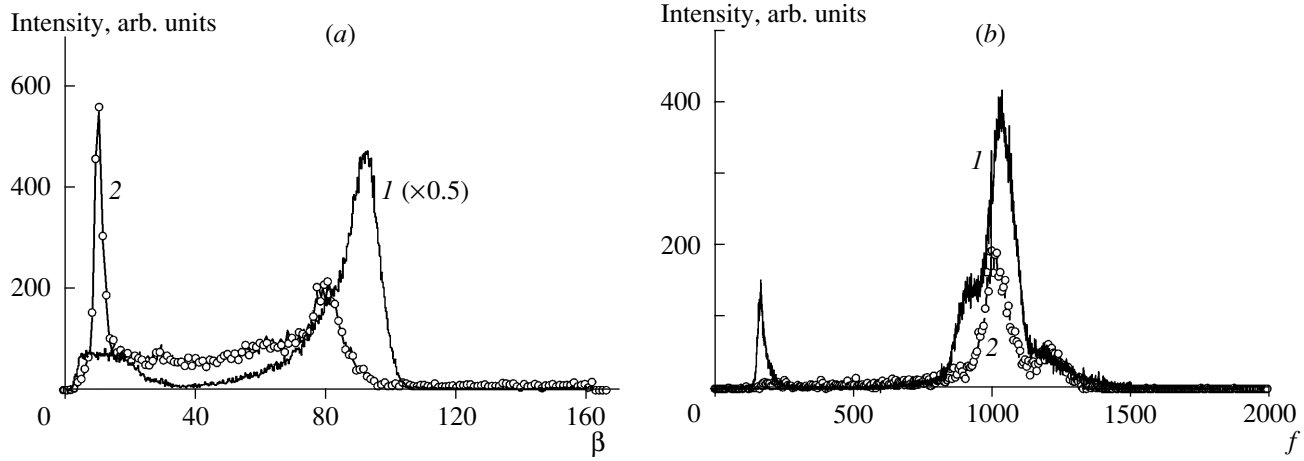

Fig. 2. (*a*) Energy spectra of (PC1 + PC2) signals for (*1*) type-1 and (*2*) type-2 events for the ^{109}Cd source and the MWPC krypton filling; (*b*) corresponding f distributions (*1* and *2*, respectively). Curves *1* are multiplied by a factor of 0.5.

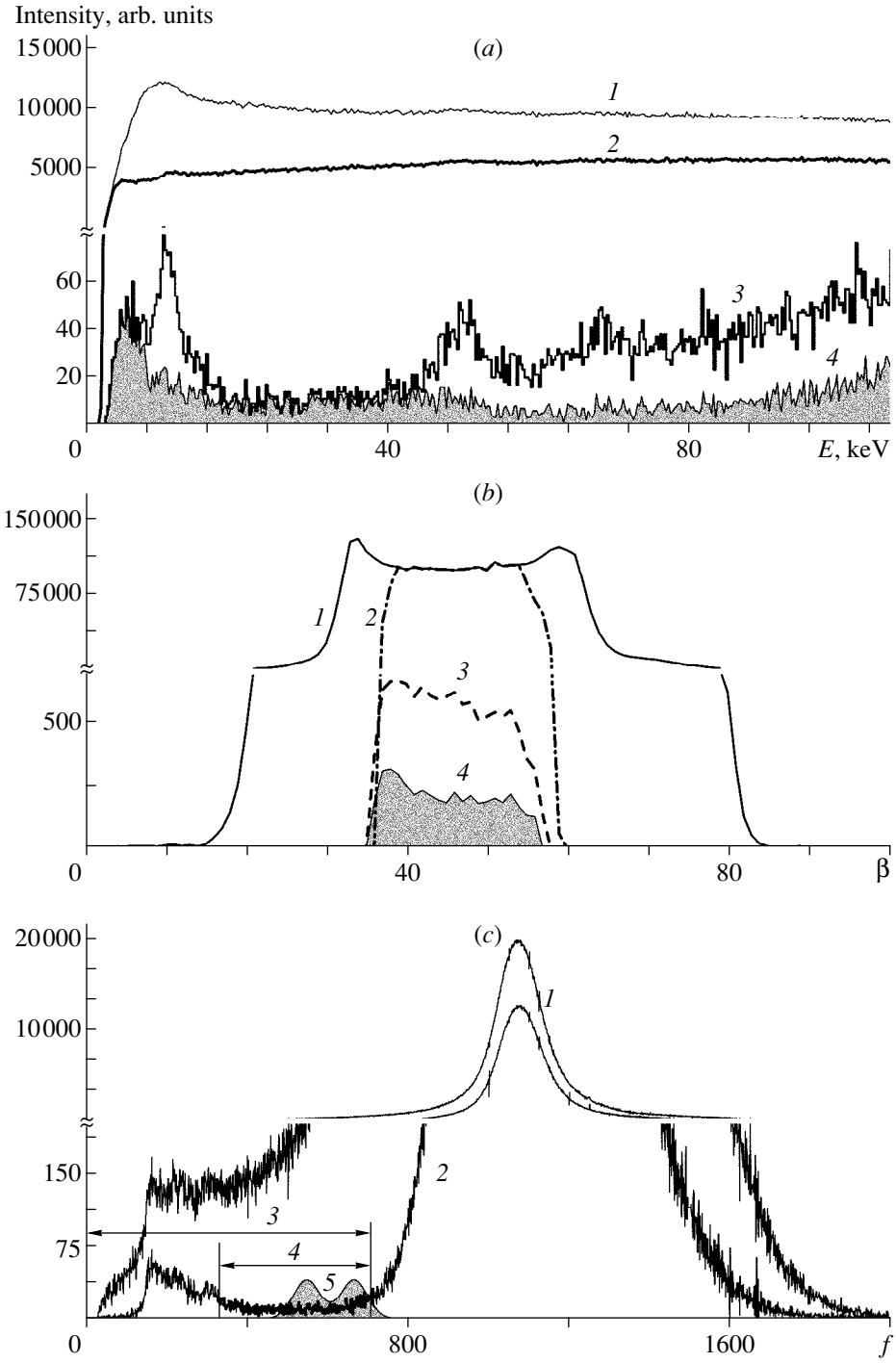

Fig. 3. (*a*) Background energy spectra and (*b* and *c*) corresponding β and *f* distributions: (*1*) $0 \le \beta \le 100$, $1 \le f \le 2000$; (*2*) $36 \le \beta \le 58$, $1 \le f \le 2000$; (*3*) $36 \le \beta \le 58$, $1 \le f \le 710$; (*4*) $36 \le \beta \le 58$, $330 \le f \le 710$; and (5) expected *f* distribution for the 2*K*-capture ^{78}Kr events.

shown in Fig. 2*b* with the same scaling and notation. One can see a peak on curve *1* with a maximum at $f_1 = 166$, which corresponds to two-point events from the total absorption peak when the KrK_α-ray ionization is collected first on the MC anode. If the photoelectron ionization is collected first, the relevant events form a peak with a maximum at $f_2 = 920$. The calculated *f* values of these maxima should be equal to $f_1 = 1000 \times 12.6/88 = 143.2$ and $f_2 = 1000 \times (88 - 12.6)/88 = 856.8$ in the calibration when the P12 amplitude is equal to the (PC1 + PC2) one for single-point events. Actual values calculated on the basis of experimental data dif-

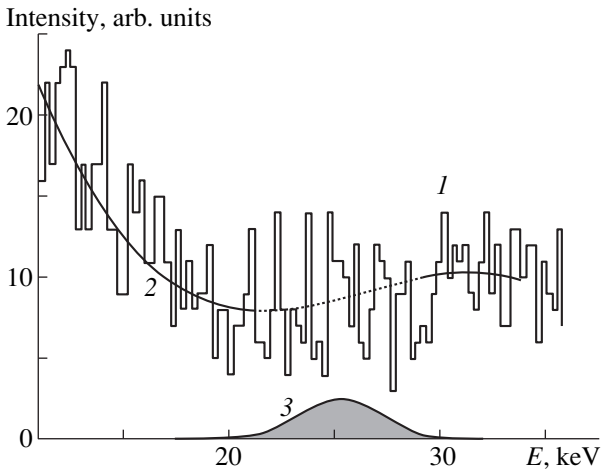

Fig. 4. (*1*) Residual energy spectrum of the background; (*2*) best fit; and (*3*) expected spectrum of the effect.

fer slightly from the theoretical ones. This could be explained by nonideality of the experimental setup. The parameter f depends on energy for the same reason. The energy spectrum represented by curve *2* in Fig. 2*a* is formed primarily by one-point events, and its f distribution (curve *2* in Fig. 2*b*) has no multipoint peaks. The peaks at $f = 1015$ and $f = 1239$ are one-point peaks for, respectively, the energy region above 16 keV and the krypton 12.6-keV x-ray peak. The f distribution represented by curve *1* has a one-point peak with a maximum at $f = 1039$.

The background energy spectrum of the MWPC with krypton due to type-1 event is shown in Fig. 3*a* (curve *1*). It was collected for 1817 h. The counting rate is 1506 h^{-1} for the energy range 20–100 keV. The corresponding β and f distributions are shown in Fig. 3*b* (curve *1*) and Fig. 3*c* (curve *1*). One can see peaks at the ends of the β distribution that are caused by events from a high-energy part of the ^{85}Krβ spectrum mainly collected in an ionization mode, the end-effect corrections associated with bugles of the anode being taken into account. In order to eliminate this background component, it is sufficient to perform the β selection of events in the range $36 \le \beta \le 58$ (Fig. 3*b*, curve *2*). The energy spectrum represented by curve *2* in Fig. 3*a* and the f distribution represented by *2* in Fig. 3*c* correspond to this selection. One can see from this f distribution that background events corresponding to $f \le 710$ are mainly suppressed. The energy spectrum of events characterized by $36 \le \beta \le 58$ and $f \le 710$ is shown in Fig. 3*a* (curve *3*). The shape of this spectrum follows that of the spectrum represented by curve *1* in Fig. 1, with the exception of the escape peaks. This means that almost all one-point events from the ^{85}Krβ spectrum are eliminated by the selection used. Curve *5* in Fig. 3*c* shows roughly the shape and the place of the f distribution expected for the ^{78}Kr$(2K, 2\nu)^{78}$Se multipoint events.

For a final analysis, we used events corresponding to $36 \le \beta \le 58$ and $330 \le f \le 710$ because, for such a selection, there are no peaklike distortions of the residual energy spectrum *4* in Fig. 3*a* in the region of interest.

A low-energy part of this spectrum is shown in Fig. 4 (curve *1*). A sample of this spectrum and the location of the ^{78}Kr$(2K, 2\nu)^{78}$Se effect is shown as curve *3* (Fig. 4). The energy region 25.3 ± 3.8 keV includes 95% of the events. The background was fitted by using points below and above this region (curve *2*). The net fitted background for 25.3 ± 3.8 keV was found to be 266. The sum over experimental data is equal to 262. The difference is -4 ± 23 or -19 ± 111 yr^{-1}. Taking into account the event-detection efficiency (0.22) and the effective counter length (0.6 of working length), we find that the limit on the half-life of ^{78}Kr with respect to the $2K(2\nu)$ capture mode is given by $T_{1/2} \ge 2.3 \times 10^{20}$ yr (at a 90% C.L.).

ACKNOWLEDGMENTS

This work was supported by the Russian Foundation for Basic Research (project nos. 94-02-05954a and 97-02-16052) and in part by the International Science Foundation (grants RNT000 and RNT300).

REFERENCES

1. Ju. Gavriljuk *et al.*, in *Proceedings of the Ninth International School in Particles and Cosmology, Baksan Valley, Kabardino-Balkaria, Russia, 1997* (Inst. Yad. Issled., Moscow, 1998), p. 415.
2. Ju. Gavriljuk *et al.*, Yad. Fiz. **61**, 1389 (1998) [Phys. At. Nucl. **61**, 1287 (1998)].
3. M. Aunola and J. Suchonen, Nucl. Phys. A **602**, 133 (1996).
4. M. Hirsch *et al.*, Z. Phys. A **347**, 151 (1994).
5. O. Rumyantsev and M. Urin, Phys. Lett. B **443**, 51 (1998).
6. M. Doi and T. Kotani, Prog. Theor. Phys. **87**, 1207 (1992).

Physics of Atomic Nuclei, Vol. 63, No. 12, 2000, pp. 2205–2208. From Yadernaya Fizika, Vol. 63, No. 12, 2000, pp. 2301–2304.

Calibration of Solar-Neutrino Detectors with Artificial ^{51}Cr and ^{75}Se Neutrino Sources*

V. N. Kornoukhov, *****

Institute of Theoretical and Experimental Physics, Bol'shaya Cheremushkinskaya ul. 25, Moscow, 117259 Russia

Received October 13, 1999

Abstract—The possibility of calibrating the solar-neutrino detectors GNO, BOREXINO, and LENS with the same artificial neutrino source is discussed. For this purpose, the Russian heavy-water reactor L-2 can be used to produce a 10 MCi neutrino source based on the ^{51}Cr isotope. For the first time, the possibility of producing and using a neutrino source based on the ^{75}Se isotope is demonstrated. © *2000 MAIK "Nauka/Interperiodica".*

1. INTRODUCTION

Four pioneering experiments, Clorine [1], Kamiokande [2], GALLEX [3], and SAGE [4], observed neutrino fluxes with a substantially lower intensity than that predicted by the standard solar model. This discrepancy constitutes the so-called solar-neutrino problem (SNP), which is one of the most intriguing problems in modern physics and astrophysics. The majority of physicists deem that the solution to this problem lies in new neutrino physics, a possibility of great importance for modern physics.

From the experimental point of view, the most important task for solving the solar-neutrino problem is to continue Ga–Ge experiments for the reason of sufficient accuracy (SAGE [4] and GNO [5]) and to detect low-energy neutrino fluxes from the *pp* and ^{7}Be sources with the real-time detectors BOREXINO [6] and LENS [7].

The detector BOREXINO (now under construction at the Gran Sasso underground laboratory) is intended to measure the ^{7}Be neutrino, as well as to seek the neutrino magnetic moment [8] with an artificial neutrino source (ANS).

The detector LENS [7] uses a Yb target for solar-neutrino capture. Neutrino capture by the ^{176}Yb nucleus results in excited isomer states of ^{176}Lu, which decay to the ground state of ^{176}Lu with a time delay of 50 ns. These neutrino events have a highly specific signature: two events produced at the same point in the detector with an average delay time. This signature makes it possible to discriminate the neutrino signal against the background by a factor of 10^7. The interpretation of such an experiment has one major problem: only an order of magnitude of the neutrino cross section for the transition of ^{176}Yb to the excited states of ^{176}Lu is known {this cross section is deduced from the cross sections for (*p*, *n*) or (3^3He, ^{3}H) scattering reactions on the same isotope [9]}. The only possibility of solving this problem is to calibrate the full-scale detector with an artificial neutrino source of MCi activity.

Artificial neutrino sources based on the ^{51}Cr isotope with an activity of a few MCi were successfully used to calibrate two gallium detectors, GALLEX [10] and SAGE [11]. For these detectors, an artificial neutrino source was mainly used for an overall check of the detector; for the ^{176}Yb detector, the calibration of the detector is necessary in order to measure the unknown cross section for neutrino capture with an accuracy not poorer than 5%.

A scheme for calibrating three solar-neutrino detectors (GNO, LENS, and BOREXINO) with the same high-activity artificial neutrino source is under development now. The objective of this study is to answer major questions associated with the calibration procedure and with the creation of an artificial neutrino source with a very high activity for this purpose.

2. NEUTRINO EXPERIMENTS WITH ARTIFICIAL NEUTRINO SOURCES ON THE BASIS OF ^{51}Cr AND ^{75}Se

The ^{51}Cr isotope decays by electron capture with a Q value of 751 keV and $T_{1/2}$ = 27.7 d to the ground state of ^{51}V (90.14% branching ratio) and to its first excited state (9.86%), which is deexcited to the ground state with the emission of a 320-keV γ ray. The neutrino spectrum consists of four monoenergetic lines at 746 keV (81%), 751 keV (9%), 426 keV (9%), and 431 keV (1%) [10, 11].

The ^{75}Se isotope [12] decays by electron capture with a Q value of 865 keV to the excited states of ^{75}As, which are deexcited to the ground state with the emission of several γ rays of different energies. Considering the atomic levels to which transitions can occur, we find that the neutrino energies are 452 keV (83%), 465 keV (11%), 585 keV (2%), and 600 keV (3.5%). The half-

* This article was submitted by the author in English.
** e-mail: kornoukhov@mail.ru
*** e-mail: kornoukhov@vxitep.itep.ru

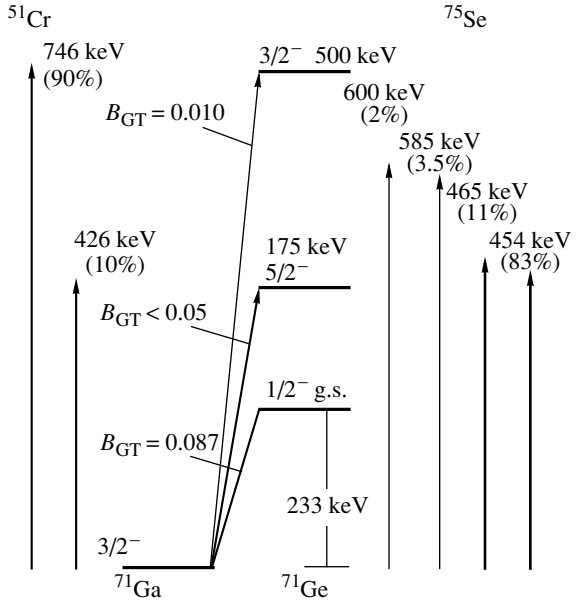

Fig. 1. Nuclear data for Ga–Ge detection of ^{51}Cr and ^{75}Se neutrinos.

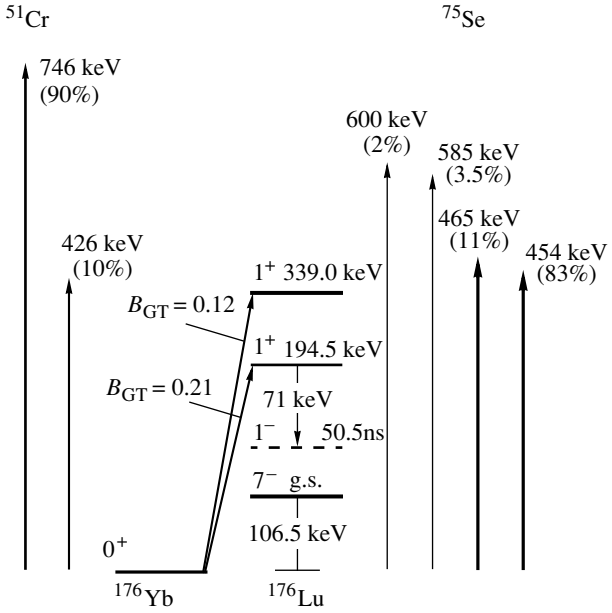

Fig. 2. Nuclear data for Yb–Lu detection of ^{51}Cr and ^{75}Se neutrinos.

life for ^{75}Se is 119.78 d; this allows one to make the calibration experiment quite uninhibitedly.

It is suggested that the neutrino source (its volume, together with passive shielding, is 0.3 m^3) will be placed at the center of the GNO (or LENS) detector (that is, in full-angle geometry). The volume of the GNO detector is 54 m^3 [3], while the volume of the LENS detector is 108 m^3.

The cross section for the inverse-beta-decay reaction was calculated according to [13]. The matrix elements for the transitions to the excited states of ^{176}Lu were evaluated by using their Gamow–Teller strengths B_{GT}, which were measured by (p, n) and (^{3}He, ^{3}H) scattering [9].

Figures 1 and 2 show the simplified nuclear data for ^{71}Ge and ^{176}Lu detection of solar neutrinos. Tables 1 and 2 list the results of the calculations of neutrino-capture events for ^{51}Cr (^{75}Se) neutrinos in the GNO and LENS detectors.

To achieve the accuracy required for the GNO detector (about 5%), the activity of the ^{51}Cr and ^{75}Se sources should not be less than 1.75 and 1.77 MCi, respectively. For the experiment with the LENS detector, the activity of the artificial neutrino source based on ^{51}Cr should not be less than 4.30 MCi (only events produced by 746-keV neutrinos are analyzed). In view of the possible problems of delivering this comparatively short-lived isotope from the reactor to the Gran Sasso underground laboratory, the ^{51}Cr activity should be more than 5.1 MCi. The required activity of the artificial neutrino source based on ^{75}Se should be more than 3.84 MCi (events produced by neutrinos with energies of 452 and 465 keV are analyzed).

Thus, if GNO and BOREXINO (and LENS in the future) are placed in the same underground laboratory, there is an opportunity to calibrate all of these detectors with the same artificial neutrino source of very high activity.

Table 1. Calculation of neutrino-capture events in the GNO detector [activity of the ^{51}Cr (^{75}Se) source is 1 MCi and exposure time is three months]

Neutrino source	E, keV	Events			
		ground state, B_{GT} = 0.0087	175 keV, B_{GT} = 0.05	500 keV, B_{GT} = 0.01	Sum
^{51}Cr	746	205	8.2	5.4	218.6
	426	10.3	0.3	–	10.6
	Sum	215.3	8.5	5.4	229.2
^{75}Se	452	177.7	5.4	–	183.1
	465	24.7	0.7	–	25.4
	585/600	17.4	0.6	–	18.0
	Sum	219.8	6.7	–	226.5

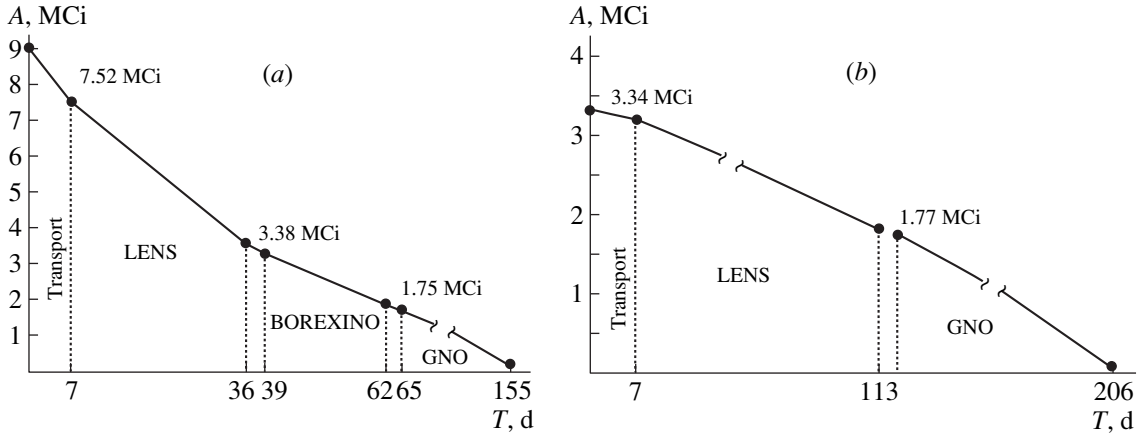

Fig. 3. Schedule of the GNO, LENS, and BOREXINO experiments with the same artificial neutrino source based on (*a*) ^{51}Cr and (*b*) ^{75}Se.

Figure 3*a* shows the schedule of the GNO, LENS, and BOREXINO experiments with the same artificial neutrino source based on ^{51}Cr and the ^{51}Cr activity at various stages of the procedure. The activity of ^{51}Cr at the instant of the reactor shutdown should be more than 8.9 MCi. The ^{75}Se isotope can be used as an artificial neutrino source for the GNO and LENS experiments, and the activity of this source should not be less than 3.48 MCi (Fig. 3*b*).

For the sake of simplicity, we assume that the time it takes to deliver an artificial neutrino source from the reactor to the laboratory is 7 d and that the time it takes to transfer it from one detector to another is 3 d.

3. PRODUCTION OF ARTIFICIAL NEUTRINO SOURCES

3.1. Artificial Neutrino Source Based on ^{51}Cr

^{51}Cr is produced by neutron capture on ^{50}Cr (a 4.5% natural abundance) with a sufficiently large cross section for thermal and epithermal neutrons (15.9 and 7.8 b, respectively). The source material must be enriched in ^{50}Cr and depleted in ^{53}Cr (because of the large cross section of this isotope equal to 18.2 b). Owing to a high cost of enriched chromium, it was proposed to use the available material produced for the GALLEX Collaboration [35.6 kg of chromium enriched in ^{50}Cr to 38.6% and depleted in ^{53}Cr to 0.7%)].

One more advantage of this material is that it is in the form of chips; therefore, it is easy to homogenize their irradiation and to perform the sampling procedure. As a result, one can determine the activity of the neutrino source by direct methods and by calorimetry [10]. But it should be noted that there is a need for a large volume (about 10 l) in a reactor to place this material because of its low density and a certain temperature of a starting material to avoid sintering of Cr chips.

In Russia, there are three reactors that are suited for producing the required activity of ^{51}Cr. These are the fast breeder reactor BN-600 featuring a special irradiation assembly [14], the research reactor SM-3 [15], and the heavy-water reactor L-2 [16]. The reactor L-2 has a very large volume with a high thermal neutron flux (up to 2×10^{14} cm^{-2} s^{-1}), a very effective cooling system, and a continuous loading–unloading mode for the starting material. If one takes into account the need for unloading the starting material from the reactor at an appropriate time and the use of ^{50}Cr in the form of chips, then the choice actually has to be the heavy-water reactor L-2. It follows from the calculation [17] (Table 3) that the expected activity of ^{51}Cr after the irradiation of 35.6 kg of enriched chromium in the standard mode of the L-2 reactor is 8.5 MCi, and it can be increased to 10 MCi (in a modified mode of the reactor L-2).

3.2. Artificial Source on the Basis of ^{75}Se

^{75}Se is produced by neutron capture on ^{74}Se with a large cross section for thermal and epithermal neutrons

Table 2. Calculation of neutrino-capture events in the LENS detector [activity of the ^{51}Cr (^{75}Se) source is 1 MCi and exposure time is three months]

Neutrino source	*E*, keV	Events		
		194.5 keV, B_{GT} = 0.21	339 keV, B_{GT} = 0.12	sum
^{51}Cr	746	72.7	30.7	103.4
	426	4.2	–	4.2
	Sum	76.9	30.7	107.6
^{75}Se	452	70.2	26.8	97.0
	465	9.7	4.0	13.7
	585/600	6.3	2.6	8.9
	Sum	86.2	33.4	119.6

Table 3. Results of ^{51}Cr production at the L-2 heavy-water reactor [17]

Site of target	Number of channels	Activity, MCi	Specific activity, Ci/g
Standard mode. Irradiation time is 130 d			
Neutron traps	6	6.4	270
Core	3	2.1	180
Total	9	8.5	240
Standard mode. Irradiation time is 50 d (end of reactor campaign)			
Neutron traps	6	5.3	220
Core	3	1.7	140
Total	9	7.0	200
Modified mode with the reduced loading fuel. Increasing of the reactor power 10%. Irradiation time is 130 d			
Core	9	9.7	270

Table 4. Results of ^{75}Se production with the L-2 reactor (the isotopic composition of the starting material is 90% ^{74}Se and 10% ^{76}Se)

Target type	Specific activity, Ci	Mass for 1 MCi, kg
$\varnothing 3 \times 3$ mm	875	1.26
$\varnothing 5 \times 5$ mm	737	1.5

(51.8 and 520 b, respectively). The source material should be enriched in ^{74}Se and depleted in ^{76}Se because of the large cross section of the latter isotope (85 b). Fortunately, the enrichment can be performed by a gas centrifugation of volatile SeF_6. An optimum value of enrichment of Se in ^{74}Se is on the order of 90%.

The starting material will be in the form of tablets of pressed high-purity Se powder, sealed into a hermetic shell of highly pure Al. The size of the tablets is less than 5 to 6 mm in order to avoid the self-shielding of ^{74}Se. Table 4 presents the results of ^{75}Se production with the L-2 reactor [18].

4. CONCLUSION

The calibration of detectors involving an artificial neutrino source with well-determined characteristics with to precision not poorer than 5% is the necessary stage of the next generation of solar-neutrino experiments. The experiments with the GNO, BOREXINO, and LENS detectors can be performed with the same artificial neutrino source based on ^{51}Cr if its activity at the time of reactor shutdown is not less than 8.9 MCi. The activity of the artificial neutrino source based on ^{75}Se, which can be used for the GNO and LENS experiments, should be more than 3.48 MCi.

The best way to produce a ^{51}Cr source with an activity of up to 10 MCi is to use the Russian heavy-water reactor L-2. The starting material for this purpose is 35.6 kg of ^{50}Cr, which was previously used by the GALLEX collaboration.

The specific activity of ^{75}Se that can be produced at the L-2 reactor is 740–900 Ci/g, resulting in a total activity sufficient for the experiments in the Gran Sasso laboratory, which have been discussed in this article.

REFERENCES

1. B. T. Cleveland *et al.*, in *Proceedings of IV Solar Neutrino Conference, Heidelberg, Max-Planck-Institute für Kernphysik, 1997*, p. 85.
2. Y. Suzuki, in *Proceedings of the 17th Conference on Neutrino Physics and Astrophysics, Helsinki, 1997* (World Sci., Singapore, 1997), p. 73.
3. GALLEX Collab. (P. Anselmann *et al.*), Phys. Lett. B **342**, 440 (1995).
4. SAGE Collab. (J. N. Abdurashitov *et al.*), Phys. Lett. B **328**, 234 (1994).
5. E. Bellotti *et al.*, Proposal for a Permanent Gallium Neutrino Observatory (GNO) at Laboratori Nazionali del Gran Sasso, 1996.
6. BOREXINO Collab. (C. Arpesella *et al.*), *INFN BOREXINO Proposal*, Ed. by G. Bellini, R. Ragavan, *et al.* (Milano Univ. Press, Milano, 1992), Vols. 1, 2.
7. R. S. Raghavan, Phys. Rev. Lett. **78**, 3618 (1997); R. S. Raghavan, in *Proceedings of IV Solar Neutrino Conference, Heidelberg, Max-Planck-Institut für Kernphysik, 1997*, p. 248.
8. BOREXINO Collab. (G. Alimonti *et al.*), *Proposal to the National Science Foundation*, Ed. by F. P. Calaprice *et al.* (Princeton Univ. Press, Princeton, 1996); N. Ferrari, G. Fiorentini, and B. Ricci, Phys. Lett. B **387**, 427 (1996).
9. M. Fudjiwara, Report to the LENS Collab., Grenoble, 1999; Ch. Goodman, Report to the LENS Collab., Grenoble, 1999.
10. GALLEX Collab. (H. Hampel *et al.*), Phys. Lett. B **420**, 114 (1998).
11. E. P. Veretenkin *et al.*, in *Proceedings of the IV Solar Neutrino Conference, Heidelberg, Max-Planck-Institute für Kernphysik, 1997*, p. 126.
12. J.-F. Cavagniac and M. Cribier, private communication.
13. G. V. Domogatsky, Candidate's Dissertation (Lebedev Institute of Physics, Moscow, 1970).
14. J. N. Abdurashitov *et al.*, At. Énerg. **80**, 101 (1996).
15. G. V. Kiselev, *Technology of the Production of Radionuclides with Nuclear Reactors* (Énergoatomizdt, Moscow, 1990).
16. A. D. Dodonov *et al.*, Reports to Conference "Improvement in Heavy Water Reactors," Moscow, ITEP, 1998.
17. B. P. Kochurov *et al.*, Preprint No. 37-98, ITEP (Institute of Theoretical and Experimental Physics, Moscow, 1998).
18. B. P. Kochurov and V. N. Konev, private communication.